The $W^{\pm}W^{\pm}$ Scattering Process

Theoretical Studies, Observation, Cross-section Measurement, and EFT Reinterpretation at $\sqrt{s} = 13\,\text{TeV}$ with the ATLAS Detector

Dissertation

zur Erlangung des akademischen Grades
Doctor rerum naturalium
(Dr. rer. nat.)

vorgelegt der
Fakultät für Physik
der
Technischen Universität Dresden

von
Dipl.-Phys. Stefanie Todt

Institut für Kern- und Teilchenphysik
2022

CERN-THESIS-2022-268
02/12/2022

Eingereicht am 22.09.2022

1. Gutachter: Prof. Dr. Michael Kobel
2. Gutachter: Apl. Prof. Dr. Monica Dunford

Kurzdarstellung

Die Streuung massiver, elektroschwacher Eichbosonen (VBS) beinhaltet neben der kubischen und quartischen Selbstwechselwirkung den Austausch von Higgsbosonen. Das Zusammenspiel dieser beiden fundamentalen Prozesse, welche jeweils auf die Eichstruktur und den Mechanismus der elektroschwachen Symmetriebrechung des Standardmodells (SM) zurückzuführen sind, prägen diese Kategorie von Prozessen. Die elektroschwache Erzeugung zweier gleich geladener $W^{\pm}$-Bosonen zusammen mit zwei Hadronenjets ($W^{\pm}W^{\pm}jj$-EW6), welche unter anderem VBS-Beiträge beinhaltet, kann genutzt werden, um diese zwei grundlegenden Komponenten im Kontext des SM und darüber hinaus, zu erforschen.

Diese Arbeit beinhaltet vielfältige Studien des elektroschwachen $W^{\pm}W^{\pm}$-Streuprozesses im vollleptonischen Zerfallskanal, erzeugt aus Proton-Proton-Kollisionen bei einer Schwerpunktsenergie $\sqrt{s}$ von 13 TeV. Dabei wird ein Datensatz des ATLAS-Experiments im Umfang von $36.1\,\text{fb}^{-1}$ analysiert.

Theoretische Vorhersagen des $W^{\pm}W^{\pm}jj$- und speziell des elektroschwachen Prozesses $W^{\pm}W^{\pm}jj$-EW6, werden mithilfe von drei Monte-Carlo-Eventsimulationsprogrammen untersucht: PowhegBox mit NLO-QCD-akkuraten Vorhersagen in der VBS-Approximation, Sherpa mit Vorhersagen auf LO-Niveau für bis zu drei Hadronenjets in der Matrixelementberechnung und MadGraph5_aMC@NLO mit LO-akkuraten Vorhersagen. Die Studien zeigen Unterschiede der drei Vorhersagen auf, welche deren Unsicherheiten überschreiten. Folglich werden die Konfigurationen der genutzten Programme eingehend untersucht. Dazu zählen die nominelle Wahl der Renormierungs- und Faktorisierungskalen, sowie die Parton-Shower-Konfigurationen.

Des Weiteren wird, zum ersten Mal anhand Daten des ATLAS-Experiments, die Beobachtung des $W^{\pm}W^{\pm}jj$-EW6-Prozesses etabliert und veröffentlicht [1]. Die beobachtete Signifikanz beträgt 6.5σ bei einer Vorhersage von 4.4σ unter Zuhilfenahme der Vorhersage von Sherpa für die Beschreibung des Signal-Prozesses $W^{\pm}W^{\pm}jj$-EW6. Der gemessene Wechselwirkungsquerschnitt im Referenzphasenraum beträgt $\left(2.89^{+0.59}_{-0.56}\right)$ fb. Dieser enthält, per Konstruktion der Analyse, die Interferenz mit dem QCD-induzierten Untergrundprozess $W^{\pm}W^{\pm}jj$-EW4. Die Messung ist limitiert durch die statistische Genauigkeit der gemessenen Daten. Alle drei untersuchten Vorhersagen stimmen mit der Messung innerhalb der Fehlertoleranzen überein.

Die Bestandteile der Analyse des $W^{\pm}W^{\pm}jj$-EW6-Prozesses im SM-Kontext werden ferner benutzt, um die experimentellen Daten auf mögliche Beiträge jenseits des SM zu untersuchen. Dazu wird ein Effektiver-Feldtheorie-Ansatz (EFT) verwendet, welcher dem SM anomale quartische Kopplungen im elektroschwachen Sektor mithilfe von Operatoren mit Massendimension acht hinzufügt [2, 3]. Erstmals in dieser Arbeit werden Ausschlussgrenzen auf Koeffizienten dieser Dimension-acht Operatoren im vollleptonischen Endzustand des $W^{\pm}W^{\pm}jj$-Prozesses mit Daten des ATLAS-Experiments bestimmt. Des Weiteren stellen diese Ergebnisse die ersten Ausschlussgrenzen dieser Operatorkoeffizienten mit einem 13 TeV-Datensatz des ATLAS-Experiments dar. Diese Resultate sind, im Vergleich zu existierenden Ausschlussgrenzen in allen Endzuständen, weniger stringent.

Der Fokus dieser Arbeit liegt auf der Untersuchung grundlegender Bestandteile der Datenanalyse von Dimension-acht EFT-Modellen. Dabei wird die neuartige Methode der Amplitudendekomposition für die MC-Simulation der EFT-Signalbeiträge genutzt. Diese verbessert nicht nur die Signalvorhersagen, ihr statistische Genauigkeit und die Simulationseffizienz in den EFT-sensitiven Regionen bei hohen invarianten Massen. Die tiefgründige Validierung dieser Methode zeigt zudem, dass die konventionell genutzte Methode unzulänglich in der Beschreibung der Signalbeiträge in den relevanten Regionen ist.

Darüber hinaus wird die Anwendung der sogenannten Clipping-Unitarisierung auf die EFT-Signalbeiträge eingehend studiert und Ausschlussgrenzen, zusätzlich zu ununitarisierten Ergebnissen, unter Anwendung dieser Methode bestimmt. Erstmals im betrachteten Endzustand, $W^{\pm}W^{\pm}jj$, werden Ausschlussgrenzen in Abhängigkeit von mehr als einem Wert der Clippingenergie ermittelt. Vergleiche mit aus Ref. [4] berechneten Unitaritätsgrenzen zeigen auf, dass die ermittelten Ausschlussgrenzen noch nicht im physikalisch angemessenen Bereich liegen.

Weiterhin werden Ausschlussgrenzen bestimmt, die Effekte von Dimension-sechs EFT-

Operatoren auf den Untergrundprozess $W^{\pm}Z$-EW4 beinhalten. Diese Ergebnisse sind einzigartig in ihrer Existenz. Die Berücksichtigung dieser Effekte zeigt keinen repräsentativen Einfluss auf der ermittelten Ausschlussgrenzen auf Koeffizienten der Dimension-acht-Operatoren.

Abstract

Vector Boson Scattering (VBS) processes involving massive, electroweak gauge bosons include the fundamental interactions of the triple and quartic electroweak self-couplings, and the exchange of the Higgs boson. Hence, the interplay of the gauge structure and the Electroweak Symmetry Breaking mechanism of the Standard Model (SM) shape this class of processes. Containing VBS contributions, the electroweak production of two like-charge $W^{\pm}$ bosons in association with two jets ($W^{\pm}W^{\pm}jj$-EW6), can be employed to simultaneously probe these two fundamental components in the SM and beyond.

This thesis presents comprehensive investigations of the electroweak $W^{\pm}W^{\pm}$ scattering process in the fully leptonic final state in proton-proton collisions at a centre-of-mass energy of 13 TeV. An amount of 36.1 fb^{-1} of data, taken with the ATLAS detector, is utilised.

The theoretical predictions of the $W^{\pm}W^{\pm}jj$ and, in particular, the $W^{\pm}W^{\pm}jj$-EW6 process are studied. Three different Monte-Carlo (MC) event generation programmes are employed: the PowhegBox programme at NLO QCD accuracy with the VBS approximation, the Sherpa programme in a LO multi-jet merged setup with up to three jets in the matrix element, and the MadGraph5_aMC@NLO programme at LO accuracy. The predictions of the three nominal setups in the fiducial region are found to disagree beyond their uncertainty envelopes. Subsequently, their individual settings, such as the nominal renormalisation and factorisation scales in the matrix-element calculations and the parton shower configurations, are investigated.

The first observation of the $W^{\pm}W^{\pm}jj$-EW6 process with data from the ATLAS experiment is established and published in Ref. [1] by rejecting the background-only hypothesis with a significance in experimental data of 6.5σ. The expected significance, employing the prediction from Sherpa for the $W^{\pm}W^{\pm}jj$-EW6 process, is 4.4σ. The fiducial cross-section of the $W^{\pm}W^{\pm}jj$-EW6 process as predicted by the SM is measured as $\left(2.89^{+0.59}_{-0.56}\right)$ fb, which, per construction of the analysis, includes the contribution of the interference with $W^{\pm}W^{\pm}jj$-EW4 process. This measurement is dominated by the statistical uncertainty of the data sample. All three studied theoretical predictions agree with the measured fiducial cross-section within the total uncertainty envelopes.

The components of the analysis of the SM $W^{\pm}W^{\pm}jj$-EW6 process are reutilised for a reinterpretation of the experimental data in terms of an Effective Field Theory (EFT) model describing beyond SM extensions which generate anomalous quartic gauge couplings in the electroweak sector through operators of mass dimension eight [2, 3]. For the first time, one-dimensional exclusion bounds on the coefficients of these operators are determined in the fully leptonic $W^{\pm}W^{\pm}jj$ final state with data from the ATLAS experiment, at the same time presenting the first overall dimension-eight EFT parameter exclusion bounds derived with $\sqrt{s} = 13$ TeV data from the ATLAS experiment. Comparisons with existing results of all final states show that the obtained results are less stringent.

The thesis' focus for this part lies in the investigation of the fundamental ingredients for the analysis of dimension-eight EFT models. The novel technique of amplitude decomposition is employed for the MC generation of the EFT signal contributions. It considerably improves the signal predictions and accuracy, as well as the simulation efficiency in the sensitive regions of the EFT contribution at high invariant masses. Moreover, along the profound validation of this new approach, it is found that the conventional simulation technique is insufficient in terms of phase space integration accuracy in the MC event generation.

The application of the clipping unitarisation on the EFT signal contributions is thoroughly investigated, and exclusion limits obtained with this approach are derived, alongside the ununitarised exclusion bounds. For the first time in the $W^{\pm}W^{\pm}jj$ final state, exclusion bounds scanning multiple values of the clipping energy are shown in this thesis. Comparisons with unitarity bounds calculated from Ref. [4] shown that the obtained results do not yet reach physically reasonable regions in terms of unitarity.

Moreover, exclusion bounds are studied, including the impact of dimension-six EFT operators on the $W^{\pm}Z$-EW4 background process. The results of this study constitute the first of their kind across final states and experiments. The inclusion of effects of dimension-six EFT operators with coefficients at their current best limit values yields no sizable effect on the exclusion bounds of the dimension-eight coefficients in the tested configuration.

Contents

1 Introduction **1**

2 Theoretical Foundations **3**
2.1 The Standard Model of Particle Physics 3
2.2 Electroweak Vector Boson Scattering in the Standard Model 13
2.3 Effective-Field-Theory Approach 18

3 Experimental Setup **25**
3.1 The Large Hadron Collider 25
3.2 The ATLAS Detector 27
3.3 Data-Taking and Preparation 34
3.4 Object Reconstruction and Identification 39

4 Simulation of Proton-proton Collisions at the LHC and the ATLAS Detector **47**
4.1 The Cross-section of Proton-proton Collisions 48
4.2 The Structure of Monte-Carlo Event Generation 49
4.3 Preparation of MC Simulated Events for Analysis 54

5 Electroweak Vector Boson Scattering at the LHC **57**
5.1 Definition of the Electroweak VBS Process at LO at the LHC 57
5.2 Categorisation of Feynman Diagrams at LO 59
5.3 Experimental Signature in the Fully Leptonic Final State 62
5.4 VBS at NLO in QCD and EW Couplings 63
5.5 Overview of VBS Final States and Measurements at the LHC 68

6 Theoretical Predictions **73**
6.1 Current Status of Theoretical Predictions 74
6.2 Review of the Modelling in LHC Analyses 78
6.3 Simulation of the $W^{\pm}W^{\pm}jj$ Process at the LHC 79
6.4 Definition of Inclusive and Fiducial Regions 85
6.5 Evaluation Strategy of Modelling Uncertainties 87
6.6 Predictions of the $W^{\pm}W^{\pm}jj$ Processes 91
6.7 Studies on the Predictions of the $W^{\pm}W^{\pm}jj$-EW6 Process 103
6.8 Conclusions and Final Sample Choices 118
6.9 Prospects of Theoretical Predictions for Future LHC Analyses 119

7 Overview of the Experimental Analyses **123**
7.1 Measurement Objectives and Analysis Strategies 124
7.2 Data and Simulated Data Samples 125
7.3 Object Selections 125
7.4 Event Selection in the Signal Region 128
7.5 Background Processes 128
7.6 Systematic Uncertainties 131
7.7 Expected Event Counts and Uncertainties in the Signal Region 144

8 Observation and Cross-section Measurement **147**
8.1 Review of Existing Results . . . 147
8.2 Strategy of the Statistical Analysis . . . 149
8.3 Strategy of the Fiducial Cross-section Measurement . . . 154
8.4 Control Regions . . . 156
8.5 Treatment of Uncertainties . . . 160
8.6 Results . . . 169
8.7 Potential of Future Analyses . . . 180

9 Exclusion Limits on Dimension-8 EFT Parameters **183**
9.1 Review of Existing Results and Their Measurement Strategies . . . 184
9.2 Simulation of EFT Signal Samples . . . 194
9.3 Strategy of the Statistical Analysis . . . 222
9.4 Systematic Uncertainties . . . 226
9.5 Exclusion Limits with Systematic Uncertainties . . . 232
9.6 Exclusion Limits Employing the Clipping Unitarisation Approach . . . 239
9.7 Impact of Dimension-6 EFT Effects from the $W^{\pm}Zjj$ QCD Process . . . 248
9.8 Discussion of Results and Potential Directions for Improvement . . . 254

10 Summary & Outlook **261**

A Details on the MC Event Generation **265**
A.1 Input Parameters and Generator Specifications . . . 265
A.2 Steering Cards and Job Options . . . 266
A.3 Inconsistencies in the Event Generation . . . 278
A.4 Technical Information for the Evaluation of Modelling Uncertainties . . . 278

B Additional Information on the Theoretical Studies **289**
B.1 Sample Statistics, Generator Cross-sections, Acceptances, and Fiducial Cross-sections for All Setups . . . 289
B.2 Comparison of Scale Setting for the $W^{\pm}W^{\pm}jj$-EW4 Process . . . 294
B.3 Comparison of Contributions to the $W^{\pm}W^{\pm}jj$ process . . . 295
B.4 Detailed Information on the Modelling Uncertainties . . . 299
B.5 Comparison of Scale Settings . . . 308
B.6 Comparison of Shower Configurations . . . 310
B.7 Effect of the QED FSR Radiation in the Parton Shower . . . 311

C Details of MC Simulated Event Samples at Reconstruction Level **313**
C.1 Reconstruction Level SM Samples . . . 313
C.2 Reconstruction Level EFT Samples . . . 319
C.3 Reconstruction Level aTGC Samples . . . 319

D Additional Analysis Details **323**
D.1 Object and Event Selection . . . 323
D.2 Background Estimates . . . 325
D.3 Validation of the Background Modelling . . . 341
D.4 Systematic Uncertainties . . . 350

E Additional Details on the Cross-section Measurement **355**
E.1 Control Regions . . . 355
E.2 Modelling Uncertainties in the Signal and Low-m_{jj} Control Region . . . 358
E.3 Results . . . 360

F Simulation of EFT Signal Samples **365**
F.1 Sample Generation using Madgraph 365
F.2 Technical Implementation of the Variable m_{WW} at Matrix-Element Level . . 369
F.3 The True Invariant Mass of the $W^{\pm}W^{\pm}$ System 369
F.4 Distributions of Two-dimensional EFT Effects 371
F.5 Investigation of the Decomposition Non-closure 374
F.6 Sample Statistics, Cross-sections, and Acceptances for the Final Setup 375

G Additional Details on the EFT Reinterpretation **377**
G.1 Exclusion Bounds Without Systematic Uncertainties 377
G.2 Event Yields in Bins of m_{ll} 377
G.3 Systematic Uncertainties 380
G.4 The Clipping Unitarisation Approach 385
G.5 Impact of Dimension-6 EFT Effects from the $W^{\pm}Z$-EW4 Process 385

Acronyms and Conventions

SM Standard Model

QFT quantum field theory

EFT Effective Field Theory

BSM beyond the Standard Model

QCD quantum chromodynamics

EW electroweak

EWSB Electroweak Symmetry Breaking

SSB spontaneous symmetry breaking

QED quantum electrodynamics

LO leading order

NLO next-to-leading order

VBS Vector Boson Scattering

aQGC anomalous quartic gauge couplings

aTGC anomalous triple gauge couplings

QED quantum electrodynamics

LHC Large Hadron Collider

CERN European Organisation for Nuclear Research

LEP Large Electron-Positron Collider

IBL insertable b-layer

SCT semi-conductor tracker

TRT Transition Radiation Tracker

MDT Monitored Drift Tubes

CSC Cathode Strip Chambers

RPC Resistive Plate Chambers

TGC Thin Gap Chambers

TDAQ trigger and data aquisition

HLT High Level Trigger

GRL good runs list

LAr liquid argon

AOD analysis object data

BDT boosted decision tree

WP working point

JES jet energy scale

JER jet energy resolution

JVT jet vertex tagger

I/FSR initial/final state radiation

MC Monte-Carlo

PDF parton distribution function

ME matrix element

EW electroweak

MPI multi-parton interactions

VR validation region

CR control region

BDT boosted decision tree

p.d.f. probability density function

NP nuisance parameter

C.L. confidence level

Lagrangian is used throughout this thesis as a term where most of the times it describes a Lagrangian density.

Masses are given in units of eV which arises from the convention in particle physics to use "natural units" ($c = \hbar = 1$).

Particle - Antiparticle: The corresponding term for particles will always refer to the particle and the anti-particle, e.g. the notation "lepton" comprises leptons and anti-leptons, especially in the experimental chapters, unless explicitly stated otherwise.

ATLAS coordinates: A right-handed coordinate system is used to describe the experimental set-up, where the z-axis is along the beam direction and the x-axis is pointing towards the centre of the LHC ring.

Definition of Variables

Primary Vertex
– Interaction point of interest;
– Origin of the right-handed coordinate system.

Azimuthal angle Φ – Is measured around the beam pipe in the transverse $x-y$ plane

Polar angle θ
– Defines the angle between the measured particle (or system of particles) and the positive z-axis;
– Is not invariant under Lorentz boosts.

Rapidity Y
– For massive particles;
– Invariant under Lorentz boosts;

$$Y = \frac{1}{2} \ln \left[\frac{E + p_z}{E - p_z} \right].$$

Pseudorapidity η
– For massless particles;
– Is invariant under Lorentz boosts;

$$\eta = -\ln \tan \left(\frac{\theta}{2} \right).$$

Distance parameter ΔR
– Between two (systems of) particles;

$$\Delta R = \sqrt{(\Delta\eta)^2 + (\Delta\phi)^2}, \text{ or } \Delta R = \sqrt{(\Delta Y)^2 + (\Delta\phi)^2}.$$

Transverse quantities – Such as p_{T}, E_{T}, and E_T^{miss}:

$$s_T = \begin{pmatrix} s_x \\ s_y \end{pmatrix}, \qquad s_T^2 = s_x^2 + s_y^2;$$

Zeppenfeld variable of object i (possibly leptons or the 3$^{\mathrm{rd}}$ jet):

$$z(i) = \frac{Y(i) - \frac{1}{2}\left(Y(j_1) + Y(j_2)\right)}{|Y(j_1) - Y(j_2)|};$$

Lepton centrality:

$$\begin{aligned} \zeta = \min \{ \; & \min\{Y(l_1), Y(l_2)\} - \min\{Y(j_1), Y(j_2)\}, \\ & \max\{Y(j_1), Y(j_2)\} - \max\{Y(l_1), Y(l_2)\} \}; \end{aligned}$$

Transverse mass of the combined system of particle i (usually a lepton) and E_T^{miss}:

$$m_T = \sqrt{2 p_T(i) E_T^{\mathrm{miss}} (1 - \cos \Delta\Phi(i, E_T^{\mathrm{miss}}))}$$

Chapter 1

Introduction

Beginning with the last century, the field of elementary particle physics has advanced enormously. Based on the theoretical description of electroweak interactions [5, 6], a theory emerged which is capable of describing the properties and fundamental interactions of the full spectrum of observed particles – the Standard Model (SM) of Particle Physics. Since then, it became well-established through various precision measurements [7] of the vast range of natural phenomena it can explain, ranging from low-energy interaction of atoms to particle collisions at unprecedentedly high energies. The success story culminated in the discovery of the Higgs boson in 2012 at the Large Hadron Collider (LHC) [8, 9], completing the SM particle set.

Nevertheless, the SM is incapable of explaining observations such as the baryon asymmetry [10], the hierarchy problem [11], or the existence of dark matter [12]. Moreover, the origin of the Electroweak Symmetry Breaking (EWSB) and the elementary fermion masses remain unresolved by the SM. Hence, it is widely accepted that it must be extended by a more general theory including the descriptions of new physics phenomena. However, experimental evidence for such phenomena is rare and mostly unstable with an increasing amount of data. Thus, directions for possible new physics searches are countless, a situation which has led to a new era in particle physics.

After the milestone achievement of the Higgs discovery, the field's focus evolved towards the precise measurement of even rarer processes, hoping to find insights into the nature of new physics. Among these are the class of Vector Boson Scattering (VBS) processes. Their compelling nature arises from the fundamental interactions they comprise: triple and quartic self-interactions, as well as the exchange of a Higgs boson between the electroweak bosons. As such, VBS offers a unique opportunity to study the gauge structure and the symmetry breaking mechanism of the electroweak sector of the SM and possible new-physics extensions thereof.

First evidence for the existence of a process involving VBS was found with the measurement of the electroweak production of two like-charged $W^{\pm}$ bosons and two jets, short $W^{\pm}W^{\pm}jj$-EW6, at a centre-of-mass energy $\sqrt{s}$ of 8 TeV with the ATLAS experiment [13]. A special and advantageous feature of this process is the reduced contribution of irreducible backgrounds compared to other VBS final states. A natural consequence was therefore the first observation of a process containing VBS in this same measurement channel, accomplished by the CMS collaboration with data at $\sqrt{s} = 13\,\text{TeV}$ [14]. A measurement by the ATLAS collaboration confirmed the observation of this process shortly after [1]. This experimental analysis, conducted with $36.1\,\text{fb}^{-1}$ of data at $\sqrt{s} = 13\,\text{TeV}$, constitutes one of the three main parts of this thesis. The observation of many other processes involving VBS followed in recent years [15–18].

The $W^{\pm}W^{\pm}$ scattering process does not only drive the experimental measurements of this class of processes. Owing to its comparably simple theoretical structure, it like-wise pioneers theoretical predictions in the field of VBS. Recent publications present the first computation of the full corrections at next-to-leading order (NLO) in both, electroweak and strong couplings, of the $W^{\pm}W^{\pm}jj$ process [19]. In present times, in which the Run 3 data-taking period of the LHC has just begun, measurements of processes involving VBS are on

the verge of not being limited by the statistics of the experimental data any more. Therefore, theoretical predictions are necessary that exhibit a precision in the range of the experimental uncertainties of future measurements. Hence, their thorough investigation, including the theoretical uncertainties, is presented in this thesis with suitable setups and in appropriate phase space regions. This is a vital ingredient of the preparation of experimental measurements. The gained knowledge does not only improve the accuracy of SM measurements. It is furthermore crucial for the reliable separation of new physics effects from SM background contributions in beyond the Standard Model (BSM) analyses.

Various new concepts for extensions of the SM have been formulated that affect its electroweak interactions, for example theories involving composite Higgs particles or supersymmetry. Evidence for these theories include but are not limited to new resonances with reasonably high masses above 1 TeV. However, their exploration is complicated due to the restricted energy range accessible by current high-energy collider experiments. Effective Field Theories (EFTs) come to the rescue in these situations, as these are designed to model-independently describe the low-energy effects of a new massive resonance outside the experimental reach.

Quartic couplings are rare and exceptional in the SM. The fine-tuned interplay between the EWSB and the quartic and triple self-interactions of the electroweak bosons in the SM further motivates their study beyond the SM. Therefore, the VBS processes are ideally suited for the study of anomalous quartic gauge couplings (aQGC) in the electroweak sector employing the EFT approach. The third part of this work focuses on the interpretation of the experimental data in light of aQGC in the $W^{\pm}W^{\pm}$ scattering process. For this study, the theoretical description of the SM is extended for an EFT model incorporating additional operators of mass dimension eight, which generate anomalous couplings to the quartic vertices of the electroweak gauge bosons [2, 3]. The event generation of this model follows the novel technique of amplitude decomposition. The profound validation of this new simulation approach is one of the main objectives in this work. Eventually, the impact of dimension-eight EFT operators is compared to experimental data and exclusion bounds on their coefficients can be derived. The implications of these results must be thoroughly discussed. This includes the reasonability of these results in the light of the allowed region of the EFT approach, which is affected by the allowed energy range of the EFT, its unitarisation bounds, and further assumptions made. Considering these aspects, the impact of the clipping unitarisation method and effects of dimension-six EFT operators on the exclusion limits is studied.

This thesis is organised as follows. Chapter 2 outlines the underlying theoretical concepts with emphasis on electroweak interactions and the description of the EFT approach in the context of aQGC. The experimental setup and conditions at the LHC and the ATLAS detector relevant for the analyses are briefly described in Chapter 3. The basic concepts of event generation and simulation of proton-proton collisions for this setup are given in Chapter 4. The process of VBS at the LHC is defined and characterised in Chapter 5. In Chapter 6 profound studies on the simulation of the $W^{\pm}W^{\pm}jj$ process in the context of the experimental conditions are presented. In Chapter 7 the goals of the SM and EFT reinterpretation analyses and their common components are described. The experimental analysis for the observation and cross-section measurement of the electroweak production of two like-charge $W^{\pm}$ bosons in association with two jets as predicted by the SM are detailed in Chapter 8. Studies on the simulation of the EFT signal process and exclusion bounds on dimension-eight EFT coefficients in the electroweak $W^{\pm}W^{\pm}jj$ process are presented in Chapter 9. The major aspects of this thesis and their future potential are summarised in Chapter 10.

Chapter 2

Theoretical Foundations

Experimental measurements in high-energy physics are based on a theoretical framework of the fundamental interactions between the elementary objects that form our universe. It is called the Standard Model (SM) of Particle Physics and as such is one of the best tested theories of our times. The SM is formulated as a relativistic quantum field theory (QFT). It has been established in the last century, combining the many standalone theories of that time. Based on the thorough inspection in the to-date experimentally accessible energy ranges, it is become incredibly structured and complete. Yet, it is today commonly accepted that the SM must be a subset of a larger theory which reaches to higher energies, eventually unravelling the origin of its characteristics and parameter values that cannot be described by the SM, such as the origin of the Higgs potential or the particles' masses. Many candidates for theories BSM come to the rescue in these cases, none of which has yet been experimentally confirmed.

This chapter begins with a brief sketch of the theoretical concepts of the SM in the first section. The relativistic notion and a basic understanding of QFT is assumed to be known by the reader. This section is based on established material, a detailed presentation of the fundamental theory can be found in textbooks, such as [20–23]. This work's main objective is the investigation of the scattering of massive electroweak vector bosons, and especially, the quartic couplings in the electroweak sector. Section 2.2 defines Vector Boson Scattering (VBS) in the context of this work, and highlights the special characteristics of these processes. The theoretical approach to explore beyond the Standard Model (BSM) physics in this thesis is based on the concept of Effective Field Theories (EFTs). It is introduced in Section 2.3. Further reading into EFTs can be found in Ref. [24, 25].

2.1 The Standard Model of Particle Physics

Over the past century, the understanding of nature in its fundamental constituents and interactions has remarkably progressed. Experiments, by far not only those at collider facilities, have expanded the knowledge of the underlying theory, culminating in the Standard Model of Particle Physics (SM) as we know it today. It describes the dynamic motions of the elementary components of matter and their fundamental interactions, the electromagnetic, the weak and the strong force into a renormalisable, relativistic quantum field theory. Gravity, the fourth fundamental force in nature, is not described by the SM.

The vital essence of modern theories such as the SM is the underlying principle of gauge invariance. Self couplings of gauge bosons are particularly interesting to this work, more precisely those of the electroweak part of the theory. These self couplings unfold directly from the principle of gauge invariance. Thereafter, we construct the Lagrangian of the SM with special emphasis on the electroweak interactions. Then, the mechanism of Electroweak Symmetry Breaking (EWSB) is introduced for the inclusion of particle masses in the model. Further, from this, we will see the crucial role of the EWSB in vector boson scattering. Having collected all necessary ingredients, the particle content is summarised, and the interactions are structured by developing Feynman rules from the Lagrangians. Eventually, the

connection to the calculation of observables that are measured in the experiment, such as the cross-section, is briefly sketched.

2.1.1 Gauge Structure and Symmetries

The SM was formulated aiming to establish a theoretical description of the known electromagnetic, weak and the strong interactions[1]. This was only achieved after developing the idea of local gauge symmetries by Yang and Mills [6] in the 1960s. These theories are innovative in the sense that the structure of the interactions is fully determined by the underlying gauge symmetry.

Local gauge invariance effectively means the invariance of the matter field ψ under local phase transformations of the kind:

$$\psi \longrightarrow \ e^{\mathrm{i}\,\varphi(x)}\ \psi, \tag{2.1}$$

where the phase $\varphi(x)$ is space-time dependent. Requiring the invariance of the Lagrangian and hence physical observables of the system under these transformations results in additional transformations, which have to be conducted simultaneously. This reveals the presence of associated fields and particles with spin one. The fields are called gauge fields and the associated particles are the gauge or vector bosons.

In case of the SM the gauge structure follows from the non-Abelian symmetry group product:

$$SU(2)_L \otimes U(1)_Y \otimes SU(3)_C, \tag{2.2}$$

where $SU(2)_L \otimes U(1)_Y$ describes the electroweak interactions and $SU(3)_C$ quantum chromodynamics (QCD), the strong interaction. Similarly to Noether's theorem [26] of classical mechanics, the invariance under these transformations leads to the conservation of the associated charges. Central to this work is precisely that the SM obeys a set of non-Abelian symmetry groups which lead to non-commuting generators and hence charges. This directly means, there exist self-interactions of those vector bosons that are described by the non-Abelian structures.

In addition to the gauge structure, the SM obeys the space-time translation symmetries yielding to the well established conservation laws of energy, momentum and angular momentum.

2.1.2 The Standard Model Lagrangian

Knowing the symmetries of the SM its Lagrangian can be constructed. It can be subdivided into three constituents:

$$\mathcal{L}_{\mathrm{SM}} = \mathcal{L}_{\mathrm{EW}} + \mathcal{L}_{\mathrm{QCD}} + \mathcal{L}_{\mathrm{SSB}}, \tag{2.3}$$

where the first two terms describe the interactions based on the gauge group. The last term, $\mathcal{L}_{\mathrm{SSB}}$, comprises the mathematical description of the spontaneous symmetry breaking of the electroweak theory which is necessary to give mass to particles.

The first two terms of Eq. (2.3) can further be schematically separated into a term characterising the kinematics and interactions of fermions, and a pure gauge term describing the dynamics of the spin one gauge bosons:

$$\mathcal{L}_{\mathrm{INT}} = \mathcal{L}_{\mathrm{fermion}} + \mathcal{L}_{\mathrm{gauge}}. \tag{2.4}$$

Electroweak Theory and Spontaneous Symmetry Breaking

The first unified electromagnetic and weak theory based on the Yang-Mills approach has been formulated in the 1960s by Glashow [5]. As such, Glashow's theory superseded the former independent theory of electromagnetism and Fermi's weak theory based on four-fermion interactions [27]. His theory, however, solely incorporated massless gauge bosons, which was later in this decade completed by Salam and Weinberg [28, 29].

[1] There has been constant efforts to incorporate gravity into the model, which however has not been successful to date.

Experimental evidence for this electroweak theory was originally found in 1973 with the Gargamelle experiment, which discovered the Z boson mediated neutral current interactions [30]. A decade later the $W^{\pm}$ and Z bosons have been discovered at the SPS accelerator at CERN [31–34].

The electroweak theory distinguishes between left- and right-handed components of the Dirac fermion field spinors ψ. The left-handed fermions ψ_L form $SU(2)_L$ doublets, while right-handed fermions ψ_R are singlets under the associated transformation. The components are built by the action of the projection operators $P_{L/R} = \frac{1}{2}(1 \mp \gamma_5)$ on them: $\psi_{L/R} = P_{L/R}\psi$. The Lagrangian describing the fermions takes hence the form:

$$\mathcal{L}_{\text{fermion}} = \sum_{f_L, f_R} \bar{\psi}_f \mathrm{i}\, \gamma^\mu D_\mu \psi_f, \tag{2.5}$$

with the sum over all fermions $f_{L/R}$, the adjoint spinor $\bar{\psi} \equiv \psi^\dagger \gamma^0$ and the covariant derivative built to obey the $SU(2)_L \otimes U(1)_Y$ gauge structure:

$$D_\mu = \partial_\mu + \mathrm{i}\, g_W T^a W_\mu^a + \mathrm{i}\, g_Y Y B_\mu. \tag{2.6}$$

According to their degrees of freedom, the three generators of the $SU(2)_L$ group give rise to three gauge fields, W_μ^a $(a = 1, 2, 3)$, while the $U(1)_Y$ generates the field B_μ to ensure invariance under the local transformations. The corresponding couplings are g_W, and g_Y, respectively. Note that the values of these couplings remain undetermined by the gauge structure and hence the theory. $T^a = \frac{1}{2}\tau^a$ with τ^a being the Pauli matrices, and the hypercharge Y are the generators of the $SU(2)_L$ and $U(1)_Y$, respectively. The corresponding transformations are:

$$\begin{aligned} \psi_L &\longrightarrow U_L \quad U_Y \quad \psi_L \\ &\longrightarrow e^{\mathrm{i}\,\alpha_a(x) T^a} \; e^{\mathrm{i}\,\beta(x) Y} \; \psi_L, \\ \psi_R &\longrightarrow U_L \quad U_Y \quad \psi_R \\ &\longrightarrow \mathbb{1} \quad e^{\mathrm{i}\,\beta(x) Y} \; \psi_R, \end{aligned} \tag{2.7}$$

where $\alpha_a(x)$ and $\beta(x)$ are the space-time dependent gauge parameters. For the gauge fields, the Tailor expanded infinitesimal transformations then take the form:

$$\begin{aligned} W_\mu^a &\longrightarrow W_\mu^a - \frac{1}{g_{\mathrm{W}}} \partial_\mu \alpha^a(x) - \epsilon^{abc} \alpha^b(x) W_\mu^c, \\ B_\mu &\longrightarrow B_\mu - \frac{1}{g_{\mathrm{Y}}} \partial_\mu \beta(x), \end{aligned} \tag{2.8}$$

containing the group structure constants ϵ^{abc}.

The part of the Lagrangian forming the dynamics of the electroweak gauge fields:

$$\mathcal{L}_{\text{gauge}} = -\frac{1}{4} W_{\mu\nu}^a W^{a\,\mu\nu} - \frac{1}{4} B_{\mu\nu} B^{\mu\nu}. \tag{2.9}$$

contains the antisymmetric field strength tensors:

$$B_{\mu\nu} = \partial_\mu B_\nu - \partial_\nu B_\mu, \tag{2.10a}$$

$$W_{\mu\nu}^a = \partial_\mu W_\nu^a - \partial_\nu W_\mu^a + g_W \epsilon^{abc} W_{b,\mu} W_{c,\nu}. \tag{2.10b}$$

As a result of the non-Abelian structure of the gauge group, terms in Eq. (2.9) occur that contains cubic and quartic self-interactions among the gauge fields.

According to experimental results, the observation of charged and neutral currents, the gauge fields have to mix to form the charged $W^{\pm}$ bosons fields:

$$W_\mu^{\pm} = \frac{1}{\sqrt{2}} \left(W_\mu^1 \mp \mathrm{i}\, W_\mu^2 \right), \tag{2.11}$$

with the charged current coupling g_W and the neutral photon and Z bosons fields:

$$\begin{pmatrix} A_\mu \\ Z_\mu \end{pmatrix} = \begin{pmatrix} \cos\theta_{\mathrm{W}} & \sin\theta_{\mathrm{W}} \\ -\sin\theta_{\mathrm{W}} & \cos\theta_{\mathrm{W}} \end{pmatrix} \begin{pmatrix} B_\mu \\ W_\mu^3 \end{pmatrix}. \tag{2.12}$$

The mixing of the neutral fields is determined by the observed equal couplings of left- and right-handed fermions to the photon with the strength of the electric charge value e. Additionally, no couplings of photons to neutrinos is observed. This fixes the rotation and the fermion couplings to the electroweak gauge bosons have the relation:

$$g_{\mathrm{W}} \sin\theta_W = g_Y \cos\theta_W = e. \tag{2.13}$$

The generators of the $U(1)_{\mathrm{QED}}$ gauge symmetry, giving the electric charges, can then be expressed as:

$$Q = I_3^W + Y, \tag{2.14}$$

and the coupling to the Z boson takes the form:

$$g_Z = \frac{e}{\sin\theta_W \, \cos\theta_W}. \tag{2.15}$$

As to this point, no particles have gained mass in the theory. As suggested above, the electroweak theory was only completed when Salam and Weinberg included masses of the bosons into the mathematical descriptions. This was achieved through spontaneous breaking of the $SU(2)_L \otimes U(1)_Y$ symmetry group via the Brout-Englert-Higgs mechanism (short Higgs mechanism) proposed by several parties in 1964 [35–37]. Though, the initial motivation was giving mass to the gauge bosons, fermion masses can be added manually with the same ingredients through Yukawa couplings.

The necessity for the additional effort being that mass terms of the form:

$$\frac{1}{2} m_W^2 W_\mu^a W^{a\,\mu} + \frac{1}{2} m_B^2 B_\mu B^\mu, \tag{2.16}$$

for spin one bosons and:

$$m\psi\bar{\psi}, \tag{2.17}$$

for fermions are not invariant under the electroweak gauge group $SU(2)_L \otimes U(1)_Y$. This can be seen when applying the transformations of Equations (2.8) and (2.7), respectively.

The solution is introducing a non-symmetric vacuum ground state $v = \langle 0|\Phi|0\rangle \neq 0$ (vacuum expectation value) for a new complex, scalar field:

$$\Phi = \begin{pmatrix} \theta^2(x) + \mathrm{i}\,\theta^1(x) \\ \frac{1}{\sqrt{2}} \left(v + H(x) + \mathrm{i}\,\theta^3(x)\right) \end{pmatrix}, \tag{2.18}$$

and hence breaking the electroweak symmetry spontaneously, while leaving the Lagrangian itself fully $SU(2)_L \otimes U(1)_Y$ symmetric. Φ is a $SU(2)_L$ doublet with non-zero $U(1)_Y$ hypercharge. It exhibits four degrees of freedom $H(x)$ and $\theta^i(x)$, the real-valued Higgs field and Goldstone modes, respectively. A scalar field Lagrangian:

$$\mathcal{L}_\Phi = \left(D^\mu \Phi\right)^\dagger \left(D_\mu \Phi\right) - V(\Phi), \tag{2.19}$$

with a kinetic term described by the covariant derivative in Eq. (2.6) and the explicit form of the $SU(2)_L$ invariant potential:

$$V(\Phi) = \mu^2 \left|\Phi\right|^2 + \lambda \left|\Phi\right|^4. \tag{2.20}$$

can be added to the electroweak theory. For $\mu^2 < 0$ and $\lambda > 0$ the potential has degenerate non-zero minima. Arbitrarily choosing:

$$\Phi_0 = \begin{pmatrix} 0 \\ \frac{1}{\sqrt{2}} v \end{pmatrix} = \begin{pmatrix} 0 \\ \frac{1}{\sqrt{2}} \sqrt{\frac{-\mu^2}{\lambda}} \end{pmatrix}, \tag{2.21}$$

as the ground state leads to the desired behaviour the symmetry breaking was introduced to reveal. The electrically charged component of the scalar field is chosen $\Phi_0^+ = 0$ such that the

electromagnetic $U(1)_{\mathrm{QED}}$ remains unbroken and hence resulting in a massless photon and massive electroweak bosons $W^{\pm}$ and Z:

$$m_W = v\frac{g_W}{2}, \tag{2.22}$$

$$m_Z = \frac{m_W}{\cos\theta_W}. \tag{2.23}$$

Additionally, the new kinetic term of the Lagrangian features the interaction of the Higgs field with the massive gauge bosons and a mass term for the scalar Higgs boson:

$$m_H = v\sqrt{2\lambda}. \tag{2.24}$$

Self-interactions of the Higgs field are following from the potential $V(\Phi)$. Note, that μ and λ are free parameters of the SM which are to be determined by experiment. The non-vanishing vacuum expectation value v can be related to G_F the Fermi coupling constant, which is historically been determined from the decay of the muon described in the Fermi theory [27, 38]:

$$v = \frac{1}{\sqrt{\sqrt{2}G_F}} = 246\,\mathrm{GeV}, \tag{2.25}$$

and which quantifies the weak scale.

With the breaking of the electroweak gauge group $SU(2)_L \otimes U(1)_Y$ to $U(1)_{\mathrm{QED}}$, the four degrees of freedom of Φ are absorbed into the longitudinal polarisation states of the now massive $W^{\pm}$ and Z bosons, and the Higgs boson. The interactions of the Higgs field with the massive gauge bosons reveals a crucial phenomenon, which is the restoration of a unitary scattering amplitude in longitudinal vector boson scattering. This is in detail discussed in Sec. 2.2.3.

Eventually mass terms for the fermions can be formulated via Yukawa couplings y_i:

$$\mathcal{L}_{\mathrm{Yukawa}} = y_1^f \bar{\psi}_L^f \Phi \psi_R^f + y_2^f \bar{\psi}_L^f \Phi^{\mathrm{c}} \psi_R^f + \mathrm{h.c.}. \tag{2.26}$$

With the Higgs doublet, an operator connecting left- and right-handed fermions can be formulated. The first term with y_1^f produces masses for the charged leptons and the down-type quarks. The charge-conjugate $\Phi^{\mathrm{c}} = \mathrm{i}\,\sigma_2\Phi^*$ enables the mass terms for the up-type quarks. Neutrino masses are generally not seen to be part of the SM. Masses of the fermions then have the form:

$$m_f = v\frac{y_{1,2}^f}{\sqrt{2}}. \tag{2.27}$$

In addition, interaction terms between the Higgs boson and the massive fermions are generated. The full spontaneous symmetry breaking (SSB) Lagrangian is then:

$$\mathcal{L}_{\mathrm{SSB}} = \mathcal{L}_{\Phi} + \mathcal{L}_{\mathrm{Yukawa}}. \tag{2.28}$$

Quantum Chromodynamics

The theory of strong interactions, quantum chromodynamics has been established shortly after the electroweak theory by employing the $SU(3)_C$ gauge group [39, 40]. The corresponding Lagrangian is of the form[2]:

$$\mathcal{L}_{\mathrm{QCD}} = \sum_f \bar{q}_f \mathrm{i}\,\gamma^\mu D_\mu q_f - \frac{1}{4} G^j_{\mu\nu} G^{j\,\mu\nu}, \tag{2.29}$$

with the covariant derivative:

$$D_\mu = \partial_\mu + \mathrm{i}\,g_S \lambda^j G^j_\mu. \tag{2.30}$$

The fermionic part only acts on the quarks q_f, which carry the three-valued quantum number colour. G^j_μ are the eight gauge fields whose excitations are the eight gluons carrying colour

[2]The kinetic term is added here again for a complete description of the quarks in the SM in this section. However, when adding this Lagrangian to Eq. 2.3, the kinetic term must be omitted as it is already included in Eq. 2.5.

Table 2.1: Spin-1/2 fermions of the SM and their quantum numbers of the $SU(2)_L \otimes U(1)_Y \otimes SU(3)_C$ symmetry group. Left-handed fermions form $SU(2)_L$ doublets whereas right-handed fermions are $SU(2)_L$ singlets. I_3^W denotes the third component of the weak isospin, the charge of $SU(2)_L$, Y is the hypercharge corresponding to $U(1)_Y$, Q is the electric charge, and colour represents the charge of the QCD group $SU(3)_C$. The corresponding antifermions have opposite charges.

	Generation			$\mathrm{SU(2)_L \otimes U(1)_Y}$			$\mathrm{SU(3)_c}$
	1st	2nd	3rd	I_3^W	Y	Q	colour
Leptons	$\begin{pmatrix}\nu_e\\ e^-\end{pmatrix}_L$	$\begin{pmatrix}\nu_\mu\\ \mu^-\end{pmatrix}_L$	$\begin{pmatrix}\nu_\tau\\ \tau^-\end{pmatrix}_L$	$+\frac{1}{2}$	$-\frac{1}{2}$	0	–
				$-\frac{1}{2}$	$-\frac{1}{2}$	-1	–
	e_R^-	μ_R^-	τ_R^-	0	-1	-1	–
Quarks	$\begin{pmatrix}u\\ d\end{pmatrix}_L$	$\begin{pmatrix}c\\ s\end{pmatrix}_L$	$\begin{pmatrix}t\\ b\end{pmatrix}_L$	$+\frac{1}{2}$	$+\frac{1}{6}$	$+\frac{2}{3}$	rgb
				$-\frac{1}{2}$	$+\frac{1}{6}$	$-\frac{1}{3}$	rgb
	u_R	c_R	t_R	0	$+\frac{2}{3}$	$+\frac{2}{3}$	rgb
	d_R	s_R	b_R	0	$-\frac{1}{3}$	$-\frac{1}{3}$	rgb

and anticolour, and λ^j represent the generators of the group. The corresponding coupling strength is $g_S = \sqrt{4\pi\alpha_S}$.

As a result of the non-Abelian structure of the $SU(3)_C$ group and the strong coupling, QCD exhibits the properties of asymptotic freedom and confinement. These characteristics strongly affect the dynamics of partons in high-energy proton-proton collisions, the experimental handle of this work. This will be discussed in Sec. 4.1. Particles that consist of quarks are called hadrons.

2.1.3 Particle Content and Parameters of the Standard Model

Tables 2.1[3] and 2.2 summarise the particle content, the fermions and boson, respectively of the SM. They are characterised by their quantum numbers or charges of the gauge structure $SU(2)_L \otimes U(1)_Y \otimes SU(3)_C$. I_3^W denotes the third component of the weak isospin, the charge of $SU(2)_L$, Y is the hypercharge corresponding to $U(1)_Y$, Q is the electric charge of the unbroken $U(1)_{\mathrm{QED}}$, and colour represents the charge of the QCD group $SU(3)_C$.

Left-handed fermions form $SU(2)_L$ doublets, whereas right-handed fermions are $SU(2)_L$ singlets. They come in three generations, with increasing masses from the first to the third generation and varying flavour. Consequently, only particles of the first generation are stable and create matter as we know it. Masses of all particles are shown in Tab. 2.3 and 2.4. Other quantum numbers are identical across generations, hence revealing identical couplings to all spin-one bosons.

All fermions take part in the weak interactions mediated by the Z boson, while only left-handed particles interact with the $W^\pm$ boson. As a result of their colour quantum numbers, fermions can be classified into leptons which are colour neutral and quarks that occur in three colour states. Hence, only quarks take part in the strong interaction mediated by the gluon. All electrically charged particles participate in the electromagnetic interaction. Each fermion can be associated with an antiparticle, which has opposite charges and equal mass and spin.

The gauge bosons of the theory carry spin one. The photon, Z and $W^\pm$ boson are gauge bosons of the $SU(2)_L \otimes U(1)_Y$ symmetry group. The gluon is the gauge boson of the

[3]Notice that this table does not comprise right-handed neutrinos, since they have not been observed in any experiment so far and therefore are considered to not interact with any of the SM forces, i. e. all corresponding quantum numbers are zero. However, most scenarios for neutrino masses require the existence of right-handed neutrinos.

Table 2.2: Bosons of the SM and their quantum numbers of the $SU(2)_L \otimes U(1)_Y \otimes SU(3)_C$ symmetry group. I_3^W denotes the third component of the weak isospin, the charge of $SU(2)_L$, Y is the hypercharge corresponding to $U(1)_Y$, Q is the electric charge, and colour represents the charge of the QCD group $SU(3)_C$. Bosons of spin-1 are the gauge bosons of the theory.

	Bosons		$\mathrm{SU}(2)_L \otimes \mathrm{U}(1)_Y$			$\mathrm{SU}(3)_c$
			I_3^W	Y	Q	coloured
Spin-1	Photon	γ	0	0	0	–
	$W^\pm$ boson	$W^\pm$	± 1	0	± 1	–
	Z boson	Z	0	0	0	–
	Gluons	g	0	0	0	yes
Spin-0	Higgs boson	H	$-\frac{1}{2}$	$+\frac{1}{2}$	0	–

Table 2.3: The Standard Model fermions with their experimental masses and its precision. The quark masses are approximate values since they depend on the applied renormalisation scheme. For the neutrinos only upper limits on the mass have been confirmed experimentally. The given upper limits correspond to the linear parametrisation of the flavour eigenstates ν_α ($\alpha \in \{e, \mu, \tau\}$) with respect to the mass eigenstates ν_i ($i \in \{1, 2, 3\}$), e. g. $\nu_\alpha = \sum_i U_{\alpha i} \nu_i$ and therefore $m_{\nu_\alpha} = \sum_i |U_{\alpha i}|^2 \, m_i$. Note the wide spectrum of the fermion masses covering a range of at least 11 orders of magnitude from the electron-neutrino to the top-quark. Numbers are taken from Ref. [41].

Particle name		Mass m (GeV)	Rel. precision ($1\,\mathrm{ppm} = 10^{-6}$)
1^{st} generation:			
e-neutrino	ν_e	$< 1.1 \times 10^{-9}$	–
Electron	e^-	511.0×10^{-6}	0.006
Up quark	u	2.16×10^{-3}	$(1.2 - 2.3) \times 10^5$
Down quark	d	4.67×10^{-3}	$(0.4 - 1.0) \times 10^5$
2^{nd} generation:			
μ-neutrino	ν_μ	$< 1.1 \times 10^{-9}$	–
Muon	μ^-	105.7×10^{-3}	0.023
Charm quark	c	1.27	0.2×10^5
Strange quark	s	95×10^{-3}	$(0.5 - 1.2) \times 10^5$
3^{rd} generation:			
τ-neutrino	ν_τ	$< 1.1 \times 10^{-9}$	–
Tau lepton	τ^-	1.78	68
Top quark	t	172.76	1737
Bottom quark	b	4.18	$4785 - 7177$

Table 2.4: The Standard Model bosons with their experimental masses and its precision. For the gluons, the theoretical value is listed. A mass as large as a few MeV may not be precluded. Numbers taken from Ref. [41].

Particle name		Mass m (GeV)	Rel. precision ($1\,\text{ppm} = 10^{-6}$)
Photon	γ	$< 10^{-27}$	–
$W^{\pm}$ boson	$W^{\pm}$	80.379	149
Z boson	Z	91.1876	230
Gluons	g	0	–
Higgs boson	H	125.10	1119

strong interaction and has eight colour representations. Photons and gluons are massless in the SM since their corresponding gauge symmetries are unbroken. Nevertheless, masses of $< 10^{-18}\,\text{eV}$ and a few MeV for the photon and gluon, respectively, are not ruled out by experiment [41]. The Higgs boson is introduced as a scalar boson in the course of the EWSB of the electroweak theory. It was discovered in 2012 at the LHC with a mass of 125 GeV [8, 9].

As indicated above, the SM cannot predict some parameters of the theory. Hence, those parameters have to be measured by experiments. In total, there are 18 input parameters in the SM. The inclusion of neutrino masses adds 7 parameters. The masses of all fermions are summarized in Tab. 2.3 and enter the theory through the Yukawa couplings. The masses of all bosons in the SM are displayed in Tab. 2.4. In addition, the three coupling constants for the gauge interactions, and the two parameters of the Higgs potential cannot be predicted. The four remaining parameters come from the mixing of the quarks in the Cabibbo–Kobayashi–Maskawa (CKM) matrix, which are not discussed in detail here. With the neutrinos being massive, four parameters describing their cross-generational mixing, need to be added.

Generally, conventions as to how to define the set of input variables exist. The simulation studies in this thesis use the set of input parameters with the masses of the $W^{\pm}$, Z and the Higgs boson m_W, m_Z, and m_H respectively, and the Fermi coupling constant G_F. This set is called the G_μ scheme. The weak coupling constants and weak boson masses are then evaluated via the weak mixing angle θ_W through the relations from Equations (2.13), (2.15), (2.22), (2.24), and (2.25) at tree-level:

$$\sin^2\theta_W \approx 0.223, \tag{2.31}$$

$$g_W \approx 0.641, \tag{2.32}$$

$$g_Z \approx 0.727, \tag{2.33}$$

$$\alpha_{\text{QED}} = \frac{e^2}{4\pi} \approx \frac{1}{137.036}. \tag{2.34}$$

The latter is the electromagnetic fine-structure constant. In addition the strong coupling constant serves as input via:

$$\alpha_S = \frac{g_S^2}{4\pi}. \tag{2.35}$$

Tab. 2.5 summarises the additional input parameters of the SM.

2.1.4 Predictions and Feynman Calculus

Completing the brief introduction to the SM theory, leaves us with connecting the theoretical foundations with the actual calculation of experimental observables, such as scattering cross-sections or decay rates. However, this is not very straightforward. To this day, no interacting quantum field theories of more than two space-time dimensions are known which can be solved

Table 2.5: Additional input parameters of the SM which serve as input for simulations in this work. The value of the strong coupling constant α_S is evaluated at the mass of the Z boson m_Z. Numbers taken from Ref. [41].

Parameter		Value	Rel. precision ($1\,\text{ppm} = 10^{-6}$)
Fermi constant	G_F	$1.1663787 \times 10^{-5}\,\text{GeV}^{-2}$	0.514
Strong coupling constant	$\alpha_S(m_Z)$	0.1179	8.5×10^5

exactly. This includes the SM. Consequently, some assumptions have to be made to obtain an applicable approach that can give meaningful predictions.

Tomonaga, Schwinger and Feynman achieved a great advancement in this direction by applying perturbation theory to originally solve quantum electrodynamics (QED) problems [42]. The key in this ansatz is to treat the interaction term of the Lagrangian as a small time-dependent perturbation of the free field solutions. This can be done as long as the coupling constant, which is used to expand the series, is small. Only then the perturbation series can be used to calculate predictive quantities, as the truncation at finite orders produces meaningful results. As we will see later, the perturbative orders are used to characterise the level of accuracy for any given process. A leading order (LO) process is calculated by omitting all terms in the perturbation series that are beyond the first coupling dependent term. Next-to-leading order (NLO) processes are consequently defined by taking one more order of couplings into account, and so on.

The obtained perturbation series have a structure that can be visualised using of Feynman diagrams. These diagrams can thus be used to derive rules for the calculation of measurable observables. They are called Feynman rules. They are derived from the Lagrangian and contain a prescription for the calculation of the propagation and interaction of the involved fields. The exact form in the SM is not in the scope of this work, as it strongly depends on the chosen gauge and others. A summary can e. g. be found in Ref. [21].

An essential quantity to deduce from collider experiments as ATLAS is the cross-section of a scattering process. It is the likelihood with which any particular final state can occur in a given theory and with known initial states. It is a quantity that is intrinsic to the colliding particles and the underlying theory. From the quantum mechanical approach of computing a probability amplitude that a given initial state i propagates to the final state f:

$$S_{fi} = \langle f|S|i\rangle\,, \tag{2.36}$$

the scattering matrix (S-matrix) can be defined. The S-matrix can be divided into:

$$S_{fi} = \delta_{fi} + \mathrm{i}\,\mathcal{M}_{fi}, \tag{2.37}$$

a part that describes no scattering and a part that represents the non-trivial scattering amplitude $\mathcal{M}_{fi}$. In this, the interaction rules of the model are encoded from the SM Lagrangian. The Feynman rules organise the contributions to a given process in terms of diagrams. The cross-section can then be connected to the non-trivial scattering probability:

$$\sigma \sim \int_{PS} |\mathcal{M}_{fi}|^2\, d\theta, \tag{2.38}$$

that contains the sum of all diagrams and is integrated over a given Lorentz-invariant phase space. The proportionality factor is not Lorentz-invariant, but invariant under boosts along the direction of the incoming particles, and transforms as an area which is the unit of the cross-section. This can be seen from scattering theory described in standard literature [21, 22].

The success of the SM and the predictions it imposes has been evaluated in many experiments. Fig. 2.1 shows a summary of measurements conducted at the ATLAS experiment at CERN with comparison to SM predictions.

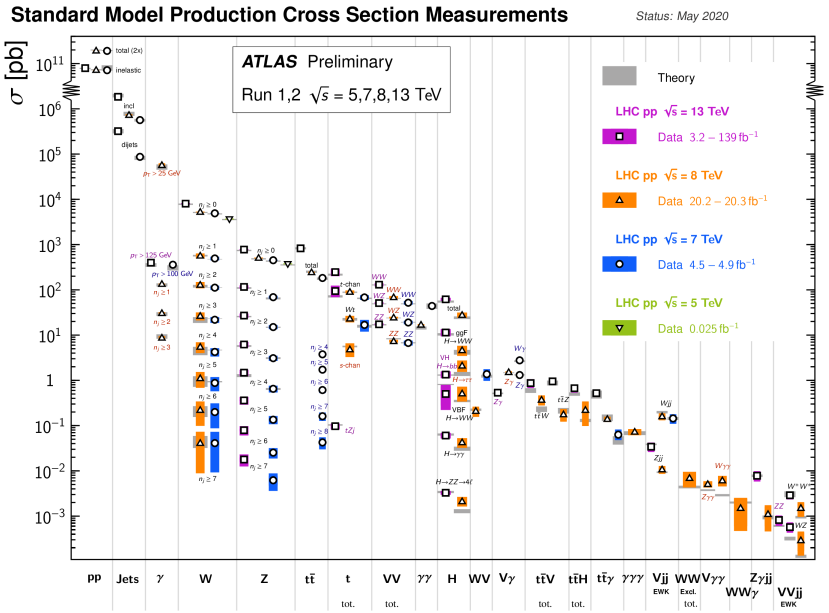


Figure 2.1: Summary of several Standard Model total and fiducial production cross section measurements with the ATLAS experiment, corrected for branching fractions, compared to the corresponding theoretical predictions with the precision available for the relevant processes. Figure taken from Ref. [43].

2.1.5 Open Questions

Albeit the great performance and incredible success of the SM in predicting aspects and structuring the many elementary particles of modern particle physics, there are many unanswered questions, here listing an excerpt that is interesting in the context of this work:

- What is the origin of the over 20 arbitrary parameters; Especially, what motivates the values of the particle masses, that spread over so many magnitudes, the form of the Higgs potential, or the "hierarchy problem" [11];
- Why are there so many elementary particles (61), why three fermion families;
- What motivates the gauge group of the SM; or
- How can a theory of gravity be incorporated into the SM.

These kinds of questions all hint to a possible existence of a more general theory, a "Grand Unification" [44, 45], that typically reduces the number of free parameters by incorporating the SM formulation into a larger gauge group. One recent example for hints of new physics constitute the measurements of the anomalous magnetic moment of the muon, whose results remain in slight tension with SM predictions after a refined measurement and combination with previous results [46].

There exist many approaches on how to extend the SM and formulate a larger theory that embeds the SM while finding answers to some of the questions. A very valid attempt lies in extending the SM in a minimal fashion that fixes a selection of requirements and leaves the rest to be found by experiment. This can be achieved by the concepts of EFTs, which, in the context of this work of electroweak physics, are discussed later in this next section.



Figure 2.2: Triple self-interaction vertices of the electroweak gauge bosons with coupling factors derived from Feynman Rules at LO. LO triple self-interaction vertex amplitudes are linearly proportional to the respective coupling.

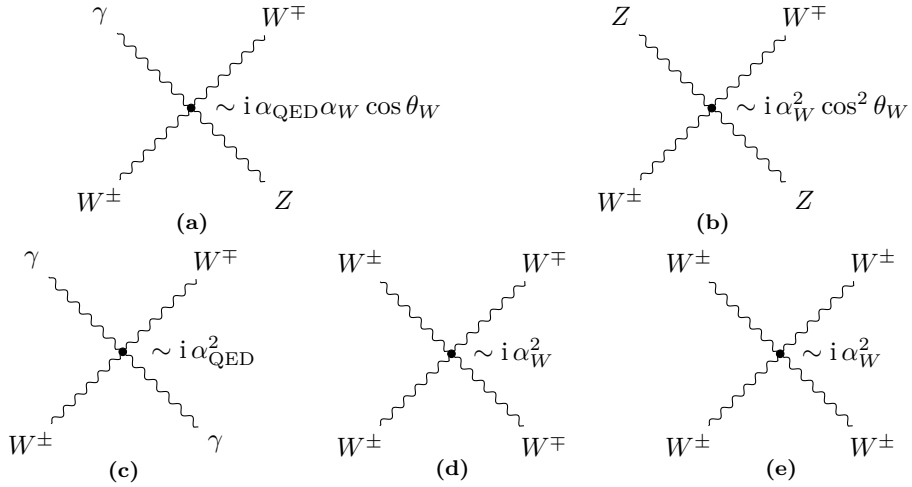


Figure 2.3: Quartic self-interaction vertices of the electroweak gauge bosons with coupling factors derived from Feynman Rules at LO. LO quartic self-interaction vertex amplitudes are proportional to the square of the respective couplings.

2.2 Electroweak Vector Boson Scattering in the Standard Model

2.2.1 Relevant Processes and their Feynman Rules

From the Lagrangian of the electroweak gauge theory in Eq. (2.9) follows, due to the non-abelian structure of the gauge group, the existence of triple and quartic self-interaction vertices between the electroweak gauge bosons. Fig. 2.2 and 2.3 show the Feynman diagrams for the triple and quartic self-interactions, respectively, with the electroweak coupling factors at each vertex. Here α_W, is similarly to the electromagnetic fine-structure constant, defined as:

$$\alpha_W = \frac{g_W^2}{4\pi}. \tag{2.39}$$

Other than the self-interaction vertex combinations shown in these two figures are not allowed in the SM, especially forbidding self-interactions where only neutral bosons are involved.

In addition, processes with vertices involving the Higgs boson and electroweak gauge fields are prerequisite for the discussion of electroweak vector boson scattering. They are a consequence of the kinetic term of the Higgs Lagrangian in Eq. (2.19) due to the covariant derivative. Fig. 2.4 shows the allowed LO vertices in the SM together with the coupling factors for each vertex.

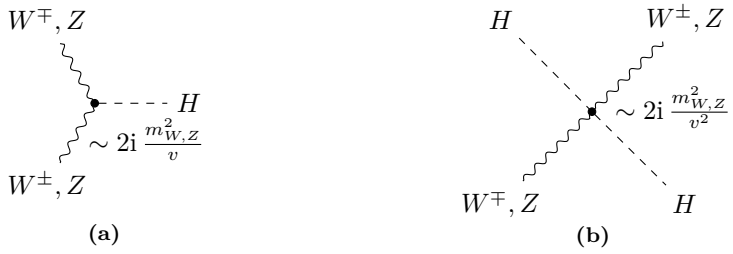


Figure 2.4: Interaction vertices for the Higgs boson with the electroweak gauge bosons with coupling factors derived from Feynman Rules.

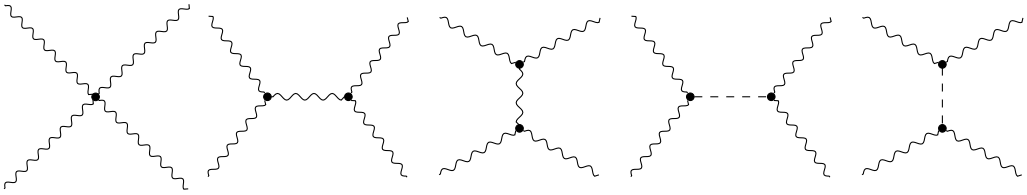


Figure 2.5: Feynman diagrams contributing to the process of vector boson scattering $VV \to VV$ at LO.

2.2.2 Definition of Electroweak Vector Boson Scattering

The process referred to as electroweak VBS is defined as the sum of processes that connect two incoming electroweak gauge bosons of any kind with two, potentially different outgoing electroweak vector bosons and is denoted as $VV \to VV$. Fig. 2.5 shows all relevant Feynman diagrams that can contribute to VBS as allowed in the SM. It comprises the quartic self-interaction vertex, as well as the s- and t/u-channel triple gauge boson interaction processes, and the interaction of the Higgs boson with the massive electroweak gauge bosons. From Fig. 2.2 to 2.4 all possible processes with different initial and final state electroweak gauge bosons can be deduced. It should be noted, for a specific VBS process with fixed initial and final state, typically a subset of the shown diagrams do actually contribute.

2.2.3 The Virtue of Electroweak Vector Boson Scattering

With its unique composition of relevant processes, VBS is a handle to study:

1. The fundamental gauge structure of the underlying $SU(2)_L \otimes U(1)_Y$ electroweak symmetry group of the SM through the quartic and triple self-interaction vertices;

2. EWSB through its contribution from Higgs exchange processes.

In addition, VBS allows studying these phenomena at energy ranges much higher than, e. g. direct Higgs boson measurements, which makes its exploration beautifully interesting.

Albeit very much desirable, the study of each of the contributing processes in Fig. 2.5 independently is not possible due to the fact that single diagrams are not observable, but only the combination of gauge invariant set of diagrams is. The reason for this is as compelling as beautiful, since it follows directly from the elemental and primary assumption of the theory: local gauge invariance and EWSB.

The invariance under local gauge transformations in non-abelian theories is impossible without the existence of both quartic and triple self-interactions of the gauge bosons. The phenomenon is also referred to as gauge cancellation.

Further, these bosons are massive, and the covariant derivative occurs in the Lagrangian terms that describe the EWSB which at the same time describe the interaction of the gauge bosons with the Higgs field. Of course, after all, it is possible that the Higgs mechanism, as considered part of the SM today, is not the full picture. However, it has one striking aspect that has to be part of any other theory that might come to supersede EWSB as constructed from the Higgs mechanism: Without the Higgs boson interaction with the electroweak gauge

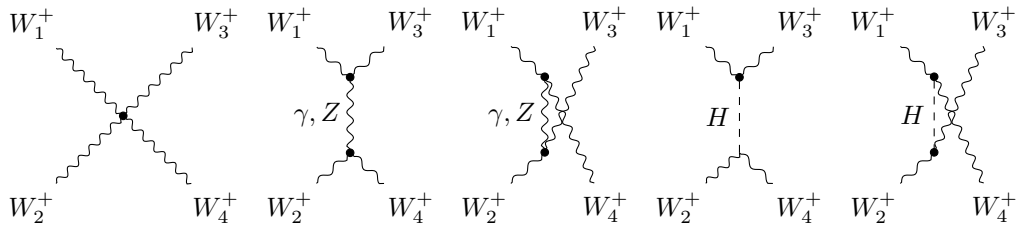


Figure 2.6: Feynman diagrams of the seven processes contributing to the vector boson scattering $W^+W^+ \to W^+W^+$ at LO, including the quartic self-coupling vertex, the triple gauge boson interactions via a photon γ or Z boson, and the Higgs exchange in the t- and u-channels, respectively.

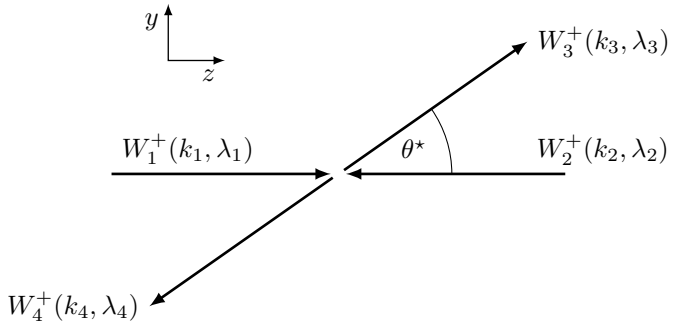


Figure 2.7: Kinematic sketch of the scattering reaction $W_1^+(k_1, \lambda_1)W_2^+(k_2, \lambda_2) \to W_3^+(k_3, \lambda_3)W_4^+(k_4, \lambda_4)$ in the centre-of-mass frame of the W^+W^+ system. Figure modified from Ref. [49].

bosons the scattering of the longitudinally polarised vector bosons is violating the basic principle of probability conservation, called unitarity. At high energy, the production rate of the boson self-interactions processes calculated from the S-matrix elements rises with energy, and this continuous increase is unphysical. The violation of unitarity is mitigated only when all relevant processes to VBS are considered in the computation of its amplitude.

The cancellation of the unphysical behaviour at energies much higher than the boson masses, $E^2 \gg m^2$, is briefly sketched in the following. The example is the longitudinal W^+W^+ scattering to demonstrate the gauge cancellation as well as the restoration of unitarity through the Higgs boson exchange. This has been discussed quantitatively for $W^+W \to W^+W^-$ scattering in Ref. [47] and for $W^+W^+ \to W^+W^+$ in Ref. [48, 49]. In Ref. [50], Monte Carlo simulations for additional boson final states have been studied.

To begin with, the process of $W^+W^+ \to W^+W^+$ scattering has seven contributing Feynman diagrams which are shown in Fig. 2.6. The scattering amplitude of this process hence has four main parts, the quartic vertex, the triple vertices of the photon and the Z boson, respectively and the Higgs exchange interaction:

$$\mathrm{i}\,\mathcal{M} = \mathrm{i}\,\mathcal{M}^{\times} + \mathrm{i}\,\mathcal{M}^{\gamma} + \mathrm{i}\,\mathcal{M}^{Z} + \mathrm{i}\,\mathcal{M}^{H}. \tag{2.40}$$

It can be expressed through the polarisation states of the external bosons $\varepsilon_i^\mu(\lambda_i)$, where $\lambda_i = 0$ denotes longitudinal polarisations of the W^+ bosons, and $\lambda_i = \pm 1$ correspond to the transverse polarisations. The differential cross-section for a specific polarisation state is then given as [47]:

$$\left(\frac{d\sigma}{d\theta}\right)_{\lambda_1\lambda_2\lambda_3\lambda_4} = \frac{1}{64\pi^2 s}\left|\mathcal{M}_{\lambda_1\lambda_2\lambda_3\lambda_4}\right|^2. \tag{2.41}$$

The coordinate system is chosen such that the incoming particles W_1^+ and W_2^+ with four-momentum k_1 and k_2, respectively, travel along the z-axis and get scattered into the z-y plane with the scattering angle $\theta^\star$. The outgoing particles are W_3^+ and W_4^+ with four-momentum k_3 and k_4. The kinematic reaction is sketched in Fig. 2.7.

In the centre-of-mass frame of the W^+W^+ system, the four-momenta can be written as:

$$k_1^\mu = \begin{pmatrix} E \\ 0 \\ 0 \\ p \end{pmatrix}, \quad k_2^\nu = \begin{pmatrix} E \\ 0 \\ 0 \\ -p \end{pmatrix}, \quad k_3^\rho = \begin{pmatrix} E \\ 0 \\ p\sin\theta^\star \\ p\cos\theta^\star \end{pmatrix}, \quad k_4^\sigma = \begin{pmatrix} E \\ 0 \\ -p\sin\theta^\star \\ -p\cos\theta^\star \end{pmatrix}, \tag{2.42}$$

and the longitudinal polarisation vector at rest $\varepsilon^\mu(\lambda = 0) = (0, 0, 0, 1)^\top$ transforms to:

$$\varepsilon_1^\mu(0) = \frac{1}{m_W}\begin{pmatrix} p \\ 0 \\ 0 \\ E \end{pmatrix}, \; \varepsilon_2^\nu(0) = \frac{1}{m_W}\begin{pmatrix} p \\ 0 \\ 0 \\ -E \end{pmatrix}, \; \varepsilon_3^\rho(0) = \begin{pmatrix} p \\ 0 \\ E\sin\theta^\star \\ E\cos\theta^\star \end{pmatrix}, \; \varepsilon_4^\sigma(0) = \begin{pmatrix} p \\ 0 \\ -E\sin\theta^\star \\ -E\cos\theta^\star \end{pmatrix}, \tag{2.43}$$

for the two incoming and two outgoing particles. The matrix elements for the different contributions read [48]:

$$\mathrm{i}\,\mathcal{M}^\times = -g_W^2\left[(\varepsilon_1\varepsilon_3)(\varepsilon_2\varepsilon_4) + (\varepsilon_1\varepsilon_4)(\varepsilon_2\varepsilon_3) - 2(\varepsilon_1\varepsilon_2)(\varepsilon_3\varepsilon_4)\right], \tag{2.44a}$$

$$\begin{aligned}\mathrm{i}\,(\mathcal{M}^\gamma + \mathcal{M}^Z) = -g_W^2\left[\frac{\sin^2\theta_W}{t} + \frac{\cos^2\theta_W}{t - m_Z^2}\right]\Big[&-(\varepsilon_1\varepsilon_3)(\varepsilon_2\varepsilon_4)(k_1 + k_3)(k_2 + k_4) \\ &- 8(\varepsilon_3 k_1)(\varepsilon_4 k_2)(\varepsilon_1\varepsilon_2) - 8(\varepsilon_3 k_1)(\varepsilon_2 k_4)(\varepsilon_1\varepsilon_4) \\ &+ 4(\varepsilon_3 k_1)(\varepsilon_2\varepsilon_4)\varepsilon_1(k_2 + k_4) + 4(\varepsilon_4 k_2)(\varepsilon_1\varepsilon_3)\varepsilon_2(k_1 + k_3)\Big],\end{aligned} \tag{2.44b}$$

$$\mathrm{i}\,\mathcal{M}^H = -g_W^2\frac{m_W^2}{t - m_H^2}(\varepsilon_1\varepsilon_3)(\varepsilon_2\varepsilon_4), \tag{2.44c}$$

and in addition the u-channel contributions for $\mathcal{M}^\gamma + \mathcal{M}^Z$ and $\mathcal{M}^H$ which are obtained by the replacement of $k_3 \leftrightarrow k_4$ and $t \leftrightarrow u$ simultaneously. They incorporate the full kinematic and polarisation information. The quantities t, u, and s are the Mandelstam variables:

$$s = (k_1 + k_2)^2 = 4E^4, \tag{2.45}$$

$$t = (k_1 - k_3)^2 = -2p^2(1 - \cos\theta^\star), \tag{2.46}$$

$$u = (k_1 - k_4)^2 = -2p^2(1 + \cos\theta^\star). \tag{2.47}$$

By calculating the longitudinal scattering amplitudes from Eq. (2.44a) with the polarisation vectors from Eq. (2.43), it can already be seen that each external W^+ boson adds a factor of E/m_W to the amplitude. Already here it is obvious that without cancellations the longitudinal scattering amplitude rises strongly with energy, violating unitarity eventually. In order to see the high-energy behaviour when $\sqrt{s} = m_{WW} \gg 2m_W$, the amplitudes can be expanded in terms of E/m_W. Computing and simplifying the matrix elements with all necessary ingredients then results in:

$$\mathrm{i}\,\mathcal{M}^\times = g_W^2\left[\frac{E^4}{m_W^4}(6 - 2\cos^4\theta^\star) - 4\frac{E^2}{m_W^2} + \mathcal{O}(E^0)\right], \tag{2.48a}$$

$$\mathrm{i}\,(\mathcal{M}^\gamma + \mathcal{M}^Z) = g_W^2\left[\frac{E^4}{m_W^4}(-6 + 2\cos^4\theta^\star) + 3\frac{E^2}{m_W^2} + \mathcal{O}(E^0)\right], \tag{2.48b}$$

$$\mathrm{i}\,\mathcal{M}^H = g_W^2\left[\frac{E^2}{m_W^2} + \mathcal{O}(E^0)\right], \tag{2.48c}$$

It can be seen that the cross-section for the quartic and triple gauge boson interactions individually grow with $E^4 \sim s^2$. However, after adding all pure gauge boson interaction terms in the expansion leaves the resulting amplitude proportional to $E^2 \sim s$. The inclusion of the Higgs interaction contributions cancels furthermore the E^2 dependencies. The resulting SM amplitude shows a $\sim 1/s$ dependency [47]. This behaviour has been presented for the $W^+W^- \to W^+W^-$ scattering case in Ref. [47], and is shown in Fig. 2.8. As we have seen, qualitatively similar results are obtained for the $W^+W^+ \to W^+W^+$ scattering case. Fig. 2.9 shows the universal importance of the Higgs exchange processes in massive VBS. Interestingly, the energy range at which the effect of the cancellations is destroyed depends on the specific boson initial and final state.

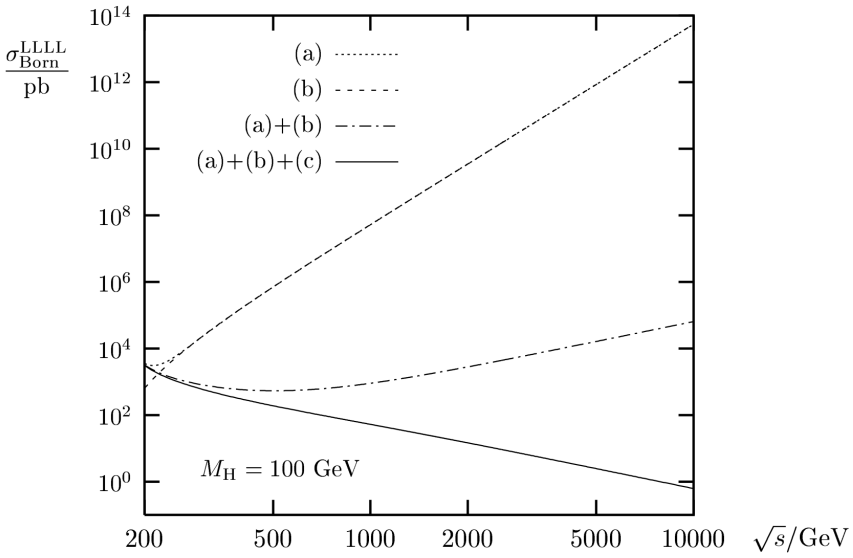


Figure 2.8: Cross-section of longitudinally polarised gauge-boson scattering in the $W^+W^- \to W^+W^-$ channel as a function of the centre-of-mass energy $\sqrt{s}$ for different (sub-)sets of the diagrams contributing in the SM. The cross-section rises dramatically for the individual contributions of the triple (a) and quartic (b) gauge boson interactions. The phenomenon of gauge cancellation can be shown when considering both processes together, yet still exposing a rise of the cross-section at large energies. Eventually, the Higgs exchange contribution (c) makes the SM cross-section physically solid without unitarity violation in the high-energy regime. Figure taken from Ref. [47].

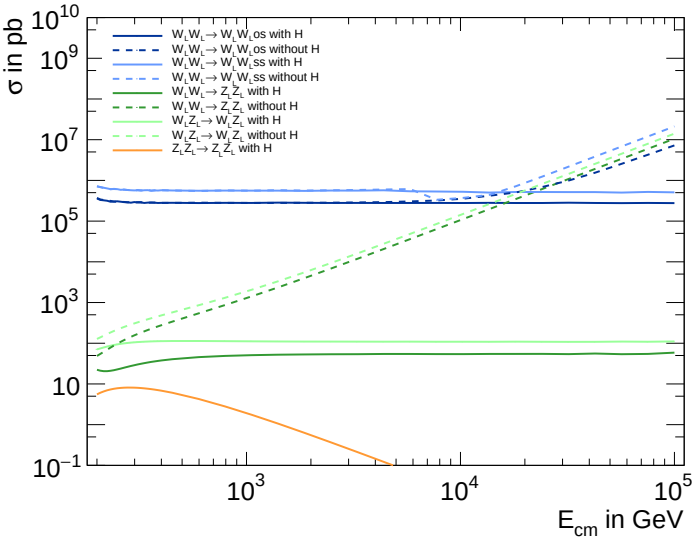


Figure 2.9: Cross-section of the polarised gauge-boson scattering in all possible massive boson final states $V_LV_L \to V_LV_L$ as a function of the centre-of-mass energy E_{CM} with and without including the Higgs exchange contributions. Solid lines show the SM case with the Higgs boson, dashed lines the case without the Higgs boson contributions. Figure taken from Ref. [50].

2.3 Effective-Field-Theory Approach

The SM, as has been pointed out previously and in more detail in Section 2.1.5, features some unsolved puzzles. These mysteries push for investigations of manifold BSM scenarios that tackle any desired aspect of them. The aim of this work is to profoundly examine VBS and incidentally quartic couplings of electroweak vector bosons. With the contributions to electroweak VBS in mind (see Section 2.2.2), new physics scenarios can be explored which extend the electroweak gauge structure of the SM or affect the EWSB mechanism. Popular extensions of the spontaneous symmetry breaking sector of the SM include additional Higgs multiplets, for example in the MSSM[4] [51]. These are compatible with the discovery of a light Higgs boson of mass 125 GeV, and could as well solve the mass problem in a $SU(2)_L \otimes U(1)_Y$ theory. Further, BSM scenarios which assume composite electroweak particles could extend the theory's collection of fundamental particles and modify the production rates of VBS [52–56]. Various models exist that could be tested, none of which has been hinted on by experimental data yet. It is a period of time in this field in which experiments give indications, where the search for new signs is most promising.

Given this to-date situation, a convenient strategy for building a BSM model ought to be as model-independent as possible and should make just a few generic assumptions. The framework of Effective Field Theories serves these requirements as a quantum field theory that describes the new phenomena in a restricted range of validity, the energy range in the case at hand. As such, it is a simplified version of a full theory which is yet to be unknown. The so-called bottom-up EFT approach parametrises extensions of the theory such that new operators are added manually to the SM Lagrangian. In such a way, the SM is recovered in the low-energy regime up to the currently accessible energy range in experiments and the theory is not specific about the hidden heavy states that evolve in the high-energy limit.

First in this section, we illuminate the Fermi theory, the predecessor of the SM electroweak theory, as an example of a four-point interaction in the EFT framework. Further, key aspects of an EFT in the bottom-up approach are discussed. Eventually, the specific EFT model for the analysis of anomalous contributions to quartic interactions in VBS gets introduced.

2.3.1 Fermi's Theory of Weak Interactions in the EFT Formalism

Before embarking on details on the EFT formalism used in this thesis, we take a brief deflection into a historic example of a four-point interaction, Fermi's theory of the β-decay which he developed in 1933. This theory can be classified as a bottom-up approach to the weak interaction, since the weak mediator bosons, $W^{\pm}$ and Z, were not known by the time Fermi formulated his theory. The situation today is expected to be comparable, thinking of an unknown interaction which reveals itself and its mediators only at larger energies than the current experimental reach. The SM then remains the valid low-energy effective theory of this larger representation.

Not knowing the underlying theory, Fermi started by modifying the theory of QED to incorporate a formulation of the flavour changing β-decay:

$$d \to u + e^- + \nu_e.$$

Since the QED Lagrangian is flavour symmetric, any supplement describing the neutron decay as a weak, flavour-changing charged current must break this symmetry. Additionally, the interaction has to connect four fermion lines, leading to possible operators of mass dimension six. A general operator set that describes this effective four-point interaction can be written as [57]:

$$\mathcal{L}_{\text{eff}} = \sum_{f_L, f_R} s_{ijkl}(\bar{\psi}_{fi}\psi_{fj})(\bar{\psi}_{fk}\psi_{fl}) + v_{ijkl}(\bar{\psi}_{fi}\gamma^{\mu}\psi_{fj})(\bar{\psi}_{fk}\gamma_{\mu}\psi_{fl}), \tag{2.49}$$

with the sum over all fermion families f_L/R and arbitrary couplings s_{ijkl} and v_{ijkl}. Comparing with experimental results reveals that many structures can be neglected. The lowest order

[4] Minimal Supersymmetric Standard Model.

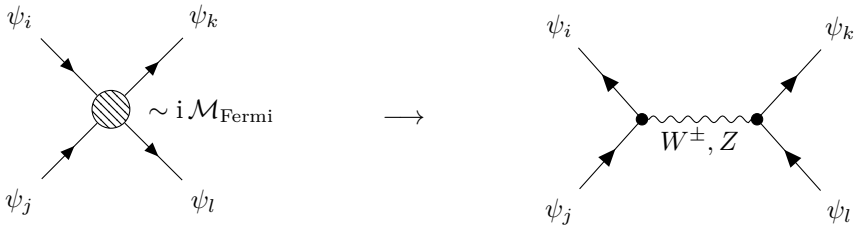


Figure 2.10: The four-fermion vertex in the Fermi theory translates into the exchange of a $W^{\pm}/Z$ boson in the full electroweak SM (here the s-channel exchange as one example Feynman diagram is shown).

operator that describe low-energetic four-fermion interactions can be expressed in terms of charged and neutral currents[5]:

$$-4\sqrt{2}G_F\left(2J_\mu^+ J^{\mu-} + J_\mu^0 J^{\mu 0}\right), \tag{2.50}$$

where Fermi only described the charged current equivalently as:

$$J_\mu^+ J^{\mu-} = 4\left(\bar{\psi}_{fi}\gamma^\mu\psi_{fj}\right)\left(\bar{\psi}_{fk}\gamma_\mu\psi_{fl}\right)^\dagger + h.c.\,. \tag{2.51}$$

The matching of Fermi's model to the SM expression for the amplitude of tree level exchange of a $W^{\pm}$ boson at the lowest order in energy is then [25]:

$$i\mathcal{M} = \left(-\mathrm{i}\,g_W\right)^2 J_\mu^+ J^{\mu-}\frac{-ig_{\mu\nu}}{q^2 - m_W^2} = -i\frac{g_W^2}{m_W^2}J_\mu^+ J^{\mu-} + \mathcal{O}\frac{q^2}{m_W^2}, \tag{2.52}$$

and we get the relation between G_F and the SM electroweak scale, introduced in Eq. (2.25). Hence, Fermi's theory is an effective description of the weak interaction at low energies which evolves into the known weak boson exchange processes at high energies, as depicted in Fig. 2.10.

2.3.2 Key Features of an EFT in the Bottom-Up Approach

An EFT is constructed as a generic parametrisation of a hidden theory at larger energy scales than the current experimental reach. It is "effective" in the sense, that it is only valid in a restricted energy range as it parametrises the low-energy effect of this new physics which manifests itself only at scales above the characteristic scale Λ. New interactions are included into the theoretical model via operators of dimensions higher than the space-time dimensions of the SM Lagrangian. The SM, with its gauge symmetry $SU(2)_L \otimes U(1)_Y$ and its breaking, appears as the low-energy limit of the new theory. Hence, the new operators involve SM fields, and obey SM symmetries and are added in the form of a series, where the expansion parameter is given by the energy scale Λ:

$$\mathcal{L}_{\mathrm{EFT}} = \mathcal{L}_{\mathrm{SM}} + \sum_{n=5}^{\infty}\sum_{i=0}^{N_n}\frac{f_i^{(n)}}{\Lambda^{n-4}}\mathcal{O}_i^{(n)}, \tag{2.53}$$

with dimension-n operators $\mathcal{O}_i^{(n)}$ and coefficients $f_i^{(n)}$. This expansion introduces an infinite number of free parameters. The conditions under which this expansion can be used are [58]:

1. There is a finite number of parameters N_n to describe the interactions at each given dimension n.
2. The coefficients for the dimension $(n-4)$ are at most of the order of $\mathcal{O}(1/\Lambda^n)$ with $E < \Lambda$.

[5]The exact definition of the currents can be derived from Chapter 2.1.2 or taken from Ref. [57].

The first condition means, at any fixed order of this expansion, only a finite subset of these parameters must be relevant, to be testable experimentally. Secondly, any contribution of a $(n+1)$ term in the expansion series cannot exceed the contribution from the n^{th} term. As the experimental accessible energy $\sqrt{s}$ approaches Λ, the contributions of operators with higher dimensions become more relevant. Eventually, the limit of validity of the EFT is approached when the expansion series breaks down. Condition two indicates, that this is not necessarily the case when $\sqrt{s} = \Lambda$, but more realistically much earlier. This implies $\Lambda \gg \sqrt{s}$.

Eventually, this expansion into higher dimensional operators mimics the effect of heavy states in the new theory at low energies, so that they leave a signature which can be studied at an energy range that is currently experimentally accessible. Said from a theorist perspective, the decoupling of heavy particles leads to the appearance of higher dimensional operators in the SM Lagrangian [58].

It can be shown that the dimension of any possible operator that fulfils the SM symmetries, i. e. Lorentz and gauge symmetries, must be even to not violate lepton- or baryon-number conservation [59]. Therefore, the Lagrangian from Eq. (2.53) can be written as:

$$\mathcal{L}_{\text{EFT}} = \mathcal{L}_{\text{SM}} + \sum_{i=0}^{N_6} \frac{f_i^{(6)}}{\Lambda^2} \mathcal{O}_i^{(6)} + \sum_{i=0}^{N_8} \frac{f_i^{(8)}}{\Lambda^4} \mathcal{O}_i^{(8)} + \dots \,, \tag{2.54}$$

and explicitly only writing terms of relevant dimensions for this work.

A few very relevant remarks may be added, concluding this introduction. Effective field theories are designed to function best when there is a large separation between the energy scale of interest (experiment, low energy) and the energy scale of the underlying dynamics (heavy states, high energy). Furthermore, when constructing an EFT the focus is not necessarily laid on the UV completeness of the theory. Hence, the EFT predictions must be manually prevented from violating unitarity, by introducing a formalism that prohibits the scattering amplitudes to raise with energy at large centre-of-mass energies $\sqrt{s}$. The possibilities to introduce such formalism are shortly outlined in the last section of this chapter.

2.3.3 The Parametrisation of Dimension-Eight EFT Operators

Model Assumptions and Motivation

One of the major goals of this work is to set limits on BSM contributions to the quartic vertices that appear in VBS processes which, as a reminder, is presented by the first Feynman diagram in Fig. 2.5. The chosen scenario in this thesis is based on Ref. [2] and has been refined in Ref. [3]. The model's assumptions are:

- The Lagrangian preserves the SM symmetries: electroweak gauge group $SU(2)_L \otimes U(1)_Y$ and Lorentz invariance;
- BSM effects are solely generated in the quartic self-coupling vertices of the electroweak gauge bosons.

The most generic and lowest dimension extension to the SM Lagrangian that meets these requirements is obtained by exclusively adding operators with mass dimension eight:

$$\mathcal{L}_{\text{EFT}} = \mathcal{L}_{\text{SM}} + \sum_{i} \frac{f_i^{(8)}}{\Lambda^4} \mathcal{O}_i^{(8)}. \tag{2.55}$$

Especially the latter of the afore-mentioned assumptions causes the model to disregard any effects due to operators with mass dimension six. Although, this group of operators already introduces BSM effects on the quartic self-couplings of the gauge boson, these are always accompanied by non-SM effects on triple self-couplings as well.

From an experimental viewpoint, this is a very reasonable choice as dimension-six operators, which generate BSM effects on triple and quartic gauge interactions, are much better constrained in measurements of diboson final states formerly at LEP [60–65] and since Run-2 further at the LHC, e. g. in Ref. [66–68]. Processes with two bosons in the final state are much more frequent (a factor of $\sim \mathcal{O}(10^5)$, cf. Fig. 2.1) than VBS processes at the LHC.

Table 2.6: Dimension-eight operators in the model of Éboli and Gonzalez–Garcia [3] and the quartic vertices each operator is contributing to [70].

	Dimension-eight operator in Ref. [3]:					
Contribution to quartic vertex:	$\mathcal{O}_{S0}$ $\mathcal{O}_{S1}$ $\mathcal{O}_{S2}$	$\mathcal{O}_{M0}$ $\mathcal{O}_{M1}$ $\mathcal{O}_{M7}$	$\mathcal{O}_{M2}$ $\mathcal{O}_{M3}$ $\mathcal{O}_{M4}$ $\mathcal{O}_{M5}$	$\mathcal{O}_{T0}$ $\mathcal{O}_{T1}$ $\mathcal{O}_{T2}$	$\mathcal{O}_{T5}$ $\mathcal{O}_{T6}$ $\mathcal{O}_{T7}$	$\mathcal{O}_{T8}$ $\mathcal{O}_{T9}$
$W^\pm W^\pm W^\pm W^\pm$	✓	✓	–	✓	–	–
$W^\pm W^\mp W^\pm W^\mp$	✓	✓	–	✓	–	–
W^+W^-ZZ	✓	✓	✓	✓	✓	–
$W^+W^-Z\gamma$	–	✓	✓	✓	✓	–
$W^+W^-\gamma\gamma$	–	✓	✓	✓	✓	–
$ZZZZ$	✓	✓	✓	✓	✓	✓
$ZZZ\gamma$	–	✓	✓	✓	✓	✓
$ZZ\gamma\gamma$	–	✓	✓	✓	✓	✓
$Z\gamma\gamma\gamma$	–	–	–	✓	✓	✓
$\gamma\gamma\gamma\gamma$	–	–	–	✓	✓	✓

Hence, looking at effects on EFT operators with mass dimension six in VBS processes would not add much additional insight in the to date experimental conditions.

From a physical as well as mathematical standpoint, however, ignoring effects of the dimension-six operators is quite a severe constraint on the underlying model. This assumption is equivalent as to set coefficients of any dimension-six operator equal to zero. As stated in Ref. [3], this can be motivated in models with "new heavy bosons which generate a tree level contribution to quartic self-couplings of the gauge boson, while its effect in the triple gauge vertex would only appear at one-loop level" [69]. Consequently, the BSM effects on the triple self-coupling vertices would be suppressed with respect to the effect on the quartic vertices.

The Dimension-Eight Operator Basis

Now, with the collection of the assumptions from above, a set of non-redundant operators can be constructed. From the over 70 Lorentz structures that have been found in Ref. [2], 17 independent operators of dimension eight can be constructed containing solely SM fields and derivatives. Tab. 2.6 summarises all possible operators and the quartic vertices they are contributing to.

The operators can be categorised in three groups, depending on their field decomposition. The group of "S"-operators comprises operators with four covariant derivatives (cf. Eq. (2.6)) acting on the Higgs field:

$$\mathcal{O}_{S0} = \left[\left(D_\mu\Phi\right)^\dagger \left(D_\nu\Phi\right)\right] \times \left[\left(D^\mu\Phi\right)^\dagger \left(D^\nu\Phi\right)\right], \tag{2.56}$$

$$\mathcal{O}_{S1} = \left[\left(D_\mu\Phi\right)^\dagger \left(D^\mu\Phi\right)\right] \times \left[\left(D_\nu\Phi\right)^\dagger \left(D^\nu\Phi\right)\right], \tag{2.57}$$

$$\mathcal{O}_{S2} = \left[\left(D_\mu\Phi\right)^\dagger \left(D_\nu\Phi\right)\right] \times \left[\left(D^\nu\Phi\right)^\dagger \left(D^\mu\Phi\right)\right], \tag{2.58}$$

hence, only affecting quartic gauge boson vertices with only longitudinally polarised boson.

It must be noted here that, in fact, the operator $\mathcal{O}_{S2}$ is the hermitian conjugate of $\mathcal{O}_{S0}$. It has not been considered until [71] and was eventually added in Ref. [3] as a separate operator. Nevertheless, this work follows the notation in Ref. [3] as this corresponds to the

model parameters that are implemented in the FeynRules [72] model for the Monte Carlo simulation of the process. Hence, this convention is an artefact of the notation which requires that the coefficients for $\mathcal{O}_{S2}$ and $\mathcal{O}_{S0}$ must always be equal, $f_{S2} = f_{S0}$, which is indicated with the use of the $S02$ subscript in this work when referring to these parameters. This reduces the 18 operators listed in Ref. [3] to 17 independent ones.

The second class of operators, the "M"-operators, contain field strength tensors[6] $\hat{W}_{\mu\nu} \equiv \sum_a W^a_{\mu\nu} \frac{\tau^a}{2}$ together with the contributions with covariant derivatives acting on the Higgs field, affecting the vertices with mixed longitudinally and transversally polarised vector bosons:

$$\mathcal{O}_{M0} = \mathrm{Tr}\left[\hat{W}_{\mu\nu}\hat{W}^{\mu\nu}\right] \times \left[(D_\rho\Phi)^\dagger (D^\rho\Phi)\right], \tag{2.59}$$

$$\mathcal{O}_{M1} = \mathrm{Tr}\left[\hat{W}_{\mu\nu}\hat{W}^{\mu\rho}\right] \times \left[(D_\rho\Phi)^\dagger (D^\mu\Phi)\right], \tag{2.60}$$

$$\mathcal{O}_{M7} = \mathrm{Tr}\left[(D_\mu\Phi)^\dagger \hat{W}_{\rho\nu}\hat{W}^{\rho\mu} (D^\nu\Phi)\right]. \tag{2.61}$$

Note here, that only those three operators are explicitly listed, which contribute to the $W^\pm W^\pm W^\pm W^\pm$ quartic vertex, the subject of study in this thesis.

The third class of operators, the "T"-operators, contain solely field strength tensors, hence affecting only quartic vertices with four transversally polarised vector bosons:

$$\mathcal{O}_{T0} = \mathrm{Tr}\left[\hat{W}_{\mu\nu}\hat{W}^{\mu\nu}\right] \times \mathrm{Tr}\left[\hat{W}_{\rho\sigma}\hat{W}^{\rho\sigma}\right], \tag{2.62}$$

$$\mathcal{O}_{T1} = \mathrm{Tr}\left[\hat{W}_{\rho\nu}\hat{W}^{\mu\sigma}\right] \times \mathrm{Tr}\left[\hat{W}_{\mu\sigma}\hat{W}^{\rho\nu}\right], \tag{2.63}$$

$$\mathcal{O}_{T2} = \mathrm{Tr}\left[\hat{W}_{\rho\mu}\hat{W}^{\mu\sigma}\right] \times \mathrm{Tr}\left[\hat{W}_{\sigma\nu}\hat{W}^{\nu\rho}\right]. \tag{2.64}$$

Again here, only those operators are listed which make a contribution to the $W^\pm W^\pm W^\pm W^\pm$ quartic vertex. It can easily be seen from the field content, that the extra operators do not contribute to this vertex, since they contain at least one field strength tensor $B_{\mu\nu}$. The exact mathematical form of the full set of operators in this model can be found in Ref. [3, 71].

Unitarity in Effective Field Theories

As outlined in Sec. 2.2, electroweak Vector Boson Scattering processes involving massive bosons include fundamental interactions such as the triple and quartic electroweak gauge couplings, but also the exchange of the Higgs boson. With these both, the theoretical implementation of the gauge structure of the SM and the EWSB mechanism shape the VBS process. Through the interplay of amplitudes from the possible Feynman diagrams in the SM, the high-energy behaviour of the VBS process receives exact cancellations, which renders the total amplitudes finite. Models describing new physics in the quartic coupling of vector bosons destroy the precise cancellation, which leads to a rising scattering amplitude and hence its violation of unitarity at large energies.

EFTs are rarely formulated as UV complete theories. Hence, the unitarity violating behaviour remains part of the theory unless it is manually prevented. In the case of the dimension-eight EFT model under study, unitarity is violated at lower energies than the scale Λ. The energy for which a certain partial wave of a scattering process violates unitarity can be calculated. The unitarity bound is defined as the energy at which one of the decomposed partial waves of the scattering amplitude violates unitarity. It depends on the analysed scattering process and the considered parameter set f_i/Λ^4. Through the latter, it also depends on the new physics scale Λ. For the EFT model and the $W^\pm W^\pm$ scattering process considered here, the unitarity bounds for the one-dimensional scenario where solely one EFT parameter is non-vanishing, are calculated in Ref. [4].

Different procedures exist on how the violation of unitarity can be prevented. Several have been used in the interpretation in terms of aQGC of experimental data at the LHC so far. While it was common to use form factor [73, 74] or K/T-matrix [71, 75–77] unitarisation

[6] As a reminder, $W^a_{\mu\nu}$ is the field strength tensor as defined in Eq. (2.10) and τ^a being the Pauli matrices.

methods in publications based on the Run-1 data-taking period of the ATLAS collaboration, the focus has now been shifted towards a simpler approach. The reason for this is mainly that these formerly used procedures introduce additional parameters. In the case of VBS and dimension-eight EFT extensions, the unitarisation schemes have large impact on differential and total cross-sections (cf. e. g. Ref. [13]). Hence, the parameters introduced by the unitarisation scheme become part of the signal model and dependencies on these, both on the chosen process and phase-space, cannot be easily reconstructed by theorists.

As a result, this work follows a different strategy which got incorporated into LHC analyses in recent times and follows the "Recommendations from the Anomalous Gauge Coupling Taskforce" initiated by the LHC EW working group [78]: the so-called "clipping" approach. This strategy will be explained later in Chapter 9 together with an overview of previous analyses and their use of unitarisation methods when setting limits on aQGC or dimension-eight EFT parameters.

Chapter 3

Experimental Setup

The experimental measurements presented in this thesis are conducted with the ATLAS experiment installed at the Large Hadron Collider (LHC), which is hosted by the European Organisation for Nuclear Research (CERN).

This chapter begins with a brief introduction to the LHC and CERN. Thereafter, the specifics of the ATLAS detector are examined by shortly summarising the purpose and technical details of the subdetectors. Further, this chapter enlightens the basic concepts of data-taking with the ATLAS detector: triggering, data quality assessment, and luminosity measurements. Lastly, the procedure of reconstructing physics objects from the detectors' signatures is briefly outlined and specified.

Most of this chapter's content is taken from the design reports of the LHC and the ATLAS detectors in Refs. [79] and [80], respectively. In-depth information on the design, construction, and operation can be found therein.

3.1 The Large Hadron Collider

CERN

The CERN was founded in 1954 as "Centre Européen pour la recherche Nucléare" near Geneva, at the border between France and Switzerland. By the time of the establishment, the council counted 12 European member countries. To this date, the organisation has 23 member states, with Serbia having joined most recently in 2018, and several associate members and observers. Since 2016 Fabiola Gianotti is the first female Director-General. With the LHC and its current experiments, it hosts the most powerful particle accelerator and collider to date. However, many other accelerator and non-accelerator based experiments, as well as design studies for future colliders and detectors are constituents of CERN's active research programme, making it the leading international research facility for particle and high-energy physics.

Technical Details

The LHC is a circular proton and heavy ion (Pb) accelerator and collider with a circumference of almost 27 km. Its tunnel is situated between 45 m and 170 m underground, and formerly hosted the Large Electron-Positron Collider (LEP). The LHC started to operate in 2008 as an accelerator of unprecedented energy and luminosity range. It accelerates two concentric particle beams, which travel in opposite direction in separate beam pipes. Before reaching the LHC, the particles are pre-accelerated in various accelerators of increasing size and energy, forming an entire system of acceleration devices. The full complex of accelerator facilities is sketched in Fig. 3.1 [81]. A number of eight cavities per beam accelerate the particles along the path. Almost 10000 magnets form and steer the beams inside the beam pipes, among these 1232 superconducting dipole magnets with a magnetic field strength of maximum 8.3 T which allow for the bending of the trajectory of the particle beams. They are operated at a temperature of 1.9 K induced by a cryogenic system filled with super-fluid helium-4.

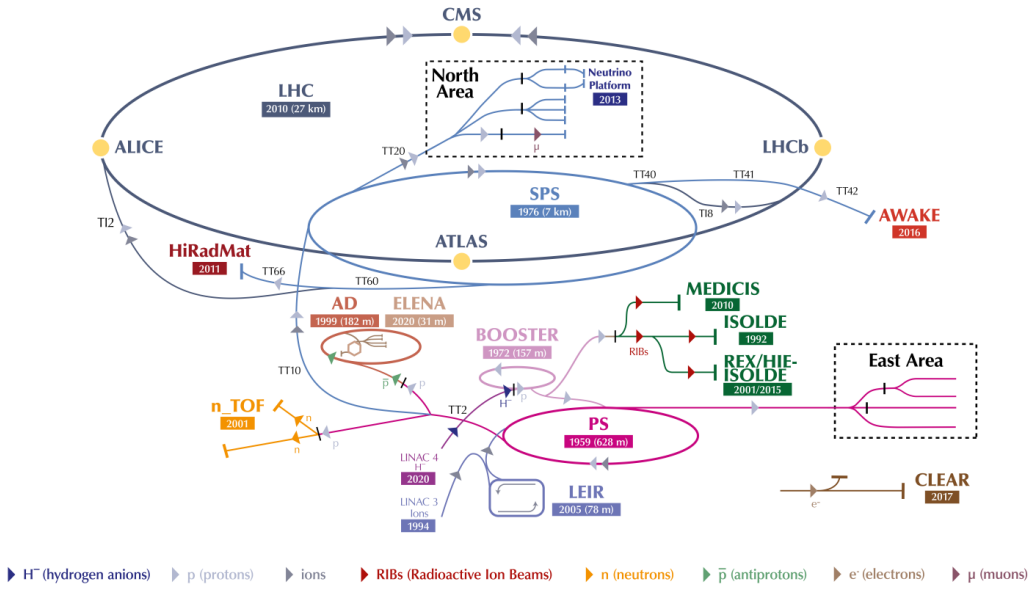


Figure 3.1: Scheme of the CERN accelerator complex. Figure taken from Ref. [81].

Table 3.1: Summary of parameters of the LHC proton-proton Runs 1 and 2, together with their design values, taken from Ref. [79].

Technical parameter	Value		
	Run 1 2010 - 2012	Run 2 2015 - 2018	Design
Centre-of-mass energy $\sqrt{s}$ (TeV)	7/8	13	14
Bunch spacing (ns)	50	25	25
Number of bunches (peak)	1380	2544	2808
Bunch population (10^{11} p)	1.6	1.25	1.15
Peak instantaneous luminosity ($10^{34}\,\mathrm{cm^{-2}s^{-1}}$)	0.77	2.1	1
Delivered total integrated luminosity ($\mathrm{fb^{-1}}$)	5.5/22.8	156	–

This is required to ensure superconductivity, inevitable to reach this immense magnetic field strength.

The beam pipes intersect at the location of the four major experiments: ALICE [82], ATLAS [80], CMS [83], LHCb [84]. Further experiments at the LHC are LHCf, TOTEM, MoEDAL, and FASER.

LHC Operation and Schedule

The LHC is designed to collide two proton beams at a centre-of-mass energy of 14 TeV with peak instantaneous luminosity of $10^{34}\,\mathrm{cm^{-2}s^{-1}}$. Further design parameters are summarised in Tab. 3.1 together with the actually achieved values in the two runs of the LHC up to date. The first phase of data-taking, Run 1, was conducted between the years 2010 and 2012, followed by a Long Shutdown (LS1) of approx. two years. The second round of data-taking, Run 2, started in spring 2015 and concluded at the end of 2018, interrupted only by the usual technical stops at the turn of the years. A full schedule of the accomplished and future LHC data-taking periods and shutdowns is sketched in Fig. 3.2. Currently, the LHC and its experiments are in Long Shutdown 2 (LS2) where major updates of the accelerators, as well



Figure 3.2: Outline of the LHC schedule as of 2020, modified from Ref. [85].

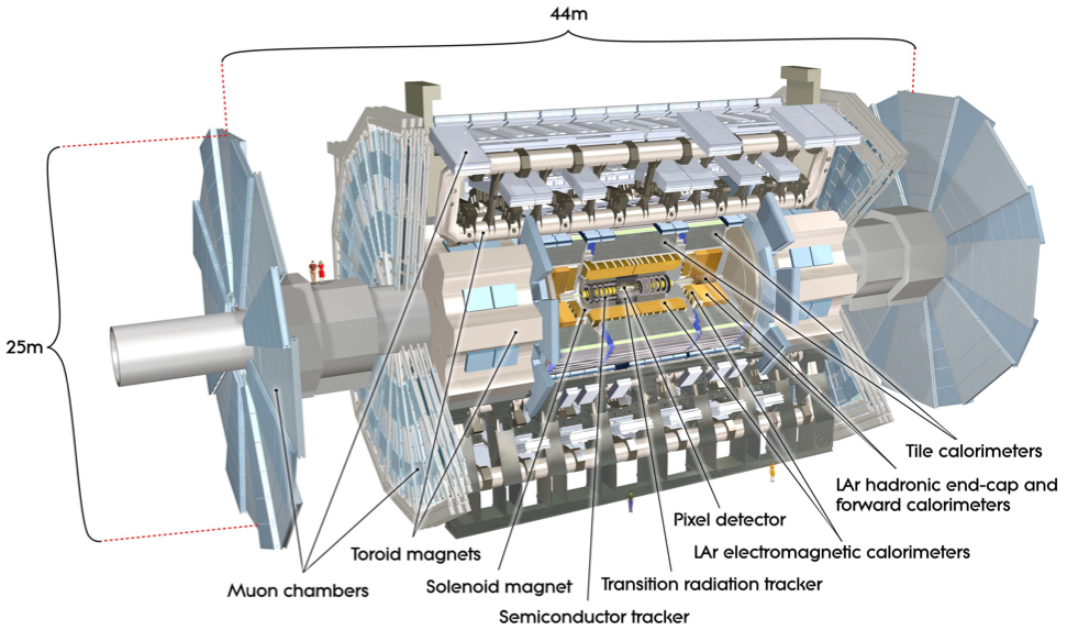


Figure 3.3: Schematic view of the ATLAS detector at the LHC, taken from Ref. [80].

as the experiments, are planned.

While the design energy has not been reached in the two previous runs, the design peak instantaneous luminosity has been more than doubled in Run 2. It is planned to reach full design energy in the next data-taking period, Run 3, which is scheduled to begin in 2022. After Run 3, the LHC and the experiments are planned to be upgraded to prepare for the high-luminosity phase of the accelerator.

This work is based on a subset of data taken in the years 2015 and 2016 of the Run 2 data-taking period. It aims at enhancing the knowledge in the field of VBS gained in Run 1, see e. g. in Ref. [13, 86].

3.2 The ATLAS Detector

The ATLAS detector is a general purpose detector designed both for the precise measurement of the properties of known particles and for the search for new physic's phenomena in the directions described in the previous section. As such a machine, it is able to detect and reconstruct all groups of elementary particles with distinct signature, except neutrinos, which interact too weakly to be measured in the ATLAS detector. It is designed, constructed and run by the ATLAS collaboration, which currently counts over 5500 members of 103 nationalities and 253 institutes [87].

The construction, sketched in Fig. 3.3, is realised in concentric layers around the central beam pipe adding up to a highly hermetic, cylindrical detector – 44 m in length and 25 m

in diameter. Featuring a central barrel region and two end-cap regions on either side of the installation, it is built symmetric in the forward and backward direction with respect to the interaction point. There are four major layers or detection elements: the inner detector, the electromagnetic and the hadronic calorimeters, and the muon spectrometer. The inner detector and the muon spectrometer are both tracking devices immersed in magnetic fields to measure the momentum of charged particles. The magnetic system comprises a solenoid which encompasses the inner detector, and three large toroidal arrangements, one in the barrel region and two on either end-cap side. The toroids provide the magnetic field for the muon spectrometer measurements and, with the octuple symmetric shape, guided the appearance of the detector. Altogether, the detector has approx. 100 million electronic channels.

The essential purpose remains the identification and reconstruction of the kinematics of high energetic collisions, which can be done by precisely measuring the energies, transverse momenta and charges of particles. Beyond this substantial requisites, the main design requirements have been driven by the physics goals and limited by the times technical advancement. Shortly summarised, they have been the following [80]:

- Fast, radiation-hard electronics and sensor elements, and high detector granularity are needed to handle the particle fluxes and to reduce the influence of overlapping events (pile-up).
- Large acceptance in pseudorapidity η with almost full azimuthal angle (Φ) coverage is required.
- Good charged-particle momentum resolution and reconstruction efficiency in the inner tracker are essential, as well as the observation of secondary vertices with vertex detectors close to the interaction region.
- Very good electromagnetic calorimetry for electron and photon identification and measurements, complemented by full-coverage hadronic calorimetry for accurate jet and missing transverse energy measurements, are important requirements.
- Good muon identification and momentum resolution over a wide range of momenta are fundamental requirements.
- Highly efficient triggering on low transverse-momentum objects with sufficient background rejection, is a prerequisite to achieve an acceptable trigger rate for most physics processes of interest.

The choices of materials for the various subdetectors depends essentially on the detection mechanisms of the different particles they are to measure. The following sections summarise the specifics of the main subsystems. Variables and quantities that are referring to the detector layout and operation and are used throughout this thesis, are summarised on page xiv.

3.2.1 The Tracking Systems

Reconstructing the path of a particle through the detector provides a powerful means to determine the charge and transverse momentum of a charged particle. Tracking detectors are hence a valuable tool in high energy physics experiments. The ATLAS detector has two main tracking systems, the inner detector at the very centre close to the beam pipe, as well as the muon spectrometer which builds the outer rim of the detector. These detector types utilise the interaction via ionisation of charged particles with the detector material, often ionising gases or silicon devices. Only charged particles interact via the process of ionisation. For energetic particles it is mostly non-destructive, allowing to build tracking detectors of multiple layers of active material, each recording the passage of a charged particle. Its trajectory can hence be reconstructed with special tracking algorithms.

The installation of a suitable magnetic system enables transverse momentum[1] and charge measurement through the Lorentz force. In the magnetic field with strength B, charged

[1] The definition of transverse momentum can be found on page xiv.

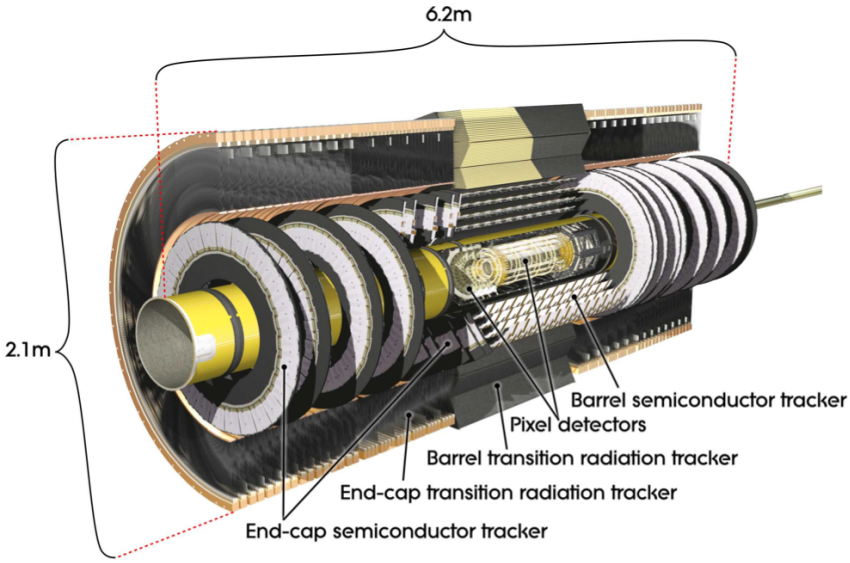


Figure 3.4: Schematic view of the ATLAS inner detector with all subcomponents and its overall dimensions, taken from Ref. [80].

particles trajectories bend perpendicular to the magnetic field lines. From the curvature of the particle (with radius r_T perpendicular to the beam pipe), the transverse momentum p_T can be deduced:

$$p_\mathrm{T} = |q|\, B r_T. \tag{3.1}$$

The direction of the curvature reveals the sign of the charge of the particle under study.

The Inner Detector

The inner detector is designed to measure the transverse momentum and charge of charged particles in a region which is exposed to huge particle fluxes. It has to be hermetic and robust against high irradiation doses and at the same time exhibit a fine granularity for high-resolution measurements of momenta and vertex positions, as well as solid pattern recognition for track reconstruction. Nominally, owing to the solenoidal magnetic field of 2 T, charged tracks with momenta as low as 0.5 GeV can be reconstructed. The inner detector is composed of three independent types of subdetectors. The transition radiation tracker in the outermost region complement the two inner semiconductor devices, a silicon pixel detector and a strip detector. A scheme of the inner detector can be seen in Fig. 3.4. The specific detector parts are arranged in layers, in the barrel region as concentric cylinders around the beam pipe and in the end-cap region as disks perpendicular to the beam direction. The inner detector is not part of the first stage of the trigger, the hardware component. The features of the three distinct detector components are summarised subsequently.

Closest to the beam pipe, in the region with the highest density of tracks, the silicon pixel detector is situated. Consequently, it has the highest granularity, with a minimum pixel sensor layout of $50 \times 400\,\mu\mathrm{m}^2$ in size. It consists of four discrete pixel layers. The innermost insertable b-layer (IBL) has only been added in LS1 [88]. A zoomed-in view of the upgraded pixel detector is illustrated in Fig. 3.5. The pixel detector covers a region of $|\eta| < 2.5$ in pseudorapidity. Each particle typically traverses three pixel layers, which exhibit an accuracy of $10\,\mu\mathrm{m}$ in $R - \phi$ and $115\,\mu\mathrm{m}$ in z or R for the barrel or end-cap region, respectively. The number of readout channels in all layers sums up to approximately 80.4 million.

The middle part of the inner detector is the multi-layered semi-conductor tracker (SCT). It is a silicon strip detector with microstrips arranged in discrete layer pairs with a slight tilt of 40 mrad against each other. This layout allows for measurements in both $(R - \phi)$ and z directions simultaneously in each of the layers. The strip pitch averages to $80\,\mu\mathrm{m}$. The

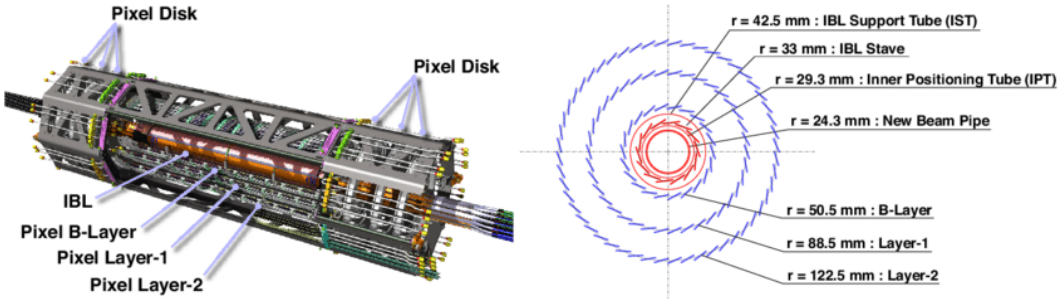


Figure 3.5: Schematic view of the ATLAS pixel detector with the insertable b-layer (IBL), the fourth and innermost layer, upgraded in LS1. Figure taken from Ref. [89].

resulting space point accuracy of this assembly is 17 μm in $R-\phi$ and 580 μm in z direction in the barrel and R direction in the end-cap region, respectively. Each particle crosses four double layers of the SCT with a pseudorapidity coverage of $|\eta| < 2.5$, alike to the pixel detector. Circa 6.3 million readout channels constitute the electronic structure of the SCT.

The outermost component of the inner detector is the Transition Radiation Tracker (TRT), a straw tube detector with many layers of straws. The tubes are 4 mm in diameter with a 0.03 mm diameter gold-plated tungsten wire in the centre and filled with a xenon-based gas mixture. In contrast to the silicon detectors, particles traverse typically 36 straw tubes of the TRT in a pseudorapidity range of $|\eta| < 2.0$. Moreover, it provides, per construction, only information in the $R-\phi$ plane. The achieved accuracy is approx. 130 μm per straw. The straw tubes of the TRT are enclosed by a material that fosters the generation of transition radiation[2]. The detection of this transition radiation enables the discrimination between electrons and other types of typically heavier particles, improving the electron identification over a range of energies between 0.5 GeV and 150 GeV. Together with the large number of hits per particle, the TRT increases the robustness of the particle identification and pattern recognition provided by the silicon tracking detectors as well as the calorimeters. The TRT has a relatively small number of readout channels compared to the other inner detector parts, approx. 350000 .

Altogether the inner detector components synergise for a robust track reconstruction, electron identification and high-precision momentum and vertex measurement. The inner detector in total reaches a transverse momentum resolution of

$$\frac{\sigma_{p_\mathrm{T}}}{p_\mathrm{T}} = 0.05\% \; p_\mathrm{T}(\mathrm{GeV}) \oplus 1\%. \tag{3.2}$$

The measurement of the curvature in a magnetic field gives the dependence in the first term, while the second term in dominated by multiple scattering effects.

The Muon Spectrometer

The muon spectrometer is designed to measure the momentum and charge of muons. As the inner detector, it is a tracking device with multiple layers and components. Due to their properties (mass and interaction behaviour)[3] muons are the almost only (known) particles which, by construction, can escape the calorimeters, the middle layer of the ATLAS detector (see next section). Exception are certainly neutrinos which cannot be detected at all by the detector and very energetic particles. For this reason, the muon spectrometer is incorporated as the outmost shell of the ATLAS detector and provides complementary measurements compared to the inner tracker.

[2]Transition radiation is produces when a relativistic, charged particle transits the surface between two media with differing dielectric constants. The properties of the generated transition radiation are, among others, dependent on the mass of the particle.

[3]Muons are leptons, 200 times heavier than electrons. They interact primarily via ionisation in contrast to electrons who, because of their smaller mass, lose most of their energy through bremsstrahlung. Thus, muons loose only a small fraction of their energy in the preceding detector layers.

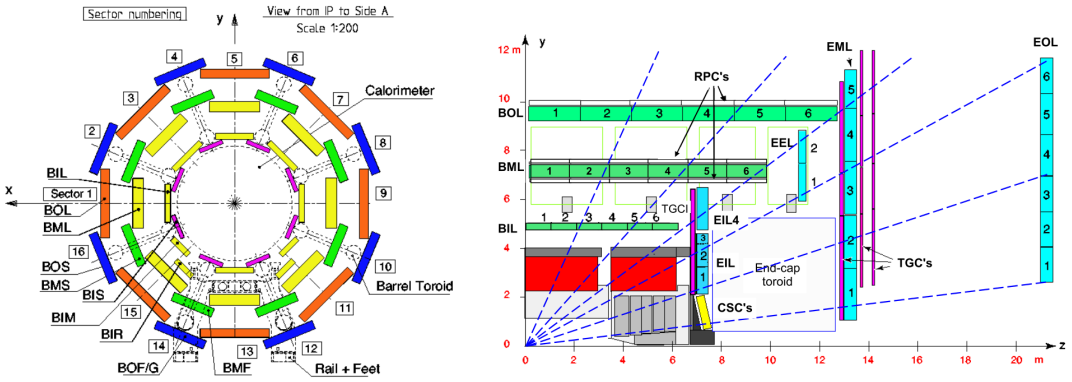


Figure 3.6: Cross-sectional, schematic view of the ATLAS muon spectrometer in the $R-\phi$ plane (non-bending plane) in the barrel region (left) and the $R-z$ plane (bending plane, right), with all subcomponents and its overall dimensions. Figure taken from Ref. [80].

The muon spectrometer is constructed both to precisely measure properties of and provide trigger information for muons. It is equipped with a toroidal, air-filled magnet system composed of three magnets, one barrel and one end-cap magnet on either side of the detector. The magnetic field is highly complex yet designed to run predominantly perpendicular to the muon trajectories, defining a bending plane in $R-z$ and a non-bending plane $R-\phi$. The air-core system minimises effects from multiply scattered muons. The whole muon instrumentation consists of four different types of ionisation chambers. Monitored Drift Tubes (MDT) and Cathode Strip Chambers (CSC) provide high-precision tracking, while Resistive Plate Chambers (RPC) and Thin Gap Chambers (TGC) are included separately for triggering and measurement of the space component in the non-bending direction. The overall coverage in pseudorapidity is $|\eta| < 2.7$ for tracking and $|\eta| < 2.4$ for triggering. The entire system has over one million readout channels. It is arranged in three general layers in both, the barrel ($|\eta| < 1.05$) and end-cap region. Each layer has a different composition of instrumentation owing to the divers experimental environment and performance goals. The overall layout and position of the sub-elements is shown in Fig. 3.6 and detailed in [80].

The MDTs typically provide 20 hits per track with a resolution in the bending direction z of 35 μm per chamber. The maximum drift time is 700 ns, insufficient for triggering. CSCs are employed in the very forward region ($2.0 < |\eta| < 2.7$) and innermost layer, where the muon track density and particle rates are highest. These chambers have a higher granularity and rate capability, and permit to measure both, R and z coordinates. The per chamber resolution is 40 μm in R and 5 mm in z direction.

One of the major limiting aspects of the precision momentum measurement lies in the alignment of the muon chambers within each other and over the large area of operation in the detector. A synergy between optical alignment systems and track-based algorithms ensure to achieve the relative resolution goal: approx. 10% for muons with transverse momentum of 1 TeV, and solid measurement capability down to approximately 3 GeV in p_{T}.

The trigger system is composed of RPCs in the barrel region inside $|\eta| < 1.05$, and TGCs in the pseudorapidity region $1.05 < |\eta| < 2.4$, where a higher granularity and rate capability is desired. The location of the chambers of the trigger system can be seen on the right of Fig. 3.6. Both types have a timing spread below 25 ns, suitable for the main purposes of the trigger system [80]:

- discrimination on muon transverse momentum;
- bunch-crossing identification;
- fast and coarse tracking information;
- robustness towards random hits due to n/γ-background in the experimental hall.

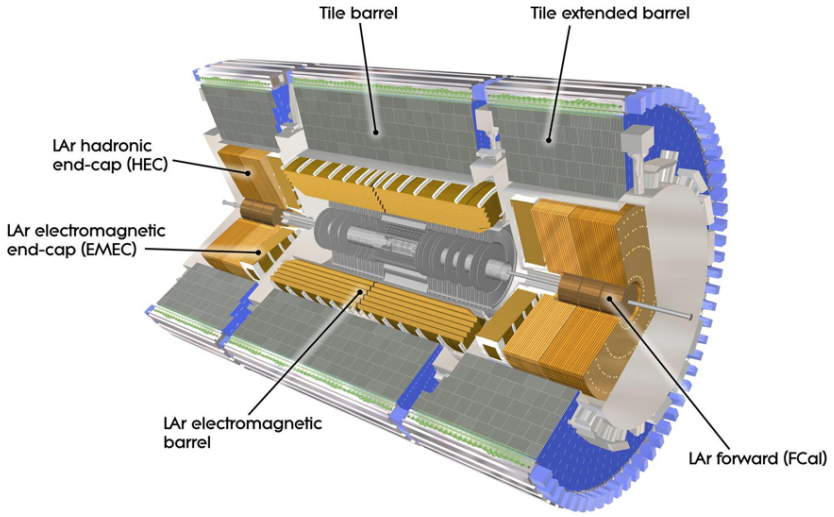


Figure 3.7: Schematic view of the ATLAS calorimeter system, taken from Ref. [80].

3.2.2 The Calorimeters

The energy of a particle, electromagnetically charged or neutral, can be measured via total absorption in calorimeters. They are specially designed for different types of particles, according to whether the particle primarily interacts via the electromagnetic or strong force. The fundamental key aspect is the way of interaction with dense matter.

Electrons, positrons, and photons above a certain energy threshold (a few MeV) primarily interact via bremsstrahlung and pair production, respectively, producing electromagnetic showers. Hadrons form hadronic showers by disintegration into secondary particles, mainly light mesons, photons, or muons. Hadronic showers, as a result, are much more complex and have an electromagnetic shower component. The longitudinal shower development, besides the incident energy of the particle, depends on the radiation or nuclear interaction length[4], respectively, for electromagnetic and hadronic showers. This quantity is substantially larger for hadrons than electromagnetically interacting particles, which is the reason for stacking the electromagnetic in front of the hadronic calorimeter. As explained in the previous section, due to their larger mass, muons are not stopped by the calorimeters, which are, as a consequence, placed between the inner detector and the muon spectrometer. The thickness of the calorimeter must be chosen such that hadronic showers are expected to be fully contained inside the active material to ensure good energy resolution as well as prevent leakage into the muon system.

The ATLAS calorimeter system consists of a combination of different sampling calorimeters with varying absorption and two main detection materials which alternate in numerous layers. A sketch is shown in Fig. 3.7. The main parts are the electromagnetic barrel, the hadronic barrel and extended barrel, the end-cap electromagnetic (EMEC) and hadronic (HEC) calorimeters, and closest to the beam pipe and most forward, the forward calorimeter (FCal). A highly hermetic construction is important for the energy measurement of hadronic jets, formed by quarks or gluons, as well as the determination of the missing transverse energy $\vec{E}_T^{\,\text{miss}}$ in the event with adequate resolution.

Besides, in the barrel region of the hadronic calorimeter where scintillation tiles are used, the active detection medium is liquid argon. This choice arises from the intrinsic linear behaviour and stability in response, as well as its radiation hardness. The absorption material, a dense metal such as lead, steel or tungsten, as well as its thickness varies from

[4]The radiation length X_0 is defined for particles that interact via the electromagnetic force as the mean distance the particle has to travel for it to loose all but $1/e$ of its energy. For photons, it is defined as 7/9 of the mean free path for pair production. The mean free path between two inelastic interactions for hadrons is called interaction length λ.

Table 3.2: Relative energy resolution requirements for the different calorimeter components of the ATLAS detector [80].

Calorimeter component	Target resolution
Electromagnetic calorimeter	$\sigma_E/E = 10\,\%/\sqrt{E(\mathrm{GeV})} \oplus 0.7\,\%$
Hadronic calorimeter	$\sigma_E/E = 50\,\%/\sqrt{E(\mathrm{GeV})} \oplus 3\,\%$
Forward calorimeter	$\sigma_E/E = 100\,\%/\sqrt{E(\mathrm{GeV})} \oplus 10\,\%$

part to part and boosts the propagation of the showers. Except for the FCal, the absorber geometry is accordion-shaped. The sampling implementation enforces the estimation of the energy deposited in the non-active material, therefore diminishing the energy resolution.

The total pseudorapidity coverage is $|\eta| < 4.9$, with multiple transition regions, so-called crack regions, between the calorimeter parts at $1.375 < |\eta| < 1.52$, $2.47 < |\eta| < 2.5$, and $3.16 < |\eta| < 3.35$. The coverage in Φ is without any cracks around the beam pipe.

At $\eta = 0$, the thickness of the electromagnetic and hadronic active calorimeter is above $22\,\mathrm{X}_0$ and $9.7\,\lambda$, respectively, and approximately $24\,\mathrm{X}_0$ and $10\,\lambda$ in the end-cap and forward regions.

The number of layers and the granularity of each calorimeter component decreases with pseudorapidity. Full details can be found in Tab. 1.3 in [80]. In the region of $|\eta| < 2.5$ each calorimeter part is equipped with three layers and fine granularity complementing the high-precision measurement of the inner tracker. In this region, signatures and directional information, from e. g. longitudinal shower evolution, from the calorimeters, can be matched to track information obtained in the inner detector. For triggering, readout channels are grouped together to so-called trigger towers, reducing the granularity to $\Delta\eta \times \Delta\Phi = 0.1 \times 0.1$ for the fast hardware-based trigger system. In total, the calorimeter instrumentation has almost 200000 channels.

One crucial feature of calorimeters is the energy resolution ΔE, statistically dominated and hence proportional to the full-width-at-half-maximum (FWHM) of a Gaussian-like signal peak. It is a performance measure that quantises the capability to differentiate two particles nearby energies. A parameterisation of the relative energy resolution of calorimeters is given by:

$$\frac{\Delta E}{E} = \frac{a}{\sqrt{E(\mathrm{GeV})}} \oplus b \oplus \frac{c}{E(\mathrm{GeV})}, \tag{3.3}$$

where the contribution of each term is to be added in quadrature to obtain total relative resolution. The first, called stochastic term, includes effects from intrinsic statistical fluctuations due to sampling and quantum fluctuations. The latter contains the intrinsic limitation of the resolution due to quantum physical fluctuations in the shower evolution. Ionisations in the pure physical shower process fluctuate according to a Poisson distribution, and the number of secondary particles produced is proportional to the incident energy. It follows:

$$\frac{\Delta E}{E} \propto \frac{\sqrt{N}}{N} = \frac{1}{\sqrt{N}} \quad \longrightarrow \quad \frac{\Delta E}{E} \propto \frac{1}{\sqrt{E}}, \tag{3.4}$$

and the energy resolution improves with the incident energy of the particle. The second, constant term, arises from instrumental effects, such as inhomogeneities in material and detector response, constructional variations, non-linearity of the readout electronics, and longitudinal shower leakage due to the finite size of the calorimeter. The third, called noise term, includes not only the effects from electronic noise but also from natural radio-activity of the detector material and pile-up fluctuations.

Tab. 3.2 shows the relative target energy resolution of each calorimeter component of the ATLAS detector. As evident, the statistical fluctuations are the limiting factor in the energy resolution, due to the adjustment of the thickness as a design requirement to minimise longitudinal leakage. The complementarity of the measurement in the inner detector and the calorimeters can be seen by a comparison of Equations (3.2) and (3.3), quantising the transverse momentum resolution in the inner detector and the energy resolution in

the calorimeters, respectively. While the energy resolution improves for higher values, the transverse momentum resolution decreases with increasing p_{T}.

3.3 Data-Taking and Preparation

This section provides all necessary information of the data taken in the years 2015 and 2016 that has been used for the measurements in this thesis. It will outline the path of the data from its origin from LHC provided collisions towards the data format that is used in the analysis. Moreover, the determination of important meta-data is sketched briefly. This includes:

- The reduction of the amount of data by the triggering algorithm and the general data acquisition;
- The data quality assessment;
- The luminosity measurements and determination;
- The pileup conditions; and
- The data preparation towards offline usage and further reduction for final analyses.

All these items are key components for physics analysis and hence will be explained briefly in the following subsections.

3.3.1 Trigger and Data Aquisition

The LHC, with its minimal bunch spacing of 25 ns, provides a maximum event rate of 40 MHz. The energy deposited by the particle debris of these collisions is read out by the almost 100 million channels of the ATLAS detector. Only those channels are sending data which actually measure a signal, totalling to a raw average data size of 1.5 MB per event. The resulting data flow of 60 TB/s exceeds both, the attainable data rate and disk storage capacities. In fact, it is unnecessary to store all of these events since many interesting processes occur at a rate which is orders of magnitude lower than the total proton-proton cross-section, as can be deduced from Fig. 2.1. A triggering mechanism is in place to reduce the data size which is kept for permanent storage.

The triggering algorithm in ATLAS consists of two levels, the fast, low precision Level-1 (L1) and the high-precision High Level Trigger (HLT) system, reducing the data rate in two steps to a final rate of 1 kHz of physics data on average. A schematic view of the operating concept is shown on the left-hand side of Fig. 3.8.

The L1 trigger system is purely hardware-based and analyses coarse-granularity information from the calorimeters and the muon chambers, reducing the event rate to approx. 100 kHz in less than 2.5 μs. It determines Regions of Interest (RoIs) and passes them to the HLT system, which uses full granularity detector information in these regions plus information from the inner detector. The HLT is purely software-based and forms an accept decision upon complex selection criteria determined by so-called trigger chains in approximately 200 ms. The whole collection of trigger chains is called trigger menu, which includes possible prescaling factors for each trigger chain. Once the HLT accept is received, all detector data and meta-data is sent to the TIER-0 processing farm where the data is kept on a waiting loop for 48 h (the "calibration loop") for data quality assessment before final processing.

The trigger algorithms create so-called "trigger objects". In the LAr and tile calorimeters, jets and electromagnetic objects (electrons or photons) are determined by the trigger towers of the L1-Calo algorithm. In the muon chambers, dedicated for triggering, muon trigger objects are formed. Different kinematic selection criteria, such as transverse momentum, pseudorapidity or isolation thresholds, can be posed on these objects and are critical for the rate reduction. Later in the final analysis the trigger objects must be matched to the offline reconstructed objects which undergo a much more thorough calibration and reconstruction (see later in this section). In addition, it must be accounted for inefficiencies in the trigger performance, which are important characteristics in the physics analysis.

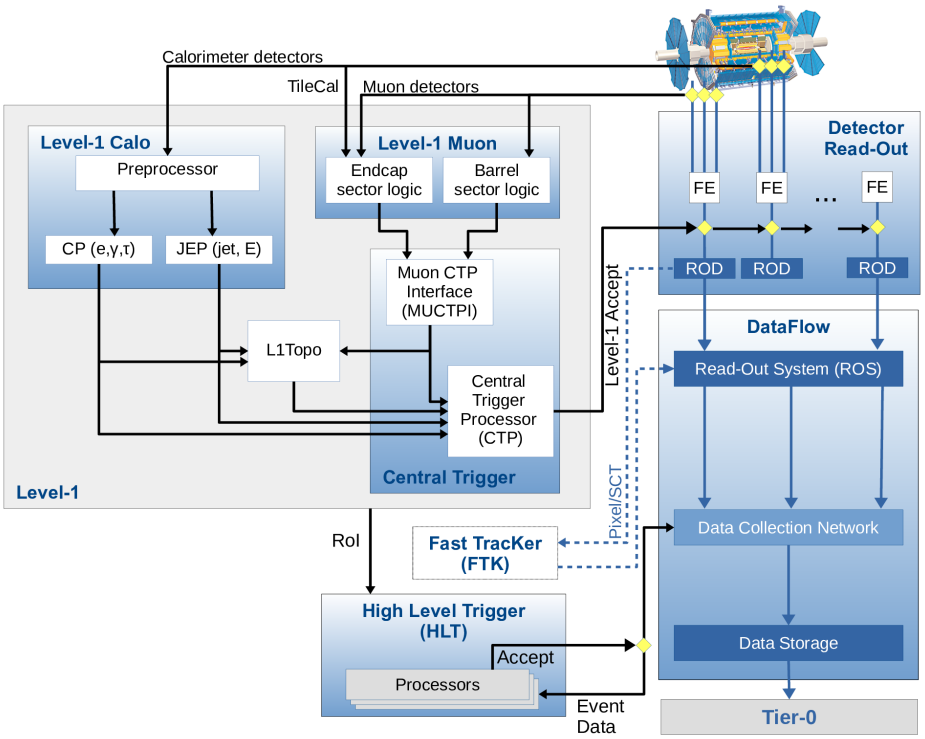


Figure 3.8: The ATLAS trigger and data aquisition (TDAQ) system in Run 2 showing the components relevant for triggering as well as the detector read-out and data flow. Figure taken from Ref. [90].

Table 3.3: Luminosity and pileup conditions summary of the relevant data-taking years 2015 and 2016. The "good total integrated luminosity" is the value used in the subsequent analysis. Numbers taken from Ref. [91].

Year	2015	2016
Delivered total integrated luminosity	$4.2\,\text{fb}^{-1}$	$38.5\,\text{fb}^{-1}$
Recorded total integrated luminosity	$3.9\,\text{fb}^{-1}$	$35.6\,\text{fb}^{-1}$
Good total integrated luminosity	$3.2\,\text{fb}^{-1}$	$32.9\,\text{fb}^{-1}$
Peak instantaneous luminosity ($10^{34}\,\text{cm}^{-2}\text{s}^{-1}$)	0.5	1.3
Luminosity-weighted mean inel. interactions/crossing ($< \mu >$)	13.7	24.9

3.3.2 Data Quality Assessment

The data quality (DQ) monitoring is a crucial step in the data preparation. It is done online and offline, and includes the assessment of the functionality of each subdetector as well as a careful scan of the performance of physics object reconstruction (see next section). Each subsystem or physics performance DQ task force reviews the data shortly after the end of a run (usually within 48 h, the so-called "calibration loop") and a second time after full reconstruction. This review can result in two defect types:

- Either in a set of event-by-event based defects that are passed on as flags to the data reconstruction algorithms via databases; or
- In the rejection of entire luminosity blocks (LB), a typical luminosity interval of approximately 60 s, registered in "good runs lists" (GRLs).

Reasons for bad data are divers, examples being noise bursts in the LAr calorimeters or incomplete or corrupt (meta)data information. Besides the effect of rejecting events or event blocks in the analysis, the removed data must be accounted for in the luminosity calculation. The GRLs used in the analyses of this thesis are:

```
data15_13TeV.periodAllYear_DetStatus-v79-repro20-02_DQDefects-00-02-02_
PHYS_StandardGRL_All_Good_25ns.xml
```

and

```
data16_13TeV.periodAllYear_DetStatus-v88-pro20-21_DQDefects-00-02-04_
PHYS_StandardGRL_All_Good_25ns.xml
```

for the 2015 and 2016 data-taking periods, respectively. The losses compared to ATLAS recorded data amount to $82,1\%$ and $92,4\%$ for the years 2015 and 2016, respectively, as can be deduced from Tab. 3.3.

3.3.3 Luminosity Determination and Pile-up

The instantaneous luminosity L_{inst} is the quantity that relates the cross-section of a given process σ_{process} with the event rate occurring in a specific experimental setup:

$$\frac{dN_{\text{process}}}{dt} = L_{\text{inst}} \cdot \sigma_{\text{process}}. \tag{3.5}$$

While the cross-section encodes the theory of a certain model under study and is energy-dependent, the luminosity is purely determined by the experimental conditions and machine parameters:

$$L_{\text{inst}} = \frac{N_b^2 f n_b}{4\pi\sigma_x\sigma_y} \cdot F, \tag{3.6}$$

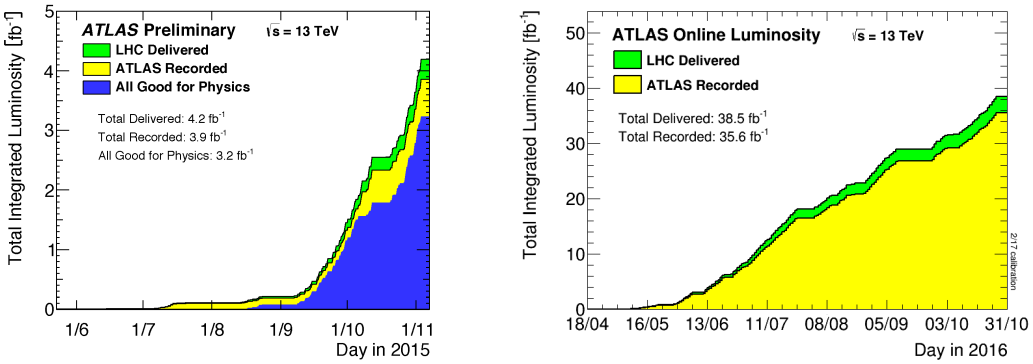


Figure 3.9: Cumulative luminosity versus time delivered to (green), and recorded by the ATLAS detector (yellow) during stable beams for proton-proton collisions at 13 TeV centre-of-mass energy in 2015 and 2016, as well as certified to be good quality data (blue) in 2015 Figures taken from Ref. [91].

where N_b denotes the population of protons in one bunch, f the revolution frequency of the LHC, n_b the number of bunches and $\sigma_{x,y}$ the width of the beam in x and y directions, respectively, for Gaussian distributed beam profiles. The parameters of operation in Run 2 are summarised in Tab. 3.1. In addition, a number of complex geometric corrections need to be included in the calculation for real shaped beams favouring high beam intensities and a high centre-of-mass energy for the LHC [92]. Particularly for cross-section measurements - one of the analysis interests of this thesis - a precise assessment of the integrated luminosity[5] of the dataset at hand is crucial. While the concept of the cross-section is explained briefly in Sec. 2.1.4, the measurement and determination of the luminosity is addressed now.

The instantaneous luminosity for physics runs is measured in a multistep procedure. First, the detectors dedicated to the luminosity measurement, the LUCID2 Cherenkov detector [93] and the ATLAS beam conditions monitor (BCM), need to be calibrated. This absolute calibration is evaluated during so-called van der Meer (vdM) scans. These scans are carried out with dedicated LHC beam conditions, during which the position of the beams is moved in x and y directions to scan the overlap between the beams' areal cross-section. The average number of interaction per bunch crossing $< \mu >$ increases with the overlap of the beam areas, and the absolute luminosity can be derived. The vdM scans need to be conducted in a low $< \mu >$ environment.

The LUCID2 and BCM detectors equally and complementary measure the luminosity during physics runs, which feature substantially higher $< \mu >$ values and bunch density. In order to extrapolate the calibration obtained from the vdM scans, a so-called track counting algorithm is employed. This algorithm counts the number of tracks in the inner detector, and it particularly benefits from a good linear coverage of $< \mu >$ values in both, the vdM scan and physics run environments. This procedure is called "calibration transfer".

The luminosity value relevant for physics analysis is not the total integrated luminosity delivered by the LHC machine but rather the value corrected for the losses due to the detector not ready for recording, trigger configurations used in the analysis, and data rejected from quality measures collected in the good runs list (GRL). These stages of luminosity evaluation for both relevant years of data-taking are listed in Tab. 3.3, the "good total integrated luminosity" being the final value used in the analysis. It sums to 36.1 $\mathrm{fb}^{-}1$ in both data-taking years. In addition, the peak instantaneous luminosity as well as the $< \mu >$ values for each year are summarised. The time evolution of the integrated luminosity recording in 2015 and 2016 is shown in Fig. 3.9.

The $< \mu >$ parameter, in fact, is a highly relevant quantity. It is the average number of interactions occurring in the same bunch crossing and commonly referred to as pileup[6]

[5]The integrated luminosity is given over a specific period of time and relates to the total number of events occurring during this time of data-taking.

[6]This specific phenomenon is exactly called in-time pileup while there is also the out-of-time pileup which labels the collisions that happen in bunch crossings before and after the crossing of interest.

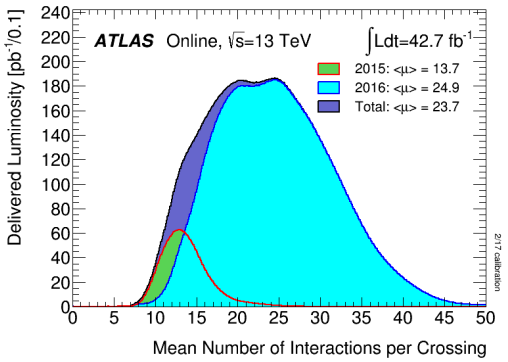


Figure 3.10: Luminosity-weighted distribution of the mean number of interactions per crossing combined for the relevant data-taking years 2015 and 2016. The mean number of interactions per crossing corresponds to the mean of the Poisson distribution of the number of interactions per crossing calculated for each bunch. Figure taken from Ref. [91].

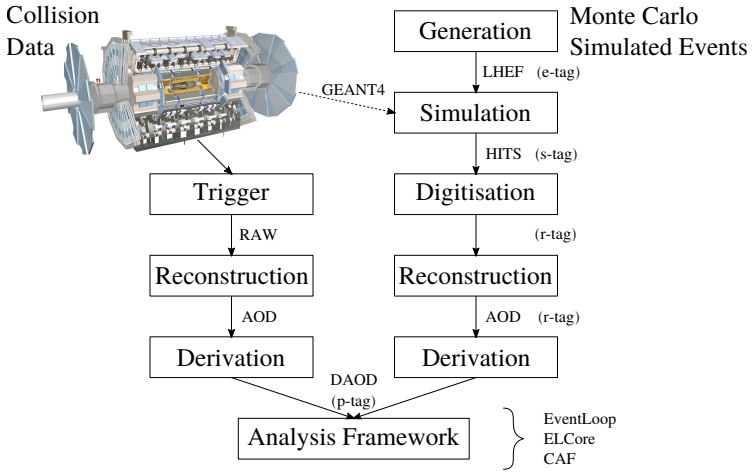


Figure 3.11: Schematic processing chain and data formats from recorded data and Monte Carlo simulated events to analysis level. Figure modified from Ref. [95].

parameter. It is related to the total averaged instantaneous luminosity at any given time. While large pileup values enhance the number of total collisions, it complicates the data analysis significantly as the unique assignment of debris of each collision event is impossible, leading to unavoidable backgrounds. The pileup conditions for the relevant years of data-taking are summarised in Fig. 3.10 showing the mean number of interactions per crossing.

The relative uncertainty of the luminosity measurement values to 2.1% in both years combined [94].

3.3.4 Prompt Reconstruction and Event Format Preparation

After the online selection via the trigger algorithm and the first selection based upon DQ criteria, the stored data is ready for reconstruction and further preparation towards final offline usage. A scheme of the data (and Monte Carlo simulated data) path from the detector (respectively event generation) towards final analysis application is shown in Fig. 3.11.

In the prompt reconstruction step, the time-dependent alignments, calibrations, and defects stored in the conditions' database are applied to the "RAW" data from the detector. The algorithms used for this are optimised for making fast decisions and refined later in the analysis step (see next section). Simultaneously, the detector signals are assembled into event information data and physics objects, such as electrons, muons, jets, etc. This processing

is computationally very intense and consumes the majority of the resources of Tier-0. The most important output formats are ROOT-readable analysis object data (AOD), a major improvement over the Run 1 data handling. Occasional reprocessing campaigns are launched with improved software, object reconstruction performance and conditions databases.

Since Run 2, an additional, centrally initiated step is the production of derived AODs (DAODs), which contain only a subset of information compared to the AODs. Near to 90 different DAOD formats are produced, each of the size of mega- to gigabytes, which makes handling of the data that runs through the analysis much more convenient. The DAOD pre-selection criteria are based on physics analyses needs and must always be looser than the actual analysis selection. The possible reductions can be the following:

- Skimming: Removal of entire events,
- Thinning: Removal of entire objects inside events,
- Slimming: Removal of variables inside objects.

Besides the lowering, extra information can be added to the events remaining inside the DAODs through attachment of additional containers, i. e. derived analysis objects, or the decoration of variables to existing objects.

The DAODs are the data format passed to the analysis framework. In this thesis, the analysis has been done with the EventLoop [96] based framework ElCore [97] and a Common Analysis Framework (CAF) [98, 99], the first being developed and both maintained at TU Dresden. All of these algorithms internally use Root [100]. The `AnalysisBase` release used is 2.4.29. The derivation used in the reconstruction level analysis in this work is STDM3 and the tag used is `p3314` for skimmed DAODs and `p3317` for unskimmed DAODs. At truth level, the TRUTH1 derivation is used with tag `p3317`.

3.4 Object Reconstruction and Identification

Each type of particle leaves a specific signature in the detector which can be used to reconstruct and identify those particles which match a certain final state. In this thesis, the fully leptonic final state of the scattering of two same-charge $W^{\pm}$ is explored. A detailed discussion of the topology for this process is given later in Chapter 5. Besides the leptonic decay products of the $W^{\pm}$ bosons, two jets are key components of every VBS final state at the LHC. The neutrinos are invisible for the ATLAS detector. However, its presence can be inferred from energy and momentum conservation in the transverse plane.

With regard to the final state at hand, this section contains a brief summary of the object preparations for electrons, muons, and jets, including the tagging of b-jets which are relevant for background suppression in this analysis. In addition, the reconstruction of missing transverse energy is outlined, a handle on the neutrinos escaping the ATLAS detector. The preparation procedures include “offline” reconstruction and calibration, identification, and primary vertex association of these objects. For leptons, additionally, the charge reconstruction and isolation determination are of importance. As the reconstruction of physics objects is performed completely independent of each other, detector signals can be allocated to multiple objects at the same time. In order to resolve signal ambiguities, a procedure called “overlap removal” is applied, explicitly removing objects when overlapping signals exist. The decisions of which objects to keep or reject is highly analysis specific and summarised at the end of this section.

3.4.1 Primary Vertex

An event, defined as one bunch crossing in the detector, can have multiple reconstructed vertices, due to in-time pileup. The vertex with the largest sum of squared tracks' transverse momentum associated is specified to be the vertex of interest, called primary vertex [101]. A reconstructed primary vertex is required to have at least two associated tracks, which are required to have a minimum transverse momentum of 0.5 GeV.

3.4.2 Leptons

The kinematic properties of leptons are especially interesting in the context of the EFT reinterpretation carried out in this thesis. Hence, highly efficient reconstruction and identification of "prompt" leptons which originate from the decay of heavier particles ($W^{\pm}$, Z, or Higgs bosons) as well as stringent isolation criteria are crucial in this analysis. Moreover, a precise determination of the charge of electrons is vital to select the required same-charge final state.

Owing to the challenging conditions of data-taking in the early Run 2 which featured unprecedented and gradually increasing peak instantaneous luminosities and pileup conditions in the ATLAS detector, more robust reconstruction and identification techniques have to be adopted compared to the Run 1 strategies.

Electrons

The signature of an electron in the central region of the ATLAS detector is a track in the inner detector pointing towards an energy shower deposit in the electromagnetic calorimeter. The insertion of the IBL as the innermost tracking layer considerably impacts the electron reconstruction and identification as well as the distinction between electrons and (converted) photons, which is critical to suppress charge misidentification of electrons. The overall reconstruction and identification requirements, including charge and isolation determination is based on [102], while the calibration procedure for early Run 2 is described in detail in [103] and based on the Run 1 strategy [104].

Reconstruction Energy clusters in the second layer of the electromagnetic calorimeter found via a sliding-window algorithm [105] initiate the electron reconstruction. These seed clusters can potentially origin from either an electron or a photon. The spatial matching of an inner detector track and a potentially existing vertex from a converted photon helps to distinguish between the two particle types. The tracks and conversion vertices are obtained by fitting the space-point measurements in the inner detector layers with a GSF algorithm [106]. Only high-quality tracks with at least four hits in the silicon layers of the inner detector and without association to a conversion vertex are classified as electrons. A refined classification is based on the particle candidate's kinematic properties (such as the transverse momentum of the track and the ratio of the cluster energy over the track momentum), the characteristics of the secondary vertex, and the presence of a measurement in the innermost silicon layer of the detector, the IBL. The decision is reflected in the `Author` quantity which values to 1 for electrons, 4 for photons and 16 for an ambiguous classification as either electron or photon.

The reconstruction efficiencies of both, the calorimeter cluster and the track finding algorithms are pseudorapidity $|\eta|$ and E_T dependent and vary between 65% at $E_T = 4.5\,\text{GeV}$ and more than 99% above $E_T = 15\,\text{GeV}$, and 80% at $E_T = 1\,\text{GeV}$ to more than 98% above $E_T = 10\,\text{GeV}$, respectively [102].

The final spatial direction in η and ϕ for the electron candidates are calculated from track properties, while the energy is determined from the calibrated cluster deposits. Further information are then decorated to the final electron object, such as object quality used for identification and isolation information.

Energy Calibration The energy of the reconstructed electron candidates is corrected in scale and resolution to account for losses due to detector geometry and operation conditions, as well as deficiencies in the simulations. The true energy spectrum of electrons is estimated from multivariate and template techniques using both, real data and simulation.

The calibration procedure constitutes three major steps. First, electromagnetic cluster properties are corrected for energy leakage, e. g. through deposits in the material in front of or beyond the active calorimeter or outside the dimensions of the cluster window. These adjustments are estimated with single electron simulations employing a boosted decision tree (BDT) and precursory data-driven studies regarding material and layer characteristics. They are applied to simulation and data likewise. A second step corrects the real collision data for regional non-uniformities in detector geometrics and operation conditions, such as

varying layer, high voltage or LAr temperature settings. Due to data statistics limitations in early Run 2, some of these effects are derived from Run 1 data. In this case, additional systematic uncertainties are assigned to account for extrapolation effects. The calibration of electromagnetic objects is completed with the alignment of the energy scale and resolution in data and simulation. With the use of simulated Z boson decays to electrons, the energy scale in data is shifted to the expected value and the resolution in simulated events is smeared to match the slightly poorer resolution in data. For the latter, an additional constant term is added to Equ. (3.3). Systematic uncertainties are estimated from the event selection criteria, the intrinsic calibration procedure, and the data-driven inputs in the three steps.

Identification The selection of the electron candidates can be adjusted to the needs of the physics analysis at hand. The studies in this thesis require multiple electrons samples with different reconstruction quality based on their purpose in the analysis. For signal electrons a clean, high-quality set of electrons is desirable, while for background rejection a large efficiency of the selection is preferable.

For electrons inside the acceptance region of the inner tracker ($|\eta| < 2.47$), five different identification working points are provided based on their selection efficiency and background rejection factors. The working points are constructed from an $|\eta|$ and E_T dependent optimisation of a likelihood discriminant. The inputs to this discriminant include measurements of reconstructed quantities such as electromagnetic shower shape variables, the quality of the associated track, its number of measurements in the silicon detectors (pixel or SCT), the detection of transition radiation in the TRT, and the quality of the matching of the inner detector track to the corresponding calorimeter cluster. A detailed list of input variables can be found in Table 1 in [102].

The working points (WPs) used in the studies in this thesis are, with increasing yet inclusive reconstruction quality requirements, `Loose+IBL`, `Medium`, and `Tight`. All of these WPs include a requirement on a measurement in the IBL which reduces the selection of background signatures from converted photons and hence the probability of charge misidentification backgrounds in the analysis.

The efficiency for the identification of prompt electrons, extracted from J/Ψ and Z boson decays, ranges between 55% at $E_T = 4.5\,\text{GeV}$ to 90% at $E_T = 100\,\text{GeV}$ for the `Tight` WP, and from 85% at $E_T = 20\,\text{GeV}$ to 96% at $E_T = 100\,\text{GeV}$ for the `Loose` WP, while the background rejection factor increases by a factor of five between the `Loose` and `Tight` WP [102].

Muons

As muons traverse all detector layers, their reconstruction, and identification is based on the combination of measurements in the inner detector, the calorimeters, and the muon spectrometer. Before the start of Run 2, additional muon chambers have been installed into the ATLAS detector which, together with the insertion of the IBL and an improved reconstruction software, allow for a refined muon reconstruction, calibration, and identification strategy. The details are described in [107] and briefly presented here.

Reconstruction & Identification Initially, muon track candidates are reconstructed independently in the inner detector and the muon spectrometer and finally statistically combined to form physics objects. In the muon spectrometer, tracks are assembled in two steps. First, the hits from the MDTs and CSCs are combined with the hits from the trigger chambers in each layer to form track segments. These segments are then matched across all three layers of the muon spectrometer as well as loosely with the area of interaction to form a full track, called MS track.

Eventually, MS tracks are combined with information from the inner detector and the calorimeters resulting in four different muon types, all of which are potentially used in the analysis of this thesis [107]:

- Combined (CB) muons are formed from the combination of MS and inner detector

tracks with a global outside-in refit of the corresponding hits. The majority of reconstructed muons are CB muons.

- Segment-tagged (ST) muons are reconstructed from an inner detector track, which is extrapolated to the muon spectrometer and can be matched to at least one MS track segment. In the studies presented in this thesis, ST muons are enhancing the acceptance in the very central region of the detector ($|\eta| < 0.1$) where the muon spectrometer instrumentation is incomplete.

- Calorimeter-tagged (CT) muons are reconstructed from an inner detector track, which can be extended into the calorimeter by matching to an energy deposit pattern consistent with a minimum-ionizing particle. As ST muons, CT muons are enhancing the acceptance in the very central region of the detector ($|\eta| < 0.1$).

- Extrapolated (ME) muons are reconstructed solely with an MS track compatible with originating from the interaction point. With this type of muons the acceptance for muon reconstruction is expanded into the region not covered by the inner detector ($2.5 < |\eta| < 2.7$). This is relevant for background rejection in the analysis.

The efficiency to reconstruct muons above a transverse momentum of $p_{\mathrm{T}} > 5\,\mathrm{GeV}$ and inside $|\eta| < 2.5$ is close to 99% for most of the acceptance region [107].

For identification, muons are, like electrons, categorised into WPs defined by their respective efficiency, background rejection and uncertainties. The selection is based on the quality of the fit, the hit pattern, and the kinematic difference between the inner detector and MS tracks identified with the respective muon. The studies in this thesis use the `Loose` and `Medium` WPs for background rejection and signal muons. While `Medium` muons only comprise CB and ME muons, all muon types with less strict requirements are considered for the `Loose` WP, hence yielding a higher identification efficiency for the latter.

The overall reconstruction and identification efficiency, derived from simulated $t\bar{t}$ events, for prompt `Loose` muons range between 96% and 98% and for prompt `Medium` muons between 95% and 96%, depending on their transverse momentum and pseudorapidity.

Momentum Calibration In contrast to the electron energy calibration, the muon momentum is exclusively corrected in the simulated events to match the observations in data. The procedure is aligning the simulated scale and relative resolution of the muon momentum similarly as for electrons, however not only correcting the constant term but also the contribution of the scale and relative resolution linearly dependent on the muon momentum (ref. Eq. (5) and (6) in [107]).

The calibration constants are independently derived for the transverse momentum correction in the inner detector and the muon spectrometer, starting with the first and taking into account the energy loss in the calorimeters for the latter. The procedure uses solely CB muons compatible with stemming from J/Ψ and Z boson decays in 18 different pseudorapidity regions and two azimuthal regions for MS track calibration separating the small and large sectors of the muon spectrometer.

Lepton Isolation

The concept of lepton isolation especially has been introduced in order to discriminate between prompt leptons originating from the decay of heavier particles ($W^{\pm}$, Z, or Higgs bosons) and non-prompt leptons, which either originate from heavy quark-flavour decays or which are misidentified hadrons or converted photons (predominantly in the case of electrons). It is a measure to quantify the activity in the detector in an area in azimuth and pseudorapidity, $\Delta R = \sqrt{(\Delta\eta)^2 + (\Delta\phi)^2}$, around the particle candidate of interest. The isolation requirements for electrons are given in [102] while for muons they are summarised in [107].

Two discriminating variables are employed based on the track transverse momentum or on transverse energy deposits in the calorimeters, called `ptvarcone` and `topoetcone`, respectively. The `ptvarcone` variable is built from the sum of the transverse momenta of the

tracks ($p_{\mathrm{T}} > 1\,\mathrm{GeV}$, longitudinal association to interaction point $|z_0 \sin\theta| < 3\,\mathrm{mm}$) in a cone of radius $\Delta R = \min\{10\,\mathrm{GeV}/p_{\mathrm{T}}, x_\ell\}$ around the lepton, excluding the track of the lepton under study. x_ℓ values to 0.2 for electrons and 0.3 for muons, defining `ptvarcone20` and `ptvarcone30`, respectively. The variable cone size results in smaller cone radii for particles with increasing p_{T}. The `topoetcone` variable is built from the sum of the transverse energy of topological clusters corrected for pileup and underlying event effects and subtracted by the energy deposit of the particle under study. For both, electrons and muons, a cone size of $\Delta R = 0.2$ is used, defining `topoetcone20`.

Both, the `ptvarcone` and `topoetcone` measures are combined to form the `Gradient` isolation WP used in the studies in this thesis for both electrons and muons. It is defined with gradient efficiency targets: $\varepsilon(25\,\mathrm{GeV}) = 90\%$ and $\varepsilon(60\,\mathrm{GeV}) = 99\%$. The detailed definition and cut maps can be retrieved from [108].

3.4.3 Jets

When protons collide at the energies reached at the LHC, a vast number of quarks and gluons are produced. Due to QCD confinement, these particles cannot be separated, hence forming energetic hadrons. As a result, quarks and gluons are observed through collimated showers of hadrons, called jets, in the ATLAS detector. The goal of the jet reconstruction and calibration is to relate the kinematics of the observed jet to the kinematics of the underlying physics object defining the final state in question.

The reconstruction and calibration procedure used for data relevant in this thesis is similar to the one used for data taken in 2012 and is described in detail in [109]. The increase in centre-of-mass energy and bunch frequency, and the improvements of the ATLAS detector as outlined in Sections 3.1 and 3.2 lead to adjustments of the methods' key parameters, such as the noise threshold of the energy reconstruction in the calorimeters or the pileup conditions.

Reconstruction The analyses throughout this thesis use the jet collection, which is called `AntiKt4EMTopoJets`. These jets are reconstructed at the electromagnetic scale from three-dimensional, topologically connected energy deposits in calorimeter cells containing a significant amount of energy signal above a noise threshold, called topo-clusters [105, 110]. The topo-clusters are combined into jet objects using the anti-k_T jet finding algorithm [111] with radius parameter $R = 0.4$ and the FastJet software package [112] version 2.4.3.

Calibration The calibration procedure for jets consists of several consecutive steps. First, a set of simulation-based corrections is applied which compare the reconstructed jet four-momentum to the true particle level one. The procedure is further completed by multiple in-situ measurements in data and simulated events.

The calibration aims to reduce the effects of energy loss due to dead material in the detector, below noise threshold effects, or leakage arising from the clustering procedure or high energetic jets punching through the calorimeter active length. In addition, the reduction of pileup effects is targeted.

First, the direction of the reconstructed jet is corrected to point to the identified primary vertex instead of toward the centre of the detector. This leaves the jet energy unchanged while improving the resolution in η. Following, the effect of pileup is subtracted based on the parametrisation [113]:

$$p_{\mathrm{T}}{}^{\mathrm{corr}} = p_{\mathrm{T}}{}^{\mathrm{EM}} - \rho \times A - \alpha \times (N_{PV} - 1) - \beta \times < \mu > . \tag{3.7}$$

The momentum of the jet at the electromagnetic scale, $p_{\mathrm{T}}{}^{\mathrm{EM}}$ is first corrected for an area-based estimate of the mean pileup energy density per event $\rho \times A$ (first subtraction term). Further residual dependencies on in-time (second term, dependent on the number of hard scattering vertices N_{PV}) and out-of-time pileup (last term, dependent on the average interactions per bunch crossing $< \mu >$) are removed by fitting the parameters α and β in simulated events, especially affecting jets in the forward region of the detector. The next step calibrates the reconstructed jet four-momentum to the true simulated jet energy scale (JES) by fitting the core jet response distribution, $R = E_{\mathrm{reco}}/E_{\mathrm{truth}}$ in dijet events with a Gaussian

parametrisation. Additionally, biases in the jet pseudorapidity are resolved which are caused by the calorimeter composition (transition regions, granularity differences) in the detector. The second to last step is the global sequential calibration, a successive correction based on variables describing the jet shower, including track-based observables and activity in the muon spectrometer behind the jets. This reduces the dependence on leakage effects and jet flavour composition. Finally, residual difference in the jet response are corrected in data only with in-situ measurements of the balance in transverse momentum between a jet and a recoiling reference object, such as a Z boson, a photon, or multijet system.

Pile-up Jet Suppression After the subtraction of pileup effects in the calibration procedure, local pileup energy fluctuations can remain, leading to spuriously reconstructed jets, called pileup jets. The suppression of these jets is crucial in the analyses at hand, which requires jets in the final state. The strategy pursued in Run 2 is detailed in [114] and briefly outlined here.

Aiming to distinguish jets originating from the primary vertex and pileup jets, two track-based variables are combined into a multivariate likelihood discriminant, called jet vertex tagger (JVT). It includes the pileup-corrected jet vertex fraction, corrJVT, which denotes the fraction of a jet's total momentum of tracks associated with the primary vertex, corrected for the dependency on the number of reconstructed vertices. The second variable is R_{p^T}, the ratio of the scalar transverse momentum sum of the tracks associated with the jet and the primary vertex divided by the total jet transverse momentum after calibration. The JVT value ranges between zero and one, representing pile-up-like and hard scatter-like jets, respectively.

Analyses throughout this thesis use the `Medium` JVT WP with a discriminant cut at JVT < 0.59 and a resulting average efficiency of 92% for jets originating from the hard scattering. It is applied to jets in the central region $|\eta| < 2.4$ with transverse momentum in the range of $20\,\text{GeV} < p_\text{T} < 60\,\text{GeV}$.

B-Jet Tagging Top quarks almost exclusively decay into a $W^\pm$ boson and a bottom (b) quark [41]. In order to reduce the contribution of background from processes with top quark decays in the analyses at hand, the identification of jets originating from the hadronisation of b quarks, called b-jets, is beneficial.

The strategy of b-jet tagging exploits the lifetime of B-hadrons which allows the particles to travel a significant distance before decaying (up to a few millimetres). These decays are measurable by the ATLAS detector through the identification of displaced, so-called secondary vertices inside jets and hence tracks inside jets whose origin is displaced from the primary vertex. B-jet tagging is hence only possible within an absolute pseudorapidity range of $|\eta| < 2.5$ where track information from the inner detector is available. The installation of the IBL significantly enhances the performance of b-jet tagging in comparison to Run 1, especially for jets with medium transverse momentum.

In the analyses in this thesis, the `MV2c10` b-jet tagging algorithm [115] is employed to discriminate b-jets from c-jets and jets originating from light quark flavours (u, d, or s quarks) and gluons. The algorithm combines information on secondary vertices and tracks inside each jet into a BDT discriminant. A detailed list of input variables can be found in Tab. 2 in [116].

The analyses in this thesis use the fixed-cut WP with a b-jet identification efficiency of 85% and light(c)-quark jet rejection of 33(3.1) evaluated in simulated $t\bar{t}$ events.

3.4.4 Missing Transverse Momentum

The concept of missing transverse momentum E_T^miss is a powerful instrument in physics analyses, especially when looking for processes with leptonically decaying $W^\pm$ bosons in the final state. It is based on the conservation of momentum perpendicular to the beam axis, from which the total transverse momentum of all particles from the hard scattering of interest is inferred to be zero. Any particle that leaves the ATLAS detector undetected leaves an imbalance of momentum in the transverse plane, and can hence be related to the missing

transverse momentum. These can be invisible particles of any kind. In the context of this thesis, these are neutrinos, but they can generally also represent particles in BSM theories.

The reconstruction of missing transverse momentum is explained in [117] for the data-taking period of 2015 and 2016 which is the basis for the following summary.

Signals from all parts of the ATLAS detector are used to reconstruct the missing transverse momentum per event. It has two components, $\vec{E}_T^{\text{miss}} = \left(E_x^{\text{miss}}, E_y^{\text{miss}}\right)^\top$ which are determined from the negative sum of momenta of fully reconstructed and calibrated particles ("hard term") as well as unassociated soft detector signals ("soft term"):

$$E_{x(y)}^{\text{miss}} = \underbrace{-\sum_{\substack{\text{selected}\\\text{electrons}}} p_{x(y)}^{e} - \sum_{\substack{\text{selected}\\\text{muons}}} p_{x(y)}^{\mu} - \sum_{\substack{\text{accepted}\\\text{jets}}} p_{x(y)}^{\text{jet}}}_{\text{hard term}} \underbrace{- \sum_{\substack{\text{unused}\\\text{tracks}}} p_{x(y)}^{\text{track}}}_{\text{soft term}} . \tag{3.8}$$

The reconstruction process must ensure that no detector signals are double counted. The order of terms represents hence the priority assigned to include the objects in the missing transverse momentum calculation. Detector signals assigned to leptons are considered first, with only those leptons included that are used in the analysis (electrons e and muons μ) and that pass specific selection criteria. This allows for consistency within the analysis event selection, especially concerning the calibration and propagation of systematic uncertainties. In contrast to this, jets are only included in the calculation if they are not rejected due to signal overlap with any of the leptons. Further, only central(forward) jets ($|\eta| < (>)2.4$, respectively) with transverse momentum above 20 GeV(30 GeV) are considered. Pile-up dependence is mitigated by rejecting central jets with transverse momentum up to 60 GeV tagged with JVT < 0.59. The signal ambiguity resolution and pileup jet rejection is further detailed in [118].

The soft term includes detector signals that are not matched to any of the objects already included in the missing transverse momentum calculation from the hard term. The analyses in this thesis utilise the missing transverse momentum representation, which is called `MET_Reference_AntiKt4EMTopo` and the soft term specification `PVSoftTrk`. Hence, the soft term solely includes charged particle tracks with $p_{\text{T}} > 0.4$ GeV, which are associated to the primary vertex via selections on the impact parameters, but are not matched to any of the hard objects mentioned above. Including the soft activity of the event in the calculation improves both its scale and resolution.

The reconstruction of E_T^{miss} is highly sensitive to the accuracy of the energy scale and the resolution of the reconstructed leptons and jets, as well as to mismeasurements and defects of the detector, e. g. when particles traverse regions not covered by active sensor material. In addition, contributions stemming from pileup interactions may contaminate the calculations. These are suppressed by only considering fully calibrated objects in the hard term, which already receive pileup corrections through the calibration process. Moreover, the use of tracks over calorimeter signals in the soft term, where the tracks can be matched to the primary vertex, minimises the effects of pileup.

3.4.5 Overlapping Object Treatment

All the above outlined reconstruction algorithms of the different physics objects are applied autonomously of each other. Thus, detector signals can be assigned to two or more physics objects simultaneously. For example, a calorimeter cluster can be reconstructed as an electron/photon energy deposit or as associated with a jet. This duplication is artificial, as intrinsically created by the reconstruction procedure, and needs to be removed. However, the production of two real physics objects can naturally occur very close to each other. In this case, it needs to be decided whether to retain both objects or not. This decision is fundamentally motivated by the underlying physics that created the close-by objects. An example would be the leptonic decay of a meson inside a jet. In these cases, the concept of lepton isolation, as explained in Sec. 3.4.2, is a helpful discriminant. Consequently, the nature of overlaps depends on the object identification criteria and is highly analysis-specific.

A harmonised overlap removal procedure is defined in [119] and refined during Run 2 data-taking in [120]. Unless stated otherwise, the `heavy flavour` (`HF`) WP of the centralised

overlap removal tool [121] is used in this work[7]. This WP favours b-jets over leptons and is used here to optimise the background rejection efficiency of events with leptonic heavy flavour decays.

The procedure is again priority ordered, beginning with the resolution of lepton-lepton overlaps before handling jet-lepton overlaps. As recommended in [119], the objects with the loosest identification requirements per class are passed to the algorithm. Details are specified later in the section which outlines the object selections in the analyses (cf. Sec. 7.3). The rapidity defined distance between two objects is, among other conditions, used to measure a potential overlap.

Lepton-Lepton Overlap Removal Two electrons are regarded as overlapping, if they share an inner detector track or have overlapping clusters in the second layer of the electromagnetic calorimeter. The electron with the lower transverse momentum is discarded.

Duplications between muons are resolved during muons classification in the object reconstruction step.

The reconstruction of overlapping electron-muon pairs may happen when the muon radiates photons (FSR or bremsstrahlung). This phenomenon is characterised by the electron and muon sharing the same inner detector track. In this case, the muon is kept unless it is a calorimeter-tagged muon (see Sec. 3.4.2).

Lepton-Jet Overlap Removal Resolving overlaps between leptons and jets is a very delicate endeavour as it has to separate between its different origins.

Reconstructing prompt electrons erroneously as jets is an intrinsic property of the jet clustering algorithm. However, jets originating from light quarks have the potential to imitate ("fake") an electron. Moreover, jets stemming from heavy quarks may comprise non-prompt electrons from semileptonic decays of mesons. The goal is hence to remove the duplicate while preserving the real jet objects (light or heavy flavour).

The resulting procedure maintains the electron when the jet-electron distance is small, $\Delta R_{e-j} < 0.2$, unless, due to the usage of the `HF` WP, the jet is tagged as a heavy flavour jet. The electron is removed when it is at a distance of $0.2 < \Delta R_{e-j} < 0.4$ from the jet.

Prompt muons can overlap with spurious jets that have the same origin as falsely reconstructed electrons near muons (final state radiation or bremsstrahlung). Further, in the same way as electrons, non-prompt muons may originate from semileptonic decays of mesons inside jets. Jets reconstructed from photon radiation off the prompt muon are characterised by a very limited number of tracks, assumingly only the muon track itself. Therefore, the muon is kept, if the number of tracks associated to the jet is below three and the distance between the two objects $\Delta R_{\mu-j}$ does not exceed 0.2 or when the muon's inner detector track is ghost associated [122] to the jet, which is equivalent to the distance requirement. Here again, if the jet is tagged as a heavy flavour originating jet or if $0.2 < \Delta R_{\mu-j} < 0.4$ the jet is always kept, and the muon is removed.

[7] In the course of the estimate of background contribution from heavy flavour jets the overlap removal procdure is altered.

Chapter 4

Simulation of Proton-proton Collisions at the LHC and the ATLAS Detector

The simulation of high-energy physics events at hadron colliders, based on theoretical descriptions outlined in Chapter 2, form a key aspect in today's experimental analysis of collision data. Simulations are not only used for designing and understanding detectors. They have become a central element in experimental data analyses, from understanding and modelling of background estimates and the measurement of SM parameters to novel analysis techniques involving artificial intelligence and the search for and interpretation of BSM physics. Hence, high-energy physics collider experiments spend a substantial portion of their computing resources on the simulation of collision events.

In this thesis, the simulation of high-energy physics events plays an important role beginning from the thorough investigation of the modelling of the SM signal process in Chapter 6 to the study and validation of the simulation of a BSM physic's scenario with a new modelling technique in Chapter 9. While these aspects are in the focus of this work, simulations accompany the whole chain of the analyses.

Collisions at hadron colliders, such as the LHC, are governed by QCD interactions which typically produce a number of particles of order $\mathcal{O}(100-1000)$ in the final state with momenta ranging over multiple orders of magnitude. Hence, the simulation of these collision events is an intricate task.

This chapter starts with outlining the physics motivations and ground works for the event simulation of proton-proton (pp) collision events, based on [123, 124], which necessary to describe measurements in the given experimental setup. It focuses on the simulation of events with a high-energy core process of interest, also called the hard scattering process, and its subsequent evolution towards lower energies. While the hard scattering event can be described by arbitrary underlying physics models, the evolution is independent of it and based on SM phenomena, some of which can be derived by first principles of perturbation theory and some which need to be modelled phenomenologically. When discussing details of the simulation, this chapter refers to the generation of the process under study, the scattering of two $W^{\pm}$ boson at the LHC. Hence, this chapter is designated to give the ingredients for the studies presented in the following chapters.

The second part of this chapter briefly outlines the stages of the simulation of the ATLAS detector, which follows the purely theoretical event generation. It closes with a summary on the preparatory steps necessary for the utilisation of simulated events in experimental analyses.

4.1 The Cross-section of Proton-proton Collisions

Collisions of protons at a centre-of-mass energy of 13 TeV proceed at very small distances, i. e. at the level of elementary, point-like particles, the quarks and gluons (referred to as "partons") inside the protons. Built upon the short theoretical introduction in Sec. 2.1.4, the cross-section of pp collisions for a given final state at the LHC can be derived from the SM Lagrangian via Feynman diagrams and the tool of perturbation theory. Furthermore, the parton distribution functions (PDFs) of the protons need to be included in the calculation. These are necessary to describe parton interactions from an initial state exhibiting protons. The goal is to derive quantitative predictions for the process of interest, which mostly involves large transfer of momentum or the creation of heavy objects.

Due to the large separation in energy scales usually present in the collisions, the factorisation theorem can be employed to compute the cross-section for a scattering process with n final state particles $pp \to n$ [123]:

$$\sigma(pp \to n) = \sum_{a,b} \int_0^1 \int_0^1 dx_a dx_b \int f_a^{h_1}(x_a, \mu_F) f_b^{h_2}(x_b, \mu_F) d\hat{\sigma}_{ab\to n}(\hat{s}, \mu_R, \mu_F). \tag{4.1}$$

The parton distribution functions (PDFs) $f_a^{h_1}(x_1, \mu_F)$ give the probability to find parton a with momentum fraction x_a (Bjorken variable) inside hadron h_1. These functions depend on the factorisation scale μ_F introduced by the factorisation method, and so does the parton level cross-section $\hat{\sigma}_{ab\to n}$ for producing the final state n through the initial partons a and b. The latter additionally depends on the centre-of-mass energy reduced by the Bjorken variables of both incoming partons $\hat{s} = x_1 x_2 s$, and the renormalisation scale μ_R. The sum over all possible partons $\sum_{a,b}$ ensures that all partons enter the calculation that can participate in the given process.

The factorisation separates the components describing low-energy phenomena, i. e. the PDFs, from the high-energy hard scattering process $ab \to n$. The first cannot be described by perturbation theory any longer, as they occur at energies too low for the expansion in the strong coupling constant α_S.

The PDFs are obtained via a global fit to data collected in deep inelastic scatting experiments. These can include fixed-target experiments, as well as collider experiments with electrons, protons, or anti-protons in the initial state (HERA [125], Tevatron [126], and the LHC). Due to the complementary kinematic reach of these experimental setups, PDFs can be evaluated over a large range in the corresponding Bjorken variable x and scale μ_F^2. The role of the LHC-collected data is thereby increasing, helping to constrain the PDFs. Presently, six groups published results for unpolarised PDFs up to an NNLO accuracy in perturbative QCD, among them MMHT [127], NNPDF [128], and CT(EQ) [129]. Fig. 4.1 illustrates the PDFs for all partons obtained by the NNPDF3.0 analysis at QCD order NNLO at two different scales with their obtained value for the strong coupling constant $\alpha_S(m_Z^2) = 0.118$.

The differential partonic cross-section for the subprocess $ab \to n$ can be calculated as:

$$d\hat{\sigma}_{ab\to n}(\hat{s}, \mu_R, \mu_F) = d\Phi_n \frac{1}{2\hat{s}} \left|\mathcal{M}_{ab\to n}\right|^2 (\Phi_n, \mu_R, \mu_F). \tag{4.2}$$

The theoretical prescription of the SM is encoded in the squared matrix element $\left|\mathcal{M}_{ab\to n}\right|^2$, with the average over initial state and the sum over final state degrees of freedom of spin and colour. The initial state conditions are considered via the parton flux $1/(2\hat{s})$. The kinematic information of the final-state is encoded in the $3n-4$ dimensional phase space element:

$$d\Phi_n = \prod_{i=1}^{n} \frac{d^3 p_i}{(2\pi)^3 2E_i} (2\pi)^4 \delta^{(4)}(p_a + p_b - \sum_{i=1}^{n} p_i), \tag{4.3}$$

which constrains the four-momenta of the outgoing particles p_i via energy and momentum conservation. The integration over the large and variable dimensions of this final state phase space concludes the calculation.

Eq. (4.1) is valid for all orders of the perturbation series. However, effectively, the calculation remains always fixed order regardless of the computation method. This, in fact, leaves

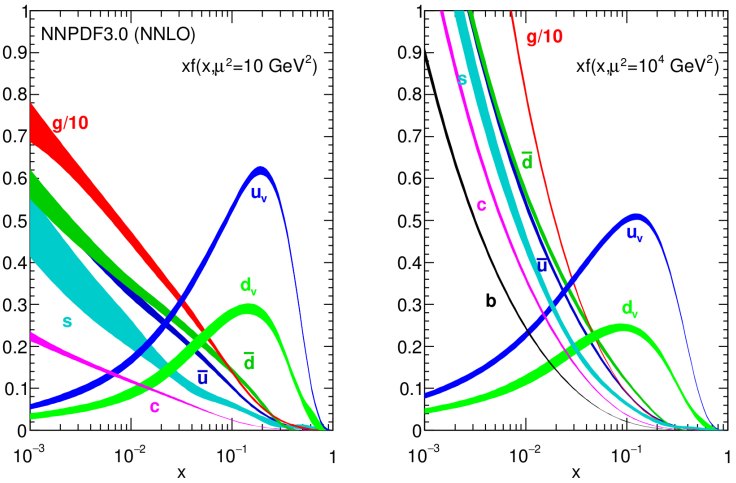


Figure 4.1: Unpolarised NNLO NNPDF3.0 [128] parton distribution functions (PDFs) multiplied by the Bjorken variable, $x \cdot f_a^p(x)$ (where $a = u_v, d_v \bar{u}, \bar{d}, s, \bar{s}, c, \bar{c}, b, \bar{b}, g$ and $f_s \approx f_{\bar{s}}$, $f_c = f_{\bar{c}}$, $f_b = f_{\bar{b}}$) for protons obtained in global fits at scales $\mu^2 = 10\,\mathrm{GeV}^2$ (left) and $\mu^2 = 10^4\,\mathrm{GeV}^2$ (right) and with $\alpha_S(m_Z^2) = 0.118$. Figure taken from [41].

the calculation dependent on the factorisation and renormalisation scales, while in the full expansion these dependencies cancel entirely. Consequently, these scales have to be set manually, the choice of which is made by experience (though limited by the known logarithmic structure of QCD).

4.2 The Structure of Monte-Carlo Event Generation

The computation of the *pp* cross-section as outlined above constitutes the heart of the event generation at hadron colliders. However, to reach observable final states of stable[1] and colourless particles, the generation of a collision event is completed by the simulation of subsequent QCD effects, decays, and QED radiation. The goal of this section is to briefly summarise the process of event generation at the LHC while highlighting the specifics that need to be considered for the studies in this thesis.

Figure 4.2 illustrates the structure of event generation. Alongside the hard scattering process in the centre of the scheme, the event generation is dominated by QCD reactions. Consequently, the process typically includes the production of hundreds of particles with momenta ranging over numerous orders of magnitude. The spread in momenta can be classified into three regimes with decreasing scales involved in the QCD interactions. The hard process of interest occupies the highest energy scales. At the lowest scales, observable particles are produced which form the final state hadrons seen by the detectors, usually referred to as soft QCD interactions. The QCD parton shower bridges the two regimes via an evolutionary procedure. Through the ansatz of factorisation, these regions of momenta can be simulated independently according to their momentum transfer scales involved. This is crucial as perturbation theory breaks down in the course of the evolution, culminating in the non-perturbative confinement of QCD partons at low-energy scales. For all three regimes, MC techniques can be employed which make the accuracy of the numerical evaluation scale with $\sim 1/\sqrt{N_I}$ of the number of integration points N_I and independent of the dimension of the final state. Further reading into the basic MC techniques used in high-energy physics event generation can be found in [123].

While the generation of the hard scattering process is commonly incorporated in matrix element generators, the modelling of all subsequent components of the event generation is generally combined in so-called parton shower generators. The major steps of the event generation are described in more detail hereafter based on [123, 124]. The technical imple-

[1] The term "stable" refers to the scale, and hence the time frame of the detecting devices.

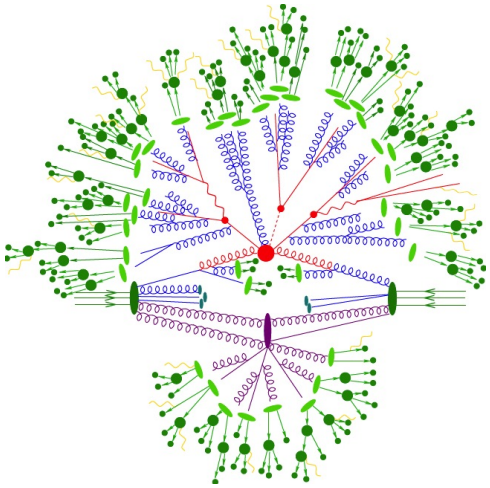


Figure 4.2: Scheme of the structure of Monte Carlo event generation for pp-collisions. The hard scattering process is depicted in red, the parton shower contributions in blue, the formation of hadrons and decays of unstable particles in green, the underlying event in violet and QED final state radiation in orange. Figure taken from [130].

mentation of these steps is to a high degree tool specific and will only be discussed briefly.

4.2.1 The Hard-scattering Subprocess

The first step of simulating events occurring at the LHC is to model the hard scattering subprocess as it defines the highest scales in the event and describes the parton-parton interaction which can be evaluated with the tools described above. The incoming and outgoing particle types of the subprocess are well-defined. Obviously, the explicit physics model under study with its associated Feynman rules has to be specified, as well as the values for the free parameters of this model (for the free parameters of the SM see Section 2.1.3). In addition, the orders in perturbation theory of the interaction, both in electroweak (EW) and QCD couplings, need to be given, if not assumed automatically by the respective programme.

Via Eq. (4.1), the evaluation of the matrix element is intrinsically dependent on the choice of the PDF set from which initial state partons are randomly picked, in type as well as kinematic properties. The fixed-order matrix element is ultimately constructed by summing over the contributing Feynman diagrams determined via the Feynman calculus (see Section 2.1.4).

While many processes have been calculated and incorporated into simulation tools beyond LO in QCD to this day, interactions in higher orders in EW couplings have only been computed recently and for a few designated processes. The studies in this thesis comprise predictions at LO and NLO accuracy, both in QCD and EW. NLO accurate calculations amend the LO matrix element with the virtual and real-emission corrections. The first includes extra particles in internal loops, while the latter adds one additional external particle to the final state phase space. The truncation of the perturbation series can result in remaining divergences which are either mitigated by approximation schemes in the matrix element calculation or, when possible, regularised via dedicated selection criteria on the integration phase space. The treatment of these divergences is not further detailed here. The reader is referred to [123, 131] for more explanations. The combination with the subsequent parton shower in the NLO case is not straightforward and needs dedicated so-called matching algorithms, briefly introduced below.

As mentioned above, the finite order in perturbation theory and the factorisation of the partonic cross-section introduce the dependence on the choice of renormalisation and factorisation scales. The effects of these choices, including the one of the PDF set, are typically evaluated as modelling uncertainties on the matrix element in the analyses. The evaluation of variations to the final result caused by alternative settings of these parameters can already be included during the generation process via internal reweighting and are provided

via so-called on-the-flight weights on an event-by-event basis, a feature which has come to use during Run 2 of the LHC.

Finally, in giving the phase space information via so-called generator level selection requirements, all ingredients for the calculation of the hard scattering matrix elements and momentum integration are provided by the user. The physically inevitable phase space restrictions (typically on transverse momenta of partons or other objects, or related observable such as distance parameters between decay products) to avoid divergences, introduced for example by t-channel particle exchange or infrared QED radiation, are naturally accompanied by selections delimited by the fiducial acceptance of the detector at hand. The integration over the n-particle final state of the hard scattering process employing MC methods eventually delivers "parton-level" cross-sections and events.

Many programmes are on the market today which perform hard scattering matrix element computations and phase space integrations. The programmes used to model the signal process of the analyses in this thesis are Sherpa [132, 133], MadGraph5_aMC@NLO (short MG5_aMC) [134], and PowhegBox [135, 136]. Their special features with respect to the VBS process are detailed in the following chapters.

4.2.2 QCD Parton Showers

The occurrence of QCD parton showers in the collision of hadrons is a direct consequence of the non-abelian nature of QCD interactions and its colour confinement at small scales/long distances. This means, that high-energy inelastic collisions of hadrons, which are composite particles of coloured QCD partons, are inevitably accompanied by a cascade of many additional partons eventually forming hadrons itself. Hence, fixed-order calculations involving partons are inaccessible by hadron collider experiments.

Parton shower algorithms are thus formulated to dress the fixed order calculation of the hard scattering cross-section with additional real emissions of QCD partons off the initial and final-state partons taking part in the hard scattering process. Their goal is to formulate an inclusive result which approximates all higher order corrections of these real emissions to the hard scattering event. This is achieved by employing the principles of perturbative QCD and its factorisation to simulate the evolution of step-by-step single-parton branchings down to a scale where the formation of observable, colour-neutral hadrons sets in. As such, parton shower algorithms can be thought of as the transition from a final state of few partons of high energy to a final state with many partons of low energy.

The evolution of the branchings of initial and final state partons is based on the collinear factorisation of the subsequent emissions employing evolution equations and parton splitting functions. These are combined into an unconditional non-splitting probability between two scales for a single parton or colour dipoles and expressed via Sudakov form factors. In this way, the multiplicity of the final state is increased iteratively and independent of other partons in the event. This is crucial, as it makes it possible to solve these differential equations with iterative MC techniques that add one parton to the event at a time. The exact functional form depends on the choice of the evolution and the splitting variable. The evolution variable is usually a momentum-transfer-like variable, such as the opening angle or relative transverse momentum of the emitted parton with respect to the initial parton, and takes the role of the renormalisation scale in the parton shower algorithm. The splitting variable can be an energy or momentum fraction.

There are two commonly used approaches to ensure a colour coherent emission, i. e. to include the prescription of soft gluons and their interferences with harder gluons, in the parton shower formalism. One way is to choose the opening angle between the initial and the emitted parton as the evolution parameter, which intrinsically guarantees coherence in the emission. Another possibility is to use colour dipoles in the formulation of the splittings. These are referred to as dipole parton showers.

Eventually, the parton shower has to be reconnected to the hard scattering event by reassuring energy and momentum conservation after each branching. This is handled by the so-called recoil schemes implemented in the parton shower programmes. These can be realised globally or locally. The first distributes the energy among the whole hard scattering

event, while in the latter the recoil only affects those partons which are colour-connected to the splitting.

In addition, the initial state parton shower needs to be carefully connected to the PDF sets used in the hard scattering calculation. This is not further outlined here.

The resulting parton shower algorithms respect four-momentum and flavour conservation, as well as unitarity. The algorithms are universal and not dependent on the hard scattering core process[2].

The physics principles outlined here are implemented in different ways in current parton shower programmes. Not only the mathematical form of the algorithms itself leave many choices, such as the exact form of the splitting kernels and variables, or the evolution variable. Furthermore, they have various parameters which cannot be exactly determined but only guided by first principles. Comparing different parton shower setups against experimental data allows to specify these parameters and commonly collect them in so-called "tunes" of the programmes. These tunes comprise recommended prescriptions of parameter variations to assess modelling systematics of the predictions of the respective parton shower programmes.

Prominent examples of such parameters are the choice of some undetermined scales in the parton shower. These include:

- The resummation scale, i. e. the starting scale for the shower evolution;
- The evolution cutoff at low scales, i. e. the energy scale of the transition of the parton shower evolution into the formation of hadrons; and
- the renormalisation scale, which enters as argument of the running of the strong coupling constant α_S in the initial and final state emissions.

For the event generation of the signal process in this thesis, three parton shower programmes are employed: Pythia 8 Ref. [137], Herwig 7 [138, 139] and the default internal parton shower implemented in the Sherpa programme [140].

The default Pythia 8 setup uses the relative transverse momentum of the gluon with respect to the initial parton's direction k_T^2 as the evolution variable. It employs per default a global recoil scheme which is recently found to be non-optimal for processes involving VBS as the initial state partons are not colour connected which is ignored by the parton shower in this case [141].

Herwig 7 employs a default parton shower with angular ordering of the emission evolution. It also features a parton shower implementation based on dipoles and ordered in relative transverse momentum of the parton branching.

In the CSSHOWER implemented in the Sherpa programme, the evolution variable is again the relative transverse momentum of the gluon with respect to the initial parton's direction k_T^2. Colour coherence is assured via the dipole formalism.

4.2.3 Matching and Merging

A delicate matter now, after introducing the calculation of hard scattering events and subsequent QCD parton showers, is the consistent combination of these two when beyond LO QCD matrix elements are involved in the computation. The goal is to utilise each of the two descriptions in regions where they develop their full strengths, while preserving their respective accuracy and removing possible double counting of QCD emissions.

Many approaches have been invented in the last two decades. Only the techniques relevant for the generation of the signal samples in this thesis are discussed briefly here. These are:

- The combination of LO predictions from matrix elements with multiple final states of different parton multiplicities with QCD parton showers, called LO multi-jet merging; and
- The combination of NLO QCD accurate matrix elements with parton showers, called NLO matching.

[2]Though it has been observed that the global recoil scheme is non-optimal for processes which exhibit colour disconnected initial state partons, such as VBS.

LO Multi-jet Merging describes the additive combination of final states with different parton multiplicities at matrix element level, i. e. $pp \to X$, $pp \to Xj$, $pp \to Xjj$, ... up to a maximum parton multiplicity, into one sample. Higher parton multiplicities are then generated by the parton shower emissions off the matrix element with the highest parton multiplicity.

In order to circumvent double-counting, the QCD emission phase space is divided into a regime occupied by the hard emissions from the matrix element and a regime of soft and collinear emissions generated by the parton shower. The separation is realised via a requirement on the jet resolution scale, commonly denoted Q_{CUT}. The result is a prediction which is LO accurate in inclusive observables and exclusive quantities up to the maximum matrix element multiplicity, while retaining leading logarithmic accuracy for additional parton production.

The merging procedure is independent of the hard scattering core process X which in turn can already have jets in the final state at tree level. In this work, the CKKW-L prescription [142] is employed in the event generation of LO multi-jet merged signal predictions. The requirement on the jet resolution scale is hence denoted $Q_{\mathrm{CUT}} \equiv \mu_{\mathrm{CKKW}}$ and usually takes values around 20 GeV. Other methods exist [143] which are not further detailed here.

NLO Matching solves the problem of double-counting when attaching parton showers to NLO QCD accurate matrix element calculations which already include a first real emission. Two common approaches exist, the MC@NLO [144] and the Powheg [145, 146] method, where the latter is used for one of the nominal signal predictions in this work.

The Powheg method generates the hardest emission before and independent of the subsequent parton shower algorithm. The latter must, however, either be order in a momentum-like observable, or capable of imposing a veto in this observable. An advantage of the Powheg method is that it only gives events with positive weights.

4.2.4 Soft QCD Components, Decays and QED Radiation

After the parton shower evolution, the event generation is finalised with soft QCD phenomena, decays of unstable particles, and QED radiation. The first include the underlying event generation, and the hadronisation process. These rely on models which cannot be derived from first principles, as they take place at low scales where the strong perturbation series breaks down. The model parameters have to be derived with fits to experimental data and are collected in the different tunes of the programmes. The parton shower programmes used in this work, Pythia 8 [137], Herwig 7 [138, 139], and Sherpa [140] implement these phenomena in different ways. The exact implementation is not discussed in great detail here as they are not very relevant in this work. The focus rather lies upon the general physics motivation.

Underlying Event

The term underlying event encapsulates multiple phenomena, such as pileup reactions (cf. Sec. 3.3.3), multi-parton interactions (MPI), and the behaviour of the soft fragments of the protons. As such, it connects the hard scattering process to the protons of the incoming beams.

MPI describes additional interactions of the remaining constituents of the protons after taking part in the initial hard scattering process of interest. While these are per definition softer than the scattering process of interest, they can occur to be in the hard regime of QCD interactions.

All of these phenomena originate in the composite nature of the protons as the beam particles. They result in the modification of the number of particles occurring in the collision and observables related to the description of jets.

Hadronisation

During the parton shower evolution, the energy and momentum of the involved partons decreases until eventually the strong coupling constant becomes as large as one and perturbation series break down and confinement set in. This is understood to occur around 1 GeV. At this stage, the coloured partons are converted into colour-neutral, yet not necessarily stable, hadrons. This transition process is called hadronisation and is per definition non-perturbative. Models are used to describe this process, which are inspired by QCD and consider the momenta and flavour and colour structure of the partons in the event. Two common implementations are used in current programmes: the Lund string fragmentation [147] (Pythia 8) and the cluster model [148] (Herwig 7 and Sherpa).

Hadron and τ Lepton Decays

The hadrons created in the process of hadronisation can be exited, unstable states which further decay into lighter particles which are stable in the range of the detector dimensions (essentially protons, neutrons, kaons, pions, charged leptons, photons, and neutrinos). The τ lepton is also unstable in these dimensions, and its decays are generated within the MC event simulation chain. The many possible decay chains and particles involved make the modelling and implementation complex.

QED radiation

The radiation of photons is implemented in the MC event generation to account for soft photon emission processes, called bremsstrahlung, of charged particles in the event.

4.3 Preparation of MC Simulated Events for Analysis

This chapter so far deals with the generation of physics events based on the underlying theory. The result is a series of events, each consisting of a set of (many hundreds of) particles with all necessary physics properties. The events at this stage of simulation are referred to as "truth level" or "particle level" events.

In order to compare these events to actual data taken in an experiment, the response of the detector needs to be simulated, and the events need to be prepared for analysis. The steps necessary for this are presented in Fig. 3.11 and briefly outlined next. The resulting simulated and prepared events are referred to be at "reconstruction" or "detector" level. After normalising the simulated predictions to the luminosity collected in the relevant data-taking period, they can be used for the analyses.

4.3.1 Simulation of the ATLAS Detector and Reconstruction

The preparation of the physics events for analysis follows the steps outlined in Fig. 3.11. These are complex and resource intense. The simulation of the detector, in which the interaction of the particles with the material of the detector is simulated, follows the MC event generation. It is based on an implementation in the Geant4 software [149].

Subsequently, the simulation of the detector output, referred to as digitisation, and the reconstruction of physics objects from this information follows. These steps also include the simulation of the trigger and the pileup modulation, the latter of which is discussed in more detail in the next section. As for experimental data, also simulated data preparation is finalised with creating subsets of events serving special physics analysis needs, called derivations (cf. Sec. 3.3.4).

All these steps are subject to constant improvements and changes in the underlying software structures. Stages are tracked in so-called tags, which represent a given status of the software and physics models.

All simulated data samples used for the analyses in this thesis are summarised in App. C, including the tags, they have been simulated with and their explanation. Some of the samples of the signal process employed in the special studies in Chapter 6 and all samples used for

the EFT reinterpretation in Chapter 9 have been produced privately. All other samples have been produced within the ATLAS MC production framework.

4.3.2 Pile-up Handling and Reweighting

Pileup is injected into the MC simulated samples after the detector simulation step by overlaying Pythia 8 simulated minimum-bias events, i. e. events with low momentum transfer. The MC event samples used in this thesis are generated within an ATLAS wide MC production campaign, which defines the settings in the simulation. However, by the time of the running of this campaign, the LHC conditions, which highly influence the pileup conditions, have not been known. Hence, the average number of interactions per beam bunch crossing $<\mu>$, which defines the pileup, has to be guessed in the MC simulations and demands reweighting to the actual distribution once the data has been taken. Variations of the pileup modelling are provided in order to derive systematic uncertainties originating from the reweighting in MC simulated events.

In the same procedure, the distribution of average interactions per bunch crossing in data is shifted by a factor of 1/1.09.

4.3.3 Object Truth Matching

In many cases during the analyses, it can be advantageous to be able to identify a reconstruction level object with a physics object at truth level in simulated events, either created in the matrix element or the subsequent parton shower. This process is called truth matching of objects.

In the analysis of this work it is primarily used to identify prompt objects in the simulated events compared to non-prompt objects which either can be an artefact from misidentified detector responses or from non-prompt decays of primary hadrons.

In the procedure of truth matching, the objects get assigned a particle `type` and `origin` which produced the given particle. These properties are provided by the `MCTruthClassifier` tool [150]. Prompt leptons are then required to have truth `type IsoElectron` or `IsoMuon`, unless stated otherwise. In some cases, e. g. the analysis selection, the charge of the lepton is also truth matched.

4.3.4 Efficiencies and Scale Factors

Efficiencies on the reconstruction, identification, and selection requirement of all object types (cf. Sec. 3.4) are measured in data as well as in MC simulated events. Discrepancies between these efficiencies in data versus MC simulation are accounted for by applying so-called scale factors (SF) to simulated events. These factors are derived for all particle types and selection steps. Usually, they are provided in multiple bins of multiple observables, most commonly the transverse momentum of the object and its rapidity. For some pileup dependent selection procedures, these scale factors are also derived as a function of the number of primary vertices or the average interaction per bunch crossing. For electrons, muons, and jets, the procedures to obtain and apply these scale factors are discussed in detail in Ref. [102], [107], and [114, 151], respectively.

Chapter 5

Electroweak Vector Boson Scattering at the LHC

This chapter aims at giving the process definition and motivation for analyses involving electroweak Vector Boson Scattering (VBS) at the LHC. Commencing from the description of the self-couplings of electroweak gauge bosons from the SM Lagrangian, the process of VBS is constructed with the initial state conditions at the LHC when colliding two proton beams. The supreme aim is to gain knowledge about the self-couplings of the vector bosons, as well as the effect of the Higgs boson exchange in this class of processes. However, we will see in this chapter, that these contributions cannot be accessed directly and rather have to be measured together with irreducible and gauge invariantly inseparable background contributions. Yet, the different processes, exhibiting the same final states, can be separated and classified. This is explained in detail alongside the kinematic properties and the experimental signatures, which are expected for processes involving VBS, especially in the fully leptonic final state.

Further, as can be seen from Fig. 2.1, the VBS process has a very low cross-section compared to other processes of the SM that have already been measured at the LHC. It is even lower than for most Higgs boson channels.

Hence, both the theoretical description and the analysis of VBS are particularly challenging. At the LHC, it defines a process with up to six particles in the final state at LO and hence makes theoretical computations complicated. Nevertheless, theoreticians are pushing forward, publishing the computation of VBS (inclusive and differential) cross-sections at NLO accuracy in both, QCD and EW couplings. A short review of the VBS process' characteristics at NLO accuracy and common approximations in the calculations will complete the theoretical description and categorisation of the process. The chapter concludes with an overview of measurements including the VBS process in various final states conducted at the LHC experiments to date.

5.1 Definition of the Electroweak VBS Process at LO at the LHC

At the LHC, the electroweak VBS process at the partonic tree-level can be defined via the schematic Feynman diagram shown in Fig. 5.1. The partons, explicitly quarks or anti-quarks, inside the incoming protons accelerated by the LHC each radiate a vector boson which scatter off each other. The scattering among the quarks evolves via a t-channel exchange interaction, which can be identified as the subprocess $VV \to VV$ with $V = W^{\pm}, Z$, or γ. The Feynman diagram shown in Fig. 5.1, is schematic in the sense, that it signifies a collection of possible Feynman diagrams. The interaction of the vector bosons in the subprocess $VV \to VV$ occurs in multiple ways in the SM, defined by the quartic and triple self-interaction Feynman diagrams as shown in Fig. 2.5. For massive vector boson scattering, the $VV \to VV$ subprocess can also be mediated by the exchange of a Higgs boson in the t-, u- and/or s-channel depending on the involved vector bosons.

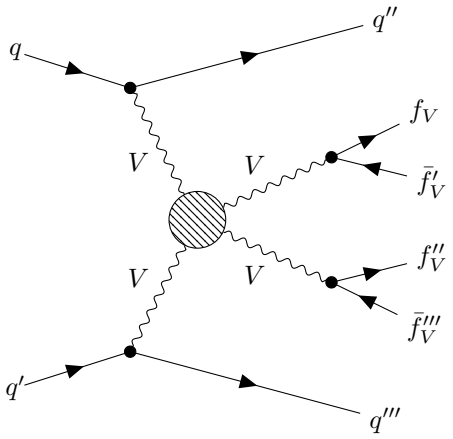


Figure 5.1: Schematic Feynman diagram illustrating the collection of VBS processes at the LHC. The Feynman diagram represents all processes with all possible incoming, outgoing, and intermediate particles as allowed by the SM. The hatched circle represents the collection of possible vector boson self-interactions as shown in Fig. 2.5. This diagram has the perturbative coupling order $\mathcal{O}(\alpha_{EW}^6 \alpha_S^0)$.

As a reminder from Chapter 2.2.3, this process is especially interesting due to the special role of the Higgs boson unitarising the VBS cross-section of longitudinally polarised vector bosons as assumed in the EWSB mechanism of the SM. This motivates to focus henceforth on VBS processes with massive vector bosons in the final state of the scattering subprocess. In this case, the scattered vector bosons being a $W^\pm$ or Z boson, decay promptly into fermions (quarks[1], charged leptons and/or neutrinos) with any flavour f_V. At LO, the partonic process can be expressed as:

$$qq' \to f_V \bar{f}'_V f''_V \bar{f}'''_V q'' q''', \tag{5.1}$$

where q denotes any quark or anti-quark possibly occurring in this process, as allowed by the SM. The two quarks in the final state evolve into hadronic jets in the detector of the experiments.

From the form of the squared matrix element the special, so-called "VBS topology" can be derived [131]. It is proportional to the four-momenta of the outgoing quarks. This implies a large cross-section for the VBS process when their momenta are large. Further, the propagators of the incoming vector bosons in the scattering process appear as denominator which is found to be minimal when the outgoing quarks'[2] deflection from the initial quarks (travelling along the beam line) is small. Consequently, the two outgoing quark jets' energy is predicted to be large while their scattering angle with respect to the beam line is fairly small. Together, this implies moderate transverse momentum p_T, a large invariant mass m_{jj}, and a large separation in rapidity:

$$\Delta Y_{jj} = |Y(j_1) - Y(j_2)|\,, \tag{5.2}$$

of the outgoing jets. As such, they are a special feature of the VBS process at the LHC and called tagging jets.

The decay modes of the outgoing vector bosons, $W^\pm$ or Z bosons, define three classes of final states:

- The fully leptonic final state, where both vector bosons decay into charged leptons or neutrinos, with a total of four leptons in the final state;
- The semi-leptonic final state, where one vector boson decays hadronically and the other one leptonically, exhibiting two leptons and two (additional) quarks in the final state; and

[1] In the following, quark denotes both quark and anti-quark. In the same way, lepton means any lepton or anti-lepton.

[2] Here, the quarks are considered to be massless which is a valid assumption in the typical experimental energy range of the process.

- The fully hadronic final state adds four quarks from the vector boson decays to the two quarks already present from the initial scattering.

Despite the branching fractions of the leptonic vector bosons decays, $W^{\pm} \to \ell^{\pm}\nu_{\ell}$ and $Z \to \ell^{\pm}\ell^{\mp}$, being small (21% and 6.7% with $\ell^{\pm} = e^{\pm}$ or $\mu^{\pm}$, respectively) compared to the hadronic decay fractions, the fully leptonic final states are the primary analysis interest at the LHC experiments. The reason for this is the overwhelmingly large cross-section of processes producing multi-jet final states at hadron colliders such as the LHC compared to the very small cross-section of VBS processes in this experimental setup. Due to the absence of colour connection between the two incoming and hence outgoing quark lines in the VBS process at LO, the hadronic activity in the central region of the detector is predicted to be reduced compared to processes involving QCD interactions. This can, of course, best be exploited in the fully leptonic final state where no additional hadronic jets from the decay of the vector bosons are present – another virtue of the fully leptonic final states.

From an experimental view point, the process of VBS can only be determined through the particles measured in the final state, which are the tagging jets and the decay products of the vector bosons, possibly charged leptons, missing transverse momentum from the escaped neutrinos, and/or more jets[3].

The perspective from a theoretical viewpoint, however, adds another important aspect to the process definition. In addition to the external particles, the perturbative order in strong and electroweak couplings can be assigned to a given process. At tree-level, the VBS process is defined at the order $\mathcal{O}(\alpha_{EW}^6\alpha_S^0)$ when including the decay products of the massive vector bosons. No strong couplings occur. Since photons can still occur in the $VV \to VV$ scattering, the electroweak coupling needs to be defined as $\alpha_{EW} \in \{\alpha_{QED}, \alpha_W\}$ in this notation, including both the QED and the weak fine-structure constants.

An attempt to experimentally measure a VBS process naturally entails the measurement of non-VBS contributions with the same final state, called irreducible backgrounds, at the same time. Moreover, from the theoretical side, the collection of scattering processes as defined with Fig. 5.1 alone is not gauge invariant. There are additional processes at the same coupling order $\mathcal{O}(\alpha_{EW}^6\alpha_S^0)$, not exhibiting the scattering of bosons, however, necessary to form a gauge invariant set of Feynman diagrams. The next section will systematise the possible contributions, proceeding via a classification in coupling orders.

5.2 Categorisation of Feynman Diagrams at LO

The full process of all possible contributions at LO in the SM is the production of two massive vector bosons in association with two jets, henceforth called $VVjj$. At tree-level, the set of signal and irreducible background processes occur at two different coupling orders at the amplitude level, $\mathcal{O}(\alpha_{EW}^3)$ and $\mathcal{O}(\alpha_{EW}^2\alpha_S)$, respectively. The cross-section of the $VVjj$ process, which is proportional to the squared amplitude, then receives contributions as:

$$\sigma_{VVjj} \sim \left|\mathcal{M}_{VVjj\text{-EW6}} + \mathcal{M}_{VVjj\text{-EW4}}\right|^2, \tag{5.3}$$

$$\sim \underbrace{\left|\mathcal{M}_{VVjj\text{-EW6}}\right|^2}_{\sim\alpha_{EW}^6} + \underbrace{\left|\mathcal{M}_{VVjj\text{-EW4}}\right|^2}_{\sim\alpha_{EW}^4\alpha_S^2} + \underbrace{2Re(\mathcal{M}_{VVjj\text{-EW6}}\mathcal{M}^*_{VVjj\text{-EW4}})}_{\sim\alpha_{EW}^5\alpha_S}, \tag{5.4}$$

$$\sigma_{VVjj} \equiv \sigma_{EW6} + \sigma_{EW4} + \sigma_{INT}. \tag{5.5}$$

Accordingly, three gauge invariant contributions to the $VVjj$ process exist. The definition of the individual contributions is adopted as: $VVjj$-EW6 or electroweak production at order $\mathcal{O}(\alpha_{EW}^6\alpha_S^0)$, $VVjj$-EW4 or strong or QCD-induced production at order $\mathcal{O}(\alpha_{EW}^4\alpha_S^2)$, as well

[3]The final state with outgoing photons in the $VV \to VV$ subprocess has a different experimental signature. The reason is that high-energetic photons are detected directly in the detector and not via their decay products, contrary to the $W^{\pm}$ and Z bosons. Hence, experimentally, final states with outgoing photons in the $VV \to VV$ subprocess are not considered here any longer. It is to be noted, that this does not exclude the processes with photons in the initial state of the VV scattering, e. g. in the W^+W^- final state. From the theoretical side, outgoing photons of the $VV \to VV$ are not excluded in this process definition as these can occur off their mass shell.

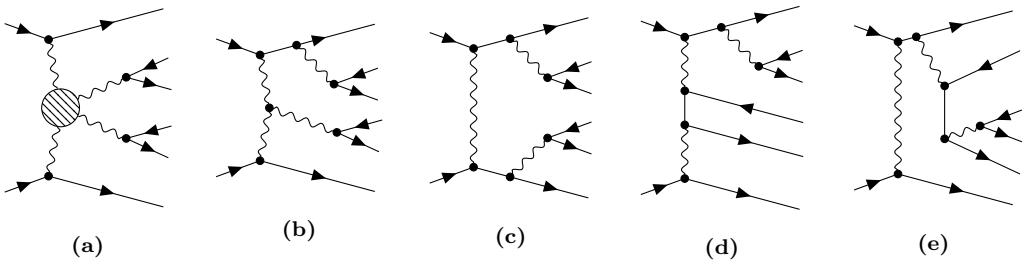


Figure 5.2: Examples of Feynman diagrams representing the process of $VVjj$-EW6 at LO in the t- and u-channels.

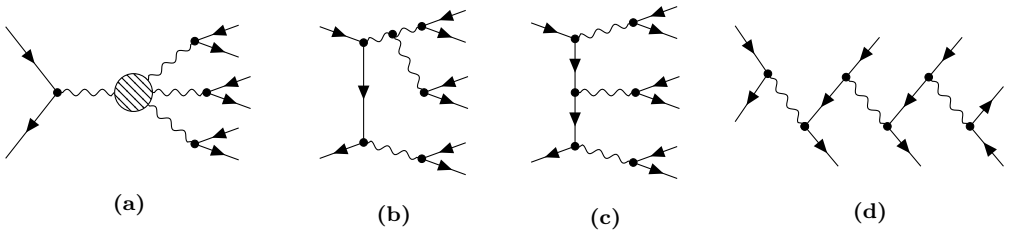


Figure 5.3: Examples of Feynman diagrams representing the process of $VVjj$-EW6 at LO in the s-channel.

as the interference between these two contributions at $\mathcal{O}(\alpha_{EW}^5 \alpha_S)$, denoted $VVjj$-INT. Here again, V stands for the outgoing vector bosons, a $W^\pm$ or Z boson as defined via the process definition in Eq. (5.1). While this chapter is meant to be a general overview of the classes of contributing processes to the $VVjj$ process, emphasis lies on the characteristics of the fully leptonic final states, the final state of the process under study in this thesis.

5.2.1 Electroweak Production

The electroweak production mode $VVjj$-EW6, at order $\mathcal{O}(\alpha_{EW}^6 \alpha_S^0)$, receives contributions from Feynman diagrams in the t/u-channel and s-channel as exemplarily depicted in Figures 5.2 and 5.3, respectively. From these figures, the different channels can be identified according to the distinct flow of the quark lines. In the t- and u-channels the initial state quark lines are connected to the final state ones, while for the s-channel diagrams the initial state quarks are connected with each other and hence also the final state ones. Clearly, depending on the particular final state considered, some of the diagrams may not be present.

At LO, the t/u-channels are characterised by the exchange of QCD colour neutral gauge bosons between the two quark lines. In addition to the genuine VBS process (Diagram 5.2 (a)), the t-channel comprises many more diagrams. One possibility is the radiation of one (Diagrams 5.2 (b), (d), and (e)) or two (Diagram 5.2 (c)) vector bosons directly off either of the quark lines. Moreover, especially when considering the full fermionic final state, diagrams with non-resonant vector bosons occur, where fermions are appearing in the t-channel (Diagrams 5.2 (d) and (e)). It is predicted that the contribution from these diagrams is fairly small (of the order of a few percent), owing to the suppression of these contributions by a factor Γ_V/m_V for each non-resonant vector boson, Γ_V being the decay width of the gauge boson [131]. Feynman diagrams in the u-channel are obtained from the t-channel ones when crossing the quark lines, which is only possible in processes with identical quark flavour combinations.

The s-channel is characterised by diagrams, where the two initial state quarks annihilate, hence are colour connected, emitting one or more gauge bosons in the s-channel. The emitted vector bosons can be resonant (Diagrams 5.3 (a)-(c)) or non-resonant (Diagrams 5.3 (d)). The resonant case is generally also referred to as triboson production. A special feature of all s-channel configurations is that (at least) one of the gauge bosons has to decay hadronically, to match the considered full final state of Eq. (5.1) with a minimum of two jets. Consequently,

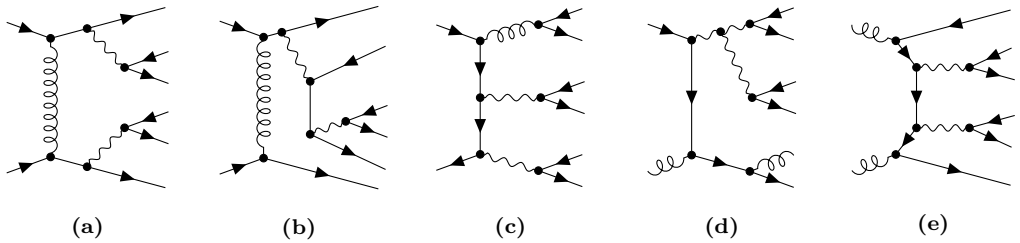


Figure 5.4: Examples of Feynman diagrams representing the process of $VVjj$-EW4 at LO.

the outgoing quarks are colour connected and the kinematics of the two jets is considerably different from the VBS tagging jet signature. Their invariant mass follows a Breit-Wigner distribution featuring a peak around the mass of the s-channel resonant gauge boson with decay width Γ_V. At LO, the main share of this contribution is thus occupying lower values in the m_{jj} spectrum compared to the VBS process.

In summary, the $VVjj$-EW6 production mode contains the signature process of VBS. However, irreducible background contributions from non-resonant diagrams are included to form a gauge invariant set of Feynman diagrams and hence obtain meaningful results. The s-channel configurations may be separated gauge-invariantly, however, including all possible contributions into the theoretical prescription ensures a sound description of the $VVjj$-EW6 process including all interferences between the different channels. Approximations with regard to the exclusion of certain contributions will be discussed later in this chapter.

In the literature, especially in earlier publications, the $VVjj$-EW6 contribution is sometimes referred to as VBS production even when including non-VBS configurations.

5.2.2 Strong or QCD-induced Production

The QCD-induced production mode $VVjj$-EW4, at order $\mathcal{O}(\alpha_{EW}^4\alpha_S^2)$, receives contributions from Feynman diagrams as exemplarily depicted in Fig. 5.4. One possible contribution of diboson production in association with two jets is the exchange of a gluon between the initial quark lines (diagrams 5.4 (a) and (b)), where the gauge bosons are radiated off the quark lines either in a resonant ((a)) or non-resonant ((b)) configuration. Secondly, processes where the two final state quarks emerge from a gluon splitting can occur (diagram 5.4 (c)). Further, contributions from processes with gluons in the initial and/or final state exist. Here again, depending on the particular final state at hand, some of the diagrams may not contribute. One remarkable feature of the fully leptonic final state is that there exist solely diagrams with colour connected initial state quark lines. Accordingly, the process $VVjj$-EW4 features much more hadronic activity in the central region, due to the jets being produced via QCD interactions. As a result, the distribution of the two jets' rapidity separation is maximal at zero, certainly a difference compared to the electroweak production.

As a consequence of the appearing strong couplings in this process, but also of the additional partonic processes which are possible, the cross-section of the strong production $VVjj$-EW4 is generally expected to be dominant over the electroweak production mode $VVjj$-EW6 (with one exception being the $W^\pm W^\pm jj$ final state which will be discussed in detail later). However, as a result of the considerably different colour structure of the two classes of processes, their kinematic properties are highly different, i. e. their respective contributions are large in very different phase space regions. This fact can be utilised to suppress the strong production sizeably.

5.2.3 Interference between the Electroweak and the Strong Production

The interference of the electroweak production $VVjj$-EW6 and the QCD-induced production $VVjj$-EW4, at coupling order $\mathcal{O}(\alpha_{EW}^5\alpha_S)$, contributes solely to those partonic subprocesses that exhibit identical external quarks. Already from this, one can infer that the interference

is colour suppressed. Due to the colour singlet configuration of the electroweak process, interference with the QCD-induced process is non-zero only when the propagation of the quarks is different for the two processes. This means only the connection of different channels at amplitude level, i. e. connecting t- and u-channel or t- and s-channel, gives a contribution. The kinematics of the final-state jets is, however, quite different for the electroweak and the strong process. As a result of the different colour structure, the QCD-induced process exhibits jets which are much more central than in the electroweak process. In order for the interference to become large, the jets in the strong production would need to radiate in the backward region, which is rather unlikely [131]. Also in Ref. [19] the interference between the $VVjj$-EW6 and the $VVjj$-EW4 production is stated to be small at LO (within a few percent) when imposing typical VBS cuts. The nature of these VBS cuts is discussed in the next section.

5.3 Experimental Signature in the Fully Leptonic Final State

Earlier in this chapter (Sec. 5.1), the key features in terms of the topology of the VBS process at the LHC have been identified. The tagging jets originating from the quarks deflected by the radiation of the initial gauge bosons are expected to exhibit a large invariant mass and rapidity separation. While almost all published analyses of the LHC experiments containing the study of the VBS process enhance the VBS contribution via selections on these two observables, other variables exist that are predicted to separate the VBS process from other background processes. The selections on these variables are commonly referred to as VBS cuts, where the focus lies on the suppression of the QCD-mediated process $VVjj$-EW4 and the enhancement of the electroweak contribution $VVjj$-EW6 in a certain fiducial region. Moreover, suppressing the contribution of the interference, $VVjj$-INT, is a main goal of many analyses. One of the reasons for this is, that the modelling of this contribution is not straightforward and has not been trusted very much[4]. As we have seen in Sec. 5.2.1, it is not possible to extract the VBS contribution of the electroweak process exclusively. However, it is possible to reduce the impact from processes which do not contain the scattering of vector bosons. At LO for example, a requirement on the invariant mass of the two leading jets around 200 GeV suppresses the triboson contribution substantially [141].

Since there is no colour exchange between the two quark lines in VBS production, the jet activity in the central region is small. This is especially true for the fully leptonic final state, where this property can be exploited via the use of the Zeppenfeld variable [152]:

$$z(i) = \left| \frac{Y(i) - \frac{Y(j_1)+Y(j_2)}{2}}{|Y(j_1) - Y(j_2)|} \right|, \tag{5.6}$$

where i denotes the object of which this quantity should be derived. Small values of the Zeppenfeld variable correspond to the object being more central with respect to the tagging jets while large values indicate the object being rather forward compared to these jets. In analyses, it is typically used for the charged leptons where a maximal value is required in order to select events where the leptons are produced more central in the detector. Rather used in theoretical studies and only rarely in analyses (see e. g. [153]) so far[5], the Zeppenfeld variable can also be derived for the third jet. Used in this manner, the observable is sensitive to the additional radiation's rapidity distribution.

A second option to study the kinematics of the charged leptons is the use of the lepton centrality variable [154]:

$$\begin{aligned} \zeta = \min \{ \; & \min\{Y(l_1), Y(l_2)\} - \min\{Y(j_1), Y(j_2)\}, \\ & \max\{Y(j_1), Y(j_2)\} - \max\{Y(l_1), Y(l_2)\} \}. \end{aligned} \tag{5.7}$$

[4]Only with the recent development in the modelling of EFT predictions, this field has been more investigated (cf Chapter 9).

[5]The reason for this is that additional jets are predominantly modelled by the parton shower due to the limited NLO QCD predictions in VBS today.

Table 5.1: Comparison of the predicted cross-section for fully leptonic final states of the $VVjj$-EW6 and the $VVjj$-EW4 processes calculated with SHERPA at LO in a typical phase space. The calculations include leptons of the first and second generation only, $\ell^\pm = e^\pm, \mu^\pm$; (anti-)neutrinos are labelled collectively ν. Statistical uncertainties on the cross-section from the phase space integration are below 2%. Numbers taken from Ref. [49], where detailed information on the process generation and the fiducial phase can be found. The last column shows the ratio of the $VVjj$-EW6 over the $VVjj$-EW4 induced cross-section.

Final state	Sensitive VBS channel	σ_{EW6} [fb]	σ_{EW4} [fb]	$\frac{\sigma_{EW6}}{\sigma_{EW4}}$
$\nu_\ell\nu_\ell\nu'_\ell\nu'_\ell jj$	$ZZjj$	1.68	1.38	1.22
$\ell^\pm\nu_\ell\nu'_\ell\nu'_\ell jj$	$W^\pm Zjj$	7.64	15.5	0.49
$\ell^\pm\nu_\ell\ell'^\pm\nu'_\ell jj$	$W^\pm W^\pm jj$	3.97	0.346	11.5
$\ell^\pm\ell^\mp\nu_\ell\nu_\ell jj$	W^+W^-, $ZZjj$	12.3	21.8	0.56
$\ell^\pm\ell^\mp\ell'^\pm\nu'_\ell jj$	$W^\pm Zjj$	2.34	4.38	0.53
$\ell^\pm\ell^\mp\ell'^\pm\ell'^\mp jj$	$ZZjj$	0.098	0.100	0.98

It is characterised to be negative if one or both leptons have a larger absolute rapidity than the closest jet, and positive for events where both leptons are enclosed in rapidity within the two tagging jets.

In terms of the reduced jet activity of the electroweak compared to the QCD mediated process, a central jet veto can also be employed to reduce the strong production. In practise this means to discard events with additional jets, besides the two tagging jets, in the central region. Here, the exact definition of the jets is crucial, usually being selected with a minimum requirement on their transverse momentum. The modelling of the jet related kinematics must be reliable, ideally with the jet coming from the matrix element calculation. At LO this is not the case. Until recently, imposing a jet veto has been challenging and led to large modelling uncertainties due to issues with the setting in some parton shower programmes [141] (see Sec. 6.1 for more details). One more obstacle when using a jet veto is the experimental conditions with increasing pileup contributions in the LHC Run 2.

When imposing restrictions on the standard observables for the selection of the VBS process, the QCD induced $VVjj$-EW4 can be reduced sizeably. Tab. 5.1 shows the fiducial cross-section of the $VVjj$-EW6 and the $VVjj$-EW4 process in a typical phase space in VBS analyses. Besides selection requirements for the decay products of the vector bosons and basic kinematic restrictions on the jets, requirements on the invariant mass and rapidity separation have been imposed:

$$m_{jj} > 500\,\text{GeV}, \qquad \Delta Y_{jj} > 2.4. \tag{5.8}$$

Tab. 5.1 includes the ratio of the fiducial cross-section of the $VVjj$-EW6 over the $VVjj$-EW4 production. It can be noted that the cross-section for the latter is reduced to the same order of magnitude as the $VVjj$-EW6 process for almost all final states. One exception is the final state with two like-charge leptons in the final state, which is sensitive to the scattering channel $W^\pm W^\pm \to W^\pm W^\pm$. This final state is the subject of this thesis.

5.4 VBS at NLO in QCD and EW Couplings

Recent results of analyses including the study of the VBS process with the complete dataset of Run 2 of the LHC show that the statistical uncertainties of the fiducial cross-section measurements are still dominant (see e. g. Ref. [155]). Theoretical uncertainties, if not yet comparable in magnitude (e. g. in Ref. [156] theoretical uncertainties amount to 1/3 of the statistical uncertainty of the measurement), will become important once the LHC Run 3

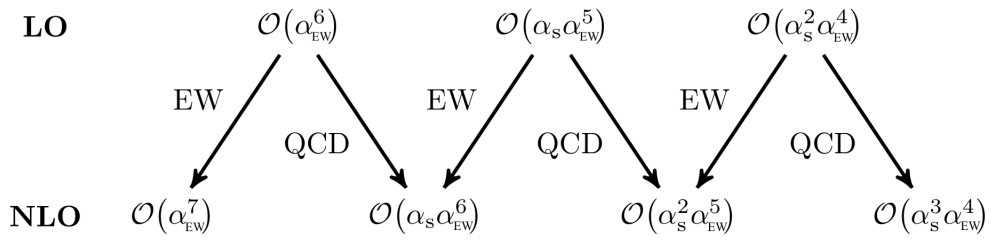


Figure 5.5: Contributing perturbative orders of the $VVjj$ process at LO and NLO at the LHC. Figure modified from Ref. [19].

dataset is being analysed, where the final accuracy for $VVjj$-EW6 processes is expected to amount to a few percent. Predictions at LO will then not suffice to gain useful insight when comparing experimental data to theoretical predictions. Moreover, as discussed above, it would be beneficial to exploit the characteristics of an additional jet, which only becomes reasonable once it is described in the matrix element calculation. Thus, the necessity of next-to-leading order (NLO) corrections to the various $VVjj$ processes is largely accepted and many calculations became available in recent time.

As depicted in Fig. 5.5, contributions of four different orders enter the complete NLO calculation of the $VVjj$ process, precisely being the orders $\mathcal{O}(\alpha_{EW}^7)$, $\mathcal{O}(\alpha_{EW}^6\alpha_S)$, $\mathcal{O}(\alpha_{EW}^5\alpha_S^2)$, $\mathcal{O}(\alpha_{EW}^4\alpha_S^3)$. At order $\mathcal{O}(\alpha_{EW}^7)$ only the NLO electroweak corrections to the $VVjj$-EW6 process enter. The order $\mathcal{O}(\alpha_{EW}^4\alpha_S^3)$ solely receives contributions from the QCD corrections of the $VVjj$-EW4 process. For the remaining two orders at $\mathcal{O}(\alpha_{EW}^6\alpha_S)$ and $\mathcal{O}(\alpha_{EW}^5\alpha_S^2)$ a simple separation between the electroweak and strong production mode is no longer possible as these orders receive contributions from at least two LO contributions. Hence, only the orders $\mathcal{O}(\alpha_{EW}^7)$ and $\mathcal{O}(\alpha_{EW}^4\alpha_S^3)$ can unambiguously be assigned to a given tree-level process. Theoreticians hence advise to conduct combined measurements of the full $VVjj$ process and add refined studies of the $VVjj$-EW6 component on top [141, 157].

Before we embark on the discussion of possible physics processes contributing at NLO and the current status of the available computations, the commonly used approximations of the theoretical calculations of the $VVjj$-EW6 process are briefly outlined.

5.4.1 Common Approximations in the Theoretical Calculation of the Electroweak Process

Without question, the dedicated study of the pure VBS process is compelling, however physically not well motivated. Approximations to the full calculation of the $VVjj$-EW6 process can help to select subsets of diagrams only, including those featuring the VBS process. These are formulated in a physically sound manner, respecting gauge invariance of the subset of diagrams considered. Nonetheless, they remain approximations which neglect parts of the full process. Their impacts need to be studied case by case in a careful manner, as they can depend on the particular final state and the fiducial region.

This section reviews the approximations used when computing the electroweak process $VVjj$-EW6 at LO and/or NLO. While many of the approximations can and have been used in the past for LO calculations, some of them are not used any longer in novel approaches today. Those, which can be employed at NLO are systematised and studied in the $W^\pm W^\pm jj$ process in Ref. [141].

Effective Vector Boson Approximation (EVA) [158–160] This approximation considers only the diagrams which include the $VV \to VV$ scattering explicitly. As pointed out before, this set of diagrams alone is not gauge invariant. This is circumvented in this approximation by considering solely the onshell projection of both, the incoming and outgoing vector bosons. For the incoming gauge bosons, this procedure is not trivial. The solution presented in Ref. [158–160] split these bosons into one part which participates in the $VV \to VV$ scattering process. The part where the gauge bosons are radiated off the

quark lines is further described by vector boson luminosities. Historically, this approximation is also called EWA, since it was first described for the scattering of $W^{\pm}$ bosons. Due to the theoretical shortcomings, this approximation should not be used further. In fact, the following approximations supersede it.

VBS Approximation [161–164] This approximation considers solely the contribution of t- and u-channel diagrams, neglecting their interference as well as the complete s-channel contribution (plus any interferences with the other channels) [141, 165]. It is hence usually denoted as $|t|^2 + |u|^2$ contribution. It is expected that the interference between the t- and u-channel is small because of colour and phase space suppression. This set is gauge invariant. This can be anticipated when considering the two incoming quarks as copies of two separate $SU(3)_C$ gauge groups, inferring two separate colour charges. As a consequence, no s-channel contributions are allowed due to the conservation of each of the two colour charges. In addition, the $VVjj$-INT contribution also cancels. This approximation is calculated at NLO [161–164] and implemented in the VBFNLO [164, 166, 167] and PowhegBox programmes [135].

VBS Approximation + s-Channel [164, 166, 167] This approximation carries forward the VBS approximation by adding the s-channel squared matrix element, leading to the computation of the contributions from $|t|^2+|u|^2+|s|^2$. Interferences between the channels are still neglected. Both, this and the VBS approximation have been invented at LO. They can be extended to NLO for the computation of NLO QCD correction to the $VVjj$-EW6 process, when being careful as to only consider gauge invariant subsets for the real emission contributions. This especially affects processes with gluons in the initial state. This approximation can be used within the VBFNLO framework [164, 166, 167].

Discarding Non-Factorisable QCD Corrections [134] The next stage of approximations towards the full NLO calculation is to consider all real emission contributions with all interferences, while only including a part of the virtual corrections. In particular, those virtual corrections which connect the two different incoming quark lines can be neglected and hence only considering factorisable corrections to the NLO QCD contribution. This has the advantage to avoid contributions with loops diagrams with many external legs. (An example for a non-factorisable contribution would be Diagram 5.6 (e) discussed in the next section.) This approximation is implemented in the MadGraph5_aMC@NLO [134] programme.

Resonant V Approximation [134] This approximation explicitly requires the exchanged vector bosons to be resonant, i. e. neglecting all non-resonant contributions. As discussed earlier, the non-resonant contributions are phase space suppressed proportional to the gauge boson's mass. This approximation can be implemented in a straightforward manner at LO and NLO. While at LO it is not so much relevant for the $VVjj$ processes any more, this approximation is to date, from a technical standpoint, one of the most complete implementations in any simulation programme, e. g. in MadGraph5_aMC@NLO [134] with the usage of MadSpin [168] in the notation:

```
p p > V V j j, V > [decay].
```

However, this approximation can become problematic on analysis level, as usually simulation samples which are signal samples for one final state analysis can be background samples for other final state analyses. These analyses can exhibit vastly different fiducial phase spaces. It is then not ensured that the missing non-resonant contributions are negligible. In particular, it discards contributions involving virtual photons.

5.4.2 The Nature of NLO Corrections

NLO corrections to the full $VVjj$ process have many facets, some of which shall be described here exemplarily for all contributing orders in α_{EW} and α_S, $\mathcal{O}(\alpha_{EW}^7)$, $\mathcal{O}(\alpha_{EW}^6\alpha_S)$, $\mathcal{O}(\alpha_{EW}^5\alpha_S^2)$, $\mathcal{O}(\alpha_{EW}^4\alpha_S^3)$. The discussion is based on Ref. [19, 131].

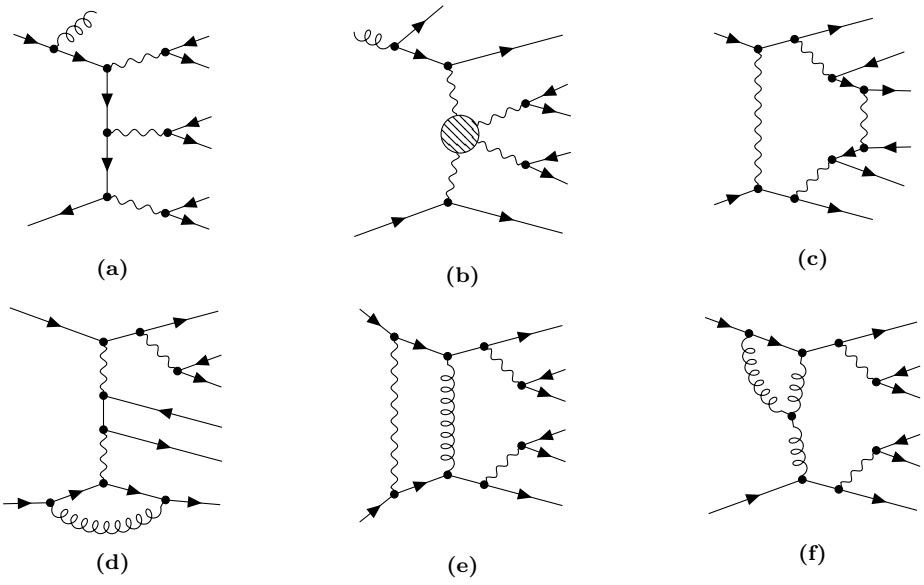


Figure 5.6: Examples of Feynman diagrams representing NLO corrections in QCD and EW to both the $VVjj$-EW6 and $VVjj$-EW4 process: (a), (b), and (d) show NLO QCD real ((a) and (b)) and virtual one-loop ((d)) corrections to the $VVjj$-EW6 process; (c) shows virtual one-loop EW corrections to the $VVjj$-EW6 process; (e) can be interpreted twofold: it can be seen as one-loop QCD correction to the $VVjj$-EW6 or as one-loop EW correction to the $VVjj$-EW4 process; (f) shows virtual one-loop QCD corrections to the $VVjj$-EW4 process. Examples adapted from Ref. [19, 131].

The real corrections at NLO $\mathcal{O}(\alpha_{EW}^7)$ to the electroweak process $VVjj$-EW6 solely include the radiation of photons off any of the involved charged particles, leading to the partonic process $qq \to f_V \bar{f}_V f'_V \bar{f}'_V qq\gamma$ with one additional photon in the matrix element calculation. Care must be taken when matching these kinds of processes to parton shower programs, which simulate QED radiation. The radiation of massive gauge bosons is not included as this would lead to a process definition which is certainly distinguishable, because of extra decay products that can be measured in the detectors. Due to the crossing symmetry, photons can also occur in the initial state at this order. In this case, PDFs with photons need to be used for a full factorised treatment.

At order $\mathcal{O}(\alpha_{EW}^6 \alpha_S)$, real corrections receive contributions from two types of radiation. One of this is the gluon radiation off any coloured particle of the $VVjj$-EW6 process (Diagram 5.6 (a)), leading to the partonic process $q(q/g) \to f_V \bar{f}_V f'_V \bar{f}'_V qq(g/q)$. Due to the crossing symmetry, this also leads to contributions with gluons in the initial state (Diagram 5.6 (b)). It is important to note that these extra emissions tend to be radiated close to one of the tagging jets due to the absent colour connection in the electroweak process. Hence, the gap in rapidity should only be affected mildly. The second category of real correction contribution to the order $\mathcal{O}(\alpha_{EW}^6 \alpha_S)$ is the radiation of a photon from the underlying $VVjj$-INT contribution. Again here, photons can occur in the initial state due to the crossing symmetry.

The same procedure can be applied to understand the real corrections contributing to the order $\mathcal{O}(\alpha_{EW}^5 \alpha_S^2)$, namely photon radiation from the strong production, as well as QCD radiation of the interference between the $VVjj$-EW6 and $VVjj$-EW4 process.

At order $\mathcal{O}(\alpha_{EW}^4 \alpha_S^3)$, only the real QCD radiation to the strong production enters the computation, leading again to a three parton final state at matrix element level.

The virtual corrections to the $VVjj$ process are rich, especially for the case of electroweak corrections. Only a few possibilities shall be discussed here. The key aspect here will be that different sources of corrections, QCD and electroweak are not distinguishable any longer, reinforcing the need for measurements of the full $VVjj$ process.

Virtual corrections at order $\mathcal{O}(\alpha_{EW}^7)$ include the connection of the two quark lines with yet another gauge boson, or possibly also between the decay products of the outgoing vector

bosons (Diagram 5.6 (c)). These corrections induce diagrams with loops up to eight external legs, which undoubtedly challenges the state-of-the-art computer programmes. Moreover, diagrams featuring corrections to the Higgs, the triple or quartic gauge boson self-interaction appear, either by loops involving gauge bosons or heavy fermions. As well, corrections to the qqV vertices occur.

Now, at order $\mathcal{O}(\alpha_{EW}^6\alpha_S)$, multiple types of corrections contribute. Gluon exchanges in the electroweak production (Diagram 5.6 (d) and (e)) appear, where the latter presents an example of non-factorisable QCD corrections to the electroweak process. Electroweak corrections to the $VVjj$-EW4 process can occur at the same order. Both types of corrections can be depicted by the Feynman diagram 5.6 (e), hence their separation is not meaningful and physically impossible. Moreover, at this order, the mixing of the electroweak and strong production occurs at another level, namely when electroweak corrections to the $VVjj$-EW6 process are contracted with the $VVjj$-EW4 Born amplitude [19]. Similar types of contributions enter at order $\mathcal{O}(\alpha_{EW}^5\alpha_S^2)$.

At order $\mathcal{O}(\alpha_{EW}^4\alpha_S^3)$, virtual one-loop QCD corrections to the strong production occur (Diagram 5.6 (f)).

While the example Feynman diagrams in Fig. 5.6 are shown for one of the LO contributions only, many of the corrections can contribute to both the $VVjj$-EW6 and $VVjj$-EW4 process. Again, depending on the final-state, some of the diagrams may not contribute.

5.4.3 Current Status of the Theoretical Calculations

Moving to NLO accuracy in the strong coupling constant for the $VVjj$ process entails some approaches to meet the complexity of the process. First of all, there is the high dimensionality with six final state particles already at leading order, adding a seventh for the real-emission corrections. Moreover, already mentioned, loops with up to eight external particles occur in the calculations. Due to the delicate colour structure of the pure electroweak process at LO, adding QCD loop corrections changes the overall structure of the process. In addition, the problem of soft photon divergencies can occur for the real emission contributions, when imposing only momentum requirements to the first two jets. In this case, it can happen that the quark line off which the photon is radiated remains unconstrained in terms of a minimum momentum selection.

This section mainly discusses the case of fully leptonic final states. Inclusive predictions at NLO accuracy for semi-leptonic final states are rare due to their multi-jet signatures. Calculations have only been found in Ref. [131] or with b quarks in the final state. The latter are regarded to be of less interest due to most VBS analyses imposing b-jet vetoes.

Next-to-leading order QCD calculations to the $VVjj$-EW6 production (order $\mathcal{O}(\alpha_{EW}^6\alpha_S)$) have first been calculated in the fully leptonic final states by excluding s-channel and non-factorisable contributions [161, 162, 169–172]. The exclusion of the latter are found to be fairly small, depending on the definition of the fiducial region, the choice of factorisation and renormalisation scales, and the particular process. These fixed-order computations have been matched to parton showers via an implementation in the PowhegBox Monte-Carlo programme since a decade now [135, 173–175], which has implemented the VBS approximation. The parton shower matched results show modest ($10-15\%$) effects on the normalisation and shape of kinematic distributions when compared to the fixed order NLO calculations.

The use of other MC programmes and matching schemes has only been presented recently, and in the case of a theoretical study of the $W^\pm W^\pm jj$-EW6 final state [141]. This includes the VBFNLO and MadGraph5_aMC@NLO progammes. The first can be used within the Matchbox framework of the Herwig 7 programme [138, 139] and employes the VBS approximation. The latter can be interfaced to Pythia 8 [137] or Herwig 7, as well as used within the Matchbox framework of the Herwig 7 programme. It employs the non-factorisable QCD approximation and is technically tested only with the resonant V implementation so far. None of these have been utilised in experimental measurements yet.

An extensive summary of LO and NLO QCD corrected fixed order cross-section at centre-of-mass energy 13 TeV is shown in Tab. II of Ref. [131]. Not only does it include almost all VBS final states, but also vector boson fusion and Higgs production modes. A fairly loose

phase space is chosen for the computation which aims at mitigating divergences of the cross-section (transverse momentum restrictions on jets, leptons, and photons), as well as emulating the detector conditions (rapidity selections). Computed k-factors, defined as the ratio of the NLO with respect to the LO cross-section:

$$k = \frac{\sigma(\text{NLO})}{\sigma(\text{LO})}, \tag{5.9}$$

range between 0.98 and 1.08 for fully leptonic VBS final states, and between 0.99 and 1.03 for VBS processes involving photons. QCD NLO k-factors for semi-leptonic VBS final states are considerably larger and all above 1 ranging from 1.07 to 1.19.

Fixed order NLO computations of the QCD induced processes, at order $\mathcal{O}(\alpha_{EW}^4\alpha_S^3)$, are available for some of the fully leptonic final states [163, 164, 176, 177] and matched to parton showers so far only for the $W^\pm W^\pm jj$ final state [136] within the POWHEGBOX Monte-Carlo programme. Note that these calculations include the full NLO corrections at order $\mathcal{O}(\alpha_{EW}^4\alpha_S^3)$ without any approximations. For processes other than $W^\pm W^\pm jj$, the computation of NLO corrections to the $VVjj$ process becomes challenging, due to the processes with lower jet multiplicity, which need to be considered in the calculations when analysing a two jet final state. In $W^\pm W^\pm jj$, the final state with two jets constitutes the one with the lowest possible jet multiplicity in the SM at tree-level.

It is not expected that calculations beyond NLO in QCD will become available in the near future for processes involving VBS due to the challenging characteristics described above. Another reason for this is the hierarchy of corrections contributing at the different NLO orders, found to be rather unintuitive in recent publications.

This brings us to the discussion of the NLO correction at order $\mathcal{O}(\alpha_{EW}^7)$. From the perspective of the perturbative evolution, comparing the size of the strong and electroweak coupling constants, corrections at NLO in the electroweak coupling should match the order of magnitude of next-to-next-to-leading order (NNLO) correction in α_S. This consideration is generally valid for the total cross-section, while no overall statement can be made for differential distributions. This statement holds when regarding inclusive diboson production [178–180] where the corrections at the level of the total cross-section amount to a few percent.

Publications in the past few years, which cover the computation of NLO EW corrections to the $VVjj$-EW6 process, however draw a substantially different picture, e. g. in the case of $W^\pm W^\pm jj$ scattering [181]. Corrections of the order $\mathcal{O}(\alpha_{EW}^7)$ are large already at the total cross-section level, reaching up to -16%, and even larger in the tails of differential distributions. The large corrections are due to large Sudakov logarithms arising from the virtual t-channel exchange of massive vector bosons. These usually affect the tails of distributions, such as invariant masses or transverse momenta, because of their logarithmic suppression at high energies. Large negative electroweak corrections to the $VVjj$-EW6 process are hence an intrinsic feature of the process structure at the LHC and not caused by the selection criteria imposed in VBS analyses [131].

Very recently then, computations of the full NLO corrections to $VVjj$ processes have been presented in Ref. [19, 182, 183] including all possible orders. From these results, it can be seen that the corrections at order $\mathcal{O}(\alpha_{EW}^7)$ are the largest of all, an observation that is independent on the considered VBS final state. Moreover, comparing to the high-luminosity plans of the LHC experiments in the future, measurements at $3000\,\text{fb}^{-1}$ will most probably show to be sensitive to these corrections. A major step in the direction of making these calculations available for comparison with experimental data, has been the automated implementation of the full fixed-order calculation of NLO corrections in the MC programme SHERPA using the matrix element generator RECOLA [184–186].

5.5 Overview of VBS Final States and Measurements at the LHC

The fiducial cross-sections for the electroweak production, $VVjj$-EW6, are of the order of a few femtobarns in pp collisions at 13 TeV centre-of-mass energy, as can be seen in Tab. 5.1.

As such, they rank among the smallest which have been measured in the LHC experiments ATLAS and CMS (refer to Fig. 2.1) [43, 187]. Besides studies on the measurement potential of such processes published by the LHCb experiment [188], only these two experiments have published results on so-called VBS measurements.

The latest results of the measurements of many $VVjj$-EW6 final states are summarised in Tab. 5.2 for the two experiments. All results are based on partial or full data delivered by the LHC in the Run 2 data-taking period between 2015 and 2018, superseding the Run 1 measurements. Besides for the semi-leptonic, many of the possible final states of the $VVjj$-EW6 process have been observed for the first time by at least one of the experiments with this dataset.

Many of the results solely measure the electroweak component of the $VVjj$ process. Only very recent analyses [155, 189] move towards presenting fiducial cross-section measurements of the full $VVjj$ process together with separate refined analyses of the $VVjj$-EW6 contribution only. This follows the recommendations of the theory community with view of higher order accurate predictions. In addition, several analyses published bounds on dimension-8 Effective Field Theory (EFT) parameters [17, 18, 154, 155, 189, 190] or the production cross-section of doubly charged Higgs bosons [14]. Current limits of dimension-8 EFT parameters will be discussed in greater depth in Chapter 9.

Except for final states with two same-charge leptons, which are sensitive to the $W^{\pm}W^{\pm} \rightarrow W^{\pm}W^{\pm}$ scattering process, the $VVjj$-EW4 process constitutes one of the major irreducible backgrounds in the analyses of the electroweak component. Other major background contributions are listed in Tab. 5.2, which can be instrumental backgrounds where, e. g. charged leptons/photons are misidentified from other objects, as well as single or diboson production in association with jets, where charged leptons/photons fall outside the detector acceptance.

The fully leptonic, together with the photon-involved final states, possess the cleanest signatures in the hadron collider experiments. First evidences and observations of processes involving VBS have been claimed in the fully leptonic final state of two same-charge leptons plus neutrinos [13, 14]. The analyses of these final states move toward the phase of precision measurements, publishing unfolded distributions [15, 155] and first polarisation studies [193].

Thus far, there have been no measurements conducted in the final state with four neutrinos, and in the $\ell^{\pm}\nu_{\ell}\ell'^{\mp}\nu'_{\ell}jj$ final state involving the scattering of two oppositely charged $W^{\pm}$ bosons. The latter are challenging at hadron colliders due to the background contributions from top quark pair production with leptonic $W^{\pm}$ boson decays. Such a final state needs a high veto efficiency for b-jets entailing larger experimental uncertainties.

Analyses of semi-leptonic final states typically utilise hadronic boson tagging in a resolved and/or merged topology for the hadronically decaying vector bosons. The resolved analysis branch selects two separate small radius (usually $R = 0.4$) jets whose invariant mass is close to the $W^{\pm}$ and Z boson mass. In the merged[6] case, one large radius jet ($R = 0.8$ or 1.0, indicated by J in Tab. 5.2) is reconstructed which is required to comprise two main subjets whose invariant mass is close to the $W^{\pm}$ and Z boson mass. The jet energy resolution in these analyses is typically not precise enough to distinguish between a hadronic $W^{\pm}$ or Z boson. Hence, mixed final states are measured. The advantage of higher branching ratios for hadronically decaying gauge bosons is flattened by large background contributions. Large jet p_{T} requirements reduce the backgrounds, however, also the sensitivity to the $VVjj$ processes. This special phase space, however, is suitable for the search for BSM effects, which arise at very high energies.

None of the LHC experiments has published analyses involving only hadronically decaying gauge bosons. Due to the overwhelming background contribution from multijet production, it is claimed that analyses covering these final states are solely possible with the selection of two boosted vector bosons [157]. This leaves limited potential for the study of the SM $VVjj$ processes, while conceivably exhibiting good sensitivity to BSM effects.

While not involving the mechanism of Electroweak Symmetry Breaking (EWSB), the $VVjj$ production involving photons is still interesting. Experimentally, these final states involve the direct detection of energetic photons, which has large efficiencies and hence a

[6] This analysis strategy is sometimes also referred to as boosted topology, especially in the search for new physics signatures, when large Lorentz factors are expected.

Table 5.2: Overview of measurements involving VBS with the ATLAS and CMS experiments at a centre-of-mass energy $\sqrt{s} = 13\,\text{TeV}$ in the fully leptonic, and the semi-leptonic final state, as well as final states involving photons. Included are the most recent publications or the last publication where an observation has been claimed for a specific process. Details on the major background contributions exclude the $VVjj$-EW4 process which is a main background in all analyses, except for the $W^\pm W^\pm jj$ final state. The analysis of the $W^\pm W^\pm jj$ final state with the ATLAS experiment published in Ref. [1] is subject of the SM analysis of the subsequent chapters of this work.

		ATLAS experiment		CMS experiment		
Final state	Sensitive VBS channel	Luminosity [fb^{-1}]	Obs. (exp.) significance	Luminosity [fb^{-1}]	Obs. (exp.) significance	Major background contributions (besides $VVjj$-EW4)
Fully leptonic VBS final states:						
$\ell^\pm\nu_\ell\ell'^\pm\nu'_{\ell'}jj$	$W^\pm W^\pm jj$	36.1	$6.5(4.4)\,\sigma$ [1]	35.9	$5.5(5.7)\,\sigma$ [14]	$W^\pm Z$ lept. final states, instrumental bkgs.
$\ell^\pm\ell^\mp\ell'^\pm\nu'_{\ell'}jj$	$W^\pm Zjj$	36.1	$5.3(3.2)\,\sigma$ [15]	137	$6.8(5.3)\,\sigma$ [155]	ZZ lept. final states, instrumental bkgs.
$\ell^\pm\ell^\mp\ell'^\pm\ell'^\mp jj$	$ZZjj$	139	$5.5(4.3)\,\sigma$ [16]	137	$4.0(3.5)\,\sigma$ [189]	instrumental bkgs.
$\ell^\pm\ell^\mp\nu_\ell\nu_\ell jj$				–	–	$W^\pm Z$ leptonic final states
Semi-leptonic VBS final states:						
$\ell^\pm\ell^\mp(jj/J)jj$				35.9	only BSM interpr. [154]	$W^\pm/Z$ in association with jets or top production
$\ell^\pm\nu_\ell(jj/J)jj$	$(W^\pm/Z)Vjj$	35.5	$2.7(2.5)\,\sigma$ [190]	137	$4.4(5.1)\,\sigma$ [191]	
$\nu_\ell\nu_\ell(jj/J)jj$				–	–	
VBS final states with photons:						
$\ell^\pm\nu_\ell\gamma jj$	$W^\pm\gamma jj$	–	–	35.9	$5.3(4.8)\,\sigma$ [17]	$W^\pm/Z$ in association with jets or γ, instrumental bkgs.
$\ell^\pm\ell^\mp\gamma jj$	$Z\gamma jj$	36.1	$4.1(4.1)\,\sigma$ [192]	137	$9.4(8.5)\,\sigma$ [18]	

comparably large fiducial cross-section. Theoretically, the gauge structure of the SM can be equally probed through scattering where photons participate.

The typical experimental signatures of processes involving VBS have been outlined in Sec. 5.1 and 5.3. Tab. 5.3 collects the selection criteria for the analyses covered in Tab. 5.2. All analyses define their tagging jets to be the two with the largest transverse momentum. Some ATLAS analyses, however, impose the criterion of the jets having to occupy opposite rapidity hemispheres of the detector $Y(j_1) \cdot Y(j_2) < 0$ which replaces the rapidity separation requirement ΔY_{jj}. This quantity, however, is not Lorentz invariant under boosts along the z axis. The transverse mass requirements of the tagging jets are consistently applied, with values ranging between 300 and 500 GeV for most of the analyses. The selection of the rapidity separation, if applied, is steady around the values between 2.0 or 2.5. The Zeppenfeld variable, defined in Eq. (5.6), is established in many CMS analyses and used for particular (systems of) objects under study, while the centrality measure, defined in Eq. (5.7), is only used rarely. Especially, the analyses studying the $ZZjj$ final states present multiple regions to measure the $ZZjj$-EW6 process. A veto in selecting additional central jets inside the rapidity region that is spanned by the tagging jet system is not applied in any of the considered analyses. It is rather used in Vector Boson Fusion (VBF) analyses, e. g. in Ref. [194, 195].

Table 5.3: Overview of selection criteria used in recent analyses to extract the $VVjj$-EW6 component involving VBS at the LHC. The quantities are defined as follows: m_{jj} is the invariant mass of the tagging jet system, ΔY_{jj} denotes the rapidity separation of the tagging jets defined in Eq. (5.2), $z(i)$ is the Zeppenfeld variable of object i defined in Eq. (5.6), and ζ is the centrality variable defined in Eq. (5.7). Values summarised from measurements shown in Tab. 5.2.

VBS channel	Experiment	Tagging jet selection: Highest p_{T}+ ...	$m_{jj} >$ [GeV]	$\Delta Y_{jj} >$	$z(i)$	ζ	Ref.
Fully leptonic VBS final states:							
$W^{\pm}W^{\pm}jj$	ATLAS	–	500	2.0	–	–	[1]
	CMS	–	500	2.5	$\max(z(l)) < 0.75$	–	[14]
$W^{\pm}Zjj$	ATLAS	$Y(j_1) \cdot Y(j_2) < 0$	500	–	–	–	[15]
	CMS	–	500	2.5	$\max(z(l)) < 1.0$	–	[155]
$ZZjj$	ATLAS	$Y(j_1) \cdot Y(j_2) < 0$	300(400)	2.0	–	–	[16]
	CMS	–	400	2.5(5.0)	–	–	[189]
Semi-leptonic VBS final states:							
$(W^{\pm}/Z)Vjj$	ATLAS	$Y(j_1) \cdot Y(j_2) < 0$	400	–	–	–	[190]
$ZVjj$	CMS	–	800	4.0	$z(W) < 0.3$, $z(V) < 0.3$	> 1.0	[154]
$W^{\pm}Vjj$	CMS	–	500	2.5	–	–	[191]
VBS final states with photons:							
$W^{\pm}\gamma jj$	CMS	–	500	2.5	$z(W\gamma) < 1.2$	–	[17]
$Z\gamma jj$	ATLAS	–	150	1.0	–	< 5.0	[192]
	CMS	–	500	2.5	$z(Z\gamma) < 2.4$	–	[18]

Chapter 6

Theoretical Predictions

Among all possible processes involving VBS at the LHC, the final state with two equally charged leptons and two neutrinos is certainly exceptional. It is referred to as $W^{\pm}W^{\pm}$ scattering or the $W^{\pm}W^{\pm}jj$-EW6 process and is one of the few processes occurring at the LHC and predicted by the SM that produces exactly two charged leptons with equal charge. Solely the QCD induced process $W^{\pm}W^{\pm}jj$-EW4 appears as an irreducible background in the SM.

As a consequence of charge conservation, only a limited number of partonic channels participate in this scattering process. Moreover, initial states with b quarks do not contribute since these would result in final states with top quarks which create clearly distinguishable final states at the LHC. In addition, no s-channel boson exchanges are possible in the pure VBS process (see Fig. 5.1). These reductions of possible Feynman diagrams make the particular process of $W^{\pm}W^{\pm}$ scattering quantitatively easier accessible from a theoretical perspective.

At LO, no external gluons are allowed for the $W^{\pm}W^{\pm}jj$-EW4 process, discarding e. g. Diagrams 5.4 (d) and (e) from the collection of possible interactions. This induces a suppression of the QCD mediated irreducible background, compared to other $VVjj$ final states (refer to Tab. 5.1). The final state with solely leptonic decay products of the $W^{\pm}$ bosons is advantageous over semi-leptonic or fully-hadronic final states with reasons being discussed in the previous chapter. The superior branching fractions of leptonic decays of the $W^{\pm}$ compared to the Z boson add another benefit to the $W^{\pm}W^{\pm}jj$ final state. Together, these findings arrange the process of $W^{\pm}W^{\pm}$ scattering as a favourable experimental measurement at the LHC.

Indeed, the first evidence for a process involving VBS was found in 2014 (at a centre-of-mass energy $\sqrt{s}$ of 8 TeV in the Run 1 data-taking period of the LHC) in the $W^{\pm}W^{\pm}jj$ final state with the ATLAS experiment [13] and confirmed by the CMS experiment shortly after [196]. The first observation of the $W^{\pm}W^{\pm}jj$-EW6 process followed in 2017 in analyses of the partial Run 2 dataset taken at $\sqrt{s} = 13$ TeV first by the CMS experiment [14] and later by the ATLAS experiment [1]. These results state the first observation of a process involving the scattering of vector bosons, including the quartic and triple self-couplings of vector bosons.

It is no surprise that also with this final state, the study of the VBS processes enters the period of precision measurements. Analysing the full Run 2 dataset of the LHC, unfolded cross-section measurements [155] and polarisation studies [193] have been published in recent times. While measurements of $W^{\pm}W^{\pm}$ scattering are still dominated by the statistical uncertainty of the full Run 2 dataset, this will not be the case any longer in Run 3 of the LHC [197, 198]. Precise theoretical predictions at higher orders will then become indispensable, with theoretical uncertainties at minimum comparable with the expected experimental uncertainties. The foundation for this is laid in meticulous studies and comparisons to current measurements. As the $W^{\pm}W^{\pm}jj$ final state is the least complex process involving VBS in view of the theoretical prescriptions, it is particularly suited to test the modelling.

As will be shown later in this thesis, the $W^{\pm}W^{\pm}$ scattering process also shows decent sensitivity to new physics effects, though not reaching the performance of semi-leptonic

final states at the LHC. The search for BSM effects requires a solid understanding of the underlying SM processes and its uncertainties in order to acquire the best constraints on these models' parameters.

This chapter will begin with a short overview of the status of the theoretical calculations of the $W^{\pm}W^{\pm}jj$ process and summarise the most common or recent event generation programmes available today. Many of these have been discussed and compared in [141] whose main findings will be reviewed briefly. Then, the event generation setups for the $W^{\pm}W^{\pm}jj$ process used in this thesis are described, as well as the assessment of theoretical uncertainties from these predictions. Further, an extensive series of comparisons of the fiducial cross-section and kinematical distributions is shown in the fiducial region of the Run 2 ATLAS publication in this channel [1], which is subject of this thesis. Fiducial cross-sections are further compared in the regions defined by the Run 2 analysis of the CMS experiment [14] and the studies in [141]. The comparison studies are completed with a summary of the impact of the VBS approximation at NLO QCD, as well as the impact of NLO EW corrections in the analysis' fiducial phase space. As such, they confirm and extend the discussions in [199, 200]. The chapter concludes with sketching the prospects of theoretical tools available for the next generation of particle level predictions and the needs in future physics analyses of the $W^{\pm}W^{\pm}$ scattering process.

6.1 Current Status of Theoretical Predictions

Due to its comparably simple structure mentioned above, the landscape of next-to-leading order predictions for VBS has mostly been driven by the theoretical development of the $W^{\pm}W^{\pm}jj$ process. This section aims at giving a brief overview of the theoretical predictions available today both for the electroweak- and the QCD-mediated processes, $W^{\pm}W^{\pm}jj$-EW6 and $W^{\pm}W^{\pm}jj$-EW4, respectively. It is based on Ref. [141] where a comprehensive summary of the present status and extensive comparison studies have been presented for the $W^{\pm}W^{\pm}jj$-EW6 process[1]. As such, it constitutes the key literature work of the present theoretical status of the $W^{\pm}W^{\pm}jj$ scattering process.

Referring to Sec. 5.4, the full matrix element of the $W^{\pm}W^{\pm}jj$ process at NLO involves four distinct orders in electroweak and strong couplings, α_{EW} and α_S respectively: $\mathcal{O}(\alpha_{EW}^7)$, $\mathcal{O}(\alpha_{EW}^6\alpha_S)$, $\mathcal{O}(\alpha_{EW}^5\alpha_S^2)$, $\mathcal{O}(\alpha_{EW}^4\alpha_S^3)$.

Approximately a decade ago, first NLO calculations covered the QCD corrections to the electroweak process $W^{\pm}W^{\pm}jj$-EW6 at order $\mathcal{O}(\alpha_{EW}^6\alpha_S)$ in the VBS approximation [161–164]. These fixed-order computations have been matched to parton showers in the framework of the PowhegBox [135] or VBFNLO [164, 166, 167] shortly after. Both employ the VBS approximation for the calculation of the $W^{\pm}W^{\pm}jj$-EW6 matrix element. Around the same time, the QCD corrections to the strong production $W^{\pm}W^{\pm}jj$-EW4, at order $\mathcal{O}(\alpha_{EW}^4\alpha_S^3)$, have been published in Ref. [163, 176] and matched to parton showers, again within the PowhegBox programme [136]. It took several years until the first full NLO electroweak corrections, including non-resonant contributions, have been calculated at order $\mathcal{O}(\alpha_{EW}^7)$ for the $W^{\pm}W^{\pm}jj$-EW6 process [181]. Only one year later in 2017, complete NLO corrections to the full $W^{\pm}W^{\pm}jj$ process, including all orders, have been calculated in Ref. [19].

The latter two publications have been a breakthrough in several directions. First, they include the computation of the first NLO electroweak corrections for a process involving VBS. Second, the full NLO computations render it possible to assess the impact of the various approximations used in the calculation of NLO QCD corrections to the $W^{\pm}W^{\pm}jj$-EW6 process. Third, they include the computation of the order $\mathcal{O}(\alpha_{EW}^5\alpha_S^2)$ which have not been presented before. Lastly, with the full computation at all orders at NLO it is possible for the first time to rank the individual corrections by their magnitude. This renders it possible to prioritise the efforts of tool developement into directions where corrections are large.

Tab. 6.1 sketches again all possible orders in the electroweak and strong couplings at LO and NLO including the corrections of the LO processes that make up the NLO contributions. It also summarises the relative size of the correction at each next-to-leading order with respect to the full LO cross-section computed in Ref. [19] which confirms what has been discussed

[1] In Ref. [141] only the subprocess $pp \to \mu^+\nu_m u e^+\nu_e jj$ is considered.

Table 6.1: Summary of possible orders of the strong and electroweak couplings, α_S and α_{EW}, respectively, at LO and NLO including the type of the corrections of the LO contributions that make up each contribution at NLO. The fixed-order NLO corrections are stated as relative to the full LO cross-section of the $W^\pm W^\pm jj$ process. The availability of parton shower matched predictions of each NLO contribution is shown as well. The order $\mathcal{O}(\alpha_{EW}^6\alpha_S)$ is currently only available with approximations, indicated by *. Numbers are taken from Ref. [19]. Availability of NLO + parton shower matched predictions is modified from Ref. [157]. For further explanations see the text.

Leading order	$\mathcal{O}(\alpha_{EW}^6\alpha_S^0)$		$\mathcal{O}(\alpha_{EW}^5\alpha_S)$		$\mathcal{O}(\alpha_{EW}^4\alpha_S^2)$	
Correction	EW ↙	↘ QCD	EW ↙	↘ QCD	EW ↙	↘ QCD
Next-to-leading order	$\mathcal{O}(\alpha_{EW}^7)$	$\mathcal{O}(\alpha_{EW}^6\alpha_S)$		$\mathcal{O}(\alpha_{EW}^5\alpha_S^2)$		$\mathcal{O}(\alpha_{EW}^4\alpha_S^3)$
Fixed-order NLO corrections [19]:						
$\delta\sigma(NLO)/\sigma(LO)$	−13.2%	−3.5%		0.0%		−0.4%
Availability of NLO + parton shower matched predictions [157]:						
	✓	✓*	×	×	×	✓

universally for VBS processes in Sec. 5.4.3. The NLO electroweak corrections are negative as expected and clearly the dominant contribution to the full fixed-order NLO corrections which amount to −17.1% for the $W^\pm W^\pm jj$ process. In addition, Tab. 6.1 states the availability of NLO + parton shower matched predictions. The order $\mathcal{O}(\alpha_{EW}^6\alpha_S)$ is currently only available with approximations. Among the MC programmes, which have been presented to be capable of giving these predictions, are:

$\mathcal{O}(\alpha_{EW}^7)$:

- POWHEGBOX with RECOLA matrix element [201];

$\mathcal{O}(\alpha_{EW}^6\alpha_S)$:

- MG5_aMC@NLO [134] (excluding non-factorisable QCD corrections and non-resonant contributions) tested in Ref. [141, 199];
- POWHEGBOX with VBFNLO matrix element [135] (VBS approximation);
- HERWIG 7 MATCHBOX [138, 139] with VBFNLO matrix element (VBS approximation) tested in Ref. [141]; and

$\mathcal{O}(\alpha_{EW}^4\alpha_S^3)$:

- POWHEGBOX with VBFNLO matrix element [136].

This listing does not claim completeness, but rather focuses on those setups which have been used in theoretical studies or compared to data in experimental analyses.

The finding of the electroweak corrections to the $W^\pm W^\pm jj$-EW6 process being the dominant ones, caused the very recent implementation of such computations matched to parton showers in the POWHEGBOX framework [201]. It employs the matrix element obtained from RECOLA [202, 203] at order $\mathcal{O}(\alpha_{EW}^7)$. The matching to a QED as well as QCD parton shower is handled by PYTHIA 8 [137] to which this setup can be interfaced.

The NLO QCD setup of MG5_aMC@NLO has, until today, only been tested with the resonant electroweak process definition:

```
p p > W W j j, W > l vl QCD=0 [QCD],
```

which generates two stable $W^\pm$ bosons subsequently decaying via MADSPIN [168] before the parton showering. This only includes doubly resonant $W^\pm$ bosons contributions [141, 199]. In principle, this setup can also be used to generate the strong process at order $\mathcal{O}(\alpha_{EW}^4\alpha_S^3)$,

replacing `QCD=0` with `QED=2 QCD=2`, which has however not been tested yet. The latter is likewise true for the Herwig 7 Matchbox setup [138, 139] which uses the VBFNLO matrix element and phase spaces. Both setups have only been used to study the QCD corrections to the electroweak process.

The PowhegBox and the MG5_aMC@NLO can be matched to both, the Pythia 8 and Herwig 7 parton showers. For the NLO matching to parton showers, the PowhegBox uses the Powheg method [145, 146] while MG5_aMC@NLO employes the MC@NLO method [144]. The Matchbox setup in contrast can be used with the Herwig 7 parton showers only, but with both the Powheg as well as the MC@NLO matching, where only the latter option has been tested in Ref. [141].

To this day, no technical implementation exists which can combine and match the full QCD and EW NLO predictions to parton showers in one process definition. An important step in this direction is the implementation of an automated interface between Recola and the Sherpa MC generator in order to perform full fixed-order computations at NLO accuracy [185].

At leading order the following MC programmes have been used:

- Sherpa [132, 133],
- MG5_aMC [134],
- Whizard [204] with O'Mega matrix element [205], and
- Phantom [206].

Again, this is not a complete list. The selection of mentioned programmes rather focuses on those that have been utilised in theoretical studies or compared to data.

While Sherpa can be used at LO, it is mostly used in multi-jet merged setups employing the CKKW-L method [140, 142], e. g. in Ref. [1, 13]. The MG5_aMC programme is utilised at LO, e. g. in Ref. [14, 196]. Both, the Whizard [204] and Phantom [206] MC programme are included in the theoretical studies in Ref. [141]. The first is mostly used for BSM interpretations, e. g. in Ref. [49, 86]. The Sherpa event generator hosts its own parton shower algorithms, the Whizard programme output can be interfaced to Pythia 8, and Phantom [206] can be used with both the Pythia 8 and Herwig 7 parton shower programmes.

For the $W^{\pm}W^{\pm}jj$-EW6 process at LO and NLO QCD (order $\mathcal{O}(\alpha_{EW}^6\alpha_S)$), many of these configurations have been systematically studied in Ref. [141]. It however excludes the Sherpa setup. Including predictions from Sherpa is one of the extensions, this chapter aims to present to this study. The comparison at both fixed-orders in Ref. [141] is completed with presenting the various setups and predictions matched to parton showers. The most important findings are summarised here.

One major result in Ref. [141] is the large variation of the parton shower matched predictions compared to the fixed-order results when examining observables sensitive to additional radiation. Naturally, larger discrepancies are expected for parton shower matched predictions, due to the different matching as well as parton shower algorithms and their tunable parameters. For the fiducial cross-section at order $\mathcal{O}(\alpha_{EW}^6\alpha_S)$ ($\mathcal{O}(\alpha_{EW}^6\alpha_S^0)$) agreement within approx. 7% (5%) is found, with larger discrepancies in many differential distributions. Fig. 6.1 shows the differential distribution of the Zeppenfeld variable of the third-leading jet in transverse momentum $z(j_3)$ (see Eq. (5.6)) at LO and NLO plus parton shower accuracy as obtained in Ref. [141] for various setups. Predictions using the Pythia 8 shower yield substantially more radiation in the central region compared to the Herwig 7 setup.

An explanation for this behaviour lies in the dipole based parton shower description of Pythia 8, which, with its default settings, distributes the recoil of an initial-state radiation among all final-state particles. This is however not favoured by nature when the final-state partons are colour disconnected as in the case of the $W^{\pm}W^{\pm}jj$-EW6 process [207][2]. As a consequence, the default Pythia 8 parton shower generates excessive radiation in the central

[2]This has been seen in the modelling of deep inelastic scattering events which feature similarly special colour structures.

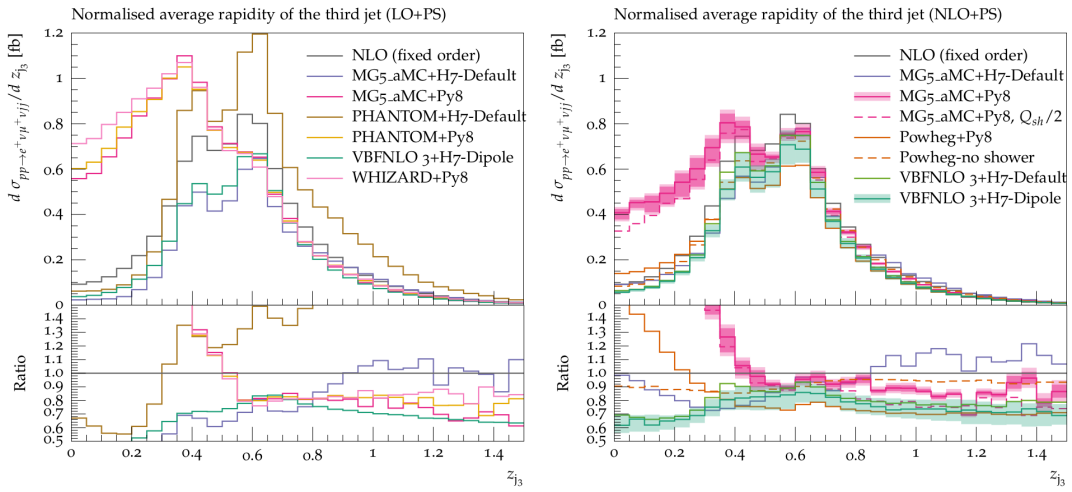


Figure 6.1: Differential distribution of the Zeppenfeld variable of the third-leading p_T jet $z(j_3)$ from predictions matched to parton showers at LO (left) and NLO (right) accuracy. The lower panel shows the ratio with respect to the full fixed next-to-leading order result computed with VBFNLO. Detailed descriptions of the exact setups, fiducial region, and computation of the uncertainty bands can be found in Ref. [141], where this figure is taken from.

rapidity region between the two tagging jets. This behaviour can be alleviated by using a non-default so-called local dipole recoil scheme, which distributes the kinematic recoil of the initial-state radiation solely to one of the final-state partons [207]. The colour flow of the hard event motivates the choice of the parton which receives the kinematic correction. With setting the option:

```
SpaceShower:dipoleRecoil=on
```

this non-default recoil scheme can be used in Pythia 8 at LO as well as NLO, the impact of which is studied in this chapter and published in Ref. [200]. At NLO, it has to be noted, however, that this option is not compatible with the MC@NLO matching used in MG5_aMC@NLO.

When using the PowhegBox with the Powheg NLO matching, this effect is not visible in the third jet quantity because this setup generates the additional radiation directly in PowhegBox. The Pythia 8 parton shower then only fills additional radiation, i. e. mostly starting from the fourth leading jet[3].

Another main finding lies within the comparison of the full fixed next-to-leading order prediction to the one obtained with the VBS approximation (refer to Sec. 5.4.1), the result of which will be discussed in detail in Sec. 6.7.4 of this chapter.

The studies in Ref. [141] conclude with precise recommendations for experimental analyses of VBS processes. The major points are:

- The inclusion of NLO EW corrections to the $W^{\pm}W^{\pm}jj$-EW6 process at order $\mathcal{O}(\alpha_{EW}^7)$ is recommended, even if only possible in an additive manner to this date;
- Care has to be taken when using approximations together with looser fiducial regions for control measurements in the analyses;
- A combined measurement of the full $W^{\pm}W^{\pm}jj$ process, including all orders (at LO) should be presented, due to the theoretical reason explained previously (see Sec. 5.4).

[3]This means that this issue would again appear for the fourth leading p_T jet, whose kinematics is barely looked at in studies.

Table 6.2: Review of the event generation specifics of the $W^{\pm}W^{\pm}jj$ process used in previous analyses with the ATLAS and CMS experiments conducted during the LHC Run 1 and Run 2 [1, 13, 14, 155, 196], the ATLAS Run 2 analysis being the subject of this thesis. Note that both experiments use different Pythia underlying event tunes.

LHC Run	Experiment	MC programme	Accuracy	Parton shower
Run 1 (8 TeV)	ATLAS [13]	Shape: Sherpa (version 1.4.2)	ME+PS multi-jet merged with 2, 3 jets at LO	Sherpa
		Normalisation: PowhegBox	NLO QCD	Pythia 8
	CMS [196]	MG5_aMC (version 2)	LO	Pythia 6.4
Run 2 (13 TeV)	CMS ($35.9\,\text{fb}^{-1}$) [14]	MG5_aMC (version 2)	LO	Pythia 8.205
	CMS ($137\,\text{fb}^{-1}$) [155]	MG5_aMC (version 2.4.2)	LO	Pythia 8.226 & 8.230
	ATLAS ($36.1\,\text{fb}^{-1}$) [1]	Sherpa (version 2.2.2)	ME+PS multi-jet merged with 2, 3 jets at LO	Sherpa
		PowhegBox	NLO QCD	Pythia 8.230

6.2 Review of the Modelling in LHC Analyses

Before specifying on the simulation samples used throughout this thesis, a short summary of the setups for the modelling of the $W^{\pm}W^{\pm}jj$ process in previous LHC analysis is given in Tab. 6.2.

From the tools described in Sec. 6.1, only a few have been used in data analyses in the LHC experiments and hence have been compared against data.

The first publication of an experimental analysis of the $W^{\pm}W^{\pm}jj$ process from the ATLAS experiment in the Run 1 data-taking period [13] already used a fairly sophisticated simulation setup. The baseline for the strong and electroweak process, as well as its interference, is simulated with version 1.4.2 of the Sherpa event generator with multi-jet merged LO accuracy with up to three jets in the matrix element. The fiducial cross-section measurement and the normalisation of differential distributions obtained with Sherpa uses the prediction from PowhegBox at NLO QCD accuracy with the VBS approximation and matched to the Pythia 8 [137] parton shower.

The CMS experiment employs a LO accurate setup in LHC Run 1 using version 2 of the MG5_aMC [134] programme interfaced to Pythia 6 [208] for the separate generation of all orders of the process, including the interference between the electroweak and the strong $W^{\pm}W^{\pm}jj$ production. This general setup does solely change in the programme versions and tunes used for the Run 2 analyses [14, 155].

For completeness, the setups used for the Run 2 ATLAS publication are added in Tab. 6.2. These will be subject to further studies in this thesis and hence will be discussed in detail in the next sections.

It is to be noted, that although both experiments use the Pythia programme for parton showering, different tunes, i. e. parameter sets, are used not only in between experiments but also in between different data-taking periods. In the most recent CMS publication the CUETP8M1 [209, 210] and CP5 [211] tunes are used for the underlying event parametri-

sation, while in the analysis with the ATLAS experiment the AZNLO [212] tune is used. In addition it has to be noted that none of these setups includes the non-default dipole recoil option mentioned previously, leading to non-optimal shower configuration regarding the additional radiations after the matrix element calculations.

The simulated samples used in the most recent publication of each experiment are, together with other configurations, compared in Ref. [200].

6.3 Simulation of the $W^{\pm}W^{\pm}jj$ Process at the LHC

In the following, a number of MC samples modelling the $W^{\pm}W^{\pm}jj$ process with different configurations at LO and NLO QCD shall be compared. The focus is laid upon the $W^{\pm}W^{\pm}jj$-EW6 process, the major motivation being the sizable differences in the prediction of the fiducial cross-section found in Ref. [1]. This section summarises the details of the simulation for these samples.

The configurations are based on the aforementioned findings in several previous studies and are shown in Tab. 6.3 for the $W^{\pm}W^{\pm}jj$-EW6 process at different accuracies.

The samples are generated at a centre-of-mass energy of 13 TeV for the core process:

$$pp \to \ell'^{\pm}\nu_{\ell'}\ell^{\pm}\nu_{\ell}jj, \tag{6.1}$$

where p and j include all possible quark flavours[4], as well as gluons[5]; $\ell^{\pm}$ include all charged lepton flavours, electrons $e^{\pm}$, muons $\mu^{\pm}$, as well as tau leptons $\tau^{\pm}$[6]; ν_{ℓ} represent all (anti-)neutrinos as allowed by the SM. Depending on the accuracy of the sample, additional jets are added to the process definition.

Three main MC generation setups are used for the modelling:

- PowhegBox [145, 146, 214] at NLO QCD with the VBS approximation matched to parton showers from either Pythia 8 [137] or Herwig 7 [138, 139];
- Sherpa [184] multi-jet merged at LO [142] with up to three jets in the matrix element, or purely at LO;
- MG5_aMC [134] at LO interfaced to either Pythia 8 [137] or Herwig 7 [138, 139].

Two samples are produced centrally within the MC production machinery of the collaboration: the PowhegBox setup interfaced to Pythia 8 with the default AZNLO tune (with `dipoleRecoil=off`), labelled PB+Py8, and the Sherpa multi-jet merged setup, labelled Sherpa23jLO, affected by a mismodelling discussed below. These samples go through the full simulation chain, i. e. are also available at reconstruction level, and are used in the publication of the ATLAS collaboration in Ref. [1]. These two samples predict sizeably different fiducial cross-sections which motivates a thorough study of their differences in the modelling setup. Both samples use the NNPDF3.0 PDF set, at NLO for the PowhegBox setups and NNLO for the Sherpa setups. This has only a minor impact on the predictions, which can be inferred from the modelling uncertainties evaluated when using various PDF sets (see Sec. 6.6.2). These samples, however, substantially differ in the choice of the renormalisation and factorisation scales. This has the potential of sizable changes in the predictions at LO and motivates a thorough comparison of different scale settings at tree-level, which is detailed in Sec. 6.7.1 and extends the comparisons in Ref. [199] and [141].

The default shower configuration in this Sherpa version suffers from a non-optimal implementation of the colour flow assigned to the matrix element for VBS-like processes, such

[4] Top quarks are excluded, due to their prompt decay which consequently excludes also bottom quarks in the $W^{\pm}W^{\pm}jj$ process.

[5] In the $W^{\pm}W^{\pm}jj$-EW6 process, gluons in the initial or final state are only possible at NLO in QCD. This opens up a whole new partonic channel for this process at next-to-leading order accuracy, see beginning of this chapter.

[6] Tau leptons are later excluded via a tau lepton veto in the fiducial region. However, since they are included in the official productions, which are used for the reconstruction level analysis, they are included in all simulations for consistency.

Table 6.3: Summary of event generation details for the modelling of the $W^{\pm}W^{\pm}jj$-EW6 process at particle level at different levels of accuracy. The PowhegBox samples are generated at NLO in QCD in the VBS approximation. Samples using the Sherpa event generator are generated at LO multi-jet merged with the parton shower with up to three jets in the matrix element, as well as at LO. MG5_aMC samples are generated at LO. Renormalisation and factorisation scales differ between the different generator setups but not within one setup. The number of events refer to the particle level. Samples indicated with (*) are centrally produced samples that go through the full simulation chain, i. e. are also available at reconstruction level, and are used in the publication of the ATLAS collaboration in Ref. [1].

	Sample label	MC programme	Scales	Parton shower	N_{evnt}	Comment
NLO QCD accuracy with VBS approx. (only $\lvert t^2\rvert + \lvert u^2\rvert$ matrix element)	PB+Py8 (*)	PowhegBox	Fixed: m_W	Pythia 8.235 AZNLO tune	730000	
	PB+Py8drec			Pythia 8.235 AZNLO tune + `dipoleRecoil=on`	730000	
	PB+H7			Herwig 7.07 (default shower)	730000	
	PB+H7DS			Herwig 7.07 Dipole Shower	730000	
ME+PS merged with 2,3j@LO accuracy:						
	Sherpa23jLO (*)	Sherpa 2.2.2	dynamic: m_{WW}	Sherpa	500000	Normalization issue [213]
LO accuracy	MG5+Py8	MG5_aMC	dynamic: H_T	Pythia 8.235 A14 tune	150000	Missmodelling of third-leading jet
	MG5+Py8drec			Pythia 8.235 A14 tune + `dipoleRecoil=on`	150000	
	MG5+H7			Herwig 7.07 (default shower)	150000	
	MG5+H7DS			Herwig 7.07 Dipole Shower	150000	
	SherpaLO	Sherpa 2.2.2	dynamic: m_{WW}	Sherpa	5800000	Missmodelling of third-leading jet

Table 6.4: Summary of event generation details for the modelling of the $W^{\pm}W^{\pm}jj$-EW4 process at particle level at different levels of accuracy. The PowhegBox samples are generated at NLO in QCD. Samples using the Sherpa event generator are generated at LO multi-jet merged with the parton shower with up to three jets in the matrix element. MG5_aMC samples are generated at LO. Renormalisation and factorisation scales differ between the different generator setups but not within one setup. The number of events refer to the particle level. Samples indicated with (*) are centrally produced samples that go through the full simulation chain, i. e. are also available at reconstruction level, and are used in the publication of the ATLAS collaboration in Ref. [1].

Sample label	MC programme	Scales	Parton shower	N_{evnt}
NLO QCD accuracy:				
PB+Py8 (*)	PowhegBox	Fixed: m_W	Pythia 8.235 AZNLO tune	680000
PB+H7	PowhegBox	Fixed: m_W	Herwig 7.07 (default shower)	672000
ME+PS merged with 2,3j@LO accuracy:				
Sherpa23jLO (*)	Sherpa 2.2.2	dynamic: m_{WW}	Sherpa	500000
LO accuracy:				
MG5+Py8drec	MG5_aMC	dynamic: H_T	Pythia 8.235 A14 tune `dipoleRecoil=on`	150000
MG5+H7	MG5_aMC	dynamic: H_T	Herwig 7.07 (default shower)	150000

as $W^{\pm}W^{\pm}jj$-EW6. This leads to an excess of parton shower emissions in the central region between the two tagging jets [213]. While the multi-jet merged setup generates one additional emission in the matrix element, it corrects the kinematic shape for this emission. However, this leads to a significantly reduced cross-section prediction due to large suppression from spuriously remaining Sudakov factors. Further details can be found in Ref. [213]. The $W^{\pm}W^{\pm}jj$-EW4 process modelling is not affected by this.

In addition, a smaller set of samples modelling the $W^{\pm}W^{\pm}jj$-EW4 process at LO and NLO QCD has been generated for the MC generator sets labelled as:

- PB+Py8,
- Sherpa23jLO,
- MG5+Py8.

The generation specifics is held very close to the ones for the electroweak process and summarised in Tab. 6.4. Here again, the PB+Py8 and Sherpa23jLO samples have been produced centrally within the ATLAS MC production framework.

Moreover, samples modelling the interference of the electroweak and strong production at LO $\mathcal{O}(\alpha_{EW}^5\alpha_S)$, as well as a fully inclusive sample including all orders of the $W^{\pm}W^{\pm}jj$ process at LO have been generated in the MG5+Py8 setup. The sample specifics are summarised in Tab. 6.5. These samples, together with the QCD samples will be included in the detailed explanations following.

Tab. A.1 in Appendix A.1 summarises the SM input parameters and their values used in the event generation within the three generator setups. All setups use the G_μ scheme, detailed in Sec. 2.1.3, as the choice of the input parameters of the electroweak theory, massless light quarks at matrix element level and a unit CKM matrix neglecting the mixing between different quark generations. The impact of t quarks is neglected which consequently also discards b quarks in the process definition.

Table 6.5: Summary of event generation details for the modelling of the interference between the $W^{\pm}W^{\pm}jj$-EW6 and $W^{\pm}W^{\pm}jj$-EW4 processes at LO, corresponding to order $\mathcal{O}(\alpha_{EW}^{5}\alpha_{S})$, as well as an inclusive sample for the $W^{\pm}W^{\pm}jj$ process including all leading orders. The default MG5_aMC setup with modified dipole recoil scheme is used for consistency. The number of events refer to the particle level. None of these samples have been produced centrally.

Sample label	MC Programme	Scales	Parton shower	N_{evnt}
Interference between $W^{\pm}W^{\pm}jj$-EW6 and $W^{\pm}W^{\pm}jj$-EW4 processes (at LO):				
MG5+Py8drec	MG5_aMC	dynamic: H_T	Pythia 8.235 A14 tune `dipoleRecoil=on`	150000
Inclusive $W^{\pm}W^{\pm}jj$ process (at LO):				
MG5+Py8drec	MG5_aMC	dynamic: H_T	Pythia 8.235 A14 tune `dipoleRecoil=on`	150000

6.3.1 $W^{\pm}W^{\pm}jj$ at NLO Accuracy in QCD

The $W^{\pm}W^{\pm}jj$-EW6 and $W^{\pm}W^{\pm}jj$-EW4 processes at NLO QCD, representing the orders $\mathcal{O}(\alpha_{EW}^{6}\alpha_{S})$ and $\mathcal{O}(\alpha_{EW}^{4}\alpha_{S}^{3})$, respectively, are generated with the PowhegBox version 2 [214].

The electroweak process has been produced with the process specific toolbox `POWHEG-BOX/vbf_wp_wp` [135]. Its technical implementation is based on the calculations in Ref. [161] and previous implementations in the VBFNLO framework [167]. As discussed above, the calculations of the electroweak process are realised in the VBS approximation, neglecting all s-channel contributions. It is argued via Ref. [215] that these processes are strongly suppressed in phase space regions where VBS processes can be experimentally observed [161]. However, in Ref. [215] only the VBS diagrams with Higgs boson exchanges are considered, neglecting a major part of the $W^{\pm}W^{\pm}jj$-EW6[7] process. As shown in Ref. [141] and discussed later in this work, this approximation is insufficient when regarding the full $W^{\pm}W^{\pm}jj$-EW6 process at NLO QCD accuracy and imposing moderate VBS requirements. As an effect of the VBS approximation and colour conservation, contributions from non-factorisable NLO QCD corrections vanish in the calculation. Hence, diagrams such as depicted in Fig. 5.6 (e) are ignored in the generation with PowhegBox. Besides that, the generation includes non-resonant contributions by respecting off-shell effects and spin correlations of the decay products of the $W^{\pm}$ bosons.

The strong process uses the `POWHEG-BOX/Wp_Wp_J_J` [136] process specification which is based on the calculations in Ref. [176].

The integration grid and LHE event files at parton level before showering for both processes have been produced privately [216] within the central ATLAS MC production framework. Enabling the `zerowidth` switch ensures to generate off-shell $W^{\pm}$ bosons following a Breit-Wigner distribution. For the production of the strong process, the latter switch is disabled, producing the $W^{\pm}$ bosons on their mass-shell only. The colour flow at matrix element level is unambiguous and follows the propagation of the quarks and gluons. Further technical details, e. g. the toolbox versions, steering scripts, and setups, can be found in Appendix A.2.1.

The `NNPDF30_nlo_as_0118` [128] PDF set with the strong coupling constant $\alpha_S(m_Z) = 0.118$ is chosen for the matrix element calculation for both processes. The central value for the factorisation and renormalisation scales is chosen to be the nominal $W^{\pm}$ boson mass m_W. It is especially noted that this is a fixed scale setting for all events. No phase space restrictions are imposed at generator level for both processes as the LO total cross-section is

[7] The notations $W^{\pm}W^{\pm}jj$-EW6 and $W^{\pm}W^{\pm}jj$-EW4 will be equally used in the context of LO and NLO QCD accuracy, disregarding the fact of representing different orders in the strong couplings.

found to be finite [161, 176].

The LHE event files are further interfaced to the Pythia 8 and Herwig 7 parton shower programmes, labelled "Py8" and "H7" in tables and figures, respectively, which also generate the hadronisation and underlying event steps (cf. Sec. 4.2.4). Samples interfaced with Pythia 8 use version 8.235 and the AZNLO tune´. Two samples are generated for the electroweak process with the global and the dipole recoil scheme, labeled "PB+Py8" and "PB+Py8drec", respectively. For the strong process only the default global recoil scheme is used. Samples interfaced with Herwig 7 use version 7.07 with default underlying event tunes. The Herwig 7 default angular ordered shower is used. For the electroweak process the dipole shower model is investigated as well. Samples are labeled "PB+H7" and "PB+H7DS", respectively.

An inconsistency regarding the lepton flavour universality has been found in the course of the studies for the MC sample describing the $W^{\pm}W^{\pm}jj$-EW4 process with PowhegBox. Its impact is described and summarised in Appendix A.3.1. The implementation of the $W^{\pm}W^{\pm}jj$-EW6 process is not affected by this inconsistency.

The samples include variations of parameters in the matrix element modelling via an internal reweighting procedure. This allows for an efficient evaluation of the modelling uncertainties. The variations include the choice of PDF sets and their eigentunes, as well as the central value of the factorisation and renormalisation scales. For the uncertainty estimate induced by the parameters of the shower prescription, additional samples with varied parameters are generated.

6.3.2 $W^{\pm}W^{\pm}jj$ with ME+PS merging at LO

The Sherpa event generator in the release version 2.2.2 is used to generate both processes, the $W^{\pm}W^{\pm}jj$-EW6 and $W^{\pm}W^{\pm}jj$-EW4, with up to three partons in the matrix element at LO. This setup uses the Comix [132] matrix element generator and the multi-jet merging with the default Sherpa Ssshower parton shower model [140] via the CKKW-L prescription [142].

The electroweak and strong processes are specified via the electroweak coupling order, being set to six and four, respectively via the `Order` command in the process definition. The merging scale is set to 20 GeV. Both samples are centrally produced within the structures of the ATLAS MC production framework. Further information on the technical details, e. g. the steering scripts and setups, can be found in Appendix A.2.2.

The `NNPDF30_nnlo_as_0118` PDF set [128] with the strong coupling constant $\alpha_S(m_Z) = 0.118$ is used for the matrix element calculation for both processes. This choice is motivated as it uses the same set as for the dedicated shower tuning with Sherpa. The central value for the factorisation and renormalisation scales is chosen to be the $W^{\pm}W^{\pm}$ system invariant mass at matrix element level:

$$m_{WW} = \sqrt{P^{\mu}_{WW} P_{\mu\, WW}}. \tag{6.2}$$

It is a dynamic scale which is set event-by-event.

As described above, this setup suffers from the non-optimal implementation of the colour flow assignment, leading to a significantly reduced cross-section prediction for the electroweak $W^{\pm}W^{\pm}jj$-EW6 process. The $W^{\pm}W^{\pm}jj$-EW4 process is not affected.

The selection criteria on matrix element level are listed in Tab. 6.6. Jets are selected with the `NJetFinder` and the anti-k$_t$ algorithm [111] with radius parameter $R = 0.4$. All massless QCD partons are clustered into jets. Selections on the minimum transverse momentum of the leptons and jets are motivated by the fiducial phase space selections. They are required to be substantially looser than in the fiducial region to capture possible migration effects during the showering process. The selection requirement on the invariant mass of electron-positron pairs m_{ee} cuts out the singular region of infrared photon production in the generator phase space. The technical implementation can be found in the example steering script in Appendix A.2.2.

For the uncertainty estimation, samples are generated including event-by-event variations as explained in the NLO case. Additionally, variations of the merging scale are included for the Sherpa setup.

Table 6.6: Generator level selection criteria in the SHERPA setup for the generation of all samples of the $W^{\pm}W^{\pm}jj$ process.

Variable	Value	Explanation
$p_{\mathrm{T}}(\ell)$	5.0	Minimum p_{T} of charged leptons (in GeV)
$p_{\mathrm{T}}(j)$	15.0	Minimum p_{T} of anti-k$_T$ jets with $R = 0.4$ (in GeV)
$n(j)$	2	Minimum number of anti-k$_T$ jets with $R = 0.4$
m_{ee}	0.1	Minimum invariant mass of electron-positron pairs (in GeV)

Table 6.7: Generator level selection criteria in the MG5_aMC setup for the generation of all LO samples of the $W^{\pm}W^{\pm}jj$ process.

Variable	Value	Explanation
$p_{\mathrm{T}}(\ell)$	4.0	Minimum p_{T} of charged leptons (in GeV)
$p_{\mathrm{T}}(j)$	15.0	Minimum p_{T} of light partons (in GeV)
$\lvert\eta(\ell)\rvert$	3.0	Maximum $\lvert\eta\rvert$ of charged leptons
$\lvert\eta(j)\rvert$	5.5	Maximum $\lvert\eta\rvert$ of light jets
$\Delta R(jj)$, $\Delta R(j\ell)$, $\Delta R(\ell\ell)$	0.2	Minimum distance of pairs of light jet and lepton (any combination)
$\Delta R(\gamma\ell)$	0.1	Minimum distance of pairs of photon and charged lepton

6.3.3 $W^{\pm}W^{\pm}jj$ at LO

At LO accuracy two sets of samples are generated, employing MG5_aMC and SHERPA.

The MG5_aMC setup uses version 2.6.5 and a local framework for the event generation which automatically creates all steering scripts upon some simple configuration inputs [217]. The `sm` model is used. The values of the parameters are left unchanged with respect to the default. The process at LO is defined in the `proc_card.dat` as:

```
generate p p > l+ vl l+ vl j j QCD=0
add process p p > l- vl~ l- vl~ j j QCD=0
```

where the `QCD=0` provides the electroweak process by setting the order of the strong coupling to zero. The strong process can be generated with specifying `QED=4` instead which only includes processes of order $\mathcal{O}(\alpha_{EW}^4\alpha_S^2)$. The interference between the $W^{\pm}W^{\pm}jj$-EW6 and the $W^{\pm}W^{\pm}jj$-EW4 process at LO can be obtained by setting `QCD^2==2`, which sets the order at matrix element level and hence generates the order $\mathcal{O}(\alpha_{EW}^5\alpha_S)$. In addition, an inclusive sample is generated specifying `QCD=2`, which includes the full process at LO. Example steering scripts and more technical details can be found in Appendix A.2.3.

The `NNPDF30_nlo_as_0118` [128] PDF set with the strong coupling constant $\alpha_S(m_Z) = 0.118$ is chosen for the matrix element calculation for all processes. The central value for the factorisation and renormalisation scales is chosen to be the sum of the transverse masses of all matrix element particles:

$$H_T = \sum_i^n \sqrt{m_i^2 + p_{Ti}^2}. \tag{6.3}$$

This is a dynamically set scale which is evaluated event-by-event.

The relevant generator level selections which are specified in the `run_card.dat` are summarised in Tab. 6.7. The selection criteria are imposed on parton level, i. e. before the showering. All massless QCD partons are considered in the selections. Criteria on the minimum transverse momentum of the leptons and jets are motivated by the fiducial phase space selection. Criteria on the absolute pseudorapidity of the leptons and jets are motivated by the detector acceptance. The separation in the azimuthal-pseudorapidity space is defined as:

$$\Delta R = \sqrt{(\Delta\eta)^2 + (\Delta\phi)^2}. \tag{6.4}$$

All samples are interfaced to the Pythia 8 parton shower programme using the version 8.235 and the A14 set of tunable parameters [218]. For consistency all samples use the dipole recoil scheme, although the $W^{\pm}W^{\pm}jj$-EW4 sample per se does not suffer from the non-optimal colour flow with the default global scheme. These are labelled with "MG5+Py8drec".

Additionally, the electroweak sample is generated with multiple shower configurations. The sample labelled "MG5+Py8" uses the default global recoil scheme. Samples are also interfaced with Herwig 7 using version 7.07 with default underlying event tunes and the default angular ordered shower model. This samples is labelled "MG5+H7".

For the uncertainty estimation, samples are generated including event-by-event variations as explained in the NLO case. For the samples showered with Pythia the variations of certain parameters of the shower prescription is included in the MG5_aMC setup.

In addition, LO accurate samples are generated within the Sherpa setup described above for the $W^{\pm}W^{\pm}jj$-EW6 process. Technically, this is realised by removing the possible third jet in the process definition in the steering scripts (rf to App. A.2.2). All other settings remain untouched. This includes the selection criteria summarised in Tab. 6.7. As described above, however, for the $W^{\pm}W^{\pm}jj$-EW6 process, this setup suffers from the non-optimal colour flow settings in the shower prescription, leading to an excess of additional radiation in the central region, and hence a mismodelling of observables sensitive to this [213].

6.4 Definition of Inclusive and Fiducial Regions

The major motivation for the definition of the fiducial region is to build a kinematic region where the electroweak production process, $W^{\pm}W^{\pm}jj$-EW6, is dominant over the strong production, $W^{\pm}W^{\pm}jj$-EW4. The fiducial region is used for the measurement of the fiducial cross-section of the $W^{\pm}W^{\pm}jj$-EW6 process in the analysis of experimental data in Chapter 8. The theoretical cross-section predicted by simulation in the fiducial region can be expressed as:

$$\sigma_{\text{theo}}^{\text{fid}} = A \cdot \sigma_{\text{theo}}^{\text{gen}}, \tag{6.5}$$

where the acceptance factor A translates the cross-section at generator level $\sigma_{\text{theo}}^{\text{gen}}$, i. e. the cross-section obtained in the course of the matrix element generation from each simulation programme, into the fiducial region. A general notation with the subscript "theo" is adopted here for the labelling of the predicted cross-section. It is used whenever the knowledge of the specific prediction is unneccessary. It is replaced by the labels of the explicit signal predictions when these are discussed.

In order to avoid large extrapolation factors, the definition of the fiducial phase space is motivated by the capabilities of the detector such as the transverse momentum and energy resolutions, the trigger thresholds, and the rapidity acceptances for the several types of particles involved. It is defined at particle level after the showering but before the detector simulations. Detector effects are later accounted for with efficiency factors in the final measurement. The selection criteria that events are required to pass to enter the fiducial region are listed in Tab. 6.8. It has been designed for Ref. [1] based on the studies of this chapter.

Events are selected based on the process definition in Eq. (6.1), requiring exactly two electrons or muons, with the same electric charge q_ℓ, which fulfil a set of kinematic object selections as defined in Tab. 6.8. In order to account for collinear QED bremsstrahlung, the momenta of all photons within a radius of $\Delta R(\gamma, \ell) = 0.1$ of a charged lepton are added to the lepton momentum, hence obtaining "dressed" charged leptons. This definition minimises the modelling dependence of the charged lepton kinematics. Events where charged leptons originate from a τ lepton decay are excluded. The effect of non-prompt leptons from these decays is accounted for in the efficiency calculation when measuring the fiducial cross-section.

A selection on the vectorial sum of the transverse momenta of the two highest p_{T} neutrinos accounts for the presence of the neutrinos and mimics the missing transverse momentum requirement at reconstruction level.

Table 6.8: Definition of the nominal fiducial phase space used in Ref. [1] and intermediate stages employed for different sets of studies in this thesis. The full list of selection criteria is used for the final cross-section measurement of the analysis presented in Chapter 8.

Variable	Value	Explanation
Object selection:		
$p_{\mathrm{T}}(\ell)$	$> 27\,\mathrm{GeV}$	Minimum p_{T} of charged leptons (e or μ)
$\lvert\eta(\ell)\rvert$	< 2.5	Maximum abs. pseudorapidity of charged leptons
$p_{\mathrm{T}}(j)$	$> 35\,\mathrm{GeV}$	Minimum p_{T} of jets
$\lvert\eta(j)\rvert$	< 4.5	Maximum abs. pseudorapidity of jets
Lepton event selection:		
$N(\ell)$	$== 2$	Number of charged leptons (e or μ)
Phase space referred to as: *Loose phase space*		
Lepton event selection cont.:		
$N(\tau)$	$== 0$	Veto any event where charged leptons stem from τ decays
$\Delta R(\ell\ell)$	> 0.3	Minimum distance between leading lepton pair
$q(\ell_1) \times q(\ell_2)$	> 0	Same electrical charge for two leading charged leptons
$m_{\ell\ell}$	$> 20\,\mathrm{GeV}$	Minimum invariant mass of leading lepton pair
$p_{\mathrm{T}}(\nu\nu)$	$> 30\,\mathrm{GeV}$	Minimum p_{T} of leading neutrino pair
Jet event selection:		
$N(j)$	≥ 2	Minimum number of jets
$p_{\mathrm{T}}(j_1)$	$> 65\,\mathrm{GeV}$	Minimum p_{T} of leading jet
$\Delta R(j\ell)$	> 0.3	Minimum distance of all lepton-jet pairs
Phase space referred to as: *Inclusive phase space*		
VBS selection:		
m_{jj}	$> 500\,\mathrm{GeV}$	Minimum invariant mass of leading jet pair
$\Delta Y(jj)$	> 2.0	Minimum rapidity separation between leading jet pair

Hadronic particle jets are reconstructed at particle level by clustering together all stable particles, excluding prompt leptons and neutrinos, with the collinear- and infrared-safe anti-k_t clustering algorithm [111] with radius parameter $R = 0.4$. The leading jets are defined to be the jets with highest transverse momentum in the event. At least two jets with kinematic restrictions, motivated by the detector specifics, have to be present in the event. The two leading jets are defined as the tagging jets in the VBS context. An increased transverse momentum requirement on the first leading jet is shown to be beneficial at the reconstruction level [219] and included in the fiducial region to avoid large extrapolation.

Characteristic VBS selection requirements (cf. Sec. 5.3) are applied on the two tagging jets. Studies on the reconstruction level including the selection optimisation with respect to the signal process via Poisson significance as well as the modelling performance of these observables [220] consolidate to utilize the invariant mass and the rapidity separation between the tagging jets. This is in accordance with the selections used in many other VBS analyses in Run 2, as well as Run 1 of the LHC data-taking (cf. Sec. 5.5).

The definition of the fiducial region is implemented in a Rivet routine and published on `HepData` [221].

The following studies include a comparison of the predictions of the fiducial cross-section in different phase spaces utilized by several publications investigating the $W^{\pm}W^{\pm}jj$ signal process at hand. This comparison includes the first measurement of the CMS collaboration at 13 TeV centre-of-mass energy [14] as well as the publication of the theoretical studies in Ref. [141]. In Tab. 6.9 the respective definitions of the fiducial regions are compared to the nominal definition outlined above.

In Ref. [141], only the subprocess $pp \to \mu^+\nu_m u e^+\nu_e jj$ is considered. This makes the τ lepton veto redundant. The definition of the fiducial regions is reasonably similar between the considered studies. All utilize the invariant mass and rapidity separation of the tagging jet system to enhance the electroweak production in the fiducial region. The object selections in Ref. [14] and [141] are, however, largely looser compared to the nominal selections in Ref. [1] and this thesis with the exception of the lepton isolation requirements in [14]. This observation to a great extent also holds for the event selection. No requirement on the invariant mass of the two leptons is posed in both studies. Also, the leading jet transverse momentum is not further constrained. In Ref. [14], even the selection criteria on the transverse momenta of the leading neutrino system is dropped, which in turn is stricter in Ref. [141]. Only the selection on the rapidity separation of the two tagging jets is consistently chosen to be stricter with respect to the requirements in Ref. [1] and this thesis.

6.5 Evaluation Strategy of Modelling Uncertainties

Predictions of physics observables, such as the fiducial cross-section, obtained from MC generation are subject to uncertainties originating from the limited theoretical understanding in the simulations. Those are commonly called modelling uncertainties and computed with respect to nominal choices of the parameters used in the MC event generation. In this context the description of uncertainties in divided into uncertainties from the calculation of the perturbative QCD matrix element parameters and the modelling of the parton showering and soft QCD components.

This section outlines the strategy of estimating the theoretical uncertainties at particle level in the fiducial region. These prescriptions can equivalently be applied for the modelling in the actual measurement on reconstruction level. However, especially when computing parton shower uncertainties, the approaches might differ.

In App. A.4 information on the technical implementation, and the detailed weight names for the on-the-fly event generation are summarised for all nominal setups.

The total uncertainty on fiducial level quantities can be obtained by adding all components of the theoretical uncertainties in quadrature.

Table 6.9: Comparison of fiducial phase space definitions used in the first analysis of the $W^{\pm}W^{\pm}jj$ final state with the CMS experiment at 13 TeV centre-of-mass energy [14] and in Ref. [141] with respect to the nominal phase space definition used in Ref. [1] and the studies in this thesis. The symbol "✓" indicates that the same selection is applied as in the nominal fiducial phase space definition, defined in Tab. 6.8. The symbol "–" indicated no selection is applied. In Ref. [141] only the final state $\mu^+\nu_\mu e^+\nu_e jj$ is considered, hence a τ veto is implicit (as indicated with *).

Variable	Value in fid. phase space of	
	Ref. [14] (CMS)	Ref. [141]
Object selection:		
$p_{\mathrm{T}}(\ell)$	$> 20\,\mathrm{GeV}$	$> 20\,\mathrm{GeV}$
$\lvert\eta(\ell)\rvert$	✓	✓
$p_{\mathrm{T}}(j)$	$> 30\,\mathrm{GeV}$	$> 30\,\mathrm{GeV}$
$\lvert\eta(j)\rvert$	< 5.0	✓
Lepton event selection:		
$N(\tau)$	✓	✓*
$N(\ell)$	✓	✓
$\Delta R(\ell\ell)$	> 0.4	✓
$q(\ell_1) \times q(\ell_2)$	✓	✓
m_{ll}	–	–
$p_{\mathrm{T}}(\nu\nu)$	–	$> 40\,\mathrm{GeV}$
Jet event selection:		
$N(j)$	✓	✓
$p_{\mathrm{T}}(j_1)$	–	–
$\Delta R(j\ell)$	> 0.4	✓
VBS selection:		
m_{jj}	✓	✓
$\Delta Y(jj)$	> 2.5	> 2.5

6.5.1 Perturbative QCD Matrix-element Uncertainties

The perturbative matrix element computation, as outlined in Sec. 4.1, has two main categories of parameters. Those which are introduced by the calculation strategy, and the ones which are input parameters of the SM and as such have been obtained from measurements which are subject to distinct uncertainties itself. The first category includes the renormalisation and factorisation scales, respectively μ_R and μ_F, whose choice is not constrained but rather limited by the QCD structure and made by experience. The latter include the choice of the PDF set, its measurement uncertainties, as well as the choice of the strong coupling value α_S for the QCD evolution of the PDF description.

With the beginning of the Run 2 of the LHC these variations are available as internal weights directly computed within the nominal LHE files, known as "on-the-fly" event weights.

Factorisation and Renormalisation Scale Uncertainties

The variation of the renormalisation and factorisation scale around its central value is a measure of the uncertainty of the cross-section calculation due to missing higher-order corrections of the perturbative expansion.

As recommended, the attached uncertainty is assessed with the use of the 7-point variation approach. In this method, the nominal choice of both scales, μ_R and μ_F, are varied pairwise up and down by a factor of 2 while rejecting the off-diagonal variations in different directions. This variation is then propagated to the final parameter of interest and combined to a final scale uncertainty by taking the envelope of all variations:

$$\Delta^{\pm}_{\text{scale}}\mathcal{O} = \begin{matrix}\max\\ \min\end{matrix} \left[\mathcal{O}(\mu_{R,i}, \mu_{F,i}) - \mathcal{O}(\mu_{R,0}, \mu_{F,0})\right], \tag{6.6}$$

where $\mathcal{O}$ is the observable of interest and $0, i$ are the nominal scale and the i'th variation, respectively.

PDF and α_S Uncertainties

As briefly outlined in Sec. 4.1, sets of PDFs are obtained by fitting to experimental datasets including various kinds of measurements. Uncertainties attached to each PDF set originate from the experimental uncertainties of the measurements itself, and the choice of the functional form of the PDFs used in the fitting procedure. In order to propagate these uncertainties to the final observables, a set of variations of the internal parameters of the central PDF set values is published alongside each nominal PDF set.

All MC samples studied in the context of this chapter use the NNPDF set [128] as the nominal choice. The estimate of its internal uncertainty follows the prescriptions in Ref. [157]. The NNPDF collaboration provides an ensemble of 100 PDF sets which is created from fits to the ensemble test on the input data. Hence, the best value of this PDF set is defined by the mean value of all the ensembles and its uncertainty is given by the standard deviation of the $N = 100$ sets in the ensemble:

$$\Delta^{\pm}_{\text{PDF}}\mathcal{O} = \sqrt{\frac{1}{N}\sum_{i=1}^{N}\left(\mathcal{O}(\text{PDF}_i) - \mathcal{O}(\text{PDF}_0)\right)^2}, \tag{6.7}$$

which is again propagated to the observable of interest $\mathcal{O}$.

Another means to assess the uncertainty originating from the choice of the PDF set is to calculate the difference between the nominal sets of different PDF sets. In this work, the differences of the CT14 [129] and the MMHT2014 [127] PDF sets (at the corresponding expansion order used for the nominal set) with respect to the nominal NNPDF set are evaluated.

The final uncertainty due to the choice of the PDF set is computed as the envelope obtained with the two approaches, the internal PDF set parameter variations and the difference with respect to alternative sets.

Uncertainties on the choice for the value of the strong coupling α_S arise from the strategy of using truncated fixed-order calculations when evaluating α_S, as well as the experimental

uncertainty in the determination of α_S. The nominal value of α_S is calculated at the scale m_Z, $\alpha_S(m_Z) = 0.118$. The variation of α_S to 0.117 and 0.119 is propagated to the baseline PDF set and further to the observable of interest.

Both sources of uncertainties, from the choice of PDF set and α_S value are eventually combined in quadrature.

The conceptual approach outlined here follows the recommendations given in Ref. [222].

6.5.2 Merging and Matching, Parton Shower and Non-perturbative QCD Modelling Uncertainties

These types of modelling uncertainties are manifold since they depend on the implementations and models used in the respective MC programmes. This includes especially the merging and matching strategies, and the description of the non-perturbative QCD components, such as the hadronisation, underlying event and MPI. Therefore, while the matrix element systematics have well established and unified recommendations, this is not the case for the prescriptions of these uncertainties. Nevertheless, a general description of the components can be given.

Merging and matching uncertainties are commonly evaluated by varying a scale, which is related to the truncated shower technique and the jet resolution in this context. It is not defined by first principles.

Parton shower uncertainties include the variation of the resummation scale, i. e. the starting scale of the parton shower which defines the high-energy cutoff for the QCD parton shower evolution. In addition, one can vary the PDF set used for the ISR shower description, and the renormalisation scale for the QCD parton emissions in the ISR and FSR showers. These uncertainties are recommended to be combined with the respective matrix element uncertainties. Both envelopes obtained from PDF set variation in the matrix element and the parton shower are to be added in quadrature to form the final PDF uncertainty for the observable of interest. The scale variations are recommended to be varied in a correlated manner between the matrix element and the parton shower computations. This, however, is efficiently realisable only with the reweighting method to obtain all necessary weights within one sample. In other cases the scales are varied independently in the matrix element and the parton shower computations and their envelopes are added in quadrature.

Lastly, variations of the tunable parameters of the parton shower and non-perturbative QCD components, such as the description of the hadronisation, underlying event and MPI, are subject of the internal parameter modelling uncertainty consideration.

For some generator setups (e.g Pythia 8), some of the variations are defined as a set of statistically independent variations, called eigentune or eigenvector variations. If these exist, they can be added in quadrature to form the final uncertainty from the internal parameter variation. In all other cases, the variations are to be combined in the envelope style, taking the largest variation in each of the negative and positive direction, to form the total internal parameter uncertainty.

The collection of possible variations described here are generally referred to as “internal parton shower variations” in this work, although these include the merging/matching variations.

The explicit variations of all nominal setups used in this thesis are briefly outlined here and quantitatively summarized in App. B.4.

For the nominal Sherpa setup the internal variations are obtained by generating separate samples for each variation. They have been officially produced within the ATLAS MC production machinery. Specific information on these samples is listed in Tab. A.4 in the appendix. Variations include the value of the merging scale μ_{CKKW} and the resummation scale μ_{QRES}, whose nominal value is defined to be the lowest invariant mass or negative virtuality in the core process, as well the variation of the kinematic recoil scheme. This totals to five variations which are combined into the final shower uncertainty via their unsymmetrised envelope.

The type of internal variations of the Pythia 8 event generator depend on the applied tune.

For the nominal PowhegBox + Pythia 8 setups the AZNLO tune is used which is designed for this setup. For the variations for this tune the prescriptions in Ref. [223, 224] are followed. They include the variation of two eigenvectors, as well as the FSR renormalisation scale μ_R^{FSR} and the MPI cutoff scale. NLO matching uncertainties, provided by the variation of the `hdamp` parameter, are not evaluated for this setup. All variations are implemented in separate samples via the set of commands listed in App. A.4.1.

For the nominal MG5_aMC + Pythia 8 setups the A14 [218] tune is used. Variations are provided on-the-fly via reweighting in the Pythia 8 setup. They include renormalisation scale variations in the ISR and FSR showers $\mu_R^{\text{ISR/FSR}}$, the variation of the inclusion of finite terms in the ISR QCD emission c_{NS}^{ISR}, and ISR PDF set variations.

For the Pythia 8 setups, it is in addition possible to compare to the predictions with the Herwig 7 event generator while using the same matrix element computations. In this way, two systematically different algorithms for the parton shower and non-perturbative modelling can be compared. However, it is not easily reconstructable which effects cause the observed differences.

The total uncertainty related to the merging and matching methods, and parton shower and non-perturbative QCD modelling is to be evaluated as the envelope of the difference between the Pythia 8 and Herwig 7 predictions, and the internal variations, excluding the scale and PDF set variations which are added to the respective uncertainties of the matrix element calculations:

$$\Delta_{\text{ps}}^{\pm}\mathcal{O} = \min^{\max}[\mathcal{O}(\text{Pythia 8}) - \mathcal{O}(\text{Herwig 7}), \Delta_{\text{internal}}^{\pm}\mathcal{O}]. \tag{6.8}$$

6.6 Predictions of the $W^{\pm}W^{\pm}jj$ Processes

This section presents studies on the $W^{\pm}W^{\pm}jj$ processes in general before focusing on the electroweak production process, $W^{\pm}W^{\pm}jj$-EW6, in the next section. The studies include the comparison of the predictions for the contributions at LO including the evaluation of the impact of the interference contribution at order $\mathcal{O}(\alpha_{EW}^5\alpha_S)$. Further, the centrally produced nominal MC samples are compared for both, the $W^{\pm}W^{\pm}jj$-EW6 and $W^{\pm}W^{\pm}jj$-EW4 processes, and their modelling uncertainties are discussed. The theoretical predictions focused on in this section include the PB+Py8, the Sherpa23jLO, and the MG5+Py8drec event generator setups. Inclusive fiducial cross-sections, as well as differential kinematic distributions are compared. Statistics and detailed numbers on cross-sections and acceptances for all setups are summarised in App. B.1.

6.6.1 Comparison of Contributions to the $W^{\pm}W^{\pm}jj$ process at LO and Impact of the Interference Contribution

For the comparison of the three contributions at LO for the $W^{\pm}W^{\pm}jj$ process, described in detail in Sec. 5.2.3, the MG5+Py8drec setup is employed. Three samples with the explicit orders $\mathcal{O}(\alpha_{EW}^6\alpha_S^0)$, $\mathcal{O}(\alpha_{EW}^4\alpha_S^2)$, and $\mathcal{O}(\alpha_{EW}^5\alpha_S)$, labelled EW6, EW4 and INT, respectively, are generated as well as an inclusive sample including the full $W^{\pm}W^{\pm}jj$ process at LO, labelled INCL.

Tab. 6.10 summarises the cross-sections for the three decomposed EW6, EW4 and INT contributions, together with their summed cross-section, labelled SUM, and the cross-section from the inclusively generated sample. The relative contributions to the summed cross-section is also given. Numbers for three different phase space selections are quoted, the generator level phase space, the inclusive, and the fiducial phase space.

Several findings can be observed. The cross-sections in the generator phase space between the summed contributions and the inclusive generation agree excellently, validating the approach of summing the individual contributions. However, as the selection requirements tighten, the discrepancy between the two predictions increases. In the inclusive phase space, the difference of 2% is still moderate and within statistical accuracy of the MC samples. It increases drastically to 18% in the fiducial region. The reason for this can be seen in Fig. 6.2, which displays the Zeppenfeld variable for the third-leading jet (cf. Eq. (5.6))

Table 6.10: Summary of cross-sections for the three explicit orders at LO of the $W^{\pm}W^{\pm}jj$ process, $\mathcal{O}(\alpha_{EW}^{6}\alpha_{S}^{0})$, $\mathcal{O}(\alpha_{EW}^{4}\alpha_{S}^{2})$, and $\mathcal{O}(\alpha_{EW}^{5}\alpha_{S})$, labelled EW6, EW4 and INT, respectively, as well as their sum, labelled SUM, and the cross-section for an inclusive production of the full $W^{\pm}W^{\pm}jj$ process, labelled INCL. Relative contributions are given with respect to the sum of the three explicit contributions. The MG5+Py8drec setup is employed with the scale choice H_T. Uncertainties are statistical uncertainties from the MC generation only. Numbers are quoted for the generator phase space (cf. Tab. 6.7), the inclusive and the fiducial phase phase (cf. Tab. 6.8).

	Cross-section [fb]				
	EW6	EW4	INT	SUM	INCL
Generator phase space:					
	34.05 ± 0.09	18.01 ± 0.08	2.52 ± 0.03	54.58 ± 0.20	54.56 ± 0.24
Rel. contr. to SUM	62%	33%	5%		
Inclusive phase space:					
	4.20 ± 0.05	2.17 ± 0.03	0.38 ± 0.01	6.75 ± 0.06	6.89 ± 0.09
Rel. contr. to SUM	62%	32%	6%		
Fiducial phase space:					
	2.59 ± 0.02	0.23 ± 0.01	0.08 ± 0.01	2.90 ± 0.04	2.38 ± 0.05
Rel. contr. to SUM	89%	8%	3%		

in the fiducial region without VBS selection requirements. Its distribution for the inclusive $W^{\pm}W^{\pm}jj$ process shows a clear excess of radiation in the central region compared to the sum of all process contributions despite employing the dipole recoil scheme in the Pythia 8 setup. The distribution of other observables in this setup, shown in App. B.2 support this finding, especially seeing the discrepancy in the lepton observables is flat and mild. This can also be seen in Tab. B.6 in the appendix, where the cross-sections for the different contributions is shown in a phase space, where only lepton and no jet event selection requirements are imposed. Here, the difference between the summed and the inclusive contributions is within the statistical accuracy of the MC samples.

This indicates that the dipole recoil scheme applied on the full $W^{\pm}W^{\pm}jj$ process generation is not providing the desired effect in the inclusive prediction of reducing the central radiation from the parton shower. Hence, further on, the prediction of the sum is considered the appropriate prediction for the full $W^{\pm}W^{\pm}jj$ process.

The relative size of each contribution with respect to the sum of all leading order contributions is barely modified when selecting events in the inclusive region. Once the requirements on the invariant mass and the rapidity separation of the tagging jets are imposed, the electroweak component of the $W^{\pm}W^{\pm}jj$ process is, expectedly, significantly enhanced to 89%, leaving the strong production and the interference contributions at 8% respectively 3% in the fiducial region.

The size of the relative contributions in the inclusive region observed here agrees well with the results obtained in Ref. [141], which are quoted to be 57%, 37%, and 6% for the electroweak, the strong and the interference process. Note that in this publication, a slightly different selection is applied and the renormalisation and factorisation scales are set to:

$$\mu_R = \mu_F = \sqrt{p_T(j_1) \cdot p_T(j_2)}. \tag{6.9}$$

In addition, the MC sample setup in Ref. [141] employs the default global recoil scheme.

In conclusion, the strong production mode remains a relevant background process also with the VBS selection requirements, and the interference contribution is small but not negligible, especially in looser phase spaces employed in the measurements later on.

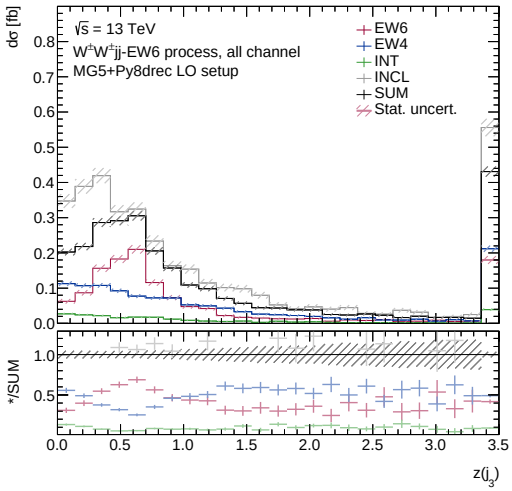


Figure 6.2: Distribution of the Zeppenfeld variable for the third-leading jet (cf. Eq. (5.6)) for all leading orders of the $W^{\pm}W^{\pm}jj$ process, $W^{\pm}W^{\pm}jj$-EW6, $W^{\pm}W^{\pm}jj$-EW4 and their interference, labelled EW6, EW4, and INT, respectively, together with their sum, labelled SUM and compared to an inclusively generated sample including all leading orders of the $W^{\pm}W^{\pm}jj$ process, labelled INCL. Distributions are shown in the inclusive phase space (cf. Tab. 6.8). The MC samples are produced in the MG5+Py8drec setup with the scale choice H_T. The lower panel shows the ratio with respect to the SUM contribution. Uncertainties are statistical uncertainties from the MC generation only. The last bin includes the overflow.

Figures 6.3 and 6.4 show several distributions of the separate and summed contributions of the $W^{\pm}W^{\pm}jj$ process at LO in the inclusive region. The differential predictions in the m_{jj} and ΔY_{jj} observables motivate very well the choice of their cut values for the fiducial region at 500 GeV and 2.0, respectively. As expected, the shape of the distribution of the number of jets in the event $N(j)$ is different, showing higher jet multiplicities for the strong production relative to the still dominant two jet process. In contrast, the lepton kinematic variables show less separation power between the $W^{\pm}W^{\pm}jj$-EW6 and $W^{\pm}W^{\pm}jj$-EW4 process. Here, the invariant mass of the two charged leptons in the event is shown exemplarily. The differential distributions for the Zeppenfeld variable for the leading charged lepton and the lepton centrality, shown in Fig. 6.4 are both used to enhance the VBS contribution over all others in various VBS analyses (cf. Sec. 5.3). The Zeppenfeld variable for the subleading charged lepton looks very similar to the one of the leading lepton and hence a combination of both is subject to selection requirements in Ref. [14]. For the electroweak production mode, the charged lepton Zeppenfeld variables tends to small values, indicating the charged leptons being more central than the jets. The lepton centrality distribution peaks at positive values for the $W^{\pm}W^{\pm}jj$-EW6 process, indicating again that the leptons are enclosed in between the jets from the rapidity perspective. For the $W^{\pm}W^{\pm}jj$-EW4, in contrast, the peak is below zero. Interestingly, the lepton centrality exhibits a region $\zeta > 1.0$, where the strong production background drops almost to zero, while the electroweak signal still has reasonable contributions beyond that.

As expected and visible in both figures, the interference contribution is only sizable, where both, the $W^{\pm}W^{\pm}jj$-EW6 and the $W^{\pm}W^{\pm}jj$-EW4 components have a considerable effect. This in turn means, when cutting away the strong production component, the interference contribution will be diminished largely as well. This is in accordance with the picture from Tab. 6.10.

Figures B.3 and B.4 in the appendix show the comparison of kinematic distributions of the $W^{\pm}W^{\pm}jj$-EW6 and $W^{\pm}W^{\pm}jj$-EW4 processes for the two other nominal setups, the Sherpa23jLO and PB+Py8 setup, respectively. For these two setups, no interference contribution is generated. For the Sherpa23jLO setup, the separation between the two processes in the typical VBS kinematic observables is less pronounced than for the MG5+Py8drec and

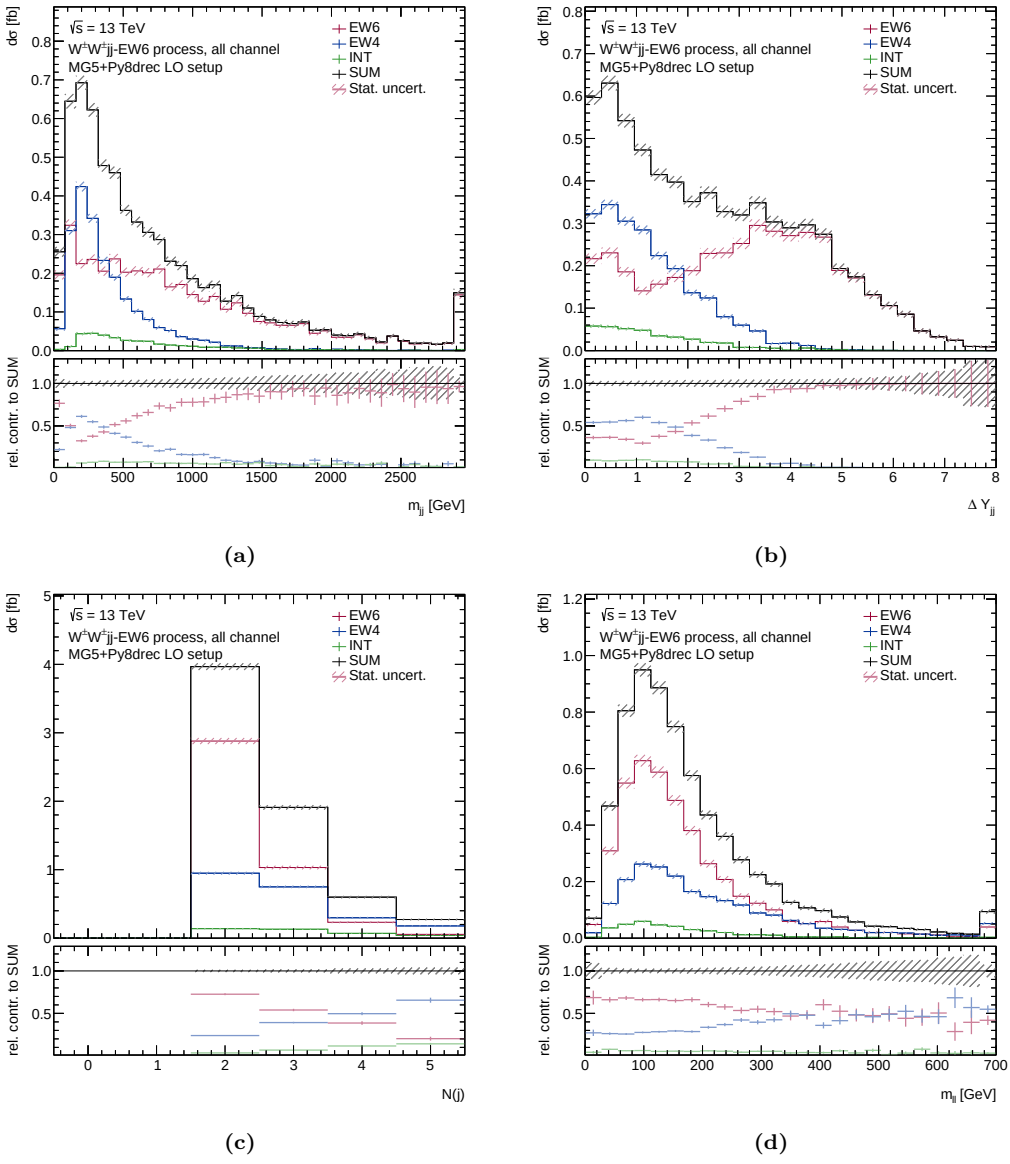
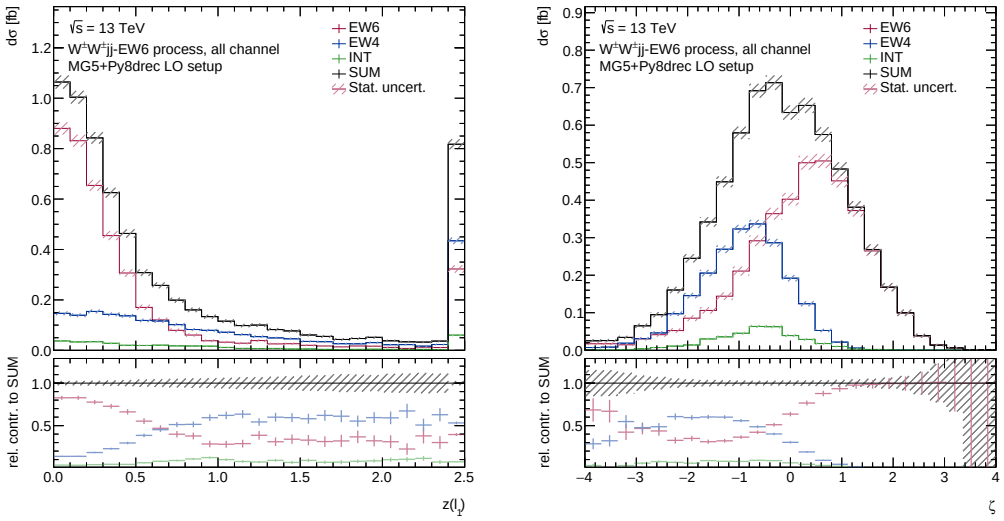


Figure 6.3: Kinematic distributions comparing the LO contributions of the $W^{\pm}W^{\pm}jj$ process, the electroweak and the strong production, and its interference, labelled EW6, EW4, and INT, respectively. The sum of all contributions is also shown, labelled as SUM. The invariant mass m_{jj} (a) and rapidity separation ΔY_{jj} (b) of the tagging jet system, the exclusive jet multiplicity $N(j)$ (c), and the invariant mass m_{ll} of the charged lepton pair (d) are shown. Distributions are shown in the inclusive phase space (cf. Tab. 6.8). The MC samples are produced in the MG5+Py8drec setup with the scale choice H_T. The lower panel shows the relative contribution with respect to the sum. Uncertainties are statistical uncertainties from the MC generation only. The last bin includes the overflow.



(a) **(b)**

Figure 6.4: Kinematic distributions comparing the LO contributions of the $W^{\pm}W^{\pm}jj$ process, the electroweak and the strong production, and its interference, labelled EW6, EW4, and INT, respectively. The sum of all contributions is also shown, labelled as SUM. The Zeppenfeld variable of the leading charged lepton $z(l_1)$ (a), and the lepton centrality ζ (b) are shown. Distributions are shown in the inclusive phase space (cf. Tab. 6.8). The MC samples are produced in the MG5+Py8drec setup with the scale choice H_T. The lower panel shows the relative contribution with respect to the sum. Uncertainties are statistical uncertainties from the MC generation only. The last bin includes the overflow.

PB+Py8 setups. Especially for the PB+Py8 setup, the contributions at low values of the invariant mass of the tagging jet pair and their rapidity separation are less populated in the $W^{\pm}W^{\pm}jj$-EW6 process, where the s-channel contributions are expected to be located. As explained in Sec. 6.3.1, these are missing for the PowhegBox setups.

It is especially noticeable, that the distinct feature of the centrality variable seen in the MG5+Py8drec setup, is not as pronounced in the other two setups. It would be interesting to further explore the reasons for this beyond the inconsistencies found in the PB+Py8 and Sherpa23jLO setups, and especially, its behaviour at NLO without approximations. It might give the opportunity to select a very pure $W^{\pm}W^{\pm}jj$-EW6 sample for specific studies in future analyses where data statistics increases.

The two-dimensional distributions of the invariant mass m_{jj} and the rapidity separation ΔY_{jj} of the tagging jet system, as used here for the selection of the VBS phase space, is shown in Fig. 6.5. In these illustrations, the different behaviour of the three leading order components is clearly visible, the electroweak production populating the diagonal, while the strong component is centered around low values for both, the m_{jj} and ΔY_{jj} observable. They also match the observations in Fig. 3 of Ref. [141], which serves as another validation of the setup used in this work. The analytic expression for the correlation at LO between these two variables in the case of massless jets is presented e. g. in Ref. [131].

6.6.2 Comparison of the Official MC Samples

Continuing the investigation of the $W^{\pm}W^{\pm}jj$ process, this section provides a comparison of the nominal setups of the three generator configurations further used in this work, both for the $W^{\pm}W^{\pm}jj$-EW6 and the $W^{\pm}W^{\pm}jj$-EW4 process. The Sherpa23jLO and PB+Py8 setups are employed in the measurement of the fiducial cross-section with the analysis of ATLAS data at reconstruction level in Run 2 [1]. The MG5+Py8drec setup is used for the reinterpretation of the data in terms of the dimension-eight EFT prescriptions. In addition, a LO MG5_aMC setup is used in all previous CMS publications on the $W^{\pm}W^{\pm}jj$ VBS final state [14, 155, 196] (cf. Tab. 6.2), which further motivates to include this setup in the

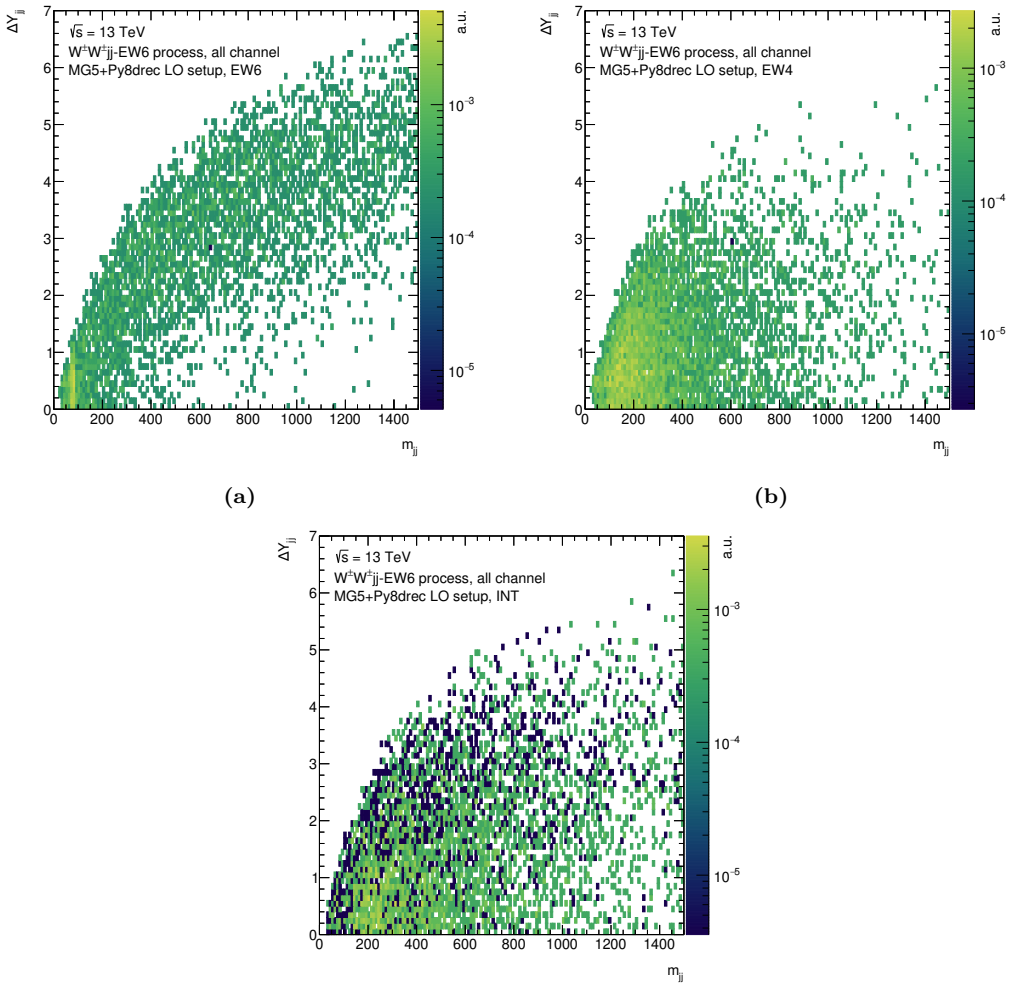


Figure 6.5: Two-dimensional distributions of the invariant mass m_{jj} and the rapidity separation ΔY_{jj} of the tagging jet system for the three LO components $W^{\pm}W^{\pm}jj$-EW6 (a), $W^{\pm}W^{\pm}jj$-EW4 (b), and their interference (c). The MC samples are produced in the MG5+Py8drec setup with the scale choice H_T. Distributions are shown in the inclusive phase space (cf. Tab. 6.8).

Table 6.11: Predictions on the cross-section in the fiducial region, defined in Tab. 6.8, for the $W^{\pm}W^{\pm}jj$-EW6 process for the PB+Py8, Sherpa23jLO, and MG5+Py8drec MC event generation setups at NLO QCD accuracy, LO multi-jet merged accuracy with up to three jets in the matrix element calculation, and pure LO accuracy, respectively. The setups employ different choices for the central values of the renormalisation and factorisation scales as explained in the text. Uncertainties are quoted split into their contributions. These include the statistical accuracy of the MC event generation, the choices for the central scales and PDF set (including the choice of the strong coupling α_S in the set prescription), and the parton shower modelling.

Sample label	Scale choice	Fiducial cross-section [fb]				
		$\sigma^{\text{fid}} \cdot (1$	$\pm\Delta_{\text{stat.}}$	$\pm\Delta_{\text{scale}}$	$\pm\Delta_{\text{PDF}+\alpha_S}$	$\pm\Delta_{\text{ps}})$
PB+Py8	Fixed: m_W	3.08	±0.02	$^{+0.02}_{-0.05}$	±0.05	±0.03
Sherpa23jLO	m_{WW}	2.01	±0.01	$^{+0.30}_{-0.23}$	$^{+0.05}_{-0.03}$	$^{+0.16}_{-0.04}$
MG5+Py8drec	H_T	2.59	±0.02	$^{+0.21}_{-0.17}$	±0.04	$^{+0.02}_{-0.03}$

detailed studies.

Tab. 6.11 summarises the cross-section for the $W^{\pm}W^{\pm}jj$-EW6 process in the nominal fiducial phase space used by the ATLAS data analysis, defined in Tab. 6.8, for the three nominal setups PB+Py8, Sherpa23jLO, and MG5+Py8drec. As detailed in Sec. 6.3, the accuracy of the respective cross-section is NLO in QCD with the VBS approximation for the PB+Py8 setup, LO merged with up to three partons in the matrix element for the Sherpa23jLO setup, and LO for the MG5+Py8drec setup. The central values of the predicted cross-section is evaluated at different renormalisation and factorisation scales for each MC generation setup. For the PB+Py8 prediction the scales are set to the fixed value of the $W^{\pm}$ boson mass for all events. Sherpa23jLO employs the invariant mass of the $W^{\pm}W^{\pm}$ system at matrix element level m_{WW}, which is dynamically set in each event. For the MG5+Py8drec configuration the scales are set to H_T, defined in Eq. (6.3). The predictions on the fiducial cross-sections are given with their statistical uncertainty on the MC sample generation, as well as with their uncertainties on the modelling parameter choices. The uncertainties are evaluated as explained in Sec. 6.5 and quoted split into their sources. Uncertainties on the choice of the nominal scales and PDF set together with their evolution uncertainty on the strong coupling α_S are combined numbers from the matrix element and parton shower effects for MG5+Py8drec and PB+Py8, while for Sherpa23jLO solely effects from the matrix element modelling are included.

The total modelling uncertainties range between 7% to 8% for the MG5+Py8drec setup, 12% to 17% for the Sherpa23jLO setup, and 2% to 3% for the PB+Py8 prediction. Detailed numbers for all variations and envelope compositions entering the total modelling uncertainty can be found in App. B.4.

For the inclusively LO accurate predictions of Sherpa23jLO and MG5+Py8drec, the modelling uncertainties are clearly dominated by the scale variations in the matrix element. However, as the strong coupling α_S does not enter the calculation of the cross-section at LO, the scale uncertainties is purely driven by the factorisation scale variation for the MG5+Py8drec prediction, while for the multi-jet merged setup of Sherpa23jLO the strong coupling enters with the inclusion of one real emission in the matrix element. The variation of both scales yield comparable effects for the latter setup. The exact numbers can be compared from Tab. B.7 in the appendix. The observations are in agreement with the findings in Ref. [141] and [131]. Uncertainties from the parton shower modelling are small for the MG5+Py8drec setup, while the variations of the resummation and merging scale have a sizable effect in the Sherpa23jLO setup. Uncertainties due to the choice of the PDF set and its α_S value are small compared to the effect of the leading source for both of these setups.

Uncertainties on the prediction of the PB+Py8 setup are comparable in size for all but one investigated sources. As expected, the scale uncertainty reduces significantly at NLO

QCD compared to LO accuracy.

The predictions for the central value of the fiducial cross-section disperse significantly for the three setups. The Sherpa23jLO setup features a significantly lower cross-section than the other two predictions, yielding a relative difference to the PB+Py8 prediction of over thirty percent. As discussed earlier in Sec. 6.3.2, one reason for this is expected to be the non-optimal colour flow implementation for this process in the SHERPA parton shower.

The prediction from MG5+Py8drec at LO accuracy is almost 16% lower than the cross-section predicted by PB+Py8 at NLO QCD accuracy. The modelling uncertainties do not cover the difference. Considering the fixed-order NLO QCD corrections derived in Ref. [19] and quoted in Tab. 6.1 being mild but negative, further enhances the discrepancy between the two predictions. The source of this discrepancy is further investigated in the following.

Fig. 6.6 show significant kinematic distributions of the $W^{\pm}W^{\pm}jj$-EW6 process in the inclusive region. In this phase space, the predictions of the inclusive cross-section of the three setups agree within a few percent, yielding a difference of 4%(1%) of the Sherpa23jLO (MG5+Py8drec) setup with respect to the PB+Py8 prediction.

The differential cross-section of jet-related quantities are, however, largely different in shape. In the region of low tagging jet invariant mass and rapidity separation, the peak caused by s-channel triboson production is clearly visible for the Sherpa23jLO and MG5+Py8drec setup, while these contributions are missing in the PB+Py8 prediction. In m_{jj}, the peak originates from one of the three vector bosons decaying hadronically, only in this case exhibiting the same final state as the $W^{\pm}W^{\pm}jj$ process. Due to charge conservation this peak is solely caused by decaying $W^{\pm}$ bosons in this final state. The amount of cross-section coming from this contribution with respect to the full process is considerable. While most of this contribution is rejected by requiring $m_{jj} > 500\,\text{GeV}$ in the fiducial region, it still has an overwhelming effect in the fitting phase space at reconstruction level where the m_{jj} requirement is lowered to 200 GeV. The missing s-channel diagrams in the PB+Py8 prediction cause the central region of ΔY_{jj} to be significantly less populated with hadronic jets.

The tails of the m_{jj} and ΔY_{jj} distributions show a difference of almost 25% (50%) for the MG5+Py8drec (Sherpa23jLO) setup with respect to PB+Py8. The latter exhibits the hardest spectrum in m_{jj} due to more forward and energetic jets. Hence, the same hierarchy is observed in the region of large rapidity separation.

The difference due to the missing s-channel contribution in PB+Py8 is neither accounted for in the modelling uncertainties, nor can these cover the differences in the tails, as expected. However, also the differences between the LO inclusively accurate prediction of Sherpa23jLO and MG5+Py8drec do not agree within their full modelling uncertainties.

Many aspects could cause these large differences in the tails. First, scale uncertainties, especially for the LO accurate MG5+Py8drec setup, where variations on the renormalisation scale are not considered, might be underestimated. Second, jet-related observables of the Sherpa23jLO prediction suffer from the normalisation issue due to the non-optimal shower configuration. Moreover, the recoil issue of PYTHIA 8 with the global recoil setting, affects the PB+Py8 prediction for $N(j)$ larger than 3 and hence, overall jet quantities due to their colour connection.

The distribution of the exclusive jet multiplicity shows fair agreement in the two jet bin which is clearly dominant for this process. The predictions from PB+Py8 exhibit the largest fraction of dijet events compared to the other setups. The modelling of the third jet shows discrepancies in the PB+Py8 setup, while Sherpa23jLO and MG5+Py8drec agree well. This is surprising as MG5+Py8drec is the only setup which completely relies on the parton shower for the modelling of the third jet, while the other two are LO accurate for third jet quantities. This is true, of course, besides migration effects in picking a different jet from the parton shower instead of the real emission from the matrix element.

Differential distributions of the purely leptonic kinematics, shown exemplarily for the invariant mass of the two charged leptons in the event, in contrast, agree well to a few percent for the three setups. This is not only important for the modelling of the acceptance into the fiducial region, but especially critical for the reinterpretation within the EFT prescription following later in this work, as this observable is employed to set limits on the parameters of this BSM model.

The modelling of the third-leading jet is further investigated in Fig. 6.7 which shows

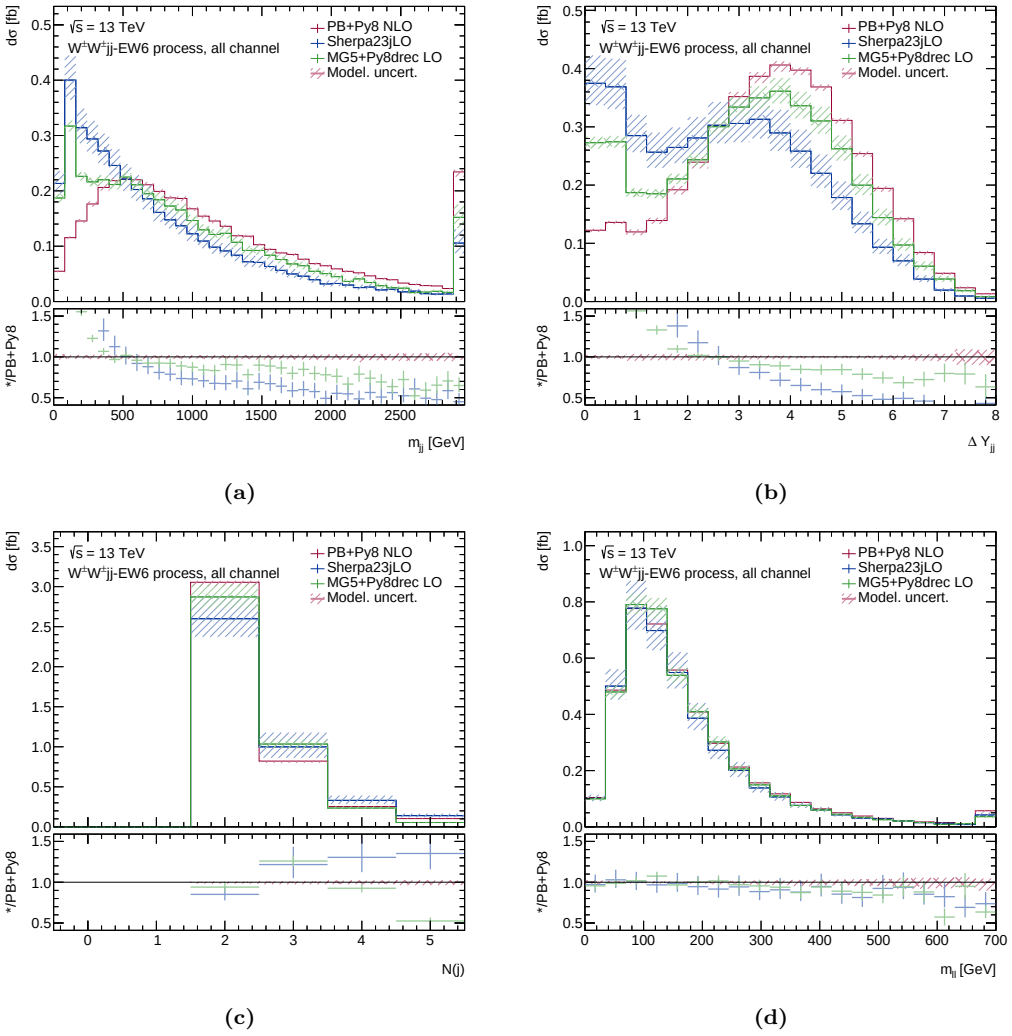
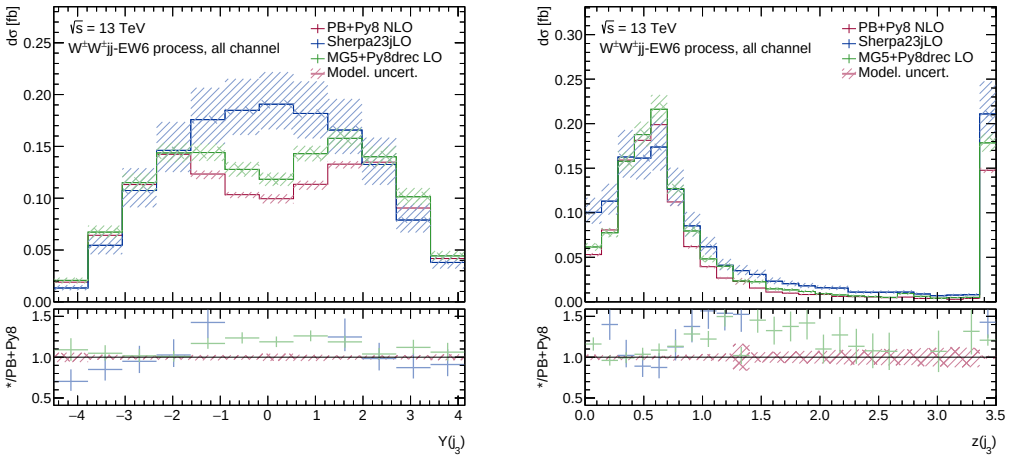


Figure 6.6: Kinematic distributions comparing the different nominal modelling setups for the $W^{\pm}W^{\pm}jj$-EW6 process, PB+Py8 (red), Sherpa23jLO (blue), and MG5+Py8drec (green) in the inclusive region (cf. Tab. 6.8). The invariant mass m_{jj} (a) and rapidity separation ΔY_{jj} (b) of the tagging jet system, the exclusive jet multiplicity $N(j)$ (c), and the invariant mass m_{ll} of the charged lepton pair (d) are shown. The lower panel shows the relative difference with respect to the PB+Py8 prediction. The uncertainties bands are the total modelling uncertainties. The last bin includes the overflow.



(a) **(b)**

Figure 6.7: Rapidity (a) and Zeppenfeld (b) distribution for the third-leading jet comparing the different nominal modelling setups for the $W^{\pm}W^{\pm}jj$-EW6 process, PB+Py8 (red), Sherpa23jLO (blue), and MG5+Py8drec (green) in the inclusive region (cf. Tab. 6.8). The lower panel shows the relative difference with respect to the PB+Py8 prediction. The uncertainties bands are the total modelling uncertainties. The last bin includes the overflow. It is to be noted that these distributions only show the fraction of events possessing at least a third jet with transverse momentum exceeding 35 GeV, according to the object selections summarised in Tab. 6.8, which is the reason of the smaller overall cross-section in this figure.

the rapidity and Zeppenfeld distribution for this jet. PB+Py8 and MG5+Py8drec show a more or less mild depletion of the central region, contrary to Sherpa23jLO. The difference is eye-catching in the rapidity distribution and less pronounced in the Zeppenfeld observable. Recently, the latter is commonly used to characterise the third-leading jet kinematics within the event.

While a number of studies [141, 199, 200] exist for the electroweak process, the strong $W^{\pm}W^{\pm}jj$-EW4 process is much more seldomly looked at. Clearly, the VBS process is the driving motivation to study the electroweak process. However, a solid modelling of the QCD-induced process is necessary, since, as seen in Tab. 6.10, it composes a non-negligible background for the $W^{\pm}W^{\pm}jj$-EW6 process in important analysis regions. Moreover, with moving in the direction of full NLO accurate predictions, the separation is non-trivial, as to be remembered from the discussion in Sec. 5.4, and the combined measurement needs to be considered.

Tab. 6.12 summarises the cross-section for the $W^{\pm}W^{\pm}jj$-EW4 process in the nominal fiducial phase used by the ATLAS data analysis, defined in Tab. 6.8, for the three nominal setups PB+Py8, Sherpa23jLO, and MG5+Py8drec. It is to be noted again that for this process no approximation is made in the calculation of the NLO QCD corrections. Besides the process definition, all settings in the MC event generation are left unchanged with respect to the production of $W^{\pm}W^{\pm}jj$-EW6 for the Sherpa23jLO and MG5+Py8drec setups. When using PB+Py8 for the $W^{\pm}W^{\pm}jj$-EW4 some changes have been made, which is a consequence of the separate implementation of the electroweak and strong process in the PowhegBox framework (cf. App. A.2.1). Especially the choice of the renormalisation and factorisation scales are identical to the $W^{\pm}W^{\pm}jj$-EW6 case, as well as the evaluation of the modelling uncertainties[8]. The predictions on the fiducial cross-section are given with their statistical uncertainty on the MC sample generation, as well as with their uncertainties on the modelling parameter choices.

[8]One difference is the absence of internal PDF set variations for the PB+Py8 $W^{\pm}W^{\pm}jj$-EW4, which should have minor effects given the availability of the alternative PDF sets for the evaluation of the envelope and the overall expected size of the PDF set uncertainties compared to the remaining sources.

Table 6.12: Predictions on the cross-section in the fiducial region, defined in Tab. 6.8, for the $W^{\pm}W^{\pm}jj$-EW4 process for the PB+Py8, Sherpa23jLO, and MG5+Py8drec MC event generation setups at NLO QCD accuracy, LO multi-jet merged accuracy with up to three jets in the matrix element calculation, and pure LO accuracy, respectively. The setups employ different choices for the central values of the renormalisation and factorisation scales as explained in the text. Uncertainties are quoted split into their contributions. These include the statistical accuracy of the MC event generation, the choices for the central scales and PDF set (including the choice of the strong coupling α_S in the set prescription), and the parton shower modelling.

QCD sample label	Scale choice	Fiducial cross-section [fb]				
		$\sigma^{\text{fid}} \cdot (1$	$\pm\Delta_{\text{stat.}}$	$\pm\Delta_{\text{scale}}$	$\pm\Delta_{\text{PDF}+\alpha_S}$	$\pm\Delta_{\text{ps}})$
PB+Py8	Fixed: m_W	0.64	±0.01	±0.08	$^{+0.03}_{-0.01}$	$^{+0.10}_{-0.01}$
Sherpa23jLO	m_{WW}	0.44	±0.00	$^{+0.17}_{-0.11}$	±0.01	±0.02
MG5+Py8drec	H_T	0.23	±0.01	$^{+0.06}_{-0.05}$	±0.01	±0.01

The reader is reminded here, that an inconsistency in the lepton flavour universality is found in the POWHEGBOX implementation of the $W^{\pm}W^{\pm}jj$-EW4 process in the course of these studies (cf. App. A.3.1).

The total modelling uncertainties range between 23% to 27% for the MG5+Py8drec setup, 26% to 39% for the Sherpa23jLO setup, and 13% to 21% for the PB+Py8 prediction. Detailed numbers for all variations and envelope compositions entering the total modelling uncertainty can again be found in App. B.4. Compared to the $W^{\pm}W^{\pm}jj$-EW6 process, the modelling uncertainties are sizeably larger which is mostly driven by the scale uncertainties. As for the electroweak production, the uncertainties on the renormalisation and factorisation scales are dominant in the LO case, i. e. for MG5+Py8drec and Sherpa23jLO. The exact numbers can be compared from Tab. B.7 in the appendix.

Uncertainties from the parton shower modelling are small for the MG5+Py8drec and Sherpa23jLO setups. The uncertainty on the prediction from the PB+Py8 setup yields comparable effects from the scale variations and the modelling differences between the PYTHIA 8 and HERWIG 7 parton shower programmes. Also for the $W^{\pm}W^{\pm}jj$-EW4, the scale uncertainty reduces significantly at NLO QCD compared to LO accuracy, dropping by roughly 50%. Uncertainties due to the choice of the PDF set and its α_S value are again small compared to the effect of the leading source for all three setups.

The predictions for the central value of the fiducial cross-section disperse significantly for the three setups also for the strong process, yet the hierarchy between the different setups alternates. While the largest cross-section is predicted again by PB+Py8, MG5+Py8drec features the lowest cross-section in the fiducial region, which is more than 60% reduced with respect to PB+Py8. The prediction from Sherpa23jLO yields a cross-section reduced by one third compared to PB+Py8. It is to be noted that the non-optimal shower configuration in the SHERPA setup should not affect the predictions in the $W^{\pm}W^{\pm}jj$-EW4 process. The overall spread of the three predictions is not covered by the modelling uncertainties. The effect of NLO QCD corrections, predicted to be below the percent level in Ref. [19] (cf. Tab. 6.1), is negligible in light of the size of the modelling differences.

Fig. 6.8 shows kinematic distributions of the $W^{\pm}W^{\pm}jj$-EW4 process in the inclusive region. The discrepancies of the predictions in this phase space are as pronounced as in the fiducial region, or, for the Sherpa23jLO setup even larger with almost 50% difference to PB+Py8. For this reason, the distributions are shown normalised to the same area. It can be observed that the shape difference in the typical VBS observables is not as pronounced as for the $W^{\pm}W^{\pm}jj$-EW6 process. Especially in the distribution of the rapidity separation of the tagging jets, which peaks at zero for the $W^{\pm}W^{\pm}jj$-EW4 process, the discrepancies are large only at large values. For the invariant mass of the tagging jet system m_{jj}, the shape of the predictions from PB+Py8 and MG5+Py8drec agree fairly well within uncertainties,

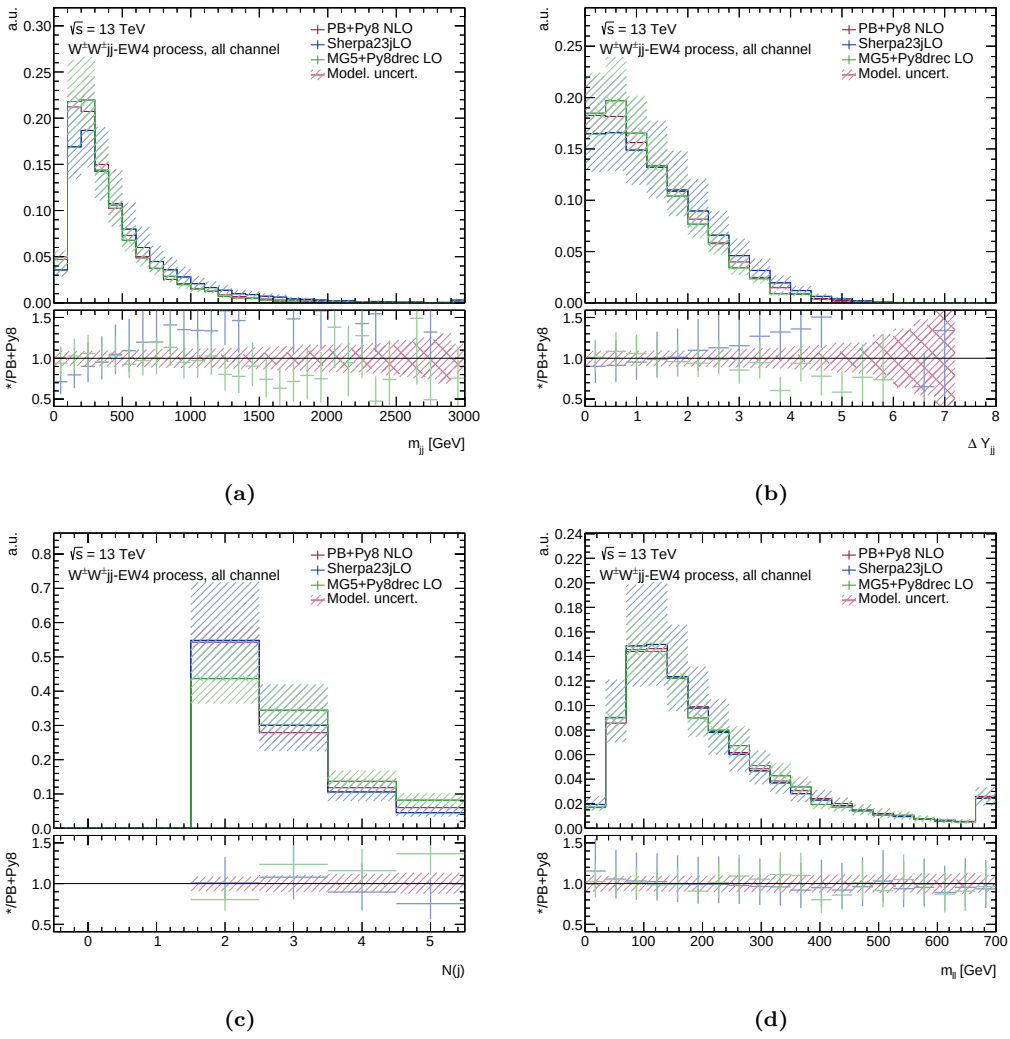


Figure 6.8: Kinematic distributions comparing the different nominal modelling setups for the $W^{\pm}W^{\pm}jj$-EW4 process, PB+Py8 (red), Sherpa23jLO (blue), and MG5+Py8drec (green) in the inclusive region (cf. Tab. 6.8). The invariant mass m_{jj} (a) and rapidity separation ΔY_{jj} (b) of the tagging jet system, the exclusive jet multiplicity $N(j)$ (c), and the invariant mass m_{ll} of the leading charged lepton pair (d) are shown. The lower panel shows the relative difference with respect to the PB+Py8 prediction. The uncertainties bands are the total modelling uncertainties. The distributions are normalised to unit area. The last bin includes the overflow.

while the Sherpa23jLO setup exhibits a harder spectrum. The predictions in the exclusive jet multiplicity agree in shape within the large uncertainty bands. As for the $W^{\pm}W^{\pm}jj$-EW6 process, kinematic distributions of the leptons agree well in shape between the three setups. Again, the invariant mass of the two charged leptons in the event is shown exemplarily.

As there is no dedicated section on the impact of the scale choice for the $W^{\pm}W^{\pm}jj$-EW4 process in this work, some remarks on the findings with a limited set of MC samples are given here. Subsequent studies on this should be done with NLO QCD accurate prediction for this process, since the theoretical predictions for this process are complete at this order in contrast to the $W^{\pm}W^{\pm}jj$-EW6 process (cf. Sec. 6.1). These are not subject of this work. Tab. B.3 summarises, among other results, the fiducial cross-section for predictions with all setups used in this thesis for the $W^{\pm}W^{\pm}jj$-EW4 process. This includes different nominal settings for the renormalisation and factorisation scales. The hierarchy between the prediction for different nominal scale setting of one MC generator setup is found to be identical as for the $W^{\pm}W^{\pm}jj$-EW6 process, discussed in the next section. Predictions employing the fixed scale of the $W^{\pm}$ boson mass, m_W are largest, while the one using $\sqrt{s}$ as the nominal scales is smallest. The differences between the scales are larger than for the $W^{\pm}W^{\pm}jj$-EW6 process. Fig. B.1 shows kinematical distributions for the $W^{\pm}W^{\pm}jj$-EW4 process employing the PB+Py8 and Sherpa23jLO setup with identical scale choices of m_W.

6.7 Studies on the Predictions of the $W^{\pm}W^{\pm}jj$-EW6 Process

Following the large discrepancies between the cross-section predictions of the three nominal setups in the fiducial region in Tab. 6.11, detailed studies of the predictions of the $W^{\pm}W^{\pm}jj$-EW6 process are pursued. These include the impact of the nominal choice for the renormalisation and factorisation scales, as well as parton shower configurations. Moreover, the predictions for the $W^{\pm}W^{\pm}jj$-EW6 process are compared with those obtained from Ref. [141] and in the first Run 2 publication of the CMS collaboration on this final state [14] by studying the cross-section in the fiducial regions of both publications.

While the studies presented here follow the lines of Ref. [141], they do extend their work substantially not only with the additional investigations mentioned, but also by including prediction of the Sherpa event generator, and using the full final state (see Eq. (6.1)) compared to the reduced process $pp \to \mu^+\nu_\mu e^+\nu_e jj$. Some of the findings presented here, have been published in Ref. [199].

As outlined below, the LO predictions are important for BSM interpretations, which is the reason to include them in these studies as well. In order to facilitate the comparison and reduce the degree of ambiguity, a Sherpa LO MC sample is included in the studies, labelled SherpaLO.

To conclude the examination of the $W^{\pm}W^{\pm}jj$-EW6 process, the impact of the VBS approximation at NLO in QCD is discussed, as well as the impact of the NLO EW corrections to this process in the fiducial region defined in this work.

Likewise for these studies, the statistics and detailed numbers on the cross-section predictions, and acceptances for all setups are summarised in App. B.1.

6.7.1 Comparison of Scale Settings

The dependence on the renormalisation and factorisation scales of the predicted cross-section originates purely from the approach to use truncated perturbative series for its calculation. If it were possible to include all orders in the calculation, this dependence would vanish entirely. As such, the variation of the predicted cross-section with the nominal scales choice can serve as an estimate of the impact of higher-order corrections not included in the predictions at hand.

If assumed that the ansatz of perturbation theory holds in the calculation, the scale dependence is expected to reduce with the inclusion of higher orders. The observations made in the previous sections confirm this assumption, seeing a significant reduction of scale

Table 6.13: Predictions on the cross-section of the $W^{\pm}W^{\pm}jj$-EW6 process in the fiducial region, defined in Tab. 6.8 for different renormalisation and factorisation scale settings, as explained in the text, in the PB+Py8, Sherpa23jLO, MG5+Py8drec, and the SherpaLO MC event generation setups. Cross-sections are arranged in descending order referencing the Sherpa23jLO predictions. Uncertainties due to the statistical accuracy of the MC event generation are quoted for all setups. For the nominal setup of each event generation programme, the scale uncertainty envelope is quoted as well.

Scale choice	Fiducial cross-section [fb]			
	PB+Py8	Sherpa23jLO	MG5+Py8drec	SherpaLO
Fixed: m_W	$3.08 \pm 0.02^{+0.05}_{-0.02}$	3.00 ± 0.04	3.31 ± 0.05	3.32 ± 0.13
SqrtPtJets		2.34 ± 0.03	2.93 ± 0.05	2.98 ± 0.07
$H_T/2$		2.02 ± 0.03	2.78 ± 0.03	2.63 ± 0.07
m_{WW}		$2.01 \pm 0.01^{+0.30}_{-0.23}$	3.08 ± 0.05	$2.60 \pm 0.00^{+0.21}_{-0.18}$
H_T		1.95 ± 0.09	$2.59 \pm 0.02^{+0.19}_{-0.17}$	2.34 ± 0.03
SqrtS		1.65 ± 0.03	2.33 ± 0.02	2.10 ± 0.04

variation for the PB+Py8 setup, which is NLO accurate in the strong coupling, compared to the LO accurate predictions from Sherpa23jLO and MG5+Py8drec.

Especially, the choice of the scales set to the fixed value of the mass of the $W^{\pm}$ boson, m_W, for the PB+Py8 setup has motivated this study as a fixed scale is said to be unfavourable to capture higher-order effects for the VBS process [161].

The effect of the choice of the renormalisation and factorisation scale on the predicted cross-section is investigated using five different dynamical scale choices together with the fixed scale choice of $\mu_{R/F} = m_W$. The dynamical scale choices include the invariant mass of the $W^{\pm}W^{\pm}$ system, m_{WW}, defined in Eq. (6.2), which is the default scale of the Sherpa23jLO setup. Moreover, the scale defined in Eq. (6.9) as the square root of the transverse momenta of the (sub-)leading jet $p_T(j_{1/2})$ is studied. It is a scale which has been shown to provide reasonably stable predictions at NLO QCD accuracy [162] and which is hence used throughout the studies in Ref. [141]. It is labelled "SqrtPtJets" in the following. Further, the impact of three scales are investigated which are pre-implemented in the MG5_aMC programme: H_T, as defined in Eq. (6.3), its half $H_T/2$, and the scale:

$$\text{SqrtS} := \sqrt{\hat{s}}, \tag{6.10}$$

with $\hat{s}$ defined as the centre-of-mass energy of the partonic system (see Eq. (4.1)).

All scales are defined at matrix-element level for the Sherpa and MG5_aMC setups. The details of the technical implementation are summarised in App. A.2.2 and A.2.3 for the respective MC programme. Especially the implementation of the scales m_{WW} and SqrtPtJets in the MG5_aMC code is technically sophisticated as this requires the modification of its `FORTRAN` code. The patches for their implementation are also provided in App. A.2.3. While the nominal scales are altered, all remaining parameters within one generator setup are left unchanged. A change of the default scale has not been done in the PowhegBox setup and is left for further studies.

Tab. 6.13 summarises the predictions of the cross-section in the fiducial phase space, for the different choices of the central value of the renormalisation and factorisation scales for the three nominal setups PB+Py8, Sherpa23jLO, MG5+Py8drec, and the not merged LO accurate SherpaLO setup. Uncertainties from the renormalisation and factorisation scale envelope are quoted only for the setup with the nominal scale choice. The uncertainty built from the envelope of the renormalisation and factorisation scale variation cannot cover the spread in predictions observed for the variety of scale choices for all studied setups at LO accuracy. The spread reaches a relative size with respect to the nominal scale choice of 45%, 30%, and 37% for the Sherpa23jLO, MG5+Py8drec, and the SherpaLO, respectively.

The predictions of the Sherpa23jLO setup are consistently lower than the cross-sections from the other two MC programmes (due to the already mentioned non-optimal setup, see

Sec. 6.3.2). The agreement between the MG5+Py8drec, and the SherpaLO predictions, both being purely LO accurate without any merging, is good for the fixed scale m_W, as well as the SqrtPtJets and the $H_T/2$ scale choice. The cross-section predictions for the m_{WW}, H_T, and SqrtS scale choices, however, show differences between 10% and 16%. The hierarchy between the predictions for different scale choices within one setup is preserved over different setups, except for the m_{WW} scale choice, which might be explained with different internal implementations between Sherpa and MG5_aMC.

For the scale choice m_W, a direct comparison between all setups is possible. Predictions employing this scale choice show by far the largest cross-section for all setups. Kinematic distributions in the inclusive region are shown in Fig. 6.9. The agreement between the different predictions improved in the VBS region at high invariant mass m_{jj} and rapidity separation ΔY_{jj} of the tagging jet system, compared to Fig. 6.6. For the low m_{jj} and ΔY_{jj} regions discrepancies remain where the PB+Py8 prediction is missing the s-channel contributions which, as discussed previously, is populating the peak around the $W^{\pm}$ mass. However this does not explain the large differences between the Sherpa23jLO and MG5+Py8drec predictions in this region, which might still be an artefact of the non-optimal implementation of the parton shower configuration in Sherpa.

This assumption might be deduced from the exclusive jet multiplicity distributions which agrees well between Sherpa23jLO and MG5+Py8drec in the two jet bin, but diverges significantly in the three jet bin. The difference between PB+Py8 and Sherpa23jLO in the latter bin is even more pronounced, although these two setups share the LO accuracy in this bin.

Again, the shape of the dilepton invariant mass distributions agree well between the three setups.

The agreement in the high m_{jj} region between the LO and NLO QCD accurate predictions is remarkable, as large k-factors where found particularly when employing the fixed scale choice of m_W. The comparison of the obtained k-factors for the scale m_W and a dynamical scale set to the momentum transfer between an incoming an outgoing parton along a fermion line [161] is shown in Fig. 6.10. There, k-factors for the fixed scale m_W are found that reach almost 0.8 in the high invariant mass region.

Although the dependence on the renormalisation and factorisation scales are predicted and seen to be reduced at NLO QCD accuracy, it is nevertheless interesting to examine those as well. This has been done in Ref. [161] and [131]. Fig. 2 in Ref. [161] and Fig. 10 in Ref. [131] both show the scale dependence of NLO QCD and LO accurate predictions of the $W^{\pm}W^{\pm}jj$-EW6 process for different central values. The scale dependence is reduced significantly at NLO QCD accuracy compared to the LO predictions, ranging in the few percent level. In addition, both studies show the same hierarchy between the predictions employing the fixed scale m_W and different dynamical scales, finding the largest predictions with the fixed scale. In Ref. [161], the difference between the fixed and dynamical scale prediction amount to 9% at LO and is below one percent at NLO QCD accuracy. In Ref. [131] the difference between the tested scales is similarly below the percent level at NLO QCD. As stated in Ref. [131], however, these small numbers are especially not reliable and underestimate the effect of known higher-order corrections when new topologies enter at these higher orders. This is the case for the $W^{\pm}W^{\pm}jj$-EW6 process, where processes with gluons in the initial state only appear at orders beyond LO.

Not only the impact on the inclusive fiducial cross-section prediction on the choice of the central value of the scales is sizable, but also its effect on the shape of several kinematic distributions. This can be seen in Figures 6.11 and 6.12 for the LO multi-jet merged setup Sherpa23jLO and the purely LO accurate setup MG5+Py8drec, respectively. All relevant distributions shown here, the invariant mass m_{jj} and rapidity separation ΔY_{jj} of the tagging jet system, the exclusive jet multiplicity and especially also the invariant mass of the two leading charged leptons m_{ll}, exhibit distortions due to the central choice of the renormalisation and factorisation scales. These are found to be consistent between Sherpa and MG5_aMC. In some regions, the discrepancies are covered by the scale uncertainty derived from the envelope approach on the nominal prediction. However, in various regions this is not the case, especially e. g. for large invariant masses, both in m_{jj} and m_{ll}. Both of these regions are highly relevant in further analyses, the first for the extraction of the cross-section using ATLAS data and the latter to extract exclusion limits to the BSM EFT

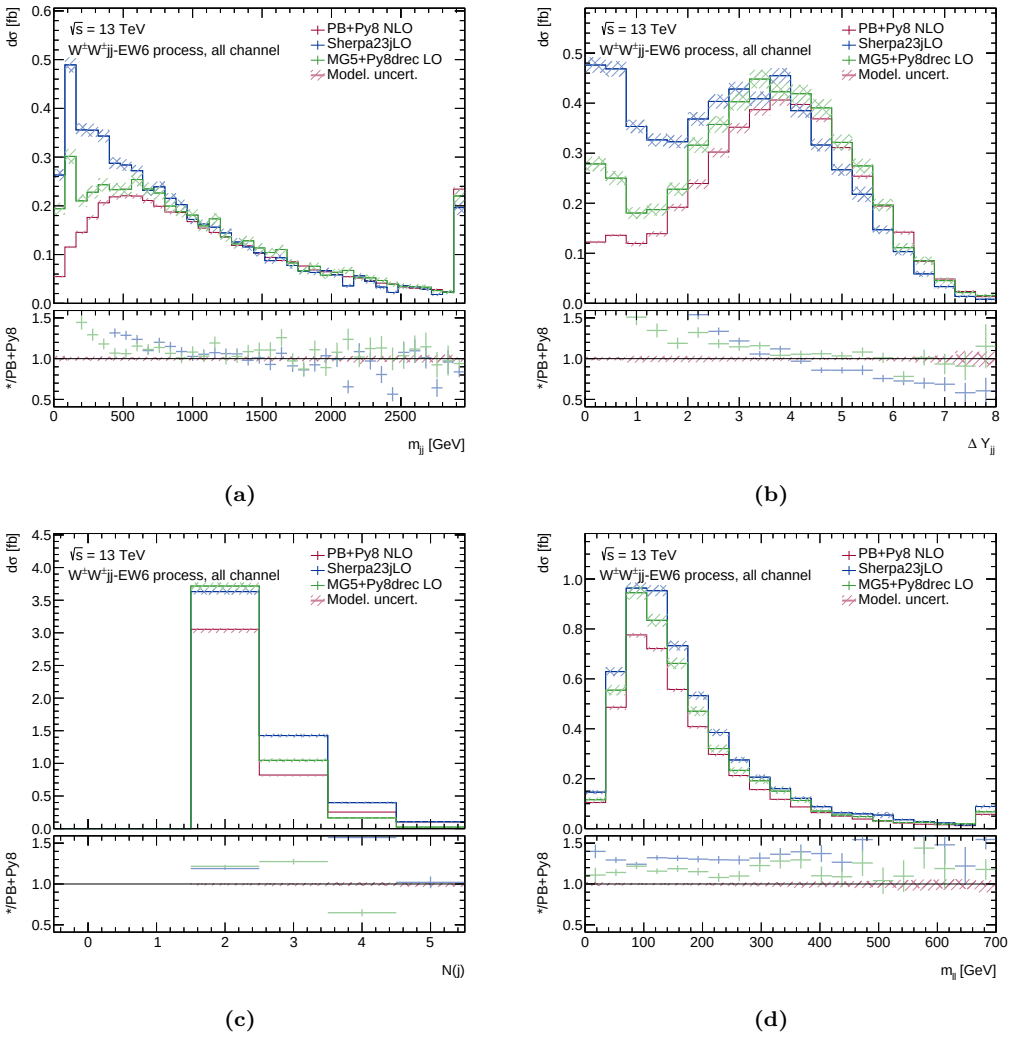


Figure 6.9: Kinematic distributions comparing the different modelling setups for the $W^{\pm}W^{\pm}jj$-EW6 process, PB+Py8 (red), Sherpa23jLO (blue), and MG5+Py8drec (green), for the same scale choice m_W. Distributions are shown in the inclusive region (cf. Tab. 6.8). The invariant mass m_{jj} (a) and rapidity separation ΔY_{jj} (b) of the tagging jet system, the exclusive jet multiplicity $N(j)$ (c), and the invariant mass m_{ll} of the charged lepton pair (d) are shown. The lower panel shows the relative difference with respect to the PB+Py8 prediction. The uncertainties bands are the total modelling uncertainties for the PB+Py8 prediction, while they are MC statistics only for Sherpa23jLO and MG5+Py8drec. The last bin includes the overflow.

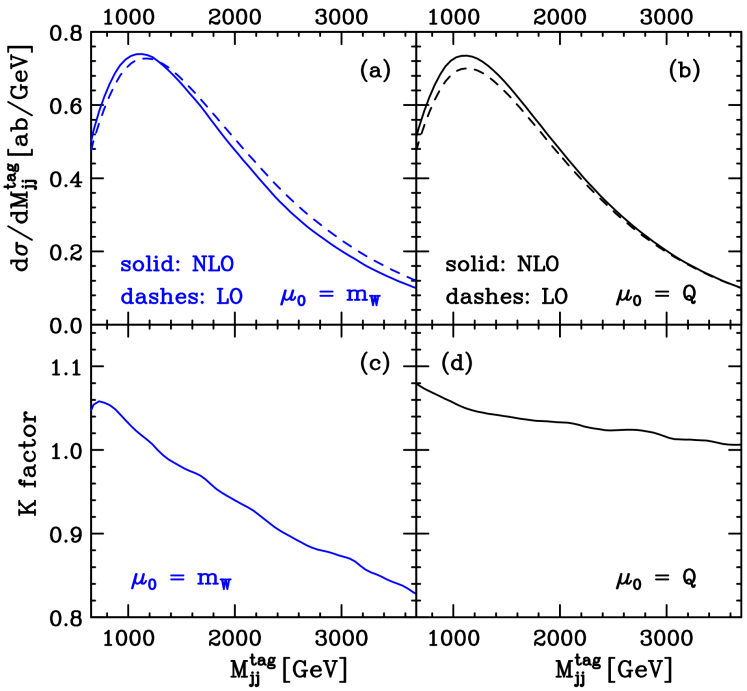


Figure 6.10: Distribution of the invariant mass m_{jj} of the tagging jet pair exemplarily for the $pp \to e^+\nu_e\mu^+\nu_\mu jj$ process at LO (dashed) and NLO QCD (solid) accuracy at a centre-of-mass energy of $\sqrt{s} = 14\,\text{TeV}$ for two different scale choices: (a) fixed scale m_W, and (b) scale Q as the momentum transfer between an incoming and outgoing parton along a fermion line. The lower panels show the k-factor as defined in Eq. (5.9). Figure taken from Ref. [161].

model parameters with these data.

The differences in shape are even more pronounced in the LO accurate SherpaLO setup, as shown in Fig. B.11 in the appendix. In addition, good agreement is seen between the two LO inclusively accurate predictions of MG5+Py8drec and SherpaLO when using the scale SqrtPtJets, as defined in Eq. (6.9) and used in the studies of Ref. [141], and shown in Fig. B.12 in the appendix.

6.7.2 Comparison of Parton Shower Configurations

As described in Sec. 4.2, the modelling of parton showers and especially of the soft components in QCD rely on a set of parameters and non-perturbative models. These parameters cannot be derived from first principles, and hence need to be tuned by comparing with experimental data. This is especially interesting when it comes to processes involving VBS. One reason is the special kinematics of the process. Moreover, due to its comparable low cross-section in the SM there has only been limited experimental access to this class of processes which made it difficult so far to derive proper conclusions. With increasing statistics in the course of Run 2 of the LHC, processes including VBS can be studied more thoroughly. This section summarises the findings when comparing different parton shower configurations for the $W^{\pm}W^{\pm}jj$-EW6 process. Only few, namely the setups employing the default Pythia 8 tunes, shown in this section have been compared to data (cf. Tab. 6.2). However, this comparison never exceeded the study of the typical VBS variables. Comparisons of third jet observables have not been done with data yet.

Tab. 6.14 summarises the inclusive predictions in the fiducial region, defined in Tab. 6.8, for the different parton shower setups used together with the MG5_aMC and PowhegBox frameworks. For both setups the default Pythia 8 tune setup, A14 and AZNLO, respectively for MG5+Py8 and PB+Py8, is compared to a Pythia 8 setup where the default global recoil scheme is changed to the dipole recoil scheme, labelled Py8drec, and to the default Herwig 7

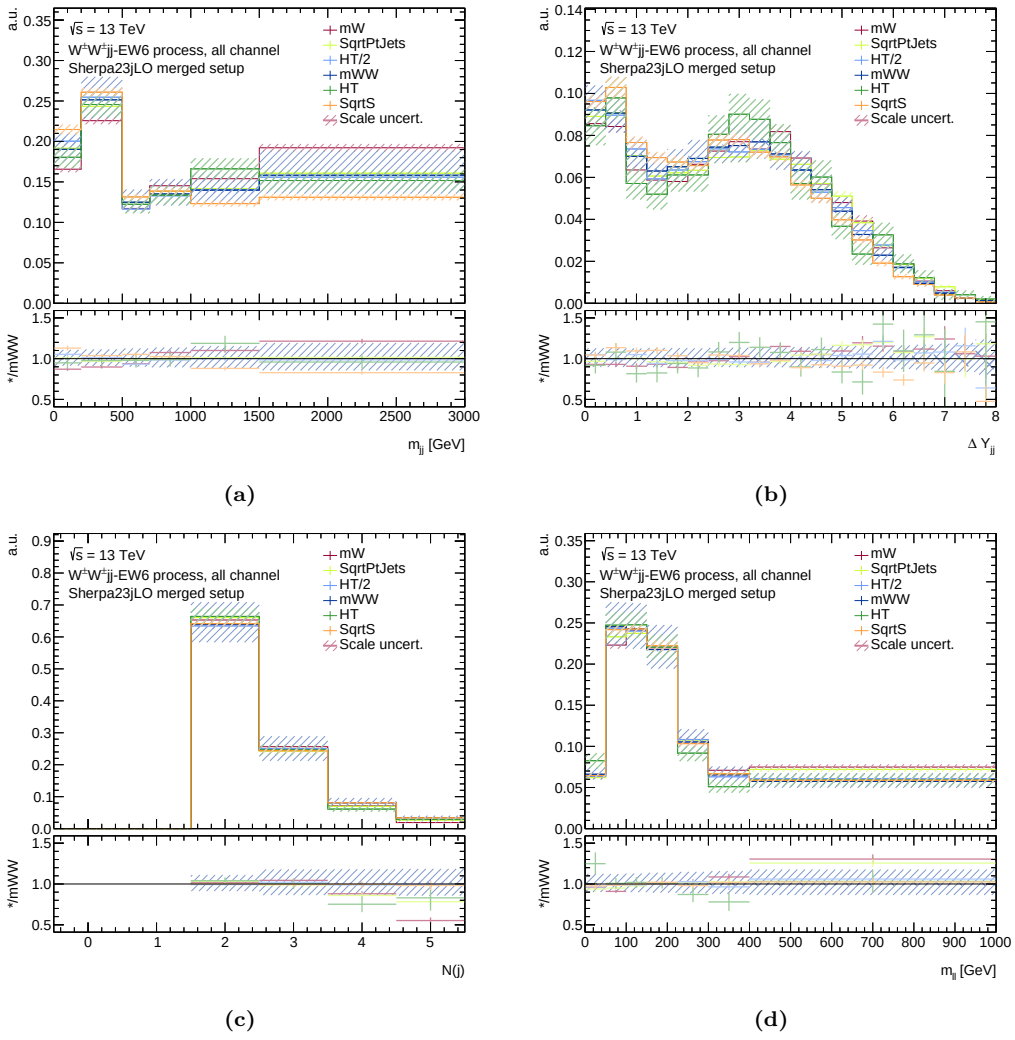


Figure 6.11: Kinematic distributions comparing the predictions of the Sherpa23jLO setup for the $W^{\pm}W^{\pm}jj$-EW6 process, for six different scale choices as defined in the text. Distributions are shown in the inclusive region (cf. Tab. 6.8) and are normalised to unit area. The invariant mass m_{jj} (a) and rapidity separation ΔY_{jj} (b) of the tagging jet system, the exclusive jet multiplicity $N(j)$ (c), and the invariant mass m_{ll} of the charged lepton pair (d) are shown. The lower panel shows the relative difference with respect to the nominal predictions employing the scale m_{WW}. The uncertainties bands are from the MC statistics only, except for the default setup which includes scale uncertainties from the envelope approach. The last bin includes the overflow.

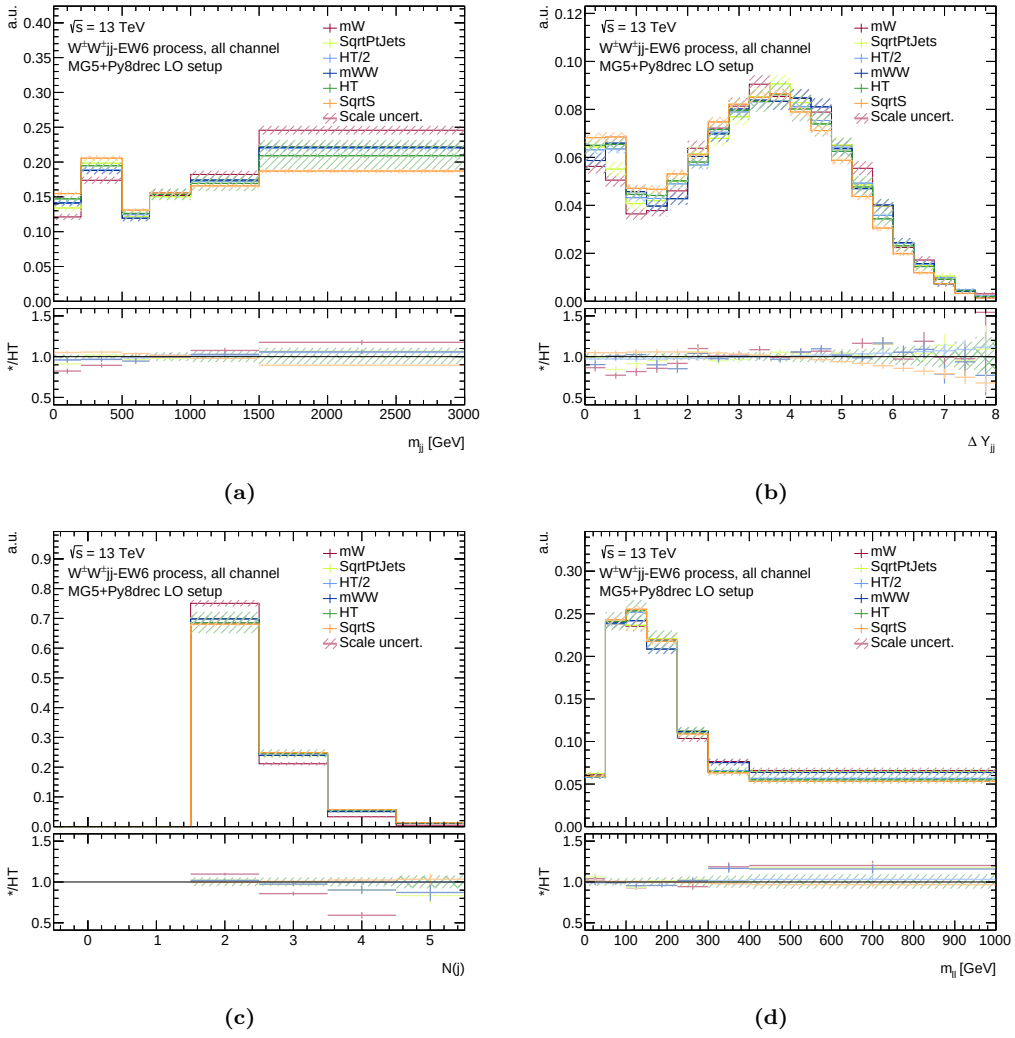


Figure 6.12: Kinematic distributions comparing the predictions of the MG5+Py8drec setup for the $W^{\pm}W^{\pm}jj$-EW6 process, for six different scale choices as defined in the text. Distributions are shown in the inclusive region (cf. Tab. 6.8) and are normalised to unit area. The invariant mass m_{jj} (a) and rapidity separation ΔY_{jj} (b) of the tagging jet system, the exclusive jet multiplicity $N(j)$ (c), and the invariant mass m_{ll} of the charged lepton pair (d) are shown. The lower panel shows the relative difference with respect to the nominal predictions employing the scale H_T. The uncertainties bands are from the MC statistics only, except for the default setup which includes scale uncertainties from the envelope approach. The last bin includes the overflow.

Table 6.14: Predictions on the cross-section in the fiducial region, defined in Tab. 6.8, for the $W^{\pm}W^{\pm}jj$-EW6 process for different parton shower setups, employing Pythia 8 and Herwig 7, for the MG5_aMC and PowhegBox MC event generations. The setups adopt different choices for the central values of the renormalisation and factorisation scales as explained in the text. Uncertainties due to the statistical accuracy of the MC event generation are quoted for all setups, while for the nominal setup of each event generation programme, the envelope from the internal parton shower variations is quoted as well.

Sample label	Scale choice	Fid. cross-section [fb]
MG5+Py8drec		$2.59 \pm 0.02 \pm 0.02$
MG5+Py8	H_T	2.40 ± 0.04
MG5+H7		2.56 ± 0.04
PB+Py8		$3.08 \pm 0.02 \pm 0.01$
PB+Py8drec	Fixed: m_W	2.98 ± 0.07
PB+H7		3.05 ± 0.02

configuration, labelled H7.

Uncertainties from the MC event generation on the fiducial cross-section are quoted for all setups. The variation of the internal parton shower parameters is only given for the nominal setups, MG5+Py8drec and PB+Py8. The latter are small and equal in size compared to the statistical accuracy of the samples for both the MG5_aMC and PowhegBox setups. The differential distributions of the internal parton shower variations can be found in Figures B.5 and B.9 in the appendix, for the MG5+Py8drec and PB+Py8 setups, respectively. Uncertainties from PDF set and scale variations are expected to be small when changing the parton shower modelling and hence are not provided here again. They can be found in Tab. 6.11 for the nominal setups.

For the MG5_aMC setup, the predictions on the fiducial cross-section are compatible between the Pythia 8 configuration with the dipole recoil scheme and Herwig 7. The default Pythia 8 tune predicts a lower cross-section. This can be explained from the observations in Fig. 6.13.

While the modelling of the invariant mass of the tagging jet system agrees well for the three setups in the fiducial region above 500 GeV, the differential prediction in the rapidity separation ΔY_{jj} is shifted towards smaller values for the MG+Py8 setup with default global recoil scheme. Hence, more events are rejected when imposing a selection requirement of $\Delta Y_{jj} > 2.0$ in the fiducial region.

The exclusive jet multiplicity shows a substantial enhancement of events with three or more jets compared to the other two setups, depleting the two jet bin via migration. According to the distribution of the Zeppenfeld variable of the third jet, the additional jets are radiated into the centre of the detector.

These findings are in agreement with the observation of additional radiation in the central region when using the global recoil scheme, and explained in detail in Sec. 6.1. As a consequence, two effects occur. First, due to the additional radiation it becomes more likely that one of the centrally radiated jets is wrongly assigned as a tagging jet. This explains the contributions at very low m_{jj} and low ΔY_{jj}. Second, the tagging jets, which are QCD colour connected to these extra radiations, are pulled towards the centre of the detector by the QCD interactions. Therefore, they are less separated in this setup. This effect is visible in the shift of the peak in the ΔY_{jj} distribution towards slightly lower values. These findings agree well with the observations from Ref. [141] shown in Fig. 6.1.

The predictions between the MG5+Py8drec and the MG5+H7 setup agree generally well for observables involving the (sub)leading jet which are dominated by the matrix element calculations. This is confirmed in the distribution of the exclusive jet multiplicity, which agrees well in the two jet bin and starts diverging for higher exclusive jet multiplicities, where parton shower effects are dominant.

Distributions related to the kinematics of the (charged) leptons are in good agreement between the three setups, exemplarily shown for the invariant mass of the two charged leptons

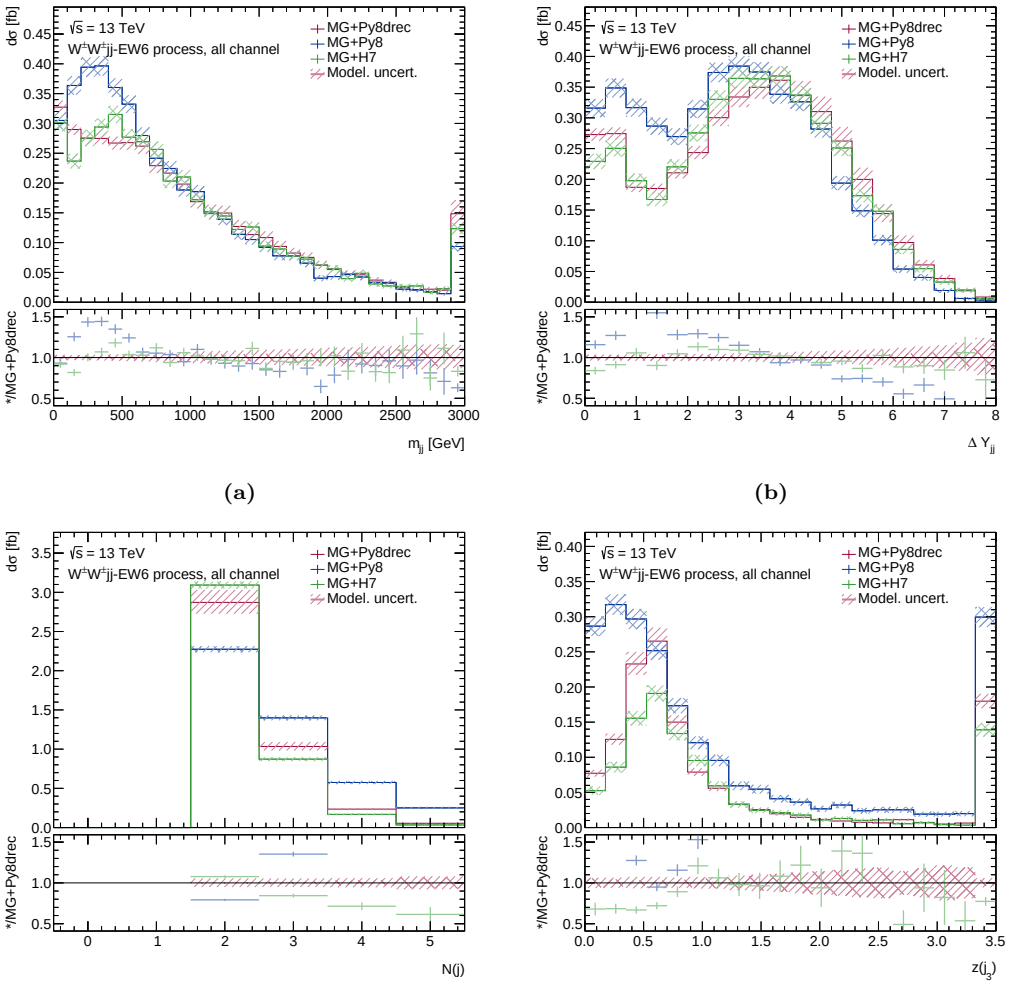


Figure 6.13: Kinematic distributions comparing the predictions of different parton shower setups at LO of the $W^{\pm}W^{\pm}jj$-EW6 process with the MG5_aMC event generator. The nominal setup MG5+Py8drec, using Pythia 8 with the dipole recoil option, is compared against the default Pythia 8 tune (MG+Py8) and the default Herwig 7 setup (MG+H7). Distributions are shown in the inclusive region (cf. Tab. 6.8). The invariant mass m_{jj} (a) and rapidity separation ΔY_{jj} (b) of the tagging jet system, the exclusive jet multiplicity $N(j)$ (c), and the Zeppenfeld variable for the third-leading jet, $z(j_3)$ (d) are shown. The lower panel shows the relative difference with respect to the nominal setup MG5+Py8drec. The uncertainties bands are from the MC statistics only, except for the nominal setup which includes the full modelling uncertainties. It is to be noted that the distribution for the Zeppenfeld variable in panel (d) only shows the fraction of events possessing at least a third jet with transverse momentum exceeding 35 GeV, according to the object selections summarised in Tab. 6.8, which is the reason of the smaller overall cross-section in this figure. The last bin includes the overflow.

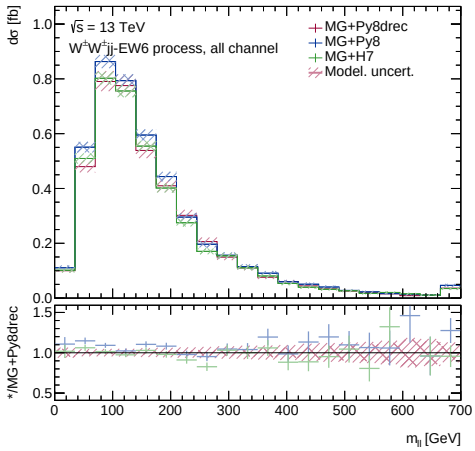


Figure 6.14: Distribution of the invariant mass of the two charged leptons, m_{ll}, comparing the predictions of different parton shower setups at LO of the $W^{\pm}W^{\pm}jj$-EW6 process with the MG5_aMC event generator. The nominal setup MG5+Py8drec, using Pythia 8 with the dipole recoil option, is compared against the default Pythia 8 tune (MG+Py8) and the default Herwig 7 setup (MG+H7). Distributions are shown in the inclusive region (cf. Tab. 6.8). The lower panel shows the relative difference with respect to the nominal setup MG5+Py8drec. The uncertainties bands are from the MC statistics only, except for the nominal setup which includes the full modelling uncertainties. The last bin includes the overflow.

in the event in Fig. 6.14. It is expected that these observables are less sensitive to parton shower effects.

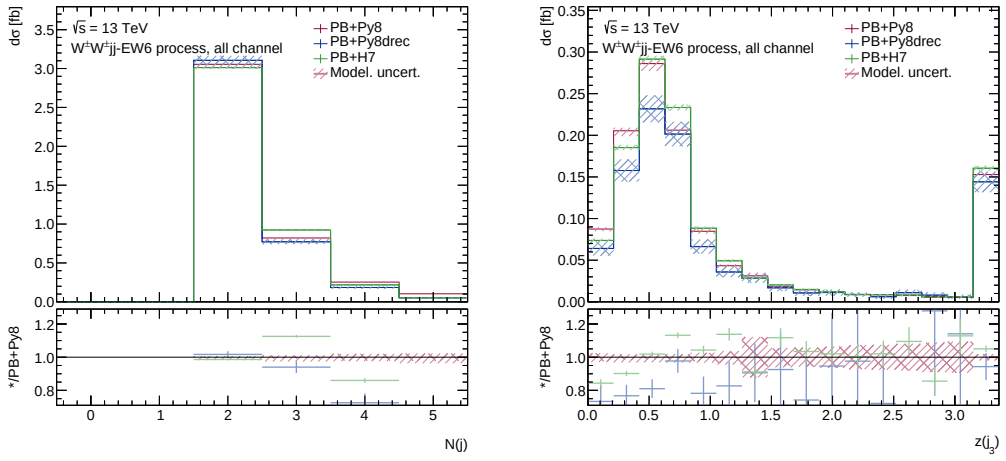
The predictions in the fiducial region employing the PowhegBox framework are comparable for all three setups, as shown in Tab. 6.14. Turning on the dipole recoil scheme reduces the cross-section prediction for this setup, which simultaneously has the largest statistical uncertainty due to a reduced number of MC events used for this cross-check. As explained in Sec. 6.1, the effect of the change of the recoil scheme is reduced when using PowhegBox. The reason for this is that the prediction from PowhegBox is NLO accurate in QCD and in addition, the PowhegBox framework fills the first emission with an internal Sudakov factor. This leaves the description of the first emission, i. e. the third jet, entirely within the PowhegBox framework. Only the second extra emission is generated by the Pythia 8 parton shower, which affects only a very small fraction of the events.

Fig. 6.15 shows the exclusive jet multiplicity $N(j)$ and the Zeppenfeld variable of the third jet $z(j_3)$. The latter shows the divergence of the predictions for events with more than three jets. Additional kinematic distributions of this study are shown in Fig. B.13 in the appendix.

As a final remark in this section, the size of the variations of the internal shower parameters is revisited. These are very small and comparable in size to the statistical uncertainties of the MC samples (cf. Sec. B.4.2). In Ref. [225] the relevance of the study of soft QCD effects is outlined in the case of VBF Z boson production, where especially the impact of the variation of the MPI model is found to play a sizable role. It is stated that the variations of the pure perturbative parton shower evolution are insufficient to assess the full uncertainties given by parton shower programmes. The reliability of models of soft QCD, describing multi-parton interactions, colour reconnection, and hadronization, as well as their interplay have to be carefully evaluated and accounted for in the uncertainty estimate.

6.7.3 Comparison in Different Phase-spaces

As a further investigation, cross-sections have been calculated in phase spaces rebuilt from the definitions in Ref. [14] and [141]. The selection requirements of these phase spaces have been collected in Tab. 6.9.



(a) **(b)**

Figure 6.15: Kinematic distributions comparing the predictions of different parton shower setups at NLO QCD accuracy of the $W^{\pm}W^{\pm}jj$-EW6 process with the POWHEG-BOX event generator. The nominal setup PB+Py8, using PYTHIA 8 with the default global recoil option, is compared against the a PYTHIA 8 setup with the dipole recoil scheme (PB+Py8drec) and the default HERWIG 7 setup (PB+H7). Distributions are shown in the inclusive region (cf. Tab. 6.8). The exclusive jet multiplicity $N(j)$ (a), and the Zeppenfeld variable for the third-leading jet, $z(j_3)$ (b) are shown. The lower panel shows the relative difference with respect to the nominal setup PB+Py8. The uncertainties bands are from the MC statistics only, except for the nominal setup which includes the full modelling uncertainties. The last bin includes the overflow.

This section includes only numbers for those configurations which either appear in and can be compared with the respective publications or are the nominal setups used in this thesis. Numbers for further configurations can be found in Tab. B.5 in the appendix.

The cross-section predictions of various configurations in the phase space defined in Ref. [14], in which the first measurement of the CMS collaboration at 13 TeV centre-of-mass energy has been published, are summarised in Tab. 6.15. Version and tune details of the generation programmes utilised therein are summarised in Tab. 6.2. Settings of the recoil scheme and the renormalisation and factorisation scales are left at its default values. The central values of the dynamical scales in MG5_aMC are predefined as the squared transverse mass m_T^2 after the clustering of event fragments with the k_t algorithm [226], labelled "cluster" scale in this work. However, according to the discussion in Ref. [227], based on findings within the studies of this work, the cluster scale is not a favourable choice for the $W^{\pm}W^{\pm}jj$ process. This is the reason why this scale is not included in any of the studies presented above.

The predicted cross-section with a comparable setup using MG5_aMC and PYTHIA 8 obtained in these studies is in reasonable agreement with the value obtained in Ref. [14]. It has to be noted here, that different tunes of the PYTHIA 8 generator have been used. Information on the PDF set used in Ref. [14] are, however, not available. No systematic uncertainties are quoted in this phase space for these studies, except the statistical error of the MC sample.

The cross-section predicted with the default LO setup in this work, MG5+Py8drec, is lower than the reference value. This prediction agrees well with the measured fiducial cross-section of the CMS publication [14], which is stated to be $3.83 \pm 0.66(\text{stat.}) \pm 0.35(\text{syst.})$ fb for the $W^{\pm}W^{\pm}jj$-EW6 process, where the uncertainties quoted are the statistical uncertainty of the dataset and the total experimental uncertainties, respectively.

The nominal setups of the POWHEGBOX and SHERPA event generators in this work, PB+Py8 and Sherpa23jLO, respectively, predict a cross-section for the $W^{\pm}W^{\pm}jj$-EW6 process in this phase space which is larger, respectively lower than the reference in Ref. [14].

Table 6.15: Predictions of the cross-section of the $W^{\pm}W^{\pm}jj$-EW6 process in the fiducial phase space defined in Ref. [14] for various MC generation configurations. The central values of the renormalisation and factorisation scales are stated as defined in Sec. 6.7.1 and the text. The first line states the predicted theoretical cross-section at LO obtained in Ref. [14].

Sample label	Scale choice	Cross-section in fid. phase space of Ref. [14] [fb]
Reference from [14]:		
MG5+Py8	Cluster	4.25 ± 0.27(tot.)
MG5+Py8	Cluster	4.35 ± 0.06(stat.)
MG5+Py8drec	H_T	3.78 ± 0.03
PB+Py8	Fixed: m_W	4.44 ± 0.02
Sherpa23jLO	m_{WW}	2.78 ± 0.02

Both of these tendencies match the picture of previous results of these studies.

Tab. 6.16 summarises the predicted cross-section of the reduced process $pp \to \mu^+\nu_\mu e^+\nu_e jj$ obtained in this work in the fiducial phase space rebuilt from the studies in Ref. [141].

Predictions at NLO accuracy in QCD, employing the PowhegBox framework with various parton shower configurations, explained in Sec. 6.7.2, show reasonable agreement with the result in Ref. [141] quoted to be 1.3642 ± 0.0004(stat.) fb. It has to be noted here, that the configurations used in this study differ in the choice of the central value for the renormalisation and factorisation scales, as well as the Pythia 8 tune. In Ref. [141] the scale SqrtPtJets is used as central value. In addition, Pythia 8 is set up with the tune presented in Ref. [209] and disabled MPI in Ref. [141].

The predictions at LO accuracy employing the MG5_aMC event generation programme and various parton shower configurations show a slightly lower cross-section than obtained in Ref. [141]. One difference between the setups in this work and in Ref. [141] is again the Pythia 8 tune. Moreover, in Ref. [141] only resonant contributions of the $W^{\pm}W^{\pm}jj$-EW6 process are generated with the process definition employed, neglecting diagrams such as shown in Fig. 5.3 (d) and (e).

Predictions employing the Sherpa event generator are not included in Ref. [141]. Using as the central value for the renormalisation and factorisation scales the SqrtPtJets, the LO accurate setup agrees well with the predictions in Ref. [141]. All other cross-sections predicted with Sherpa are substantially lower. This is again expected from the findings of the previous studies and summaries.

6.7.4 Impact of the VBS approximation at NLO QCD

As outlined in Sec. 6.1, the VBS approximation, helped in gaining an insight into the first NLO QCD accurate predictions of the $W^{\pm}W^{\pm}jj$-EW6 process. Due to the exclusion of all s-channel contributions and their interference with the other channels, the calculation of the process can be simplified and Feynman diagrams omitted (cf. Sec. 5.4.1).

The impact of the VBS approximation at LO accuracy has been studied in several publications [19, 131, 163]. In the fiducial region, where selection requirements are placed on the typical VBS variables, explicitly with $m_{jj} > 500\,\text{GeV}$ and $\Delta Y_{jj} > 2.5$ in these studies, the difference between the full calculation and the VBS approximation is below the percent level at the order $\mathcal{O}(\alpha_{EW}^6\alpha_S^0)$. Only when moving close to the resonant triboson contribution, which peaks at invariant masses of the tagging jet system at the mass of the $W^{\pm}$ boson, m_W, the difference between the two predictions is becoming large, naturally. These observations are confirmed in Ref. [141].

With the first full calculations at NLO accuracy in QCD in Ref. [19] the impact can be calculated for the first time at this order. While in this publication, the studies are still

Table 6.16: Predictions of the cross-section of the reduced process $pp \to \mu^+\nu_\mu e^+\nu_e jj$ in the fiducial phase space defined in Ref. [141] for various MC generation configurations. The central values of the renormalisation and factorisation scales are stated as defined in Sec. 6.7.1.

Sample label	Scale choice	Cross-section in fid. phase space of Ref. [141] [fb]
PB+Py8	Fixed: m_W	1.31 ± 0.01
PB+Py8drec		1.26 ± 0.04
PB+H7		1.32 ± 0.01
PB+H7DS		1.25 ± 0.07
Sherpa23jLO	SqrtPtJets	0.99 ± 0.02
Sherpa23jLO	m_{WW}	0.83 ± 0.01
MG5+Py8drec	SqrtPtJets	1.24 ± 0.03
MG5+Py8drec	H_T	1.12 ± 0.02
MG5+Py8	SqrtPtJets	1.19 ± 0.05
MG5+H7DS	SqrtPtJets	1.23 ± 0.05
SherpaLO	SqrtPtJets	1.36 ± 0.08
SherpaLO	m_{WW}	1.07 ± 0.00

confined to the typical VBS fiducial region ($m_{jj} > 500\,\text{GeV}$, $\Delta Y_{jj} > 2.5$), and again find a negligible impact, the studies in Ref. [141] extend the discussion to outside these selection criteria. Fig. 6.16, which is taken from Ref. [141], shows the impact of the VBS approximation at NLO accuracy in QCD for the $W^{\pm}W^{\pm}jj$-EW6 process.

The impact of the VBS approximation in the typical VBS region is observed to be negative and does not exceed a few percent also at NLO QCD accuracy. However, outside this region, the difference to the full calculation can be as large as 50%. This result is relevant as analysis techniques are advancing trying to extract as much information as possible with the use of control regions and multivariate analyses outside the VBS region for fits to experimental data. Analyses of processes involving VBS at the LHC are becoming more sophisticated and eventually more sensitive to more subtle modelling effects. Predictions beyond the VBS approximation are hence required.

A first step towards this direction is the inclusion of the s-channel while still neglecting the inference between the different channels. The impact of this approximation is shown on the right side of Fig. 6.16. It is positive and sizable only for small invariant masses m_{jj} with simultaneously large rapidity separations ΔY_{jj} of the tagging jet system.

Due to the different setups used with many possible sources for discrepancies, a quantitative conclusion cannot be made from the figures and numbers shown in the previous sections of this chapter.

6.7.5 Impact of NLO EW Corrections

In Ref. [19], and summarised in Tab. 6.1, first full corrections in all orders at NLO of the complete $W^{\pm}W^{\pm}jj$ process are calculated. With these calculations it has been shown that corrections of the order $\mathcal{O}(\alpha_{EW}^7)$, i. e. NLO electroweak corrections to the $W^{\pm}W^{\pm}jj$-EW6 process, are dominant in size over all other corrections at NLO. This result motivates to include these corrections in the predictions of the $W^{\pm}W^{\pm}jj$-EW6 process of this analysis. Following the prescription in Ref. [19], predictions for the fixed-order $\mathcal{O}(\alpha_{EW}^7)$ (NLO EW) and $\mathcal{O}(\alpha_{EW}^6\alpha_S^0)$ (LO) of the $W^{\pm}W^{\pm}jj$ process are kindly provided by Ref. [228][9]. Both are given as a function of the invariant mass of the tagging jet system m_{jj} and applying the

[9] Real radiation from photon-induced contributions of the type $\gamma q \to \ell^{\pm}\nu_\ell\ell^{\pm}\nu_\ell jjj$ are not included in the computation of the NLO EW accurate process at order $\mathcal{O}(\alpha_{EW}^7)$.

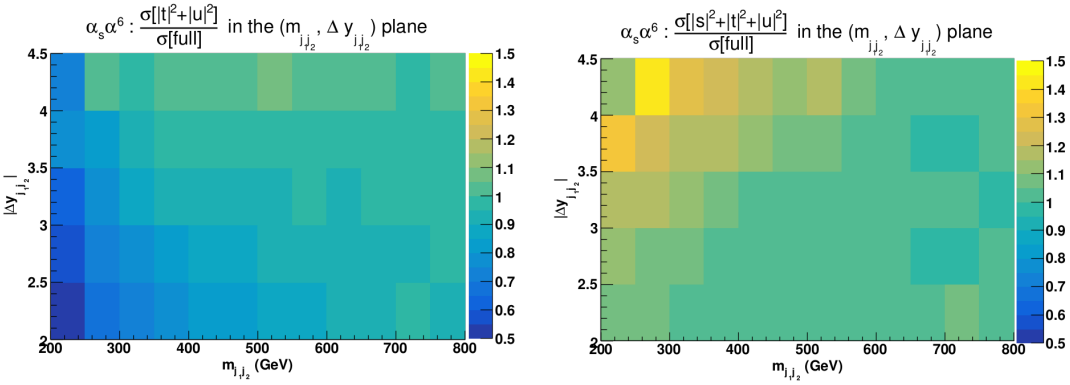


Figure 6.16: Differential distributions in the 2-dimensional plane of the transverse mass m_{jj} and the rapidity separation ΔY_{jj} of the tagging jets showing the ratio of the approximated squared amplitudes of the $W^\pm W^\pm jj$-EW6 process at NLO accuracy in QCD in the VBS approximation ($\left|t^2\right| + \left|u^2\right|$) (left) and $\left|t^2\right| + \left|u^2\right| + \left|s^2\right|$ (right) to the full matrix element calculation in the fiducial region defined in Tab. 6.9 with less tight requirements on the VBS observables, $m_{jj} > 200\,\text{GeV}$, and $\Delta Y_{jj} > 2.0$. Figure taken from Ref. [141].

nominal fiducial selection of this work (except the requirement on m_{jj} itself). No parton shower is applied. From this information the k-factor is derived which allows to rescale the LO prediction to the NLO EW result. Following Eq. (5.9), it is defined in this matter as:

$$k(\text{NLO EW}) = \frac{\sigma(\text{NLO EW})}{\sigma(\text{LO})}, \tag{6.11}$$

$$= \frac{\sigma(\mathcal{O}(\alpha_{EW}^7))}{\sigma(\mathcal{O}(\alpha_{EW}^6\alpha_S^0))}. \tag{6.12}$$

The distribution of the k-factor as a function of m_{jj} is displayed in Fig. 6.17. As expected, the correction is negative throughout the whole spectrum. It is below 10% in absolute value for smaller and medium invariant masses below the fiducial region requirement of 500 GeV. The correction does significantly affect the tail of the m_{jj} distribution, due to the large Sudakov logarithms in the calculation of the NLO EW corrections at large energy-momentum transfer. Hence, this is expected for all energy-momentum-like observables. As a result, events with large tagging jet invariant mass are significantly suppressed at NLO EW accuracy. In the case at hand, the suppression reaches approx. -20% for m_{jj} of 2000 GeV and above.

In the fiducial region, i. e. with $m_{jj} > 500\,\text{GeV}$, the total correction factor and its statistical uncertainty amount to:

$$k(\text{NLO EW}) = 0.834 \pm 0.002(\text{stat.}). \tag{6.13}$$

This result matches closely the numbers presented in Ref. [19] (-13.2%, cf. Tab. 6.1) and Ref. [181] (-16.0%), which employ very similar fiducial phase space definitions. It shall now be used to rescale the nominal predictions of PB+Py8, Sherpa23jLO, and MG5+Py8drec. Before doing so, however, some further remarks and examinations have to be made.

As described in Sec. 5.4.2, electroweak corrections at NLO of the $W^\pm W^\pm jj$-EW6 process include the radiation of real photons off any charged particle of the LO process. Also, the MC samples to which the correction shall be applied here include the resummation of QED radiation off charged final-state particles via their (interface to) parton shower programmes (cf. Sec. 4.2.4). Hence, simply applying the correction factor to these samples leads to a double counting between the real NLO EW correction and the first photon emission from the parton shower.

This effect is estimated through an additional MC sample in which the QED final-state radiation is switched off. For reasons of simplification and in light of the magnitude of the effect, this study is performed with the Sherpa23jLO setup and taken to be largely universal as to be applicable to the MC setups which use Pythia 8, i. e. PB+Py8 and MG5+Py8drec.

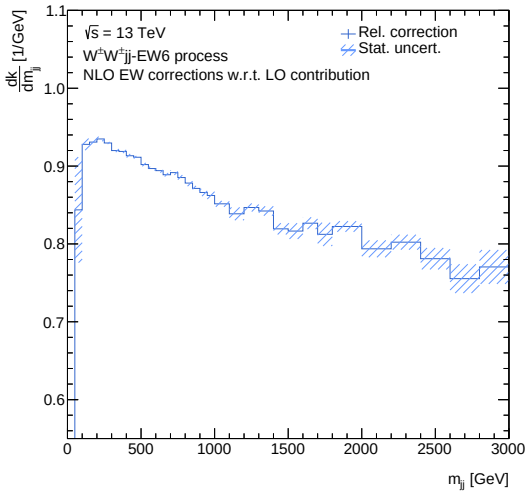


Figure 6.17: Distribution of the relative NLO EW correction at order $\mathcal{O}(\alpha_{EW}^7)$ to the LO $W^{\pm}W^{\pm}jj$-EW6 process at order $\mathcal{O}(\alpha_{EW}^6\alpha_S^0)$, k(NLO EW), as a function of the invariant mass of the tagging jet system m_{jj} in the fiducial region, defined in Tab. 6.8 without the m_{jj} requirement. Inputs to the computation have been given by Ref. [228] based on Ref. [19].

Table 6.17: Predictions on the cross-section in the fiducial region, defined in Tab. 6.8, for the $W^{\pm}W^{\pm}jj$-EW6 process for the nominal setup Sherpa23jLO and with QED FSR radiation switched off. Uncertainties are the statistical errors of the MC generation only.

Sample label	Fid. cross-section [fb]
Sherpa23jLO	2.01 ± 0.01
Sherpa23jLO w/o QED FSR	1.93 ± 0.05

The technical details can be studied in App. B.7. With this technical approach, all QED FSR is excluded, i. e. also radiation beyond the first one. Hence, this comparison is by nature a conservative estimate as it overestimates the actual effect under study. It is shown for the fiducial cross-section in Tab. 6.17 and results in a reduction of the prediction of 4% when turning off the QED FSR. The statistical uncertainty of the alternative MC sample is below 3%.

Even if slightly larger than the statistical uncertainty of the alternative sample, the effect is still considered to be small, also since as stated above, it constitutes a conservative estimate. Results for the prediction of the cross-section from the nominal MC event generation setups rescaled by the NLO EW correction, k(NLO EW) (cf. Eq. (6.13)) are summarised in Tab. 6.18 and should be interpreted in the light of the result of the study above. Uncertainties are rescaled in equal manner for this simple approach. The accuracy in QCD couplings is unaffected by this scaling, as the respective processes are independent and have different orders (cf. Tab. 6.1). The rescaled PB+Py8 predictions hence includes NLO QCD and EW corrections of the $W^{\pm}W^{\pm}jj$-EW6 process, respectively of orders $\mathcal{O}(\alpha_{EW}^6\alpha_S)$ and $\mathcal{O}(\alpha_{EW}^7)$, in an additive manner.

The selection sequence and differential distributions comparing the predictions with and without QED FSR are shown in Fig. B.14 in the appendix. The largest impact on the selection sequence is seen when requiring the events to pass selections on jet event observables (cf. Tab. 6.8). The distributions of the invariant mass m_{jj} and rapidity separation ΔY_{jj} of the tagging jets only show differences between the two setups at high values of the respective observable in the inclusive region. The impact is mild, however, precise predictions at NLO EW are required to include these in the signal definition in an experimental analysis. Upon these findings it is decided to include the impact of the NLO EW corrections as a

Table 6.18: Predictions on the cross-section in the fiducial region, defined in Tab. 6.8, for the $W^{\pm}W^{\pm}jj$-EW6 process for the PB+Py8, Sherpa23jLO, and MG5+Py8drec MC event generation setups rescaled to NLO EW accuracy with the correction factor k(NLO EW) shown in Eq. (6.13). The setups employ different choices for the central values of the renormalisation and factorisation scales. Uncertainties are the total modelling uncertainties including the statistical accuracy of the MC event generation, the choices for the central scales and PDF set (including the choice of the strong coupling α_S in the set prescription), and the parton shower modelling.

Sample label	Scale choice	Fiducial cross-section [fb]
PB+Py8	Fixed: m_W	$2.57^{+0.05}_{-0.07}$
Sherpa23jLO	m_{WW}	$1.68^{+0.28}_{-0.20}$
MG5+Py8drec	H_T	$2.16^{+0.18}_{-0.15}$

(conservative) uncertainty on the $W^{\pm}W^{\pm}jj$-EW6 process prediction in the reconstruction level analysis in this work and, hence, in Ref. [1]. Another important reason for this decision is the lack of modelling uncertainty estimates on the NLO EW corrections at this point.

6.8 Conclusions and Final Sample Choices

The effort on theoretical calculations of the $W^{\pm}W^{\pm}$ scattering process is pioneering the field of VBS predictions. First full NLO corrections for a process involving VBS are calculated for the $W^{\pm}W^{\pm}jj$ process [19]. Efforts are being made towards the implementation of the full NLO computation in MC programmes and their interface to QED and QCD parton shower programmes [185, 201].

A variety of different MC programmes with interfaces to different parton shower programmes exist that can model the $W^{\pm}W^{\pm}jj$ process at LO, LO multijet merged, and NLO in perturbative QCD. However, few of these setups have been tested against experimental data (cf. Tab. 6.2).

The studies of this chapter use three nominal MC sample setups, PB+Py8, Sherpa23jLO, and MG5+Py8drec, whose default parameters are varied and their impact investigated.

The interference between the $W^{\pm}W^{\pm}jj$-EW6 and the $W^{\pm}W^{\pm}jj$-EW4 process at LO, i. e. order $\mathcal{O}(\alpha^5_{EW}\alpha_S)$, is small in the fiducial region. In the inclusive region it amounts to 9% with respect to the electroweak process and hence is not negligible. From the studies in this chapter, it is decided to add the effect of the $W^{\pm}W^{\pm}jj$-INT contribution as systematic uncertainty on the $W^{\pm}W^{\pm}jj$-EW6 prediction in the analyses, as it employs fits in regions with relaxed requirements on the VBS observables for the cross-section measurement.

The predictions from the nominal MC samples for both, the $W^{\pm}W^{\pm}jj$-EW6 and the $W^{\pm}W^{\pm}jj$-EW4 process, differ substantially. The spread is not covered by the total modelling uncertainties in both cases.

The known non-optimal implementation of the colour flow assignment for VBS-like processes in the default parton shower configuration in the Sherpa programme [213] is leading to a significantly reduced cross-section prediction with the Sherpa23jLO setup for the $W^{\pm}W^{\pm}jj$-EW6 process.

The study of the scale dependence of the three different setups for the $W^{\pm}W^{\pm}jj$-EW6 process show a hierarchy between the tested scales. Setting the scales to the fixed value of the $W^{\pm}$ mass, m_W, yields the largest predictions for all varied setups. This might explain the cross-section prediction being largest for the PB+Py8 setup despite the inclusion of the negative NLO QCD corrections for the $W^{\pm}W^{\pm}jj$-EW6 process as predicted by Ref. [19] and the exclusion of the s-channel contributions and all channel interferences in this sample.

The scale uncertainties assigned as the envelope of the variation of the renormalisation and factorisation scales cannot cover the spread of the predictions with varied central scales at LO and LO multi-jet merged.

The investigations of different parton shower configurations employing Pythia 8 and

Herwig 7 show good agreement in the fiducial cross-section predictions when switching to the dipole recoil scheme in the Pythia 8 setup. The non-optimal behaviour of observables describing the third-leading jet in the event is confirmed when using the default recoil scheme in Pythia 8 with a LO accurate setup, such as MG5_aMC + Pythia 8. It is to be noted however, that the Pythia 8 setup with the dipole recoil scheme has not been included in the commonly used tunes and hence is not tested against experimental data yet. It is therefore recommended to change the default recoil scheme setting only where strictly necessary.

The NLO EW corrections of the $W^{\pm}W^{\pm}jj$-EW6 process are negative and the largest in size compared to all other NLO corrections of the full $W^{\pm}W^{\pm}jj$ process. They increase with large invariant masses of the tagging jet system, the region which is most dominantly used in experimental analyses to extract the $W^{\pm}W^{\pm}jj$-EW6 cross-section and significance.

Based on the findings in this chapter, the final choice on the nominal samples employed in the analysis of the SM $W^{\pm}W^{\pm}jj$-EW6 process are made. Only the nominal predictions Sherpa23jLO and PB+Py8 are at disposal at this point, because only for these setups, official fully detector simulated samples at reconstruction level existed by the time of the completion of this analysis. The MG5+Py8drec setup has not been produced on reconstruction level by the time of the SM analysis. It has only been fully simulated for the EFT reinterpretation analysis[10].

The impact of the VBS approximation at NLO QCD accuracy, employed in the PB+Py8 setup, is seen to be sizable in the regions employed in this analysis, especially in the control regions where the typical VBS requirements are relaxed. The missing contributions, as an effect of the VBS approximation, clearly distort the shape of the invariant mass spectrum of the tagging jet system m_{jj}, the observable which is used for the extraction of the significance and the measurement of the $W^{\pm}W^{\pm}jj$-EW6 process' cross-section in this analysis.

Moreover, the choice of a fixed scale in the PB+Py8 setup is considered unfavourable by theoreticians. The studies presented in this work show, that the scale choice has a large impact on the normalisation as well as the shape of important kinematic distributions.

In addition, in the course of the studies, an inconsistency in the lepton flavour universality is found in the PowhegBox implementation of the $W^{\pm}W^{\pm}jj$-EW4 process (cf. App. A.3.1). This prevents from utilising this setup for a statistical analysis at reconstruction level, where not only channel dependent selection criteria are imposed but also flavour split regions are fitted. Aiming for a consistent setup for the description of both contributions of the $W^{\pm}W^{\pm}jj$ process in the analysis, the PB+Py8 setup cannot be used.

The decision on the nominal signal prediction is hence made in favour of the Sherpa23jLO setup. By the time of the decision, the effects of the non-optimal parton shower configurations in the Sherpa event generation setup have not been identified. However, these are expected to solely affect the normalisation in the multi-jet merged setup and not the shape of any kinematic distribution. In the statistical analysis of the cross-section measurement, normalisation effects on the signal prediction are adjusted by including the unconstrained normalisation nuisance parameter of the signal strength. Hence, the normalisation of the signal prediction utilised to extract the measured cross-section, does not affect its result. Clearly, however, the measured signal strength, is affected by this non-optimal configurations.

6.9 Prospects of Theoretical Predictions for Future LHC Analyses

While most of the predictions employed in LHC experimental analyses investigating the $W^{\pm}W^{\pm}jj$ process to date are inclusively accurate at LO, efforts of the theoretical community are moving towards full NLO accurate computations. It has been shown throughout this chapter that precise predictions beyond inclusive LO accuracy are necessary to capture all effects that are relevant considering the advanced analysis techniques used in current and future analyses. Not only the increasing statistical accuracy of the data samples is forcing in this direction but also the use of control regions outside the typical VBS selections and

[10] In addition, it has not been produced within the official ATLAS MC production structures.

Table 6.19: Summary of MC event generation setups capable of the generation of the $W^{\pm}W^{\pm}jj$ process, including the matrix element providers within the referenced MC programme, its accuracy and possible NLO matching respectively LO merging methods, and common parton shower programmes possible to interface it with. The last column indicated whether this setup has been studied against LHC data yet. Setups that cannot be matched/merged to parton showers are not included (besides the full NLO prediction), as well as programmes that are only capable of providing LO predictions. MG5_aMC@NLO stands short for MadGraph5_aMC@NLO. Notes on the available accuracy of the programmes are specified with (cf. Sec. 6.1): * only available with the VBS approximation for the $W^{\pm}W^{\pm}jj$-EW6 process , ** no non-factorisable QCD corrections for the $W^{\pm}W^{\pm}jj$-EW6 process, *** available for $W^{\pm}W^{\pm}jj$-EW6 process only. Information based on Ref. [230].

MC Programme (ME from)	ME accuracy (ME+PS method NLO matching/ LO merging)	Possible parton shower programmes	Probed in LHC analyses?
PowhegBox (VBFNLO)	NLO QCD* (Powheg)	Pythia 8	✓
		Herwig 7	–
MG5_aMC@NLO	NLO QCD** (MC@NLO)	Pythia 8	–
		Herwig 7	–
	LO multi-jet merged (CKKW-L)	Pythia 8	–
		Herwig 7	–
Sherpa 3.0	LO multi-jet merged (CKKW-L)	internal	–
Matchbox (via Herwig 7)			
(VBFNLO)	NLO QCD*	Herwig 7	–
(MG5_aMC@NLO)	NLO QCD**		–
PowhegBox (Recola)	NLO EW***	Pythia 8	–
Sherpa 3.0 (Recola)	Full NLO (fixed-order only)	None	–

multivariate techniques which are sensitive to more subtle information in the theoretical predictions.

Tab. 6.19 attempts to summarise the available MC event generation setups for the $W^{\pm}W^{\pm}jj$ process beyond LO accuracy at the time of writing of this work. This list by no means claims completeness. Rather it focuses on setups which have been used in recent studies [141, 199] or for predictions of other VBS channels [229]. An extensive summary of currently available and commonly used MC programmes for the generation of VBS processes can be found in Ref. [229].

None of the presented setups have been used for cross-section or significance measurements of the $W^{\pm}W^{\pm}jj$-EW6 process in experimental analyses at the LHC yet. Solely the PowhegBox setup is used for normalising the Sherpa multi-jet merged setup in the ATLAS analysis at 8 TeV [13] and for cross checks but not the main measurements in Ref. [1]. It uses the VBS approximation for the predictions at NLO QCD accuracy of the $W^{\pm}W^{\pm}jj$-EW6 process.

Moreover, unless not studied further, the inconsistency regarding the lepton flavour universality found in the PowhegBox setup for the $W^{\pm}W^{\pm}jj$-EW4 process (cf. App. A.3.1)

currently strongly discourages to employ this implementation for predictions of this process. The reasons for this are the channel dependent selection requirements at reconstruction level (cf. Sec 7.3), and the cross-section extraction employing separate fits to the different lepton channels. Hence, the PowhegBox implementation of the $W^{\pm}W^{\pm}jj$-EW4 process cannot be used for the description of the $W^{\pm}W^{\pm}jj$-EW4 process considered as a background to the electroweak production in this work. Moreover, a combined measurement of the cross-section of the strong and electroweak production modes, which is strongly recommended to be pursued with a consistent set of MC samples, is not possible with this setup.

The MadGraph5_aMC@NLO (short MG5_aMC@NLO) setup is used in Ref. [141, 199] for comparisons of different predictions of the $W^{\pm}W^{\pm}jj$-EW6 process at NLO QCD accuracy. It has not been tested for the $W^{\pm}W^{\pm}jj$-EW4 process yet. In addition, it is so far only used with resonant V approximation and does not include non-factorisable QCD corrections [141, 199].

The LO multi-jet merged setup within MG5_aMC@NLO has not been used for the description of any of the components of the $W^{\pm}W^{\pm}jj$ process yet. Though only LO accurate it has multiple advantages. This setup is in principle ready to use, including the handling of theoretical uncertainties. In addition, the predictions do not include any approximations and it can be interfaced to parton showers capable of providing adequate colour flow implementations for the $W^{\pm}W^{\pm}jj$-EW6 process. It is hence viewed as a good alternative to investigate besides next-to-leading order accurate setups.

Version 3.0 of the Sherpa event generation programme has only been released recently. It is expected to improve the prescription of the colour flow assignment in the parton shower for the $W^{\pm}W^{\pm}jj$-EW6 process. In view of the non-optimal settings of the colour flow treatment in the version 2.2.2 of the programme, future analyses should make an effort to thoroughly investigate the newer version. In principle, this setup is capable of providing automated NLO QCD accurate predictions. However, these have never been studied for the $W^{\pm}W^{\pm}jj$ process. This might be a further step in the investigation of the Sherpa setup.

Full NLO corrections to the full $W^{\pm}W^{\pm}jj$ process, including all orders, and implemented in the Sherpa MC programme are provided in Ref. [185]. Though not matched to parton showers yet, it is one further step in the direction of full NLO predictions for the full $W^{\pm}W^{\pm}jj$ process.

The Matchbox tool box has not been used in the context of the $W^{\pm}W^{\pm}jj$ process so far. It is considered an alternative to other NLO QCD accurate predictions once the programme is capable of providing on-the-fly weights for parton shower variations. It can be used with both common matching methods, the Powheg and the MC@NLO implementations. It has to be noted though, that Matchbox employs external matrix elements from VBFNLO and MG5_aMC@NLO, both of which use approximations in the NLO QCD corrections of the $W^{\pm}W^{\pm}jj$-EW6 process.

The PowhegBox framework has recently been extended to be used with the Recola matrix element providing NLO EW accurate predictions matched to both QCD and QED parton showers [201]. This effort pushes forward in the direction of full NLO predictions for the $W^{\pm}W^{\pm}jj$-EW6 process. Once scrutinised it can be combined with the established predictions at NLO QCD accuracy of this process from the PowhegBox programme in an additive manner outlined in Ref. [201]. This setup then can provide the first combined NLO corrections for the $W^{\pm}W^{\pm}jj$-EW6 process matched to parton showers.

Chapter 7

Overview of the Experimental Analyses

After having thoroughly discussed the modelling of the processes of interest at particle level, we turn to introducing all necessary ingredients for the statistical analyses at reconstruction level following in the next chapters of this thesis. These involve the first view on experimental data from proton-proton collisions recorded with the ATLAS detector at a centre-of-mass energy of 13 TeV in the Run 2 data-taking period of the LHC within this work. One candidate event exhibiting the key features of same-charge $W^{\pm}W^{\pm}$ scattering in the fully leptonic final state, as outlined in Sec. 5.3, is displayed in Fig. 7.1.

This chapter aims at focusing on the commonalities of both analyses conducted in this thesis. It begins with stating the measurement objectives and introducing the general analysis strategy pursued in these measurements. Accordingly, the next section briefly outlines the subsequent structure of this chapter.

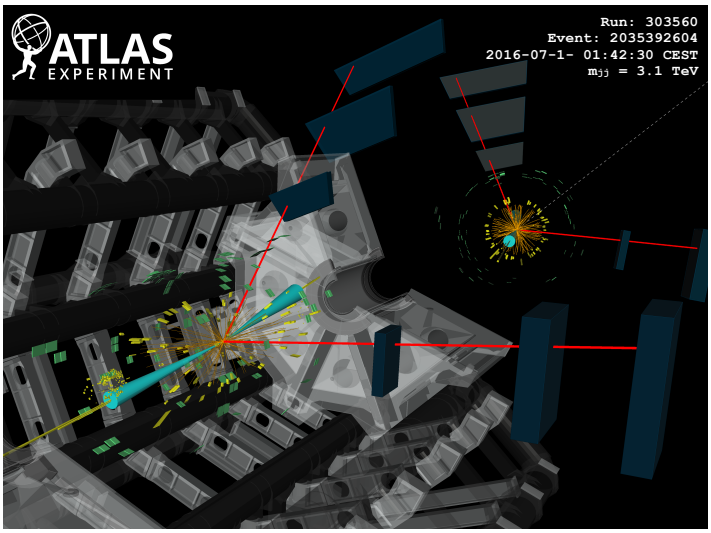


Figure 7.1: Display of an experimental event from proton-proton collisions at a centre-of-mass energy of 13 TeV recorded with the ATLAS detector in the Run 2 data-taking period of the LHC. The hard scattering interaction produce two energetic muons (red lines) traversing the inner detector and the muon spectrometer, two energetic hadronic jets (cyan cones) depositing energy in the calorimeters (yellow squares), and missing transverse momentum (dashed gray line in the azimuthal plane display). As such, it constitutes a candidate event of the process $pp \to W^{\pm}W^{\pm}jj \to \mu^{+}\nu_{\mu}\mu^{+}\nu_{\mu}jj$. The muons exhibit transverse momenta of 123 GeV and 120 GeV each. The hadronic jets have transverse momenta of 291 GeV and 118 GeV, and an invariant mass and rapidity separation of $m_{jj} = 3.1$ TeV and $\Delta Y_{jj} = 5.6$, respectively. Figure taken from Ref. [1].

7.1 Measurement Objectives and Analysis Strategies

The experimental analyses presented in this thesis have three main measurement objectives:

1. The observation of the $W^{\pm}W^{\pm}jj$-EW6 process as predicted by the Standard Model of Particle Physics;

2. The measurement of the fiducial cross-section of the SM $W^{\pm}W^{\pm}jj$-EW6 process and its comparison to theoretical predictions; and

3. The extraction of exclusion limits for various parameters of a BSM physics scenario based on an Effective Field Theory model employing dimension-8 operators [2, 3].

The first two goals are achieved in one analysis further referred to as the "SM analysis". It is presented in Chapter 8 and published in Ref. [1]. The latter objective is accomplished with a reinterpretation of the SM analysis in terms of the EFT model at hand. It is detailed in Chapter 9 and being prepared for publication by the time of writing of this work. The intention of this "EFT reinterpretation" analysis is to utilise ingredients of the SM analysis where possible and solely alter the signal definition and the statistical methodology. The commonalities of both analyses shall be collected and discussed in this chapter.

Before doing so, the overall strategy of the experimental analyses is outlined. The exact theoretical definition of the signal process, including possible decay channels, needs to be established. In the context of this work, this is especially delicate as outlined in Chapter 5. Once this is settled, the modelling of the signal process with the help of MC simulations (cf. Chapter 4) is designed, launched and thoroughly validated. In this process, the fiducial region for the cross-section measurement is defined and refined. This procedure is elaborated in Chapter 6. The conclusions from these studies on the definition of the signal process are summarised in Sec. 6.8.

According to the experimental and theoretical signatures of the signal process, suitable and tentative object and event selection criteria of the experimental data at reconstruction level are compiled. These are subject to refinements throughout the phase of the SM analysis conceptualisation. The final requirements for objects and events to pass the various selections employed in the analyses are summarised in Sections 7.3 and 7.4, respectively.

Further, contributions of background processes are evaluated, MC simulated and validated. For the estimation of background processes poorly modelled by simulations, stable and sufficiently accurate data-driven methods for their estimations need to be established. Possible background processes are summarised in Sec. 7.5. Estimation methods are discussed in App. D.2 and their modelling is validated in App. D.3.

Moreover, all signal and background estimates are complemented with estimates on their theoretical and experimental accuracy. All attainable sources of systematic uncertainties and their impacts are discussed in Sec. 7.6.

The interplay between the signal definition, possible background contributions, and their systematic uncertainties define and refine the object and signal region selection criteria, usually in an optimisation procedure iterating over the main steps of the analysis chain. This procedure is detailed in Ref. [219] and not further discussed in this thesis.

Finally, all ingredients are collected and inserted into the statistical analysis which is characterised by the statistical methodology chosen, the definition of the signal and control regions, the template observable(s), the treatment of systematic uncertainties, and naturally by the measurement objective. Hence, details on the statistical analysis are discussed in subsequent and separate chapters for the two analyses.

In the meantime, experimental data from the ATLAS experiment has been collected, preselected and cleaned for the experimental analyses. All necessary stages have been outlined in Chapter 3. While these data are used for validation purposes throughout many steps of the analyses, they must not be used for any optimisation procedure in the analysis and are only run through the full statistical framework once every detail of the respective analysis is settled. This prevents the analyses from experimental biases on the final result.

7.2 Data and Simulated Data Samples

Experimental Data

The experimental data analysed in this thesis are pp collisions recorded with the ATLAS experiment in the partial Run 2 data-taking period of the LHC, precisely the years 2015 and 2016, at a centre-of-mass energy $\sqrt{s}$ of 13 TeV. The total integrated luminosity of good data after cleaning amounts to $36.1\,\text{fb}^{-1}$. Details on the data-taking conditions and data preparation are presented in Sec. 3.3.

SM Signal Process – Simulated Data

For the different analysis goals in this thesis, the definition of the signal process varies.

The signal process of the SM analysis is defined to be the $W^{\pm}W^{\pm}jj$-EW6 process. The nominal theoretical prediction, which is used for all optimisation studies, uncertainty estimates, and the final fits for the discovery and cross-section measurement, is taken from the nominal Sherpa MC event simulation, labelled Sherpa23jLO, without any corrections, i. e. without NLO EW corrections or the interference between the $W^{\pm}W^{\pm}jj$-EW6 and $W^{\pm}W^{\pm}jj$-EW4 process. Its production within the official ATLAS MC production framework follows the procedure outlined in Chapter 4. At particle level, it is studied in detail in Chapter 6, together with the alternative prediction from PowhegBox + Pythia 8, labelled PB+Py8, which is used for reconstruction-level cross-checks only.

For the EFT reinterpretation analysis, the signal processes are defined as the effect of new operators introduced in the theoretical prescription of the $W^{\pm}W^{\pm}jj$-EW6 process. Hence, the contributions of the $W^{\pm}W^{\pm}jj$-EW6 process described by the SM are considered to be a background in this analysis. The choice of the prediction used for the SM contribution in the EFT reinterpretation analysis is the nominal MG5_aMC + Pythia 8 setup, MG5+Py8drec. Its choice is discussed in detail in the respective chapter. There, also the signal predictions including EFT effects are investigated extensively.

Background Processes – Simulated Data and Data-driven Methods

The modelling of background processes entering the regions of interest of the analyses is taken from MC simulation at reconstruction level as well as evaluated with data-driven methods.

The MC simulated samples are produced within the official ATLAS MC production framework in which they undergo the event generation, detector simulation, and preparation process as outlined in Chapter 4. Details on the samples used in the analyses, e. g. their perturbative order, matrix element configurations, production tags, cross-sections, filter efficiencies, and k-factors, are listed in App.App. D.2 C.

The data-driven techniques employed to estimate the background contributions arising from electron charge misidentification and non-prompt leptons are discussed in App. D.2.

7.3 Object Selections

Prior to the selections in the analyses presented here, objects are reconstructed, identified, and calibrated according to the procedures outlined in Sec. 3.4. Details on the object collections utilised in the analyses can also be found in the respective section, as well as the lepton isolation and missing transverse momentum determination, and specifics on the b-tagging algorithm for hadronic jets.

In the analyses, multiple sets of objects, precisely of charged leptons and jets, with different selection criteria are employed. They are used at different stages of the event selection, serving particular needs in the analyses. The following Tables 7.1, 7.2, and 7.3 show these stages of the object selection together with the precise selection criteria for electrons, muons and jets, respectively. Per construction, these stages are inclusive, implying tighter selections moving from left to right, i. e. moving from "`baseline`" to "`analysis`" objects.

The `baseline` selection of all objects refers to the least common selection of the different stages of the event selection, including the estimate of background sources. As such, `baseline`

Table 7.1: Summary of electron sets used in the analyses with their selection criteria. Details on the identification, including the "author" quantity, and isolation WPs can be found in Sec. 3.4.2.

Observable	Cut value	
	`Baseline/Veto`	`Analysis`
p_{T}	$> 6\,\mathrm{GeV}$	$> 27\,\mathrm{GeV}$
$\lvert\eta\rvert$	< 2.47	< 2.47 and not in $(1.37 < \lvert\eta\rvert < 1.52)$
Identification WP	`Loose+IBL`	`Tight`
$\lvert z_0 \times \sin\theta\rvert$	$< 0.5\,\mathrm{mm}$	✓
d_0/σ_{d_0}	< 5	✓
Isolation WP	–	`Gradient`
Author	–	$== 1$

Table 7.2: Summary of muon sets used in the analyses with their selection criteria. Details on the identification and isolation WP can be found in Sec. 3.4.2.

Observable	Cut value		
	`Baseline`	`Veto`	`Analysis`
p_{T}	$> 6\,\mathrm{GeV}$	✓	$> 27\,\mathrm{GeV}$
$\lvert\eta\rvert$	< 2.7	✓	< 2.5
Identification WP	`Loose`	✓	`Medium`
$\lvert z_0 \times \sin\theta\rvert$	$< 0.5\,\mathrm{mm}$	✓	✓
d_0/σ_{d_0}	< 10	< 3	✓
Isolation WP	–	–	`Gradient`

Table 7.3: Summary of jet sets used in the analyses with their selection criteria. Central and forward `analysis` jets are required to have different transverse momentum thresholds. Details on the pile-up rejection procedure via the jet vertex tagger (JVT) measure can be found in Sec. 3.4.3.

Observable	Cut value		
	`Baseline`	`Analysis`	
		Central	Forward
p_{T}	$> 20\,\mathrm{GeV}$	$> 25\,\mathrm{GeV}$	$> 30\,\mathrm{GeV}$
$\lvert\eta\rvert$	< 4.5	< 2.4	< 4.5
JVT	–	✓	–

objects are used for the removal of object overlaps as outlined in Sec. 3.4.5, the calculation of missing transverse energy E_T^{miss} as explained in Sec. 3.4.4, and the jet-based event cleaning procedure [231]. The selection in pseudorapidity is motivated by the detector geometry, i. e. the inner detector and muon chamber acceptances or the calorimeter coverage (cf. Sec. 3.2). Considerations on the detector resolution and pile-up characteristics affecting reconstruction efficiency uncertainties drive the transverse momentum requirements. `Baseline` charged leptons are identified to be at least of `Loose`(`+IBL`) quality. The additional requirement of a hit in the insertable b-layer (IBL) for electron reduces signatures from converted photons and charge misidentification (cf. Sec. 3.4.2). No isolation requirements are imposed on `baseline` leptons.

Objects used in the analyses shall originate from the primary vertex in the event in order to reduce pile-up effects. For both, electrons and muons, this is ensured by imposing selection requirements on $|z_0 \times \sin\theta|$ and d_0/σ_{d_0}. These are measures including the transverse and longitudinal impact parameters, d_0 and z_0, respectively. d_0 is defined as the shortest distance in the transverse plane between the beam line and the corresponding track. z_0 is defined as the distance in z direction between the location on the track used to assess d_0 and the primary vertex. θ is the polar angle of the ATLAS coordinate system and σ_{d_0} is the resolution of the transverse impact parameter. For central `analysis` jets, the jet vertex tagger (JVT) is used for this purpose. Its methodology and application is briefly explained in Sec. 3.4.3.

`Analysis` leptons are used in the signal region of the analyses. Tightened selection requirements are imposed in order to obtain a lepton sample with a high contribution of prompt leptons. They are required to have a transverse momentum larger than 27 GeV, a value slightly larger than the threshold of the lowest unprescaled single lepton triggers used in the analyses (cf. Sec. D.1.1) in order to reduce the impact of migration effects after offline reconstruction.

Only electrons with `Tight` quality are accepted in the `analysis` selection. Moreover, electrons that traverse the transition region of the barrel and end-cap electromagnetic calorimeters ($1.37 < |\eta| < 1.52$) are rejected in the signal region, due to the considerable resolution reduction in this region.

`Analysis` muons are required to stay within the acceptance of the inner tracking detector and have `Medium` quality. These requirements imply that only combined muons are accepted in the signal region of the analyses (cf. Sec. 3.4.2). Transverse vertex selection requirements are tightened for `analysis` muons.

Both, `analysis` electrons and muons, are required to be isolated from hadronic activity in the detector employing the `Gradient` WP, which includes calorimeter and track based isolation requirements. Thus, contributions from leptons, especially muons, from hadronic decays inside jets, as well as from jets misidentified as leptons, especially electrons, are reduced.

The `analysis` electron sample used in the signal region is cleaned from ambiguous contributions (cf. Sec. 3.4.2), reducing contributions from converted photons and hence charge misidentified electrons in the signal region cia the author requirement.

`Analysis` jets have pseudorapidity dependent transverse momentum thresholds. Forward jets are required to have larger transverse momentum in order to reduce the contribution from pile-up jets in the region where track information is not available and hence pile-up suppression is more complicated. A JVT requirement is only applied to central jets with $p_{\text{T}} < 60$ GeV (cf. Sec. 3.4.3).

All central `analysis` jets are considered for b-jet identification. As outlined in Sec. 3.4.3, the MV2c10 b-tagging algorithm is used in the analyses with its 85% efficiency WP.

The missing transverse momentum E_T^{miss} is calculated with the `METMaker` tool which is provided with the calibrated `baseline` leptons outlined above and jets without any requirements, following the procedure explained in Sec. 3.4.4. No other objects are fed to the tool for the calculation.

All relevant selection requirements are complemented with scale factor corrections to adjust the (in)efficiencies in the MC simulations compared to experimental data as outlined in Sec. 4.3.4.

7.4 Event Selection in the Signal Region

The signal region is designed and optimised [219] to efficiently select events with the typical properties of this process in the fully leptonic final state:

$$pp \to \ell'^{\pm}\nu_{\ell'}\ell^{\pm}\nu_{\ell}jj, \tag{7.1}$$

where[1] $\ell^{\pm} = e^{\pm}, \mu^{\pm}$ and as outlined in Sec. 5.3. In addition, the event selection shall reduce the contributions from possible background processes and hence increase the signal-to-background ratio.

The selection requirements for events to enter the analyses' signal region are summarised in Tab. 7.4. Experimental data events are preselected with the data quality assessment tools summarised in Sec. 3.3.2, employing the final good runs list (GRL) and event-by-event error flags, whose exact names are detailed in Sec. 3.3.2 and App. D.1.1, respectively. Both, experimental and simulated data events have to fire at least one of the single lepton triggers detailed in App. D.1.1. Trigger selection efficiencies are corrected in simulated events as outlined in Sec. 4.3.4. At least one primary vertex has to be found in the event with properties outlined in Sec. 3.4.1. Events are vetoed if a bad jet is found with the jet-based event cleaning procedure, excluding jets originating from pile-up, outlined in Ref. [231].

Events with exactly two `analysis` leptons ($e^{\pm}$ or $\mu^{\pm}$) with identical electric charges are selected. One of these two leptons must have activated one of the single-lepton triggers considered for the analyses. Both leptons and their electrical charges must be matched to a particle-level truth lepton in MC simulated events, as explained in Sec. 4.3.3, in order to prevent double-counting when data-driven background estimates are included.

In order to lessen background contributions from processes with multiple leptons, such as fully leptonic $W^{\pm}Z$ and ZZ final states, a veto on additional leptons with `veto` lepton object requirements is placed in the signal region.

The invariant mass of the two `analysis` leptons m_{ll} is required to exceed 20 GeV such that Drell-Yan processes with low invariant masses are suppressed. In addition, the $e^{\pm}e^{\pm}$ channel selection features a resonant Z veto via a window cut on m_{ee} of 15 GeV around the mass of the Z boson and requires both electrons to lie within the barrel region ($|\eta_e| < 1.37$).

In order to account for the two neutrinos occuring in the fully leptonic final state, the missing transverse momentum is required to be above 30 GeV.

As a result of the selection optimisation procedure, detailed in Ref. [219], the leading and subleading jets in transverse momentum are required to have transverse momentum larger than 65 GeV and 35 GeV, respectively. These two jets are referred to as the tagging jets to reflect the special nature of the VBS signal process.

Events where at least one `analysis` jet is identified as a b-jet are rejected in order to decrease contributions for top quark processes.

Finally, in order to enhance the $W^{\pm}W^{\pm}jj$-EW6 process, with its VBS contribution, over the $W^{\pm}W^{\pm}jj$-EW4 process, only those events are selected that feature an invariant mass m_{jj} and rapidity separation ΔY_{jj} of the tagging jets to be above 500 GeV and > 2.0, respectively. These selection criteria reflect the findings on the properties of the contributions of the $W^{\pm}W^{\pm}jj$ process at LO in Sec. 6.6.1.

7.5 Background Processes

The signal process of interest, defined in Eq. (6.1), exhibits exactly two same-charge leptons, neutrinos, and jets in the final state. Background processes that enter the signal region, defined in Tab. 7.4, hence are expected to produce two same-charge leptons in association with multiple jets and missing transverse momentum. Besides the $W^{\pm}W^{\pm}jj$-EW6 signal process,

[1] Final states with τ leptons are not considered in the experimental analyses, as these decay within the dimension of the ATLAS detector. Events with τ leptons in the final state can nevertheless enter the measurement selections when the τ lepton decays leptonically. The selection efficiency, however, is much reduced as the resulting electrons and muons have to share the available energy-momentum with their decay products (neutrinos) in the τ lepton decay. In the following, hence, the term "leptons" refers to electrons and muons unless explicitly stated otherwise.

Table 7.4: Definition of the selection requirements for events to enter the signal region, i. e. the nominal analysis phase space, with intermediate stages as used in Ref. [1] and for different sets of studies in this thesis. The full list of selection criteria is used for the final measurement objectives outlined in Sec. 7.1.

Observable	Cut value	Explanation
Event preselection:		
GRL	✓	Data cleaning (cf. Sec. 3.3.2)
Error flags	✓	Data cleaning (cf. Sec. 3.3.2 and App. D.1.1)
Trigger	✓	Event fired at least one single lepton trigger (cf. App. D.1.1)
$N(\text{pv})$	> 0	Minimum number of primary vertices
Jet cleaning	✓	Veto if bad jets are found (excluding pile-up jets)
Lepton event selection:		
$N(\ell_{\text{ana}})$	$== 2$	Number of charged leptons ($e^{\pm}$ or $\mu^{\pm}$) with `analysis` selection
Region referred to as: *Loose region*		
$q(\ell_1) \times q(\ell_2)$	> 0	Same electrical charge for two leading charged leptons
$N(\ell_{\text{veto}})$	$== 0$	Veto if additional leptons ($e^{\pm}$ or $\mu^{\pm}$) with `veto` selection requirements exist
Trigger match	$\ell_1 \,\|\|\, \ell_2$	At least one `analysis` lepton fired the event trigger
m_{ll}	$> 20\,\text{GeV}$	Minimum invariant mass of the lepton pair
$\lvert m_{ee} - m_Z \rvert$	$> 15\,\text{GeV}$	Veto on resonant Z boson production ($e^{\pm}e^{\pm}$ channel only)
$\lvert\eta_e\rvert$	< 1.37	Pseudorapidity restriction for electrons ($e^{\pm}e^{\pm}$ channel only)
E_T^{miss}	$> 30\,\text{GeV}$	Minimum missing transverse energy
Jet event selection:		
$N(j)$	≥ 2	Minimum number of `analysis` jets
$p_{\text{T}}(j_1)$	$> 65\,\text{GeV}$	Minimum p_{T} of leading jet
$p_{\text{T}}(j_2)$	$> 35\,\text{GeV}$	Minimum p_{T} of subleading jet
$N(\text{b-jet})$	$== 0$	Veto if any `analysis` jet is identified as b-jet
Region referred to as: *Inclusive region*		
VBS selection:		
ΔY_{jj}	> 2.0	Minimum rapidity separation between leading jet pair
m_{jj}	$> 500\,\text{GeV}$	Minimum invariant mass of leading jet pair

the SM predicts only few processes with exactly two same-charge leptons, the most prominent one being the QCD-induced production of two same-charge $W^{\pm}$ bosons, $W^{\pm}W^{\pm}jj$-EW4, studied together with the signal process in Chapter 6. Therefore, the major background contributions emerge from the limited detector acceptance or finite resolution to properly reconstruct and identify certain types of objects, especially leptons. The overall contributions can be divided into three categories:

- SM processes producing two (or more) prompt leptons, two of which have the same electrical charge;
- SM processes producing opposite charge leptons, where one of the leptons' charge is wrongly reconstructed, eventually forming a same-charge pair;
- SM processes producing non-prompt leptons originating from jets or photons.

Besides the $W^{\pm}W^{\pm}jj$-EW4 process, the first category involves processes where one or more prompt leptons fall outside the detector acceptance or fail the `analysis` lepton requirements, resulting in the selection of a same-charge lepton pair. These are predominantly fully leptonic $W^{\pm}Z$ production in association with jets. Further, less frequently, contribute fully leptonic ZZ +jets, $t\bar{t}V$, and triple boson (VVV, $V \in \{W^{\pm}, Z\}$) production. A veto on additional leptons with looser selection requirements (`veto` leptons) helps in reducing this class of background processes. Their modelling is estimated from MC simulation. Detailed modelling information are summarised in App. C. The $W^{\pm}Z$ process yields the largest source of background events. Hence, in the SM analysis, its normalisation is further constrained in the final fitting procedure using a dedicated control region, discussed in Sec. 8.4.1.

The second category mainly comprises fully leptonic $W^{+}W^{-}$ or Z/γ production in association with jets, or $t\bar{t}$ production with leptonic decays, where the charge of one of the electrons is wrongly identified. The veto in the dilepton invariant mass around the Z boson mass and the restrictions in pseudorapidity[2] of electrons in the $e^{\pm}e^{\pm}$ channels reduce the background contributions from the overwhelmingly large rate of Z and γ^{*} boson production. Furthermore, the b-jet veto, affecting the $t\bar{t}$ event yield, lessens these backgrounds' contributions. Background contributions from electron charge misidentification are estimated from a data-driven method explained in detail in App. D.2.1 based on Ref. [219].

Background processes producing non-prompt leptons originating from jets are mainly leptonic $W^{\pm}$+jets or semi-leptonic $t\bar{t}$ production with small contributions from single top and QCD multijet processes. Stringent requirements on the lepton isolation and vertex association, as well as the b-jet veto and the minimum missing transverse momentum requirement reduce these background contributions. The remaining yields are estimated with a data-driven method explained in detail in App. D.2.2 based on Ref. [232, 233].

Background processes with photons identified as leptons mainly comprise $W^{\pm}\gamma$ production. Its normalisation in the signal region is adjusted from experimental data to MC simulation comparisons in a dedicated region, summarised in App. D.2.3 based on Ref. [220].

The modelling of all relevant background processes is validated in dedicated regions, collectively called validation regions (VRs). While this step of the analysis is not directly involved in obtaining the final measurement result, it is crucial for helping to understand the background predictions from the methods described above.

In total seven VRs are investigated. Some validation regions are defined such that one or very few background contributions are isolated to better study their predictions while still being connected to the definition of the signal region (e. g. by inverting signal region requirements). Other validation regions are employed to understand the overall background composition in regions very close to the signal region. The contribution from the signal process is negligible in most of the validation regions. The agreement between experimental data and the background estimates is generally good. A detailed summary of all background validation regions, including selection requirements and example kinematic distributions, is given in App. D.3.

[2]It is shown in Ref. [102] Fig. 13, that the wrong charge assignment to electrons is significantly enhanced in the end-cap region with pseudorapidity $1.5 < |\eta| < 2.5$ compared to the central barrel region.

Table 7.5: Estimated event yields and statistical uncertainties of all relevant background processes in the combined $\ell^{\pm}\ell^{\pm}$ channel in the signal region before the statistical analyses.

Process	Event yield $\ell^{\pm}\ell^{\pm}$ channel
$W^{\pm}Z$	35.06 ± 0.79
$W^{\pm}W^{\pm}jj$-EW4	7.34 ± 0.09
Other prompt	2.36 ± 0.13
- $t\bar{t}V$	1.04 ± 0.09
- ZZ	0.98 ± 0.07
- VVV	0.33 ± 0.05
Non-prompt	23.32 ± 4.23
Charge misID	8.93 ± 0.42
$V\gamma$	4.47 ± 0.84
- $W^{\pm}\gamma$	4.35 ± 1.48
- $Z\gamma$	0.12 ± 0.07
Total	81.48 ± 4.41

7.5.1 Final Background Estimates in the Signal Region

The final event yields and their statistical uncertainties of all relevant background processes in the signal region in the combined $\ell^{\pm}\ell^{\pm}$ channel are summarised in Tab. 7.14. The largest background contributions come from $W^{\pm}Z$ production followed by processes exhibiting non-prompt leptons. The event yield of the $W^{\pm}Z$ process is the summed contribution of the electroweak-induced $WZjj$-EW6 and the QCD-induced $W^{\pm}Z$-EW4 processes. The latter is dominant with a fraction of 85% with respect to the sum in the signal region. In the following, the notation "$W^{\pm}Z$" refers to the sum of the two contributions, while the specific process labels are used when referring to one of the two.

Consistent with the findings in Sec. 6.6.1, the QCD-induced same-charge $W^{\pm}W^{\pm}$ process, $W^{\pm}W^{\pm}jj$-EW4, yields a sizable background contribution in the signal region. Other prompt contributions, such as $t\bar{t}V$, ZZ, and triboson production have a small impact. In the following, these processes are grouped together under the label "other prompt" contributions. Equivalently, the diboson processes with photons in the final state are grouped together as "$V\gamma$" contribution.

7.6 Systematic Uncertainties

Various sources of systematic uncertainties are considered for all event yield estimates in all regions and observables utilised for results of the final measurements. This sections aims at collecting all information on all sources of systematic uncertainties used throughout this thesis. They are categorised into:

- Experimental uncertainties:
  - Uncertainties affecting the reconstruction, identification, and selection of physics objects and whole events; and
  - Uncertainties obtained from the data-driven background estimation methods; and
- Theoretical uncertainties on the modelling of MC-simulated predictions.

Moreover in this section, a summary of the impact of all (sub)categories of uncertainties is given for all SM processes in the signal region. Particularities of the treatment of systematic

uncertainties in each of the two statistical analyses used to extract the measurement goals, the cross-section measurement of the SM $W^{\pm}W^{\pm}jj$-EW6 process and the reinterpretation in terms of EFTs, are discussed in Sections 8.5 and 9.4, respectively.

The statistical analysis of both measurement goals is based on fits to differential distributions in various different regions. Hence, systematic uncertainties can not only have an effect on the overall normalisation of a given event yield in a given region. In addition, they can also cause shape differences in the observables employed for the final fit. Most sources of systematic uncertainties include both, normalisation and shape effects. However, a few sources are constructed as normalisation uncertainties only. In addition, some uncertainties are treated differently in the one or the other analysis. This is detailed later in the respective chapters.

7.6.1 Experimental Uncertainties

ATLAS Object and Event Uncertainties

For predictions taken from MC simulations, uncertainties on the properties of all physics objects used in the analyses have to be accounted for. These comprise standard object and event uncertainties common to all ATLAS analyses. They are conceptualised and derived within the procedures for the analysis preparation of each object type outlined in Sec. 3.4. As such they result from variations of the specific measurements used to derive the properties of each object. They are provided centrally within the ATLAS combined performance efforts and need to be propagated to all relevant measurement observables and results of the analyses. In the analyses subject to this thesis, uncertainty sources comprise:

- The energy/momentum calibration (scale and resolution) of all objects (electrons, muons, jets, and missing transverse momentum);
- The efficiency of the reconstruction, identification, isolation and other relevant selection criteria of each object type; and
- The trigger efficiency for electrons and muons.

In addition, uncertainties on the luminosity measurement, outlined in Sec. 3.3.3, and the pileup reweighting procedure, outline in Sec. 4.3.2, must be included on all simulated predictions. The relative uncertainty on the integrated luminosity amounts to 2.1%.

In total a set of 93 experimental object and event uncertainties are considered in the analyses. These are collected in categories for each object type in Tab. 7.6. A list of all experimental object uncertainties with full labels and short explanations can be found in Tab. D.12 in the appendix.

The sensitivity and impact of the uncertainties on leptons are expected and confirmed later to be minor in the analyses at hand. Hence, uncertainty models with variations combined into simplified sets are chosen in almost all lepton categories. These sets contain only one or at most few uncorrelated variations. The consequence is more conservative error estimates while drastically reducing the computational effort. An exception constitutes the model picked for the electron identification efficiencies. Here, a parametrisation with intermediate level of accuracy containing 15 correlated and 16 uncorrelated variations is chosen.

As outlined in Sec. 3.4.2, the energy calibration of electrons is derived with Run 1 experimental data and methods. In order to account for changes between the detector and pileup conditions between Run 1 and Run 2, additional sources of systematic uncertainties are added to the nominal energy scale uncertainty obtained from the Run 1 measurement method. This results in a total of 5 variations considered in this category.

For muons, the transverse momentum resolution uncertainty is measured independently in the inner detector and the muon spectrometer, yielding two separate variations. Moreover, most of the efficiency measurements are provided with individually combined variations for statistical and systematic uncertainty sources. Additionally, the reconstruction and identification efficiency uncertainties are provided individually for low- and high-p_{T} muons.

Table 7.6: Summary of experimental uncertainties for all objects relevant to the analyses, as well as for the entire event prescription. These uncertainties are conceptualised and derived within the object and event preparation procedures outlined in Sections 3.4, and 3.3 and 4.3.2, respectively. They are provided centrally within the ATLAS combined performance efforts. For each object type and category, the prefix of the label used in the statistical analyses (as occurring in figures and result tables), and the number of variations N_{var} within one category are listed. A list of all 93 experimental variations with full labels and short explanations can be found in Tab. D.12 in the appendix.

Category	Label prefix	N_{var}
Electrons:		40
Energy scale	`EG_SCALE`	5
Energy resolution	`EG_RESOLUTION`	1
Reconstruction efficiency	`EL_EFF_Reco`	1
Identification efficiency	`EL_EFF_ID`	31
Isolation efficiency	`EL_EFF_Iso`	1
Trigger efficiency	`EL_EFF_Trigger`	1
Muons:		12
Momentum scale	`MUON_SCALE`	1
Momentum resolution	`MUON_ID`, `MUON_MS`	2
Reconstruction & identification efficiency	`MUON_EFF`	4
Track-to-vertex association efficiency	`MUON_TTVA`	2
Isolation efficiency	`MUON_ISO`	2
Trigger efficiency	`MUON_EFF_Trig`	1
Jets:		36
Energy scale (JES)	`JET`	21
Energy resolution (JER)	`JET_JER`	1
JVT efficiency	`JET_JvtEfficiency`	1
b-tag inefficiency	`FT_EFF`	13
E_T^{miss}:		3
Soft tracks energy scale	`MET_SoftTrk_Scale`	1
Soft tracks energy resolution	`MET_SoftTrk_Reso`	2
Event:		2
Pile-up reweighting data SF	`PRW_DATASF`	1
Luminosity	`lumi`	1

Table 7.7: Relative impact of experimental systematic uncertainties on the event yields of all predictions based on MC simulation in the combined $\ell^\pm\ell^\pm$ channel in the signal region condensed into six categories. Lepton uncertainties comprise all variations in the measurement of electrons and muons, except the trigger efficiency which is quoted as separate value. Jet uncertainties comprise all variations in the measurement of jets, except the variations of the flavour tagging which are quoted as b-tag inefficiency uncertainties. "Other prompt" comprises MC-based predictions of the processes of $t\bar{t}V$, ZZ, and triboson production. Numbers are shown for both $W^\pm W^\pm jj$-EW6 predictions, the Sherpa23jLO setup, employed in the SM analysis and the MG5+Py8drec setup, employed in the EFT reinterpretation analysis. Independent uncertainty sources are added in quadrature for each category. Detailed numbers for all channels and processes can be found in Tab. D.13 in the appendix.

Process	Systematic Uncertainty [%]					
	Leptons	Trig. eff.	Jets	b-tag ineff.	Pile-up rwt.	E_T^{miss}
$W^\pm Z$	2	< 1	6	2	3	1
$W^\pm W^\pm jj$-EW4	1	< 1	3	2	1	1
Other prompt	3	< 1	16	7	8	3
$V\gamma$	1	< 1	31	3	12	< 1
$W^\pm W^\pm jj$-EW6 (Sherpa23jLO)	1	< 1	2	2	1	< 1
$W^\pm W^\pm jj$-EW6 (MG5+Py8drec)	16	3	16	44	10	5

Uncertainties related to jets are among the leading uncertainties in the analyses. Hence a statistical model with intermediate accuracy yielding 21 parameters is used for the uncertainty estimate due to the jet energy scale measurement. This includes 8 eigenvector variations from the in-situ calibration analyses, and 4 variations due to each individual term in the pileup subtraction procedure (cf. Sec. 3.4.3). In addition, effects such as flavour and p_{T} dependence on the energy scale are considered.

The jet energy resolution variation is provided one-sided by the combined performance analysis. It is symmetrised in the statistical analyses in order to stabilise the result.

Uncertainties due to jet flavour tagging must be considered in the analyses due to the b-jet veto requirement in the signal region. These comprise 5 independent variations for light quark flavours and 3 each for c- and b quarks. Two more variations come from extrapolation effects.

Three variations are considered for the systematic uncertainty on the missing transverse momentum calculation which provide uncertainties due to the track based soft term description. Uncertainties from the hard objects used in the E_T^{miss} calculation are also propagated through the E_T^{miss} calculation.

The relative impact of these uncertainties on the event yields of all processes with MC-based predictions in the signal region are summarised in Tab. 7.7. A list of all detailed values in all lepton charge- and flavour-split channels for all processes can be found in Tab. D.13 in the appendix. An exception is the MG5+Py8drec prediction of the signal process, for which uncertainties are solely evaluated in the combined $\ell^\pm\ell^\pm$ channel.

It can be noted that the uncertainties for the MG5+Py8drec prediction of the signal process are considerably larger than for the other processes. The reason for this lies in the statistical limitation of this sample at reconstruction level[3] which especially affects the evaluation of systematic uncertainties. The statistical uncertainty in the $\ell^\pm\ell^\pm$ channel is at 2%. Differences of very few events per variation cause sizable fluctuations in the predictions. As a consequence, the total size of the uncertainty depends on the number of considered independent sources added together in quadrature. Comparing with Tab. 7.6, this in particular

[3]Since this samples has been produced privately, resources have been limited.

Table 7.8: Summary of experimental uncertainties from background estimation procedures used in the analyses. These uncertainties are conceptualised and derived within the the respective estimation methods outlined in Appendices D.2.1 to D.2.3. For each background process and category, the prefix of the label used in the statistical analyses (as occurring in figures and result tables), and the number of variations N_{var} within one category are listed.

Category	Label (prefix)	N_{var}	Comment
Electron charge misidentification:		2	Details in App. D.2.1
Charge ID SF	`CF_SFunc`	1	
Energy correction	`CF_NoCorr`	1	One-sided, symmetrised
Non-prompt leptons (jets):		4	Details in App. D.2.2
f_e stat. & syst.	`FakeEl`	2	
f_μ stat. & syst.	`FakeMu`	2	
Non-prompt leptons (photon conversion):		1	Details in App. D.2.3
Normalisation	`Conv_Model_Vgamma`	1	One-sided, symmetrised, normalisation only

affects the uncertainties on the measurement of electrons, muons, and jets, including the measurement of the b-tag inefficiency. Hence, the following discussion does only partly apply on this prediction.

Variations in the measurements of jets compose the largest source of systematic object uncertainties. For the dominant background process $W^{\pm}Z$, they reach almost 10% in the $e^{\pm}e^{\pm}$ channels. For the other prompt and $V\gamma$ processes these variations cause large uncertainties, also due to statistically limited samples in the respective channels. However, the event yield of these processes in the signal region is small compared to the $W^{\pm}W^{\pm}jj$-EW6 and $W^{\pm}Z$ processes. Among the subleading uncertainty sources are the pile-up reweighting and flavour tagging efficiency variations. Especially the latter is large for processes involving top quarks. Uncertainties due to the measurement of leptons and the missing transverse momentum are minor, as expected. Uncertainties on the Sherpa23jLO prediction of the $W^{\pm}W^{\pm}jj$-EW6 signal process are generally mild and within (1 to 2)% in all channels and categories.

Uncertainties from Background Estimation Procedures

The procedures for the estimate of backgrounds due to electron charge misidentification, non-prompt leptons, and photon conversion are outlined in Appendices D.2.1 to D.2.3, together with the discussion of the variations used to derive systematic uncertainties. The technical details of these variations, as used in the statistical analyses, are listed in Tab. 7.8. Most of the variations have a large impact on the respective event yields and the measurement observables of the analyses. Their impacts on the event yields of the background estimates in the signal region are summarised in this section.

Electron Charge Misidentification Two main sources of systematic uncertainties are considered for the estimate of the background due to the electron charge misidentification:

- Systematic and statistical uncertainties from the scale factor measurement of the charge (mis)identification probabilities; and
- Switching on/off the electron transverse momentum correction of the electron subject to charge misidentification.

The first includes systematic variations of the event selection in the SF measurement, in particular the size of the Z boson mass window, and the trigger matching to either one or both

Table 7.9: Estimated event yields of the background due to electron charge misidentification (cf. App. D.2.1) in all relevant channels in the signal region (cf. Tab. 7.4) together with the statistical uncertainties on the event selection in the opposite charge region as well as systematic uncertainties split into their sources. The $\ell^\pm\ell^\pm$ channel is the sum of all above channels, excluding the $\mu^\pm\mu^\pm$ channels, where the contribution of this background is zero. Numbers taken from Ref. [219].

Channel	Nominal yields	Statistical uncertainty	Systematic uncertainty	
			Charge ID SF	Energy corr.
e^+e^+	1.33	±0.08	$^{+0.13}_{-0.10}$	±0.05
e^-e^-	1.17	±0.08	$^{+0.10}_{-0.10}$	±0.03
$e^+\mu^+ + \mu^+e^+$	3.48	±0.42	$^{+0.11}_{+0.01}$	±0.21
$e^-\mu^- + \mu^-e^-$	2.95	±0.36	$^{+0.09}_{-0.06}$	±0.19
$\ell^\pm\ell^\pm$	8.93	±0.42	$^{+0.41}_{-0.26}$	±0.47

electrons, as well as methodological variations, i. e. switching on/off the background subtraction, and retrieving the probabilities utilising the truth information in simulated events. Together with the statistical uncertainties, this totals to five sources of charge (mis)identification scale factor uncertainties which are propagated through the final background estimation procedure. The variations of the background estimate are then added in quadrature to form the final uncertainty from the scale factor measurement, labelled "Charge ID SF".

The variation due to the energy correction of the electron subject to charge misidentification is derived one-sided and symmetrised later in the statistical analyses.

The final estimated event yields for the background contribution due to electron charge misidentification together with the two sources of systematic uncertainties in the signal region for all relevant channels are shown in Tab. 7.9. Both systematic uncertainty sources yield variations comparable in size, ranging from 2% to 9% between channels. As the explanations of this background estimate, these numbers are taken from Ref. [219].

Non-prompt Leptons from Hadron Decays or Misidentified Jets The sources of systematic uncertainties considered for the fake factor measurement are detailed in Ref. [233] and shall only briefly be reviewed here. They include:

- Individual variations of the selection requirements of the dijet region;
- Variation of the prompt lepton contamination subtraction from MC simulation derived from the discrepancy between experimental and MC simulated data in a dedicated control region;
- Variation due to the removal of the b-tag requirement on the tag jet accounts for the uncertainty due to different jet flavour composition in the dijet and the signal region;
- Variation due to the application of the reweighting of the tag jet transverse momentum to account for the difference between the tag jet and underlying jet (i. e. the non-prompt lepton candidate) p_T spectrum.

The resulting overall systematic uncertainty on the fake factor measurement is taken as the envelope of all these variations, which is then propagated to the final background estimate calculation.

The final estimates for the background contribution due to non-prompt leptons from hadron decays or misidendified jets, together with the propagated systematic uncertainties on the fake factor measurements for electrons and muons in the signal region for all relevant channels, are shown in Tab. 7.10. Systematic uncertainties from the fake factor measurement for both electrons and muons vary substantially between channels. They generally have a

Table 7.10: Estimated event yields of the background due to non-prompt leptons (cf. App. D.2.2) in all relevant channels in the signal region (cf. Tab. 7.4) together with the statistical uncertainties on the event selection in the `ana+anti-ana` region as well as systematic uncertainties from the fake factor measurement split into statistical (stat.) and systematic (syst.) sources for electrons f_e and muons f_μ. The $\ell^\pm\ell^\pm$ channel is the sum of all channels. Numbers taken from Ref. [232].

Channel	Nominal yields	Statistical uncertainty	Systematic uncertainty			
			f_e		f_μ	
			Stat.	Syst.	Stat.	Syst.
e^+e^+	4.08	±1.77	±0.61	$^{+0.63}_{-2.12}$	–	–
e^-e^-	2.31	±1.47	±0.34	$^{+0.40}_{-1.23}$	–	–
$e^+\mu^+ + \mu^+e^+$	9.35	±2.62	±0.95	$^{+0.45}_{-4.14}$	±0.45	$^{+5.78}_{-0.69}$
$e^-\mu^- + \mu^-e^-$	6.34	±2.38	±0.73	$^{+0.74}_{-2.17}$	±0.32	$^{+4.27}_{-0.46}$
$\mu^+\mu^+$	0.57	±0.14	–	–	±0.05	$^{-0.05}_{-0.01}$
$\mu^-\mu^-$	0.67	±0.17	–	–	±0.11	$^{+0.20}_{-0.10}$
$\ell^\pm\ell^\pm$	23.32	±4.23	±2.62	$^{+2.52}_{-9.67}$	±0.93	$^{+10.20}_{-1.25}$

larger impact than the statistical uncertainties from the fake factor measurement with variations of more than $50-70\%$ in some channels. The largest sources of systematic uncertainties in most of the measurement bins for both electron and muon fake factors come from the jet p_T reweighting and the removal of the b-tag requirement on the tag jet. The largest impact is seen for fake factors of large transverse momentum leptons. Exact numbers of the systematic uncertainties on the fake factor measurements can be retrieved from Tab. D.5, D.6, and D.7 in the appendix. As the explanations of this background estimate, these are taken from Ref. [232].

Non-prompt Electrons from Photon Conversions The full effect of the normalisation correction obtained from data in the $Z\gamma$ region is taken as a systematic uncertainty on the modelling of the combined $Z\gamma$ and $W^\pm\gamma$ background contributions. Its relative value amounts to 44% and is symmetrised in the statistical analyses. This uncertainty source solely affects the normalisation of the event yield, without changing the shape of any kinematic observable of the $V\gamma$ predictions.

7.6.2 Modelling Uncertainties

For MC-modelled processes with major contributions in the signal region, detailed modelling uncertainties are incorporated in the statistical analyses in order to account for uncertainties due to the limitations of the theoretical predictions of these processes. These are derived for the following predictions:

- The Sherpa23jLO prediction of the SM $W^\pm W^\pm jj$-EW6 signal process;
- The Sherpa23jLO prediction of the $W^\pm W^\pm jj$-EW4 background process; and
- The combined prediction of the $W^\pm Z$ process, comprising the processes of $WZjj$-EW6 and $W^\pm Z$-EW4, both modelled with Sherpa version 2.2.2, but different accuracy in QCD couplings (cf. Tab. C.2 in the appendix).

The common strategies to evaluate modelling uncertainties due to the usual variations are detailed in Sec. 6.5 with focus on the $W^\pm W^\pm jj$ processes. A comprehensive summary of results in the fiducial region at particle level for the two processes $W^\pm W^\pm jj$-EW6 and

Table 7.11: Summary of modelling uncertainties for all MC-based signal and background predictions. For each process and category, the prefix of the label used in the statistical analyses (as occurring in figures and result tables), and the number of variations N_{var} are listed.

Process & category	Label	N_{var}	Comment
$W^{\pm}W^{\pm}jj$-EW6:		6	
Ren. & fact. scales	`signal_EW6_TheoScale`	1	
PDF set	`signal_EW6_TheoPDF`	1	
Strong coupling α_S	`signal_EW6_TheoAlphas`	1	
Parton shower	`signal_EW6_TheoShower`	1	
EW6-EW4 interference	`TheoInterference`	1	One-sided, symmetrised
NLO EW corrections	`signal_EW6_TheoEWCorr`	1	
$W^{\pm}W^{\pm}jj$-EW4:		4	
Ren. & fact. scales	`signal_EW4_TheoScale`	1	
PDF set	`signal_EW4_TheoPDF`	1	
Strong coupling α_S	`signal_EW4_TheoAlphas`	1	
Parton shower	`signal_EW4_TheoShower`	1	
$W^{\pm}Z$:		4	
Ren. & fact. scales	`WZ_TheoScale`	1	
PDF set	`WZ_TheoPDF`	1	
Strong coupling α_S	`WZ_TheoAlphas`	1	
Parton shower	`WZ_TheoShower`	1	One-sided, symmetrised
Other prompt backgrounds: (all normalisation only)			
$t\bar{t}V$ cross-section	`top_XS`	1	
ZZ cross-section	`ZZ_XS`	1	
VVV cross-section	`triboson_XS`	1	
Non-prompt leptons from photon conversion: (all normalisation only)			
$W^{\pm}\gamma$ cross-section	`Wgamma_XS`	1	
$Z\gamma$ cross-section	`Zgamma_XS`	1	

$W^{\pm}W^{\pm}jj$-EW4 is given in Sec. B.4 in the appendix. The strategies employed at particle level can in equal manner be applied at reconstruction level, as well as for the $W^{\pm}Z$ processes. In summary, they comprise variations of the renormalisation and factorisation scales, the PDF set and its value of the strong coupling α_S, and parton shower and merging parameters or algorithms, as specifically provided for each prediction.

For processes with subdominant contributions in the signal region solely uncertainties on the overall cross-section from the MC generation, i. e. only affecting the normalisation, are considered. These affect the processes of $t\bar{t}V$, ZZ, VVV, and $V\gamma$ production.

All sources of modelling uncertainties considered for each process are listed in Tab. 7.11, together with their label used in the statistical analyses and the number of variations for each sample.

For the signal process, two additional sources of uncertainties reflecting the theoretical knowledge of the process are added. In Sec. 6.6.1, the contribution of the interference between the $W^{\pm}W^{\pm}jj$-EW6 and $W^{\pm}W^{\pm}jj$-EW4 processes is evaluated to 9% compared to the electroweak $W^{\pm}W^{\pm}jj$-EW6 contribution in the inclusive region. This non-negligible effect, is added as a relative systematic uncertainty on the nominal Sherpa23jLO signal prediction. It is mirrored around the nominal prediction, thus, providing a conservative, symmetrised

systematic uncertainty.

Further, discussed in Sec. 6.1, NLO EW corrections to the $W^{\pm}W^{\pm}jj$-EW6 process, at order $\mathcal{O}(\alpha_{EW}^{7})$, are the leading NLO corrections to this process. The nominal signal prediction Sherpa23jLO does not incorporate these corrections. The impact in the fiducial region of the analyses is shown in Sec. 6.7.5 together with a discussion on the consistency of applying these corrections to the nominal Sherpa23jLO signal prediction at reconstruction level. The exact implementation is discussed in the SM-specific analysis chapter, as it is only considered therein.

The uncertainties due to the modelling of the parton shower and subsequent phenomena (cf. Sec. 4.2.4) for the QCD-induced $W^{\pm}Z$-EW4 process are evaluated as the difference between the Powheg prediction interfaced to either Pythia 8 or Herwig++, following the concept of Eq. (6.8). Technical details on these samples are listed in Tab. C.3 in the appendix. Variations of the parton shower algorithm on the electroweak-induced $WZjj$-EW6 process are not available at reconstruction level. Hence, the relative difference between the predictions with the two alternative generators for the $W^{\pm}Z$-EW4 process is applied as uncertainty to the sum of the nominal Sherpa predictions of the $W^{\pm}Z$-EW4 and $WZjj$-EW6 processes and symmetrised for the statistical analyses. The effect of this approximate estimate is considered to be small, due to the minor contribution of the $WZjj$-EW6 process of 15% with respect to the sum in the signal region.

Viewing the theoretical prescriptions of the SM, all modelling variations are not expected to be dependent on the flavour of the final state leptons. This includes the electroweak corrections as well as the interference contribution and has been successfully verified. Moreover, only the PDF set variations are expected to be dependent on the charge of the final state leptons, as these are specifically evaluated for positively charged protons. It has been seen that the PDF set uncertainties are marginally larger for the lepton channel with negative charge. With regard of these findings and in order to profit from the increased statistical accuracy, the variations are calculated in the combined $\ell^{\pm}\ell^{\pm}$ channel. The relative impact found is applied to all lepton flavour and charge split channels in the statistical analysis of the SM $W^{\pm}W^{\pm}jj$-EW6 process.

Some of the variations used to assess the modelling uncertainties of the $W^{\pm}W^{\pm}jj$ processes summarised in Tab. 7.11 have only been generated at particle level. Mostly due to the limited computing resources or the unavailability of interfaces to parton shower algorithms, these have not been propagated through the full detector simulation chain (cf. Sec. 4.3) and hence are not available on reconstruction level. In order to assess their impact in the signal region, especially on differential distributions, the predictions for the modelling parameter variations are transferred to reconstruction level using a folding procedure. This is described in the next section. The uncertainties are then evaluated with the folded variations and the nominal prediction at reconstruction level following the same procedure as at particle level. Quantities concerned by this are:

- The variations of the parton shower and merging parameters of the nominal predictions of the $W^{\pm}W^{\pm}jj$-EW6 and $W^{\pm}W^{\pm}jj$-EW4 processes, Sherpa23jLO (cf. Sec.B.4.2 in the appendix);
- The estimate of the interference between the $W^{\pm}W^{\pm}jj$-EW6 and the $W^{\pm}W^{\pm}jj$-EW4 process at LO (cf. Sec. 6.6.1);
- The impact of the NLO EW corrections to the $W^{\pm}W^{\pm}jj$-EW6 process (cf. Sec. 6.7.5).

All of these variations have been discussed in detail at particle level in Chapter 6.

Folding – From Particle Level to Reconstruction Level Quantities

The folding procedure aims at inferring the effects of the detector simulation by utilising information from an existing MC prediction at both, particle and reconstruction level. Eventually, this permits to estimate the event yield in the signal region at reconstruction level for the prediction under test available at particle level.

The procedure is based on the assumption that similar processes with identical types of final state particles with energies in comparable ranges are subject to similar detector

effects. Hence, the existing MC prediction must be close to the predictions under test. A natural choice for this input dataset is the prediction with nominal modelling parameters for a respective process.

The differential event yield of the prediction under test $(dN/dx)(R_j)^{\text{test}}$ at reconstruction level, denoted R, in each bin j of an observable x is the quantity of interest. Since the method is independent of the exact observable at hand, the notation shall be simplified to: $(dN/dx)(R_j)^{\text{test}} =: N(R_j)^{\text{test}}$. Similarly, the corresponding event yield in bin i of observable x at particle level T is denoted: $(dN/dx)(T_i)^{\text{test}} =: N(T_i)^{\text{test}}$. This is the quantity to be folded to reconstruction level.

The regions at reconstruction/particle level used to derive all necessary quantities for the folding procedure are usually the signal/fiducial regions of the analyses. The method of folding is especially relevant for differential predictions, where migrations between bins are possible and relevant. Employing the Bayes' theorem, the probability of finding $N(R_j)^{\text{test}}$ events in bin j at reconstruction level is:

$$P(R_j)^{\text{test}} = \frac{\sum_i \left(P(R_j|T_i)^{\text{in}} \cdot P(T_i)^{\text{test}}\right)}{\sum_i P(T_i|R_j)^{\text{in}}}, \tag{7.2}$$

where $P(R_j|T_i)$ is the conditional probability of an event being reconstructed in bin j given its true existence in bin i on particle level. The final event yield can then be derived as:

$$N(R_j)^{\text{test}} = P(R_j)^{\text{test}} \cdot N(R)^{\text{test}}, \tag{7.3}$$

with $N(R)^{\text{test}} = \sum_j N(R_j)$ being the total event yield in region R at reconstruction level.

The goal is now to express the probability $P(R_j)^{\text{test}}$ with quantities easily accessible from the predictions of the input dataset. The full calculation is presented in App. D.4.2. From this, the event count of the test dataset per bin j at reconstruction level can eventually be expressed as:

$$N(R_j)^{\text{test}} = \frac{F_{\text{norm}}}{C_j^{\text{fid}}} \sum_i \left(\mathcal{M}_{ji}^{\text{res}} \cdot N(T_i)^{\text{test}}\right), \tag{7.4}$$

where $\mathcal{M}_{ji}^{\text{res}}$ is the response matrix, C_j^{fid} is called the fiducial correction, and F_{norm} is a residual normalisation factor.

The response matrix:

$$\mathcal{M}_{ji}^{\text{res}} = \frac{N(T_i \cap R_j)^{\text{in}}}{N(T_i)^{\text{in}}}, \tag{7.5}$$

$$\sim P(R_j|T_i)^{\text{in}}, \tag{7.6}$$

is a 2-dimensional matrix in the $R \cap T$ space collecting all events passing both the reconstruction level selection requirements and the selection criteria in the region at particle level of the input dataset. Each row of the matrix i is corrected with the event count $N(T_i)^{\text{in}}$ in the respective particle level bin i. In this way, the matrix can be applied to the particle level distribution of the test dataset $N(T_i)^{\text{test}}$ in a straight forward manner[4].

The fiducial correction, defined differentially in reconstruction level bins j:

$$C_j^{\text{fid}} = \frac{\sum_i N(T_i \cap R_j)^{\text{in}}}{N(R_j)^{\text{in}}}, \tag{7.7}$$

$$\sim \sum_i P(T_i|R_j)^{\text{in}}, \tag{7.8}$$

[4]This refers to the in contrast sometimes adopted strategy to define an efficiency correction C_i^{eff}, which is only needed if the response matrix is defined as normalised to unity per row, i. e. $\mathcal{M}_{ji}^{\text{res}} = \frac{N(T_i \cap R_j)^{\text{in}}}{\sum_j N(T_i \cap R_j)^{\text{in}}}$. Then, $C_i^{\text{eff}} = \frac{\sum_j N(T_i \cap R_j)^{\text{in}}}{N(T_i)^{\text{in}}}$ must be added to the equation. Its interpretation is the correction for the fraction of events passing the particle level selection criteria that do not pass the selection criteria at reconstruction level.

is the fraction of events passing the reconstruction level selection criteria that also pass the selection criteria at particle level. It corrects the numerator for the fraction of events at reconstruction level that are not entering the response matrix because they do not occur in the region T at particle level. As can be seen from the Bayes' theorem in Eq. (7.2), it acts as a normalisation correction such that the entity of numerator and denominator satisfy the normalisation axiom of the probability definition.

Both, the response matrix and the fiducial correction, are not exactly probabilities on their own. Some normalisation factors have been omitted in their definition. These are collected in F_{norm} in Eq. (7.4), which from Eq. (D.28) yields:

$$F_{\text{norm}} = \frac{N(T)^{\text{in}} N(R)^{\text{test}}}{N(T)^{\text{test}} N(R)^{\text{in}}}. \tag{7.9}$$

It collects all total event counts in the regions at particle/reconstruction level of the respective datasets. Since $N(R)^{\text{test}}$ is unknown, this factor is assumed to be equal to 1 in the calculation. This fixes the overall normalisation of the test dataset in the folding region at reconstruction level to:

$$N(R)^{\text{test}} = \frac{N(R)^{\text{in}}}{N(T)^{\text{in}}} \cdot N(T)^{\text{test}}. \tag{7.10}$$

In order to verify the final result, several tests can be made. One is to condense the mathematical form of the folding prescription to one bin in each region, i. e. to inclusive observables. For $i = j = 1$, with Equations (7.5) and (7.7), Equ. (7.4) becomes:

$$N(R)^{\text{test}} = \frac{N(R)^{\text{in}}}{N(T \cap R)^{\text{in}}} \cdot \left(\frac{N(T \cap R)^{\text{in}}}{N(T)^{\text{in}}} \cdot N(T)^{\text{test}} \right), \tag{7.11}$$

$$= \frac{N(R)^{\text{in}}}{N(T)^{\text{in}}} \cdot N(T)^{\text{test}}, \tag{7.12}$$

$$= C^{\text{eff}} \cdot N(T)^{\text{test}}. \tag{7.13}$$

The last equality uses the definition of the efficiency of the signal region selection with respect to the fiducial region selection when reducing to one bin in each region, i. e. for inclusive observables:

$$C^{\text{eff}} = \frac{N(R)^{\text{in}}}{N(T)^{\text{in}}}, \tag{7.14}$$

and leads to the expected result. However, it also shows the following: The relative normalisation of the test dataset at reconstruction level with respect to the particle level will always be identical to the input dataset when using the folding procedure.

A second test of the folding procedure is to fold the input dataset used to derive the quantities for the folding. This is a technical test. The folded distribution of the input dataset must give the exact same result as the nominal input distribution at reconstruction level. This test has successfully been performed in the course of the publication in Ref. [1]. Results are shown in Appendix G.3 in Ref. [232].

In the two main analysis parts, discussed in the next chapters, different observables are utilised for the statistical analyses:

- The invariant mass of the tagging jet system, m_{jj}, in the SM analysis for the cross-section measurement of the SM $W^{\pm}W^{\pm}jj$-EW6 process; and
- The invariant mass of the two `analysis` leptons in the event, m_{ll}, for the EFT reinterpretation analysis.

The response matrix divided by the fiducial correction $\mathcal{M}^{\text{res}}/C^{\text{fid}}$, for the $W^{\pm}W^{\pm}jj$-EW6 and the $W^{\pm}W^{\pm}jj$-EW4 process for both observables are shown in Fig. 7.2. The phase space used to extract these folding information is the fiducial region at particle level, defined in Tab. 6.8, and the signal region at reconstruction level, defined in Tab. 7.4. When extracting the folding information differentially in m_{jj}, the selection criteria on this observable is omitted at both particle and reconstruction level. In this way, migration effects in this observable can be studied.

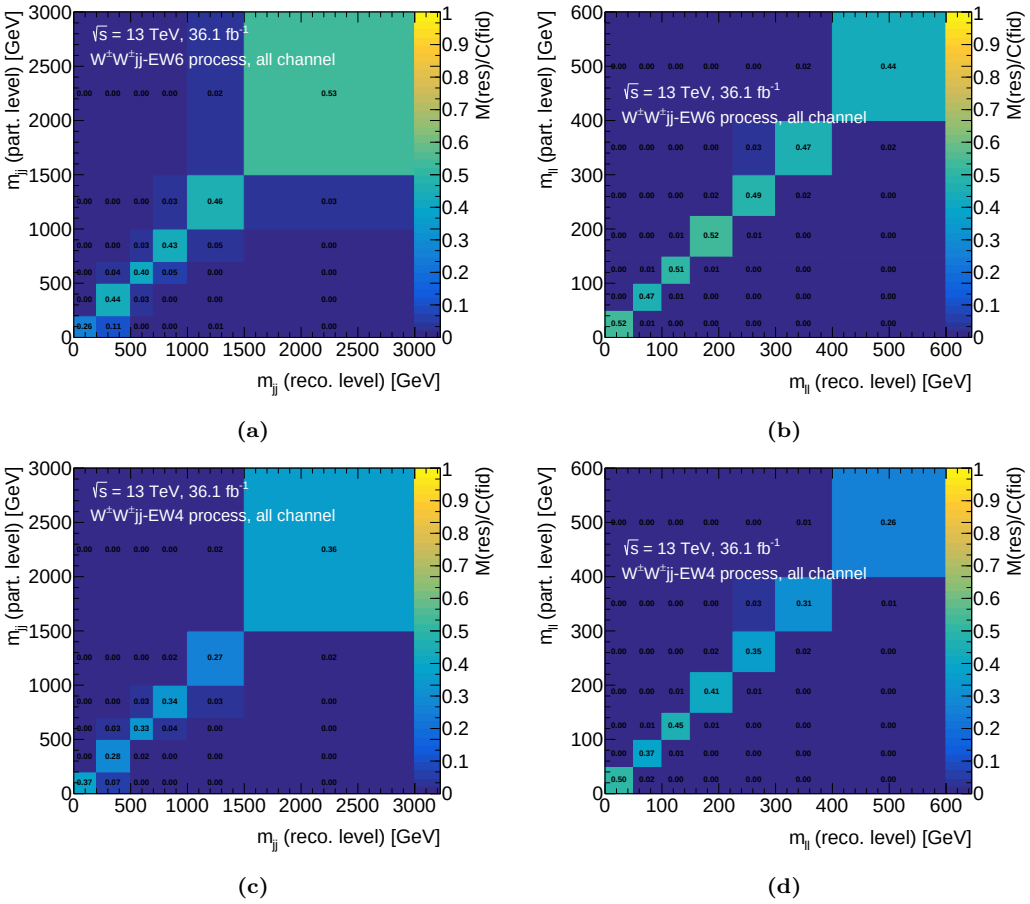


Figure 7.2: The response matrix divided by the fiducial correction $\mathcal{M}^{\text{res}}/C^{\text{fid}}$, for the $W^{\pm}W^{\pm}jj$-EW6 (a,b) and the $W^{\pm}W^{\pm}jj$-EW4 (c,d) process for the invariant mass of the tagging jets, m_{jj} (a,c), and of the `analysis` leptons in the event, m_{ll} (b,d). The phase space used to extract these folding information is the fiducial region at particle level, defined in Tab. 6.8, and the signal region at reconstruction level, defined in Tab. 7.4. For the distributions in m_{jj}, the respective selection criteria in both regions are omitted.

Table 7.12: Relative impact of modelling uncertainties on the event yields of predictions based on MC simulation for the dominant background processes $W^{\pm}Z$ and $W^{\pm}W^{\pm}jj$-EW4, and the $W^{\pm}W^{\pm}jj$-EW6 signal process in the combined $\ell^{\pm}\ell^{\pm}$ channel in the signal region. Results for the $W^{\pm}Z$ process are the combined impact on the $WZjj$-EW6 and $W^{\pm}Z$-EW4 processes. Numbers are shown for both $W^{\pm}W^{\pm}jj$-EW6 predictions, the Sherpa23jLO setup, employed in the SM analysis and the MG5+Py8drec setup, employed in the EFT reinterpretation analysis. The columns contain the effect (from left to right) from the variation of the renormalisation and factorisation scales μ_R/μ_F, the nominal PDF set and its strong coupling value α_S, the parton shower and/or merging parameters/algorithms, the interference between the respective EW6 and EW4 processes, and the NLO EW corrections to the electroweak-induced process.

Process	Modelling uncertainty [%]					
$\ell^{\pm}\ell^{\pm}$ channel	μ_R/μ_F	PDF set	α_S	Part. shower	Int.	NLO EW corr.
$W^{\pm}Z$	$^{+28}_{-18}$	$^{+2}_{-1}$	±2	±13	–	–
$W^{\pm}W^{\pm}jj$-EW4	$^{+38}_{-25}$	±2	±2	$^{+4}_{-6}$	–	–
$W^{\pm}W^{\pm}jj$-EW6 (Sherpa23jLO)	$^{+15}_{-11}$	±2	$<\pm1$	$^{+8}_{-2}$	±3	-17
$W^{\pm}W^{\pm}jj$-EW6 (MG5+Py8drec)	$^{+8}_{-7}$	±2	$<\pm1$	$^{+4}_{-1}$	±3	-17

Modelling Uncertainties in the Signal Region

The uncertainties resulting from the variation of the modelling parameters for the $W^{\pm}Z$ and $W^{\pm}W^{\pm}jj$-EW4 background processes and the $W^{\pm}W^{\pm}jj$-EW6 signal process are listed in Tab. 7.12. Detailed numbers entering the envelope calculations of the renormalisation and factorisation scale, and PDF set variations can be found in App. D.4.2. For the $W^{\pm}Z$ process, the uncertainties are quoted separately for the $W^{\pm}Z$-EW4 and $WZjj$-EW6 processes, as well as for the sum, labelled $W^{\pm}Z$, in the appendix. Tab. 7.12 only summarises the combined uncertainties which are used in the statistical analyses in the subsequent chapters. Number for the signal process are quoted for both, the Sherpa23jLO and MG5+Py8drec predictions.

The renormalisation and scale variations are the dominant source of modelling uncertainties for all processes, except for the $W^{\pm}W^{\pm}jj$-EW6 signal process, where the NLO EW corrections have a larger impact. For the QCD-induced processes, the scale uncertainties are driven by the variation of the renormalisation scale. The resulting envelopes are highly asymmetric and amount to a relative uncertainty of $20-40\%$. Scale variations for the electroweak-induced processes are milder. For the Sherpa23jLO prediction of the signal process both scales yield comparable variations. The prediction of MG5+Py8drec setup, as well as the electroweak-induced $WZjj$-EW6 process is LO accurate, hence yielding no dependence on the strong coupling. In consequence, no renormalisation scale variations exist.

Uncertainties due to the variations of the nominal PDF set are of the order of 2% for all considered processes. Uncertainties originating from the variation of the value of the strong coupling constant α_S in the nominal PDF set range in the order of the statistical accuracy of the MC prediction for the electroweak-induced processes. For the QCD-induced processes these are stable around $(2-3)\%$.

For the $W^{\pm}W^{\pm}jj$-EW6 and $W^{\pm}W^{\pm}jj$-EW4 processes, uncertainties labelled "parton shower" in addition comprise the variations of the merging of the matrix element and parton shower algorithms. Their relative impact quoted in Tab. 7.12 is the envelope of the relative variations obtained in the fiducial region at particle level (cf. Tab. B.12 in the appendix) omitting the effect of unequal migration in and outside the signal region discussed earlier, which, observing the off-diagonal elements in the response matrix and the event yields in the respective bins at particle level, is estimated to have a negligible effect (below 1% with

Table 7.13: Normalisation uncertainties on MC estimated cross-section predictions for minor backgrounds taken from Ref. [13, 234, 235].

Process	Normalisation uncertainty [%]
$t\bar{t}V$	±30
ZZ	±20
VVV	±30
$W^{\pm}\gamma$	±20
$Z\gamma$	±20

respect to the final event yield in the signal region). This accuracy shall suffice for this summary table. In the statistical analyses, more detailed differential modelling uncertainties are employed, which are then correctly folded to reconstruction level utilising the aforementioned prescription. These are stated in the respective chapters.

The same procedure is taken for the uncertainty due to the $W^{\pm}W^{\pm}jj$-INT process and the NLO EW corrections to the $W^{\pm}W^{\pm}jj$-EW6 process.

It can be noted here that the uncertainty estimates of the MG5+Py8drec signal prediction do not exhibit the statistical limitations observed for the evaluation of the experimental uncertainties. The reason lies in the different technical approaches of their estimate. Experimental uncertainties are evaluated by altering kinematic properties of the objects in the event. This causes migrations of, statistically limited, events in and outside the signal region and eventually the systematic effect compared to the nominal prediction. Together with combining many variations in one uncertainty, the statistical effect increases. On the contrary, the modelling uncertainties are evaluated by alternating event weights from the event generation and are mostly combined by taking their envelope. Hence, they are less affected by statistical effects.

Tab. 7.13 summarises the modelling uncertainties for minor MC estimated background processes taken as symmetrised normalisation uncertainties on the predicted cross-section in the statistical analyses. For the $t\bar{t}V$, ZZ and $W^{\pm}\gamma$ processes, these are extracted from the Run 1 analysis of the $W^{\pm}W^{\pm}jj$-EW6 process at $\sqrt{s} = 8\,\text{TeV}$ centre-of-mass energy [13]. For VVV production reference values are taken from the Run 1 analysis of the triple $W^{\pm}$ boson production [234]. The uncertainty on the normalisation of the $Z\gamma$ cross-section prediction is taken to be equal to the $W^{\pm}\gamma$ case. It has the smallest contribution estimated in the signal region.

7.7 Expected Event Counts and Uncertainties in the Signal Region

Concluding this overview on the aspects of the experimental analyses in this thesis, the estimated event yield and their total uncertainties in the signal region of all relevant SM processes are summarised in Tab. 7.14. The table comprises numbers for all relevant background processes estimated from data-driven methods (cf. App. D.2) or MC simulation (cf. Sec. 4, and App. C). Numbers for the $W^{\pm}W^{\pm}jj$-EW6 signal process are quoted for both, the nominal Sherpa23jLO prediction, employed in the SM analysis (cf. Sec. 6.3.2) and the MG5+Py8drec prediction (cf. Sec. 6.3.3), employed in the EFT reinterpretation analysis. For the latter, uncertainties are not evaluated in the lepton flavour- and charge-split channels. Hence, predictions are given in the combined $\ell^{\pm}\ell^{\pm}$ channel only. In addition, the measured event yields in data, taken in the years 2015 and 2016 in Run 2 of the LHC with the ATLAS detector (cf. Sec. 3.3) are given.

A total of 122 experimental data events are selected into the signal region. The total signal plus background estimate agrees with experimental data exhibiting a background only event yield of approx. 81 ± 14. While the event yields of experimental data in the $e^{\pm}e^{\pm}$ channels are lower than the total estimate, it exceeds the predictions in the $\mu^{\pm}\mu^{\pm}$ channels.

The total uncertainties are obtained from combining the independent, individual compo-

Table 7.14: Estimated event yields and their total uncertainties of all SM processes relevant to the analyses in this thesis, together with the event yields of experimental data taken in the years 2015 and 2016 in Run 2 of the LHC with the ATLAS detector. The predictions of the $W^{\pm}W^{\pm}jj$-EW6 process are shown for both, the Sherpa23jLO setup, employed in the SM analysis and the MG5+Py8drec setup, employed in the EFT reinterpretation analysis. Uncertainties on the signal predictions include the normalisation uncertainties from the modelling variations. "Other prompt" comprises MC-based predictions of the processes of $t\bar{t}V$, ZZ, and triboson production. Numbers are given in all lepton flavour- and charge-split, as well as in the combined $\ell^{\pm}\ell^{\pm}$ channel, in the signal region before the statistical analyses, except for the MG5+Py8drec signal prediction. Uncertainties for the latter are not evaluated in the lepton flavour- and charge-split channels. Hence, predictions are given in the combined $\ell^{\pm}\ell^{\pm}$ channel only. The total expected event yield is composed with the Sherpa23jLO signal prediction.

Process	Channel						
	e^+e^+	e^-e^-	$e^+\mu^+ + \mu^+e^+$	$e^-\mu^- + \mu^-e^-$	$\mu^+\mu^+$	$\mu^-\mu^-$	$\ell^{\pm}\ell^{\pm}$
$W^{\pm}Z$	1.87 ± 0.58	1.31 ± 0.42	13.81 ± 4.04	8.92 ± 2.61	5.50 ± 1.65	3.64 ± 1.15	35.06 ± 10.15
$W^{\pm}W^{\pm}jj$-EW4	0.38 ± 0.13	0.16 ± 0.05	3.02 ± 1.02	1.21 ± 0.41	1.80 ± 0.61	0.76 ± 0.26	7.34 ± 2.47
Other prompt	0.17 ± 0.05	0.14 ± 0.05	0.90 ± 0.19	0.60 ± 0.14	0.36 ± 0.10	0.19 ± 0.06	2.36 ± 0.48
Non-prompt	4.08 ± 2.30	2.31 ± 1.71	9.35 ± 4.87	6.34 ± 3.74	0.57 ± 0.15	0.67 ± 0.25	23.32 ± 9.68
Charge misID	1.33 ± 0.15	1.17 ± 0.13	3.48 ± 0.37	2.95 ± 0.33	–	–	8.93 ± 0.71
$V\gamma$	0.41 ± 0.26	0.62 ± 0.37	2.65 ± 1.60	0.80 ± 0.72	–	–	4.47 ± 2.44
$W^{\pm}W^{\pm}jj$-EW6 (Sherpa23jLO)	3.80 ± 0.93	1.49 ± 0.37	16.49 ± 4.01	6.45 ± 1.64	9.14 ± 2.25	3.50 ± 0.86	40.88 ± 10.02
$W^{\pm}W^{\pm}jj$-EW6 (MG5+Py8drec)							50.06 ± 25.94
Total expected (w. Sherpa23jLO)	12.04 ± 2.57	7.20 ± 1.84	49.70 ± 7.74	27.27 ± 4.93	17.37 ± 2.86	8.76 ± 1.48	122.36 ± 17.60
Data 2015/16	10	4	44	28	25	11	122

nents, i. e. the statistical uncertainty from the MC simulation or the data-driven estimate, the systematic uncertainties, and the modelling uncertainties if applicable (cf. Sec. 7.6) in quadrature.

The total uncertainty on the Sherpa23jLO prediction of the $W^{\pm}W^{\pm}jj$-EW6 signal process amounts to approx. 25% uniformly throughout all channels. Statistical uncertainties due to the MC simulation are negligible for the Sherpa23jLO signal prediction in all channels. For the MG5+Py8drec prediction, the evaluation of systematic uncertainties is affected by the statistical limitation the sample and amount to over 50%.

Due to the more stringent selection criteria for the $e^{\pm}e^{\pm}$ channels, event yields for the prompt backgrounds and the signal process in these channels are smaller than for the $\mu^{\pm}\mu^{\pm}$ channels, although identical branching fractions are expected for these processes.

As discussed in Sec. 7.5.1, the $W^{\pm}Z$ process contributes the largest fraction to the total background estimate in the combined $\ell^{\pm}\ell^{\pm}$ channel. However, splitting into channels defined by lepton flavour, the composition of the different background contributions changes substantially. In the $e^{\pm}e^{\pm}$ channels, the background with the largest contribution comes from processes with non-prompt leptons. Moreover, backgrounds due to electron charge misidentification and photon conversion are not present in the $\mu^{\pm}\mu^{\pm}$ channels.

Due to the initial charge configuration in the collision of protons, processes producing $W^{\pm}$ bosons exhibit a significant asymmetry in the charge dependent yields, compared to processes such as electron charge misidentification which is driven by Z boson production. Due to the signal process, featuring the production of two $W^{\pm}$, its charge asymmetry is highly distinctive. Hence, the fraction of expected signal events with respect to the overall event yield is always larger in the positive charge channels compared to the negative charge channels. It grows from 20% in the $e^{-}e^{-}$ to over 50% in the $\mu^{+}\mu^{+}$ channel considering all channels.

Chapter 8

Observation and Cross-section Measurement

In this chapter, all components of the previous chapters are combined to establish the first observation of the $W^{\pm}W^{\pm}jj$-EW6 process with the ATLAS experiment, measure the cross-section of this process and compare the results to theoretical predictions.

This chapter begins with a review on existing measurement results of the SM $W^{\pm}W^{\pm}jj$, and especially the $W^{\pm}W^{\pm}jj$-EW6 process. After outlining the mathematical strategy of the statistical analysis and the cross-section measurement, the specifics of this SM analysis, such as the control region (CR) employed and the exact treatment of the systematic uncertainties, are refined and results are presented. The chapter closes with a short assessment of the potential of and possible strategies for future analyses.

8.1 Review of Existing Results

The history of the discovery of the $W^{\pm}W^{\pm}jj$-EW6 process has already been summarised briefly in Tab. 5.2 and Chapter 6, including the first evidence at centre-of-mass energy $\sqrt{s} = 8\,\text{TeV}$ by the ATLAS experiment [13] in Run 1 of the LHC data-taking. The CMS experiment claimed the first observation of the $W^{\pm}W^{\pm}jj$-EW6 process at $\sqrt{s} = 13\,\text{TeV}$ in Ref. [14], followed shortly after by the publication of the ATLAS experiment subject of this thesis [1]. By the time of writing of this work, the CMS experiment has published two more results including cross-section measurements of the $W^{\pm}W^{\pm}jj$ process [155, 193]. Tab. 8.1 summarises the measurements of the fiducial cross-section of the $W^{\pm}W^{\pm}jj$ process at $\sqrt{s} = 13\,\text{TeV}$ utilising partial or full data of the Run 2 data-taking period of the LHC. This table excludes the results of the ATLAS experiment [1] which will be discussed in detail in this chapter.

In Ref. [14], a fit of the two-dimensional distribution in invariant masses of the tagging jets, and leading charged leptons, m_{jj} and m_{ll}, respectively, is employed to extract the significance and the fiducial cross-section of the electroweak-induced $W^{\pm}W^{\pm}jj$-EW6 process with partial LHC Run 2 data at $\sqrt{s} = 13\,\text{TeV}$. The statistical analysis is designed with a profile likelihood ratio function as the test statistic and performed simultaneously in one signal region and a $W^{\pm}Z$ control region, both of which contain events of all lepton flavour and charge combinations. In the latter region, solely the m_{jj} distribution is utilised. Dominant background contributions in the signal region come from processes exhibiting non-prompt leptons and the $W^{\pm}Z$ process, amounting to 64% and 18% of the total background event estimate before the statistical analysis, respectively. Backgrounds from electron charge misidentification plays a minor role compared to other background sources. Alltogether, the background composition differs substantially compared to the analysis of the ATLAS experiment discussed in this thesis. A first reason is clearly the difference in detector technologies and hence capabilities for e. g. electron property measurements. Secondly, the analysis in Ref. [14] imposes more stringent requirements on the VBS observables (cf. Tab. 5.3) which reduces the contribution of the QCD-induced $W^{\pm}W^{\pm}jj$-EW4 process. The cross-section

Table 8.1: Summary of existing results on the cross-section measurement of the $W^{\pm}W^{\pm}jj$ process at $\sqrt{s} = 13\,\text{TeV}$ centre-of-mass energy at the LHC in the fully leptonic final state, excluding the result of the ATLAS experiment subject of this thesis [1]. Cross-section measurements of the electroweak process $W^{\pm}W^{\pm}jj$-EW6, the full process $W^{\pm}W^{\pm}jj$, including the $W^{\pm}W^{\pm}jj$-EW6, $W^{\pm}W^{\pm}jj$-EW4 and their interference, and polarized electroweak $W^{\pm}W^{\pm}$ production (L - longitudinal, T - transverse, X - any, longitudinal or transverse) have been published by the time of writing of this thesis. Theoretical prediction are LO accurate. Those employed in the unpolarised measurements are summarised in Tab. 6.2. Measurements in Ref. [155] are additionally compared to NLO corrected theoretical predictions including the orders $\mathcal{O}(\alpha_{EW}^7)$ and $\mathcal{O}(\alpha_{EW}^6\alpha_S)$. Uncertainties on the theoretical predictions are the total modelling uncertainties quoted in the publications. The fiducial region of the measurement published in Ref. [14] is summarised in Tab. 6.9. Fiducial regions of the other measurements can be extracted from the respective publication.

Process	Measured fiducial cross-section [fb]	Theoretical predictions [fb]
CMS experiment ($35.9\,\text{fb}^{-1}$) [14]:		
$W^{\pm}W^{\pm}jj$-EW6	$3.83 \pm 0.66(\text{stat.}) \pm 0.35(\text{syst.})$	4.25 ± 0.27
CMS experiment ($137\,\text{fb}^{-1}$) [155]:		
$W^{\pm}W^{\pm}jj$-EW6	$3.98 \pm 0.37(\text{stat.}) \pm 0.25(\text{syst.})$	3.93 ± 0.57 (LO)
		3.31 ± 0.47 (NLO)
$W^{\pm}W^{\pm}jj$	$4.42 \pm 0.39(\text{stat.}) \pm 0.25(\text{syst.})$	4.34 ± 0.69 (LO)
		3.72 ± 0.59 (NLO)
CMS experiment ($137\,\text{fb}^{-1}$) [193]:		
$W_L^{\pm}W_L^{\pm}jj$-EW6	$0.32^{+0.42}_{-0.40}$	0.44 ± 0.05
$W_X^{\pm}W_T^{\pm}jj$-EW6	$3.06^{+0.51}_{-0.48}$	3.13 ± 0.35
$W_L^{\pm}W_X^{\pm}jj$-EW6	$1.20^{+0.56}_{-0.53}$	1.63 ± 0.18
$W_T^{\pm}W_T^{\pm}jj$-EW6	$2.11^{+0.49}_{-0.47}$	1.94 ± 0.21

is measured in the fiducial region as defined in Tables 6.9 and 6.8. It is compared to the theoretical prediction at LO of MG5_aMC + Pythia 8 (details in Tab. 6.2), which is also used for the modelling of the signal process in the statistical analysis. The interference of the electroweak- and QCD-induced $W^{\pm}W^{\pm}jj$ processes is taken as a systematic uncertainty on the $W^{\pm}W^{\pm}jj$-EW6 signal prediction in the analysis. Measurement and theoretical prediction agree within their uncertainties. A detailed comparison of various prediction in the fiducial region of Ref. [14] is performed in Sec. 6.7.3 of this work.

The measurement of the cross-section of the $W^{\pm}W^{\pm}jj$-EW6 with the CMS experiment at $\sqrt{s} = 13\,\text{TeV}$ is repeated with the full LHC Run 2 dataset in Ref. [155]. The analysis in this publication does not only add more data to the measurement, but also performs the statistical analysis in combination with the $W^{\pm}Z$-EW6 process, and measures the fiducial cross-section of the full $W^{\pm}W^{\pm}jj$ process inclusively and unfolded differentially in m_{jj}, m_{ll}, and the leading lepton transverse momentum. Cross-sections consistent with the SM are reported in all measurements. The statistical analysis combines two signal regions, one for the $W^{\pm}W^{\pm}jj$ and $W^{\pm}Z$ processes each, and three control regions, one for the background contributions from processes with non-prompt leptons, the ZZ and the tZj processes each, in a multibin maximum likelihood fit. The combination of the statistical analyses of the two processes yields the clear advantage of estimating the $W^{\pm}Z$ contribution, one of the major background contributions in the $W^{\pm}W^{\pm}jj$ signal region, in both signal regions simultaneously. In the $W^{\pm}W^{\pm}jj$ signal region, the two-dimensional distribution in m_{jj} and m_{ll} is again employed in the fit. In the $W^{\pm}Z$ signal region a boosted decision tree (BDT) is trained, whose output score binned in m_{jj} is utilised in the fit. In the control regions,

the m_{jj} observable is used as input to the statistical analysis. Theoretical predictions for the $W^{\pm}W^{\pm}jj$-EW6 signal process are equivalent to the ones used in Ref. [14]. However, the interference between the $W^{\pm}W^{\pm}jj$-EW6 and $W^{\pm}W^{\pm}jj$-EW4 processes is considered as part of the $W^{\pm}W^{\pm}jj$-EW6 process in this publication. In addition, the fiducial cross-section measurements extracted with information of the LO predictions, is compared to both, LO and NLO corrected theoretical predictions. The latter include corrections of the orders $\mathcal{O}(\alpha_{EW}^7)$ and $\mathcal{O}(\alpha_{EW}^6\alpha_S)$ to the $W^{\pm}W^{\pm}jj$-EW6 process only. The fiducial region is moderately tighter than in the previous publication, increasing the jet transverse momentum threshold to 50 GeV and adding the requirement on m_{ll} to be larger than 20 GeV. The inclusive cross-section measurements are considerably more accurate, not only in statistics, as expected, but also in systematics.

Further, in Ref. [193], polarized $W^{\pm}W^{\pm}jj$-EW6 production is investigated for the first time at $\sqrt{s} = 13\,\text{TeV}$ by the CMS experiment. Both an upper limit on, as well as a measurement of the fiducial cross-section of different polarisation states is reported. The observed (expected) upper limit at 95% confidence level for purely longitudinal electroweak $W^{\pm}$ boson pair production is quoted to be 1.17(0.88) fb in the $W^{\pm}$ boson pair centre-of-mass reference frame.

8.2 Strategy of the Statistical Analysis

The measurement goals of this analysis and the overall strategy to achieve them have been stated in Sec. 7.1. The approaches of the statistical analysis to complete the objectives of the SM analysis are detailed in this chapter.

The procedure of hypothesis testing is used to accomplished the first objective, the observation of the $W^{\pm}W^{\pm}jj$-EW6 process. The measurement of the fiducial cross-section of this process, the second aim, is targeted with the method of parameter estimation. Both employ the method of extended maximum likelihood in its respective implementations, where the likelihood function takes form based on:

- The theoretical foundation, i. e. the statistical nature of particle physics interactions: Poisson distributed observations in experimental data;
- The specifics of the given signal process: Definition of the signal contribution and signal region, channels, discriminating observable and its binning;
- The specifics of the background contributions: Modelling and estimation, control regions; and
- Constraints from additional measurements: Integrated luminosity, experimental and modelling systematic effects of the signal and all background expectations.

The first fundamental is driven intrinsically by the large sample size (number of collected events), and the low cross-section of the signal process. The second and third items are discussed next. The systematic effects are introduced in Sec. 7.6 and their treatments in the statistical analysis are refined in this chapter, Sec. 8.5.

Before the mathematical implementation of the model is discussed, the characteristics of the experimental measurement shall be reviewed in light of serving as the input to the statistical procedures.

8.2.1 Characteristics of the Experimental Measurement

The cross-section of the $W^{\pm}W^{\pm}jj$-EW6 shall be measured in the fiducial region defined in Sec. 6.4. The experimental measurement is conducted in the signal region, defined in Sec. 7.4 with the intention to rebuild the fiducial region at detector level considering all acceptance and resolution limitations of the experiment, as well as to reject the background and at the same time retain the signal events as efficiently as possible.

The measurement consists of the observation of a certain, discrete number of events passing the signal region selection. These events have various different kinematic properties.

As discussed in Sec. 5.3 and verified in Fig. 6.3, the $W^{\pm}W^{\pm}jj$-EW6 signal process has very distinctive features in the VBS observables, the invariant mass and the rapidity separation of the tagging jet system, m_{jj} and ΔY_{jj}, respectively. Hence, conducting the statistical analysis in the differential distributions of these variables augments the information content for the parameter estimation or respectively hypothesis testing. As both quantities are highly correlated [131], and in light of the limited statistics at hand (cf. Tab. 7.14), only one of them is chosen. It is the m_{jj} observable whose binning is optimised with respect to the expected significance in the course of the statistical analysis. The optimisation procedure is detailed in Ref. [235] and not further discussed here. It yields an optimal number of four bins in the signal region with lower bin edges rounded to whole numbers of: $m_{jj} \in \{500\,\text{GeV}, 700\,\text{GeV}, 1000\,\text{GeV}, 1500\,\text{GeV}\}$.

The prominent difference in relative lepton flavour and charge split event yields of the signal and background processes is discussed in Sec. 7.7. Splitting the signal region into six lepton flavour and charge dependent, and hence mutually exclusive channels is highly beneficial in constraining different background contributions as well as efficiently estimating the signal properties.

The $W^{\pm}Z$ process yields the largest background contribution in the signal region. In Ref. [15], a mild mismodelling of the normalisation of this process in MC simulation with respect to experimental data in a VBS phase space is reported. Thus, the normalisation of this process shall be constrained from experimental data in a dedicated $W^{\pm}Z$ control region (CR), which is implemented in the fitting procedure.

The information of events with a lower m_{jj} than those entering the signal region is exploited in a second control region. It presents a kinematic region with low signal contribution but similar background composition compared to the signal region. It is called the "low-m_{jj} control region" and like the signal region split into six lepton flavour and charge dependent channels.

All regions, the signal region with six channels and both control regions, are evaluated simultaneously in the fitting procedure in order to extract the figure of merit at hand. The information on each region is again summarised in Tab. 8.2. This table also summarises information on the processes considered in each region. The prediction for the $W^{\pm}W^{\pm}jj$-EW6 process is taken from the Sherpa23jLO setup. For the signal region, this is in detail discussed in the previous chapter. Information on the control regions is extended in Sec. 8.4.

8.2.2 Characteristics of the Statistical Model

The mathematical features of the statistical models employed in the SM analysis are briefly outlined in this section. The reader is directed to established literature on the subject of statistical data analysis in experimental physics for further details, mathematical implications and connections, such as Ref. [236, 237].

The measurement of the fiducial cross-section of the $W^{\pm}W^{\pm}jj$-EW6 process is a problem of parameter estimation which is approached with a binned, extended maximum likelihood method. The observation of this process is formulated as a hypothesis test and utilises the maximum likelihood ratio as a test statistic. The mathematical form of the likelihood function is identical for the evaluation of the two results. Thus, the basis of the statistical analysis of both objectives can be combined to a great extent. The tools for the statistical analysis employed here have been developed in the analysis group [238] based on the `HistFactory` framework within the `ROOT` libraries [239, 240].

The outcome of the measurement, i.e the number of observed events N in any considered region, is Poisson distributed:

$$\text{Pois}(N|\nu) = \frac{\nu^N}{N!} \cdot e^{-\nu}, \tag{8.1}$$

with ν being the expected event count. In case of one signal process (S) and multiple background contributions (B), the latter can be expressed as:

$$\nu(\mu, \vec{\theta}) = \mu(\vec{\theta}) \cdot \nu_S(\vec{\theta}) + \sum_B \nu_B(\vec{\theta}). \tag{8.2}$$

Table 8.2: Details on all regions entering the fitting procedure for the SM analysis, including the channels, observables and processes considered in each region. The $W^{\pm}Z$ CR is defined in a trilepton region with $\ell^{(\prime\prime)} = e^{\pm}$ or $\mu^{\pm}$. Information on the control regions are detailed in Sec. 8.4.

Region	Signal region (SR)	Control regions (CRs)	
		Low-m_{jj} CR	$W^{\pm}Z$ CR
Channels	6	6	1
	$e^{\pm}e^{\pm}$, $e^{\pm}\mu^{\pm} + \mu^{\pm}e^{\pm}$, $\mu^{\pm}\mu^{\pm}$		$\ell\ell'\ell''$
Observable (bins)	m_{jj} (4)	– (1)	– (1)
Considered processes:			
$W^{\pm}W^{\pm}jj$-EW6 (Sherpa23jLO)	✓	✓	✓
$W^{\pm}Z$	✓	✓	✓
$W^{\pm}W^{\pm}jj$-EW4	✓	✓	✓
Other prompt:			
- $t\bar{t}V$	✓	✓	✓
- ZZ	✓	✓	✓
- VVV	✓	✓	✓
Charge misID	✓	✓	–
Non-prompt	✓	✓	–
$V\gamma$:			
- $W^{\pm}\gamma$	✓	✓	✓
- $Z\gamma$	✓	✓	✓

The parameter μ is introduced as the signal strength:

$$\mu = \frac{\sigma^{\text{fid}}_{\text{meas}}}{\sigma^{\text{fid}}_{\text{theo}}}, \tag{8.3}$$

which is the ratio of the measured over the predicted fiducial cross-section. It is a continuous, uniformly distributed variable in the fit whose true value is subject of the measurement, i. e. it is the parameter of interest of the analysis. A value of $\mu = 0$ represents the background-only case where no signal is present, $\mu = 1$ reproduces the fiducial cross-section prediction of the SM template which is input to the fit. In the analysis case at hand, values of $\mu < 0$ are not allowed as the $W^{\pm}W^{\pm}jj$-INT contribution is found to be positive in the relevant phase space regions (cf. Sec. 6.6.1) and no negative interferences of the signal with other background contributions are expected.

Systematic effects are encoded in the ensemble of nuisance parameters $\vec{\theta} = \{\theta_1, \ldots, \theta_m\}$. It contains all systematic sources explained in Sec. 7.6. It is to be noted that not all systematic effects act on all quantities in Eq. (8.2).

For the analysis strategy at hand, Eq. (8.2) can be concretised as:

$$\nu(\mu, \vec{\theta}) = \mu(\vec{\theta}) \cdot \nu_{WWjj\text{-EW6}}(\vec{\theta}) + \mu_{WZ}(\vec{\theta}) \cdot \nu_{WZ}(\vec{\theta}) + \sum_{B \setminus WZ} \nu_B(\vec{\theta}), \tag{8.4}$$

where the unconstrained[1] normalisation factor for the $W^{\pm}Z$ background μ_{WZ} is introduced in equal manner as the signal strength μ. With Eq. (3.5), the number of expected events for processes which are estimated from simulation, can further be expressed in terms of their

[1] This normalisation factor is unconstrained in the sense, equal to the signal strength, in the positive region $\mu_{WZ} \in [0, \infty)$.

predicted cross-section σ_p^{fid}, their efficiency $C_p^{\text{eff}}(\theta)$, and the experimental luminosity L_{inst}:

$$\nu_p = \sigma_p^{\text{fid}} \cdot C_p^{\text{eff}}(\theta) \cdot L_{\text{inst}}. \tag{8.5}$$

The $C_p^{\text{eff}}(\theta)$ are the efficiencies defined when discussing the folding methodology in Eq. (7.14).

Eq. (8.4) does not yet incorporate all information from the measurement, which is provided in bins j of a sensitive observable for each process p in each channel of each region (together denoted as c)[2]. Collecting all of these information, the number of expected events per process, channel, and bin can then generically be written as:

$$\nu_{cjp}(\mu, \vec{\theta}) = \gamma_{cjp} \cdot \eta_{cp}(\vec{\alpha}) \cdot \mu_{cp}(\vec{\alpha}) \cdot \lambda \cdot \sigma_{cjp}(\vec{\alpha}), \tag{8.6}$$

with the following parameter definitions: γ_{cjp} are all constrained bin-by-bin nuisance parameters. They take the role as the statistical uncertainties of each expected event count of each process in each bin, channel, and region. The quantities $\eta_{cp}(\vec{\alpha})$ and $\mu_{cp}(\vec{\alpha})$ are constrained and unconstrained normalisation factors, respectively, and $\vec{\alpha}$ are all nuisance parameters with external constraints from auxiliary measurements, i. e. all η_{cp} and coherent shape variations β_{cjp}. The nuisance parameter associated to the experimental measurement of the instantaneous luminosity L_{inst} is λ. The $\vec{\theta}$ can then be specified as the collection of all nuisance parameters, except[3] the parameter of interest μ, as $\vec{\theta} = \{\gamma_{cj}, \eta_{cp}, \mu_{cp}, \lambda, \beta_{cjp}\}$. The σ_{cjp} are the predictions for each process in each channel/region and bin at reconstruction level. The $\nu_{cjp}(\mu, \vec{\theta})$ are provided in histograms to be included in the technical framework.

For the measurement at hand, the total expected event count in each channel/region and bin, with Equations (8.4) and (8.6) transforms into:

$$\begin{aligned}\nu_{cj}(\mu, \vec{\theta}) = {} & \mu(\vec{\alpha}) \cdot \lambda\gamma_{cj} \left[\sigma_{cj}(\vec{\alpha})\right]_{WWjj\text{-EW6}} + \mu_{WZ}(\vec{\alpha}) \cdot \lambda\gamma_{cj} \left[\sigma_{cj}(\vec{\alpha})\right]_{WZ} \\ & + \eta_{V\gamma}(\vec{\alpha})\lambda\gamma_{cj} \left[\sigma_{cj}(\vec{\alpha})\right]_{V\gamma} + \sum_{p\in(\text{other MC})} \lambda\gamma_{cj} \left[\sigma_{cj}(\vec{\alpha})\right]_p \\ & + \sum_{p\in(\text{data-driven})} \gamma_{cj} \left[\sigma_{cj}(\vec{\alpha})\right]_p .\end{aligned} \tag{8.7}$$

The parameter $\eta_{V\gamma}$ is the constrained normalisation nuisance parameter associated to the normalisation uncertainty of the $V\gamma$ processes, discussed in Sec. D.2.3. The discussion of the treatment of all nuisance parameters is carried on in Sec. 8.5.

The extended binned likelihood function, directly linked to the conditional probability[4] of observing N events while expecting ν, can now be formulated as:

$$\mathcal{L}(\mu, \vec{\theta}) = \prod_c \prod_j \text{Pois}(N_{cj}|\nu_{cj}(\mu, \vec{\theta}))\text{Gaus}(L_{\text{inst}}|\lambda, \Delta_L) \prod_r f_r(a_r|\alpha_r, \Delta_r). \tag{8.8}$$

The nuisance parameters α_r are constrained externally from auxiliary measurements a_r with probability density f_r, usually either Gauss or log-normal distributed. Δ_L denotes the uncertainty of the luminosity measurement for the ATLAS dataset.

Finally, $-\ln \mathcal{L}(\mu, \vec{\theta})$ is minimised[5] in order to obtain best estimates with respect to the observed data for all nuisance parameters including the parameter of interest, then denoted as $\hat{\vec{\theta}}$ and $\hat{\mu}$, respectively. The obtained value (and its uncertainty) for the best estimate $\hat{\mu}$ can then directly be inserted into Eq. (8.3) to obtain a measured fiducial cross-section from observed data. It shall be noted here that, with view on the non-optimal MC generation

[2] This generalisation is a matter of taste. Mathematically, there is no difference between summing over region and channels, or just over all channels in all regions.

[3] The parameter of interest is kept individually in all equations to explicitly point out its importance in the measurement.

[4] While the probability density function is dependent on both N and ν, the likelihood function is constructed with N already fixed from the measurement. Hence, the latter is not a probability density any longer.

[5] This method is preferred over maximising $\mathcal{L}$ for reasons of numerical stability as the Poisson density exhibits an exponential function. Since the logarithm is a monotonously increasing function, maxima of $\mathcal{L}$ and $\ln \mathcal{L}$ are identical.

of the signal process for the template using the Sherpa23jLO prediction, the result of the measured signal strength μ is always contingent on the template prediction which is input of the statistical analysis. This implies that the result of $\hat{\mu}$ must always be quoted in conjunction with the signal template used. For the result of the measured cross-section this dependency is milder as normalisation effects are accommodated by $\hat{\mu}$. Hence, solely the shape of the theoretical prediction used to perform the fit can affect the measurement of the fiducial cross-section. This must be thoroughly checked in the analysis and is done in Ref. [235] for the case at hand.

Before measuring the cross-section, it is to be determined whether the observed data support the signal hypothesis H_1 ($\mu > 0$) or rather favour the background-only, also called null hypothesis H_0 ($\mu = 0$). Both hypotheses, by construction, have different probability density functions, a fact that is exploited by the method of hypothesis testing.

The hypothesis test assigns the outcome of the measurement of the discriminating observable, called the test statistic, to one of the considered hypotheses. The assignment to the signal hypothesis, i. e. a discovery of the signal process is claimed, if the hypothesis test assuming the null hypothesis yields a probability in the observed data which is below a certain p-value. This p-value is usually translated into a significance level which is expressed in standard deviations σ, relating the probability of H_0 to be true to a Normal distribution. In experimental particle physics, it is broadly agreed to that an observation or discovery is made if the significance level exceeds 5σ, which corresponds to obtaining a probability of the null hypothesis to be true given the observed data (i. e. the p-value) below $2.87 \cdot 10^{-7}$.

The test statistic for observation, i. e. for rejecting H_0, in this analysis is chosen to be the maximum likelihood ratio defined as:

$$q(\mu = 0) = -2 \ln \frac{\mathcal{L}(H_0)}{\mathcal{L}(H_1)} \tag{8.9}$$

$$= -2 \ln \frac{\mathcal{L}(0, \hat{\hat{\vec{\theta}}})}{\mathcal{L}(\hat{\mu}, \hat{\hat{\vec{\theta}}})} \tag{8.10}$$

$$= -2 \left(\ln \mathcal{L}(0, \hat{\hat{\vec{\theta}}}) - \ln \mathcal{L}(\hat{\mu}, \hat{\hat{\vec{\theta}}}) \right) \tag{8.11}$$

$$\equiv -2\Delta (\ln \mathcal{L}) \tag{8.12}$$

which, according to the Neyman-Pearson lemma, is stated to give the most optimal test performance. The denominator represents the best estimate for the unconditional fit, i. e. with both μ and $\vec{\theta}$ being free parameters of the minimisation procedure, while the numerator is the minimised negative log-likelihood function with respect to all $\vec{\theta}$, where μ is fixed to zero, indicating the null hypothesis. The latter is also referred to as the conditional minimisation.

The test statistic defined as above holds for the best estimate $\hat{\mu}$ found to be zero or above. As stated above, it is not expected for the signal to cause negative interference phenomena with the background processes, hence $\hat{\mu} < 0$ is not part of the signal model. Therefore, a result of the test statistic given the observed data which yields $\hat{\mu}$ to be below zero does not correspond to expecting any signal contribution and $q(\mu = 0)$ is set to zero if $\hat{\mu} < 0$.

Given the test statistic defined as in Eq. (8.10), the total uncertainty on the final measurement of $\hat{\mu}$ can be extracted by the variation of $q(\mu = 0)$ of one unit up with respect to the minimum, which corresponds to a shift in $\hat{\mu}$ of ± 1 standard deviation.

Commonly, the measurement is performed twice with slight modifications yielding an *observed* as well as an *expected* measurement result. The observed result is obtained by using real experimental data for the fitting procedure. In order to be able to compare this measurement to theoretical predictions, the measurement is repeated with replacing the real experimental data with the sum of all expectations for all contributing processes, taken either from MC simulations or data-driven estimates. This is the generally accepted procedure for obtaining expected measurement results. The sum of all expectations emulating the experimental data is called the Asimov dataset. It has solely statistical Poisson uncertainties assigned to it. Ultimately, the measurement objective is to obtain an observed and expected significance for the observation of the $W^{\pm}W^{\pm}jj$-EW6 and an observed and expected $\hat{\mu}$ for the fiducial cross-section measurement.

In view of the measurement including two control regions and an unconstrained normalisation factor for the $W^{\pm}Z$ process in the statistical analysis, the method of obtaining the expected measurement results is slightly adjusted. As stated above, in light of previous results [15], it is expected that the normalisation factor μ_{WZ} is significantly different from 1 when fitting to observed data in the $W^{\pm}Z$ control region. In order to incorporate this information already in the expected quantities, μ_{WZ}, in the complete expected fit, is set to the value obtained by an upstream and independent fit in the $W^{\pm}Z$ control region to experimental data. This means, the prediction of the $W^{\pm}Z$ process in all regions of the fit of the Asimov dataset is already adjusted for the discrepancy between observed and expected event yields in the $W^{\pm}Z$ control region. This ensures that the expected and observed quantities remain comparable only in light of the change of the signal contribution. Similarly, the inclusion of information of data in the low-m_{jj} control region is expected to constrain the contribution from the non-prompt lepton background. However, this is not taken into account in the fitting strategy for the expected quantities as there is no independent normalisation factor for this background contribution.

8.3 Strategy of the Fiducial Cross-section Measurement

Extracting a fiducial cross-section from an experimental measurement necessarily involves the transition from reconstruction level to particle level quantities. The observed number of events in the signal region needs to be converted into a fiducial cross-section, defined in the fiducial region at particle level. This procedure is commonly called extrapolation of the cross-section measurement from the signal into the fiducial region. The mathematical formulation in its fundamentals is, hence, in general terms related to the folding procedure, discussed in Sec. 7.6.2, simply with inverse objective. As expected, some peculiarities arise, which are a result of the aim to compare the measured fiducial cross-section $\sigma^{\text{fid}}_{\text{meas}}$ to its theoretical prediction from MC simulations $\sigma^{\text{fid}}_{\text{theo}}$, and the utilisation of a binned measurement in the signal region to extract the fiducial cross-section. These, especially, concern the treatment of theoretical modelling uncertainties. This section aims at giving a closer look into the details of defining the ingredients of the measurement.

The theoretical cross-section predicted by simulation in the fiducial region $\sigma^{\text{fid}}_{\text{theo}}$ is defined in Eq. (6.5). It is subject to modelling uncertainties originating from the limited theoretical understanding in the simulation as discussed in Sec. 6.5. Accounting for these uncertainties and adopting the notation from the mathematical formulation of the statistical analysis, Eq. (6.5) is specified to:

$$\sigma^{\text{fid}}_{\text{theo}}(\vec{\theta}_{\text{theo}}) = \left(A \cdot \sigma^{\text{gen}}_{\text{theo}}\right)(\vec{\theta}_{\text{theo}}), \tag{8.13}$$

where the theoretical modelling nuisance parameters are indicated with $\vec{\theta}_{\text{theo}}$. Obviously, the predicted cross-section does not depend on experimental nuisance parameters. Since the theoretical cross-section is not derived differentially in this analysis, the theoretical uncertainties are normalisation uncertainties only.

The measured fiducial cross-section is extracted from the fit to observed data via Eq. (8.3):

$$\sigma^{\text{fid}}_{\text{meas}}(\vec{\theta}) = \hat{\mu}_{\text{obs}}(\vec{\theta}) \cdot \sigma^{\text{fid}}_{\text{theo}}(\vec{\theta}_{\text{theo}}). \tag{8.14}$$

It receives uncertainties from theoretical normalisation uncertainties $\vec{\theta}_{\text{theo}}$ on the signal prediction $\sigma^{\text{fid}}_{\text{theo}}$ as well as from all nuisance parameter variations included in the statistical analysis which determines $\hat{\mu}_{\text{obs}}$. The complete and possible set of uncertainties on $\hat{\mu}$ are of both experimental and theoretical origin. In general, they include the theoretical normalisation uncertainties on the signal prediction.

In the fitting procedure, however, all normalisation uncertainties on the signal prediction have no effect on the value of the best estimate $\hat{\mu}_{\text{obs}}$. They only affect its uncertainty. This is true because it is always more profitable for the fit to vary μ if possible, as it covers the same effect but is unconstrained, rather than any constrained normalisation NP of the signal prediction. Hence, the effect of any normalisation NP of the signal prediction is precisely 100% anti-correlated with the effect on $\hat{\mu}_{\text{obs}}$.

Consequently, the theoretical normalisation uncertainties of the signal prediction on the best fit value $\hat{\mu}_{\text{obs}}$ and the theoretical normalisation uncertainties $\vec{\theta}_{\text{theo}}$ on the signal prediction $\sigma^{\text{fid}}_{\text{theo}}$ in Eq. (8.14) cannot be treated independently. They are precisely 100% anti-correlated and their effects cancel each other.

The strategy, which is therefore pursued in the statistical analysis at hand is the following. Those parts of the signal modelling uncertainties, which are exactly anti-correlated with the theoretical normalisation uncertainties of $\sigma^{\text{fid}}_{\text{theo}}$ are omitted when calculating the measured fiducial cross-section from Eq. (8.14). Simultaneously, theoretical modelling uncertainties on $\sigma^{\text{fid}}_{\text{theo}}$ are not added. Hence, Eq. (8.14) transforms to:

$$\sigma^{\text{fid}}_{\text{meas}}(\vec{\theta}) = \hat{\mu}_{\text{obs}}(\vec{\theta}_{\text{red}}) \cdot \sigma^{\text{fid}}_{\text{theo}}, \tag{8.15}$$

where $\vec{\theta}_{\text{red}}$ excludes parts of the signal modelling uncertainties with normalisation effect. The derivation of the omitted parts is not straight forward in the multi-bin fit pursued in this analysis and is expanded in the following. When calculating the measured fiducial cross-section, the two quantities of the right hand side of Eq. (8.15) can be interpreted as independent and the uncertainty on $\sigma^{\text{fid}}_{\text{meas}}$ can directly be propagated from the measurement of $\hat{\mu}_{\text{obs}}$.

The strategy pursued in this analysis is a fit in multiple bins of the invariant mass of the tagging jet system, m_{jj}, in the signal region. This means that not only the normalisation of the signal expectation is subject of the measurement but also its spectrum, i. e. the shape in the differential m_{jj} distribution in the signal region. Like the normalisation, this shape is dependent on the underlying theoretical modelling and as such affected by modelling uncertainties.

With Eq. (8.5), (8.13), and (8.15) the overall expected number of events in the signal region (SR) can be expressed as:

$$\nu^{\text{SR}}_{S} = \mu(\vec{\theta}) \cdot \left[(\sigma^{\text{gen}}_{\text{theo}} \cdot A)(\vec{\theta}_{\text{theo}}) \cdot C^{\text{eff}}(\vec{\theta})\right]_{S} \cdot L_{\text{inst}}. \tag{8.16}$$

Now, by adopting the notation from the folding prescription in Sec. 7.6.2, this is translated into a differential quantity in bins of m_{jj}, with index i and j at particle and reconstruction level, respectively[6]:

$$\nu^{\text{SR}}_{j,S} = \mu(\vec{\theta}) \cdot \sum_{i} \left[(\sigma^{\text{gen}}_{\text{theo}} \cdot A_i)(\vec{\theta}_{\text{theo}}) \cdot C^{\text{eff}}_{ji}(\vec{\theta})\right]_{S} \cdot L_{\text{inst}}. \tag{8.17}$$

The acceptance A_i is binned at particle level, while the efficiency C^{eff}_{ji} is binned in both particle and reconstruction level m_{jj}. Comparing to Eq. (7.14)[7] it can be specified as:

$$C^{\text{eff}}_{ji} = \frac{N^{\text{SR}}_{j}}{N^{\text{fid}}_{i}}, \tag{8.18}$$

which shows that it receives contributions from theoretical (via N^{fid}_{i}) as well as experimental (via N^{SR}_{j}) uncertainties.

Comparing the predicted cross-section in Eq. (8.13) and the number of events as input to the statistical analysis in Eq. (8.17) it can be deduced that normalisation uncertainties on the product $(\sigma^{\text{gen}}_{\text{theo}} \cdot A)$ in the latter are not to be included as these are also included in and anti-correlated with the uncertainties on the predicted cross-section. However, the acceptance is evaluated in bins i in order to account for bin migration effects between the particle and reconstruction level bins in m_{jj} via the efficiency matrix C^{eff}_{ji}. This means, the A_i are subject to shape uncertainties originating from theoretical modelling variations. Since these are not included in the predicted cross-section, and hence, exhibit no anti-correlation, they remain

[6] Comparing to the notation of Eq. (8.6), the indices correspond in detail to: the channel/region is $c = \text{SR}$, the bin at reconstruction level is $j = j$, the process is $p = S$. Since the theoretical modelling uncertainties are derived collectively in all channels (cf. Sec. 7.6.2), the six different channels in the signal region are not further specified.

[7] Note that $R = \text{SR}$ and $T = \text{fid}$ correspond to the signal and fiducial region, respectively.

included in the measurement of μ. In practice, the modelling uncertainties are evaluated on $\nu_{j,S}^{\mathrm{SR}}$, more specifically on the product of generator level cross-section, acceptance and efficiency normalised by the luminosity. Hence, this quantity, when evaluating the theoretical modelling uncertainties on the expected signal event count, needs to be normalised by $(\sigma_{\mathrm{theo}}^{\mathrm{gen}} \cdot A)$. This leads to the following adjustments of Eq. (8.17):

$$\nu_{j,S}^{\mathrm{SR}} = \mu(\vec{\theta}) \left[\sigma_{\mathrm{theo}}^{\mathrm{gen}} \cdot A\right]_S \cdot \sum_i \left[\left(\frac{\sigma^{\mathrm{gen}} \cdot A_i \cdot C_{ji}^{\mathrm{eff}}(\vec{\theta}_{\mathrm{experim}})}{\sigma_{\mathrm{theo}}^{\mathrm{gen}} \cdot A} \right) (\vec{\theta}_{\mathrm{theo}}) \right]_S \cdot L_{\mathrm{inst}}. \tag{8.19}$$

The first product $\left[\sigma_{\mathrm{theo}}^{\mathrm{gen}} \cdot A\right]_S$ is fixed and not subject to theoretical modelling variations, while the complete term in round brackets is varied when evaluating these uncertainties. For completeness the nuisance parameter dependence of C_{ji}^{eff} is split into theoretical and experimental sets.

In the above procedure, normalisation effects of the theoretical variations can still remain. These enter via C_{ji}^{eff} if events migrate in- or outside the signal region when varying from the nominal central value of theoretical parameter that do not migrate at particle level (i. e. N_j^{SR} changes while N_i^{fid} does not and, hence does not affect A_i). This effect, as is shown in Sec. 8.5, is negligible.

With this procedure, the measured cross-section can eventually be extracted from the result of the statistical analysis with Eq. (8.15), including all information on the best estimates of all nuisance parameters considered.

8.4 Control Regions

The statistical analysis of the experimental data, alongside the signal region, includes two control regions. The exact definitions, event yields and systematic uncertainties are summarised in this section.

8.4.1 $W^{\pm}Z$ Control Region

The dominant background contribution in the signal region is the fully leptonic $W^{\pm}Z$ production in association with two jets. A mild overestimation of its normalisation in MC simulation (approx. 20%) is reported in Ref. [15]. Hence, a dedicated control region is used to measure the normalisation of this process in experimental data. This control region is part of the statistical analysis of the observed experimental data.

Events from $W^{\pm}Z$ production enter the signal region if one lepton from the Z boson decay fails kinematic (transverse momentum or rapidity), reconstruction, or identification requirements imposed on the `veto` lepton set, and the remaining two leptons identified form a same charge pair. In addition, the neutrino from the leptonic $W^{\pm}$ boson decay gives enough missing transverse momentum and the $W^{\pm}Z$ pair is produced in association with two energetic jets.

The requirements for the $W^{\pm}Z$ control region are hence focusing on selecting an additional lepton in order to enhance the $W^{\pm}Z$ contribution while at the same time staying as close to the signal region as possible to avoid large differences when utilising the normalisation obtained from this control region. The selection criteria for events to enter the $W^{\pm}Z$ control region are detailed in Tab. 8.3.

In addition to the two `analysis` selected leptons, one lepton with `veto` selection requirements and transverse momentum exceeding 15 GeV must exist. Two of the three selected leptons must form a pair with opposite electric charge and same lepton flavour. Moreover the invariant mass of the system of all three selected leptons m_{lll} must be greater than 106 GeV which reduces the contribution from Z+jets and $Z\gamma$ production.

The jet and VBS selection requirements are weakened to gain sufficient statistics. The additional requirements on the transverse momenta of the selected jets are dropped and the minimum invariant mass requirement of the two-jet system is chosen to be 200 GeV. These selection criteria move this CR quite substantially away from the signal region. Future analyses, profiting from increased statistics, have the opportunity to better align the requirements with the signal region ones.

Table 8.3: Definition of the selection requirements for events to enter the $W^{\pm}Z$ CR.

Observable	Cut value	Explanation
Event preselection as in signal region (cf. Tab. 7.4)		
Lepton event selection:		
$N(\ell_{\text{ana}})$	$== 2$	Number of charged leptons ($e^{\pm}$ or $\mu^{\pm}$) with `analysis` selection
Trigger match	$\ell_1 \,\|\|\, \ell_2$	At least one `analysis` lepton fired the event trigger
m_{ll}	$> 20\,\text{GeV}$	Minimum invariant mass of leading `analysis` lepton pair
E_T^{miss}	$> 30\,\text{GeV}$	Minimum missing transverse energy
$W^{\pm}Z$ event selection:		
$N(\ell_{\text{veto}})$	$== 1$	One additional lepton ($e^{\pm}$ or $\mu^{\pm}$) with `veto` selection
$p_{\text{T}}(\ell_{\text{veto}})$	$> 15\,\text{GeV}$	Minimum p_{T} of `veto` lepton
OCSF pair	✓	Two selected leptons (`analysis` or `veto`) form an opposite-charge-same-flavour pair
m_{lll}	$> 106\,\text{GeV}$	Minimum invariant mass of two `analysis` and one `veto` lepton
Jet event selection:		
$N(j)$	≥ 2	Minimum number of `analysis` jets
N(b-jet)	$== 0$	Veto if any `analysis` jet is identified as b-jet
VBS selection:		
$\Delta Y(jj)$	> 2.0	Minimum rapidity separation between leading jet pair
m_{jj}	$> 200\,\text{GeV}$	Minimum invariant mass of leading jet pair

The $W^{\pm}Z$ control region is evaluated in one combined channel $\ell\ell'\ell''$, with $\ell^{(\prime\prime)} = e^{\pm}$ or $\mu^{\pm}$. The estimated event yields an their total uncertainties for all processes in the $W^{\pm}Z$ control region are summarised in Tab. 8.4. The purity in $W^{\pm}Z$ events is above 86%. No events from the $W^{\pm}W^{\pm}jj$-EW4 and $W^{\pm}\gamma$ processes pass the selection criteria. The $W^{\pm}W^{\pm}jj$-EW6 signal contribution is 0.002 events. As expected, the MC predictions overestimate the experimental data in this CR. Detailed numbers for the event yields and total uncertainties of all processes of the other prompt category can be found in Tab. E.1 in the appendix.

As indicated in Tab. 8.2, backgrounds estimated with data-driven methods in the signal region are not considered in the final statistical analysis in this region, which is doubtlessly an aspect for future improvement and sanity of the analysis. This affects the background due to electron charge misidentification as well as non-prompt leptons. For completeness, the event yields of these background contributions are estimated from MC simulation in this section and listed in Tab. 8.4. For simplicity, whole process categories are attributed to either one or the other contribution. The processes of Z+jets and W^+W^- production are counted as background due to electron charge misidentification while the processes of $t\bar{t}$ and $W^{\pm}$+jets production are taken to be due to non-prompt leptons. Both backgrounds contribute below 1% and 2%, respectively, of the total expected event yield in this CR. Form the simple comparison of results in Ref. [1], on which this work is based on, and Ref. [235], their maximal impact on the final measured cross-section can be estimated to below 2%. However, studies in Ref. [235] do not assign uncertainties on these contributions. Moreover, they contain several additional slight changes w.r.t. the analysis conducted in Ref. [1].

As in the signal region, the $V\gamma$ processes are scaled to 1.77, a normalisation correction determined in a dedicated region not part of the statistical analysis (cf. Sec. D.2.3).

The relative impact of experimental and theoretical modelling uncertainties on the event yields are summarised in Tables 8.5 and 8.6 in respective categories. Dominant experimental uncertainties for all processes are jet-related parameter variations, among them the

Table 8.4: Estimated event yields and their total uncertainties of all SM processes in the $W^{\pm}Z$ control region before the statistical analysis. "Other prompt" contains MC-based predictions of the processes of $t\bar{t}V$, ZZ, and triboson production. The "non-prompt" and "charge misID" estimates are taken from the MC simulated processes $t\bar{t}$, and Z+jets and $W^{+}W^{-}$, respectively. The yields of experimental data taken in the years 2015 and 2016 in Run 2 of the LHC with the ATLAS detector are given as well. Numbers are given in the combined $\ell\ell'\ell''$ channel, with $\ell^{(\prime\prime)} = e^{\pm}$ or $\mu^{\pm}$.

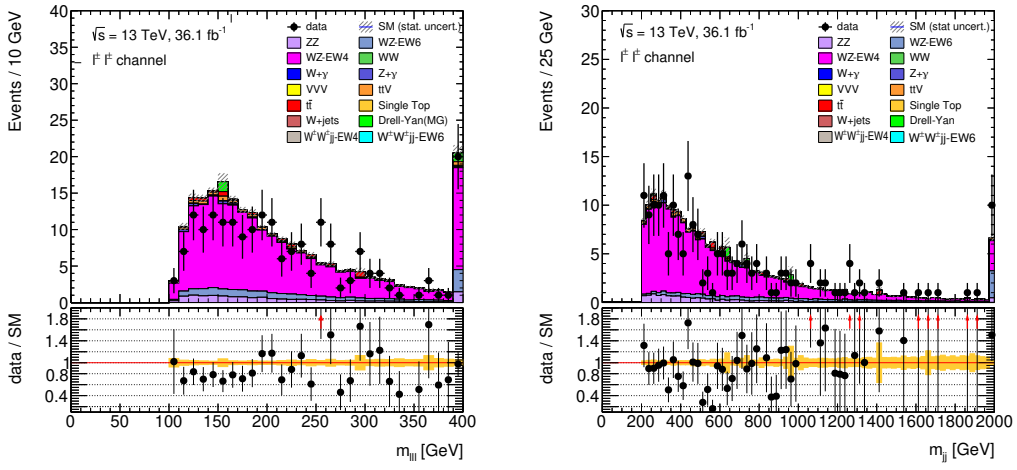
Process	$\ell\ell'\ell''$ channel
$W^{\pm}Z$	197.09 ± 68.84
$W^{\pm}W^{\pm}jj$-EW4	–
Other prompt	21.55 ± 3.93
Non-prompt	4.27 ± 1.02
Charge misID	2.56 ± 1.40
$V\gamma$	2.68 ± 1.83
$W^{\pm}W^{\pm}jj$-EW6 (Sherpa23jLO)	< 0.01
Total expected	228.15 ± 69.02
Data 2015/16	201

Table 8.5: Relative impact of experimental systematic uncertainties on the event yields of all predictions based on MC simulation in the $W^{\pm}Z$ control region condensed in six categories. Lepton uncertainties contain all variations in the measurement of electrons and muons, except the trigger efficiency which is quoted as separate value. Jet uncertainties contain all variations in the measurement of jets, except the variations of the flavour tagging which are quoted as b-tag inefficiency uncertainties. The spread in value indicates the variation of the impact for all subprocesses involved in the other prompt category. Detailed numbers for all channels and processes can be found in Tab. E.2 in the appendix.

Process	Systematic Uncertainty [%]					
	Leptons	Trig. eff.	Jet	b-tag ineff.	Pile-up rwt.	E_T^{miss}
$W^{\pm}Z$	2	< 1	6	2	1	1
Other prompt	$1 - 2$	< 1	$7 - 11$	$2 - 13$	$< 1 - 4$	$< 1 - 4$
$V\gamma$	1	< 1	61	2	7	23
$W^{\pm}W^{\pm}jj$-EW6	1	< 1	< 1	1	43	< 1

Table 8.6: Relative impact of modelling uncertainties on the $W^{\pm}Z$ and $W^{\pm}W^{\pm}jj$-EW6 event yields in the $W^{\pm}Z$ control region. Detailed numbers from all variations are summarised in App. E.1.1.

Process	Modelling Uncertainty [%]				
	MC stat.	μ_R/μ_F	PDF set	α_S	Parton shower
$W^{\pm}Z$	± 1	$^{+35}_{-19}$	$^{+2}_{-1}$	± 2	± 25
$W^{\pm}W^{\pm}jj$-EW6	± 50	± 5	± 4	± 1	–



(a) **(b)**

Figure 8.1: Distributions of the invariant mass of the trilepton and tagging jet system, m_{lll} (a) and m_{jj} (b), respectively, in the $W^{\pm}Z$ control region. The lower pad shows the experimental data relative to the sum of all SM predictions. Uncertainties on the sum of the SM predictions are statistical only. Figures taken from Ref. [232].

jet energy resolution uncertainty being the largest for almost all process. For processes including top quark production, b-jet tagging inefficiency uncertainties are dominant. For the $W^{\pm}W^{\pm}jj$-EW6 signal process, statistics is poor with only two simulated events surviving the selection criteria. Hence, uncertainties are affected by statistics as well. Detailed numbers for all channels and processes can be found in Tab. E.2 in the appendix.

Detailed modelling uncertainties are provided for the $W^{\pm}Z$ and $W^{\pm}W^{\pm}jj$-EW6 processes only. Comprehensive variation results contributing to the scale and PDF+α_S envelopes are provided in Tables E.3 and E.4 in the appendix, respectively. As in the signal region, dominant uncertainties are obtained by the variation of the renormalisation and factorisation scales for the $W^{\pm}Z$ and $W^{\pm}W^{\pm}jj$-EW6, respectively. Again as in the signal region, the renormalisation scale variations on the $W^{\pm}Z$-EW4 process have a largely asymmetric effect and are dominant among all modelling uncertainties.

Uncertainties due to the variation of parton shower, matching, and merging parameters are only provided for the $W^{\pm}Z$ process. These are calculated with the identical strategy as in the signal region, detailed in Sec. 7.6.2. This variation yields the second largest modelling uncertainty source of the $W^{\pm}Z$ process.

The reason for not providing these uncertainties for the $W^{\pm}W^{\pm}jj$-EW6 process is its very small contribution in the $W^{\pm}Z$ control region as well as the fact that these would have to be transferred to reconstruction level via folding, which is not evaluated for the $W^{\pm}Z$ control region.

Good agreement between experimental data and the SM prediction is found in differential kinematic distributions in the $W^{\pm}Z$ control region. Exemplary, the invariant mass of the trilepton and tagging jet system, m_{lll} and m_{jj}, respectively, are shown in Fig. 8.1.

8.4.2 Low-m_{jj} Control Region

The low-m_{jj} control region is designed to maximally exploit the information of the m_{jj} spectrum. It has a small signal contribution, while the composition of the different background processes is similar to the signal region.

This control region is defined identically to the signal region, defined in Tab. 7.4, except for the requirement of m_{jj} which is altered to:

$$200\,\text{GeV} < m_{jj} < 500\,\text{GeV},$$

ensuring orthogonality to the signal region. With this definition, the control region can be

added in straightforward manner to the statistical analysis. The choice of not fully exploiting the m_{jj} spectrum, but rather rejecting the region below $m_{jj} = 200\,\text{GeV}$ has several, mostly theoretically motivated reasons. From the m_{jj} distribution at particle level in Fig. 6.6(a), the contribution from diagrams with three resonant $W^{\pm}$ bosons (cf. Feynam diagram in Fig. 5.3(c)) at m_{jj} just below 100 GeV is clearly visible. These processes are included in the signal samples for reasons of completeness, however, they do not exhibit the process of interest which is the scattering of two like-charge $W^{\pm}$ bosons. Moreover, the considerable disagreement of the three signal simulations in the region of low m_{jj} is evident in this figure. Possible sources for these discrepancies have been explored in Chapter 6. In order to remain to the greatest extent possible independent from simulations in this case, this region is generously rejected in the definition of the control region.

Tab. 8.7 summarises the expected event yields and their total uncertainties of all relevant processes, together with the yields of experimental data taken in the years 2015 and 2016 in Run 2 of the LHC with the ATLAS detector in the low-m_{jj} control region. Detailed numbers for the event yields and total uncertainties of all processes of the other prompt category can be found in Tab. E.5 in the appendix.

A total of 101 experimental data events are selected into the low-m_{jj} control region. The total signal plus background estimates agrees with experimental data exhibiting a background only event yield of approx. 90 ± 16. Largest contributions in this region come from the $W^{\pm}Z$ process and processes involving non-prompt leptons misidendified as jets or from hadron decays. Since the first is primarily constrained in the $W^{\pm}Z$ control region, this region is utilised to constrain the latter processes. It is beneficial to split it into different channels defined by lepton flavours and charge, as the contributions from both dominant backgrounds vary differently in these channels. Except for the $\mu^{\pm}\mu^{\pm}$ channels, the signal contribution is approx. 10% or below.

Though, not having adjusted the normalisation of the $W^{\pm}Z$ process yet, it can be seen that the event yields of experimental data in the $e^{-}\mu^{-} + \mu^{-}e^{-}$ channel is substantially lower than the predictions, and vice versa in the $e^{-}e^{-}$ channel.

As in the signal and $W^{\pm}Z$ control region, the $V\gamma$ processes are scaled by a factor of 1.77.

Due to the proximity of the control region to the signal region, systematic uncertainties in this control region are discussed in detail together with the uncertainties in the signal region in Sec. 8.5.

8.5 Treatment of Uncertainties

As explained in Sec. 8.2.2, nuisance parameters are added to the statistical model to account for the uncertainties of a given event yield estimate. A total of 119 independent uncertainty sources are considered in this analysis. They are summarised and explained in Sec. 7.6, where the quantitative impact in the signal region is discussed as well. For the extraction of the discovery significance as well as the cross-section of the $W^{\pm}W^{\pm}jj$-EW6 signal process, the tagging jet invariant mass spectrum, m_{jj}, is utilised in the fit. Hence, detailed information on systematic uncertainties in this kinematic distribution is needed for the statistical analysis. Therefore, uncertainties, if not solely affecting the normalisation of a given prediction, are evaluated in bins of m_{jj}. In the terminology of the statistical analysis, established in Sec. 8.2.2, these are called shape uncertainties with external constraints and denoted β_{pjc}, depending on the process p, reconstruction level m_{jj} bin j, and channel/region c.

In the following, the treatment of the different categories of systematic uncertainties is specified for the SM analysis. In Tab. 8.8, the association of all nuisance parameters to the considered processes and their inclusion in the different regions of the fit are specified.

8.5.1 Experimental Systematic Uncertainties

All sources of experimental object and event systematic uncertainties are summarised in Tab. 7.6. Besides the luminosity uncertainty, these are added as shape plus normalisation uncertainty for all event yields estimated from MC simulations in all regions of the fit. The dominant experimental systematic sources for the majority of the processes in all regions

Table 8.7: Estimated event yields and their total uncertainties of all SM processes in the low-m_{jj} control region before the statistical analysis. "Other prompt" contains MC-based predictions of the processes of $t\bar{t}V$, ZZ, and triboson production. The yields of experimental data taken in the years 2015 and 2016 in Run 2 of the LHC with the ATLAS detector are given as well. Numbers are given in all lepton flavour and charge split, as well as in the combined $\ell^{\pm}\ell^{\pm}$ channel.

Process	Channel						
	e^+e^+	e^-e^-	$e^+\mu^+ + \mu^+e^+$	$e^-\mu^- + \mu^-e^-$	$\mu^+\mu^+$	$\mu^-\mu^-$	$\ell^{\pm}\ell^{\pm}$
$W^{\pm}Z$	2.02 ± 0.65	1.57 ± 0.48	13.79 ± 3.92	10.31 ± 2.99	5.76 ± 1.65	3.95 ± 1.17	37.40 ± 10.55
$W^{\pm}W^{\pm}jj$-EW4	0.24 ± 0.07	0.15 ± 0.05	1.99 ± 0.56	1.15 ± 0.32	1.16 ± 0.33	0.64 ± 0.18	5.32 ± 1.50
Other prompt	0.28 ± 0.09	0.16 ± 0.07	1.20 ± 0.25	0.77 ± 0.20	0.63 ± 0.14	0.37 ± 0.12	3.40 ± 0.64
Non-prompt	0.71 ± 0.68	4.37 ± 2.48	12.78 ± 5.68	8.62 ± 4.04	2.43 ± 2.05	1.18 ± 0.27	30.08 ± 11.09
Charge misID	1.70 ± 0.19	1.77 ± 0.21	4.00 ± 0.42	3.56 ± 0.48	–	–	11.03 ± 1.04
$V\gamma$	0.18 ± 0.10	0.26 ± 0.19	0.28 ± 1.04	2.20 ± 1.20	–	–	2.93 ± 1.90
$W^{\pm}W^{\pm}jj$-EW6 (Sherpa23jLO)	0.64 ± 0.11	0.47 ± 0.10	2.97 ± 0.50	1.99 ± 0.35	1.83 ± 0.31	1.11 ± 0.19	9.01 ± 1.53
Total expected	5.77 ± 0.98	8.75 ± 2.54	37.01 ± 7.04	28.60 ± 5.22	11.81 ± 2.67	7.25 ± 1.23	99.17 ± 15.75
Data 2015/16	5	3	39	38	10	6	101

Table 8.8: List of nuisance parameters included for each process in the signal region and low-m_{jj} ($W^{\pm}Z$) control region. NPs are categorised with effects on: shape (and normalisation) (β_{cjp}), normalisation-only (η_{cp}), and statistical (γ_{cj}) as done in the statistical framework [239]. Different treatment of NPs in the $W^{\pm}Z$ control region is indicated in parentheses. A complete list of NPs associated to experimental systematic uncertainties is given in Tab. 7.6.

	Process						
Systematic uncert.	$W^{\pm}W^{\pm}jj$-EW6	$W^{\pm}W^{\pm}jj$-EW4	$W^{\pm}Z$	Other prompt	$V\gamma$	Non-prompt	Charge misID
Shape NPs with external constraints β_{cjp} (`HistoSys`):							
All exp. (except `lumi`)	✓	✓	✓	✓	✓	–	–
`CF_SFunc/NoCorr`	–	–	–	–	–	–	✓(–)
`FakeEl/Mu`	–	–	–	–	–	✓(–)	–
`*_TheoScale/PDF/`α_S	✓	✓	✓	–	–	–	–
`*_TheoShower`	✓(–)	✓(–)	✓	–	–	–	–
`*_TheoInterference`	✓(–)	–	–	–	–	–	–
`*_TheoEWCorr`	✓(–)	–	–	–	–	–	–
Normalisation NPs with external constraints η_{cs} (`OverallSys`):							
`lumi`	✓	✓	✓	✓	✓	–	–
`Conv_Model_Vgamma`	–	–	–	–	✓	–	–
`*_XS`	–	–	–	✓	✓	–	–
Constraint bin-by-bin NPs γ_{cb} (`StatError`):							
Statistics (MC and data-driven)	✓	✓	✓	✓	✓	✓(–)	✓(–)

are the jet energy resolution and pileup reweighting data scale factor. Their impact on the MC-estimated event yields in the signal region and low-m_{jj} control region is shown in Fig. 8.2. The one-sided jet energy resolution systematic uncertainty is symmetrised for the final measurement in the statistical framework. The impact of both uncertainty sources stays below 10% in all bins for the dominant $W^{\pm}W^{\pm}jj$-EW6, $W^{\pm}W^{\pm}jj$-EW4 and $W^{\pm}Z$ contributions. For the other prompt and $V\gamma$ processes, these uncertainties are larger, mostly due to statistical limitations of the individual contributions in the signal region.

The luminosity uncertainty is identical for all regions, channels, bins, and processes and added as normalisation uncertainty for each process estimated from MC simulation in each region and channel.

8.5.2 Experimental Uncertainties on Data-driven Background Estimates

The evaluation of uncertainties on the data-driven background estimates from electron charge misidentification and non-prompt leptons is explained in Sec. 7.6.1, where associated nuisance parameters are introduced. The data driven estimates are utilised in the signal region and low-m_{jj} control region. Uncertainties are added as nuisance parameters with shape and normalisation effect in the statistical framework in these regions. In the $W^{\pm}Z$ control region these background processes are not considered due to their minor contribution.

The final estimates for the background contribution due to electron charge misidentification together with the two sources of systematic uncertainties in the signal region and low-m_{jj} control region are shown in Fig. 8.3 for all relevant channels. The one-sided energy correction systematic uncertainty is symmetrised in the final measurement. Both systematic uncertainty sources yield comparable size variations, ranging from a few percent to 20% for a small number of bins. Exact numbers in the low-m_{jj} control region for each relevant channel can be retrieved from Ref. [219], where these are taken from.

The final estimates for the background contribution due to non-prompt leptons from hadron decays or misidendified jets together with the propagated systematic uncertainties on the fake factor measurements for electrons and muons in the signal region and low-m_{jj} control region are shown in Fig. 8.4 for all channels. Systematic uncertainties for both electrons and muons vary substantially over all bins in m_{jj}. They generally have a larger impact than the statistical uncertainties from the fake factor measurement. Exact numbers in the low-m_{jj} control region for all channels can be retrieved from Ref. [232], where these are taken from.

The uncertainty on the normalisation of the $V\gamma$ processes is added as symmetrised constrained normalisation nuisance parameter to the statistical model. It is not dependent on channels or regions.

8.5.3 Modelling Uncertainties on the $W^{\pm}W^{\pm}jj$-EW6 Signal Process

The evaluation of modelling uncertainties and the associated nuisance parameters for the $W^{\pm}W^{\pm}jj$-EW6 signal process at reconstruction level are detailed in Sec. 7.6.2.

The impact of the NLO EW corrections in the fiducial region of this analysis is shown in Sec. 6.7.5 together with a discussion on the consistency of applying these corrections to the nominal Sherpa23jLO signal prediction at reconstruction level. Studies in Ref. [235] show, that the measurement result does not change significantly depending on how these corrections are incorporated in the fit, either as relative correction of the nominal signal prediction or as relative systematic uncertainty on this prediction. As a result, and for the reason of highest consistency, the NLO EW corrections are added as a symmetric, hence conservative, systematic uncertainty on the signal process in the statistical analysis. Another important reason for this decision is the lack of modelling uncertainty estimates on the NLO EW correction at this point. Technically, the relative NLO EW correction obtained from Ref. [228] and shown in Fig. 6.17 is, after folding, applied as relative uncertainty on the nominal Sherpa23jLO prediction of the $W^{\pm}W^{\pm}jj$-EW6 process in the statistical framework.

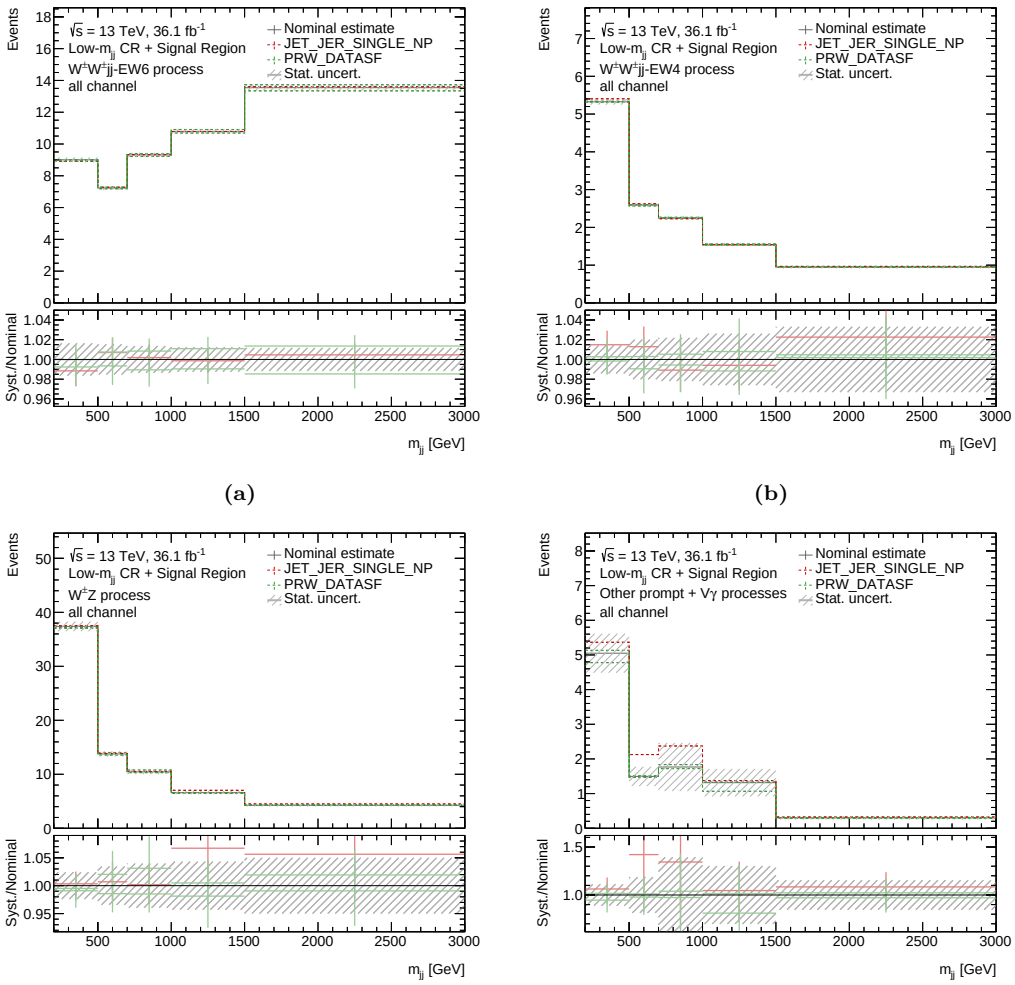


Figure 8.2: Distribution of the invariant mass of the tagging jet system m_{jj} in the signal region and low-m_{jj} control region. The nominal prediction estimated from MC simulation together with the systematic uncertainties from the jet energy resolution (red) and the pileup reweighting data scale factors (green) are shown for the $W^{\pm}W^{\pm}jj$-EW6 (a), $W^{\pm}W^{\pm}jj$-EW4 (b), $W^{\pm}Z$ (c), and the sum of the other prompt and $V\gamma$ (d) processes in the combined $\ell^{\pm}\ell^{\pm}$ channel. The one-sided jet energy resolution systematic uncertainty is symmetrised in the final measurement. The lower pad shows the relative uncertainties. Uncertainties on the nominal estimate are statistical only.

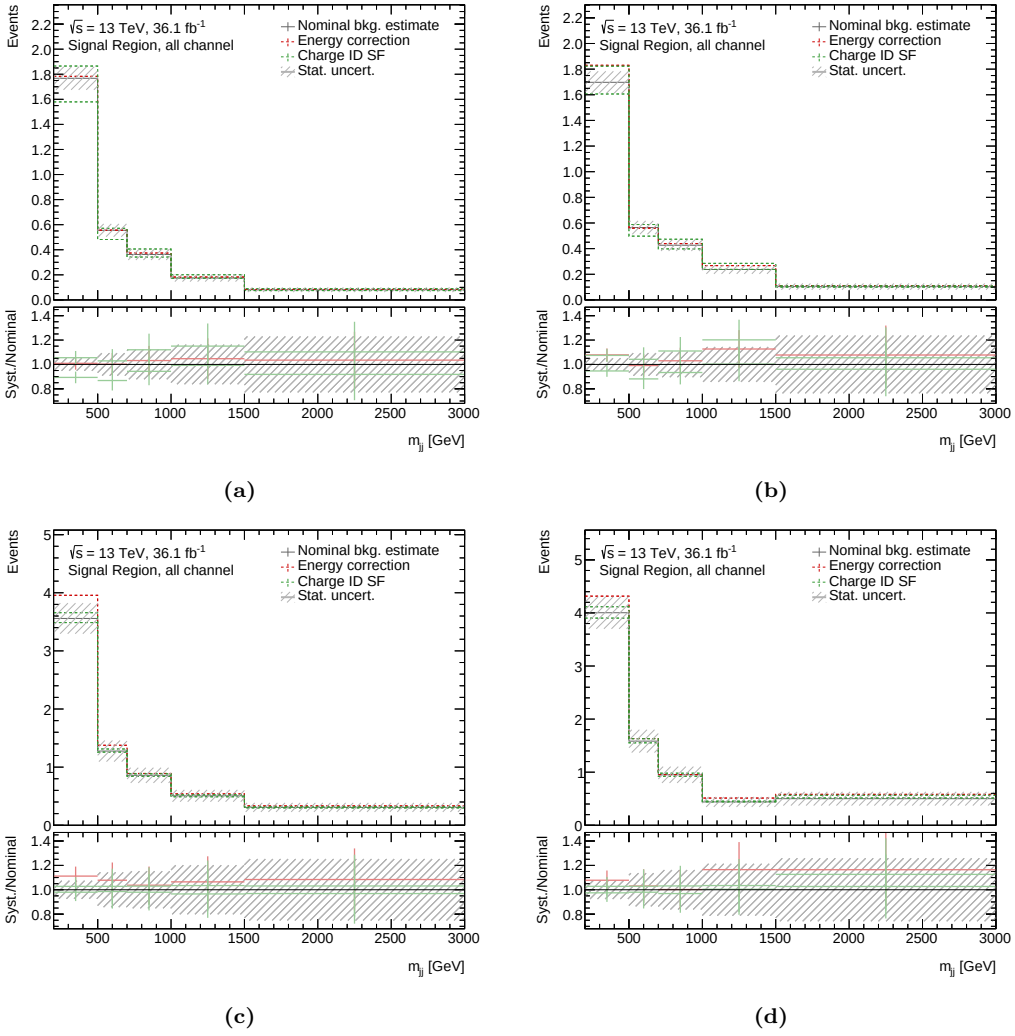


Figure 8.3: Distribution of the invariant mass of the tagging jet system m_{jj} in the signal region and low-m_{jj} control region. The nominal background estimate due to electron charge misidentification together with the systematic uncertainties from the energy correction (red) and the charge (mis)identification scale factors (green) in the channels e^-e^- (a), e^+e^+ (b), $e^-\mu^- + \mu^-e^-$ (c), and $e^+\mu^+ + \mu^+e^+$ (d) are shown. The one-sided energy correction systematic uncertainty is symmetrised in the final measurement. The lower pad shows the relative uncertainties. Uncertainties on the nominal estimate are statistical only. Calculations are based on Ref. [219].

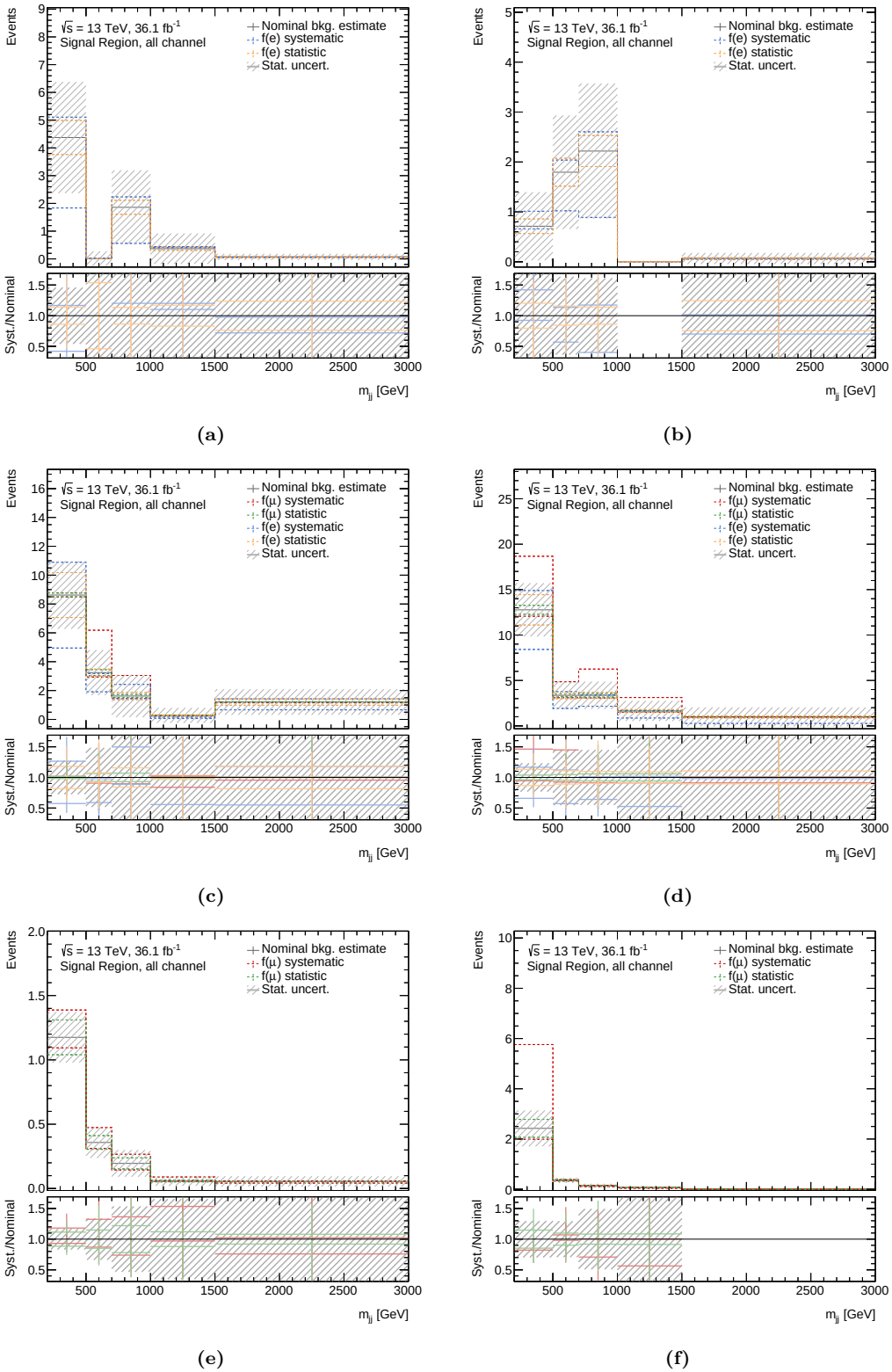
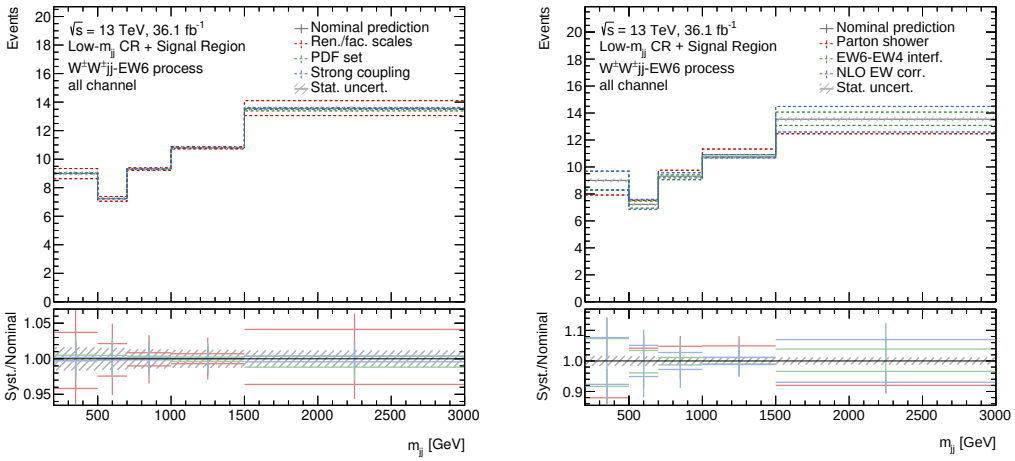


Figure 8.4: Distribution of the invariant mass of the tagging jet system m_{jj} in the signal region and low-m_{jj} control region. The nominal background estimate due to non-prompt leptons together with the separate statistical and systematic uncertainties from the fake factor measurement for electrons $f(e)$ and muons $f(\mu)$ propagated to the final background estimate in the channels e^-e^- (a), e^+e^+ (b), $e^-\mu^- + \mu^-e^-$ (c), $e^+\mu^+ + \mu^+e^+$ (d), $\mu^-\mu^-$ (e), and $\mu^+\mu^+$ (f) are shown. The systematic uncertainties are the combined uncertainties from all systematic sources of the respective fake factor measurement. The lower pad shows the relative uncertainties. Uncertainties on the nominal estimate are statistical only. Calculations are based on Ref. [232].



(a) **(b)**

Figure 8.5: Distribution of the invariant mass of the tagging jet system m_{jj} in the signal region and low-m_{jj} control region. The nominal $W^{\pm}W^{\pm}jj$-EW6 signal estimate from the Sherpa23jLO setup and theoretical modelling uncertainties from: (a) the matrix element calculation, and (b) the parton shower and merging parameter variations, the interference between the $W^{\pm}W^{\pm}jj$-EW6 and $W^{\pm}W^{\pm}jj$-EW4 processes, and the NLO EW correction of the $W^{\pm}W^{\pm}jj$-EW6 at order $\mathcal{O}(\alpha_{EW}^{7})$ (b) are shown. Uncertainties shown in (b) are obtained after folding to reconstruction level as described in Sec. 7.6.2. All modelling uncertainties are evaluated in the combined $\ell^{\pm}\ell^{\pm}$ channel. All uncertainties are normalised as explained in Sec. 8.3. The lower pad shows the relative uncertainties. Uncertainties on the nominal estimate are statistical only.

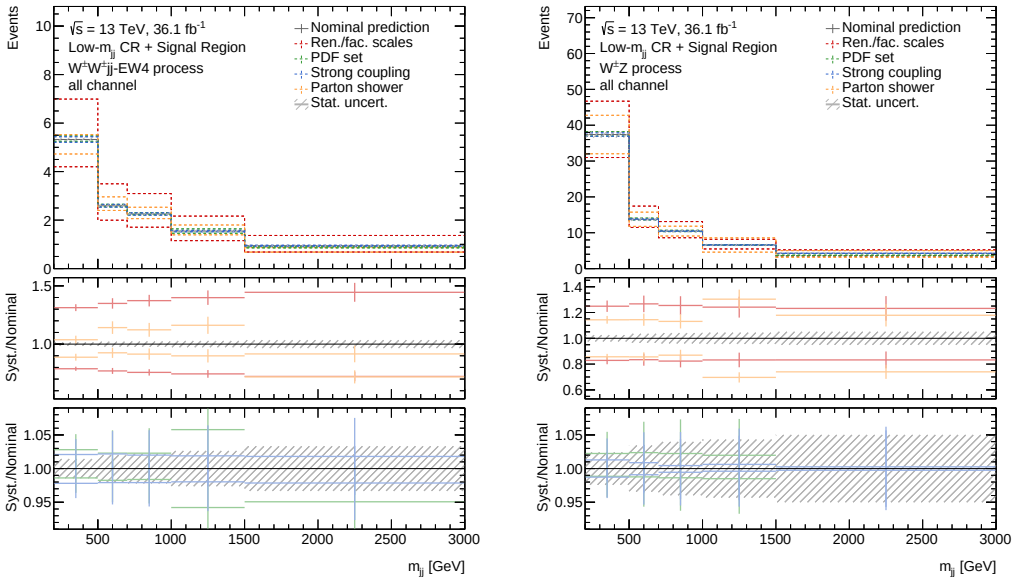
All uncertainties are normalised as explained in Sec. 8.3. As described in Sec. 7.6.2, they are evaluated for the combined $\ell^{\pm}\ell^{\pm}$ channel and the relative uncertainty in this channel is taken to be the relative uncertainty in each flavour- and charge-split channel. Their impact on the total event yield in the statistical analysis in the signal region and low-m_{jj} control region is shown in Fig. 8.5. While uncertainties from the matrix element calculation have minor impact on the shape of the m_{jj} distribution, parton shower and merging, interference and NLO EW correction uncertainties have an impact of approx. 10% at the edges of the spectrum. Distributions for the variations as ingredients to the envelopes of the renormalisation and factorisation scale at reconstruction level are shown in Fig. E.1(a). The impact of the variations of the parton shower and merging parameters as input to the folding procedure at particle level in the fiducial region without m_{jj} requirement are shown in Fig. E.2(a).

As has already been observed in the theoretical studies of the signal process (cf. Sec. B.4.2), the parton shower and merging parameter variations of the $W^{\pm}W^{\pm}jj$-EW6 process in the fiducial region at particle level are largely asymmetric, a feature that propagates to the signal region.

In the $W^{\pm}Z$ control region, only uncertainties from the matrix element calculation are considered. All other sources would have to be folded to reconstruction level, which is not provided in this region, given the very small contribution of the signal process.

8.5.4 Modelling Uncertainties on Background Estimates

Uncertainties of the matrix element calculation, and parton shower, matching and merging description of the $W^{\pm}W^{\pm}jj$-EW4 and $W^{\pm}Z$ background processes are added to the statistical analysis with effect on the shape and normalisation of the m_{jj} distribution. These are evaluated as detailed in Sec. 7.6.2. The impact of these sources of uncertainties on both processes in the signal region and low-m_{jj} control region is shown in Fig. 8.6. As already seen inclusively in the signal region, the renormalisation and factorisation scale uncertainties are the dominant sources for both processes. In both cases, these are driven by the variations of the renormalisation scale as can be seen from Figures E.1(b) and (c) in the appendix, where



(a) **(b)**

Figure 8.6: Distribution of the invariant mass of the tagging jet system m_{jj} in the signal region and low-m_{jj} control region. The nominal $W^{\pm}W^{\pm}jj$-EW4 (a) and $W^{\pm}Z$ (b) estimates and theoretical modelling uncertainties from the matrix element calculation due to the variation of the renormalisation and factorisation scale, the PDF set and its strong coupling value, and the parton shower and merging parameters are shown. The modelling uncertainties are evaluated in the combined $\ell^{\pm}\ell^{\pm}$ channel. The lower pads show the relative uncertainties. Uncertainties on the nominal estimate are statistical only.

the contributions of all scale variations to the scale envelope are shown. From the latter figure it can also be seen, that the scale variations of the $W^{\pm}Z$-EW4 process are independent of the invariant mass of the tagging jet system in the signal region. This is not the case for all other considered processes, where scale variations increase with m_{jj}. Observations described inclusively in the signal region in Sec. 7.6.2 equally hold in the differential case.

Parton shower and merging uncertainties are the second largest source of uncertainty for both processes. For the $W^{\pm}W^{\pm}jj$-EW4 process, the individual variations at particle level in the fiducial region, as shown in Fig. E.2, are folded to reconstruction level via the procedure explained in Sec.7.6.2. Parton shower uncertainties for the $W^{\pm}Z$ process, evaluated as the relative difference between the POWHEG prediction interfaced to either PYTHIA 8 or HERWIG++ on the nominal SHERPA prediction of the $W^{\pm}Z$-EW4 process, in the signal region and low-m_{jj} control region are shown in Fig. E.3 in the appendix.

Uncertainties on the cross-section of the $t\bar{t}V$, ZZ, VVV, and $V\gamma$ processes (cf. Tab. 7.13), are added as constrained normalisation nuisance parameters to the statistical model.

8.5.5 Statistical Uncertainties

Statistical uncertainties from all estimated event yields are considered as bin-by-bin independent constrained scale factors in the statistical analysis. In the statistical model described in Sec. 8.2.2, independent scale factors for each process are introduced. This strategy would hence add one nuisance parameter for each bin in each channel and region for each considered process. In order to reduce the complexity of the statistical model, statistical uncertainties from all contribution processes are combined in each bin of each channel and region according to the Beeston-Barlow method in the `HistFactory` implementation [239]. This reduces the nuisance parameter dependence on the specific process, i. e. $\gamma_{cjp} \rightarrow \gamma_{cj}$. Eventually, the relative statistical uncertainty on the sum of all contributions is taken to be the nuisance parameter in a given bin and channel/region.

8.6 Results

The combined simultaneous fit to observed data, taken at $\sqrt{s} = 13\,\text{TeV}$ centre-of-mass energy in the years 2015 and 2016 of the Run 2 data-taking period of the LHC with the ATLAS experiment, in all signal and control regions yields a signal strength of the $W^{\pm}W^{\pm}jj$-EW6 process with respect to the nominal Sherpa23jLO prediction of:

$$\hat{\mu}_{\text{obs}} = 1.44\ ^{+0.26}_{-0.24}\ (\text{stat})\ ^{+0.09}_{-0.08}\ (\text{mod})\ ^{+0.13}_{-0.11}\ (\text{sys}) \tag{8.20}$$

$$= 1.44\ ^{+0.29}_{-0.27}\ (\text{total}). \tag{8.21}$$

The sources of uncertainties are split into the following categories: statistical data uncertainties (stat), theoretical modelling uncertainties (mod), and all experimental uncertainties (sys). Modelling uncertainties quoted here exclude acceptance normalisation effects of the $W^{\pm}W^{\pm}jj$-EW6 signal process as explained in Sec. 8.3. Hence, it is explicitly noted here, that the uncertainties on μ_{obs} are not complete in this presentation. However, the form of presentation is chosen such that the result of the measured fiducial cross-section, shown later, can be reconstructed.

The result on the strength of the combined strong and electroweak $W^{\pm}Z$ process is:

$$\hat{\mu}^{\text{obs}}_{WZ} = 0.86 \pm 0.07\ (\text{stat})\ ^{+0.31}_{-0.23}\ (\text{mod})\ ^{+0.18}_{-0.08}\ (\text{sys}) \tag{8.22}$$

$$= 0.86\ ^{+0.36}_{-0.25}\ (\text{total}). \tag{8.23}$$

The corresponding two-staged fit to Asimov data, as described in Sec. 8.2.2, yields the expected signal and $W^{\pm}Z$ process strength of:

$$\hat{\mu}_{\text{exp}} = 1.00\ ^{+0.25}_{-0.23}\ (\text{stat})\ ^{+0.09}_{-0.09}\ (\text{mod})\ ^{+0.11}_{-0.12}\ (\text{sys}) \tag{8.24}$$

$$= 1.00\ ^{+0.28}_{-0.27}\ (\text{total}), \tag{8.25}$$

and:

$$\hat{\mu}^{\text{exp}}_{WZ} = 0.91 \pm 0.07\ (\text{stat})\ ^{+0.35}_{-0.23}\ (\text{mod})\ ^{+0.16}_{-0.08}\ (\text{sys}) \tag{8.26}$$

$$= 0.91\ ^{+0.39}_{-0.25}\ (\text{total}), \tag{8.27}$$

respectively.

Fig. 8.7 shows the ratio of the likelihood functions, defined in Eq. (8.12) (by omitting a scaling factor), as a function of the signal strength parameter μ with all other nuisance parameters fixed to the best estimate for the fit to observed and Asimov data. With this scan different hypotheses, with different values of μ, are tested against expected and observed data.

By construction, the minima give the best estimates for the signal strength in the expected and observed statistical analysis. The total uncertainty $\Delta\hat{\mu}$ on the best estimate of the signal strength $\hat{\mu}$ in both cases can be obtained by evaluating this scan at $(-\ln\mathcal{L}(\hat{\mu} \pm \Delta\hat{\mu}, \hat{\hat{\theta}})) = 0.5$, representing a 1σ deviation from the best estimate in this definition of the fitting function. Similarly, the total uncertainty on $\hat{\mu}_{WZ}$ is obtained from a scan of the negative log-likelihood function in this parameter, while fixing all other nuisance parameters. The uncertainties in categories, divided into statistical data, experimental and modelling systematic uncertainties, are obtained by fixing all nuisance parameters of the respective other categories to their best estimate, then reassessing the fit.

The $W^{\pm}W^{\pm}jj$-EW6 signal strength obtained from the statistical analysis of the observed data is found to be considerably larger than 1. This can be explained with an excess in data in the region of large m_{jj}, discussed in the next section, compared to the total estimate employing the Sherpa23jLO prediction. As a reminder, the non-optimal colour flow assignment for VBS processes in the parton shower description of the Sherpa event generation programme, version 2.2.2, is accompanied by a significant reduction of the predicted cross-section (cf. Sec. 6.3.2).

The $W^{\pm}Z$ strength is primarily constrained from the statistical analysis of the $W^{\pm}Z$ control region, where a deficiency of observed data with respect to expectation is present.

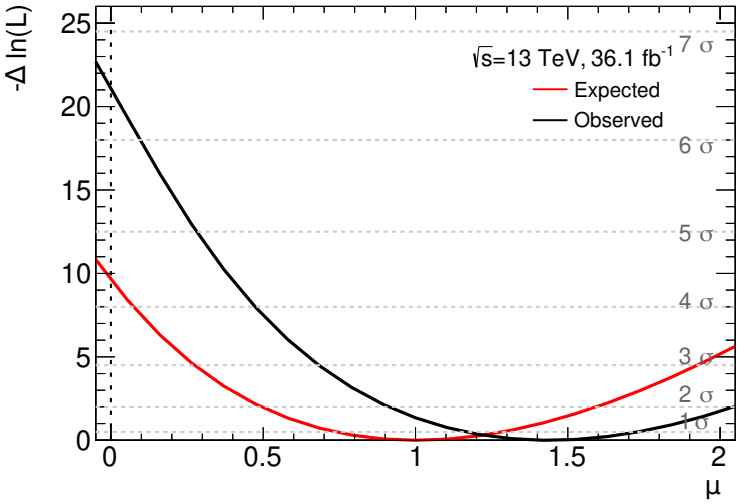


Figure 8.7: Scan of the likelihood function (cf. Eq. (8.8)) with dependence on μ for the fit to the expected, i. e. the Asimov, data (red) and the observed experimental data (black). All other nuisance parameters are fixed to their best estimate for this scan. Figure modified from Ref. [232].

The scaling factors in the observed and expected fit are compatible, especially due to the fact that observed data in the $W^{\pm}Z$ control region is used to obtain the expected results. In Ref. [15], a scaling factor of 0.80 of the combined $W^{\pm}Z$-EW4 and $WZjj$-EW6 processes after the fit to observed data in a VBS signal region is reported. This value is consistent within uncertainties with the reduction found in this analysis.

The total uncertainties on the $W^{\pm}Z$ strength amount to over 40% and are considerably asymmetric. This effect comes from the modelling uncertainties which are the dominant source of uncertainties for this measurement. In detail, the asymmetry of the uncertainties is partly caused by the asymmetry of the renormalisation scale uncertainties on the $W^{\pm}Z$-EW4 prediction.

Uncertainties for the expected and observed results are comparable for both quantities.

Further extensive studies on the results of the statistical analysis are presented in Ref. [235].

8.6.1 Yields in the Signal and Control Regions

Tables 8.9 to 8.11 present the event yields and their total uncertainties of all considered processes together with the event yields of experimental data in all signal, low-m_{jj}, and $W^{\pm}Z$ control regions after the fit to observed data. The respective numbers after the fit to Asimov data can be found in App. E.3.1.

Fig. 8.8 compares the m_{jj} spectrum in the signal region before and after the fit to observed data in the combined $\ell^{\pm}\ell^{\pm}$ channel. The m_{jj} spectra split into the six channels in the signal region after the fit are presented in App. E.3.2.

Fig. 8.9 compares the event yields and total uncertainties in all control regions before and after the fit to observed data.

The overall agreement between experimental data and the total predictions is generally increased in the individual channels and the m_{jj} distributions of the signal region, as well as the control regions. Expectation and experimental data yields agree within uncertainties in most bins of the m_{jj} spectra in all channels after the fit. Exceptions are the intermediate m_{jj} range from 700 GeV to 1000 GeV in the $\ell^{\pm}\ell^{\pm}$ combined channel in the signal region and the low-m_{jj} control region in the $e^{-}\mu^{-} + \mu^{-}e^{-}$ channel.

According to the $W^{\pm}Z$ signal strength obtained after the fit, the event yields of this process are decreased in all channels in all regions after the fit to observed data, mainly a consequence of the disagreement of experimental data and prediction in the $W^{\pm}Z$ control region.

Table 8.9: Estimated event yields and their total uncertainties of all SM processes in all channels, including the combined $\ell^{\pm}\ell^{\pm}$ channel, in the signal region after the statistical analysis. "Other prompt" contains MC-based predictions of the processes of $t\bar{t}V$, ZZ, and triboson production. The yields of experimental data taken in the years 2015 and 2016 in Run 2 of the LHC with the ATLAS detector are given as well. Uncertainties on the $W^{\pm}W^{\pm}jj$-EW6 signal process include absolute normalisation uncertainties (cf. Tab. 7.12), which are not considered in the statistical analysis (cf. Sec. 8.3).

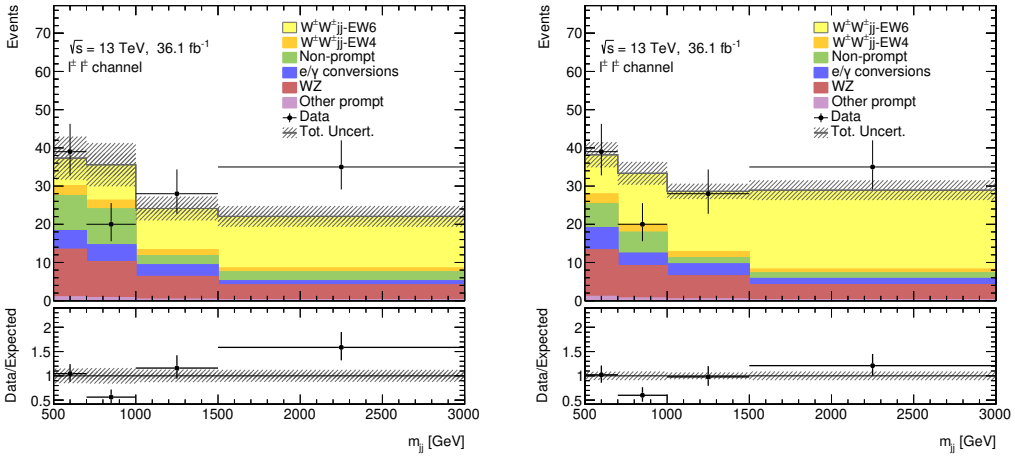
Process	Channel						
	e^+e^+	e^-e^-	$e^+\mu^+ + \mu^+e^+$	$e^-\mu^- + \mu^-e^-$	$\mu^+\mu^+$	$\mu^-\mu^-$	$\ell^{\pm}\ell^{\pm}$
$W^{\pm}Z$	1.48 ± 0.35	1.09 ± 0.30	11.56 ± 4.83	7.94 ± 1.61	4.96 ± 0.87	3.43 ± 0.65	30.46 ± 5.29
$W^{\pm}W^{\pm}jj$-EW4	0.35 ± 0.13	0.15 ± 0.05	2.92 ± 0.98	1.20 ± 0.41	1.79 ± 0.59	0.76 ± 0.25	7.17 ± 2.31
Other prompt	0.16 ± 0.04	0.14 ± 0.04	0.90 ± 0.20	0.63 ± 0.14	0.39 ± 0.09	0.22 ± 0.05	2.44 ± 0.48
Non-prompt	2.21 ± 1.21	1.18 ± 0.68	5.94 ± 2.49	4.72 ± 1.65	0.56 ± 0.05	0.68 ± 0.13	15.29 ± 5.57
Charge misID	1.21 ± 0.29	1.05 ± 0.24	3.39 ± 0.37	2.97 ± 0.41	–	–	8.61 ± 0.87
$V\gamma$	0.42 ± 0.24	0.53 ± 0.34	2.92 ± 1.59	1.38 ± 1.08	–	–	5.27 ± 2.75
$W^{\pm}W^{\pm}jj$-EW6	5.56 ± 1.37	2.20 ± 0.55	24.14 ± 5.94	9.39 ± 2.31	13.39 ± 3.32	5.15 ± 1.27	59.84 ± 14.77
Total expected	11.39 ± 1.90	6.35 ± 1.02	51.77 ± 8.28	28.23 ± 2.61	21.09 ± 3.48	10.23 ± 1.46	129.06 ± 17.06
Data 2015/16	10	4	44	28	25	11	122

Table 8.10: Estimated event yields and their total uncertainties of all SM processes in all channels, including the combined $\ell^{\pm}\ell^{\pm}$ channel, in the low-m_{jj} control region after the statistical analysis. "Other prompt" contains MC-based predictions of the processes of $t\bar{t}V$, ZZ, and triboson production. The yields of experimental data taken in the years 2015 and 2016 in Run 2 of the LHC with the ATLAS detector are given as well. Uncertainties on the $W^{\pm}W^{\pm}jj$-EW6 signal process include absolute normalisation uncertainties (cf. Tab. 7.12), which are not considered in the statistical analysis (cf. Sec. 8.3).

Process	Channel						
	e^+e^+	e^-e^-	$e^+\mu^+ + \mu^+e^+$	$e^-\mu^- + \mu^-e^-$	$\mu^+\mu^+$	$\mu^-\mu^-$	$\ell^{\pm}\ell^{\pm}$
$W^{\pm}Z$	1.85 ± 0.45	1.13 ± 0.34	12.24 ± 2.21	10.19 ± 1.95	4.98 ± 0.91	3.61 ± 0.66	34.01 ± 5.77
$W^{\pm}W^{\pm}jj$-EW4	0.23 ± 0.07	0.13 ± 0.05	2.02 ± 0.56	1.24 ± 0.35	1.18 ± 0.33	0.64 ± 0.18	5.45 ± 1.47
Other prompt	0.25 ± 0.08	0.15 ± 0.06	1.24 ± 0.26	0.98 ± 0.24	0.62 ± 0.14	0.31 ± 0.09	3.53 ± 0.67
Non-prompt	0.95 ± 0.27	2.12 ± 1.34	9.78 ± 3.03	6.47 ± 2.50	2.37 ± 0.89	1.19 ± 0.17	22.88 ± 6.64
Charge misID	1.67 ± 0.29	1.47 ± 0.41	4.17 ± 0.50	3.89 ± 0.55	–	–	11.20 ± 1.22
$V\gamma$	0.16 ± 0.09	0.24 ± 0.15	1.79 ± 1.89	2.64 ± 1.34	–	–	4.83 ± 2.96
$W^{\pm}W^{\pm}jj$-EW6	0.88 ± 0.15	0.59 ± 0.11	4.04 ± 0.66	2.67 ± 0.45	2.45 ± 0.41	1.52 ± 0.25	12.14 ± 1.98
Total expected	5.98 ± 0.88	5.83 ± 1.77	35.28 ± 4.65	28.07 ± 3.81	11.59 ± 1.47	7.27 ± 0.76	94.03 ± 9.89
Data 2015/16	5	3	39	38	10	6	101

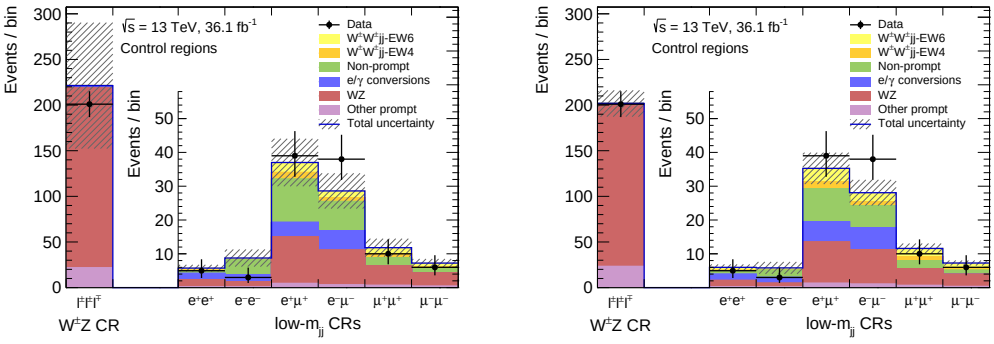
Table 8.11: Estimated event yields and their total uncertainties of all SM processes in the $W^{\pm}Z$ control region after the statistical analysis. "Other prompt" contains MC-based predictions of the processes of $t\bar{t}V$, ZZ, and triboson production. The yields of experimental data taken in the years 2015 and 2016 in Run 2 of the LHC with the ATLAS detector are given as well. Numbers are given in the combined $\ell\ell'\ell''$ channel, with $\ell^{(\prime\prime)} = e^{\pm}$ or $\mu^{\pm}$.

Process	$\ell\ell'\ell''$ channel
Data 2015/16	201
$W^{\pm}Z$	177.07 ± 15.54
$W^{\pm}W^{\pm}jj$-EW4	–
Other prompt	23.08 ± 4.31
$V\gamma$	1.58 ± 1.46
$W^{\pm}W^{\pm}jj$-EW6	< 0.01
Total expected	201.74 ± 14.44
Data 2015/16	201



(a) **(b)**

Figure 8.8: Distribution of the invariant mass of the tagging jets, m_{jj}, in the combined channel $\ell^{\pm}\ell^{\pm}$ in the signal region before (a) and after (b) the fit to observed data. Expected signal and background yields are coloured and stacked with the hatched band representing the statistical and systematic uncertainties of the background prediction. The background predictions from electron charge misidentification and $V\gamma$ processes are combined into the e/γ conversion category. The other prompt category contains predictions of the processes of $t\bar{t}V$, ZZ, and triboson production. The last bin of the distribution includes all events with $m_{jj} > 3000\,\text{GeV}$. The lower panel shows the experimental data with respect to the total expected estimate. Figures modified from Ref. [232].



(a) **(b)**

Figure 8.9: Distribution of the invariant mass of the tagging jets, m_{jj}, in the $W^{\pm}Z$ control region and all channels of the low-m_{jj} control regions before (a) and after (b) the fit to observed data. Expected signal and background yields are coloured and stacked with the hatched band representing the statistical and systematic uncertainties of the background prediction. The background predictions from electron charge misidentification and $V\gamma$ processes are combined into the e/γ conversion category. The other prompt category contains predictions of the processes of $t\bar{t}V$, ZZ, and triboson production. The backgrounds from non-prompt and electron charge misidentification processes are not considered in the statistical analysis of the $W^{\pm}Z$ control region. Figure (b) modified from Ref. [1].

As explained in Sec. 8.4.1, background expectations from processes with non-prompt leptons and electron charge misidentification are not considered in the $W^{\pm}Z$ control region in the final statistical analysis presented in Ref. [1]. Both backgrounds contribute below 2% and 1% of the total expected event yield in this region, respectively, as can be seen in Tab. 8.4. The impact of the missing contributions on the final measured cross-section is below 2% [235].

The expectation of the background due to non-prompt leptons from jet misidentification and hadron decays is reduced across all channels in the signal and low-m_{jj} control region. From Figures 8.8 and 8.9, as well as Fig. E.6 in the appendix, it can be seen that this background contributes largely in a region with low tagging jet invariant mass in all channels. In most of the channels, experimental data yields lower event numbers in this region compared to the total prediction, which is the reason for the reduction of this background contribution after the fit to observed data.

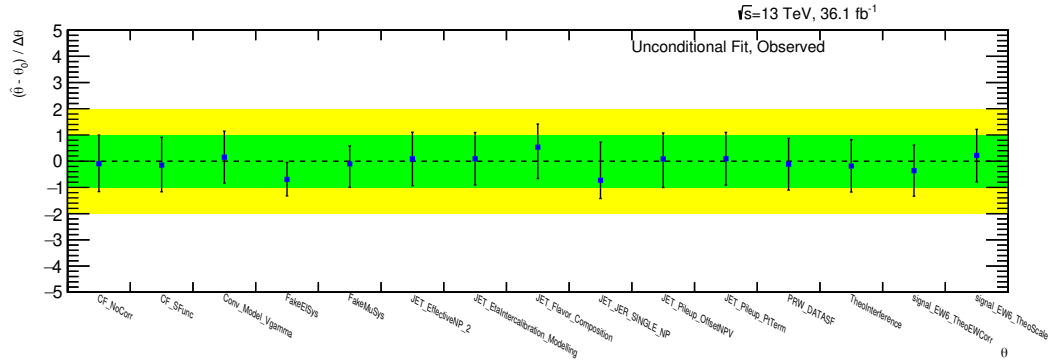
Large systematic uncertainties in the region of lower and intermediate values of m_{jj} in the channels involving electrons before the fit come from the uncertainties on the non-prompt background estimate, as can be compared from Fig. 8.4.

In contrast, the expected yields of the $W^{\pm}W^{\pm}jj$-EW6 signal process is increased in all channels after the fit to observed data, which reflects the postfit result of the value of the signal strength being considerably larger than 1. This can be understood from the spectrum in m_{jj} in the signal region, which shows a consistent excess of experimental data events compared to the total prediction above $m_{jj} = 1500\,\text{GeV}$ in all channels (cf. Fig. 8.8). This bin is dominated by the signal contribution already before the fit. The signal strength μ allows to scale the signal expectation without constraints.

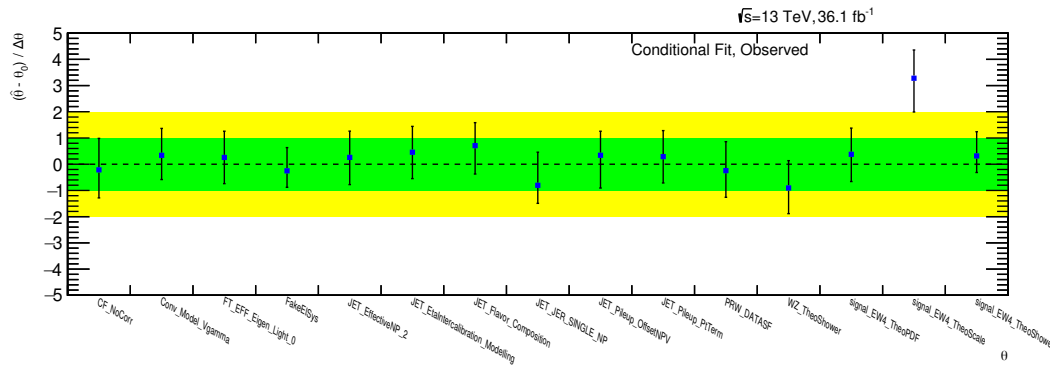
8.6.2 Nuisance Parameters

The effects on the nuisance parameters incorporated into the fit are discussed with a set of commonly used quantities, the nuisance parameter pull and impact.

In order to better fit the data, the best fit value of a NP $\hat{\theta}$ may not coincide with its central value θ_0 as predicted before the fit. In this case, the nuisance parameter is said to be "pulled" away from its prefit prediction. The difference between the central value of a NP before the fit and the most probable value after the statistical analysis is quantified with the



(a)



(b)

Figure 8.10: Pulls of the nuisance parameters for the full unconditional, i. e. including μ as a free parameter, (a) and the background-only fit, i. e. with $\mu = 0$, (b) to observed data. Only a subset of the 15 NPs with largest pulls are shown. Variations of 1σ and 2σ on the central value θ_0 before the fit are indicated with the green and yellow bands, respectively. Figure modified from Ref. [232].

pull of a nuisance parameter, defined as:

$$\frac{\hat{\theta} - \theta_0}{\Delta\theta}, \tag{8.28}$$

and expressed in units of its standard deviation.

The pulls of the NPs are shown in Fig. 8.10 for the full unconditional fit, i. e. including μ as a free parameter, and the background-only statistical fit, i. e. with $\mu = 0$, to observed data. Equivalent figures obtained from the fit to Asimov data are shown in Fig. E.4 in the appendix.

Only the 15 NPs with the largest pulls are included in the figures. After the full signal plus background fit, all NPs stay within 1σ of their uncertainty before the fit. The obvious disagreement in the shape of the m_{jj} distributions in all channels between experimental data and the predictions is adjusted with pulling some of the NPs. As the signal strength is a free parameter with normalisation effect only, it cannot cure the shape inconsistencies.

NPs with the largest pulls are associated to the following systematic uncertainties:

(1) The jet energy resolution, `JET_JER_SINGLE_NP`;

(2) The non-prompt electron systematics effects, `FakeElSys`; and

(3) The jet flavour composition, `JET_Flavor_Composition`,

followed by mildly pulled NPs associated to the $W^{\pm}W^{\pm}jj$-EW6 signal process, such as `signal_EW6_TheoEWCorr`, `signal_EW6_TheoScale`, and `TheoInterference`.

The NP associated to the jet energy resolution is pulled down with the effect of lowering the predicted event yield in the region of low tagging jet invariant mass. From Fig. 8.2, it can be seen that large effects from this variation are predicted in this region in almost all channels.

In order to lessen the disagreement in the channels exhibiting electrons in the region of low tagging jet invariant mass, where the contribution of the background due to non-prompt electrons is most sizable, the NP associated to the uncertainty due to non-prompt electron fake factor systematics is pull down.

The NP associated to the jet flavour composition is pulled up to increase the MC-predicted background event yield in the region of large m_{jj}.

Generally, NPs associated to the $W^{\pm}W^{\pm}jj$-EW6 signal process solely affect the shape of the m_{jj} distribution as their normalisation effect is insignificant per construction (cf. Sec. 8.3). Hence, the three mildly pulled NPs of the signal process are pulled in directions such that the signal expectation matches the experimental data in the region of high m_{jj}. As shape uncertainties per construction have no "up" or "down" variation, these NPs are pulled in different directions, owing to the (arbitrary) direction they are incorporated into the statistical analysis. The impact of the variations before the fit can be recapitulated from Fig. 8.5. Ultimately, the fit increases the normalisation of the $W^{\pm}W^{\pm}jj$-EW6 signal process by raising its normalisation via the signal strength μ, and further adjusts the shape mildly in order to match the experimental data.

Among the NPs with the largest pulls, is the NP associated to the normalisation uncertainty of the $V\gamma$ processes. The prefit uncertainty is large with 44%. Hence the mild upward pull results in a sizable increase of the event yield of this process category, especially in the low-m_{jj} control region.

In addition to the pull, Fig. 8.10 indicates, that some NPs are constrained by the fit, i. e. the postfit uncertainty reduces. This is the case for the fake factor systematics effects on electrons and muon from the non-prompt background estimate. Especially, in the region of low m_{jj}, these sources of uncertainties are large (cf. Fig. 8.4) and exceed the statistical data uncertainty. Hence, especially the low-m_{jj} region exhibit the potential to constrain these NPs.

Small constraints are obtained for NPs associated to the $W^{\pm}Z$ process, which mainly come from the $W^{\pm}Z$ control region.

Due to the large discrepancy between experimental data and prediction in the conditional, background-only fit, it is expected that NPs are generally pulled more to adjust the expectations.

The impact of a NP is a measure of its effect on the best fit value of the signal strength $\hat{\mu}$. It is evaluated as impact before or after the statistical analysis with an each two-fold fitting procedure in addition to the full, unconditional fit. For the prefit(postfit) impact, fits are repeated with a given NP fixed at its best fit value reduced or increased by its prefit(postfit) uncertainty, $\hat{\theta} \pm \Delta\theta$ ($\hat{\hat{\theta}} \pm \Delta\hat{\hat{\theta}}$). The alternative values for the best estimate of $\hat{\mu}$ from these additional fits are collected and NPs are ranked according to their postfit impact. NPs associated to the statistical uncertainties are not considered in this procedure.

Fig. 8.11 shows the 20 NPs with highest rank of their impact after the fit to observed data. The equivalent figure obtained from the fit to Asimov data is shown in Fig. E.5 in the appendix.

The NP associated to the parton shower uncertainty of the $W^{\pm}W^{\pm}jj$-EW6 signal process has the largest impact on the measured signal strength when considering its uncertainty after the fit. The parton shower modelling uncertainty is the largest source of systematic uncertainty on the signal process already before the fit (cf. Fig. 8.5 (b)). NPs with large correlations to the signal strength are generally ranked higher with respect to their postfit impact, as shown in Ref. [235], where the correlations are discussed in detail.

8.6.3 Observation of the $W^{\pm}W^{\pm}jj$-EW6 Process

The discovery of the $W^{\pm}W^{\pm}jj$-EW6 signal process is claimed if the background-only hypothesis is rejected with a significance of more than 5σ obtained by evaluating the test statistic of Eq. (8.10). The background-only hypothesis is represented by a signal strength of $\mu = 0$.

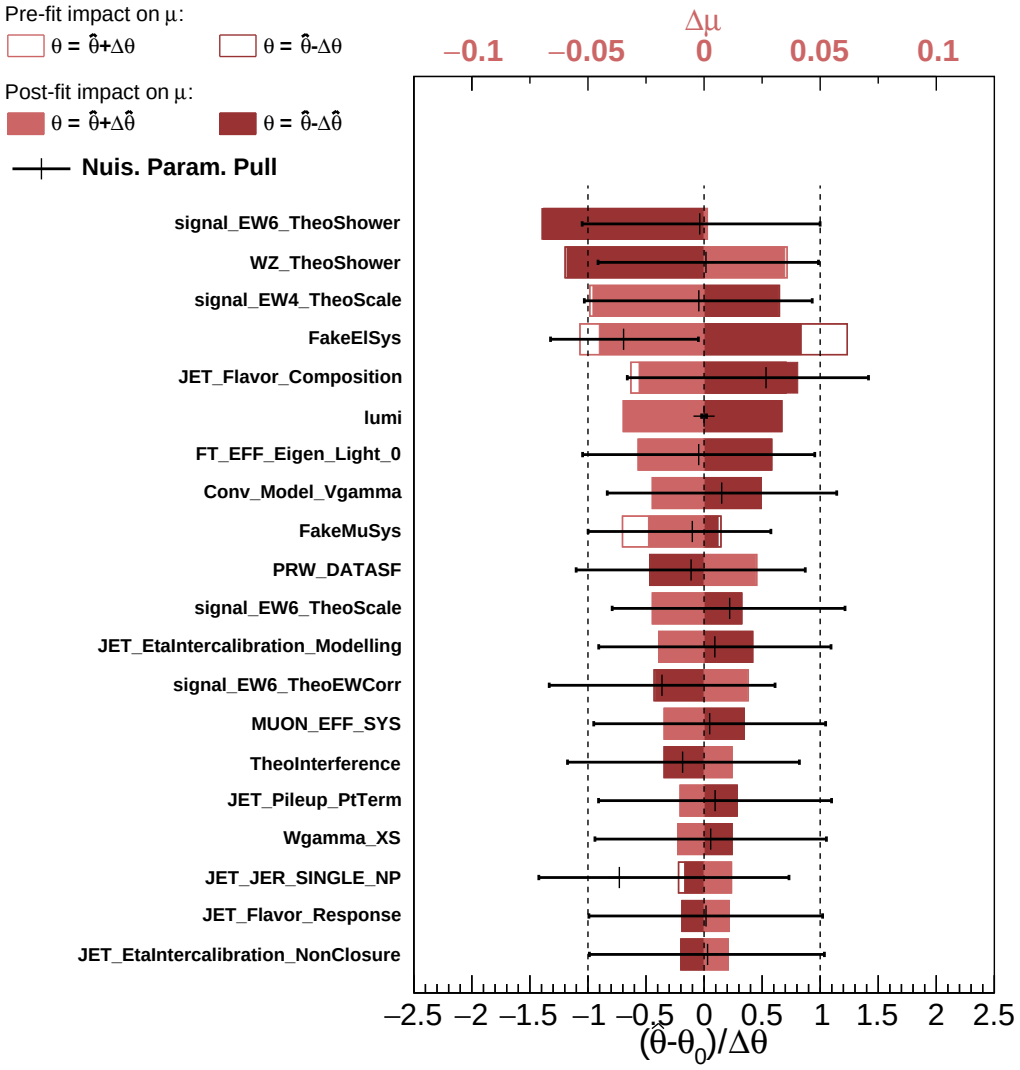


Figure 8.11: Impact of the nuisance parameters on the measured, i. e. best fit signal strength $\hat{\mu}$ before (empty brown rectangles) and after (filled brown rectangles) the fit to observed data. The impact is quantified with the upper scale. NPs are ranked by their impact after the fit including only the 20 NPs with highest impact. The black points show the pull and the relative uncertainties after the fit $\Delta\hat{\theta}$ of each NP, quantified on the lower scale. NPs associated to the statistical uncertainties of the background estimates are not considered for the impact. NPs associated with experimental uncertainties with several independent components are indicated by their index in the set. Figure taken from Ref. [232].

Employing the scan of the likelihood ratio in Fig. 8.7, both the expected and observed significance for the discovery can be obtained by identifying the value of the likelihood ratio at $\mu = 0$ and its translation into a significance[8]. The expected significance, obtained by a fit to Asimov data with the $W^{\pm}W^{\pm}jj$-EW6 signal expectation predicted by the Sherpa23jLO event generation setup, is calculated to 4.4σ. In experimental data, an excess of events in the region of high tagging jet invariant mass with respect to the estimation is measured (cf. Fig. 8.8). The background-only hypothesis is rejected by 6.5σ from the fit to observed data.

The sizable difference between the significance of the expected and observed statistical analysis is investigated further in Ref. [1, 232]. An expected significance with respect to the alternative $W^{\pm}W^{\pm}jj$-EW6 signal prediction generated with the PB+Py8 setup is reported in Ref. [1]. Due to the inconsistency in the lepton flavour universality of the $W^{\pm}W^{\pm}jj$-EW6 signal prediction of the PB+Py8 event generation programme detailed in App. A.3, however, it is not reasonable to statistically analyse the dataset with this prediction, especially since the signal region and low-m_{jj} control region is split into flavour dependent channels.

A second study is conducted by normalising the Sherpa23jLO prediction at reconstruction level by the ratio of the fiducial cross-section predicted by the MG5+Py8drec and the nominal Sherpa23jLO setup (cf. Tab. 6.11). A fully simulated event sample from the MG5+Py8drec setup and its evaluation of all associated uncertainties has not been available by the time of the analysis. With this simplified modification, the normalisation of the Sherpa23jLO prediction, which is affected by the non-optimal colour flow implementation in the parton shower algorithm (cf. sec. 6.3.2), is adjusted, while the shape of the m_{jj} distribution remains unchanged. From Fig. 6.6 (a), the latter shows large differences only in the region of low tagging jet invariant mass. The statistical analysis is repeated with this modified $W^{\pm}W^{\pm}jj$-EW6 signal prediction and an expected significance of 5.9σ is obtained. The analysis of the CMS experiment of the same final state also employs a $W^{\pm}W^{\pm}jj$-EW6 signal prediction simulated with MG5_aMC at LO (cf. Sec. 6.2), which yields an expected significance of 5.7σ [14].

8.6.4 Cross-section Measurement

From the profile likelihood fit to observed data, which yields the measured signal strength $\hat{\mu}_{\text{obs}}$, presented in Eq. (8.20), the measured cross-section in the fiducial region (cf. Sec. 6.4) can be obtained by employing Eq. (8.3):

$$\sigma^{\text{fid}}_{\text{meas}} = 2.89\ ^{+0.51}_{-0.48}\ (\text{stat})\ ^{+0.14}_{-0.16}\ (\text{mod})\ ^{+0.24}_{-0.22}\ (\text{sys})^{+0.08}_{-0.06}\ (\text{lumi})\ \text{fb}. \tag{8.29}$$

The sources of uncertainties are split into the categories: statistical data uncertainties (stat), theoretical modelling uncertainties (mod), and all experimental uncertainties (sys), except the luminosity uncertainty (lumi) which is quoted separately. Modelling uncertainties include $W^{\pm}W^{\pm}jj$-EW6 signal modelling uncertainties excluding acceptance normalisation effects (cf. Sec. 8.3). In addition, modelling uncertainties from the $W^{\pm}W^{\pm}jj$-EW6 and $W^{\pm}Z$ processes are included in this category. Theoretical modelling uncertainties on other prompt and the $V\gamma$ processes are included in the "sys" category. The total uncertainty on the cross-section measurement amounts to $^{+0.59}_{-0.55}$, which is approximately 20% of the measured cross-section. It is clearly dominated by the statistical accuracy of the experimental data. Tab. 8.12 summarises the impact of different uncertainty sources on the measured fiducial cross-section after the fit split into categories as defined in Tables 7.6, 7.8, and 7.11. Results are obtained by following the procedure outlined in the previous section, where the impact on the signal strength is discussed. The impacts of multiple variations in one category are added in quadrature. Correlations between uncertainty sources are not taken into account.

Categories with the largest impact are jet related object uncertainties, uncertainties on the estimation of the background due to non-prompt leptons misidendified as jets or from hadron decays, and uncertainties from the theoretical modelling of the $W^{\pm}Z$ and $W^{\pm}W^{\pm}jj$-EW4 background and the $W^{\pm}W^{\pm}jj$-EW6 signal processes. Nevertheless, these remain at approximately 3%, which is well below the statistical data uncertainty.

[8] The translation can be found in statistics text books, such as Ref. [236, 237]. The likelihood ratio scan in the case at hand is not parabolic. In Ref. [237] it is additionally explained that the likelihood ratio scan does not need to be parabolic, i. e. the likelihood function does not need to follow a Gauss or χ^2 distribution, in order to use the graphical method.

Table 8.12: Symmetrised impact of uncertainties on the measured fiducial cross-section split into categories as defined in Tables 7.6, 7.8, and 7.11. The impacts of multiple variations in one category are added in quadrature. Correlations between uncertainty sources are not taken into account. Numbers taken from Ref. [1].

Uncertainty category	Impact [%]
Experimental object and event:	
Electrons	0.6
Muons	1.3
Jets (except b-tagging)	3.2
b-tag ineff.	2.1
Pile-up reweighting	1.6
Luminosity	2.4
Experimental background estimation:	
Statistics	3.2
Non-prompt leptons	3.3
Electron charge misidentification	0.3
Other (including other prompt and $V\gamma$ modelling)	1.8
Theoretical modelling $W^{\pm}W^{\pm}jj$-EW6 process:	
$W^{\pm}W^{\pm}jj$-EW6-$W^{\pm}W^{\pm}jj$-EW4 interference	1.0
NLO EW corrections	1.4
Matrix-element, parton shower modelling	2.8
Theoretical modelling $W^{\pm}W^{\pm}jj$-EW4 process	2.9
Theoretical modelling $W^{\pm}Z$ process	3.3

In Fig. 8.12, the measured fiducial cross-section is compared to the nominal theoretical predictions of the Sherpa23jLO, PB+Py8, and MG5+Py8drec setups, discussed extensively in Sec. 6.6.2.

All theoretical predictions agree with the measured fiducial cross-section within the total uncertainty envelopes. The renormalisation and factorisation scale uncertainty is the leading source of uncertainty for all three setups. The disagreement within uncertainties between the predictions is discussed in detail in Chapter 6, especially in Sec. 6.6.2. The predictions from PB+Py8 and MG5+Py8drec agree better with the measurement than the Sherpa23jLO prediction, which predicts the lowest value for the fiducial cross-section. This observation matches the assumption of a too low normalisation of the Sherpa23jLO prediction due to the non-optimal colour flow assignment in the parton shower algorithm of the Sherpa programme.

As the theoretical predictions, the measured fiducial cross-section does not include the branching into τ leptons, as these are vetoed in the fiducial region (cf. Tab. 6.8). The $W^{\pm}W^{\pm}jj$-EW6 signal process template at reconstruction level does include events where $W^{\pm}$ bosons decay into τ leptons which further decay leptonically into electrons and muons. Due to the cross-section being determined via the signal strength, which relates the prediction and the measurement, the measured fiducial cross-section does not contain contribution from events with $W^{\pm}$ bosons decaying into τ leptons.

It is to be noted that the measured fiducial cross-section contains the contribution of the interference between the $W^{\pm}W^{\pm}jj$-EW6 and $W^{\pm}W^{\pm}jj$-EW4 processes, as no separate estimate for this is included in the statistical analysis. The consequence is, that the fit adjusts the free signal strength parameter such that it fits the experimental data best. The predicted contribution of the interference is at approx. 3% with respect to the $W^{\pm}W^{\pm}jj$-EW6 fiducial cross-section and positiv in the fiducial region (cf. Sec. 6.6.1).

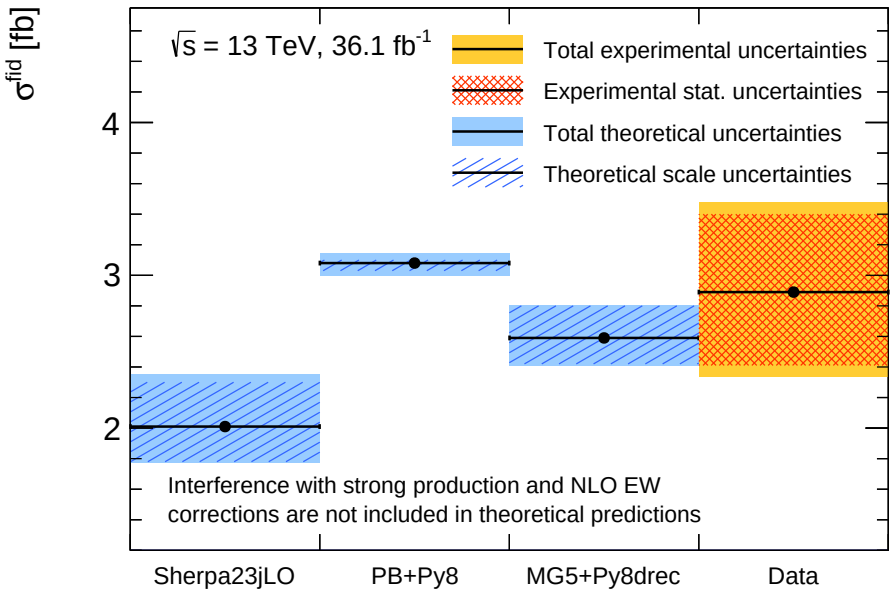


Figure 8.12: Comparison of the measured fiducial cross-section (indicated with "Data", most right) and the nominal theoretical predictions of the analysis, Sherpa23jLO, PB+Py8, and MG5+Py8drec, discussed in detail in Sec. 6.6.2. The statistical data uncertainty on the measured value is indicated as checked orange band, the total uncertainty as light orange band. Theoretical renormalisation and factorisation scale uncertainties are indicated as dashed blue bands on the theoretical predictions, total modelling uncertainties, comprising scale, PDF set, its α_S value, and parton shower plus LO merging (if applicable) uncertainties, as light blue bands. The interference between the $W^{\pm}W^{\pm}jj$-EW6 and $W^{\pm}W^{\pm}jj$-EW4 process, as well as the NLO EW corrections are not included in any of the uncertainty bands of the predicted values. Figure modified from Ref. [1].

8.7 Potential of Future Analyses

Before embarking on the reinterpretation of the experimental data in light of a BSM EFT prescription, possibilities for the improvement of future analyses of the $W^{\pm}W^{\pm}jj$ final state as predicted by the SM shall be collected and assessed.

With the partial Run 2 dataset utilised for the cross-section measurement presented here, the accuracy of the result is driven by the statistical accuracy of the experimental dataset which is approx. 18% in relative size. However both, the experimental and theoretical systematic uncertainties, on the measurement are sizable and become subsequently more important when more data is being analyses.

The increasing statistical accuracy of the measurements towards Run 3 and further the high luminosity (HL) phase of the LHC, planned to start in 2027 (cf. Fig. 3.2), motivates to utilise more sophisticated predictions including NLO effects of both, QCD and EW couplings. Calculated in Ref. [19] and outlined in Chapter 6, the NLO EW corrections of the $W^{\pm}W^{\pm}jj$-EW6 process, amounting to -13.2%, are dominant among the correction of the full $W^{\pm}W^{\pm}jj$ process at NLO and the impact further increases with the centre-of-mass energy according to calculations in Ref. [241]. Compared to this, with an expected integrated luminosity of $3000\,\text{fb}^{-1}$ of data collected after the HL phase, the uncertainty of the cross-section measurement of the $W^{\pm}W^{\pm}jj$-EW6 process with the ATLAS experiment is estimated to $5-6\%$ [241].

Dominant systematic uncertainties affect the accuracy of the background estimation procedures. One of the leading uncertainties in the measurement is caused by the variation of the background estimate due to non-prompt leptons. Some of the variations are motivated by

discrepancies between experimental data and the background estimates found in validation regions. Hence, a better understanding of the background due to non-prompt leptons will lead to an improved description of the estimates and, expectedly, to reduced uncertainties. This is confirmed by first studies in the direction of, e. g. Ref. [242].

Moreover, demanded by the theory community, is to include the measurement of the cross-section of the combined $W^{\pm}W^{\pm}jj$ process, including the contributions at all possible orders at the respective theoretical accuracy. This becomes especially important when going to NLO accuracy in both EW and QCD couplings. The motivation for this is discussed in detail in Chapter 5.

With more data being accumulated, it will be beneficial to exploit more complex strategies in the statistical data analysis. One direction is establishing multi-dimensional fits for the extraction of relevant quantities, for example employing m_{jj} and m_{ll} as in Ref. [14] by the CMS collaboration. Another possibility is to combine the measurements in the $W^{\pm}W^{\pm}jj$ and $W^{\pm}Zjj$ VBS final states. The latter being the dominant background contribution to the first motivates to utilise two dedicated regions and fit both components simultaneously. This has been pursued by the CMS collaboration in Ref. [155].

Furthermore with increasing amount of data available, a natural next analysis aim is to study unfolded distributions. Typical VBS observables, such as m_{jj} and ΔY_{jj}, can give more insight in the theoretical prescription of the VBS process. Moreover, kinematic distributions describing additional QCD radiation besides the tagging jets are of great interest. Observables like the Zeppenfeld variables of the third-leading jet or the number of jets per event help refining the description of the regime where either NLO predictions or the parton shower modelling become important.

Another analysis objective is certainly the study of different polarisation final states in the $W^{\pm}W^{\pm}$ scattering process as conducted in Ref. [193] with data from the CMS experiment. Especially the exploration of the scattering of two longitudinally polarised $W^{\pm}$ bosons is compelling to unravel the mechanism of EWSB and therein the role of the Higgs boson. The study of polarised VBS can be combined with the investigation of unfolded distributions of kinematic observables connected to the $W^{\pm}W^{\pm}$ system, for example the p_{T} of the diboson system, or the azimuthal angle between the two charged leptons.

Chapter 9

Exclusion Limits on Dimension-8 EFT Parameters

The presence of triple, and especially, quartic gauge couplings in the process of the scattering of two same-charge $W^{\pm}$ bosons allows to study the gauge structure of the SM and possible effects of new physics contributions in this process. This chapter aims at reinterpreting the experimental data taken in the years 2015 and 2016, amounting to $36.1\,\text{fb}^{-1}$ at a centre-of-mass energy of 13 TeV, in light of anomalous quartic gauge couplings. The model under study is the dimension-eight EFT expansion of the SM outlined in Sec. 2.3 and based on Ref. [2, 3]. The measurement is designed as a reinterpretation in such that it re-utilises all ingredients and knowledge from the SM analysis collected in Chapter 7. In this way, the focus can entirely be laid on the study of the EFT signal and specifics of the analysis that come with it, such as the unitarisation procedure and the inclusion of effects of dimension-six EFT operators in the measurement of exclusion bounds on dimension-eight EFT parameters. The primary goal is to address the experimental implications of the theoretical model under study which motivate and shape the analysis on the path towards the final exclusion limits. Future analyses of the full Run 2 dataset will then be able utilise the findings made here and with them pursue an optimisation of the analysis in terms of the EFT signal under study.

After the review of existing results on the EFT model under study, a comprehensive examination of the EFT signal is presented. This includes the investigation and validation of a new signal modelling technique provided by the MG5_aMC event generation programme, the amplitude decomposition method. Following this, the strategy of the statistical analysis is presented and final ingredients for the statistical analysis, the systematic uncertainties, are collected. Subsequently, this work presents the first measurement of one-dimensional exclusion bounds on dimension-eight EFT parameters in the fully leptonic $W^{\pm}W^{\pm}jj$ final state with data collected from the ATLAS experiment. As such, it seeks to complement the comparable measurements from the CMS collaboration [14, 155]. Furthermore, multiple sets of one-dimensional exclusion limits are calculated. Following a comprehensive investigation of the clipping unitarisation procedure in the $W^{\pm}W^{\pm}jj$ final state, confidence intervals including the effects of the clipping unitarisation method are presented as a function of the clipping energy. Moreover, effects of dimension-six EFT operators on the $W^{\pm}Z$-EW4 background process are studied in the VBS signal region employed in this thesis. Eventually, exclusion limits including these effects in two scenarios are computed, which constitute the first global results including dimension-six effect on a measurement of exclusion bounds on dimension-eight EFT parameters.

At the end of this chapter, the results are discussed in light of the theoretical formulation of the model as an Effective Field Theory (EFT) and its implementations. Ideas for strategies to address the shortcomings of the measurements are presented.

9.1 Review of Existing Results and Their Measurement Strategies

The interpretation of LHC data in terms of aQGC or EFT extensions of the SM has been on the agenda of the ATLAS and CMS experiments since the Run 1 data-taking period. In fact, these efforts are an extension of the measurements published by the LEP experiments. While the latter only probed anomalous triple gauge couplings (aTGC) or dimension-six EFT parameters, LHC measurements in addition investigate the aQGC or dimension-eight EFT parameter space with measurements including VBS and triple boson production. The first measurement including constraints on aQGC has been presented in the $W^{\pm}W^{\pm}jj$ final state at $\sqrt{s} = 8\,\text{TeV}$ by the ATLAS collaboration [13]. Simultaneously at the same centre-of-mass energy, first results on exclusion bounds of dimension-eight EFT parameters in the scenario considered in this thesis [2, 3] have been published in the $W^{\pm}V\gamma$ final state by the CMS experiment [243]. Many results exist today covering all high-energy runs provided by the LHC. Analyses cover a variety of final states including VBS and triple boson measurements with massive bosons decaying solely into leptons, leptons and jets, as well as channels including photons. Even final states without leptons or photons have been considered to date analysing exclusive $\gamma\gamma \to (W^{\pm}W^{\mp}/ZZ)$ production in association with intact protons [244].

The most recent results including exclusion limits on aQGC and dimension-eight EFT parameters of the ATLAS and CMS experiments are summarised in Tab. 9.1. Solely the latest publications per experiment and measurement final state are included in the table. While the CMS collaboration has superseded most of its Run 1 results with measurements of the partial or full Run 2 data at $\sqrt{s} = 13\,\text{TeV}$, the ATLAS collaboration has not published corresponding results at this centre-of-mass energy to date.

From their very first publications, both experiments follow considerably different measurement strategies. This includes the chosen BSM scenarios, and naturally with this the definition of the probed parameters. Moreover, with the different handling of unitarity and application of unitarisation procedures, two of the major considerations when comparing results diverge substantially.

Analyses of the ATLAS collaboration follow two quite disjoint strategies, depending on the probed multiboson channels. Measurements of fully and semi-leptonic final states including VBS [86, 246, 248] set exclusion bounds on the aQGC parameters α_4 and α_5 as described in Ref. [256, 257] by applying the K-matrix unitarisation procedure [75–77], both provided within the Whizard event generation programme [204, 205]. Exclusion bounds are extracted in one as well as two dimensions, where both aQGC parameters are free parameters of the fitting procedure. These analyses are the only ones which do not provide ununitarized limits. Measurements including photons in the final state, either via VBS or triple boson production, utilise the dimension-eight EFT model [2, 3] as in this thesis and present result without and with the form factor unitarisation method. One reason for the different strategies is evidently that the K-matrix unitarisation is not defined for final states with three boson or photons in general.

For the EFT parameters of mass dimension eight, two different formalisms exist, implemented in MG5_aMC and VBFNLO, respectively, which differ by the definition of the SM field strength tensors and hence the EFT operators and coefficients. Results of these two EFT and the aQGC formalisms can be converted into each other as the definition of their parameters only differ by factors of the SM $SU(2)_L$ coupling g_W or the vacuum expectation value v. The conversion is presented in Ref. [245].

The ATLAS analyses of the triple boson final states [252, 254, 255] employ the VBFNLO parameterisation, while the measurement of $Z\gamma jj$ production and interpretation [250] is the only result of the ATLAS collaboration which chooses the MG5_aMC implementation.

Results published by the CMS collaboration are more coherent. Throughout various final states and measurements at different centre-of-mass energies, the MG5_aMC implementation of the dimension-eight EFT parameters is employed and exclusion limits without unitarisation procedure are presented. In recent analyses, they move towards presenting exclusion bounds applying the clipping unitarisation method along with ununitarised results [155, 244].

The analyses of the exclusive $\gamma\gamma pp \to (W^{\pm}W^{\mp}/ZZ)pp$ production employ yet another

Table 9.1: Overview of VBS and triple boson measurements that include exclusion limits on aQGC or dimension-eight EFT parameters with the ATLAS and CMS experiments at centre-of-mass energies of 8 and 13 TeV in final states involving leptons, jets and/or photons, where $V = W^{\pm}, Z$. Solely the most recent publications per experiment for a specific channel are shown. Probed parameters in the measurements are indicated with their indices, while "×" means no measurement of parameters of this group is published. The column indicating the parameter formalism refers to the various definitions of the parameters implemented in the simulation programmes and used throughout the measurements. These formalisms are summarised in Ref. [245]. Published measurements include results without and with unitarisation applied, which is indicated by "−" and/or stating the unitarisation procedure, respectively.

Channel	Final state(s)	Experiment	$\sqrt{s}$ [TeV]	Luminosity [fb^{-1}]	Probed parameters α_i or f_i/Λ^4				Parameter formalism	Unitarisation method	Ref.
					α_i	Si	Mi	Ti			
$W^{\pm}Vjj$	$\ell^{\pm}\nu_{\ell}(\ell'^{\pm}\nu'_{\ell}/\ell'^{\pm}\ell'^{\mp})jj$	CMS	13	137	1D	×	0-1	0-1,7	0-2	MG5_aMC	−/clipping	[155]
$W^{\pm}W^{\pm}jj$	$\ell^{\pm}\nu_{\ell}\ell'^{\pm}\nu'_{\ell}jj$	ATLAS	8	20.3	2D	4-5	×	×	×	Whizard	K-matrix	[86]
$W^{\pm}Zjj$	$\ell^{\pm}\ell^{\mp}\ell'^{\pm}\nu'_{\ell}jj$	ATLAS	8	20.3	2D	4-5	×	×	×	Whizard	K-matrix	[246]
$ZZjj$	$\ell^{\pm}\ell^{\mp}\ell'^{\pm}\ell'^{\mp}jj$	CMS	13	137	1D	×	×	×	0-2,8-9	MG5_aMC	−	[247]
$VVjj$	$(\ell^{\pm}\nu_{\ell}/\ell^{\pm}\ell^{\mp})Jjj$	CMS	13	35.9	1D	×	0-1	0-1,7	0-2	MG5_aMC	−	[154]
$W^{\pm}Vjj$	$\ell^{\pm}\nu_{\ell}(jj/J)jj$	ATLAS	8	20.2	2D	4-5	×	×	×	Whizard	K-matrix	[248]
$W^{\pm}\gamma jj$	$\ell^{\pm}\nu_{\ell}\gamma jj$	CMS	13	138	1D	×	×	all	0-3,5-7	MG5_aMC	−	[249]
$Z\gamma jj$	$\ell^{\pm}\ell^{\mp}\gamma jj$	CMS	13	137	1D	×	×	all	all	MG5_aMC	−	[18]
$Z\gamma jj$	$(\ell^{\pm}\ell^{\mp}/\nu_{\ell}\nu_{\ell})\gamma jj$	ATLAS	8	20.2	1D	×	×	0-3	0,8-9	MG5_aMC	−/form factor	[250]
$(W^{\pm}W^{\mp}/ZZ)pp$	$jjjjpp$	CMS	13	100	1D	×	×	all	×	LEP	−/clipping	[244]
$W^{\pm}W^{\pm}W^{\mp}$	$\ell^{\pm}\nu_{\ell}\ell'^{\pm}\nu'_{\ell}(\ell''^{\mp}\nu''_{\ell}/jj)$	CMS	13	35.9	1D	×	×	×	0-2	MG5_aMC	−	[251]
$W^{\pm}V\gamma$	$e^{\pm}\nu_e\mu^{\pm}\nu_{\mu}\gamma$, $\ell^{\pm}\nu_{\ell}jj\gamma$	ATLAS	8	20.2	1D	×	×	all	0-3,5-7	VBFNLO	−/form factor	[252]
$W^{\pm}V\gamma$	$\ell^{\pm}\nu_{\ell}jj\gamma$	CMS	8	19.3	1D	×	×	0-3	0	MG5_aMC	−	[243]
$W^{\pm}\gamma\gamma$	$\ell^{\pm}\nu_{\ell}\gamma\gamma$	CMS	13	137	1D	×	×	2-3	0-3,5-7	MG5_aMC	−	[253]
$W^{\pm}\gamma\gamma$	$\ell^{\pm}\nu_{\ell}\gamma\gamma$	ATLAS	8	20.3	1D	×	×	2-3	0	VBFNLO	−/form factor	[254]
$Z\gamma\gamma$	$\ell^{\pm}\ell^{\mp}\gamma\gamma$	CMS	13	137	1D	×	×	×	all	MG5_aMC	−	[253]
$Z\gamma\gamma$	$(\ell^{\pm}\ell^{\mp}/\nu_{\ell}\nu_{\ell})\gamma\gamma$	ATLAS	8	20.3	1D	×	×	2-3	0,5,9	VBFNLO	−/form factor	[255]

parameterisation which is extensively used when interpreting data from the LEP experiments. In early analyses of these final states of both experiments, conversions into the dimension-eight EFT parameters f_i/Λ^4 are made by applying additional assumptions which eliminate some EFT parameters [258, 259]. Hence, exclusion bounds cannot be easily compared to newer results and are left out of this summary. Only the most recent analysis of this final state by the CMS collaboration [244] published a set of exclusion limits without these additional assumptions, which in turn make the limits substantially weaker than obtained by previous results with less data and lower centre-of-mass energy.

A commonality in all published results with this context of both experiments is that no effects of anomalous triple gauge couplings have been considered in any of the analyses to date. By disregarding operators of mass dimension six it is assumed that effects of anomalous triple gauge couplings are zero. As outlined in Sec. 2.3.3 not only the reliability of the mathematical expansion but also the model independence advertised by EFT approaches suffer. Moreover, recent theoretical studies show decent impact of operators of mass dimension six in VBS processes and phase space regions [260, 261]. It is hence desirable for future analyses to include estimates of the impact of dimension-six operators in the measurement phase spaces - a first attempt being made in this thesis.

Due to their relation to additional physical states of high mass, the introduction of anomalous quartic couplings via non-zero coefficients of EFT operators lead to more energetic final states. Hence, regions of high energy and mass of (systems of) final state particles are enhanced where contributions from SM processes are very little. Several analyses seek to exploit these characteristic experimental signatures of EFT effects with refined fiducial selection requirements beyond the typical SM VBS or triple boson regions. The most common adjustments are the requirement of large transverse or invariant diboson masses [86, 249, 254, 255] and transverse momenta or energies of (systems of) final state particles [18, 246, 248–252]. Few analyses utilise angle relations between (systems of) particles [246, 248]. The exact definition of observables are not specified here as these are highly dependent on the final state considered. Employing looser phase spaces than the SM VBS measurements is rare [247].

In addition, several analyses employ differential distributions of momentum or mass observables to gain more sensitivity for setting exclusion limits of the EFT dimension-eight parameters. The VBS analyses of both collaborations exploit the transverse mass of the diboson system $m_T(VV)$ [18, 154, 246–249]. Beyond this, the analysis in the combined final states of $W^\pm W^\pm jj$ and $W^\pm Zjj$ of the CMS collaboration utilise two dimensional information of the $m_T(VV)$ and the invariant mass of the tagging jet system m_{jj} [155]. The triple boson analysis involving photons in the final state of the CMS collaboration use the transverse momentum or energy of the (system of) photon(s) for their statistical analysis [243, 253].

Early analyses, especially by the ATLAS collaboration, are solely based on fiducial cross-section information via counting experiments for the extraction of exclusion bounds [13, 86, 250, 252, 254, 255], sometimes in many different signal regions [251].

In addition to the analyses of the ATLAS collaboration setting exclusion limits on the α_4 and α_5 parameters [13, 86, 246, 248], the first measurements of the CMS collaboration in the $W^\pm W^\pm jj$ and $W^\pm Zjj$ final states [196, 262] (which are superseded by Ref. [155]) published two dimensional exclusion limits. All remaining published results extract confidence intervals for one single parameter at a time by setting all other non-SM parameters to zero. By doing this, only specific scenarios of BSM physics are probed where only few quartic coupling channels are affected by the EFT extensions. Especially recent results move away from multi-dimensional results which make the statistical analysis complex and hard to converge.

In Figures 9.1 and 9.4, exclusion limits of all analyses summarised in Tab. 9.1 are collected. Solely results without unitarisation procedure applied are included. Untarised results are difficult to compare due to the variety of chosen unitarisation methods. Moreover, only those dimension-eight parameters of the EFT scenario in Ref. [2, 3] are presented which are relevant for the $W^\pm W^\pm jj$ channel and hence this work, precisely f_{S0}/Λ^4, and f_{S1}/Λ^4, f_{M0}/Λ^4, f_{M1}/Λ^4, and f_{M7}/Λ^4, as well as f_{T0}/Λ^4, f_{T1}/Λ^4, and f_{T2}/Λ^4.

All considered parameters are tested in multiple final states. The f_{S0}/Λ^4 and f_{S1}/Λ^4 parameters thereby are probed by the least number of final states. As can be seen from

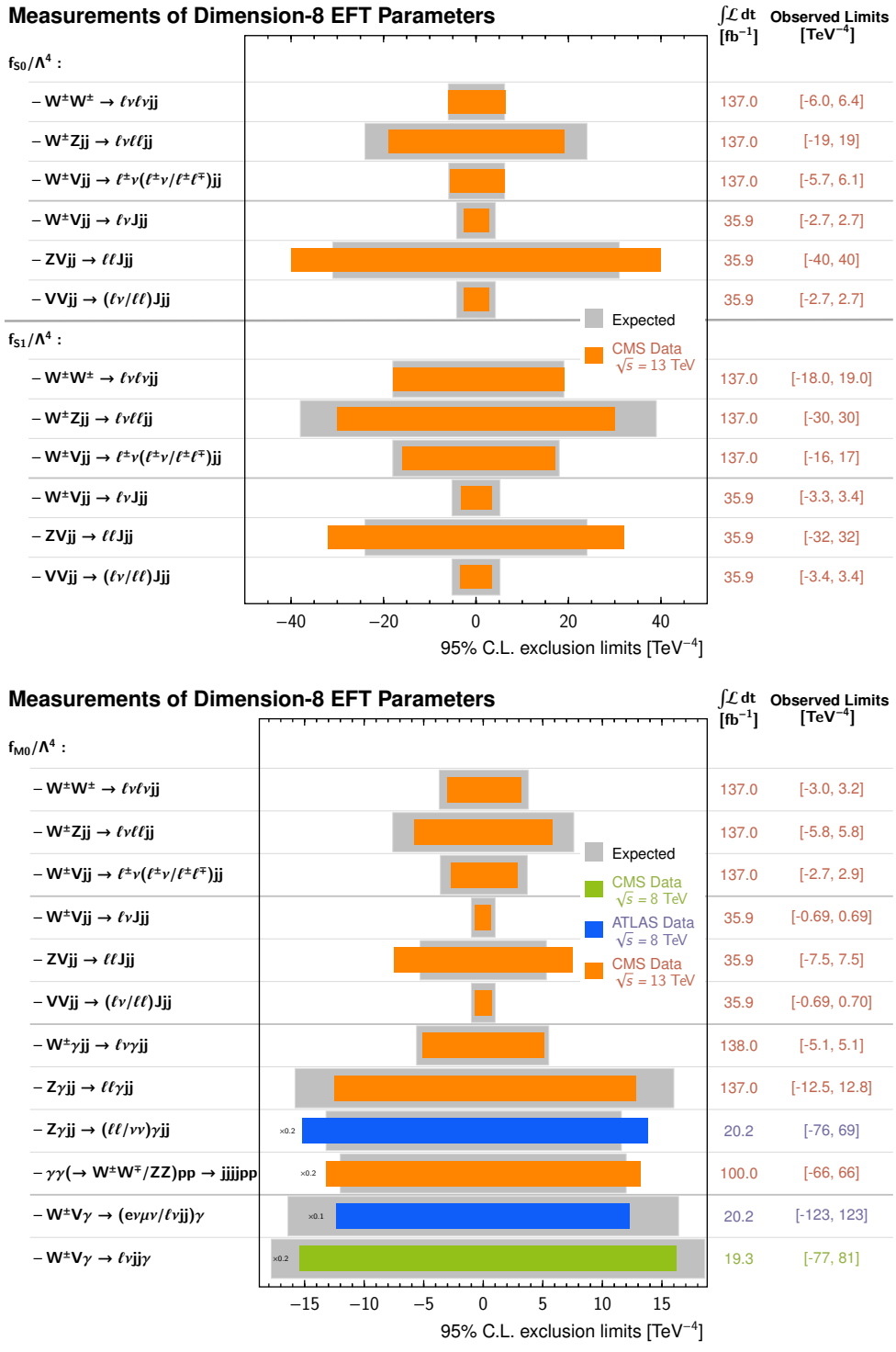


Figure 9.1: Overview of exclusion limits on dimension-eight EFT parameters f_{S0}/Λ^4 and f_{S1}/Λ^4 (top), and f_{M0}/Λ^4 (bottom) obtained in measurements with the ATLAS and CMS experiments at centre-of-mass energies of 8 and 13 TeV in final states involving leptons, jets and/or photons, where $V = W^{\pm}, Z$. Solely the most recent publications per experiment for a specific channel are shown. In order to ensure comparability, solely results without any unitarisation procedure applied are included. Exclusion limits are presented in the MG5_aMC formalism [245] and converted if necessary. Electric charges of the leptons include implicitly all combinations allowed by the SM, unless explicitly stated otherwise. Figure layout modified from Ref. [263].

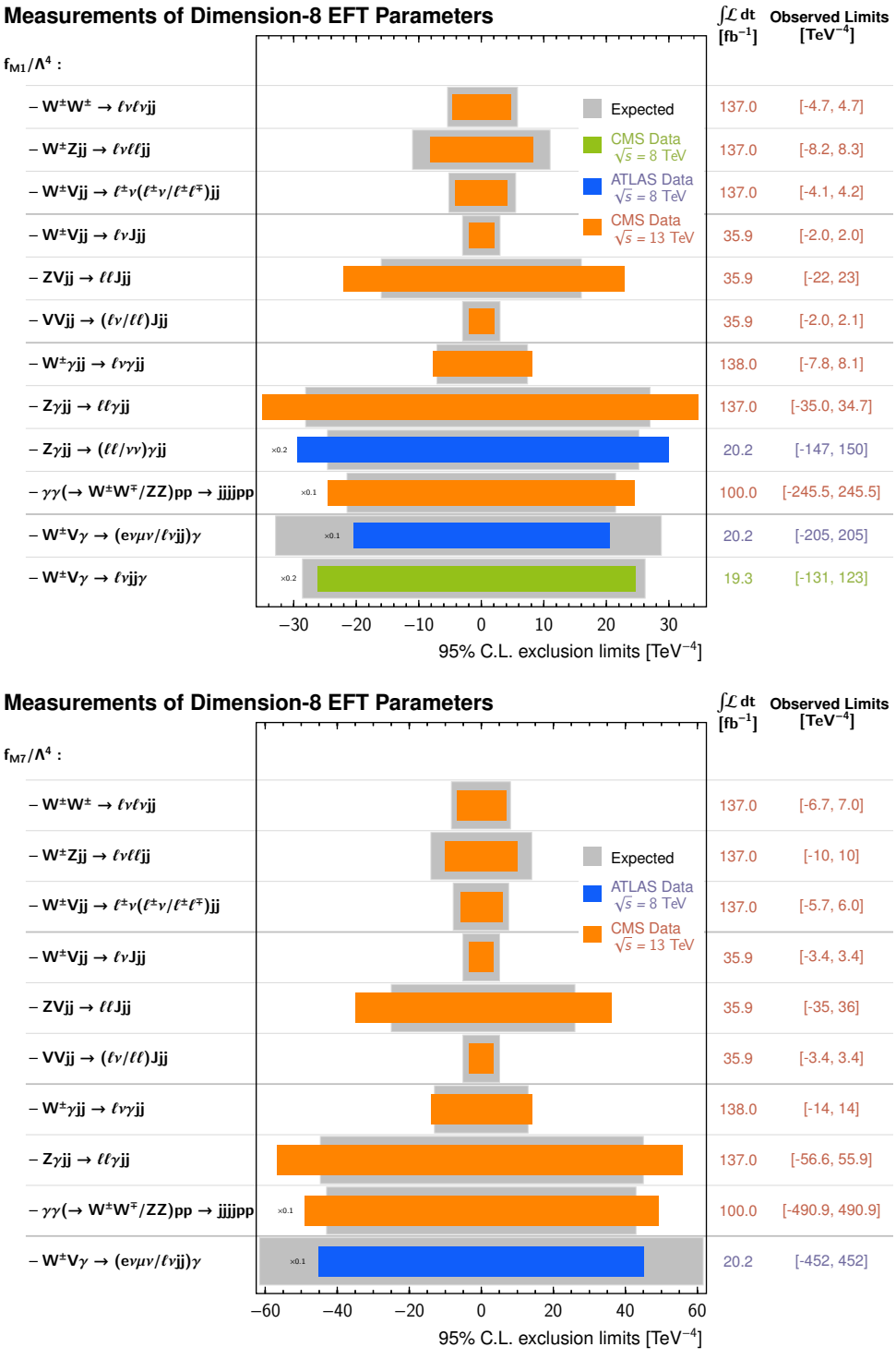


Figure 9.2: Overview of exclusion limits on dimension-eight EFT parameters f_{M1}/Λ^4 (top), and f_{M7}/Λ^4 (botom) obtained in measurements with the ATLAS and CMS experiments at centre-of-mass energies of 8 and 13 TeV in final states involving leptons, jets and/or photons, where $V = W^{\pm}, Z$. Solely the most recent publications per experiment for a specific channel are shown. In order to ensure comparability, solely results without any unitarisation procedure applied are included. Exclusion limits are presented in the MG5_aMC formalism [245] and converted if necessary. Electric charges of the leptons include implicitly all combinations allowed by the SM, unless explicitly stated otherwise. Figure layout modified from Ref. [263].

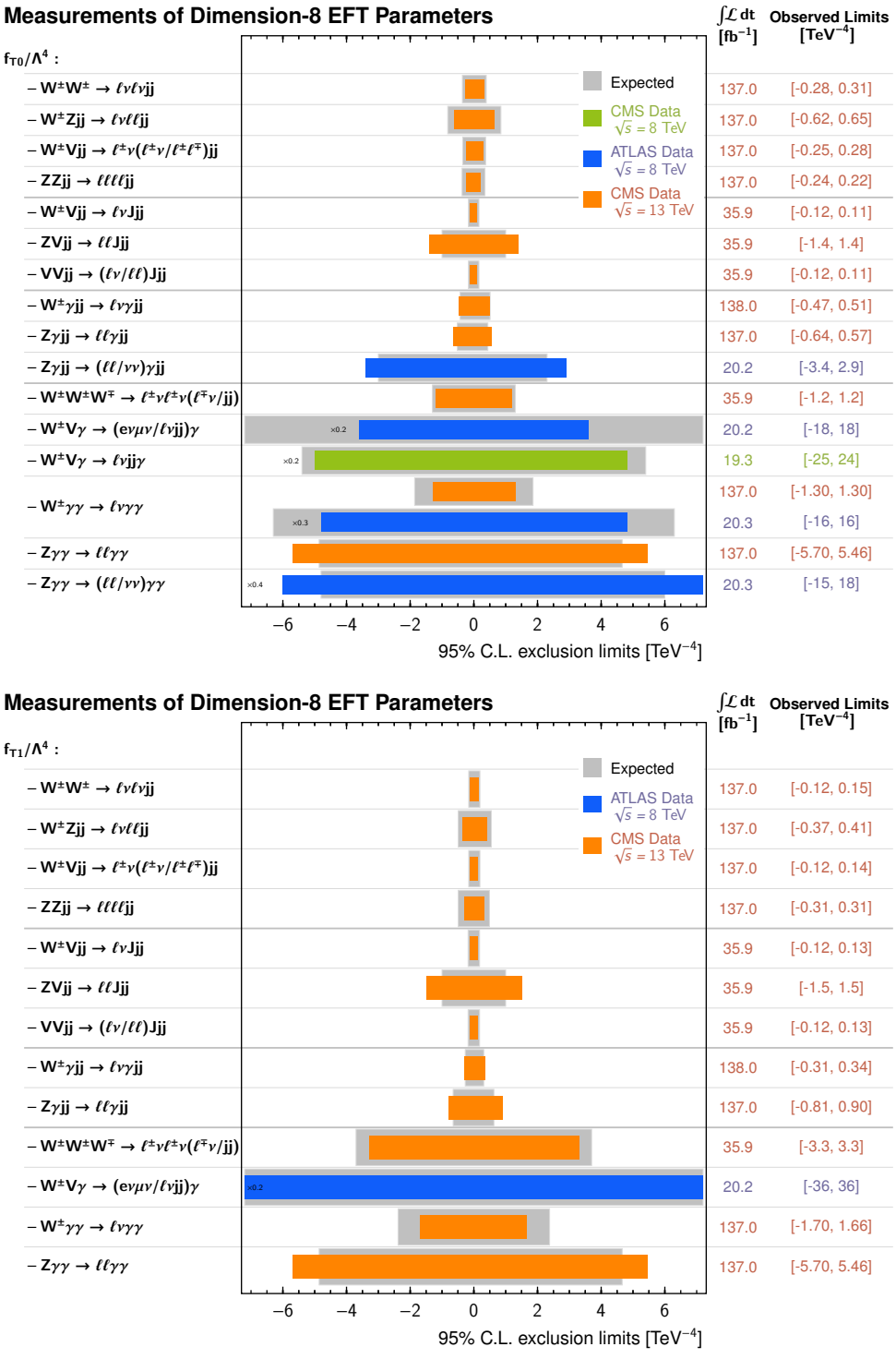


Figure 9.3: Overview of exclusion limits on dimension-eight EFT parameters f_{T0}/Λ^4 (top), and f_{T1}/Λ^4 (bottom) obtained in measurements with the ATLAS and CMS experiments at centre-of-mass energies of 8 and 13 TeV in final states involving leptons, jets and/or photons, where $V = W^{\pm}, Z$. Solely the most recent publications per experiment for a specific channel are shown. In order to ensure comparability, solely results without any unitarisation procedure applied are included. Exclusion limits are presented in the MG5_aMC formalism [245] and converted if necessary. Electric charges of the leptons include implicitly all combinations allowed by the SM, unless explicitly stated otherwise. Figure layout modified from Ref. [263].

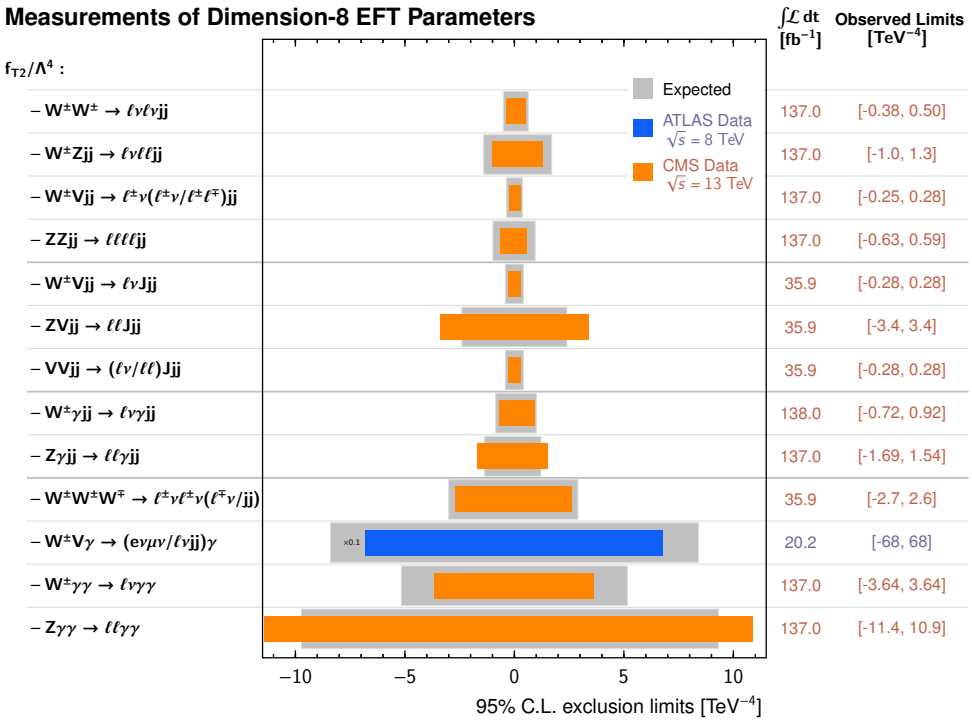


Figure 9.4: Overview of exclusion limits on dimension-eight EFT parameter f_{T2}/Λ^4 obtained in measurements with the ATLAS and CMS experiments at centre-of-mass energies of 8 and 13 TeV in final states involving leptons, jets and/or photons, where $V = W^{\pm}, Z$. Solely the most recent publications per experiment for a specific channel are shown. In order to ensure comparability, solely results without any unitarisation procedure applied are included. Exclusion limits are presented in the MG5_aMC formalism [245] and converted if necessary. Electric charges of the leptons include implicitly all combinations allowed by the SM, unless explicitly stated otherwise. Figure layout modified from Ref. [263].

Tab. 2.6 this is mainly because these parameters are not accessible by quartic couplings involving photons. Moreover, due to the chosen scenario with K-matrix unitarisation for the charged VBS final states in their analyses, no ununitarised results for these parameters from the ATLAS collaboration exist to date - a fact that is aimed to be changed with this work. Parameters of the S family have not been probed by analyses of triple boson final states yet.

On the contrary, the f_{T0}/Λ^4 parameter is probed by all of the considered analyses, except for the study of the $\gamma\gamma pp \to (W^\pm W^\mp/ZZ)pp$ process [244]. Especially in the early analyses involving photons, this parameter is considered to be the operator the most sensitive to aQGC among the group of T operators [250, 254, 255] and hence is one of the few parameters of this group that is studied in these publications.

Throughout all shown parameters, the semi-leptonic VBS final state analysis by the CMS collaboration presents the most stringent exclusion bounds with only a subset of the data delivered in Run 2 of the LHC data-taking period [154]. Solely for the f_{T1}/Λ^4 and f_{T2}/Λ^4 parameters, the combined analysis of the fully leptonic $W^\pm W^\pm jj$ and $W^\pm Zjj$ VBS final states shows comparable limits when studying the full Run 2 dataset.

The analysis of the semi-leptonic VBS final state in Ref. [154] solely studies the merged scenario, where a large radius jet with $R = 0.8$ (indicated by J in tables and figures) is selected as the hadronic $W^\pm$ or Z boson candidate. As already pointed out in the review of SM VBS analyses in Sec. 5.5, the energy resolution is not precise enough to distinguish between the two massive electroweak bosons. Hence, naturally the mixed final state is analysed. In addition, in this analysis, both the $W^\pm Vjj$ and $ZVjj$ channel are combined in the statistical analysis. However, almost all sensitivity comes from the $W^\pm Vjj$ process for the one-dimensional limits of all considered parameters. It might be interesting whether the $ZVjj$ final state can add sensitivity when studying multidimensional limits. However, since both final states are probing multiple and to some extent similar quartic couplings, it is expected that the picture does not change too much.

As stated in Ref. [248], in which the semi-leptonic VBS final state is studied in the resolved as well as merged selection by the ATLAS collaboration at $\sqrt{s} = 8\,\text{TeV}$, the merged category significantly improves the sensitivity to aQGC due to their reach to larger energies. According to this study, the exclusion limits improved by 40% when including the merged category compared to solely studying the resolved case.

VBS analyses with photons in the final state have the best sensitivity to the family of T parameters among all dimension-eight EFT parameter families. In the analysis of the $Z\gamma jj$ final state by the ATLAS collaboration [250], the charged lepton channel is combined with the channel where the Z boson decays into two neutrinos. It is stated that the latter gives most of the sensitivity in this analysis due to the larger branching fraction which can afford to place a higher threshold on the transverse energy of the photon which is used to select events for the analysis of the EFT parameters. Although the results cannot compete with the VBS analyses including $W^\pm$ and Z bosons for the parameters shown here, final states with photons are valuable for probing the neutral parameters f_{T8}/Λ^4 and f_{T9}/Λ^4 which cannot be accessed by final states with $W^\pm$ bosons.

Analyses of triple boson production are not competitive with the results obtained by the VBS analyses. This is not only because most analyses only published studies at $\sqrt{s} = 8\,\text{TeV}$ and only few have been repeated at 13 TeV.

As expected, also exclusion bounds obtained from analyses at $\sqrt{s} = 8\,\text{TeV}$ are not competitive with the new results at 13 TeV. Accordingly, results from the ATLAS collaboration at 13 TeV are anticipated with excitement to complement the range of CMS results at this centre-of-mass energy.

As stated in Sec. 5.5, no measurements in final states with four neutrinos or two opposite-charge leptons plus neutrinos have been presented to date. The study of Ref. [244] with selecting a pure hadronic final state is notably among all results, though not competitive with analyses of (semi-)leptonic final states.

Moreover, it is to be noted, that not all analyses extract exclusion limits on the full set of parameters relevant for their final state. This has several reasons. Early analyses choose parameters which can be related to dimension-six parameters constrained by results of the LEP experiments [60–65], e. g. for the parameters of the M group [250, 254, 255]. Other analyses, as indicated above, motivate their limited choice by the expected sensitivity to

parameters for their studies [250, 254, 255]

As the comparison of the sensitivity of all considered final states shows, the semi-leptonic VBS final states, and especially the $W^{\pm}Vjj$ process, profit from the larger branching fraction of hadronic final states together with a higher energy reach in the merged selection. The clean signatures of the fully leptonic and photon final states, which have their strength in the precision measurements of SM quantities (cf. Sec. 5.5), are only partially able to compete with these conditions. Without question, probing diverse final states is nevertheless essential for entirely understanding possible deviations from the SM as the coupling structure of the new physics can only be exploited with collecting all available information.

With this being said, the many uncorrelated results being presented to date possess even more potential when combining them. While the comparison of results is a valid physics motivation, the final goal is to combine all available information in order to approach a global set of exclusion bounds for the dimension-eight parameters. This implies to not only correlate information from different final states within one experiment but ultimately utilise available results from both the ATLAS and CMS experiments. Even one more step further is then the combination with studies of dimension-six parameters, whose landscape is rich in itself.

The first combination has been conducted within the ATLAS experiment at 8 TeV in the final states of $Z\gamma\gamma$ [255], $Z\gamma jj$ [250], and $W^{\pm}V\gamma$ [252], where different final states of the same process are considered. Recent results of the CMS collaboration combined multiple process categories in the simultaneous statistical analysis of information of the $W^{\pm}W^{\pm}jj$ and $W^{\pm}Zjj$ final states [155] or the $VVjj$ semi-leptonic channels [154]. Combined exclusion limits for dimension-eight EFT parameters of the $W^{\pm}W^{\pm}jj$ and $ZZjj$ final states from the CMS experiment are presented in Ref. [264] using information from HEPData [265].

Inter-experimental combinations of anomalous gauge coupling results are rare. At $\sqrt{s} = 7\,\text{TeV}$ results of the ATLAS and CMS collaboration are combined in the $ZZjj$ channel to extract exclusion bounds on aTGCs [266].

With the different analysis strategies pursued by both experiments, as stated above, combinations are difficult to achieve. For the final goal, a common ground of model assumptions, parameter definitions, unitarisation procedures, and presentation of results must be established to begin with. This requires careful focus on details beginning with the simulation of the signal contributions. Furthermore, information of measurement results must be transparent, such as for the combination of systematic and theoretical uncertainties.

In addition to the ununitarised exclusion bounds shown in Fig. 9.1 to 9.2, unitarised limits are published in various different formats. Fig. 9.5 shows the K-matrix unitarised two-dimensional exclusion bounds on the α_4 and α_5 parameters obtained with the fully and semi-leptonic VBS finales states of the ATLAS experiment at $\sqrt{s} = 8\,\text{TeV}$.

Analyses with photons in the final state from the ATLAS collaboration, alongside ununitarised measurements, present results depending on the parameters of the form factor unitarisation[1]. Analyses of the $Z\gamma\gamma$ [255], $Z\gamma jj$ [250], and $W^{\pm}V\gamma$ [252] final states derive exclusion limits depending on the form factor energy cutoff Λ_{FF}. While in the study of the latter final state, two distinct values for the cutoff are chosen, the other measurements include more measurements points, as shown in Fig. 9.6. Moreover, these analyses publish exclusion bounds at the maximally allowed value of Λ_{FF}, which is the intersection between the unitarity bound and the expected exclusion limits, obtained by the VBFNLO estimation. In the study of the $W^{\pm}\gamma\gamma$ final state, exclusion bounds dependent in the form factor exponent n are published [254].

As stated above, the CMS collaboration only recently started to implement unitarisation procedures in their analyses. For the measurements of the combined $W^{\pm}W^{\pm}jj$ and $W^{\pm}Zjj$ VBS final states they present exclusion limits clipped at the unitarisation bound employing parton-level diboson invariant masses and calculations published in Ref. [4]. The resulting limits are two to almost five times weaker than those obtained without unitarisation.

Exclusion bounds depending on the clipping energy, as recommended in Ref. [78], have

[1] In the form factor unitarisation procedure, the definition of the parameter of interest is transformed via a factor as $\frac{f_i}{\Lambda^4} \to \left(1 + \frac{s}{\Lambda_{FF}^2}\right)^{-n} \frac{f_i}{\Lambda^4}$.

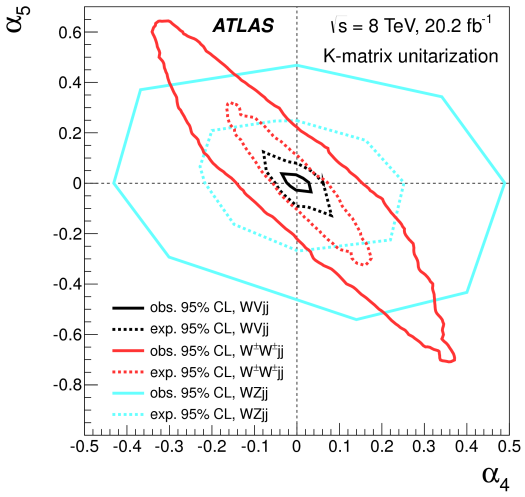
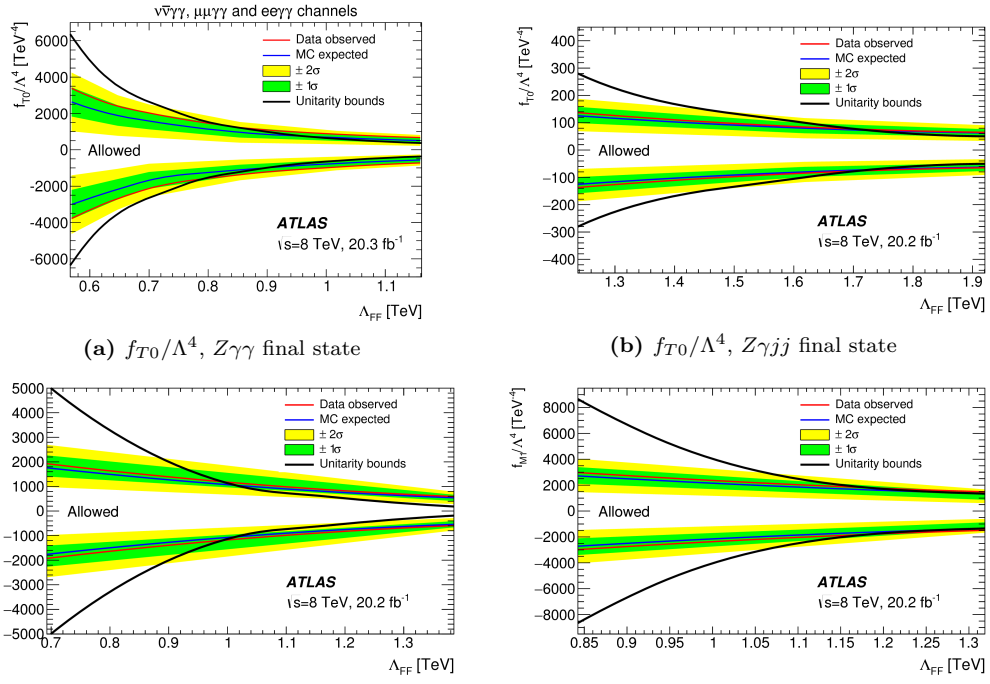


Figure 9.5: Two-dimensional expected (dotted) and observed (solid) 95% C.L. exclusion limits for the aQGC parameters α_4 and α_5 obtained by analyses of the $W^{\pm}Vjj$ (black), $W^{\pm}W^{\pm}jj$ (red), and $W^{\pm}Zjj$ (blue) VBS final states with the ATLAS experiment at $\sqrt{s} = 8\,\text{TeV}$. The K-matrix unitarisation method is applied for all results. Figure taken from Ref. [248].



(a) f_{T0}/Λ^4, $Z\gamma\gamma$ final state

(b) f_{T0}/Λ^4, $Z\gamma jj$ final state

(c) f_{M0}/Λ^4, $Z\gamma jj$ final state

(d) f_{M1}/Λ^4, $Z\gamma jj$ final state

Figure 9.6: One-dimensional expected (blue) and observed (red) 95% C.L. exclusion limits for the EFT dimension-eight parameters f_{T0}/Λ^4 (a,b), f_{M0}/Λ^4 (c), and f_{M1}/Λ^4 (d) obtained by the analyses of the $Z\gamma\gamma$ (a) and VBS $Z\gamma jj$ (b-d) final states with the ATLAS experiment at $\sqrt{s} = 8\,\text{TeV}$ depending on the form factor unitarisation cutoff scale Λ_{FF}. The unitarity bound obtained from VBFNLO is shown as well (black). Figures taken from Ref. [250, 255].

Table 9.2: One-dimensional expected and observed 95% C.L. for the aQGC parameters α_4 and α_5 with K-matrix unitarisation obtained by the analysis of the $W^{\pm}W^{\pm}jj$ final state with the ATLAS experiment at $\sqrt{s} = 8\,\text{TeV}$ and conversion into the dimension-eight EFT parameters f_{S02}/Λ^4 and f_{S1}/Λ^4 within the scenario presented in Ref. [2, 3] with Eq. (9.1) and (9.2), respectively. The vacuum expectation value is $v = 246.22\,\text{GeV}$. Numbers for α_4 and α_5 are taken from Ref. [86].

Param.	95% C.L. interval		Param.	95% C.L. interval [TeV^{-4}] (converted with Eqs. (9.1),(9.2))	
	Expected	Observed	$\frac{f_i}{\Lambda^4}$	Expected	Observed
α_4	[−0.06, 0.07]	[−0.14, 0.15]	$S02$	[−261,305]	[−609,653]
α_5	[−0.10, 0.11]	[−0.22, 0.22]	$S1$	[−435,479]	[−958,958]

not been published in analyses studying dimension-eight EFT parameters but e. g. within analyses of scenarios of aTGCs [267].

As this work focuses on the extraction of dimension-eight EFT parameters in the parameterisation presented in Ref. [2, 3] in the $W^{\pm}W^{\pm}jj$ final state with the ATLAS experiment, existing exclusion limits from ATLAS on aQGCs within the $\alpha_{4/5}$ formalism are translated into exclusion bounds of dimension-eight EFT parameters via Ref. [245]:

$$\frac{f_{S0} + f_{S2}}{\Lambda^4} = \frac{16}{v^4}\,\alpha_4, \tag{9.1}$$

$$\frac{f_{S1}}{\Lambda^4} = \frac{16}{v^4}\,\alpha_5. \tag{9.2}$$

Results are shown in Tab. 9.2. It is to be noted here again, that these numbers are obtained with the K-matrix unitarisation resulting in substantially weaker limits than without unitarisation.

9.2 Simulation of EFT Signal Samples

This section details the MC event generation of the EFT signal contributions employed in this thesis. The novel technique of amplitude decomposition, provided in the MG5_aMC event generation programme, is introduced. This approach has not been used previously in the context of analyses of dimension-eight EFT models and advantages over the conventional approach are discussed. After summarising the technical details of the MG5_aMC MC simulation setup, this new technique is thoroughly validated. The focus in the validation process not only lies in the cross-section predictions but also in the sensitive observable, whose choice is reasoned in this section. In the course of this validation, major discrepancies between the conventional method and the amplitude decomposition are found and the non-closure between the two approaches is investigated. Including all relevant distributions of all parameters is beyond the scope of a printed version of this thesis. Additional distributions of various other kinematic observables showing results for all relevant EFT parameters are collected in an auxiliary appendix, enclosed to this thesis in Ref. [268].

Eventually, the specifics of the simulation of the final signal samples are concluded from the findings in the validation procedure and the hunt for the source of the non-closure.

9.2.1 Amplitude Decomposition of the EFT Parametrisation

The squared matrix element describing EFT effects as extension of the SM can be decomposed from the individual amplitudes as:

$$\begin{aligned}\sigma_{\text{SM+EFT}} \sim \left|\mathcal{M}_{\text{SM}} + \sum_i \frac{f_i}{\Lambda^4}\mathcal{M}_i\right|^2 &= |\mathcal{M}_{\text{SM}}|^2 && \texttt{SM}\\ &+ \sum_i 2\frac{f_i}{\Lambda^4}\mathcal{R}e(\mathcal{M}_i^*\mathcal{M}_{\text{SM}}) && \texttt{LIN}\\ &+ \sum_i \frac{f_i^2}{\Lambda^8}|\mathcal{M}_i|^2 && \texttt{QUAD}\\ &+ \sum_{i,j,i\neq j} 2\frac{f_i f_j}{\Lambda^8}\mathcal{R}e(\mathcal{M}_i^*\mathcal{M}_j), && \texttt{CROSS}\end{aligned} \tag{9.3}$$

where $\mathcal{M}_{\text{SM}}$ is the SM amplitude and $\mathcal{M}_i$ describes the amplitude associated to the EFT operator $\mathcal{O}_i$ which is to be multiplied with the coefficient f_i/Λ^4. Besides the pure SM term, labelled `SM` in the following, the decomposition yields additional terms which include the BSM EFT effects and can be characterised by the order of their coefficients. The term describing the interference between the SM and EFT amplitude is linear in the coefficient f_i/Λ^4, hence further labelled `LIN`. The term quadratic in f_i/Λ^4 purely contains EFT effects of one single EFT operator. It is labelled `QUAD` in the following. The last term of Eq. (9.3) describes the interference between two different EFT operators, also referred to as `CROSS` term.

The event generation programme MG5_aMC is able to generate the individual contributions of Eq. (9.3) when using the appropriate FeynRules input model [70]. If validated thoroughly, this new method of decomposition allows to scan a wide parameter space with the generation of only very few samples. By appropriate scaling with the coefficients f_i/Λ^4, the individual samples of the `LIN`, `QUAD` and, in two-dimensional cases, the `CROSS` contributions can be combined with a preexisting SM sample to reach arbitrary points in the one- or two-dimensional parameter space of any observable as:

$$\texttt{SUM}(x = \frac{f_i}{\Lambda^4}) = \texttt{SM} + \frac{x}{x_n}\texttt{LIN}(x_n) + \frac{x^2}{x_n^2}\texttt{QUAD}(x_n), \tag{9.4}$$

in the one-dimensional case and:

$$\begin{aligned}\texttt{SUM}(x = \frac{f_i}{\Lambda^4}, y = \frac{f_j}{\Lambda^4}) = \texttt{SM} &+ \frac{x}{x_n}\texttt{LIN}(x_n) + \frac{x^2}{x_n^2}\texttt{QUAD}(x_n)\\ &+ \frac{y}{y_n}\texttt{LIN}(y_n) + \frac{y^2}{y_n^2}\texttt{QUAD}(y_n) + \frac{xy}{x_n y_n}\texttt{CROSS}(x_n, y_n),\end{aligned} \tag{9.5}$$

in the two-dimensional case. The x and y are the coefficients $\frac{f_i}{\Lambda^4}$ in the one- and two-dimensional case. The x_n and y_n are the values of the coefficients with which the individual samples have been generated (called "nominal" parameter set in the following). For simplicity one might argue that the samples can be generated with coefficients equal to $1\,\text{TeV}^{-4}$. However, we will see later that the scaling works best if the target coefficient is not too large and not too far away from the originally generated sample.

The resulting sample `SUM` is an event sample describing the full effect of the SM with EFT extensions. Its differential kinematic distributions predict the full effect expected by this extension. Ideally, one sample per operator/coefficient and contribution is needed to cover the full parameter space. For N independent operators considered from the model, N samples of the `LIN` and `QUAD` contributions each, and $N(N-1)/2$ samples of the `CROSS` contribution are necessary, resulting in $2N + N(N-1)/2$ samples.

This technique has not been used in previous analyses of dimension-eight EFT parameters since appropriate FeynRules models have only recently become available and validation studies have not yet been performed. This, especially, is aimed to be addressed in this thesis. The splitting of the contributions into individual samples has several advantages over the previously used strategies.

9.2.2 Previous Strategies for the Simulation of EFT Samples and Comparison to the Amplitude Decomposition Approach

As the different measurement strategies between the various analyses summarised in Sec. 9.1 already indicate, the approaches for the simulation of samples predicting EFT effects likewise diverge. However, all approaches involve the event generation and simulation of multiple samples per considered EFT parameter at parton/particle level and/or reconstruction level.

Analyses of the ATLAS collaboration generate a grid of samples at parton/particle level. The number of samples ranges between five and seven per considered parameter for measurements extracting one-dimensional exclusion bounds [250, 252, 254, 255, 259], and 57 [246] to over 100 [13, 86] per parameter for the two-dimensional parameter plane. In order to obtain a continuous prediction of the SM+EFT signal cross-section as a function of the EFT or aQGC parameter value, fits are performed. For the analyses probing the f_i/Λ^4 EFT parameters [250, 252, 254, 255, 259], the mathematical form of the fitting function reflects the dependency of the squared matrix elements on the EFT parameters:

$$\sigma_{\text{SM+EFT}} = p_0 + p_1 \frac{f_i}{\Lambda^4} + p_2 \left(\frac{f_i}{\Lambda^4} \right)^2 . \tag{9.6}$$

In analyses which probe the aQGC parameters α_4 and α_5 [13, 86, 246], a linear fit is performed to interpolate between the discrete cross-section values provided by the generated samples. In some cases, this fit is done for the total cross-section. Then the acceptance correction factors are usually assumed to be independent of the EFT parameter and their values, hence are taken from the SM. The differences between both are neglected as these are argued to be an order of magnitude lower than the efficiency factor corrections [255] or taken as systematic uncertainty on the EFT prediction [254]. Only in Ref. [13, 86], the acceptance corrections are computed in a fine grid of the two-dimensional α_4 and α_5 plane.

In order to utilise these information to extract exclusion bounds with events at reconstruction level, the fiducial cross-sections obtained by above's strategy, have to be translated into reconstruction level events by employing efficiency correction factors. Moreover, the assumption of the quadratic parameterisation of the fitting function of the cross-section is only valid, if the efficiency correction factor is independent of the value of the EFT parameter. Attempts have been made to show this. However, these only use one sample at reconstruction level per parameter without checking the dependency on different values of this parameter [250, 252, 255]. As a result of these tests, the efficiency correction factor obtained with the SM prediction is used for all samples of all EFT parameters, not distinguishing between parameters nor values. The maximum discrepancies between the efficiency correction obtained from the SM prediction and all considered EFT samples at reconstruction level is taken as an additional systematic uncertainty on the EFT predictions used for the limit setting [250, 255] which can reach up to 60% in some channels [255].

Solely few analyses study the impact of the detector efficiency on the BSM predictions. Within the measurement of the $W^{\pm}W^{\pm}jj$ VBS final state [13, 86], efficiency correction factors are evaluated with a coarse grid of 18 fully detector simulated samples with different values in the α_4 and α_5 plane at reconstruction level. The correction factors of these discrete points in the parameter space are then interpolated with a linear fit to obtain continuous values in the two-dimensional parameter plane and additional systematic uncertainties are propagated from this fit to the final aQGC estimate.

For the analysis of the exclusive $\gamma\gamma \to W^{\pm}W^{\mp}$ VBS channel [259] 13 samples are simulated at reconstruction level, employing either the full GEANT4 or the reduced ATLFAST-II model alternating in parameter points. The efficiency correction factor is then taken to be the average over all 13 samples and associated with an extra systematic uncertainty of a few percent from the standard deviation.

In all these analyses published by the ATLAS collaboration, unitarised limits are derived. In this case, the dependence on the parameters is no longer quadratic and Eq. (9.6) is not valid any longer. However, this effect is not considered in these analyses.

Measurements of the CMS collaboration follow two strategies. Either the parameterisation of Eq. (9.6) is employed to fit a number of samples including EFT effects. However,

this time the fit is performed at reconstruction level in order to obtain reconstructed event yields for the limit setting procedure [154, 155, 249, 253]. If the analysis employs a fit to a differential distribution to extract the exclusion limits, the quadratic fit is performed in each bin of the distribution independently. Again here, the parameterisation only holds when assuming the efficiency correction factors to be independent of the EFT effects. In other analyses [18, 247, 251, 253], predictions of multiple EFT parameter points at reconstruction level are obtained by employing the LO matrix element reweighting prescription implemented in the MG5_aMC event generator [269]. With this method, additional weights are included in the event generation which correspond to different values in the parameter space. Thus, a grid of points with different parameter values is generated within only one sample which is then fully simulated at reconstruction level. The events of these samples can then be reweighted in order to obtain predictions for a fine grid of parameter values. Two of the published analyses combine the two strategies by first simulating events with the MG5_aMC reweighting method and then interpolating between the reweighted points with the quadratic parameterisation of Eq. (9.6) [18, 247].

The LO matrix element reweighting implemented in the MG5_aMC event generator is investigated within the work of this thesis, however, not presented in detail here. In Ref. [270, 271] it is studied with MG5_aMC version 2.6.0 released in 2017. It is concluded that the method gives results which are not reliable enough to be used in a full-stack analysis chain. Multiple sets of samples have been generated, each containing reweighted and standalone samples for many points. The reweighting works fairly well for the generator cross-section predictions. However, for all sets of generated samples, few points in the parameter space are found to have considerable deviations from the cross-section predicted by a standalone generated event sample. The discrepancies reach up to 15%. Mostly, this affects cases where the reweighting was done for parameter values that are further apart from each other. However, no systematic effect could be deduced and hence the definition of "too far away" lacks a quantitative prescription. It is then difficult to estimate if a certain distance between parameter values is still behaving well without checking with a standalone sample. Thus, the gain in resources, time and computing power, is limited.

Moreover, for almost all points, differential distributions of observables exist, which differ significantly in shape between the reweighted and the standalone prediction. This affects important quantities such as the leading lepton transverse momentum and pseudorapidity or the leading jet p_{T}. Discrepancies of up to 50% are found in differential distributions for points for which the total cross-sections agree well. The reweighting procedure is especially unreliable when the shape of the nominal point used for reweighting and the target have very different shapes. This does not only lead to large discrepancies but also large statistical fluctuations.

In summary, so far published results of the ATLAS and CMS collaborations generate multiple samples per BSM parameter which describe the full SM and EFT effect in each single sample at various different parameter points at particle level and/or reconstruction level. All measurement results rely on approximations for the acceptance and detector efficiency corrections which are either obtained by interpolating between points at reconstruction level or applying the SM correction factors. Both strategies lead to additional systematic uncertainties which have to be considered in the limit setting procedure. Full detector simulations are computing resource expensive and hence are only used very restrictedly.

The new method of amplitude decomposition allows for the reduction of necessary fully simulated samples of two per parameter for one-dimensional limits. Moreover, these samples cover the full effect in acceptance and efficiency corrections without the necessity for interpolations, as will be shown within the validation in Sec. 9.2.8. Furthermore, effects from the variation of object and event kinematics to assess systematic uncertainties (cf. Sec. 7.6) can be evaluated continuously by scaling of the individual terms equally as the nominal predictions.

Moreover, with the previous methods, each sample with EFT contribution includes the full SM and EFT effect. While the EFT contributions usually populate the high-energy tails of the distributions, the SM contribution occupies the majority of the phase space. Hence, the efficiency of generating events in the phase space regions which are relevant for the analysis is small, either causing large statistical uncertainties in these regions or yet further involving

enormous resource needs. With the amplitude decomposition as explained above, the EFT contributions can be generated independently of the SM allowing for appropriate statistical accuracy in the high energy or mass tails of relevant distributions.

This new technique of amplitude decomposition needs to be validated in order to qualify it for the use in the analysis. Comprehensive studies for the validation are detailed in Sec. 9.2.6.

9.2.3 Technical Details of the Event Generation of EFT Samples

The event generation of the EFT samples with the MG5_aMC event generation programme follows the same procedure as for the SM samples, described in Sec. 6.3.3. Technical details are identical to the nominal setup, MG5+Py8drec, unless stated otherwise. The samples are LO accurate in all SM couplings.

The analysis in this thesis employs the dimension-eight EFT scenario detailed in Sec. 2.3.3. It is implemented in the FeynRules model `SM_LS012_LM017_LT012_Ind5_UFO_June19` [272] and based on Ref. [2, 3]. This model provides all operators relevant for the process under study, $W^{\pm}W^{\pm}jj$-EW6. It supports the event generation technique of the amplitude decomposition and includes `CROSS` terms between operators of the same family, however not between different families. By the time of the completion of this work a newer version of this model was published [70] which includes further operators of the scenario in the technical model implementation.

The process and parameter definitions, given in the `proc_card.dat` and `param_card.dat`, respectively, need to be altered with respect to the SM case to include information on the EFT model. Technical details are thoroughly summarised in App. F.1 including example cards for the EFT case.

Together with a suitable set of EFT samples a SM sample employing the identical settings needs to be generated for the validation of the decomposition. This includes the usage of the model describing the EFT scenario for this sample. After the validation, for the actual statistical analysis it might be possible to utilise a SM prediction that is more precise than the LO accurate EFT model provides if the k-factors that are derived for the SM predictions also apply to the EFT contribution. However, it is not possible today with the given model, to validate this assumption. Hence, this work utilises the LO accurate SM prediction of the MG5_aMC setup, MG5+Py8drec.

In the course of the validation of the decomposition, it has been stated by the authors of the MG5_aMC programme that for the interference calculation, the default dynamical renormalisation and factorisation scale, the cluster scale based on Feynman diagrams, is not defined [273]. Hence, the requested dynamical scale is internally set to a different dynamical scale in case of the generation of the interference samples. This does not only affect the `LIN`, but also the `CROSS` contribution. In addition, this holds for any model parametrisation and not only for the EFT case, e. g. it also affects the generation of the interference between the SM $W^{\pm}W^{\pm}jj$-EW6 and $W^{\pm}W^{\pm}jj$-EW4 processes, $W^{\pm}W^{\pm}jj$-INT, with the `sm` model. Moreover, within these studies, it has been found, that the cluster scale is not a favourable choice for the SM $W^{\pm}W^{\pm}jj$ process either [227].

In conclusion, the default dynamical scale is not suitable if one aims at generating a set of samples with identical settings. It is then reasonable to chose any other dynamical scale which is defined at the level of final state matrix element particles. As stated in Sec. 6.3.3, the HT dynamical scale is chosen for the final EFT samples.

9.2.4 Choice of the Nominal Parameter Values

The choice of the relevant operators for the study of BSM EFT effects in the $W^{\pm}W^{\pm}jj$-EW6 process is clearly defined by the chosen EFT model [2, 3]. It can be deduced from the form, i. e. the field content, of the operators. In the scattering process of two equally-charged $W^{\pm}$ bosons, solely the quartic vertex with four $W^{\pm}$ bosons can be probed. As summarised in Sec. 2.3.3, only the operators $\mathcal{O}_{S02}$, and $\mathcal{O}_{S1}$ of the S family, $\mathcal{O}_{M0}$, $\mathcal{O}_{M1}$, and $\mathcal{O}_{M7}$ of the M family, and $\mathcal{O}_{T0}$, $\mathcal{O}_{T1}$, and $\mathcal{O}_{T2}$ of the T family act on this quartic vertex, totalling to a number of eight operators to be probed. The reader is reminded, that the operator $\mathcal{O}_{S2}$ is the hermitian conjugate of $\mathcal{O}_{S0}$ and hence the coefficients for these two operators must

Table 9.3: Nominal values, $x_n = (f_i/\Lambda^4)_n$, of all relevant parameters as used for the amplitude decomposition method and the subsequent scaling of the individual contributions. The values are chosen based on results from Ref. [14].

Parameter $\frac{f_i}{\Lambda^4}$	Value (TeV^{-4})
$S0 = S2$	8.0
$S1$	20.0
$M0$	6.0
$M1$	10.0
$M7$	13.0
$T0$	0.6
$T1$	0.3
$T2$	1.0

always be identical, $f_{S2}/\Lambda^4 = f_{S0}/\Lambda^4$, which is indicated with the use of the $S02$ subscript in this work when referring to these parameters.

The choice of the nominal parameter values $x_n = (f_i/\Lambda^4)_n$, which are the basis for the scaling when using the method of amplitude decomposition, is based on a measurement with very similar conditions as the one conceived in this thesis. In Ref. [14], the relevant set of operators are probed in the $W^\pm W^\pm jj$ VBS channel with the CMS experiment at a centre-of-mass energy of 13 TeV with a dataset of 35.9 fb^{-1} roughly equal in size to the one utilised for this study. In addition, Ref. [14] has been the only publication that probed all relevant parameters of the model in the $W^\pm W^\pm jj$ final state by the time of the design of this measurement. The expected exclusion bounds obtained in Ref. [14] are hence employed as a benchmark for the sensitivity of this study. The nominal parameter values for the subsequent validation and the production of the samples for the final measurement are derived from these results. They are summarised in Tab. 9.3.

9.2.5 Choice of the Sensitive Observable

The exclusion limits shall be derived differentially in bins of a suitable observable. Several object and event kinematic observables are examined at particle level for all relevant parameters. The final observable is chosen based on qualitative comparisons. No quantitative evaluation is included for this study.

As pointed out previously, the EFT expansion can be related to additional physical states of high mass which are not yet accessible by the energy reach of the experiment. By setting the coefficients of EFT operators to non-zero values, the electroweak quartic gauge couplings of the SM are modified. As a result, final states are more energetic which clearly results in a modification of the whole event kinematics. However, as the outgoing gauge bosons and hence their decay products tend to be boosted compared to the SM case, it is expected that tails of observables related to energy, momentum, or masses of (systems of) these particles are affected to a greater extent. Combining information from all decay products of the gauge bosons to form invariant masses is expected to give the largest sensitivity to the effects caused by the EFT operators. Many VBS analyses studying this EFT model, exploit this behaviour by utilising invariant masses of the system of bosons under study [18, 154, 246–249].

In this thesis, one ideally wishes to explore the invariant mass of the $W^\pm W^\pm$ system. Due to the presence of the two neutrinos, it is impossible to fully reconstruct the invariant mass of the $W^\pm$ boson pair with the experimental setup at hand. Only via the measurement of the missing transverse momentum E_T^{miss}, kinematic information about the neutrinos can be attained. However, this measurement gives only two kinematic degrees of freedom while the momenta of the two neutrinos together have six. Hence, the full diboson invariant mass cannot be accessed in this final state. Only transverse masses with imposing additional constraints can be calculated. The problem of mass reconstruction in the case of the fully

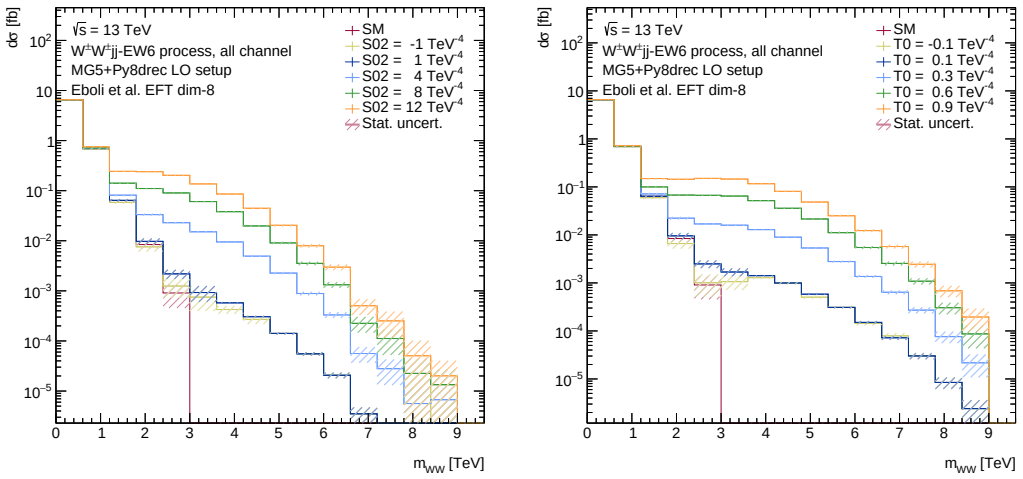


Figure 9.7: Invariant mass of the $W^{\pm}W^{\pm}$ system, m_{WW}, at matrix element level for different values of the f_{S02}/Λ^4 (a) and f_{T0}/Λ^4 (b) parameters compared to the SM prediction. The nominal value (cf. Tab. 9.3) is shown in green. The distributions are shown in the loose region (cf. Tab. 6.8) at particle level. The amplitude decomposition method is used for the EFT distributions. Note the large range of the x-axis covering values up to 10 TeV for m_{WW}. Uncertainties are statistical uncertainties from the MC generation only.

leptonic final state of like-charge $W^{\pm}$ boson scattering is extensively studied in Ref. [274] in the context of BSM electroweak resonances.

In order to compare the impact of several observables, the true invariant mass of the $W^{\pm}$ boson system at matrix element level[2], m_{WW}, is shown in Fig. 9.7 exemplarily for the parameters f_{S02}/Λ^4 and f_{T0}/Λ^4. The invariant mass is reconstructed with information from the $W^{\pm}$ bosons at matrix element level. Distributions at different values of the f_{S02}/Λ^4 and f_{T0}/Λ^4 parameters are shown[3]. Distributions for the other parameters relevant to this final state are shown in App. F.3.

To begin with, the most promising definitions of invariant (transverse) masses, as defined in Ref. [274] for the $W^{\pm}W^{\pm}$ system, are examined together with other kinematic observables related to the leptonic decay products of the $W^{\pm}$ boson pair in the loose region at particle level. A selection of observables is plotted in Figures 9.8 and 9.9 exemplarily for the f_{S02}/Λ^4 parameter. More observables for this and all other parameters can be found in Ref. [268].

Negative values of the EFT parameters compared to positive ones only result in the change of sign of the interference contribution between the EFT and the SM amplitudes. As we will see later in this chapter, this contribution is not very dominant in the realm of sensitivity of this study compared to the pure EFT contribution in the quadratic term. The difference between positive and negative values are hence only sizable for small parameter values. This is the reason for not including more negative values into the illustrations shown here.

All distributions of the invariant (transverse) masses show the expected behaviour of enhancements in the region of high masses when considering EFT effects compared to the SM prediction. The invariant mass of the two leading leptons, m_{ll}, and the transverse mass m_{o1} exhibit deviations from the SM prediction starting from lower mass values than the transverse mass $m_{1\top}$ and the vectorial mass m_{vec}.

The transverse momentum of the leading lepton $p_{\text{T}}(\ell_1)$ also shows the effect introduced by the EFT parameter at large values, however not as pronounced as for the invariant masses. An explanation is that the invariant masses combine information of both charged leptons

[2]The technical implementation is described in App. F.2.

[3]As a result of its validation covered later in this chapter, the amplitude decomposition method is utilised here and in all following figures of this section anticipatorily.

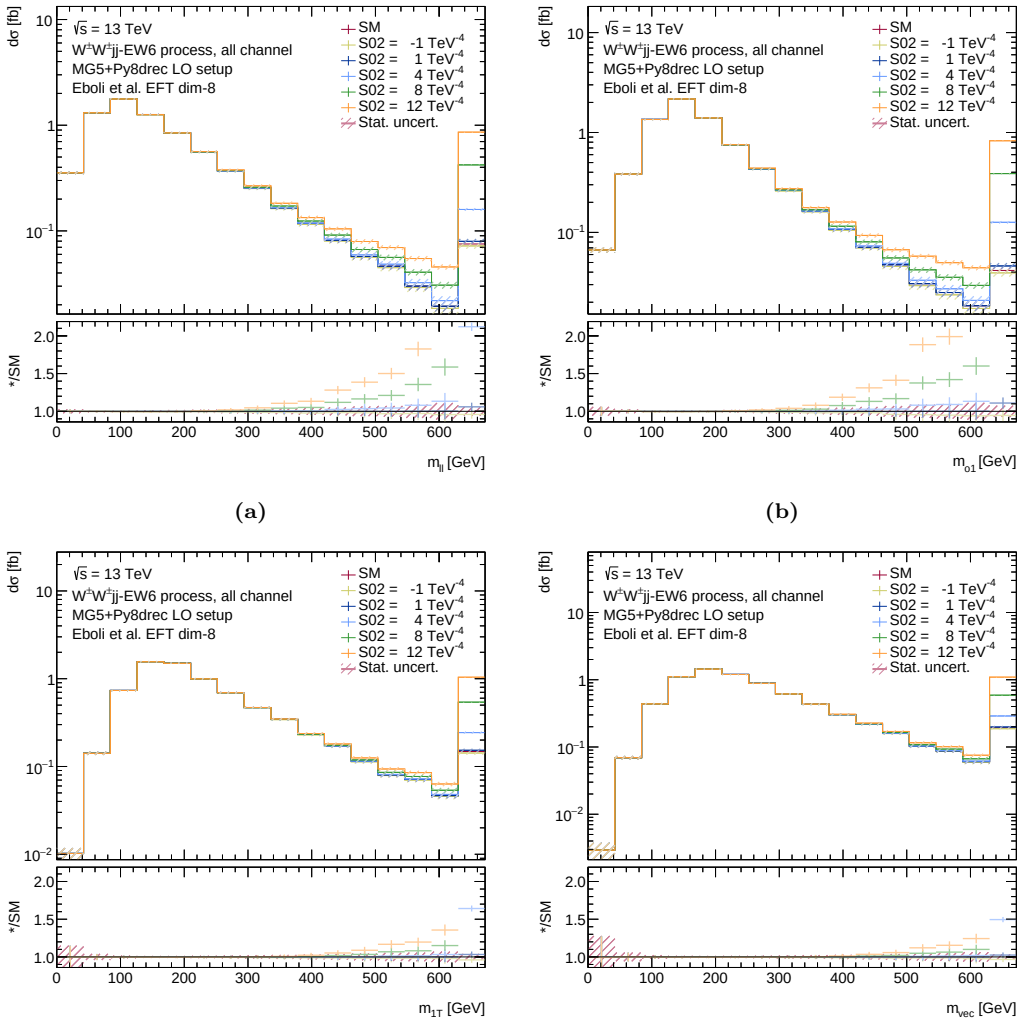
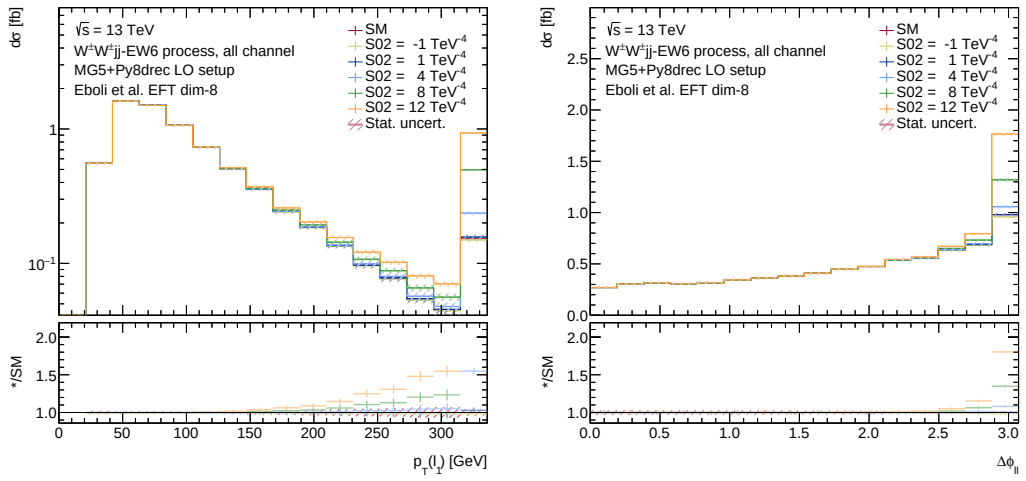


Figure 9.8: Kinematic distributions related to the leptonic decay products of the $W^{\pm}W^{\pm}$ system for different values of the f_{S02}/Λ^4 parameter and the SM prediction. The invariant mass of the lepton pair, m_{ll} (a), the transverse masses m_{o1} (b) and $m_{1\top}$ (c), and the vectorial mass, m_{vec} (d) as defined in Ref. [274] are shown. The nominal value (cf. Tab. 9.3) is shown in green. The distributions are shown in the loose region (cf. Tab. 6.8) at particle level. The amplitude decomposition method is used for the EFT distributions. The lower panel shows the ratio of the EFT contributions to the SM prediction. Uncertainties are statistical uncertainties from the MC generation only. The last bin includes the overflow.



(a) **(b)**

Figure 9.9: Kinematic distributions related to the leptonic decay products of the $W^{\pm}W^{\pm}$ system for different values of the f_{S02}/Λ^4 parameter and the SM prediction. The transverse momentum of the leading lepton $p_{\mathrm{T}}(l_1)$ (a), and the azimuthal angle between the two leading leptons $\Delta\Phi_{ll}$ (b) are shown. The nominal value (cf. Tab. 9.3) is shown in green. The distributions are shown in the loose region (cf. Tab. 6.8) at particle level. The amplitude decomposition method is used for the EFT distributions. The lower panel shows the ratio of the EFT contributions to the SM prediction. Uncertainties are statistical uncertainties from the MC generation only. The last bin in (a) includes the overflow.

from the $W^{\pm}W^{\pm}$ system while $p_{\mathrm{T}}(l_1)$ per definition only describes the leading lepton.

Moreover, the contribution from EFT predictions can be located at the largest possible separation in azimuthal angle between the two leading leptons, $\Delta\Phi_{ll}$. The reason for this lies in the increased energy content in the $W^{\pm}W^{\pm}$ boson scattering in the EFT case compared to the SM. In the first, the two bosons are boosted against each other, which is transferred to their decay products. These are hence detected back-to-back in the transverse plane where the energy-momentum balance is invariant. At the same time, this region is favoured by the SM case which makes this observable less convenient for exploring the EFT contributions as it is hard to reject the $W^{\pm}W^{\pm}jj$-EW6 background from the SM.

From Ref. [268], it can also be seen that the charged leptons are slightly more central in the detector when assuming EFT contributions compared to the SM. Furthermore, the sum of the transverse masses of the two leading neutrinos, which imitates the E_T^{miss} measurement at reconstruction level, gives sizable deviations in the region of large values. However, the E_T^{miss} reconstruction involves many particles. Hence, its resolution is inferior compared to pure charged lepton observables, which makes it less favourable for a statistical analysis of the EFT effects.

The observations for the observables related to the leptonic decay products of the $W^{\pm}W^{\pm}$ system are qualitatively comparable between all relevant parameters. In addition, it also holds when restricting the phase space to the fiducial region of the analysis. However, the deviation of the EFT contribution generally reduces in the fiducial phase space, shown in Ref. [268], compared to the loose phase space shown here. Yet, it can be seen that the reduction is larger for the family of S parameters compared to those of the M or T family. This can be understood when looking at jet-related observables, some of which show a substantial difference between the parameter of the respective families.

While for the S family of parameters, the EFT contribution can be located at small p_{T} of the leading jet, shown in Fig. 9.10, it appears at large values for the M or T parameters. This has an impact on the number of jets selected in the fiducial region which includes stringent requirements on the p_{T} of the leading and subleading jet of 65 GeV and 35 GeV, respectively. For the family of S parameters, as a result, a larger number of events has fewer selected jets compared to the SM prediction. Together with the requirement on at least two

jets in the fiducial region, this reduces the events with EFT contributions compared to the SM prediction for this family of parameters. It is a known and expected behaviour, since the jet p_{T} is different for different polarisation states of the vector bosons. As explained in Sec. 2.3.3, the parameter families are defined according to their field content which influences the effects on differently polarised boson vertices.

Moreover, for the parameter of the S family, the EFT contributions favour large rapidities of the tagging jets and hence a large separation in rapidity. For the parameters of the M and T families, the EFT contribution does not favour a specific rapidity region for the jets. This has an impact on observables mixed in leptons and jets which exhibit profitable regions for the study of the SM VBS contributions, such as the lepton centrality or the Zeppenfeld distribution of the leptons.

In general, as expected, the impact of the modification of the electroweak quartic vertex from the EFT is less pronounced in jet-related observables. Additional distributions, beyond the transverse momentum of the leading jet, $p_{\mathrm{T}}(j_1)$, can be found in Ref. [268].

In conclusion, the invariant mass of the leading lepton pair in the event, m_{ll}, and the transverse mass m_{o1} show large and comparable deviations at particle level for all parameters. The definition of the latter is more complex and includes the missing transverse momentum measurement E_T^{miss}. This, again makes m_{o1} dependent on a large number of particles in the event and hence comes expectedly with a reduced resolution and larger uncertainties than the m_{ll} variable. For simplicity, m_{ll} is chosen as the observable which is utilised for the statistical analysis of the extraction of the exclusion limits of all parameters. Its binning is not further optimised in this thesis and is taken as published in [1]. Fig. 9.11 displays the m_{ll} distributions for the f_{M0}/Λ^4 and f_{T0}/Λ^4 parameters exemplarily for the M and T family of parameters for completeness.

9.2.6 Validation of the Decomposition Method

The method of the amplitude decomposition presented in Sec. 9.2.1 shall now be validated for all relevant parameters. For this, samples with the full SM plus EFT contribution, labelled `FULL`, are generated with the otherwise identical setup as used for the decomposed samples (cf. Sec. 9.2.3 and App. F.1). The `FULL` samples are then compared to the `SUM` of the SM, `LIN` and `QUAD` contributions for identical parameter values. The `FULL` and `SUM` predictions should give identical results within the statistical accuracy of the samples. This should hold for any observable, including generator and fiducial cross-sections as well as in differential kinematic contributions. In detail, the validation covers the following steps:

1. Test if the generator cross-section fulfills:

$$\texttt{FULL}(x_n) = \texttt{SUM}(x_n) = \texttt{SM} + \texttt{LIN}(x_n) + \texttt{QUAD}(x_n); \tag{9.7}$$

2. Equally, test if the fiducial cross-section fulfills Eq. (9.7);

3. Test if Eq. (9.7) holds in differential distributions of relevant observables in all relevant phase space regions;

4. Test the scaling of the nominal samples to reach predictions for arbitrary parameter values in the one-dimensional, e. g.: $x = f_{M0}/\Lambda^4$:

$$\begin{aligned} \texttt{FULL}(x) &= \texttt{SUM}(x) \\ &= \texttt{SM} + \frac{x}{x_n}\texttt{LIN}(x_n) + \frac{x^2}{x_n^2}\texttt{QUAD}(x_n); \end{aligned} \tag{9.8}$$

5. ... and two-dimensional case, e. g.: $(x, y) = (f_{M0}/\Lambda^4, f_{M1}/\Lambda^4)$:

$$\begin{aligned} \texttt{FULL}(x, y) &= \texttt{SUM}(x, y) \\ &= \texttt{SM} + \frac{x}{x_n}\texttt{LIN}(x_n) + \frac{x^2}{x_n^2}\texttt{QUAD}(x_n) \\ &\quad + \frac{y}{y_n}\texttt{LIN}(y_n) + \frac{y^2}{y_n^2}\texttt{QUAD}(y_n) + \frac{xy}{x_n y_n}\texttt{CROSS}(x_n, y_n). \end{aligned} \tag{9.9}$$

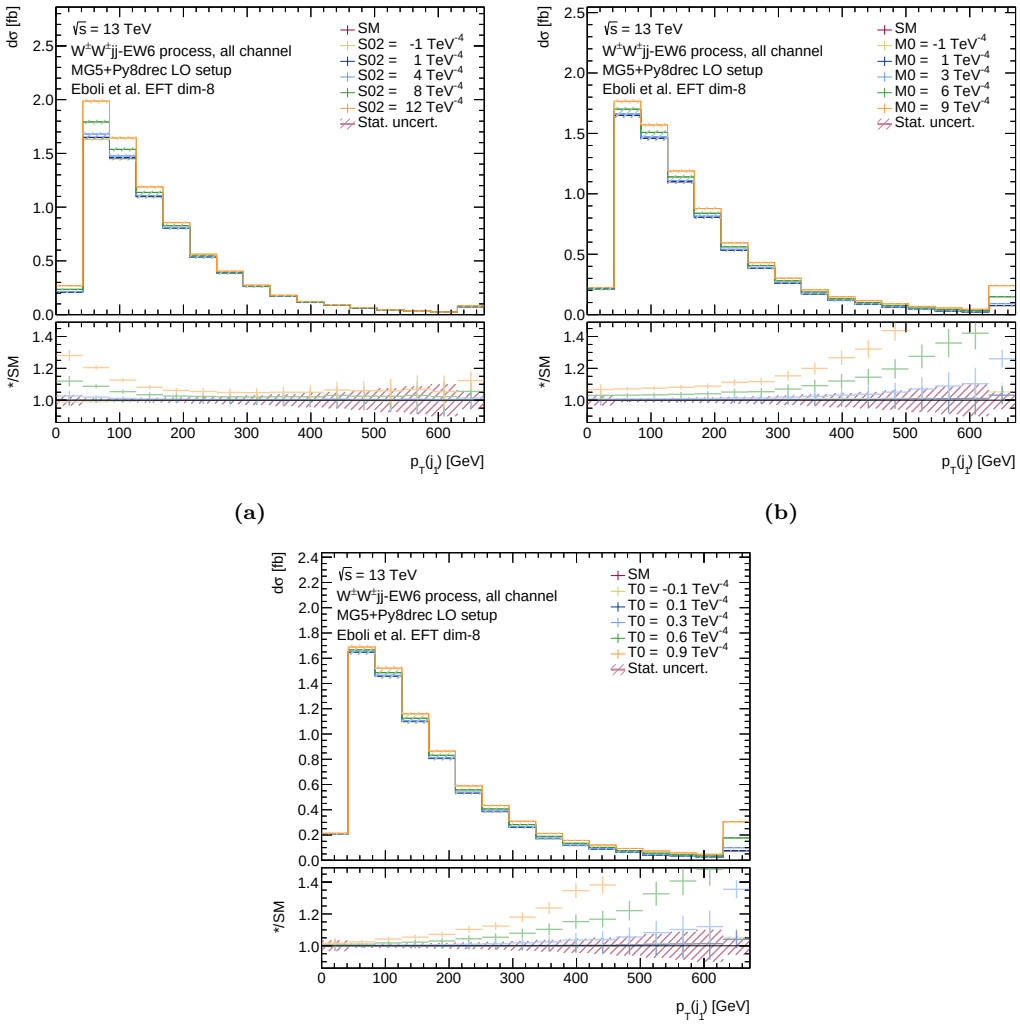
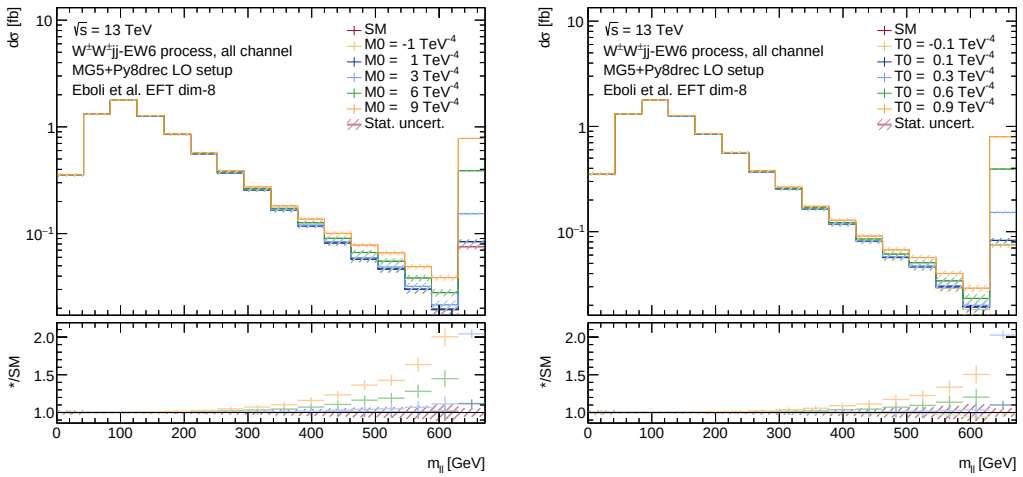


Figure 9.10: Distribution of the transverse momentum of the leading jet in the event, $p_{\mathrm{T}}(j_1)$ for different values of the f_{S02}/Λ^4 (a), f_{M0}/Λ^4 (b), and f_{T0}/Λ^4 (c) parameters compared to the SM prediction. The nominal value (cf. Tab. 9.3) is shown in green. The distributions are shown in the loose region (cf. Tab. 6.8) at particle level. The amplitude decomposition method is used for the EFT distributions. The lower panel shows the ratio of the EFT contributions to the SM prediction. Uncertainties are statistical uncertainties from the MC generation only. The last bin includes the overflow.



(a) **(b)**

Figure 9.11: Distributions of the invariant mass of the leading lepton pair, m_{ll}, for different values of the f_{M0}/Λ^4 (a), and f_{T0}/Λ^4 (b) parameters and the SM prediction. The nominal value (cf. Tab. 9.3) is shown in green. The distributions are shown in the loose region (cf. Tab. 6.8) at particle level. The amplitude decomposition method is used for the EFT distributions. The lower panel shows the ratio of the EFT contributions to the SM prediction. Uncertainties are statistical uncertainties from the MC generation only. The last bin includes the overflow.

The outcome of the tests is anticipated at this point as it explains some technical choices made for the sample generation in this section. Non-closure is found between the `FULL` and `SUM` in all steps of the validation affecting different parameters of the EFT model in different steps.

For the tests summarised in this thesis, the full $W^{\pm}W^{\pm}jj$-EW6 final state is generated (cf. Sec. 6.3.3 for the process definition in MG5_aMC) after the first iteration with a reduced process definition gave similar results[4].

The dynamical scale is set to the default cluster scale for all samples used in this section, unless stated otherwise, as the MG5_aMC internal behaviour detailed in Sec 9.2.3 has only been discussed after the finding of the non-closure.

In the following, results of the checks as mentioned above are summarised up to a point where the non-closure became apparent.

Generator Cross-section

The generator phase space for the simulation of the EFT samples is identical to the one used for the simulation of the nominal SM prediction of the MG5_aMC setup, detailed in Tab. 6.7. However, note again the differing dynamical scale choices, HT and the default cluster scale, respectively, of the MG5+Py8drec setup employed in Chapter 6 and the setup used here in the EFT decomposition validation procedure. With the differing nominal scale choice the SM predicts a cross-section in the generator phase space of (37.11 ± 0.15) fb.

The generator cross-sections for the decomposed contributions `LIN` and `QUAD`, as well as their sum with the SM contribution and the `FULL` prediction are listed in Tab 9.4 for the one-dimensional case. The `CROSS` contribution[5], together with the two-dimensional `SUM` and `FULL`

[4] In principle, the decomposition method should work independent of the lepton and quark flavour (as long as both respectively are treated equally). Hence, the first iteration used the process definition u u > d d e^+ μ^+ ν ν. However, this gives similar non-closing results as when using the full process definition in the event generation. Consequently, the full process was checked to exclude the reduced process definition as the source of non-closure.

[5] Note, that it was not possible to generate the interference term between the operators $\mathcal{O}_{M0}$ and $\mathcal{O}_{M7}$ due to an inconsistency in the version of the FeynRules model used for the validation. This has been fixed by the authors of the model after its finding in the validation procedure.

Table 9.4: Cross-section predictions in the generator phase space of the MG5_aMC setup (cf. Tab. 6.7) for the decomposed `LIN` and `QUAD` contributions, as well as their sum with the SM prediction of (37.11 ± 0.15) fb, labelled `SUM`, and the `FULL` prediction of an individual sample for all relevant parameters at their nominal values. Uncertainties are the statistical errors of the MC generation only. The last column shows the significance of the difference between the `SUM` and `FULL` contribution with respect to the statistical uncertainty of the `FULL` sample.

Param.	Value	Generator cross-section [fb]				
$\frac{f_i}{\Lambda^4}$	$\frac{1}{[\mathrm{TeV}^4]}$	LIN	QUAD	SUM	FULL	$\frac{\mathtt{SUM}-\mathtt{FULL}}{\Delta(\mathtt{FULL})}$
$S02$	8.0	-0.205 ± 0.003	2.58 ± 0.01	39.48 ± 0.15	39.39 ± 0.16	$+0.6$
$S1$	20.0	-0.123 ± 0.002	1.05 ± 0.01	38.04 ± 0.15	38.00 ± 0.15	$+0.3$
$M0$	6.0	0.098 ± 0.003	1.96 ± 0.01	39.17 ± 0.15	39.06 ± 0.16	$+0.7$
$M1$	10.0	-0.159 ± 0.003	2.47 ± 0.01	39.43 ± 0.15	39.32 ± 0.15	$+0.7$
$M7$	13.0	0.122 ± 0.003	1.80 ± 0.01	39.03 ± 0.15	39.07 ± 0.15	-0.3
$T0$	0.6	-0.096 ± 0.002	1.90 ± 0.01	38.92 ± 0.15	38.67 ± 0.15	$+0.6$
$T1$	0.3	-0.321 ± 0.002	2.18 ± 0.01	38.97 ± 0.15	38.73 ± 0.15	$+1.7$
$T2$	1.0	-0.547 ± 0.003	2.67 ± 0.01	39.24 ± 0.15	38.88 ± 0.15	$+2.4$

predictions are shown in Tab. 9.5. A total of 50000 events is generated for each individual sample.

The statistical significance, defined as:

$$\frac{\mathtt{SUM} - \mathtt{FULL}}{\Delta(\mathtt{FULL})}, \tag{9.10}$$

is utilised as a measure of (dis)agreement between the `SUM` and the `FULL` approach. It quantifies the disagreement of the two approaches in terms of the statistical uncertainty of the `FULL` sample and is expressed in standard deviations σ. The statistical accuracy of the `SUM` and `FULL` contribution is below 0.4% for all parameters.

For the one-dimensional case, the difference between the `SUM` and `FULL` prediction is within the statistical uncertainties of the `FULL` prediction for most of the parameters. Mild discrepancies of approx. 2σ are found for the f_{T1}/Λ^4 and f_{T2}/Λ^4 parameters. Regarding the agreement in the parameter families, the picture is similar in the two-dimensional case. However, the discrepancies for all parameters of the T family increase sizeably, to 7σ or even almost 10σ for the f_{T1}/Λ^4 parameter. The `FULL` prediction in these cases is always larger than the one of the `SUM`.

The inference contribution between the SM and the EFT amplitude of one operator is positive for the $\mathcal{O}_{M0}$ and $\mathcal{O}_{M7}$ operators and negative for all others at the positive nominal parameter values. At these nominal parameter values, the `QUAD` contribution is dominant over the absolute `LIN` contribution for all parameters. This dominance is as large as one order of magnitude for most of the parameters. The `CROSS` contribution is again larger than or of similar size as the `QUAD` contributions of the involved parameters. As a result, the deviations of the full EFT prediction from the SM prediction are always positive. They are sizable and approx. $6 - 16\sigma$ for all nominal parameter points in the one-dimensional case.

The picture in the two-dimensional case is different where deviations from the SM prediction become as large as 44σ for the positive S parameters. This is due to the `CROSS` contribution which is sizable and positive in this case. This observation is in agreement with the available results on two-dimensional exclusion bounds on the S parameters in the same final state. These are published at $\sqrt{s} = 8\,\mathrm{TeV}$ in Ref. [196] and show pronounced elliptical exclusion contours in the two-dimensional space of f_{S0}/Λ^4 and f_{S1}/Λ^4.

Table 9.5: Cross-section predictions in the generator phase space of the MG5_aMC setup (cf. Tab. 6.7) for the decomposed CROSS contributions, as well as the two-dimensional sum of all relevant contributions with the SM prediction of (37.11 ± 0.15) fb, labelled SUM, and the FULL prediction of an individual sample for all relevant parameters at their nominal values. Uncertainties are the statistical errors of the MC generation only. The last column shows the significance of the difference between the SUM and FULL contribution with respect to the statistical uncertainty of the FULL sample. The simulation of the CROSS contribution between the $\mathcal{O}_{M0}$ and $\mathcal{O}_{M7}$ operators was not available in the FeynRules model version used for this validation.

Parameters	Values	Generator cross-section [fb]			
$\frac{f_i}{\Lambda^4}$	$\frac{1}{[\text{TeV}^4]}$	CROSS	SUM	FULL	$\frac{\text{SUM}-\text{FULL}}{\Delta(\text{FULL})}$
$S02$ – $S1$	8.0, 20.0	3.24 ± 0.02	43.65 ± 0.15	43.69 ± 0.16	-0.3
$M0$ – $M1$	6.0, 10.0	-1.81 ± 0.01	39.68 ± 0.15	39.64 ± 0.16	$+0.3$
$M0$ – $M7$	6.0, 13.0	–	–	38.40 ± 0.15	–
$M1$ – $M7$	10.0, 13.0	-3.82 ± 0.02	37.52 ± 0.15	37.54 ± 0.15	-0.1
$T0$ – $T1$	0.6, 0.3	3.01 ± 0.01	41.93 ± 0.15	43.10 ± 0.17	-6.9
$T0$ – $T2$	0.6, 1.0	1.92 ± 0.01	40.83 ± 0.15	42.38 ± 0.16	-9.7
$T1$ – $T2$	0.3, 1.0	3.91 ± 0.01	42.88 ± 0.15	44.18 ± 0.17	-7.7

Fiducial Cross-section

The cross-sections in the fiducial phase for the decomposed contributions LIN and QUAD, as well as their sum with the SM contribution and the FULL prediction are shown in Tab. 9.6 for the one-dimensional case. The SM predicts a fiducial cross-section of (3.20 ± 0.05) fb employing the default cluster scale in the MG5_aMC setup. The CROSS contribution and the two-dimensional FULL and SUM predictions are shown in Tab. 9.7.

The statistical accuracy of both, the SUM and FULL predictions, is below 1.5% for all parameters. For each of the S and M parameters the fiducial cross-sections of the SUM and FULL predictions are similar within statistical uncertainty of the MC event generation in the one-dimensional case. The discrepancies between the SUM and the FULL predictions is now sizable for the all parameters of the T family. With up to 6σ it is largest for the f_{T0}/Λ^4. At the level of the fiducial cross-section, the SUM is always larger than the FULL prediction in these cases.

In the two-dimensional case, discrepancies between the SUM and FULL predictions affect both, the M and T families of parameters, while both predictions are consistent for the S parameters. The disagreement is milder in the fiducial region compared to the generator phase space, especially for the T parameters. Interestingly, the discrepancy changes sign in case of the interference of the $\mathcal{O}_{T0}$ and $\mathcal{O}_{T1}$ operator between the generator and the fiducial cross-section. No clear picture can be observed of whether the SUM or FULL predictions is larger.

The behaviour of the interference contribution between the SM and one EFT operator, LIN, at the nominal parameter values does not change when moving from the generator phase space into the fiducial phase space. Moreover, the pure EFT contribution of one operator, QUAD and the CROSS contributions remain dominant over the LIN contributions. The dominance is approximately similar to the one at generator level.

The deviations of the full EFT prediction from the SM prediction range between 2σ for the f_{S1}/Λ^4 and 6σ for the f_{T2}/Λ^4 parameter. In the two-dimensional case, the size of the deviations from the SM prediction is again diverse ranging from below 1σ for the $\mathcal{O}_{M1}$ - $\mathcal{O}_{M7}$ operator pair to over 20σ for the pair $\mathcal{O}_{T1}$ - $\mathcal{O}_{T2}$ depending on the sign of the CROSS contribution for the nominal parameter values.

Table 9.6: Cross-section predictions in the fiducial phase space (cf. Tab. 6.8) for the decomposed `LIN` and `QUAD` contributions, as well as their sum with the SM prediction of (3.20 ± 0.05) fb, labelled `SUM`, and the `FULL` prediction of an individual sample for all relevant parameters at their nominal values. Uncertainties are the statistical errors of the MC generation only. The last column shows the significance of the difference between the `SUM` and `FULL` contribution with respect to the statistical uncertainty of the `FULL` sample.

Param.	Value	Fiducial cross-section [fb]				
$\frac{f_i}{\Lambda^4}$	$\frac{1}{[\mathrm{TeV}^4]}$	LIN	QUAD	SUM	FULL	$\frac{\mathtt{SUM}-\mathtt{FULL}}{\Delta(\mathtt{FULL})}$
$S02$	8.0	-0.020 ± 0.001	0.246 ± 0.004	3.43 ± 0.05	3.46 ± 0.05	-0.6
$S1$	20.0	-0.011 ± 0.001	0.100 ± 0.002	3.29 ± 0.05	3.25 ± 0.05	$+0.8$
$M0$	6.0	0.017 ± 0.001	0.249 ± 0.003	3.47 ± 0.05	3.50 ± 0.05	-0.6
$M1$	10.0	-0.029 ± 0.001	0.309 ± 0.004	3.48 ± 0.05	3.48 ± 0.05	$+0.1$
$M7$	13.0	0.021 ± 0.001	0.239 ± 0.003	3.46 ± 0.05	3.50 ± 0.05	-0.8
$T0$	0.6	-0.024 ± 0.001	0.287 ± 0.003	3.46 ± 0.05	3.16 ± 0.05	$+6.0$
$T1$	0.3	-0.057 ± 0.001	0.336 ± 0.004	3.48 ± 0.05	3.29 ± 0.05	$+3.8$
$T2$	1.0	-0.101 ± 0.002	0.399 ± 0.005	3.50 ± 0.05	3.43 ± 0.05	$+1.4$

Table 9.7: Cross-section predictions in the fiducial phase space (cf. Tab. 6.8) for the decomposed `CROSS` contributions, as well as the two-dimensional sum of all relevant contributions with the SM prediction of (3.20 ± 0.05) fb, labelled `SUM`, and the `FULL` prediction of an individual sample for all relevant parameters at their nominal values. Uncertainties are the statistical errors of the MC generation only. The last column shows the significance of the difference between the `SUM` and `FULL` contribution with respect to the statistical uncertainty of the `FULL` sample. The simulation of the `CROSS` contribution between the $\mathcal{O}_{M0}$ and $\mathcal{O}_{M7}$ operators was not available in the FeynRules model version used for this validation.

Parameters	Values	Fiducial cross-section [fb]			
$\frac{f_i}{\Lambda^4}$	$\frac{1}{[\mathrm{TeV}^4]}$	CROSS	SUM	FULL	$\frac{\mathtt{SUM}-\mathtt{FULL}}{\Delta(\mathtt{FULL})}$
$S02$ – $S1$	8.0, 20.0	0.310 ± 0.005	3.83 ± 0.05	3.82 ± 0.06	$+0.2$
$M0$ – $M1$	6.0, 10.0	-0.213 ± 0.004	3.54 ± 0.05	3.68 ± 0.06	-2.3
$M0$ – $M7$	6.0, 13.0	–	–	4.02 ± 0.06	–
$M1$ – $M7$	10.0, 13.0	-0.508 ± 0.007	3.23 ± 0.05	3.32 ± 0.05	-1.8
$T0$ – $T1$	0.6, 0.3	0.457 ± 0.006	4.20 ± 0.05	3.93 ± 0.06	$+4.5$
$T0$ – $T2$	0.6, 1.0	0.284 ± 0.004	4.04 ± 0.05	4.00 ± 0.06	$+0.7$
$T1$ – $T2$	0.3, 1.0	0.583 ± 0.007	4.36 ± 0.05	4.46 ± 0.07	-1.4

Differential Kinematic Distributions

The validation in the differential distributions focuses on the one-dimensional case as inconsistencies are already found in this case and the one-dimensional distributions are most important in the course of the limit extraction of this thesis.

If observables are affected which are utilised to select events into the fiducial region, the discrepancies in the latter necessarily increase. Hence, not only the invariant mass of the leading lepton pair, m_{ll}, which is chosen as the observable for the limits extraction, is studied in detail. Also kinematic object and event distributions relevant for the fiducial region selection are investigated. Moreover, the invariant mass of the $W^{\pm}W^{\pm}$ system at matrix element level, m_{WW}, plays a crucial role in the application of the clipping procedure later in this thesis (cf. Sec. 9.6.4). It is thus included in the thorough screening for the validation of the decomposition method. Only few distributions can be included in the main body. Hence, various other distributions of all parameters in the loose and fiducial regions are shown in the collection of auxiliary material in Ref. [268].

Only distributions of the f_{S1}/Λ^4 and f_{M0}/Λ^4 parameters show good agreement in almost all tested observables in both the loose and the fiducial region, agreeing with the findings of the cross-section predictions in both regions. Exemplarily, the m_{ll} and the m_{WW} distributions for events entering the fiducial region are shown in Fig. 9.12.

Despite the good agreement in both, the generator and fiducial region cross-section predictions, discrepancies in differential distributions are found for the other parameters of the S and M families. Mostly extreme edges of the phase space are affected, most relevant here the high mass tails of the m_{ll} observable in both, the loose and the fiducial region. These distributions are shown exemplarily in Fig. 9.13 in the fiducial region, where the `FULL` prediction overshoots the `SUM` by more than 10% for the f_{S02}/Λ^4, f_{M1}/Λ^4, and f_{M7}/Λ^4 parameters.

The predictions of the `SUM` and `FULL` contributions of the T parameters diverge for the cross-section in the fiducial region, while the generator cross-section predictions are in good agreement between the two approaches. However, the differential distributions disagree in the high and/or low energy tails of some observables already in the loose region. While the disagreement is mild for the f_{T2}/Λ^4 parameter, it is most distinct for the f_{T0}/Λ^4 parameter. With these observations, the tendencies of the deviations follow those of the fiducial cross-section. Fig. 9.14 displays exemplarily the leading jet transverse momentum, $p_{\mathrm{T}}(j_1)$, and the invariant mass of the $W^{\pm}W^{\pm}$ system, m_{WW}.

The discrepancies in the $p_{\mathrm{T}}(j_1)$ observable necessarily affect more sophisticated jet-related event distributions. The `FULL` approach predicts a larger fraction of events in the region of low jet p_{T} compared to the `SUM`, while it is vice versa in the high p_{T} tails. The first affects the number of jets per event, $N(j)$, such that the `FULL` approach predicts more events with fewer jets than the `SUM` approach. The reason is that the low p_{T} jets are rejected by the fiducial region selection. The discrepancies in the high p_{T} tail are transferred to the invariant mass of the tagging jet system, m_{jj}, which lacks events in the high mass tails in the `FULL` compared to the `SUM` approach. The invariant mass of the tagging jet system is shown in the fiducial region in Fig. 9.15, together with the invariant mass of the leading lepton pair. The latter shows the same tendency as the m_{WW} observable shown in Fig. 9.14 in the loose region, where the `FULL` predictions falls short of the `SUM` predictions in all bins of the m_{ll} observable. The resulting discrepancies reach more than 20% in the tails of the m_{ll} observable in the fiducial region.

The invariant mass of the leading lepton pair is shown for completeness for the f_{T1}/Λ^4 and f_{T2}/Λ^4 parameters in the fiducial region in Fig. 9.16. While for the f_{T1}/Λ^4 parameter both approaches deviate by approx. 15% in the high mass tails, good agreement is found for the distribution of the f_{T2}/Λ^4 parameter in the whole range. Again, this reflects the disagreement in the fiducial cross-section which is mild at 2% for the latter parameter and almost 6% for the first.

It is noticeable that if discrepancies between the `SUM` and `FULL` approaches in the high mass tails of m_{ll} in the fiducial region exist, they have alternating pattern for the M and S parameters compared to the parameters of the T family. While for the first, the predictions of the `SUM` approach fall short of the `FULL`, the reverse is observed for the latter.

Moreover, the distributions at the nominal parameter values show that the `QUAD` contri-

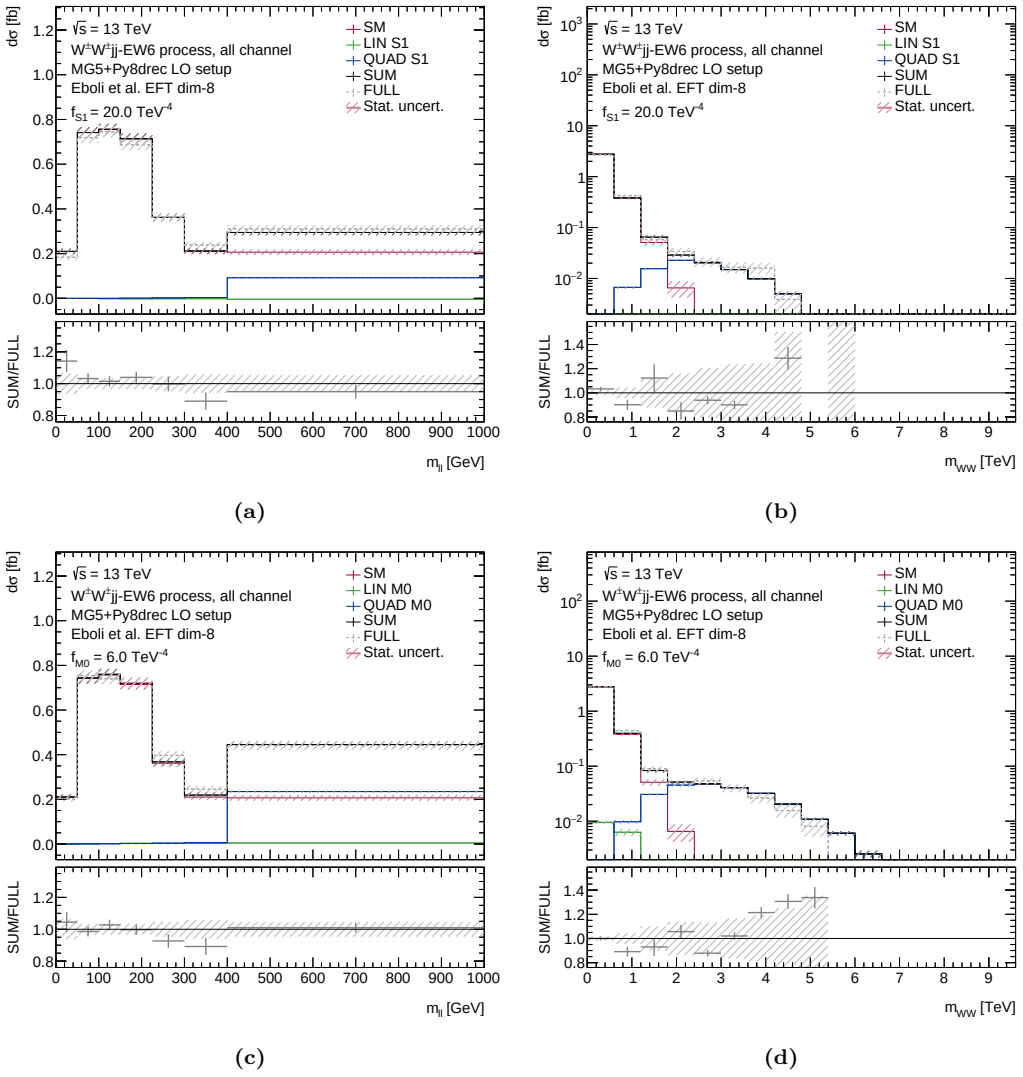


Figure 9.12: Distributions of the invariant mass of the leading lepton pair, m_{ll} (a,c), and the $W^{\pm}W^{\pm}$ system, m_{WW} (b,d), for the nominal values of the f_{S1}/Λ^4 (a,b), and f_{M0}/Λ^4 (c,d) parameters in the fiducial region. Shown are the SM prediction, the decomposed `LIN` and `QUAD` EFT contributions and their sum, labelled `SUM`, together with the prediction of an independently simulated sample of the full prediction of the SM with the EFT extension, labelled `FULL`. The lower panel shows the ratio of the `SUM` with respect to the `FULL` prediction. Uncertainties are statistical uncertainties from the MC generation only. The last bin includes the overflow.

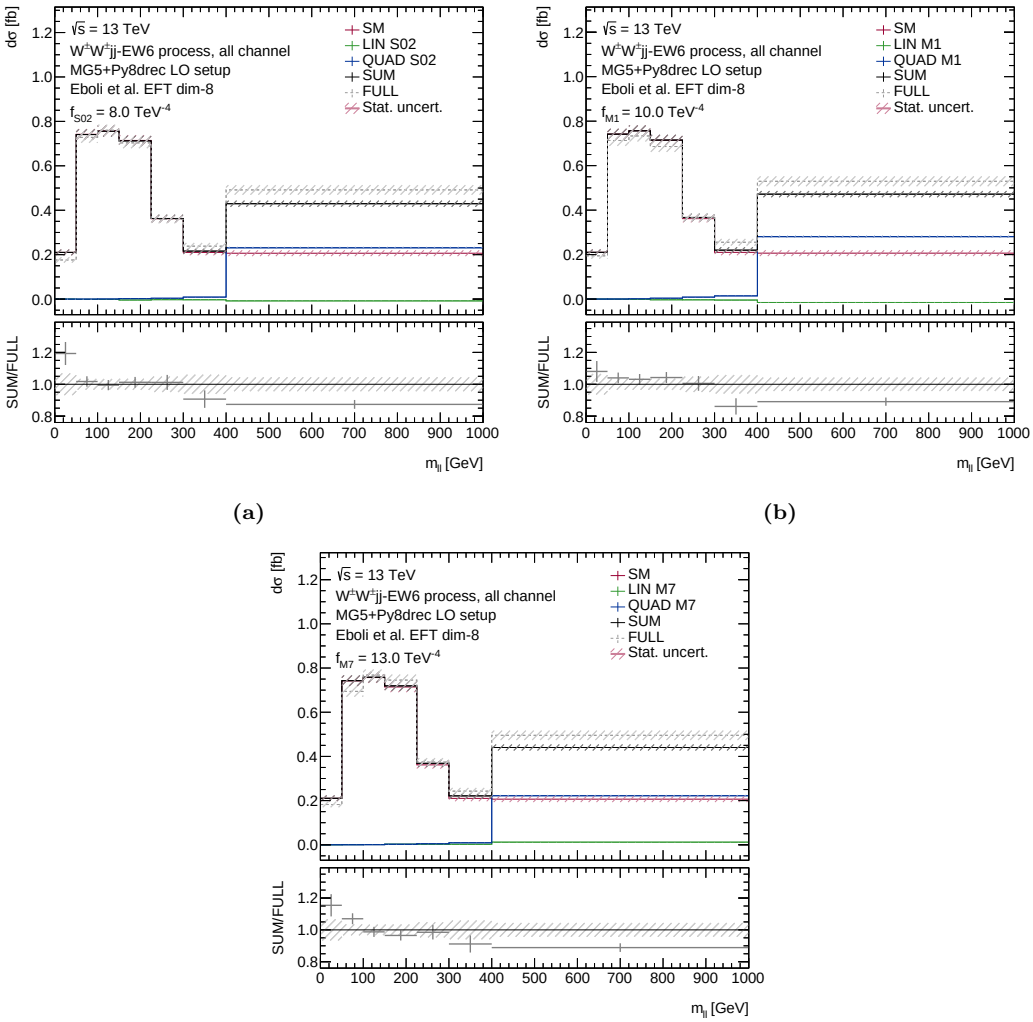
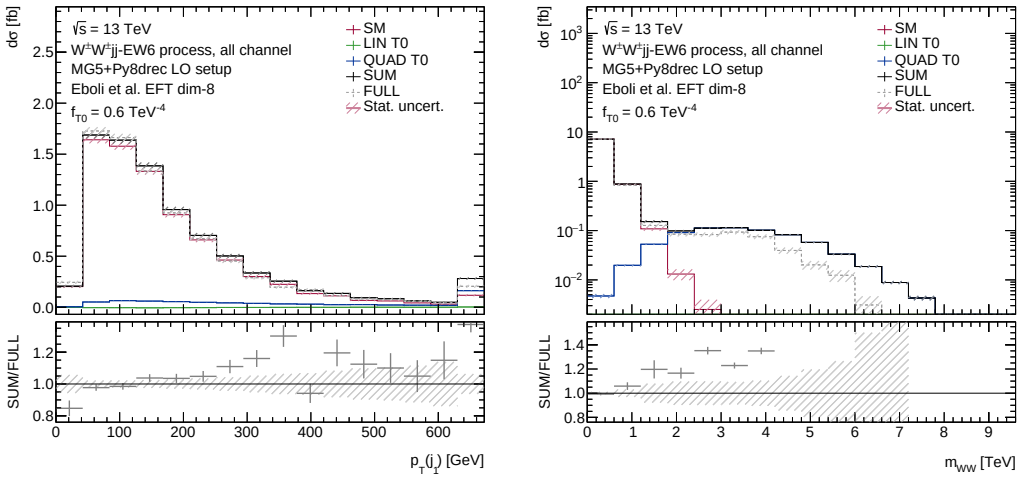
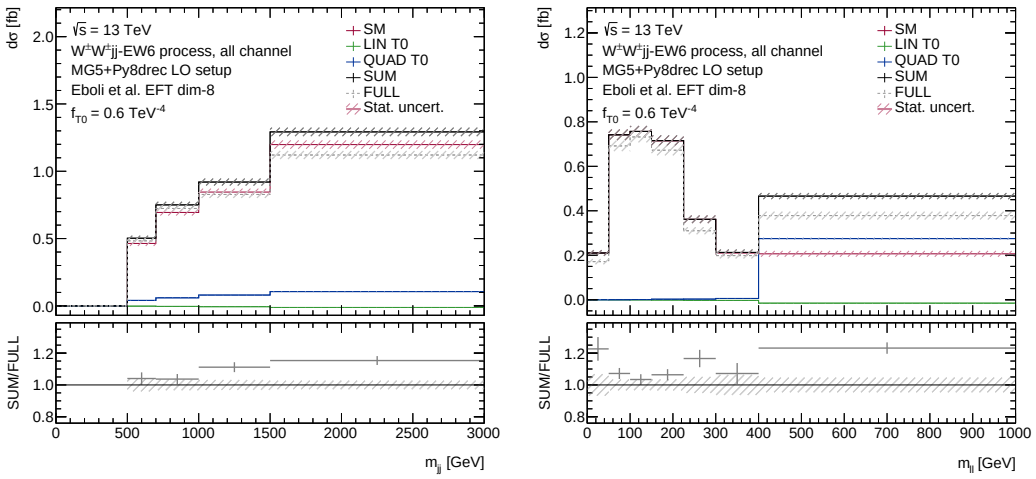


Figure 9.13: Distributions of the invariant mass of the leading lepton pair, m_{ll}, for the nominal values of the f_{S02}/Λ^4 (a), f_{M1}/Λ^4 (b), and f_{M7}/Λ^4 (c) parameters in the fiducial region. The SM prediction, the decomposed `LIN` and `QUAD` EFT contributions and their sum, labelled `SUM`, together with the prediction of an independently simulated sample of the full prediction of the SM with the EFT extension, labelled `FULL`, are shown. The lower panel shows the ratio of the `SUM` with respect to the `FULL` prediction. Uncertainties are statistical uncertainties from the MC generation only. The last bin includes the overflow.



(a) **(b)**

Figure 9.14: Distributions of the transverse momentum of the leading jet $p_{\mathrm{T}}(j_1)$ (a), and the invariant mass of the $W^{\pm}W^{\pm}$ system, m_{WW} (b), for the nominal value of the f_{T0}/Λ^4 parameter in the loose region (cf. Tab. 6.8) at particle level. The SM prediction, the decomposed `LIN` and `QUAD` EFT contributions and their sum, labelled `SUM`, together with the prediction of an independently simulated sample of the full prediction of the SM with the EFT extension, labelled `FULL`, are shown. The lower panel shows the ratio of the `SUM` with respect to the `FULL` prediction. Uncertainties are statistical uncertainties from the MC generation only. The last bin includes the overflow.



(a) **(b)**

Figure 9.15: Distributions of the invariant mass of the tagging jet pair m_{jj} (a), and the leading lepton pair, m_{ll} (b), for the nominal value of the f_{T0}/Λ^4 parameter in the fiducial region (cf. Tab. 6.8). The SM prediction, the decomposed `LIN` and `QUAD` EFT contributions and their sum, labelled `SUM`, together with the prediction of an independently simulated sample of the full prediction of the SM with the EFT extension, labelled `FULL`, are shown. The lower panel shows the ratio of the `SUM` with respect to the `FULL` prediction. Uncertainties are statistical uncertainties from the MC generation only. The last bin includes the overflow.

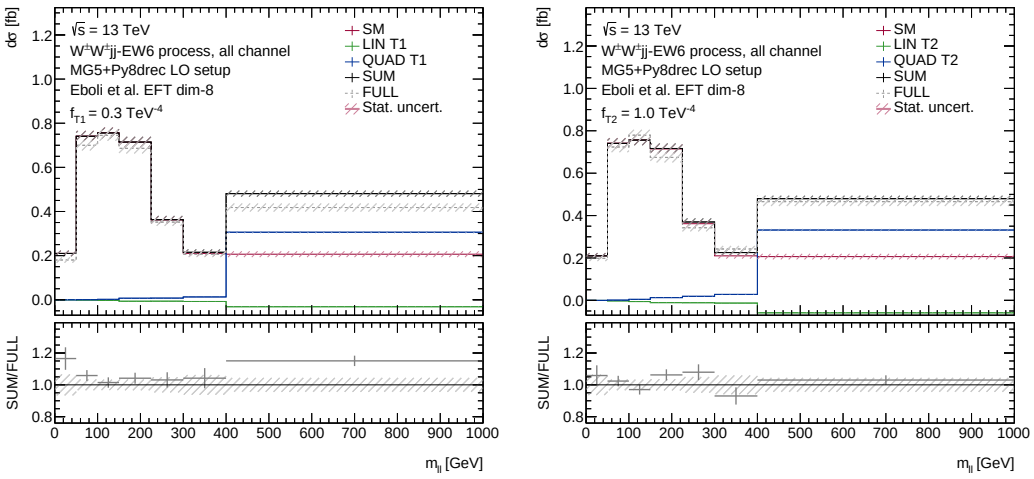


Figure 9.16: Distributions of the invariant mass of the leading lepton pair, m_{ll}, for the nominal values of the f_{T1}/Λ^4 (a), and f_{T2}/Λ^4 (b) parameters in the fiducial region (cf. Tab. 6.8). The SM prediction, the decomposed `LIN` and `QUAD` EFT contributions and their sum, labelled `SUM`, together with the prediction of an independently simulated sample of the full prediction of the SM with the EFT extension, labelled `FULL`, are shown. The lower panel shows the ratio of the `SUM` with respect to the `FULL` prediction. Uncertainties are statistical uncertainties from the MC generation only. The last bin includes the overflow.

bution is comparable to or dominant over the SM contribution in the high m_{ll} tails, except for the f_{S1}/Λ^4 parameter. Compared to the `QUAD`, which steeply rises with m_{ll} and other energy or momentum related observables, the `LIN` contribution is fairly flat over the full m_{ll} range.

Furthermore, the statistical accuracy of the `SUM` contribution is dominated by the accuracy of the SM sample in the high mass tails of m_{ll}, as the `LIN` contribution is small and the `QUAD` contribution has very good accuracy in this region. This constitutes a major advantage of the `SUM` over the `FULL` approach as the SM samples are usually simulated with very large statistics.

In the two-dimensional case, the tail of invariant mass of the leading lepton pair, as displayed in App. F.4, shows discrepancies of approximately 10% for all inter-family parameter pairs, except for the pair $f_{T1}/\Lambda^4 - f_{T2}/\Lambda^4$, where the agreement is good. For the pair $f_{M1}/\Lambda^4 - f_{M7}/\Lambda^4$ the deviations remain within the statistical accuracy of the samples.

In summary, the largest and most important discrepancies are seen at large invariant mass of the two leading leptons and the $W^\pm W^\pm$ system. Hence, it is not useful to continue the validation of the amplitude decomposition method against the `FULL` approach with testing the scaling of the samples from the nominal parameter points to various other points in the parameter space. Instead, the non-closure between the `FULL` and `SUM` predictions is illuminated further.

9.2.7 Investigation of the Decomposition Non-closure

Various tests have been made in the course of finding the cause of the decomposition non-closure. Solely a summary of the most important findings are shown in detail. Investigations that did not lead to finding the cause are not further detailed. These include:

- Checking the quadratic dependence of the `FULL` cross-section prediction;
- Testing smaller parameter values and with this the influence of the quadratic contribution, `QUAD`;

- Testing negative parameter values and with this the influence of the linear contribution, LIN;
- Testing the generation with different settings of the nominal dynamical renormalisation and factorisation scales;
- Testing an alternative process definition of the QUAD contribution;
- Testing the simultaneous simulation of the LIN and QUAD contribution in one sample.

It is further noticeable that the decomposition non-closure does not occur in all final states tested so far. Apart from the $W^{\pm}W^{\pm}jj$ final state, investigated here, it is also seen in the $ZZjj$ final state [275], while good agreement between the FULL and SUM approach is observed in the $W^{\pm}Zjj$ [276] and $Z\gamma jj$ [277] final states. In addition, non-closure between the decomposition approach and the fully generated samples is seen when testing aTGC parameter in the $W^{+}W^{-}$ final state [278].

Phase Integration and Restrictions

The non-closure is investigated in correspondence with experts from the MG5_aMC programme and the EFT dimension-eight model under study. It was first suggested that the generation and phase-space integration of the interference contribution in the MG5_aMC programme is not optimised and unexpected effects could occur [273].

In order to validate the different parts of the decomposition independently, the LIN and QUAD contributions can be obtained solely from utilising the FULL and the SM samples. From the generation of two FULL samples, each with the same absolute parameter value but different signs, both the LIN and QUAD contributions can be retrieved as:

$$|\texttt{LIN}| = \frac{1}{2}\left|\texttt{FULL}(x) - \texttt{FULL}(-x)\right|, \tag{9.11}$$

and:

$$\texttt{QUAD} = \frac{1}{2}\left(\texttt{FULL}(x) + \texttt{FULL}(-x)\right) - \texttt{SM}, \tag{9.12}$$

respectively. These can further be compared to the individual decomposed predictions.

This test is done with a reduced process definition in the MG5_aMC `process_card.dat`:

```
generate u u > e+ ve mu+ vm j j
```

and the f_{T0}/Λ^4 parameter, which shows the largest deviations comparing the SUM and FULL predictions, only. Fig. 9.17 shows the individual decomposed predictions of the LIN and QUAD contributions at both, positive and negative values for f_{T0}/Λ^4 compared to the predictions from a FULL and a SM sample by employing Equations (9.11) and (9.12). The distributions of the invariant mass of the leading lepton pair and the $W^{\pm}W^{\pm}$ system are shown exemplarily as these exhibit the largest discrepancies between the two approaches. Distributions for the f_{T1}/Λ^4 parameter show the same behaviour and are displayed in App. F.5.

The statistics is poor for the distribution of the LIN contribution when retrieved from the FULL prediction. However, the linear contribution is small and deviations remain roughly within the statistical accuracy of this prediction. The QUAD contribution when retrieved via Eq. (9.12) shows significant discrepancies in the region of high invariant masses of the leading lepton pair and the $W^{\pm}W^{\pm}$ system compared to the decomposed predictions. These deviations are similar as those observed in the non-closure, where the FULL prediction falls short of the SUM at large invariant masses for the f_{T0}/Λ^4 parameter.

With these distributions, it is shown, that also when using the FULL approach, the linear contributions are small compared to the pure quadratic EFT contribution. The discrepancies occur in regions where the quadratic term is dominant over the linear term as well as the SM prediction. Moreover, the disagreement increases with increasing invariant mass and hence energy of the events.

After these tests, it is assumed that the discrepancies can be explained by non-optimal phase space integration in the high mass tails of the FULL prediction. This is first tested with

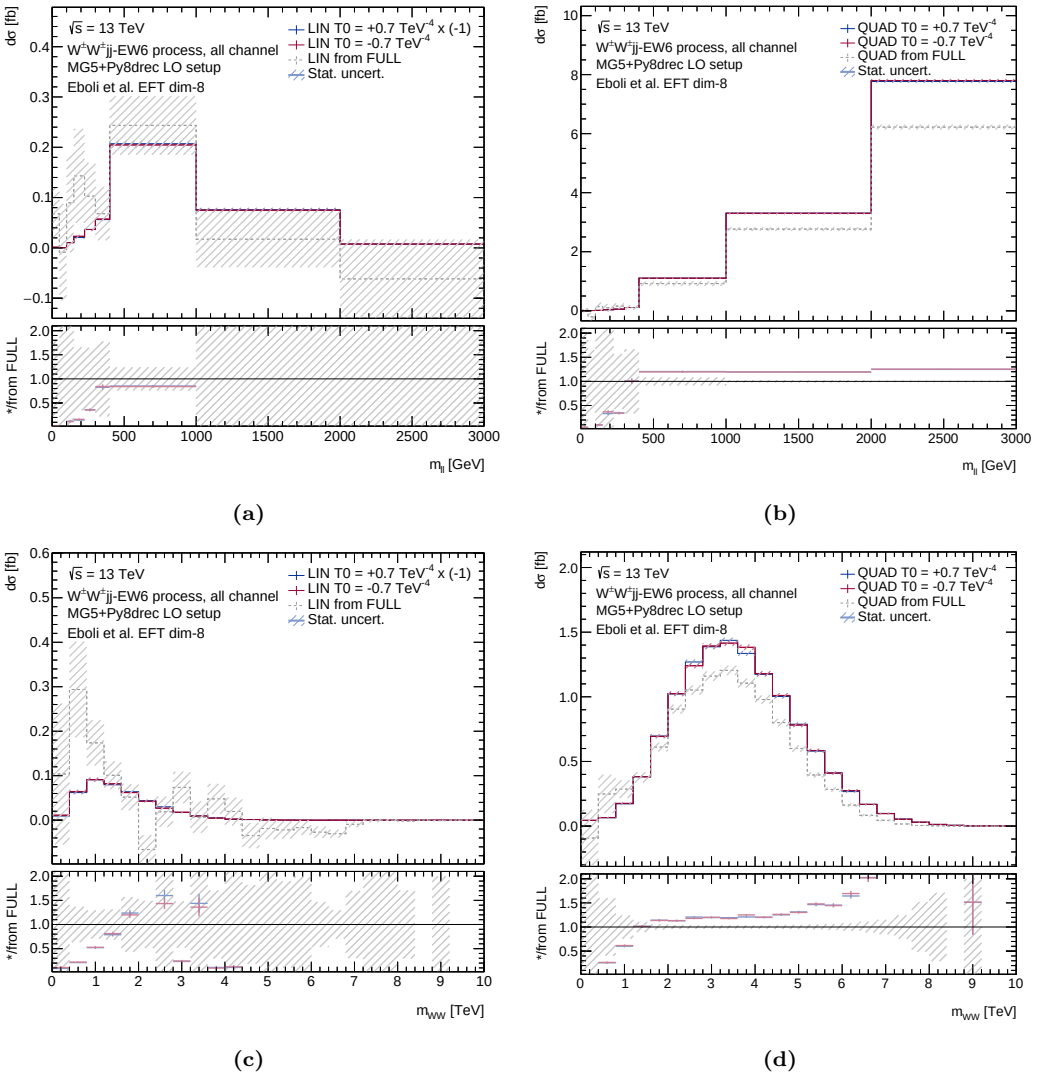


Figure 9.17: Comparison of the `LIN` (a,c) and `QUAD` (b,d) contribution obtained from the amplitude decomposition method (blue and red) compared to retrieving them from independent `FULL` and SM samples employing Equations (9.11) and (9.12) (dashed grey). The invariant mass of the leading lepton pair, m_{ll} (a,b), and the $W^{\pm}W^{\pm}$ system, m_{WW} (c,d), for the f_{T0}/Λ^4 parameter in the loose region (cf. Tab. 6.8) are shown. The contributions from the decomposition method are illustrated for identical positive (blue) and negative (red) values of f_{T0}/Λ^4. The lower panel shows the ratio of the predictions from the amplitude decomposition method with respect to the contributions obtained from the `FULL` prediction. Uncertainties are statistical uncertainties from the MC generation only. The last bin includes the overflow.

Table 9.8: Cross-section predictions in the generator (cf. Tab. 6.7) and fiducial phase space (cf. Tab. 6.8) for the SM, the decomposed `LIN` and `QUAD` contributions, as well as their sum, labelled `SUM`, and the `FULL` prediction of an individual sample for the f_{T0}/Λ^4 parameter with value $0.7\,\text{TeV}^{-4}$ in a restricted generator phase space with a minimum requirement on m_{ll} of 500 GeV. Uncertainties are the statistical errors of the MC generation only. The last column shows the significance of the difference between the `SUM` and `FULL` contribution with respect to the statistical uncertainty of the `FULL` sample.

Cross-section [10^{-2} fb]					
SM	`LIN`	`QUAD`	`SUM`	`FULL`	$\frac{\texttt{SUM}-\texttt{FULL}}{\Delta(\texttt{FULL})}$
Generator cross-section:					
2.67 ± 0.16	-0.275 ± 0.005	10.35 ± 0.04	12.75 ± 0.16	12.77 ± 0.15	-0.13
Fiducial cross-section:					
0.77 ± 0.02	-0.147 ± 0.003	3.74 ± 0.03	4.36 ± 0.03	4.33 ± 0.04	$+0.75$

restricting the underlying model in MG5_aMC by employing a `restrict_*.dat` card, that sets all redundant parameters to zero, as suggested in Ref. [277]. Using these extra settings in the event generation reduces the discrepancies in the high mass tails only marginally [279].

Another method to test the integration in the high mass tails is to restrict the phase space in the event generation with additional selection requirements at generator level. Placing a minimum requirement on the invariant mass of the charged decay products of the $W^\pm$ bosons populates the `FULL` sample in the tails and the phase space integration can become more stable.

For this test, again the f_{T0}/Λ^4 parameter and a reduced process definition[6]:

```
generate u u > mu+ vm mu+ vm j j
```

is employed. A minimum requirement on the invariant mass of the two muons in the final state at generator level is set to 500 GeV. The cross-section predictions in this restricted phase space for all samples is summarised in Tab. 9.8. The `SUM` and `FULL` approach agree well for both, the generator and fiducial phase space. This compares to the observations without the restrictions shown in Tab. 9.6, where the discrepancies are at 6σ in the fiducial region for the f_{T0}/Λ^4 parameter.

Fig. 9.18 displays the invariant mass of the $W^\pm W^\pm$ system and the leading dilepton system[7] in the loose and the fiducial region, respectively. The agreement between the `FULL` and `SUM` approach in the high mass regions is much improved compared to observations shown in Figures 9.14(b) and 9.15(b) in the loose region and consequently in the fiducial region.

After consultation with the theory community, these observations eventually render the `FULL` approach insufficient in the descriptions of the phase space regions most relevant to the extraction of exclusion bounds on the dimension-eight EFT parameters.

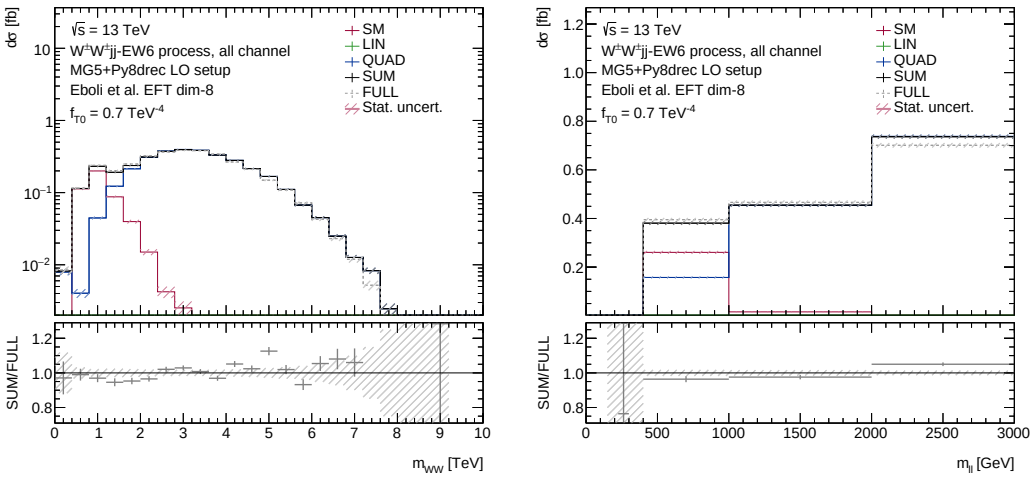
9.2.8 Validation of the Scaling of EFT Contributions

The verification of the scaling of the decomposed contributions from the nominal parameter points to arbitrary points in the parameter space cannot be pursued easily[8] against the `FULL` prediction because of the non-closure seen before. Hence, other ways to validate the scaling need to be found. Here, the scaling is tested for each contribution independently by generating multiple samples at different parameter values with the decomposition method.

[6] Due to the technical implementation of the generator level requirement of m_{ll} in MG5_aMC only same flavour final states can be utilised in this test.

[7] In this figure, events occur with m_{ll} below 500 GeV. The requirement on m_{ll} is done at matrix-element level, while the events in this figure include the effects of the parton shower, i. e. I/FSR radiations, which can reduce the momenta of the final state particles and hence, their m_{ll} distribution.

[8] It might be possible to test the scaling with `FULL` predictions sliced into disjoint m_{ll} regions in the generator phase space. However, this approach would constitute a clear increase in resource needs.



(a) **(b)**

Figure 9.18: Distributions of the invariant mass of the $W^{\pm}W^{\pm}$ system, m_{WW} (a), and the leading lepton pair, m_{ll} (b), in a restricted generator phase space with a minimum requirement on m_{ll} of 500 GeV for the f_{T0}/Λ^4 parameter. The SM prediction, the decomposed `LIN` and `QUAD` EFT contributions and their sum, labelled `SUM`, together with the prediction of an independently simulated sample of the full prediction of the SM with the EFT extension, labelled `FULL`, are shown. The m_{WW} distribution is shown in the loose region (cf. Tab. 6.8). The m_{ll} distribution is shown in the fiducial region. The lower panel shows the ratio of the `SUM` with respect to the `FULL` prediction. Uncertainties are statistical uncertainties from the MC generation only. The last bin includes the overflow.

These are then compared to predictions of the sample generated with the nominal parameter point x_n scaled by the ratio of the nominal and the new values x. According to Equations (9.4) and (9.5), the ratio of the cross-sections must fulfill:

$$\frac{\sigma^{\texttt{LIN}}(f_i/\Lambda = x)}{\sigma^{\texttt{LIN}}(f_i/\Lambda = x_n)} = \frac{x}{x_n}, \tag{9.13}$$

for the `LIN` contribution and:

$$\frac{\sigma^{\texttt{QUAD}}(f_i/\Lambda = x)}{\sigma^{\texttt{QUAD}}(f_i/\Lambda = x_n)} = \left(\frac{x}{x_n}\right)^2, \tag{9.14}$$

for the `QUAD` contribution. For the `CROSS` contribution in the two-dimensional case follows:

$$\frac{\sigma^{\texttt{CROSS}}(x,y)}{\sigma^{\texttt{CROSS}}(x_n,y_n)} = \frac{xy}{x_n y_n}. \tag{9.15}$$

These mathematical statements must again be true for all quantities at particle level in all phase space regions relevant for the analysis. This includes the generator and fiducial cross-section. Moreover, they must hold in each bin of the differential distributions of any observable i. e. the normalisation of each contribution individually must differ by the respective factor in each bin. As a consequence, the shape of the differential distributions of each contribution and parameter must be identical and independent of the value of the parameter.

The latter especially ensures that the individual contributions can also be scaled after being passed through the detector simulation and that Equations (9.4) and (9.5) are valid at reconstruction level. The reason for this is because the efficiencies of the selection requirements of the signal region usually depend on kinematic observables such as the transverse momentum or (pseudo)rapidity of the selected objects.

In summary, the efficiencies of the individual contributions, `LIN` or `QUAD` etc., change due to the scale that changes at each parameter point and not due to the shape that the distributions have. Consequently, in the signal region at reconstruction level, the individual

Table 9.9: Cross-section predictions in the generator (cf. Tab. 6.7) and fiducial phase space (cf. Tab. 6.8) for the decomposed `LIN` and `QUAD` contributions at different values of the f_{S1}/Λ^4 parameter. Columns three and five display the scaling factor between the cross-section prediction of the nominal parameter value $f_{S1}/\Lambda^4 = x_n = 20\,\text{TeV}^{-4}$ and each tested point. Uncertainties are the statistical errors of the MC generation only.

Parameter value x [TeV^{-4}]	Generator cross-section [fb]	$\frac{\sigma(S1{=}x)}{\sigma(S1{=}20\,\text{TeV}^{-4})}$	Fiducial cross-section [fb]	$\frac{\sigma(S1{=}x)}{\sigma(S1{=}20\,\text{TeV}^{-4})}$
Linear contribution:				
−5.0	0.023 ± 0.001	-0.25 ± 0.05	0.002 ± 0.000	-0.22 ± 0.16
5.0	-0.023 ± 0.001	0.25 ± 0.05	-0.002 ± 0.000	0.24 ± 0.15
−10.0	0.046 ± 0.001	-0.50 ± 0.03	0.004 ± 0.000	-0.54 ± 0.14
10.0	-0.046 ± 0.001	0.50 ± 0.03	-0.004 ± 0.000	0.50 ± 0.15
−20.0	0.092 ± 0.002	-1.00 ± 0.03	0.008 ± 0.001	-1.06 ± 0.14
20.0	-0.093 ± 0.002	–	-0.008 ± 0.001	–
−30.0	0.139 ± 0.003	-1.50 ± 0.03	0.012 ± 0.001	-1.63 ± 0.14
30.0	-0.139 ± 0.003	1.50 ± 0.03	-0.012 ± 0.001	1.57 ± 0.14
−40.0	0.185 ± 0.004	-2.00 ± 0.03	0.015 ± 0.002	-2.03 ± 0.15
40.0	-0.185 ± 0.004	2.00 ± 0.03	-0.015 ± 0.002	1.97 ± 0.15
Quadratic contribution:				
5.0	0.029 ± 0.000	0.06 ± 0.01	0.003 ± 0.000	0.06 ± 0.02
20.0	0.460 ± 0.002	–	0.053 ± 0.001	–
−30.0	1.035 ± 0.005	2.25 ± 0.01	0.117 ± 0.002	2.21 ± 0.02
30.0	1.035 ± 0.005	2.25 ± 0.01	0.119 ± 0.002	2.24 ± 0.02
−40.0	1.839 ± 0.008	4.00 ± 0.01	0.209 ± 0.003	3.94 ± 0.02
40.0	1.839 ± 0.008	4.00 ± 0.01	0.210 ± 0.003	3.96 ± 0.02

contributions can be scaled and summed together in the same manner as done at particle level.

The validation of the scaling now proceed in equal manner as for the decomposition. First, the generator and fiducial cross-sections are checked. Subsequently, differential distributions are investigated. Focus here lies on observables used for the definition of the signal region at reconstruction level. While the validation is shown for the f_{S1}/Λ^4 in the main body, numbers and distributions for the the f_{S02}/Λ^4 parameter, as well as for the two-dimensional `CROSS` term of both operators can be conferred in Ref. [268]. The findings are identical to the ones derived here.

Tab. 9.9 summarises the cross-sections at generator and fiducial level for different values of the f_{S1}/Λ^4 parameter for both, the `LIN` and `QUAD` contribution. In addition, it shows the factor between the cross-section predictions at the nominal value $f_{S1}/\Lambda^4 = x_n = 20\,\text{TeV}^{-4}$ and the respective point x. These factors agree precisely at generator level for both the `LIN` and `QUAD` contributions. In the fiducial region, the agreement is within statistical accuracy for the `LIN` contribution. In the case of the `QUAD` contribution, discrepancies of less than 2% but beyond the statistical accuracy are observed when scaling to larger values than the nominal one. This supports the earlier statement that samples should be generated with coefficients which are in the range of the expected sensitivity to avoid the scaling of the `QUAD` contributions to larger values or far away from the nominal point.

Figures 9.19 and 9.20 show lepton- and jet-related kinematic distributions, respectively, for the `LIN` and `QUAD` contributions at different values of the f_{S1}/Λ^4 parameter. The distributions are normalised to compare their shape. Due to statistical limitations, they are

shown in the loose region. The statistical accuracy for the LIN contribution is limited.

The shape of the distributions agree well between different parameter values in all phase space regions for both contributions, as well as for the contributions shown in Ref. [268]. This confirms that the efficiencies for each of the individual terms is constant with respect to the parameter values.

On the contrary, the shape of the differential distributions, especially for the lepton kinematics differ considerably between the linear and quadratic term. From Ref. [268], it can be perceived that the shape of the CROSS term is very similar to the one of the QUAD contribution, which is as expected.

This means on the one hand, the acceptance and efficiency correction factors for the linear and quadratic contributions are each independent of the parameter value. Considering that the influence of each of the terms changes for different values of one parameter, this is not true for the SUM prediction. For large values of the EFT parameter the quadratic term becomes more dominant than the linear term in the SUM contribution and vice versa. Hence, for the SUM contribution not only the acceptance correction factors but also the efficiency correction factors from the fiducial into the signal region change for different values of a given EFT parameter. In conclusion, this shows, that the approaches taken in previous analyses assuming constant acceptance and efficiency correction factors [254, 255], did not cover the full effect.

Moreover, as shown in Fig. 9.10, the shape of the transverse momentum of the leading jet varies with the parameters. Hence, previous approaches that tested the efficiency dependence of the EFT prediction for one parameter and extrapolated to other parameters [250, 252, 255], might not have caught the full effect of the differences either.

Distributions showing the full effect of differently scaled EFT predictions, obtained by summing the individual contributions of the amplitude decomposition approach with the SM prediction according to Eq. (9.4), are shown in Sec. 9.2.5 where the sensitive observable is determined.

9.2.9 Conclusions and Final Sample Specifics

In the course of the validation it is concluded that the FULL predictions suffer from deficiencies in the phase space integration of the MC sample simulation. The discrepancies occur in the cross-section predictions as well as in tails of differential distributions. Most importantly, the disagreement is seen in the tails of large invariant masses of the leading lepton pair and the true invariant mass of the $W^{\pm}W^{\pm}$ system. The first observable is chosen among a variety of kinematic distributions as the sensitive variable utilised in the statistical analysis for the extraction of the exclusion limits of the EFT parameters. The latter is employed as the variable for the implementation of the clipping to test the unitarity of the given model at the given sensitivity.

The non-closure is not only observed in this final state, but also in the $ZZjj$ final state [275]. In addition, non-closure between the decomposition approach and the fully generated samples is seen when testing aTGC parameter in the W^+W^- final state [278]. Upon the studies presented in this thesis and beyond, the possible explanation given by the theory community is the insufficient MC integration in the high energetic tails of the distributions. For the FULL prediction, the SM contribution is dominant, which is large at low energies. Hence, the MC integration is automatically optimised in this region. and not in the region where the EFT contributions become relevant. If this is true, all final states are expected to be affected by this non-closure and the extent is dependent on their energy reach. It is strongly recommended to not further utilise the FULL prediction but instead the amplitude decomposition method. An alternative strategy would be to slice the FULL predictions into multiple samples depending on some energy or mass variable. The MC generation of these samples, however, are much more resource intense than the decomposed alternative. Yet, this could be a possible procedure for the MC generation when the amplitude decomposition approach is not yet available.

Based on these findings, this work relies on the amplitude decomposition method available in the MG5_aMC event generation programme in order to simulate the EFT effects of the individual terms which are assembled together with the nominal MG5+Py8drec SM

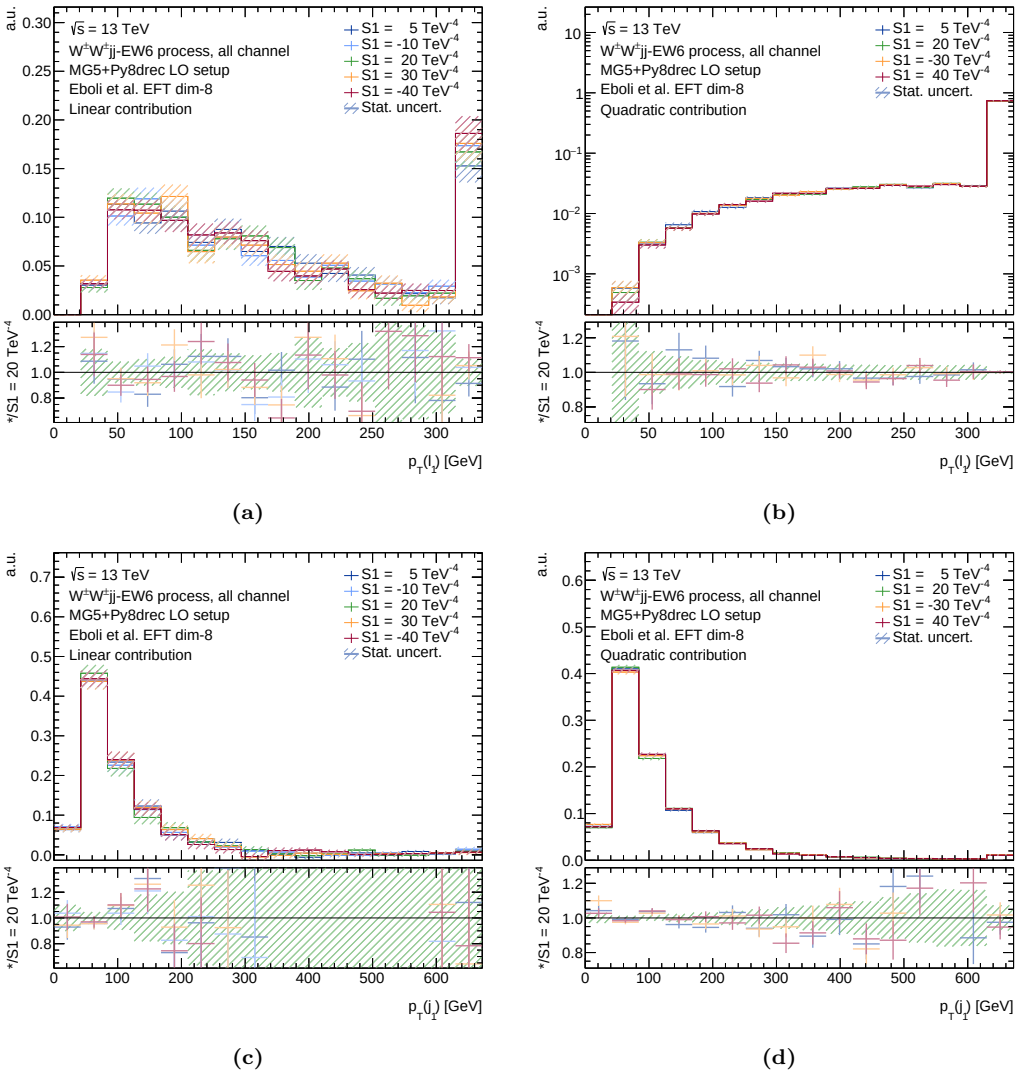


Figure 9.19: Kinematic distributions of the transverse momentum of the leading lepton $p_{\mathrm{T}}(l_1)$ (a,b), and leading jet, $p_{\mathrm{T}}(j_1)$ (c,d), of the `LIN` (a,c) and `QUAD` (b,d) contributions for different values of the f_{S1}/Λ^4 parameter. The distributions are normalised to unit area. The nominal value (cf. Tab. 9.3) is shown in green. The distributions are shown in the loose region (cf. Tab. 6.8) at particle level. The lower panel shows the ratio with respect to the nominal value. Uncertainties are statistical uncertainties from the MC generation only. The last bin includes the overflow.

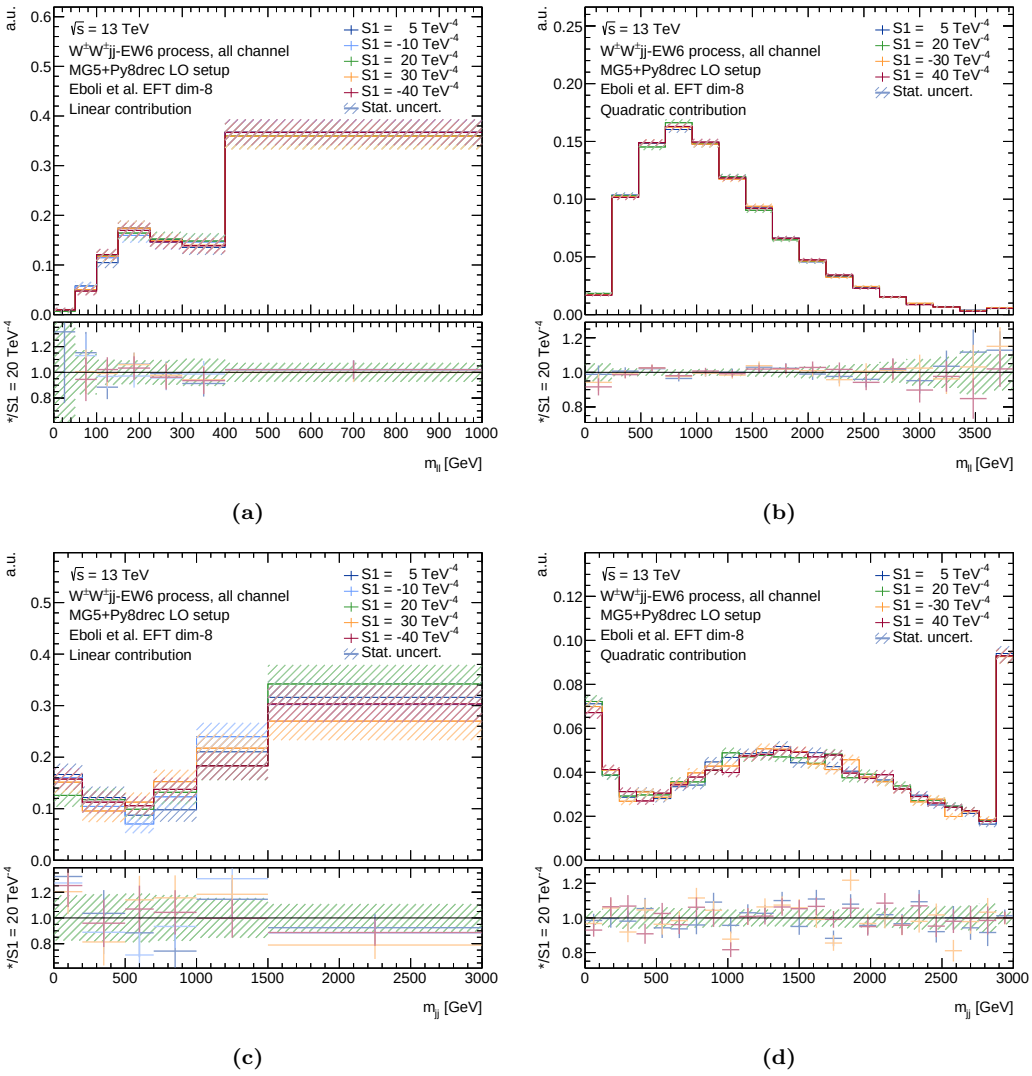


Figure 9.20: Kinematic distributions of the invariant mass of the leading lepton pair, m_{ll} (a,b), and tagging jet pair, m_{jj} (c,d), of the `LIN` (a,c) and `QUAD` (b,d) contributions for different values of the f_{S1}/Λ^4 parameter. The distributions are normalised to unit area. The nominal value (cf. Tab. 9.3) is shown in green. The distributions are shown in the loose region (cf. Tab. 6.8) at particle level. The lower panel shows the ratio with respect to the nominal value. Uncertainties are statistical uncertainties from the MC generation only. The last bin includes the overflow.

prediction according to Eq. (9.4) to a full prediction of the EFT extension of the SM described in Ref. [2, 3]. It is the first time that samples simulated with the amplitude decomposition approach are employed in the final limit setting procedure of dimension-eight EFT parameters of this model.

The FULL prediction has been used in all previous measurements of dimension-eight EFT parameters [18, 154, 155, 243, 247, 249–251, 253]. The insufficiencies found in the FULL samples, hence, affect these results. No conclusions can, however, be drawn on the size of the impact since it depends on the parameter and final state.

The decomposition method has several advantages over the conventional approach of utilising the FULL prediction. It allows to scan a wide range of the parameter space with only two samples per parameter at reconstruction level which can be used for one-dimensional exclusion limits. Moreover, the statistical accuracy in the tails of the distributions relevant for the limit setting is improved due to the specific simulation of the individual quadratic term without the regeneration of the SM for each EFT sample. Because the latter per theoretical construction occupies most of the low energetic phase space, the EFT effects are only relevant at high energy. In addition, as seen in the validation of the scaling procedure, acceptances and detector efficiencies do not need to be approximated any longer since the scaling preserves the efficiency of the assembled sample also at reconstruction level. Since the assembly and the scaling per construction is also valid for any variation used to assess systematic uncertainties, the latter can be derived continuously for each point in the parameter space at reconstruction level. Furthermore, the decomposition method allows to study the size of the individual LIN and QUAD contribution, which is important to assess the mathematical reliability of the EFT expansion.

Based on the findings of the thorough investigations of this section, MC samples are generated which are eventually employed in the limit setting procedure. Two samples per parameter, one LIN and QUAD contribution, at the nominal parameter values, summarised in Tab. 9.3, are simulated for the one-dimensional statistical analysis. After consultation with the experts, the dynamical scale is set to the sum of the transverse energy of all final state particles HT (cf. Eq. (6.3)). The generator and fiducial cross-section, together with the acceptances in the fiducial region, are summarised in App. F.6 for these final samples.

The invariant mass of the leading lepton pair is chosen as the observable for the differential analysis, because it exhibits large and qualitatively similar effects in its tails for all parameters considered here. Moreover, it excels with its simple definition over other mass variables with similar effects, such as the m_{o1} observable. However, it will be promising to explore the potential of the more sophisticated transverse mass observables studied in Ref. [274] together with an optimised binning for future analyses of the dimension-eight EFT extensions in the $W^{\pm}W^{\pm}jj$ final state.

The samples at particle level are transferred to reconstruction level with the setups detailed in App. C.2.

9.3 Strategy of the Statistical Analysis

The measurement goals of this analysis and the overall strategy to achieve them have been stated in Sec. 7.1. The statistical analysis is based on the approach of the discovery of the SM $W^{\pm}W^{\pm}jj$-EW6 process, presented in Sec. 8.2.2, and extended for the procedure of interval estimation to extract one-dimensional exclusion bounds for the EFT parameters f_i/Λ^4. It utilises information from the reconstruction level.

Again, before embarking on detailing the statistical formulation, the characteristics of the experimental measurement is outlined.

Eventually, different sets of one-dimensional exclusion limits are presented:

1. Exclusion limits without unitarisation;
2. Exclusion limits employing the clipping unitarisation approach (cf. Sec. 2.3.3) as a function of the clipping energy E_{clip}; and
3. Exclusion limits including effects of dimension-six EFT parameters on the $W^{\pm}Z$ process.

9.3.1 Characteristics of the Experimental Measurement

The measurement re-utilises major parts of the SM analysis, such as the definition of the signal region (cf. Sec. 7.4). The advantage is obviously that estimates of all background processes and their uncertainties do not need to be reevaluated. One exception is the $W^{\pm}W^{\pm}jj$-EW6 process which is now considered a background compared to the EFT signals and its prediction is taken from the MG5+Py8drec setup instead of the Sherpa23jLO setup. One reason is the inconsistency found in the Sherpa23jLO setup (cf. Sec. 6.3.2) only after the SM analysis. Moreover, the MG5+Py8drec setup provides a consistent description of the SM contribution of the $W^{\pm}W^{\pm}jj$-EW6 with respect to the EFT signals which employ the identical technical setup.

The disadvantage of reusing the signal region definition is that the event selection is not optimised with regard of the EFT signals. This becomes apparent for example in the relatively large requirements on the minimum transverse momentum of the tagging jets. The contributions of the EFT parameters of the S family favour small transverse tagging jet momenta, as shown in Fig. 9.10. Events with latter property do not enter the signal region, hence reducing the EFT sensitivity of this family.

The analysis in this thesis chooses to reuse the implementations of the $W^{\pm}W^{\pm}jj$-EW6 SM analysis as the major focus lies on the new approach of the signal modelling, the amplitude decomposition method. Moreover, the studies presented here prepare for a combination with analyses of the $W^{\pm}Zjj$ and other final states, and eventually an inter-experimental combination with results from the CMS experiment. Hence, major effort goes into the understanding of the new signal description and the deliberation of analysis choices most favourable for a statistical combination.

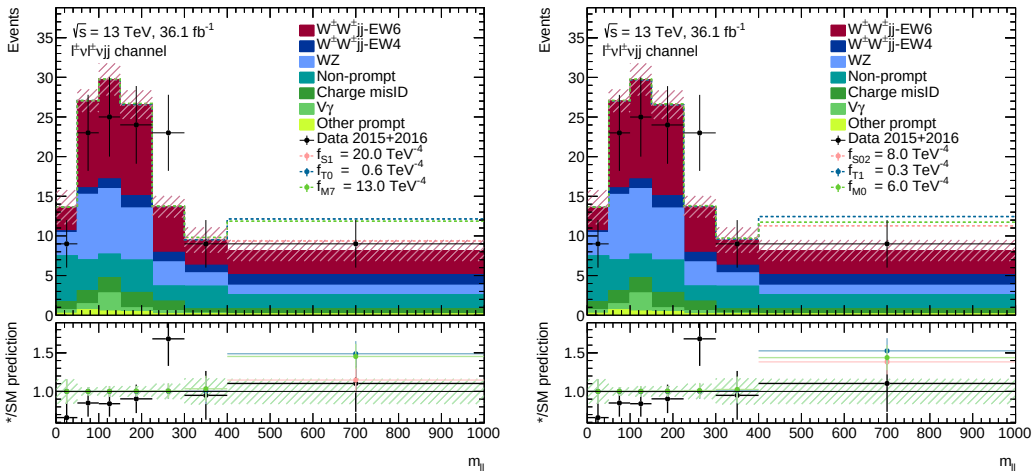
The signal is defined as the EFT contribution at reconstruction level, assembled from the linear and quadratic terms of the amplitude decomposition, detailed in Sec. 9.2.1 and validated thereafter in Sections 9.2.6 and 9.2.8.

The statistical analysis is conducted in the differential distribution of the invariant mass of the leading lepton pair, m_{ll}, in the signal region at reconstruction level, exhibiting sensitivity to EFT contributions for all relevant parameters in the high mass tail, as discussed in Sec. 9.2.5. The binning is taken to be as published for the SM analysis in Ref. [1] and not further optimised. The lower bin edges are: $m_{ll} \in \{0, 50, 100, 150, 225, 300, 400\,\text{GeV}\}$. No control regions are utilised in this analysis.

One-dimensional exclusion limits are derived in the combined channel, $\ell^{\pm}\ell^{\pm}$, in the signal region by including one parameter in the signal definition at a time and setting all other parameter of the EFT model to zero. No two-dimensional bounds are derived at this point as first attempts indicate that considerably more effort is needed in order to make the results statistically stable.

As a reminder, the event yields and their total uncertainties of all background processes, including the MG5+Py8drec prediction of the $W^{\pm}W^{\pm}jj$-EW6 process, before the statistical analysis in the combined $\ell^{\pm}\ell^{\pm}$ channel in the signal region are listed in Tab. 7.14. Event yields are taken before the statistical SM analysis as the exact same data is fitted here in the EFT analysis again. However, normalisation correction factors obtained in the SM analysis from independent fits to observed data in control regions are applied before the EFT statistical analysis. This concerns the $W^{\pm}Z$ and $V\gamma$ background processes, whose normalisation is determined from data to 0.91 (cf. Sections 8.4.1 and 8.6) and 1.77 (cf. Sec. D.2.3), respectively. The unconstrained NP on the $W^{\pm}Z$ normalisation is not included in the statistical model of the EFT. Moreover, minor backgrounds such as the VVV, ZZ and top processes, as well as the $W^{\pm}\gamma$ and $Z\gamma$ processes are grouped together in the statistical analysis to the categories "other prompt" and $V\gamma$, respectively. Systematic uncertainties from the individual contributions are added in quadrature for the combined predictions.

For the EFT signal contributions, the event yield depends on the chosen value of the respective parameter. Fig. 9.21 shows the m_{ll} distribution at reconstruction level in the binning for the statistical analysis for all background processes, experimental data taken in the years 2015 and 2016, and several signal contributions with the nominal parameter values, defined in Sec. 9.2.4. The exact event yields before the statistical analysis for all background processes and EFT signal contributions in bins of the m_{ll} variable are summarised



(a) **(b)**

Figure 9.21: Distributions of the invariant mass of the leading lepton pair, m_{ll}, in the combined $\ell^{\pm}\ell^{\pm}$ channel in the signal region at reconstruction level. The background estimates (stacked), experimental data taken in the years 2015 and 2016 with the ATLAS detector, and different signal predictions at their nominal values (stacked with background) are shown in (a) for the parameters f_{S1}/Λ^4, f_{T0}/Λ^4, and f_{M7}/Λ^4, and in (b) for the parameters f_{S02}/Λ^4, f_{T1}/Λ^4, and f_{M0}/Λ^4. The amplitude decomposition method is used for the predictions of the EFT signals. The $W^{\pm}\gamma$ and $Z\gamma$ processes, as well as the VVV, ZZ and top processes are grouped together to the categories $V\gamma$ and "other prompt", respectively. The lower panel shows the ratio with respect to the total background estimate. Uncertainties on the background estimates are the total statistical and systematic uncertainties added in quadrature. The last bin includes the overflow.

in Tables G.2 and G.3, respectively, in the appendix. For the signal contributions, these are shown for the decomposed `LIN` and `QUAD` contributions individually. With similar behavior in the fiducial region, it is no surprise, that the `QUAD` contribution is dominant in the high mass tails of m_{ll} for all nominal parameter values. For low values of m_{ll}, the `LIN` and `QUAD` contributions are of similar size.

The SM $W^{\pm}W^{\pm}jj$-EW6 process composes the largest background contribution in the signal region over the whole m_{ll} spectrum and most importantly also in the last bin of the m_{ll} distribution, where the EFT signal contributions are relevant. From Fig. 9.21 it is clear that most dominantly this last bin is sensitive to the new physics signal, while the low m_{ll} region serves to constrain the background processes, foremost the $W^{\pm}W^{\pm}jj$-EW6 process. For a future optimisation of the observable and binning used in the statistical analysis, it might be worth testing if a combination of bins in the m_{jj} and m_{ll} observable is promising. The first allows to constrain different background processes in the low and high mass regions, as seen in the SM analysis, and the latter gives the sensitivity to the EFT signal. This strategy is pursued in [155] where most recent exclusion bounds are derived for the $W^{\pm}W^{\pm}jj$-EW6 process.

It is noticeable that the prediction of the f_{S1}/Λ^4 parameter in the last bin of the invariant dilepton mass is substantially smaller than the for other parameters. This is the case although nominal parameters, which are derived from existing exclusion bounds from an analysis with similar properties, are utilised for all parameters. It can, hence, already be concluded here, that the sensitivity for this parameter is reduced compared to the other parameters. One cause may be the large requirement on the minimum tagging jet p_{T} discussed before.

9.3.2 Characteristics of the Statistical Model

The description of the mathematical approach is based on information and notations established in Sec. 8.2.2 for the SM analysis. The likelihood function of Eq. (8.8) is adjusted to

include the relevant items for the description of the BSM EFT signals. The ratio of the reformulated maximum negative logarithmic likelihood function again serves as a test statistic for the interval estimation. For the latter purpose the existing statistical tool FLIT [280] is employed. It is able to extract multidimensional exclusion limits with the asymptotic formulae [281] as well as through the generation of pseudo-experiments. The description of the EFT signal contributions, described via the functional form of the decomposition approach, is incorporated into this software tool in the course of this thesis.

The focus on the derivation of the statistical model is laid on the differences with respect to the SM analysis. To begin with, the signal definition is altered. After the $W^{\pm}W^{\pm}jj$-EW6 process in the SM is observed (cf. Chapter 8), it is considered as a background process. Solely the EFT contribution to the $W^{\pm}W^{\pm}jj$-EW6 process is considered as a signal. With the decomposed contribution of `LIN` and `QUAD`, the total expected number of signal events in the signal region at reconstruction level can be written as[9]:

$$\nu_S\left(\frac{f_i}{\Lambda^4}\right) = \nu_{\texttt{LIN}}\left(\frac{f_i}{\Lambda^4}\right) + \nu_{\texttt{QUAD}}\left(\frac{f_i}{\Lambda^4}\right). \tag{9.16}$$

The $\nu_{\texttt{LIN}}$ and $\nu_{\texttt{QUAD}}$ are parameterised as a function of the parameter f_i/Λ^4, which becomes the parameter of interest in this analysis, according to the decomposition approach as in Eq. (9.4). The total expected event count, including all background processes B estimated from MC or experimental data, is:

$$\nu\left(\frac{f_i}{\Lambda^4}, \vec{\theta}\right) = \nu_S\left(\frac{f_i}{\Lambda^4}, \vec{\theta}\right) + \sum_B \nu_B(\vec{\theta}). \tag{9.17}$$

Systematic uncertainties $\vec{\theta}$ are incorporated into the fit as NPs in a similar manner as before. Details follow in Sec. 9.4. With the above adjustments, the likelihood function from Eq. (8.8) transforms to:

$$\mathcal{L}\left(\frac{f_i}{\Lambda^4}, \vec{\theta}\right) = \prod_j \text{Pois}\left(N_j|\nu_j(\frac{f_i}{\Lambda^4}, \vec{\theta})\right) \text{Gaus}\left(L_{\text{inst}}|\lambda, \Delta_L\right) \prod_r f_r\left(a_r|\alpha_r, \Delta_r\right), \tag{9.18}$$

in seven bins j of the m_{ll} observable and with the number of events N observed in data. It is employed to define the test statistic:

$$q\left(\left(\frac{f_i}{\Lambda^4}\right)_{\text{test}}\right) = -2\ln\frac{\mathcal{L}\left(\left(\frac{f_i}{\Lambda^4}\right)_{\text{test}}, \hat{\hat{\vec{\theta}}}\right)}{\mathcal{L}\left(\frac{\hat{f}_i}{\Lambda^4}, \hat{\vec{\theta}}\right)}. \tag{9.19}$$

Equivalently to Eq. (8.10), the denominator represents the best estimate for the unconditional fit, with f_i/Λ^4 and the set of NPs $\vec{\theta}$ being free parameters of the minimisation procedure. The numerator is the minimised negative log-likelihood function with respect to all $\vec{\theta}$, where the f_i/Λ^4 is fixed to the test value. The test statistic defined as above holds for the best estimate $\widehat{f_i/\Lambda^4}$ found to be larger than the test value $\left(f_i/\Lambda^4\right)_{\text{test}}$ and is zero otherwise.

This test statistic is now utilised to assess the probability that the hypothesis under $\left(f_i/\Lambda^4\right)_{\text{test}}$ is true given the observed data (i. e. the p-value). In order to assess this probability, a number of pseudo-experiments are conducted for each hypothesis $\left(f_i/\Lambda^4\right)_{\text{test}}$. The number of signal and background events for each pseudo-experiment is estimated by randomly shifting the nuisance parameters $\vec{\theta}$ to non-zero values following the respective constraining p.d.f. f_r. For each $\left(f_i/\Lambda^4\right)_{\text{test}}$, the fraction of pseudo-events (i. e. the relative frequency) is evaluated for which the test statistic exhibits smaller values than the one obtained from observed data:

$$q_{pe}\left(\left(\frac{f_i}{\Lambda^4}\right)_{\text{test}}\right) < q_{obs}\left(\left(\frac{f_i}{\Lambda^4}\right)_{\text{test}}\right). \tag{9.20}$$

Conventionally, a signal model with parameter point $\left(f_i/\Lambda^4\right)_{\text{test}}$ is said to be excluded at 95% confidence level (C.L.) in high-energy particle physics if this fraction, representing an

[9] This definition will be refined in Sec. 9.6.4 to include information on the clipping unitarisation approach.

estimate of the p-value, is below 5%. A number of 10000 pseudo-experiments is evaluated which corresponds to a statistical uncertainty on the p-value of 0.2%.

The result is a confidence interval for the f_i/Λ^4 which contains the true value with a probability of 95%. The boundaries of the confidence interval are itself random variables with standard deviations. They constrain the allowed region of the EFT parameter space from the observed data. In the given EFT model, this is essentially the strength of possible anomalous contributions to the quartic $W^\pm$ boson vertex.

Again, expected exclusion bounds, obtained from the predicted estimates of signal and background events, are derived utilising an Asimov dataset. These can be compared to the results obtained with observed data.

9.4 Systematic Uncertainties

The definition of the signal contribution, the measurement strategy, and the statistical model has been discussed in the previous sections. The systematic uncertainties on the measurement observables are the last ingredient for the statistical analysis.

First, the systematic uncertainties on the EFT signal contributions are evaluated in the signal region. Further, the impacts of systematic uncertainties on the exclusion bounds are studied by conducting the analysis with different sets of systematic uncertainties. From this study, the final treatment of systematic uncertainties is derived by precluding an overestimation of the sensitivity and further balancing the loss of sensitivity and the computing time and stability of the statistical fits.

For the extraction of the exclusion bounds on the EFT parameters, the invariant mass of the leading lepton pair, m_{ll}, is utilised in the fit. Hence, detailed information on systematic uncertainties in this kinematic distribution is needed for the statistical analysis. Therefore, uncertainties for all signal and background processes, if not solely affecting the normalisation of a given prediction, are evaluated in bins of m_{ll}. In the terminology of the statistical analysis, established in Sec. 8.2.2, these are called shape uncertainties with external constraints and denoted[10] β_{pj} depending on the process p, and reconstruction level m_{ll} bin j.

9.4.1 Systematic Uncertainties of the EFT Signal Contributions

The signal contribution is defined as the appropriately scaled sum of the decomposed `LIN` and `QUAD` contributions. However, the `QUAD` is larger than the `LIN` contribution in almost all bins of the m_{ll} distribution. This is especially true in the last bin (cf. Sec. 9.2.6), which is expected to give the most sensitivity to the exclusion bounds, as is deduced from Fig. 9.21. Moreover, samples of the `LIN` contributions are statistically more limited than of the `QUAD` contribution (cf. Figures 9.19 and 9.20). Furthermore, a technical aspect is, that the framework utilised for the statistical analysis is not capable of handling uncertainties on both contributions. It is hence decided to asses systematic uncertainties on the total EFT prediction by applying the relative uncertainties obtained from variations of the `QUAD` contribution to the total EFT prediction. Accordingly, only relative uncertainties on the `QUAD` contribution are summarised in this thesis.

Experimental Uncertainties in the Signal Region

The evaluation of the experimental systematic uncertainties on the EFT signal processes follows the identical procedure as outlined in Sec. 7.6.1 for the SM processes. The relative impact of the experimental uncertainties on the event yields of the `QUAD` contribution of all signal processes in the signal region are summarised in Tab. 9.10.

It can be noted that the uncertainties are large, as for the MG5+Py8drec prediction of the $W^\pm W^\pm jj$-EW6 process, compared to other SM processes (cf. Tab. 7.7). The reason for this is identical to the SM case. The statistical limitation of the EFT samples at reconstruction level leads to variations with sizable fluctuations already from differences of only very few events. As a reminder, then, the total size of the uncertainty depends on the number of

[10] As the measurement solely involves one region/channel, the c is omitted.

Table 9.10: Relative impact of experimental systematic uncertainties on the event yields of the QUAD contribution of all EFT signal predictions in the combined $\ell^{\pm}\ell^{\pm}$ channel in the signal region. The uncertainty sources are condensed into seven categories as implemented in the fit. Electron and muon uncertainties comprise all variations in the measurement of electrons and muons, respectively, including the trigger efficiency. Jet uncertainties comprise all variations in the measurement of jets, except the variations of the jet energy resolution and the flavour tagging which are quoted as JER and b-tag inefficiency uncertainties, respectively. Independent uncertainty sources are added in quadrature for each category.

Param.	Contrib.	Systematic Uncertainty [%]						
		Electrons	Muons	Jets (w/o JER)	JER	b-tag ineff.	Pile-up rwt.	E_T^{miss}
$S02$	QUAD	±11	±15	±20	±3	±14	±3	±6
$S1$	QUAD	±11	±14	±18	±3	±13	±3	±5
$M0$	QUAD	±12	±14	±16	±3	±24	±1	±4
$M1$	QUAD	±12	±16	±19	±3	±22	±3	±6
$M7$	QUAD	±3	±3	±5	±1	±24	±5	±1
$T0$	QUAD	±7	±7	±8	±2	±36	±4	±2
$T1$	QUAD	±7	±10	±10	±1	±34	±3	±3
$T2$	QUAD	±13	±18	±21	±4	±35	±4	±7

considered independent sources added together in quadrature. Comparing with Tab. 7.6, this in particular affects the uncertainties on the measurement of electrons, muons, and jets, including the measurement of the b-tag inefficiency.

As discussed in Sec. 9.2.2, previous analyses with results on EFT interpretation employ systematic uncertainties of the SM prediction of the respective process [250, 252, 255] or even uncertainties extrapolated from some region into the signal region [246]. The possibility to assess experimental systematic uncertainties on the different EFT signal predictions is a step towards a refined measurement of the BSM properties. In future measurements, the statistical accuracy is to be improved by generating more events. For this study the given accuracy shall suffice. However, employing the uncertainty estimates of Tab. 9.10 result in a conservative estimate of the exclusion bounds.

Modelling Uncertainties in the Signal Region

The evaluation of the modelling uncertainties on the theoretical predictions of EFT signal processes follows similarly the procedure outlined in Sec. 7.6.2 for the SM processes. Information on the implemented variations in the MG5_aMC event generation setup employed in this thesis are detailed in App. A.4.3 and discussed in Sec. 6.5. The relative impact of the modelling uncertainties on the event yields of the QUAD contribution of all signal processes in the signal region are summarised in Tab. 9.10.

Modelling uncertainties in all categories are stable with respect to the various EFT signals. As for the SM processes, the variations of the renormalisation and factorisation scales cause the largest uncertainty on the modelling of the signal processes. Uncertainties due to the variations of the nominal PDF set are between 4% and 6% for all considered processes. Uncertainties originating from the variation of the value of the strong coupling constant in the PDF sets are below the statistical accuracy of the MC predictions for all parameters.

Parton shower uncertainties are evaluated at reconstruction level via the implemented on-the-fly weights in the event generation. No folding to reconstruction level is necessary here. The symmetrised envelope of the variations is taken as the systematic effect on the prediction. No samples interfaced to Herwig 7 are generated for the EFT contributions due to the large cost in resources compared to the gain in information. From the theoretical studies of the

Table 9.11: Relative impact of modelling uncertainties on the event yields of the QUAD contribution of all EFT signal predictions in the combined $\ell^\pm\ell^\pm$ channel in the signal region. The columns contain the effect (from left to right) from the variation of the renormalisation and factorisation scales μ_R/μ_F, the nominal PDF set and its strong coupling value α_S, and the parton shower parameters within MG5_aMC.

Param.	Contrib.	Modelling uncertainty [%]			
		μ_R/μ_F	PDF set	α_S	Part. shower
$S02$	QUAD	$^{+14}_{-12}$	±4	±1	±4
$S1$	QUAD	$^{+14}_{-12}$	±4	±1	±5
$M0$	QUAD	$^{+15}_{-12}$	±6	±1	±5
$M1$	QUAD	$^{+15}_{-12}$	±4	±1	±6
$M7$	QUAD	$^{+14}_{-12}$	±5	±1	±10
$T0$	QUAD	$^{+15}_{-12}$	±5	±1	±6
$T1$	QUAD	$^{+15}_{-12}$	±5	±1	±2
$T2$	QUAD	$^{+15}_{-12}$	±5	±1	±4

parton shower configurations of the SM prediction (cf. Sec. 6.7.2), the differences between the nominal MG5+Py8drec and MG+H7 setups is at 1% and in the same order of magnitude as the internal parton shower variations provided by the MG5+Py8drec setup. It is not expected that employing the EFT model changes this behaviour sizeably, especially in the high m_{ll} region. Hence, it is decided to assess the parton shower uncertainties in contrast to the recommended procedure, outlined in Sec. 6.5.2, and to solely utilise the envelope of the difference of the internal variations for the EFT signal predictions.

9.4.2 Impact of Systematic Uncertainties on the Exclusion Bounds

In the course of setting up the statistical measurement it is found that the fitting procedure becomes highly unstable when adding the various systematic uncertainties as nuisance parameters to the statistical model. When adding all of the more than one hundred independent NPs, the fit does not converge to meaningful results for all parameters. Hence, a suitable set of NPs is to be found which makes the statistical analysis converge and yet includes as much information as possible[11]. The primary condition is, however, to prevent the statistical fit from giving too ambitious results when neglecting part of the information.

In order to estimate the impact of a given set of systematic uncertainties on the expected exclusion bounds, several fits are performed with different sets of systematics included. In addition, the impact on symmetrising asymmetric uncertainty sources is studied. This study is conducted for the f_{S1}/Λ^4 operator only and the results are extrapolated to the other parameters. In Tab. 9.12, the information on the included sets of NPs for each fit are assembled, additionally indicating whether a certain group of systematic uncertainties is added asymmetrically or symmetrically. The expected exclusion bounds are calculated from the asymptotic formula for this study.

Starting from the fit with only statistical uncertainties on all predictions, the impact of the experimental uncertainties is studied first. For this, a "reduced" set of experimental object and event uncertainties (denoted R) on MC-simulated predictions is employed. This set adds the effect of systematic uncertainties within each object-based and predefined category in quadrature. It is defined for all considered processes, i. e. all signal and background predictions whose estimate is taken from MC simulation. The resulting effect is then added

[11] The statistical analysis converges with different sets of information for different parameters. For reasons of practicality of the statistical analysis, those sets are relevant for which the analysis converges for all parameters.

Table 9.12: Definition of various sets for the study of the impact of the systematic uncertainties on the expected exclusion bounds of the f_{S1}/Λ^4 parameter. Uncertainty sources are divided into experimental and modelling uncertainty sources. Experimental uncertainties are further separated into object and event uncertainties (cf. Sec. 7.6.1) and uncertainties from the background estimation procedures (cf. Sec. 7.6.1). The latter are subdivided into asymmetrically and symmetrically defined uncertainty sources. Only the `CF_SFunc`, `FakeElSys`, `FakeMuSys` are asymmetric while other uncertainties from the background estimation procedures are per construction symmetric. The modelling uncertainties are separated into the dominant source from the variation of the renormalisation and factorisation scales and other modelling variation sources (cf. Sec. 7.6.2). Both are subdivided further into two process categories, the EFT signals and the SM $W^{\pm}W^{\pm}jj$-EW6 process, and the $W^{\pm}Z$ and $W^{\pm}W^{\pm}jj$-EW4 background processes, respectively. Employing the reduced and full experimental object and event systematic uncertainties is indicated with an "R" or "F", respectively. Employing symmetric or asymmetric uncertainty definitions is indicated with an "S" or "A", respectively. An "−" indicates that none of these uncertainty sources are utilised for the given set. The first row states the expected exclusion bounds without systematic uncertainties. The "nominal" set is the final set employed for the extraction of the exclusion bounds in this thesis. The expected exclusion bounds are calculated from the asymptotic formulae [281] for this study.

Experimental uncertainties			Modelling uncertainties				Exclusion limits
Object & event (cf. Tab. 7.6)	Background estimates (cf. Tab. 7.8)		Ren./Fac. scales (cf. Tab. 7.11)		Other modelling (cf. Tab. 7.11)		$\frac{f_{S1}}{\Lambda^4}$
	`CF_SFunc`, `FakeElSys`, `FakeMuSys`	Others	$W^{\pm}W^{\pm}jj$-EW6 SM & EFT	$W^{\pm}Z$, $W^{\pm}W^{\pm}jj$-EW4	$W^{\pm}W^{\pm}jj$-EW6 SM & EFT	$W^{\pm}Z$, $W^{\pm}W^{\pm}jj$-EW4 Other prompt	
–	–	–	–	–	–	–	$[-46.5, 47.6]$
R	S	S	–	–	–	–	$[-48.0, 50.0]$
R	A	S	–	–	–	–	$[-48.5, 49.7]$
R	A	S	A	S	–	–	$[-49.3, 50.3]$
R	A	S	A	S	–	S	$[-49.2, 50.4]$
Nominal set:							
R	A	S	A	S	S	S	$[-50.5, 52.2]$
R	A	S	A	A	`TheoShower` A Others S	`TheoShower` A Others S	$[-50.4, 50.7]$
F	A	S	A	S	S	S	$[-50.7, 52.3]$

as independent NP to the statistical analysis. The categories are defined as follows by indicating the label prefixes listed in Tab. 7.6:

- Electrons: Adding in quadrature all systematic uncertainty sources affecting electrons in the analysis, i. e. sources with label prefix `EL` and `EG`;
- Muons: Adding in quadrature all systematic uncertainty sources affecting muons in the analysis, i. e. sources with label prefix `MUON`;
- Jets: Adding in quadrature all systematic uncertainty sources affecting jets in the analysis, except the jet energy resolution (JER) and the flavour tagging uncertainties, i. e. sources with label prefix `JET`;
- b-tag ineff: Adding in quadrature all systematic uncertainty sources affecting the flavour tagging of jets employed to define the b-jet veto in the signal region, i. e. sources with label prefix `FT`;
- E_T^{miss}: Adding in quadrature all systematic uncertainty sources affecting the missing transverse momentum measurement, i. e. sources with label prefix `MET`;
- JER: Systematic uncertainty due to the variation of the jet energy resolution, kept as separate NP;
- Pile-up rwt.: Systematic uncertainty due to the variation of the pileup reweighting scale factor, kept as separate NP; and
- Luminosity: Systematic uncertainty on the luminosity measurement, kept as separate NP.

The JER and pileup reweighting uncertainties are kept individually as these are found to be the dominant experimental uncertainty sources for all background processes. The luminosity uncertainty is kept individually because it does not add a shape but only an overall normalisation effect on the event yields. Consequently, the reduced set contains a total of 8 independent NPs compared to 100 for the full set (denoted F). The individual variations are added in quadrature combining all variations with a positive(negative) effect on the overall event yield to the up(down) variation. Further, all uncertainties in the reduced set are symmetrised by taking the direction which exhibits the larger variation in each bin.

The impact of the experimental uncertainties, employing the symmetrised, reduced set and the additional, symmetrised uncertainties from the background estimation procedures (cf. Sec. 7.6.1) on the exclusion bounds is at 3% to 5%. When adding the latter uncertainties asymmetrically where applicable[12] both boundaries of the exclusion interval are shifted towards lower values.

A further step is made, by including the dominant modelling uncertainties from the variation of the renormalisation and factorisation scales for all processes for which these are derived. For the $W^{\pm}Z$ and $W^{\pm}W^{\pm}jj$-EW4 background processes, these are included in a symmetrised manner, while they are kept asymmetric for the EFT signal and the SM $W^{\pm}W^{\pm}jj$-EW6 predictions. Solely including scale uncertainties enlarges the exclusion interval by approx. $(1-2)\%$ on both sides. Further adding the remaining, symmetrised modelling NPs (cf. Tab. 7.11) on the $W^{\pm}Z$, $W^{\pm}W^{\pm}jj$-EW4, and other prompt background predictions does not significantly affect the exclusion bounds. On the contrary, adding the symmetrised PDF set, α_{S} value and parton shower uncertainties on the EFT signal and SM $W^{\pm}W^{\pm}jj$-EW6 predictions enlarges the exclusion interval by $(3-4)\%$ on both sides.

Adding scale uncertainties for the $W^{\pm}Z$ and $W^{\pm}W^{\pm}jj$-EW4 background predictions and parton shower uncertainties on all relevant predictions in an asymmetric manner considerably improves the exclusion limits in the positive parameter direction which in turn symmetrises the exclusion interval around zero. However, asymmetric NP definitions render the fit highly unstable. As a consequence, the statistical fit does not converge for all EFT parameters when employing this set of NPs. Hence, all modelling uncertainties are kept symmetric except for

[12] Only the `CF_SFunc`, `FakeElSys`, `FakeMuSys` are asymmetric while other uncertainties from the background estimation procedures are per construction symmetric.

the renormalisation and factorisation scale uncertainties on the EFT signals and the SM $W^{\pm}W^{\pm}jj$-EW6 process.

Eventually, the impact of utilising the reduced versus the full set of experimental object and event uncertainties is shown to have an effect on the final exclusion bounds at the permille level. The nominal set of systematic NPs is, hence, concluded to include the reduced set of these uncertainties as well as symmetrised modelling uncertainties as stated above.

Including asymmetric compared to symmetric modelling uncertainties for most of the processes/sources yields more than 3% better exclusion bounds on the positive parameter side. Utilising the reduced versus the full set of experimental object and event uncertainties gives marginally worse exclusion bounds. Neglecting possible correlations between these sets of NPs it can be concluded that employing the nominal set for the final exclusion bounds gives a conservative estimate compared to using the full set of over hundred independent NPs.

9.4.3 Final Treatment of Systematic Uncertainties

The final treatment of systematic uncertainties for the EFT reinterpretation analysis is based on the treatment in the SM analysis outlined Sec. 8.5 and the results of the above studies. Only differences to the treatment in the SM analysis are summarised here.

As the statistical analysis is conducted differentially in m_{ll}, effects of systematic variations are derived for this observable. The list of systematic uncertainty categories included per process is identical to the SM analysis and detailed in Tab. 8.8. One exception are the NLO EW corrections to the $W^{\pm}W^{\pm}jj$-EW6 process which are not available differentially in m_{ll} to this date and are hence omitted.

Experimental object and event systematic uncertainties are added as reduced, symmetrised set, explained above, yielding 8 independent NPs. Their impact on the m_{ll} distribution of the two dominant background processes, the SM $W^{\pm}W^{\pm}jj$-EW6 and $W^{\pm}Z$, and the EFT signal contributions are shown in Figures 9.22 to 9.24. Detailed numbers differentially in m_{ll} for all background processes and signal contributions as well as all experimental uncertainty categories are summarised in Tables G.4 to G.6 in the appendix.

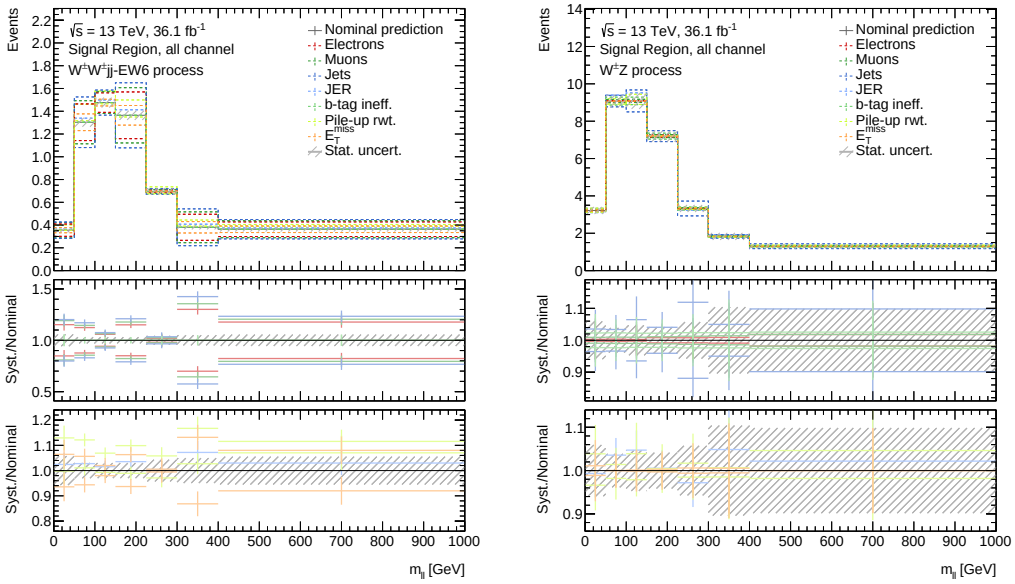
As expected, for the background processes as well as the signal contributions, the jet category has the largest impact of all combined categories. While it stays below 10% for most of the bins for the $W^{\pm}Z$ process, uncertainties in the $W^{\pm}W^{\pm}jj$-EW6 process rise to almost 50% in few bins. The predictions of the signal process show large, statistically limited variations for all parameters, consistent with the findings in Sec. 9.4.1. However, the last bin of the m_{ll} distribution, which is the most sensitive to the new physics signal, exhibits stable and consistent uncertainties of around 10% for the largest sources and almost all parameters. Solely the parameters of the S family have larger uncertainties in this bin, yet staying below 20%.

The treatment of uncertainties for the data-driven background estimation procedures is identical to the SM analysis. Their impact on the m_{ll} distribution is shown in Fig. 9.25. Detailed numbers can be found in Tab. G.7 in the appendix.

Modelling uncertainties are included for the $W^{\pm}Z$, $W^{\pm}W^{\pm}jj$-EW4, and $W^{\pm}W^{\pm}jj$-EW6 background processes as well as all signal contributions with shape and normalisation effects. Variations include the renormalisation and factorisation scale, the nominal PDF set, its value for the strong coupling α_{S}, and the parton shower modelling.

For the $W^{\pm}W^{\pm}jj$-EW6 process, these are derived in equal manner as for the SM analysis, except for the parton shower uncertainties. As the $W^{\pm}W^{\pm}jj$-EW6 prediction is taken from the MG5+Py8drec setup in the EFT analysis, parton shower uncertainties are derived with the relevant on-the-fly weights at reconstruction level without the need for folding. The envelope of the different variations is defined to be the final parton shower uncertainty. The uncertainties for the EFT signal contributions are derived in equal manner as for the $W^{\pm}W^{\pm}jj$-EW6 process.

As stated above, solely the scale uncertainties on the EFT signal contributions and the SM $W^{\pm}W^{\pm}jj$-EW6 process are added as asymmetric NPs, while all other modelling uncertainties are symmetrised. Figures 9.26 to 9.28 show the modelling uncertainties differentially



(a) **(b)**

Figure 9.22: Distribution of the invariant leading lepton mass, m_{ll}, in the combined $\ell^{\pm}\ell^{\pm}$ channel in the signal region for the two background processes with the largest contribution in the EFT reinterpretation analysis, $W^{\pm}W^{\pm}jj$-EW6 (a) and $W^{\pm}Z$ (b). The nominal predictions estimated from MC simulation (black, solid) together with the systematic variations of the experimental uncertainties in seven categories (see text) are shown. The lower pads show the relative uncertainties. Uncertainties on the nominal estimates are statistical only.

in m_{ll} for the $W^{\pm}Z$, $W^{\pm}W^{\pm}jj$-EW4, and $W^{\pm}W^{\pm}jj$-EW6 background processes, and all EFT signal contributions. Detailed numbers for all relevant processes are summarised in Tables G.8 and G.9 in the appendix.

The scale and parton shower uncertainties are the leading modelling uncertainty sources for all considered processes and especially in the last m_{ll} bin of the EFT signal contributions. For the background processes, scale uncertainties are flat in m_{ll} in contrast to their behaviour in m_{jj}.

Nuisance parameters for symmetric modelling uncertainties are implemented with a log-normal distributed constraining p.d.f. f_r in the statistical framework (cf. Eq. (9.18)). All other NPs are Gauss constrained.

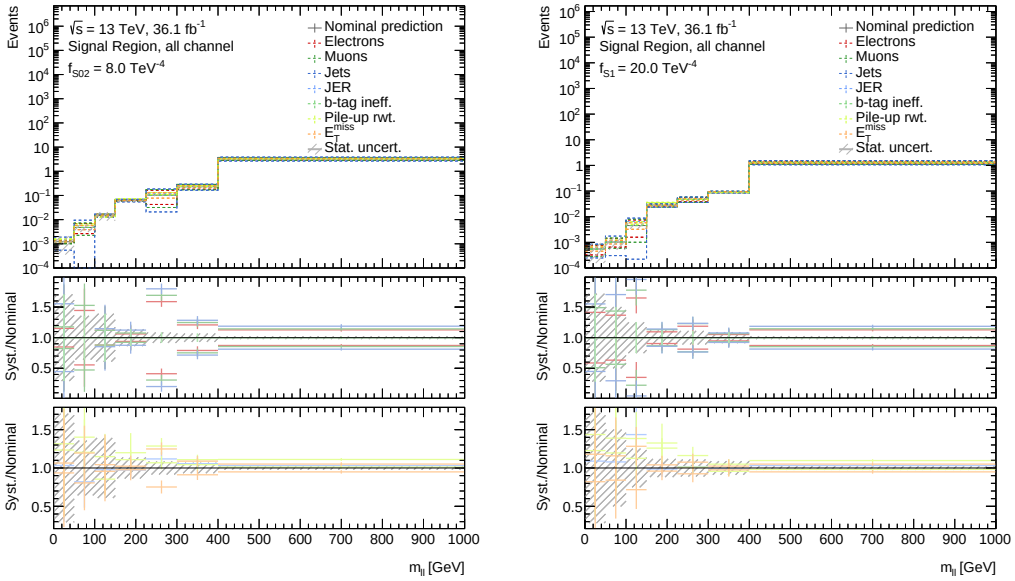
9.5 Exclusion Limits with Systematic Uncertainties

For this and all following sets of exclusion limits, the nominal set of systematic uncertainties, defined in Tab. 9.12 and the respective text, is employed. The expected and observed one-dimensional exclusion intervals at the 95% C.L. for all EFT parameters of the considered model [2, 3] relevant in the $W^{\pm}W^{\pm}jj$-EW6 process are summarised in Tab. 9.13. The expected limits are obtained with pseudo-experiments. No unitarisation procedure is applied.

The observed exclusion limits are weaker than the expected results for all considered parameters which can be explained with a slight excess of data events over the total background prediction in the last and most sensitive bin in the m_{ll} distribution (cf. Fig. 9.21).

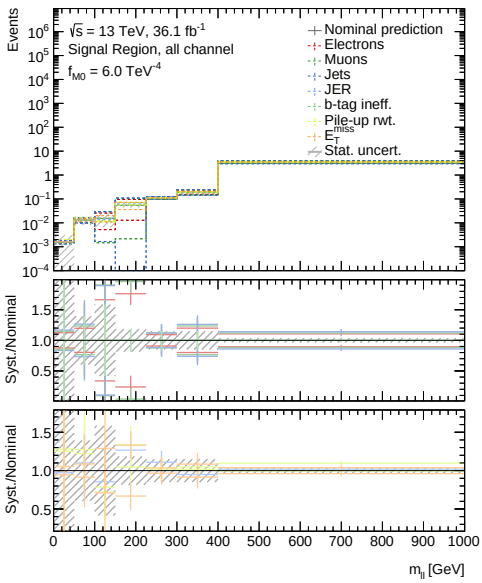
For half of the considered parameters, the limits are asymmetric. In fact, all exclusion bounds are found to be consistently asymmetric in the expected and observed case before rounding. The asymmetry can have two sources: the EFT interference contribution `LIN`, and the inclusion of asymmetric systematic uncertainties.

The results without systematic uncertainties, summarised in Tab. G.1 in the appendix, show asymmetric behaviour for more of the parameters. In this case, the effect comes purely

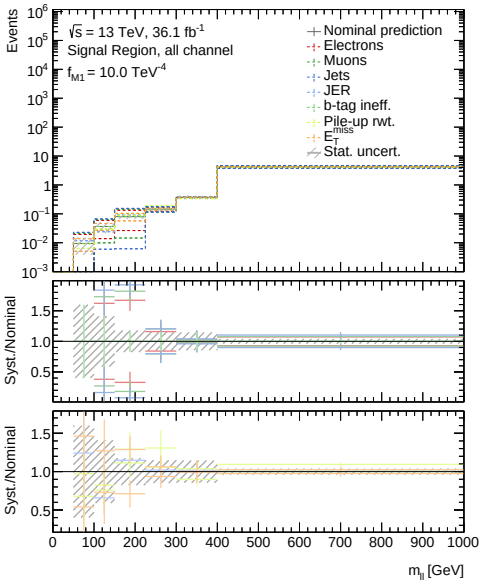


(a)

(b)

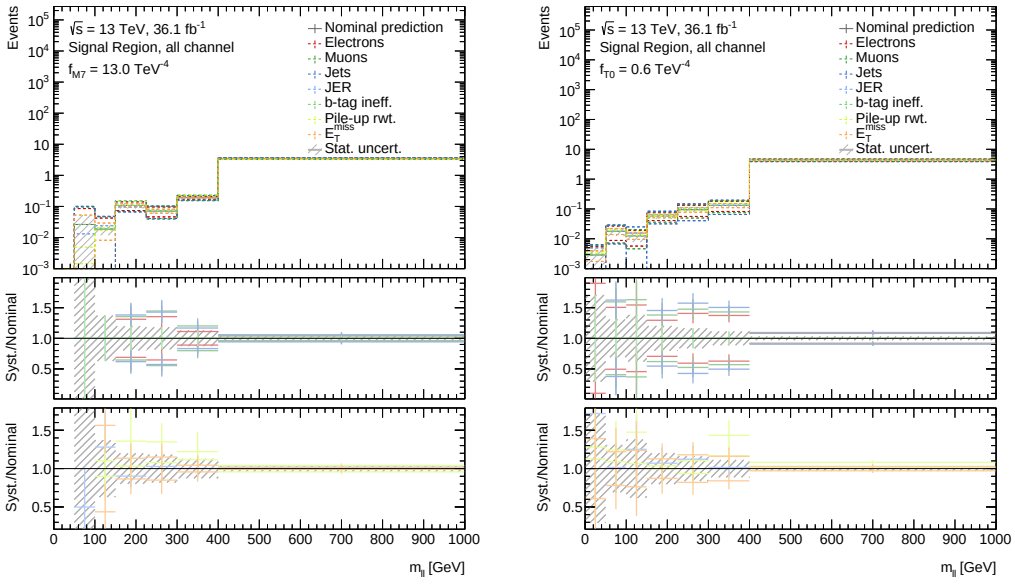


(c)



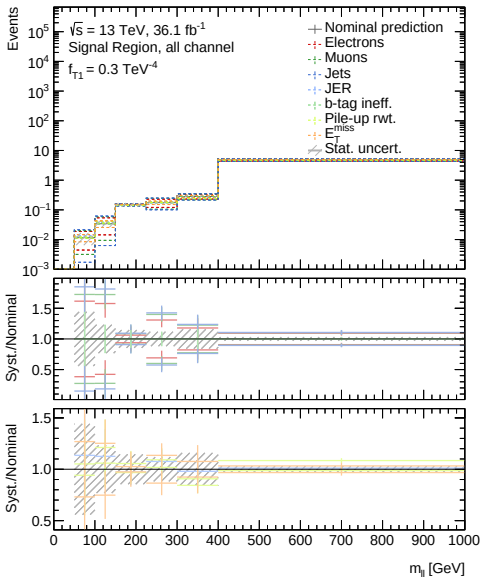
(d)

Figure 9.23: Distribution of the invariant leading lepton mass, m_{ll}, in the combined $\ell^{\pm}\ell^{\pm}$ channel in the signal region for the `QUAD` contribution of the EFT signal predictions for the parameters f_{S02}/Λ^4 (a), f_{S1}/Λ^4 (b), f_{M0}/Λ^4 (c), and f_{M1}/Λ^4 (d). The nominal predictions estimated from MC simulation (black, solid) together with the systematic variations of the experimental uncertainties in seven categories (see text) are shown. The lower pads show the relative uncertainties. Uncertainties on the nominal estimates are statistical only.

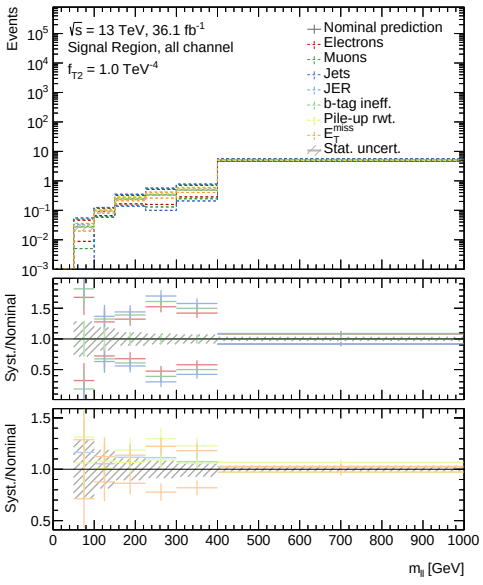


(a)

(b)



(c)



(d)

Figure 9.24: Distribution of the invariant leading lepton mass, m_{ll}, in the combined $\ell^{\pm}\ell^{\pm}$ channel in the signal region for the `QUAD` contribution of the EFT signal predictions for the parameters f_{M7}/Λ^4 (a), f_{T0}/Λ^4 (b), f_{T1}/Λ^4 (c), and f_{T2}/Λ^4 (d). The nominal predictions estimated from MC simulation (black, solid) together with the systematic variations of the experimental uncertainties in seven categories (see text) are shown. The lower pads show the relative uncertainties. Uncertainties on the nominal estimates are statistical only.

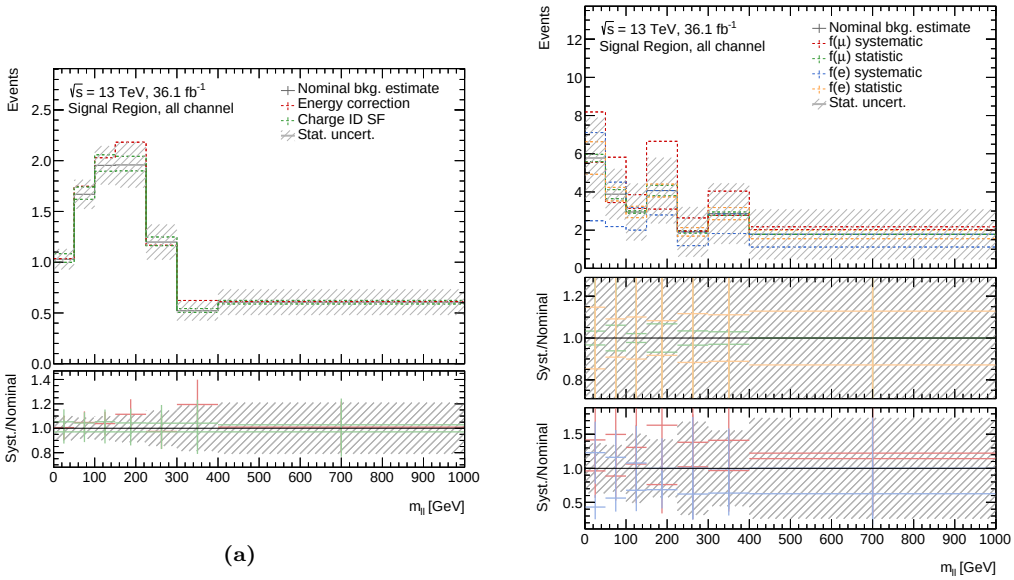
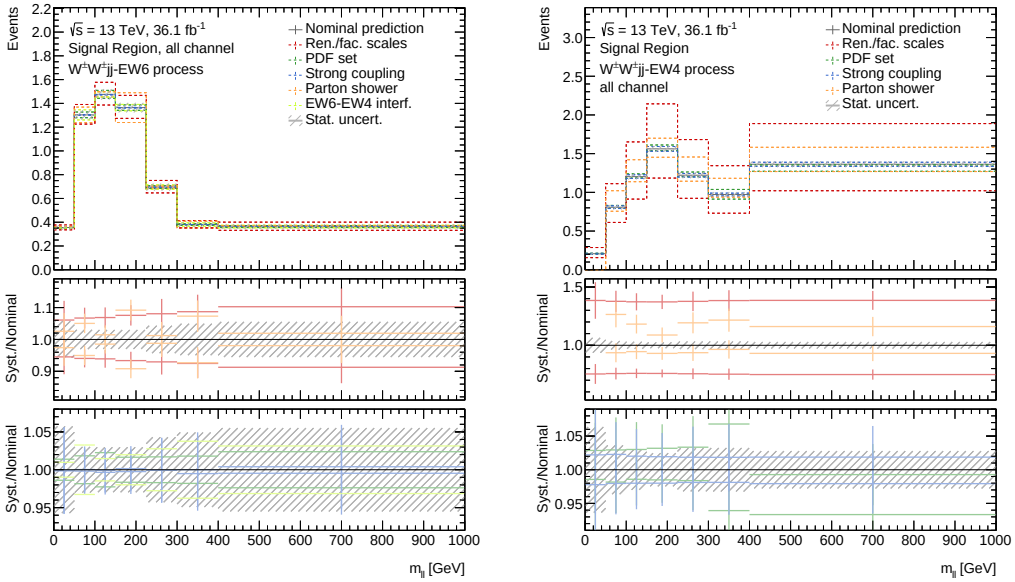


Figure 9.25: Distribution of the invariant mass of the dilepton system, m_{ll}, in the combined $\ell^{\pm}\ell^{\pm}$ channel in the signal region. (a) The nominal background estimate due to electron charge misidentification together with uncertainties from the energy correction (red) and the charge (mis)identification scale factors (green) are shown. The one-sided energy correction systematic uncertainty is symmetrised in the final measurement. Calculations are based on Ref. [219]. (b) The nominal background estimate due to non-prompt leptons together with the separate statistical and systematic uncertainties from the fake factor measurement for electrons $f(e)$ and muons $f(\mu)$ propagated to the final background estimate are shown. The systematic uncertainties are the combined uncertainties from all systematic sources of the respective fake factor measurement. Calculations are based on Ref. [232]. (a+b) The lower pad shows the relative uncertainties. Uncertainties on the nominal estimate are statistical only.

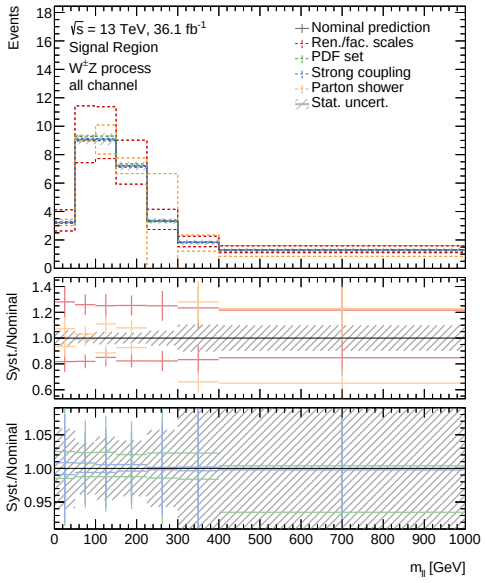
Table 9.13: Expected and observed one-dimensional exclusion intervals at the 95% C.L. for all EFT parameters of the considered model [2, 3] relevant in the $W^{\pm}W^{\pm}jj$-EW6 process. The nominal set of systematic uncertainties (cf. Sec. 9.4.2) is employed. The expected limits are obtained with pseudo-experiments. No unitarisation procedure is applied.

Parameter	95% C.L. interval [TeV^{-4}]	
$\frac{f_i}{\Lambda^4}$	Expected	Observed
$S02$	$[-13, 13]$	$[-15, 15]$
$S1$	$[-48, 50]$	$[-55, 57]$
$M0$	$[-11, 11]$	$[-12, 12]$
$M1$	$[-19, 19]$	$[-21, 22]$
$M7$	$[-24, 23]$	$[-28, 27]$
$T0$	$[-1.1, 1.1]$	$[-1.3, 1.3]$
$T1$	$[-0.51, 0.54]$	$[-0.58, 0.60]$
$T2$	$[-1.6, 1.8]$	$[-2.0, 2.2]$



(a)

(b)



(c)

Figure 9.26: Distribution of the invariant leading lepton mass, m_{ll}, in the combined $\ell^{\pm}\ell^{\pm}$ channel in the signal region for the background processes $W^{\pm}W^{\pm}jj$-EW6 (a), $W^{\pm}W^{\pm}jj$-EW4 (b), and $W^{\pm}Z$ (c). The nominal predictions estimated from MC simulation (black, solid) together with the theoretical modelling uncertainties from the matrix element calculation due to variations of the renormalisation and factorisation scale, the PDF set and its strong coupling value, and the parton shower and merging parameters are shown. For the $W^{\pm}W^{\pm}jj$-EW6 process the uncertainty due to the interference between the $W^{\pm}W^{\pm}jj$-EW6 and $W^{\pm}W^{\pm}jj$-EW4 process is shown as well. The lower pads show the relative uncertainties. Uncertainties on the nominal estimates are statistical only.

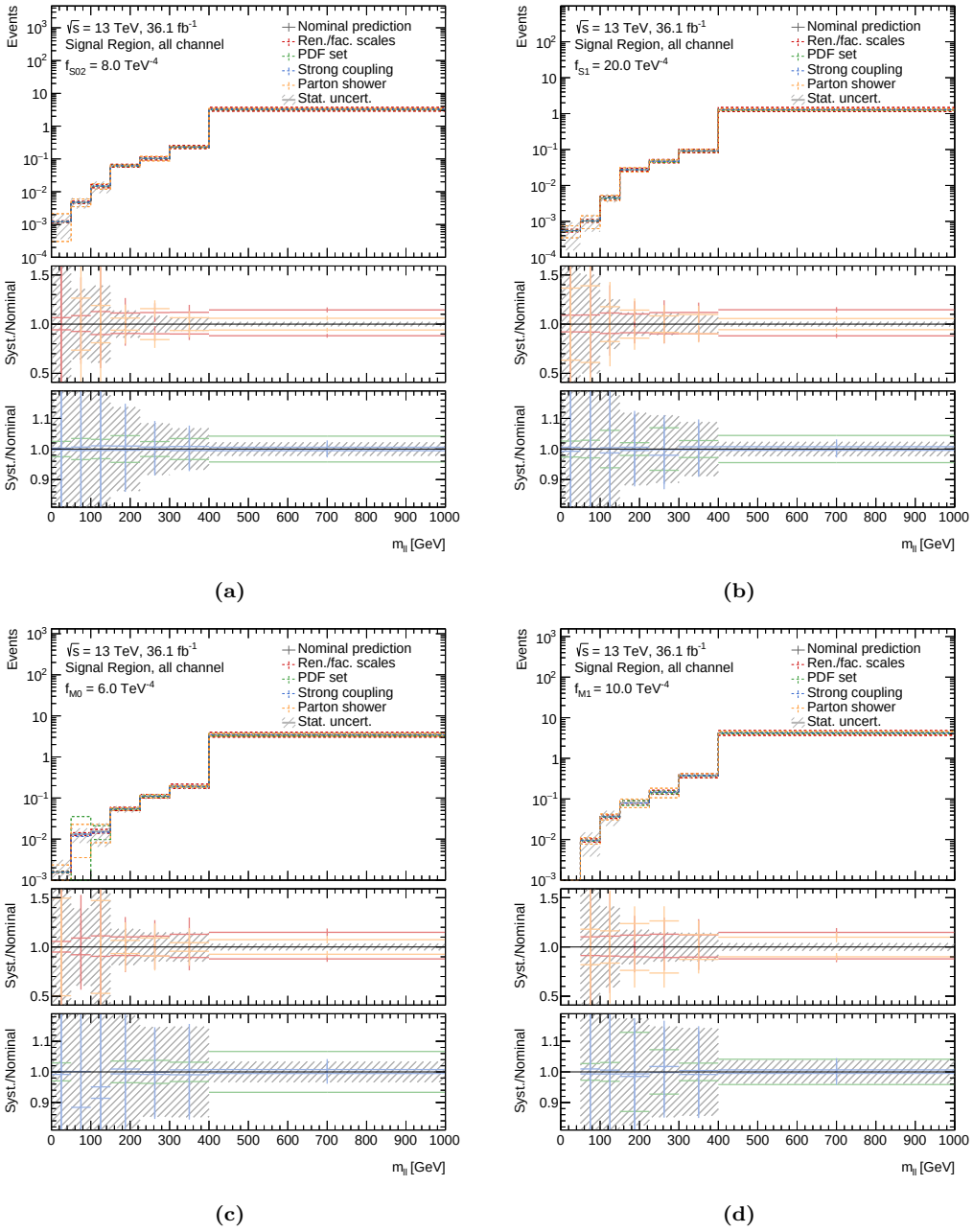


Figure 9.27: Distribution of the invariant leading lepton mass, m_{ll}, in the combined $\ell^{\pm}\ell^{\pm}$ channel in the signal region for the `QUAD` contribution of the EFT signal predictions for the parameters f_{S02}/Λ^4 (a), f_{S1}/Λ^4 (b), f_{M0}/Λ^4 (c), and f_{M1}/Λ^4 (d). The nominal predictions estimated from MC simulation (black, solid) together with the theoretical modelling uncertainties from the matrix element calculation due to variations of the renormalisation and factorisation scale, the PDF set and its strong coupling value, and the parton shower parameters are shown. The lower pads show the relative uncertainties. Uncertainties on the nominal estimates are statistical only.

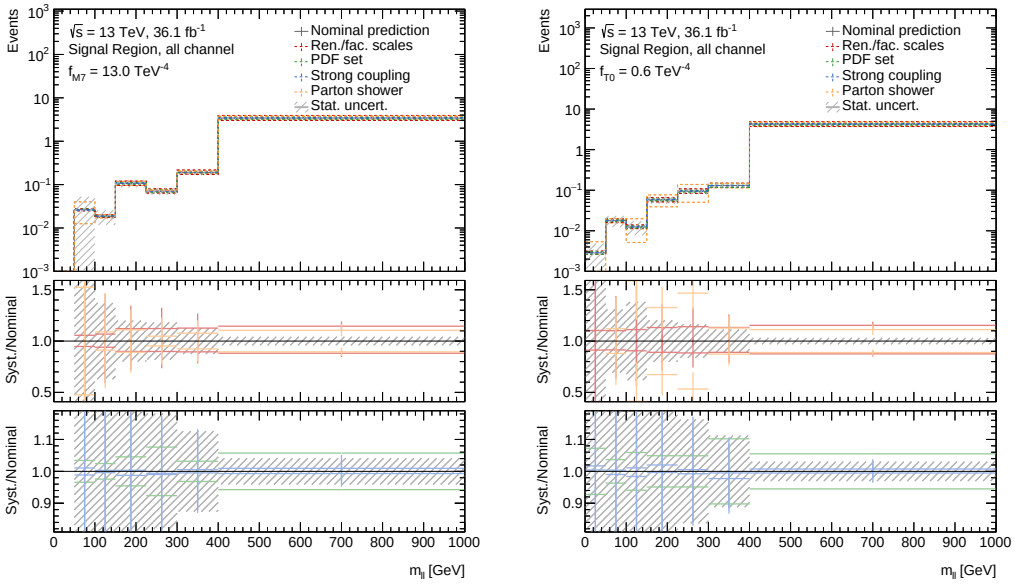


Figure 9.28: Distribution of the invariant leading lepton mass, m_{ll}, in the combined $\ell^{\pm}\ell^{\pm}$ channel in the signal region for the `QUAD` contribution of the EFT signal predictions for the parameters f_{M7}/Λ^4 (a), f_{T0}/Λ^4 (b), f_{T1}/Λ^4 (c), and f_{T2}/Λ^4 (d). The nominal predictions estimated from MC simulation (black, solid) together with the theoretical modelling uncertainties from the matrix element calculation due to variations of the renormalisation and factorisation scale, the PDF set and its strong coupling value, and the parton shower parameters are shown. The lower pads show the relative uncertainties. Uncertainties on the nominal estimates are statistical only.

from the EFT interference contribution LIN changing sign for positive versus negative parameter values. If the interference contribution is positive for positive parameter values, the exclusion bound on the positive side must be stronger than on the negative side of the interval. With this view, the asymmetry of the obtained exclusion limits is very reasonable when reviewing the interference contributions which are positive for positive parameter values only for f_{M0}/Λ^4 and f_{M7}/Λ^4 (cf. Sec. 9.2.6). The extent of the asymmetry depends on the relative contribution of the inference with respect to the quadratic term in the vicinity of the obtained limit values.

The latter aspect could also explain the reduced asymmetry of the exclusion limits including systematic uncertainties. Since the bounds become weaker in this case, the relative LIN contribution reduces, leading to more symmetric limits. In addition, the inclusion of asymmetric systematic uncertainties can influence it now as well.

The obtained limit values are larger than the nominal values, studied extensively in Sec. 9.2.6. Hence, the relative contribution of the EFT interference term LIN with respect to the quadratic term QUAD is smaller, than in the studies shown in above sections. This finding affects the reasoning of the applicability of the mathematical model of the extension in the new physics scale parameter Λ and is discussed further in the concluding section of this chapter.

The relative difference to the exclusion bounds without systematic uncertainties varies between the different parameters. While it is below 10% for the parameters of the S family, it ranges between 20% and 25% for the f_{M0}/Λ^4 and f_{M7}/Λ^4 parameters, and between 30% to 40% for the f_{M1}/Λ^4 as well as all considered T parameters.

These results constitute the first exclusion limits of EFT parameters of the considered model studying the $W^{\pm}W^{\pm}jj$ final state with data from the ATLAS experiment. Moreover, these bounds are the first overall dimension-eight EFT parameter exclusion bounds derived at $\sqrt{s} = 13\,\text{TeV}$ with data from the ATLAS experiment. Intervals obtained for the family of T parameters are the most constraining in this measurement final state, while for the f_{S1}/Λ^4 the obtained limits are the weakest, confirming the results from the CMS collaboration [14, 155].

The exclusion bounds found here are weaker than in these previous publications from CMS. Compared to Ref. [155], where almost four times the amount of data compared to this thesis is analyses, the exclusion bounds obtained here are two (f_{S02}/Λ^4) to four (f_{M1}/Λ^4) times weaker. A possible explanation for the inferior sensitivity to the f_{S1}/Λ^4 operator may be the stringent tagging jet transverse momentum requirements in the signal region, as discussed in Sec. 9.2.5.

It has to be noted, however, that the FULL prediction was used in Ref. [14, 155] which is seen to be insufficient to describe the effect of the EFT signal contributions especially in the sensitive region of large invariant dilepton mass, m_{ll}. Moreover, as stated previously, this analysis does not optimise particularly for the EFT reinterpretation.

In this light, it is again called attention to the focus of this work which lies in establishing the utilisation of the new signal modelling description using the amplitude decomposition approach, as well as studying the influence of the clipping unitarisation procedure and the effects of dimension-six EFT operators on the $W^{\pm}Z$-EW4 background process. The first and the last aspects have never been employed in an analysis on the parameters of the considered model before.

9.6 Exclusion Limits Employing the Clipping Unitarisation Approach

9.6.1 The Clipping Unitarisation Approach and Unitarity Bounds

As discussed in Sec. 2.3, EFTs are generally incomplete theories and unitarity violation in most cases occurs already at lower values than Λ. In order to prevent the predictions of the EFT to violate unitarity, thus become unphysical, unitarisation procedures are applied to these predictions. As summarised in Sec. 9.1, previous results have been published with varying unitarisation prescriptions. Motivated in Sec. 2.3.3, the “clipping” approach is employed

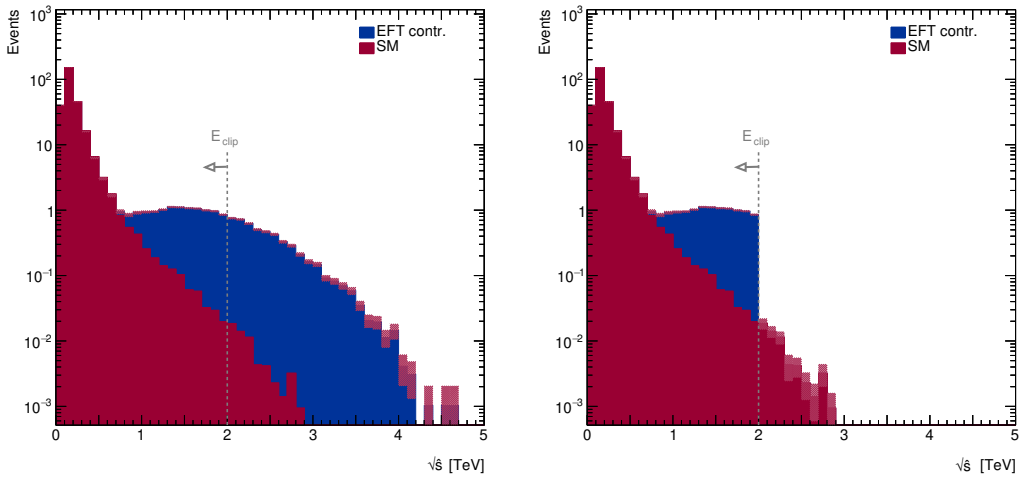


Figure 9.29: Schematic for the illustration of the clipping unitarisation procedure. The prediction from the EFT (blue) is solely considered up to a certain clipping energy E_{clip}. Beyond this energy, any contribution from this theory is set to zero. Predictions from the SM background processes (red) as well as the data remain unchanged. The clipping energy is usually defined as closely as possible to the centre-of-mass energy of the considered scattering process $\sqrt{\hat{s}}$.

for this purpose in this thesis which follows the recommendations of the anomalous coupling task force initiated by the LHC EW working group [78]. In contrast to the K-matrix and form factor unitarisation methods, this approach has the advantage that it is easily reconstructable from kinematic quantities of the scattering processes. Moreover, it depends on one single additional parameter, the so-called clipping energy E_{clip}.

In the clipping unitarisation approach, the prediction from the EFT is considered solely up to a certain energy, the clipping energy E_{clip}. Beyond this energy, any contribution from the EFT is set to zero, i. e. it is clipped. The prediction of all SM backgrounds as well as the data remain unchanged. The procedure is schematically illustrated in Fig. 9.29.

The clipping energy is usually defined as the centre-of-mass energy of the considered scattering process $\sqrt{\hat{s}}$. In the case of the $W^{\pm}W^{\pm}$ scattering analysed in this thesis, this is invariant mass of the two $W^{\pm}$ bosons, m_{WW}, defined at matrix element level, i. e. before the application of the parton shower algorithms. The relevant information for the computation of this variable can be obtained from the matrix element particles in the event record of the MG5_aMC output. The technical implementation is described in App. F.2. Fig. 9.30 shows the distribution of the m_{WW} variable separately for the `LIN` and `QUAD` contribution of the EFT prediction for all considered parameters at the nominal parameter values. For the full EFT predictions it is displayed for different parameters earlier in the course of the study and validation of the signal modelling and the decomposition approach, e. g. in Fig. 9.7 or in Sec 9.2.6.

From Fig. 9.30, however, the ranges in m_{WW} in which the `LIN` and `QUAD` contributions are located can be seen nicely. The `LIN` contribution is large only at values up to 2 TeV, while the majority of the `QUAD` contribution populates the region above 2 TeV for all parameters. The implications on the clipped EFT predictions are evident. If the `LIN` contribution is negative for a certain value of the parameter and the clipping energy is in the region of 2 TeV or below, the prediction of the EFT contribution becomes negative. The consequence is a reduced predicted event yield compared to the SM background.

This behavior can be seen in Fig. 9.31 which illustrated the impact of the clipping on the fiducial cross-section of the `SUM` EFT contribution, i. e. including the SM prediction. The figure shows the fiducial cross-section at the nominal parameter values as a function of the clipping energy E_{clip}. The last bin indicated the prediction without clipping. In

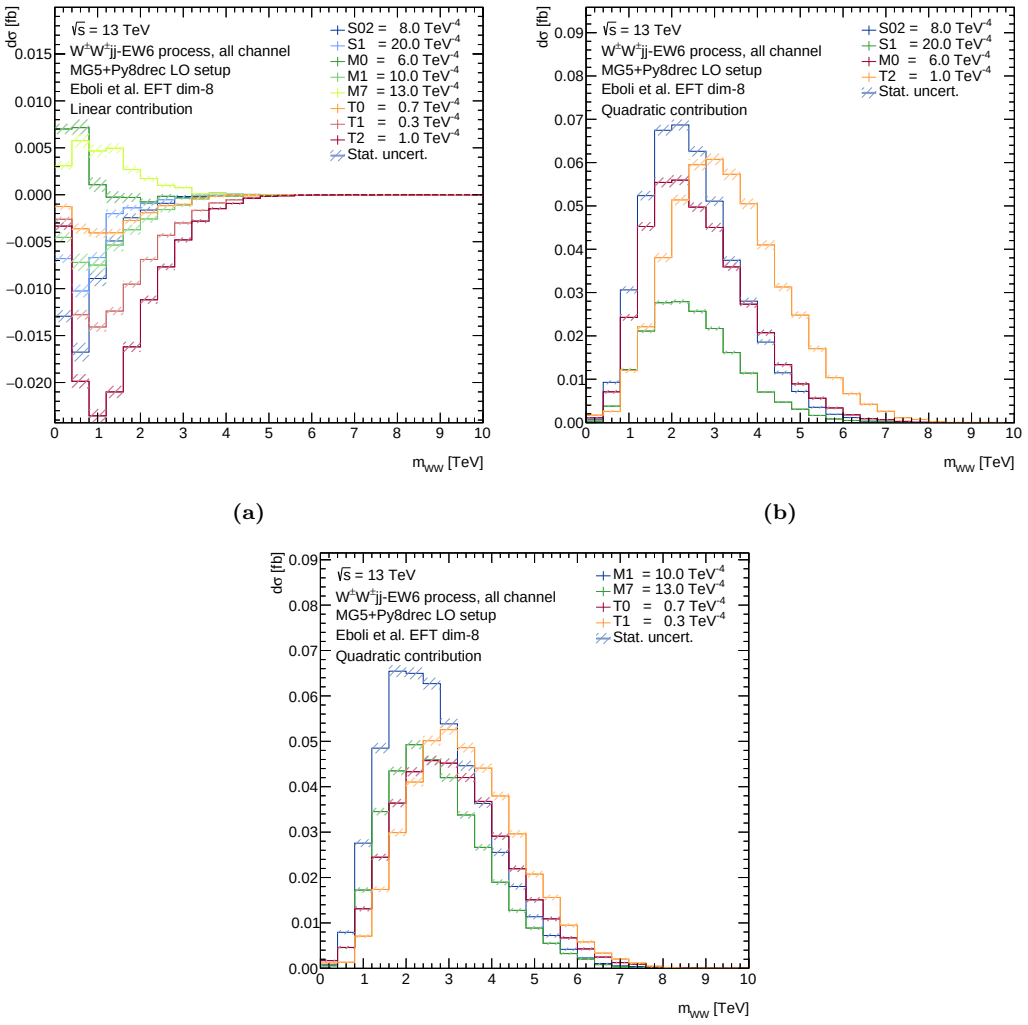


Figure 9.30: Distribution of the invariant mass of the $W^{\pm}W^{\pm}$ system, defined at matrix element level, separately for the `LIN` (a) and `QUAD` (b,c) EFT contributions for all relevant parameters set to their nominal values (cf. Tab. 9.3). The distributions are shown in the loose region (cf. Tab. 6.8) at particle level. Uncertainties are statistical uncertainties from the MC generation only.

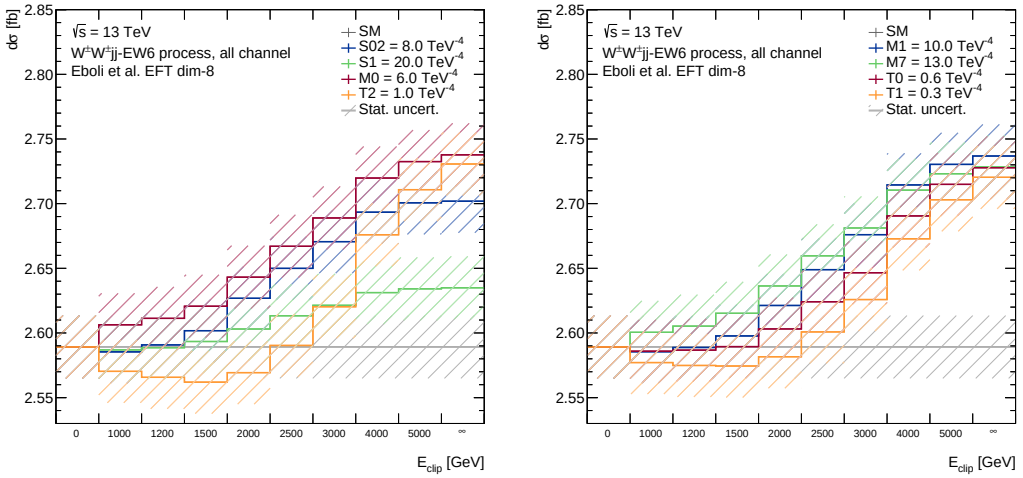


Figure 9.31: Fiducial cross-section of the `SUM` contribution as a function of the clipping energy E_{clip} for all relevant parameters set to their nominal values (cf. Tab. 9.3). The last bin shows the fiducial cross-section for the unclipped EFT signal contribution, while in the first bin, at at clipping energy of 0 TeV, solely the SM prediction remains. Uncertainties are statistical uncertainties from the MC generation only.

the first bin any EFT contribution is clipped away and the SM prediction remains. As expected from Fig. 9.30 the fiducial cross-section decreases from the unclipped prediction until a value around $(1-2)$ TeV, below which the `QUAD` term is no longer dominant. If the interference contribution is positive (for the f_{M0}/Λ^4 and f_{M7}/Λ^4 parameters), the decrease continues until solely the SM prediction remains. In all other cases, the fiducial cross-section prediction of the SM+EFT contribution becomes smaller than the pure SM prediction at very low clipping energies until it converges to the SM prediction. This behavior is especially pronounced for the f_{T1}/Λ^4 and f_{T2}/Λ^4 parameters, where the `SUM` prediction is below the SM $W^{\pm}W^{\pm}jj$-EW6 prediction already for a clipping energy of 2 TeV. However, the decrease is at largest at approx. 1% for the f_{T2}/Λ^4 parameter.

The validation of the clipping procedure is tested in distributions of m_{WW} and shown in Fig. G.1 in the appendix.

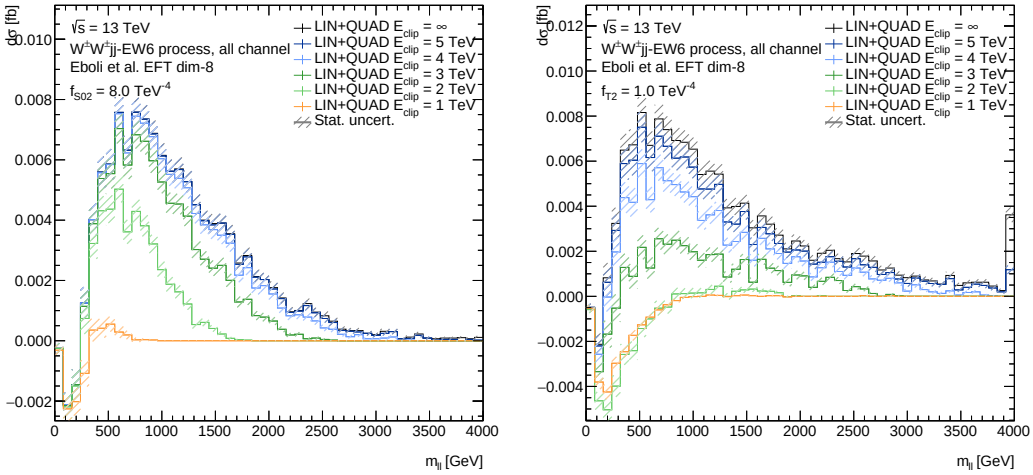
9.6.2 Impact on the m_{ll} Distribution

The impact of the clipping on the invariant mass of the two leading leptons, m_{ll}, is shown in Figures 9.32 and 9.33 in the fiducial region at particle and in the signal region at reconstruction level, respectively, exemplarily for the f_{S02}/Λ^4 and f_{T2}/Λ^4 parameters.

The particle level distributions in Fig. 9.32 show the EFT contribution without the SM $W^{\pm}W^{\pm}jj$-EW6 contribution to illustrate the change in the dominance of the `LIN` and `QUAD` contributions for large versus small values of the clipping energy.

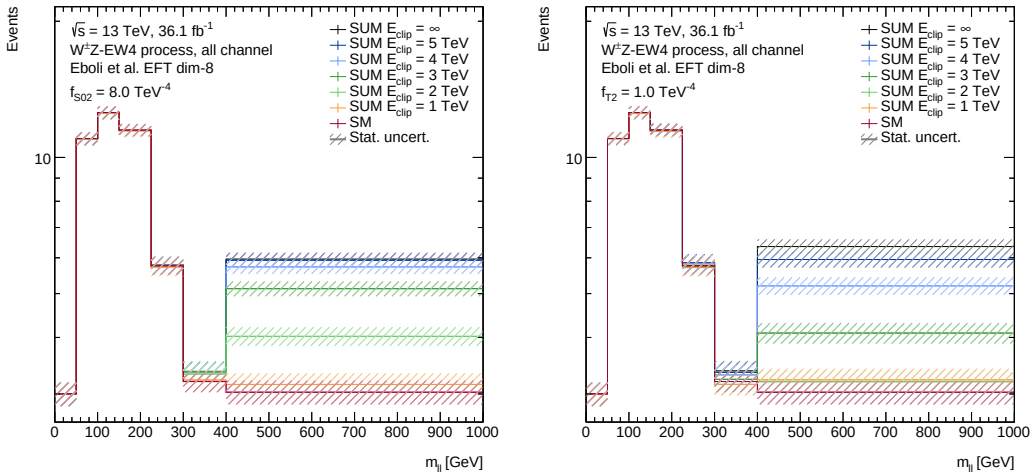
The distributions at reconstruction level in Fig. 9.33 show the impact of the clipping in the binning utilised for the statistical analysis. As the signal contribution is large only in the last bin, also the clipping mostly affects this bin of the m_{ll} distribution. The impact of the clipping at different energies is hence similar to the behavior of the fiducial cross-section. Clipping at 1 TeV removes almost all contributions from the EFT. This can be seen from Fig. 9.30. The `QUAD` contribution is seen to be small below 1 TeV and the `LIN` term peaks around or just below 1 TeV with longer tails towards larger m_{WW}.

For the EFT parameter f_{T2}/Λ^4 the predictions of the event yields for the very small clipping energy of 1 TeV rises again above the predictions when clipping at 2 TeV. This is a direct consequence of the behavior of the fiducial cross-section seen in Fig. 9.31 for this, as well as the f_{T1}/Λ^4 parameter. Distributions of the m_{ll} variable for all other considered parameters in the signal region at reconstruction level are displayed in Fig. G.2 in the appendix.



(a) **(b)**

Figure 9.32: Distributions of the invariant mass of the leading lepton pair, m_{ll}, for the EFT prediction without the SM contribution at various clipping energies E_{clip}. The distributions are shown for the f_{S02}/Λ^4 (a) and f_{T2}/Λ^4 (b) parameters set to their nominal values (cf. Tab. 9.3) in the fiducial region. Uncertainties are statistical uncertainties from the MC generation only. The last bin includes the overflow.



(a) **(b)**

Figure 9.33: Distributions of the invariant mass of the leading lepton pair, m_{ll}, for the `SUM` prediction at various clipping energies E_{clip}. The distributions are shown for the f_{S02}/Λ^4 (a) and f_{T2}/Λ^4 (b) parameters set to their nominal values (cf. Tab. 9.3) in the combined $\ell^\pm\ell^\pm$ channel in the signal region at reconstruction level. The SM prediction is shown as well (red). Uncertainties are statistical uncertainties from the MC generation only. The last bin includes the overflow.

Following the investigation of the clipping impact on several observables, the objective of this study is to derive exclusion bounds on the EFT parameters f_i/Λ^4 as a function of the clipping energy E_{clip}. From Fig. 9.33 it is concluded that clipping energy above 5 TeV and below 1 TeV do not add much information. Clipping energies are hence chosen between these two values. It is expected that the sensitivity reduces drastically with the clipping energy. In this case, the EFT predictions modelled with the amplitude decomposition approach must be scaled quite substantially from the nominal to larger parameter values. It is noted here again, that the scaling becomes slightly more inaccurate for cases when the target point is much larger than the nominal point (cf. Sec. 9.2.8).

9.6.3 The Reach of the Experimental Data

One additional point is added to the set of tested clipping energies which is the value of the equivalent of where the last event in data is observed. This is motivated by the theory community as a natural cutoff indicating the maximal energy reach of the experimental setup. However, the true invariant mass of the $W^{\pm}W^{\pm}$ is not accessible from data. Nor is the reconstructed version of this observable due to the two neutrinos in the fully leptonic final state.

The approach taken to gain information on this variable is to map the reconstructed mass of the visible decay products of the $W^{\pm}W^{\pm}$ system, i. e. the invariant mass of the two leptons in the event, m_{ll}, to the true m_{WW} in simulation. With this mapping information on the underlying m_{WW} in data can be acquired.

The template for the mapping is chosen to be the prediction of the $W^{\pm}W^{\pm}jj$-EW6 process in simulation which constitutes the largest contribution in the signal region. In Fig. 9.34 (a) it is verified that the shape of the m_{ll} distribution in data can be described by the shape of the m_{ll} distribution of the $W^{\pm}W^{\pm}jj$-EW6 process.

The two-dimensional map in m_{ll} at reconstruction level and m_{WW} at matrix element level derived from the simulation of the $W^{\pm}W^{\pm}jj$-EW6 prediction is shown in Fig. 9.34 (b). From this distribution the mean of the m_{WW} distribution at matrix element level is computed in each bin of the m_{ll} distribution at reconstruction level. The resulting mapping is shown in Fig. 9.34 (c) and fitted with a linear function. The result is:

$$m_{WW} = 164.874\,\text{GeV} + 1.271 \cdot m_{ll}. \tag{9.21}$$

The event in experimental data with the largest invariant mass of the two leptons has an m_{ll} value of 814 GeV (cf. Fig. 9.34 (a)). The resulting mapped m_{WW} amounts to 1199 GeV. Accordingly, one value in the set of the clipping energies is added at 1.2 TeV. As can be seen from above, this value is located at the very low end of the sensitivity expected for this study.

9.6.4 Impact on the Exclusion Bounds

In the following, exclusion bounds for each considered clipping energy E_{clip} shall be derived. The set of clipping energies includes:

$$E_{\text{clip}} \in [1.0\,\text{TeV}, 1.2\,\text{TeV}, 1.5\,\text{TeV}, 2.0\,\text{TeV}, 2.5\,\text{TeV}, 3.0\,\text{TeV}, 4.0\,\text{TeV}, 5.0\,\text{TeV}]\,. \tag{9.22}$$

The clipping procedure needs to be incorporated in the mathematical prescription of the statistical model. It only affects the signal definition which is adapted from Eq. (9.16) to:

$$\nu_S\left(\frac{f_i}{\Lambda^4}, E_{\text{clip}}\right) = \int_0^{E_{\text{clip}}} \frac{d\nu_S\left(\frac{f_i}{\Lambda^4}, m_{WW}\right)}{dm_{WW}} dm_{WW}, \tag{9.23}$$

$$= \int_0^{E_{\text{clip}}} \frac{d\left(\nu_{\texttt{LIN}}\left(\frac{f_i}{\Lambda^4}, m_{WW}\right) + \nu_{\texttt{QUAD}}\left(\frac{f_i}{\Lambda^4}, m_{WW}\right)\right)}{dm_{WW}} dm_{WW}, \tag{9.24}$$

to only include the EFT signal contribution up to a certain E_{clip}, where the latter is taken to be the invariant mass of the $W^{\pm}W^{\pm}$ system at matrix element level as explained above.

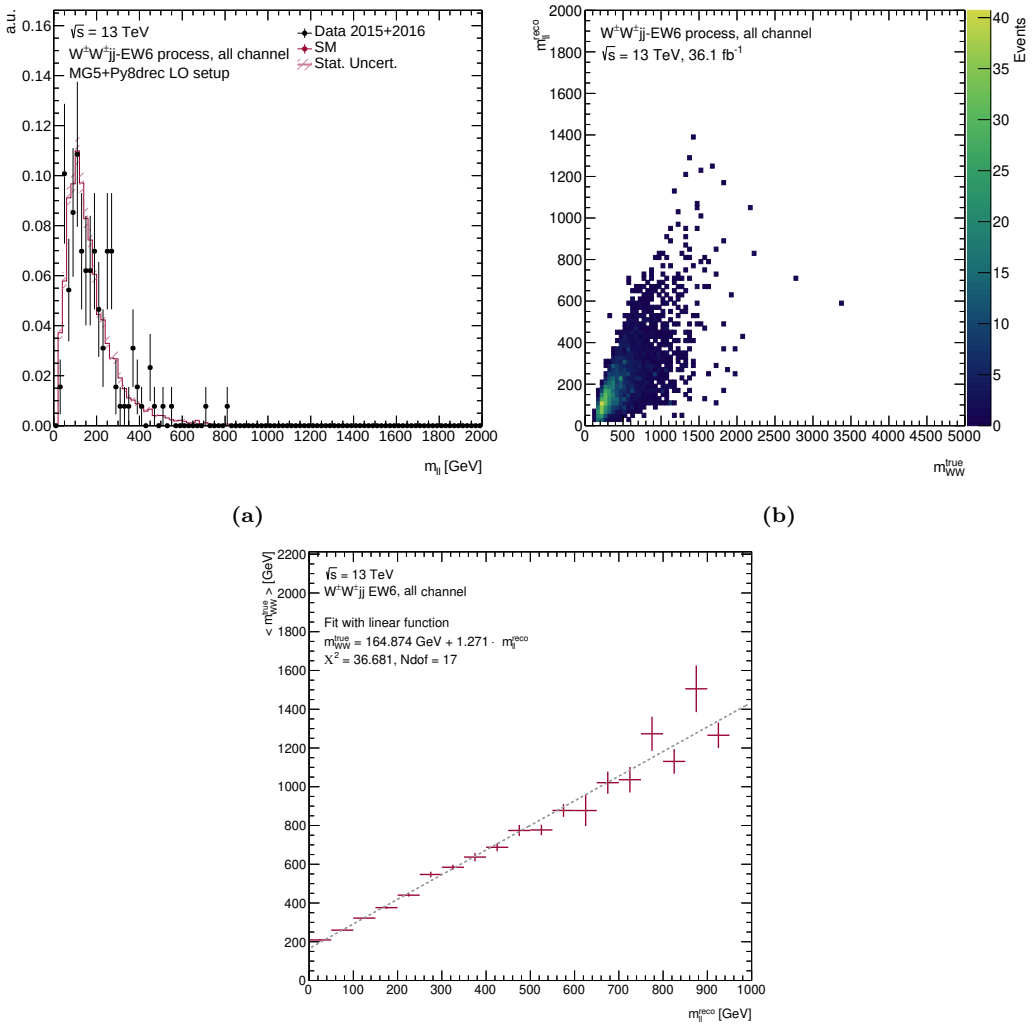


Figure 9.34: (a) Distribution of the invariant mass of the two leading leptons, m_{ll}, for the SM $W^{\pm}W^{\pm}jj$-EW6 prediction and experimental data taken in the years 2015 and 2016 with the ATLAS detector in the signal region at reconstruction level normalised to unit area. (b) Two-dimensional distribution of the invariant mass of the $W^{\pm}W^{\pm}$ system, m_{WW} at matrix-element level and m_{ll} at reconstruction level for the SM $W^{\pm}W^{\pm}jj$-EW6 process. The distribution is shown for events entering the fiducial region at particle level and the signal region at reconstruction level. (c) Mean value of m_{WW} at ME level as a function of m_{ll} at reconstruction level. A linear fit is performed on the distribution. Uncertainties in all figures are statistical uncertainties only.

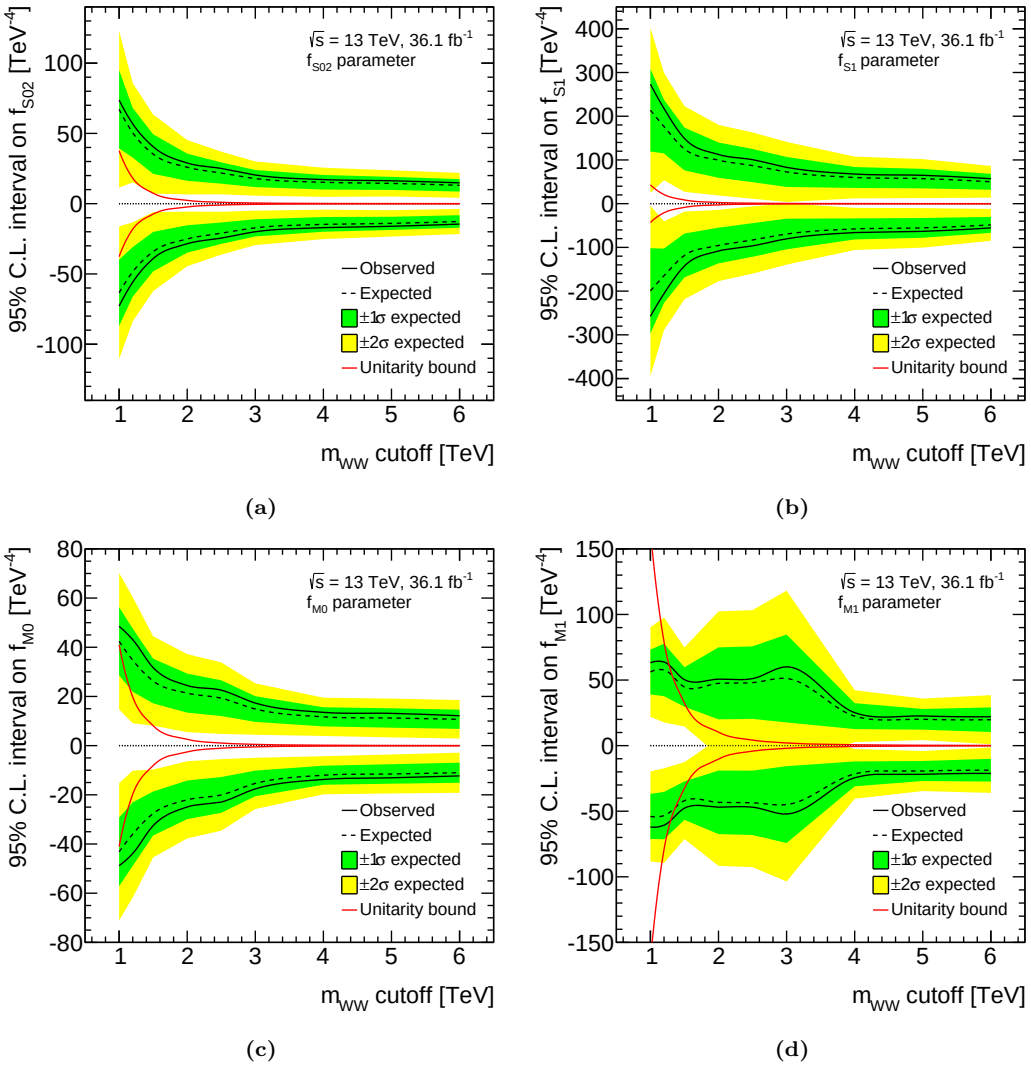


Figure 9.35: Expected (black, dashed) and observed (black, solid) upper and lower exclusion bounds at 95% C.L., and unitarity bounds (red) on the parameters f_{S02}/Λ^4 (a), f_{S1}/Λ^4 (b), f_{M0}/Λ^4 (c), f_{M1}/Λ^4 (d) as a function of the clipping energy $E_{\text{clip}} = m_{WW}$. The 1σ and 2σ uncertainty bands on the expected exclusion bounds are shown in green and yellow, respectively. Unitarity bounds are calculated from Ref. [4].

Statistical and experimental systematic uncertainties on the signal predictions are re-derived for all clipping energies. Relative modelling uncertainties are taken from the unclipped predictions.

The next step is to derive exclusion limits for the various clipping energies where each of the points in E_{clip} are fitted independently for each of the considered parameters. The results are illustrated in Figures 9.35 and 9.36.

The expected and observed upper and lower exclusion bounds as a function of the clipping energy, as well as the unitarity bounds calculated from Ref. [4] for all relevant parameters are shown. For the expected confidence intervals, derived with pseudo-experiments, the areas of the variation by 1σ and 2σ are shown. It can be seen, that the measured confidence intervals vary substantially within the set of pseudo-experiments conducted. An explanation could be the sensitivity to the EFT signals being limited to one bin at large m_{ll} where uncertainties on the background processes are large and statistics poor.

As expected, the obtained exclusion bounds weaken with smaller values of the clipping energy. Sensitivity starts to decrease substantially around a clipping energy of 2 TeV for the parameters of the S family and f_{M0}/Λ^4. In the case of the f_{M7}/Λ^4 parameter, both

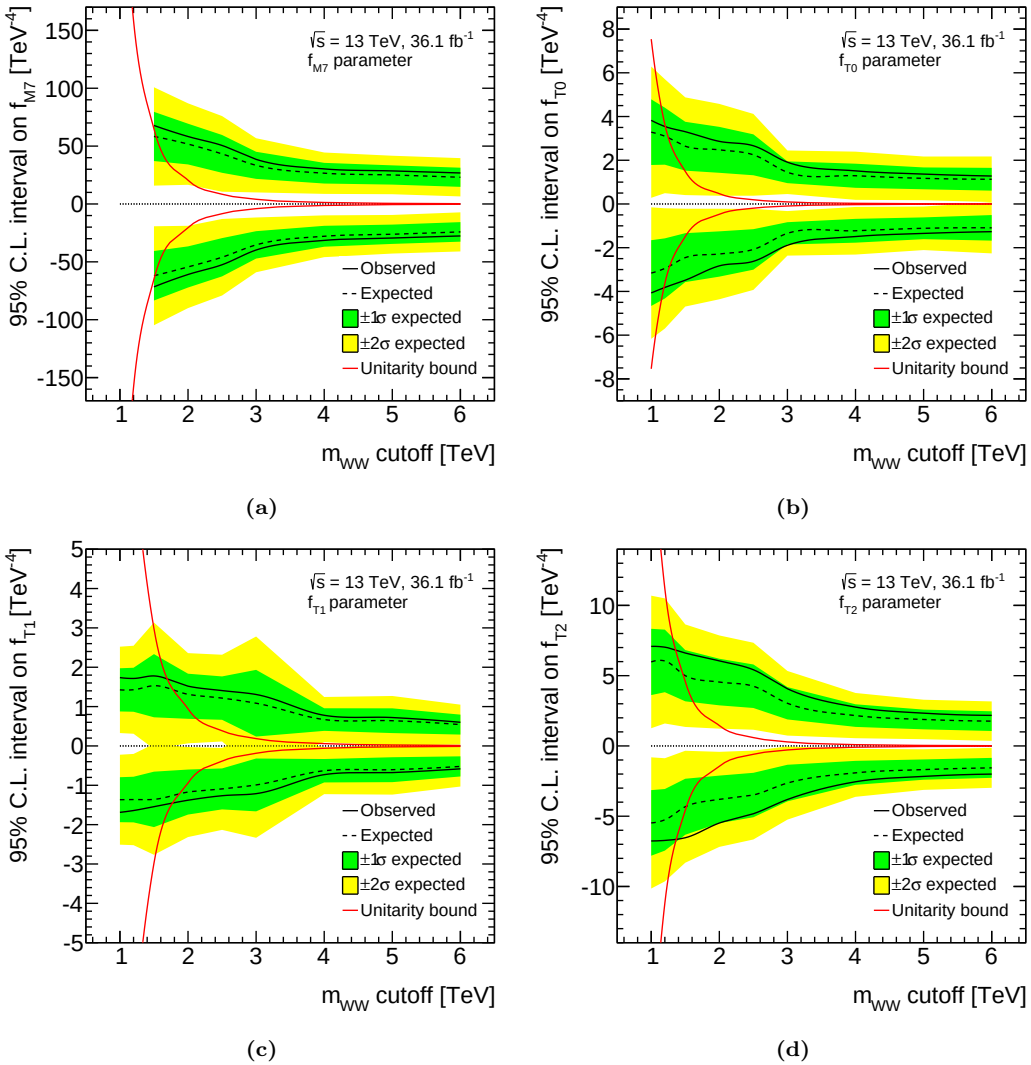


Figure 9.36: Expected (black, dashed) and observed (black, solid) upper and lower exclusion bounds at 95% C.L., and unitarity bounds (red) on the parameters f_{M7}/Λ^4 (a), f_{T0}/Λ^4 (b), f_{T1}/Λ^4 (c), f_{T2}/Λ^4 (d) as a function of the clipping energy $E_{\text{clip}} = m_{WW}$. The 1σ and 2σ uncertainty bands on the expected exclusion bounds are shown in green and yellow, respectively. Unitarity bounds are calculated from Ref. [4].

Table 9.14: Expected and observed one-dimensional exclusion intervals at the 95% C.L. for all EFT parameters of the considered model [2, 3] relevant in the $W^{\pm}W^{\pm}jj$-EW6 process applying an energy cutoff $E_{\text{clip}} = 1.5\,\text{TeV}$. The nominal set of systematic uncertainties (cf. Sec. 9.4.2) is employed. The expected limits are obtained with pseudo-experiments.

Parameter	95% C.L. interval [TeV^{-4}]	
$\frac{f_i}{\Lambda^4}$	Expected	Observed
$S02$	$[-34, 35]$	$[-39, 41]$
$S1$	$[-118, 125]$	$[-143, 149]$
$M0$	$[-28, 26]$	$[-33, 32]$
$M1$	$[-42, 45]$	$[-48, 50]$
$M7$	$[-62, 58]$	$[-72, 68]$
$T0$	$[-2.5, 2.6]$	$[-3.5, 3.3]$
$T1$	$[-1.4, 1.5]$	$[-1.5, 1.8]$
$T2$	$[-4.3, 5.0]$	$[-6.5, 6.6]$

expected and observed fits do not converge for the very low clipping energies of 1.0 TeV and 1.2 TeV. For the T parameter family exclusion bounds are more flat with the clipping energy compared to the other families.

Comparing the obtained bounds with the unitarity bounds reveals that most of the exclusion contours obtained in this study lie outside the theoretically allowed regime for all parameters. Solely for the f_{M1}/Λ^4 parameter and the parameters of the T family, exclusion bounds become reasonable at clipping energies below 1.5 TeV or even lower. The 95% C.L. exclusion intervals applying a clipping at 1.5 TeV are summarised in Tab. 9.14.

9.7 Impact of Dimension-6 EFT Effects from the $W^{\pm}Z$ Process

The exclusion limits presented above do not consider effects of EFT operators with lower mass dimension than eight. By doing so, the reliability of the mathematical expansion lacks as well as the model independence advertised by EFT approaches, as stated in Sec. 2.3.3. Moreover, recent theoretical studies show decent impact of operators of mass dimension six in VBS processes and phase space regions [260, 261]. None of the results of previous measurements of dimension-eight EFT parameters, presented in Sec. 9.1, include effects from dimension-six operators. A first attempt to include information on dimension-six effects in the extraction of exclusion bounds on dimension-eight EFT parameters is presented in this thesis.

The chosen scenario is based on a model in the LEP parameterisation [282] and considers the three independent parameters: $\Delta g_1^Z = g_1^Z - 1$, $\Delta\kappa_Z = \kappa_Z - 1$, and λ_Z. After the SM $W^{\pm}W^{\pm}jj$-EW6 contribution, the $W^{\pm}Z$ process constitutes the largest background contribution in the signal region. For the first of the processes, no study on dimension-six EFT effects has been presented to date. The technical implication is, that no samples including these effects are available and have never been produced for the $W^{\pm}W^{\pm}jj$ final state. Moreover, the $W^{\pm}W^{\pm}jj$-EW6 is a VBS process, where aTGC effects are reasonably assumed to be smaller than in diboson processes. For these reasons, the effect of dimension-six operators in the signal region of this measurement is estimated for the $W^{\pm}Z$ process only. For this, the three considered parameters are set to the most stringent observed one-dimensional exclusion bounds available by the time of the implementation of the study. These are presented in the analysis of the $W^{\pm}V \to \ell\nu J$ diboson final state at $\sqrt{s} = 13\,\text{TeV}$ by the CMS collaboration [283] without employing any unitarisation procedure. The effects in the signal region are then applied as systematic uncertainty on the $W^{\pm}Z$ process in the fitting procedure.

Dedicated MC samples at reconstruction level, which incorporate additional weights generated with a matrix element reweighting method, are employed to assess these effects. The specifics of these samples are summarised in App. C.3 together with the MC weight prescrip-

Table 9.15: Best limit values of the aTGC parameters Δg_1^Z, $\Delta\kappa_Z$, and λ_Z by the time of the implementation of this study from Ref. [283] and effect on the MC predicted event yields of the $W^{\pm}Z$ process compared to the SM prediction in the loose and signal region (cf. Tab. 7.4).

Parameter	Current best one-dim. limits [283]	One-dimensional Effect [%]	
	$[10^{-3}]$	Loose region	Signal region
Δg_1^Z	-6.1	$+0.56$	$+0.07$
	$+7.4$	-0.51	-0.05
$\Delta\kappa_Z$	-7.9	-0.06	-0.06
	$+8.2$	$+0.07$	$+0.07$
λ_Z	-6.5	$+0.00$	-0.86
	$+6.6$	$+0.30$	$+0.89$

tion to be used to transfer the nominal generated point to any point in the three dimensional space of the aTGC parameters Δg_1^Z, $\Delta\kappa_Z$, and λ_Z. The samples are NLO QCD accurate, i. e. solely the first jet is described by matrix element kinematics, which is not ideal to be used in a signal region with a minimum requirement of two jets. However, since aTGC are exclusively probed in inclusive diboson final states, or with a requirement of a maximal number of jets, a lack of alternatives restricts the choice of the simulation details. For this first study, this shall suffice. However, future analyses should elaborate the samples specifics in more detail to ensure at least LO accuracy for the second jet. The nominal point for the event generation is the SM prediction with all aTGC parameters set to zero.

The assumed values for the three dimension-six EFT parameters are listed in Tab. 9.15 together with the relative effect on the MC predicted event yields of the $W^{\pm}Z$ compared to the SM prediction process in the loose and signal regions. The effects remain below 1% in both regions. The largest effect in the signal region is generated by the λ_Z at its best exclusion limit.

The deviation from the SM prediction can be located at large invariant dilepton mass, m_{ll}, shown in Fig. 9.37 for all three parameters in the loose region. However, the event statistics in this region is already very limited and the effect remains within the statistical accuracy of the SM prediction. In the signal region, shown in Fig. 9.38, the sub-percent effect is barely visible for all three parameters.

A second set of variations is considered, where the values for the best one-dimensional exclusion limits of all three aTGC parameters are simultaneously set such that a maximal negative/positive effect is generated. This three-dimensional combination from one-dimensional limits of each parameter is expected to cause larger effects than obtained from the independent consideration of aTGC operators. However, it is not expected that the generated effect coincides with the true three-dimensional effect since interferences between the operators at amplitude level are neglected. These interference effects can be of any sign. Fig. 6 in Ref. [283] shows the two-dimensional exclusion limits of each pair of the three considered parameters. While the interference between the λ_Z parameter and both, Δg_1^Z and $\Delta\kappa_Z$, are small, it is sizable for the pair $\Delta g_1^Z - \Delta\kappa_Z$. These are, however, neglected for this set of variations in this first study.

In order to reach a maximal positive effect, the parameters have to be set to the positive or negative exclusion bound, depending on the sign of its interference with the SM amplitude. From Tab. 9.15, it can be inferred that this is the case when the exclusion bounds are chosen such that: $\Delta g_1^Z < 0$, and $\Delta\kappa_Z, \lambda_Z > 0$, and inverse for the maximal negative effect. Tab. 9.16 summarises the relative effects on the $W^{\pm}Z$ event yield compared to the SM prediction in the loose and signal regions from the simultaneous consideration of all three operators. In both regions, the resulting impact is considerably larger compared to considering only one operator at a time.

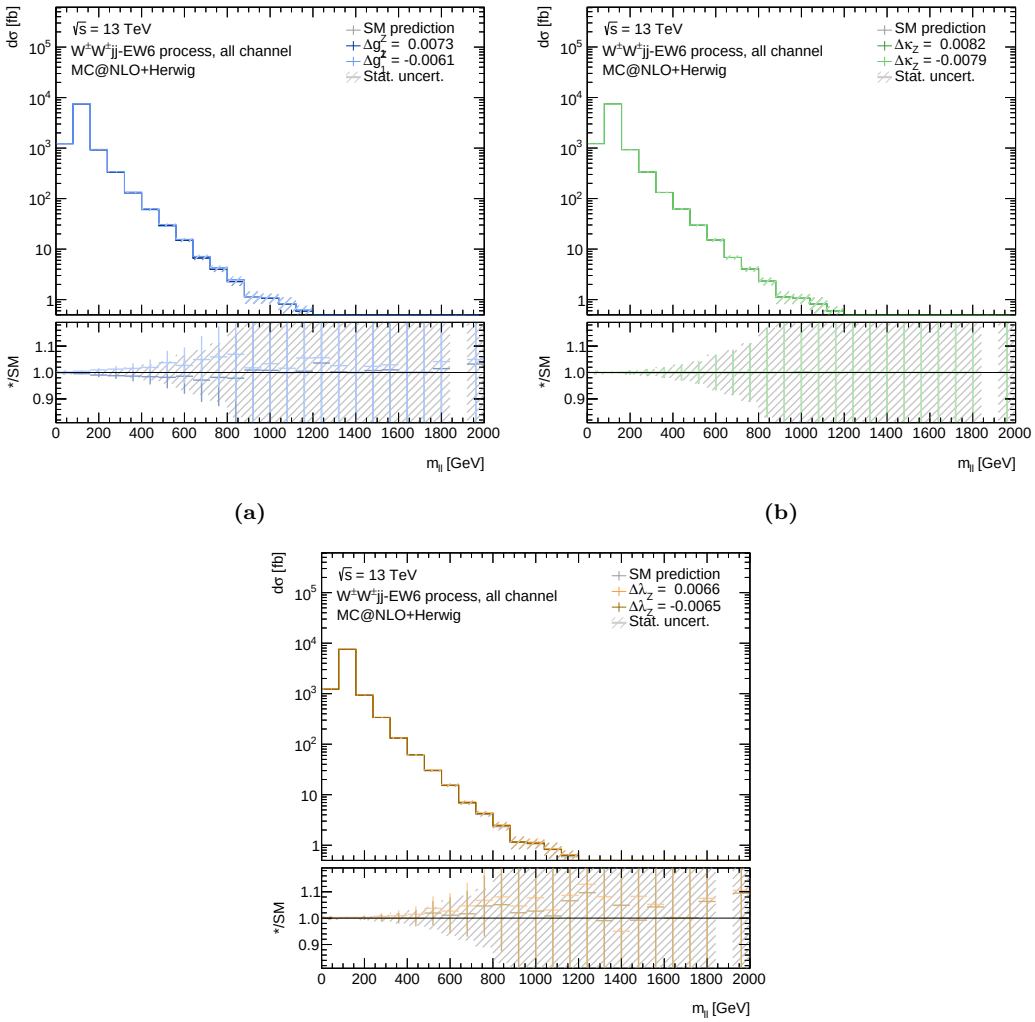


Figure 9.37: Invariant mass of the dilepton system, m_{ll}, in the loose region (cf. Tab. 7.4) at reconstruction level. The effects of the aTGC parameters Δg_1^Z (a), $\Delta\kappa_Z$ (b), and λ_Z (c) on the event yield of the $W^\pm Z$ process when set to the values of the current best exclusion limits published in Ref. [283] compared to the SM prediction are shown. The lower panel shows the ratio with respect to the SM prediction. Uncertainties are statistical uncertainties from the MC generation only.

Table 9.16: Effect of the aTGC parameters Δg_1^Z, $\Delta\kappa_Z$, and λ_Z on the MC predicted event yields of the $W^\pm Z$ process compared to the SM prediction when all three parameters are set to their best limits values [283] such that a minimal/maximal effect is generated. Numbers are shown in the loose and signal regions (cf. Tab. 7.4). Interference effects between the aTGC amplitudes and the SM cause effects alternating in sign for the different parameters.

Effect: parameter values (Best limits [283]) $[10^{-3}]$		Three-dimensional Effect [%]	
		Loose region	Signal region
Min. effect:	$(\Delta g_1^Z, \Delta\kappa_Z, \lambda_Z) = (+7.4, -7.9, -6.5)$	-11.6	-6.2
Max. effect:	$(\Delta g_1^Z, \Delta\kappa_Z, \lambda_Z) = (-6.1, +8.2, +6.6)$	$+13.8$	$+7.6$

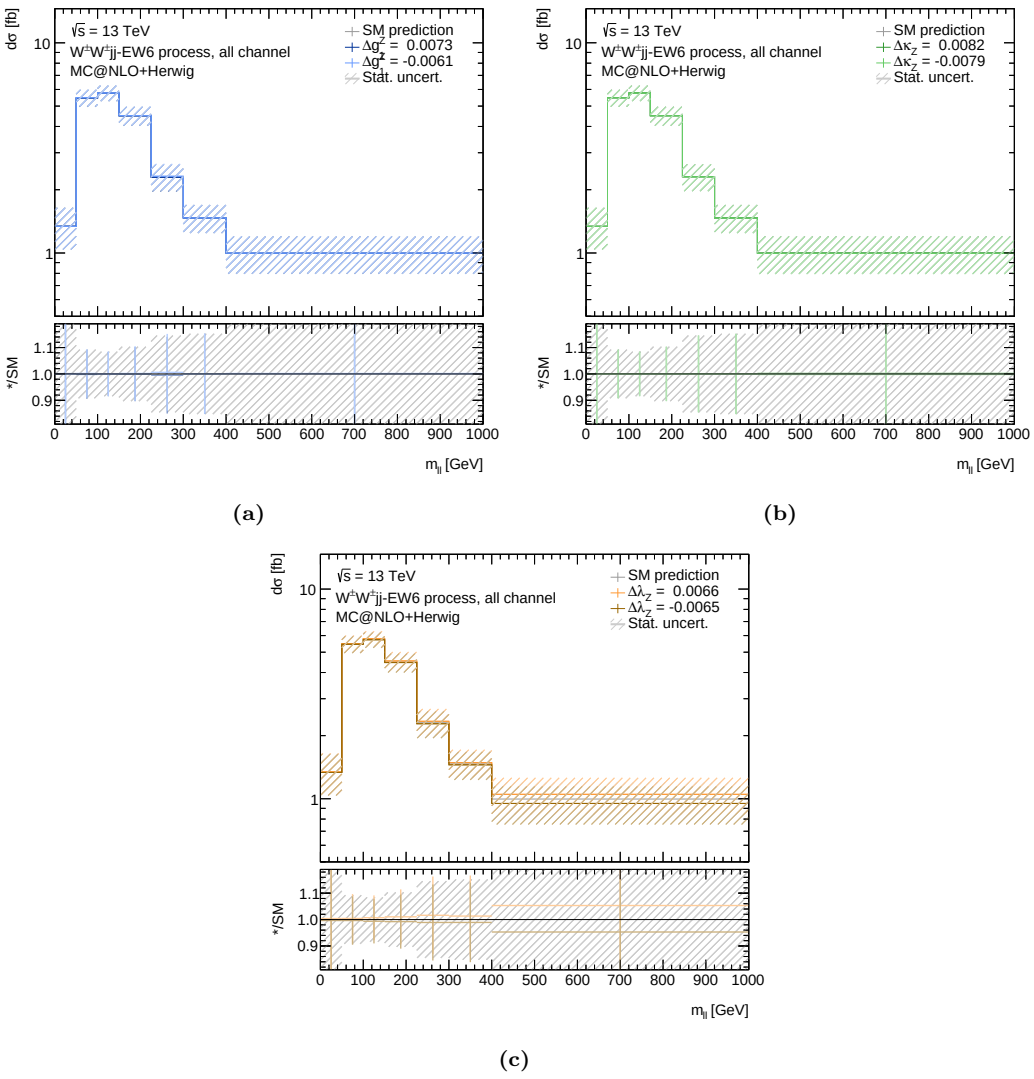


Figure 9.38: Invariant mass of the dilepton system, m_{ll}, in the signal region (cf. Tab. 7.4) at reconstruction level. The effects of the aTGC parameters Δg_1^Z (a), $\Delta\kappa_Z$ (b), and λ_Z (c) on the event yield of the $W^{\pm}Z$ process when set to the values of the current best exclusion limits published in Ref. [283] compared to the SM prediction are shown. The lower panel shows the ratio with respect to the SM prediction. Uncertainties are statistical uncertainties from the MC generation only.

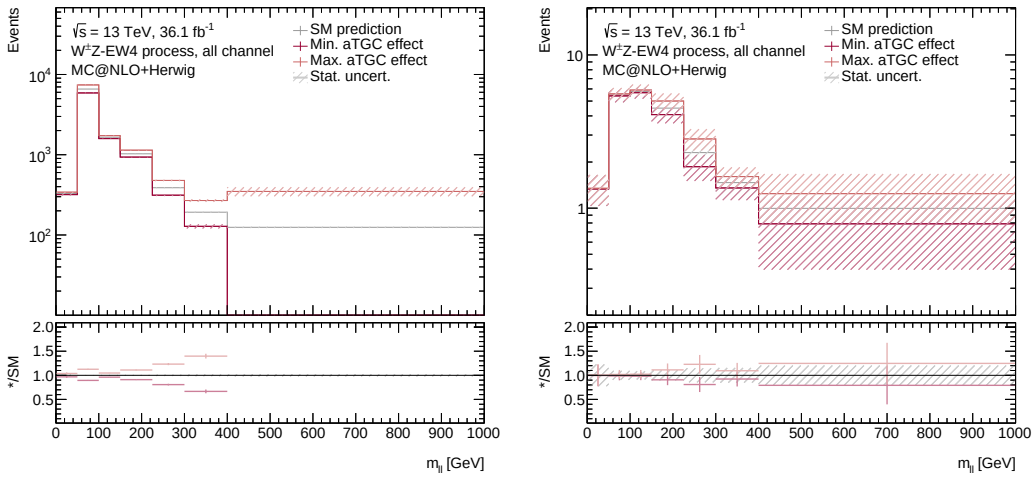


Figure 9.39: Invariant mass of the dilepton system, m_{ll}, in the loose (a) and signal region (b) at reconstruction level (cf. Tab. 7.4). The minimal and maximal effects when simultaneously setting the aTGC parameters Δg_1^Z, $\Delta\kappa_Z$, and λ_Z to the values of the current best exclusion limits published in Ref. [283] on the event yield of the $W^\pm Z$ process compared to the SM prediction are shown. The lower panel shows the ratio with respect to the SM prediction. Uncertainties are statistical uncertainties from the MC generation only.

Fig. 9.39 shows the three-dimensional impact on the $W^\pm Z$ event yield compared to the SM prediction in both regions differentially in m_{ll}. The effect at large invariant masses is clearly visible especially in the loose region. In the signal region the results again have lower statistical accuracy.

With these results, two sets of exclusion limits incorporating dimension-six EFT effects as a systematic uncertainty of the prediction of the event yield differentially in m_{ll} of the $W^\pm Z$ process are determined. For the first set, the individual effects of the three operators are added in quadrature by sign of the impact. This set is referred to as $3 \otimes 1$-dimensional set. Another set of exclusion limits is calculated by considering the effect on the $W^\pm Z$ process from all three operators simultaneously, obtained as described above and referred to as 3-dimensional set. Tab. 9.17 shows the relative impact on the event yield of the $W^\pm Z$ process compared to the SM prediction in each bin of the m_{ll} distribution for both sets. The $3 \otimes 1$-dimensional set generates deviations by at most 5% in the last bin of the distribution. Observing from Tab. G.10 in the appendix, the resulting effects of this set are dominated by the impact of the λ_Z parameter in all bins, consistent with the inclusive observations in the signal region. The 3-dimensional set generates deviations of as large as 25% in the last m_{ll} bin.

The 95% C.L. intervals for all considered dimension-eight parameters including the effect of dimension-six EFT parameters as systematic uncertainties on the event yield of the $W^\pm Z$ process are listed in Tab. 9.18. Results for both sets of considered effects are shown. The differences to the nominal set of exclusion limits (cf. Tab. 9.13) is at most 1% and within the statistical stability of the fitting procedure. In conclusion, with the definition of the impact as in this study, no impact of the inclusion of effects from the dimension-six parameters on the extracted limits on dimension-eight EFT parameters can be observed. One possible explanation might be the low event yield of the $W^\pm Z$ process in the last m_{ll} bin together with already large systematic uncertainties from the theoretical prescription of the simulation, namely the parton shower and renormalisation and factorisation scale uncertainties, amounting to 27% and 22%, respectively.

Table 9.17: Combined effect of the aTGC parameters Δg_1^Z, $\Delta\kappa_Z$, and λ_Z on the MC predicted event yields of the $W^{\pm}Z$ process compared to the SM prediction in bins of the invariant dilepton mass, m_{ll} in the signal region. The "3 $\otimes$ 1-dimensional" set summarises the total one-dimensional impact, when the three parameters are independently set to their best limits values [283], by adding the independent effects of the three parameters in quadrature. The "3-dimensional" set shows results for the minimal/maximal effect when all three parameters are simultaneously set to their best limits values.

Set label	Effect in each m_{ll} bin (lower bin edge in GeV) [%]						
(combination)	0	50	100	150	225	300	400
3 $\otimes$ 1-dim	−0.39	−0.41	−0.65	−0.78	−1.20	−1.09	−4.72
(squared sum)	+0.41	+0.46	+0.72	+1.06	+1.73	+1.33	+5.33
3-dim	−0.42	−1.31	−1.72	−9.33	−19.10	−7.71	−20.76
(simultaneous)	+0.64	+1.76	+2.31	+11.26	+22.80	+9.51	+24.72

Table 9.18: Expected and observed 95% C.L. intervals of all considered dimension-eight EFT parameters when effects of dimension-six EFT operators are included as systematic uncertainties on the event yield of the $W^{\pm}Z$ process. The results for the two considered sets of dimension-six operator effects are shown. The "3 $\otimes$ 1-dimensional" set summarises the total one-dimensional impact, when the three corresponding parameters are independently set to their best limits values [283], by adding the independent effects of the three parameters in quadrature. The "3-dimensional" set shows results for the minimal/maximal effect when all three parameters are simultaneously set to their best limits values. Expected exclusion intervals are obtained with the asymptotic formula approach. No toy experiments are generated for this study. No unitarisation procedure is applied.

Parameter	95% C.L. interval including dim-6 effect on the $W^{\pm}Z$ process [TeV^{-4}]			
	3 $\otimes$ 1-dimensional		3-dimensional	
$\frac{f_i}{\Lambda^4}$	Expected	Observed	Expected	Observed
$S02$	[−12.9 , 13.3]	[−14.6 , 14.7]	[−13.0 , 13.3]	[−14.6 , 14.9]
$S1$	[−50.3 , 52.3]	[−55.4 , 57.2]	[−50.3 , 52.3]	[−55.4 , 56.9]
$M0$	[−10.5 , 10.4]	[−12.4 , 12.3]	[−10.5 , 10.3]	[−12.4 , 12.2]
$M1$	[−16.4 , 17.1]	[−21.1 , 22.0]	[−16.7 , 17.2]	[−21.4 , 22.1]
$M7$	[−23.3 , 22.4]	[−27.6 , 26.7]	[−23.3 , 22.3]	[−27.6 , 26.6]
$T0$	[−0.98, 1.03]	[−1.26, 1.26]	[−0.98, 1.02]	[−1.27, 1.28]
$T1$	[−0.45, 0.48]	[−0.58, 0.61]	[−0.45, 0.48]	[−0.59, 0.61]
$T2$	[−1.49, 1.69]	[−1.99, 2.19]	[−1.48, 1.69]	[−2.00, 2.19]

9.8 Discussion of Results and Potential Directions for Improvement

The results presented in this chapter constitute the first exclusion bounds on dimension-eight EFT parameters of the electroweak sector in the $W^{\pm}W^{\pm}jj$ final state and overall at $\sqrt{s} = 13\,\text{TeV}$ obtained from data of the ATLAS experiment. For these confidence intervals, the new signal modelling approach with the amplitude decomposition is employed. This substantially improves the signal predictions especially in the high energy sensitive regions exploited in current analyses. The conventional simulation technique is not only inefficient in this phase space regime but also found to be insufficient in terms of phase space integration accuracy in the MC event generation.

Furthermore, while in Ref. [155] clipped exclusion limits are presented for solely one clipping energy at the unitarity bound, this thesis presents the first global exclusion bounds scanning multiple values of the clipping energy E_{clip} in the $W^{\pm}W^{\pm}jj$ final state.

In addition, exclusion bounds with the impact of dimension-six EFT effects on the $W^{\pm}Z$-EW4 background process are studied for the first time across all final states and experiments.

Comparing the nominal unclipped exclusion intervals with previous results in Figures 9.40 to 9.43, it is seen that they cannot compete with the current best limits, obtained by analyses of the $W^{\pm}Vjj \to \ell^{\pm}\nu_{\ell}Jjj$ [154] and $W^{\pm}Vjj \to \ell^{\pm}\nu_{\ell}(\ell'^{\pm}\nu'_{\ell}/\ell'^{\pm}\ell'^{\mp})jj$ [155] final states by the CMS collaboration.

However, this thesis adds valuable information to the study of the dimension-eight EFT models in the electroweak sector by investigating fundamental ingredients for future analyses, such as the new, more efficient signal modelling technique, the clipping unitarisation approach, and the possibility to include effects of dimension-six EFT operators. With these elements of the analysis being the major focus in this thesis, it is reminded here, that no optimisation of the measurement phase space or the binning of the m_{ll} observable utilised for the statistical analysis is conducted. These elements of the analysis are inherited from the SM measurement of the $W^{\pm}W^{\pm}jj$-EW6 process presented in Chapter 7 and 8.

With the new technique of the signal modelling, the amplitude decomposition method, the individual terms of the EFT contributions can be studied thoroughly for the first time. Of course, also with the conventional MC simulation technique it is in principle possible to obtain the individual contributions by utilising Equations (9.11) and (9.12). However, since this approach always includes the subtraction of one sample from another, this approach is statistically very limited. Hence, this has never been done.

Reminding of the discussion in Sec 2.3.3, in order for the EFT expansion to be reasonable, the `LIN` contribution must be larger than the `QUAD` contribution. From the validation of the amplitude decomposition approach in Sec. 9.2.6 we have learned that this is not the case for the nominal parameter points (cf. Tab. 9.3). As the obtained unclipped exclusion bounds, summarised in Tab. 9.13, are weaker than the nominal parameter points for all parameters, the interference term is even more inferior than the quadratic term in these cases. This indicates that the EFT model in its strict and straight mathematical interpretation is not as model-independent as claimed in this regime and hence it describes a very constrained physics model in which the interference of the EFT operators with the SM ones is very suppressed.

With the individual linear and quadratic EFT contributions, now available from the decomposition, it is possible to identify the parameter region where the `LIN` term is in the range or larger than the `QUAD` term. This can be done under the assumption that the decomposition approach holds in this regime. These parameter values are summarised in Tab. 9.19 together with the resulting cross-section of the pure EFT $\texttt{LIN} + \texttt{QUAD}$ contribution in the fiducial region defined in this thesis (cf. Tab 6.8).

In addition, the current best 95% C.L. intervals measured in the $W^{\pm}W^{\pm}jj \to \ell^{\pm}\nu_{\ell}\ell'^{\pm}\nu'_{\ell}jj$ final state with the full dataset of the LHC Run 2 data-taking period from Ref. [155] are displayed. Comparing these to the parameter values for which $\texttt{LIN}(x) = \texttt{QUAD}(x)$ holds, shows that the current best limits are still weaker than these values[13]. For the parameters of the S

[13]This conclusion is valid when the signal regions of this analysis and the one in Ref. [155] are fairly equivalent because the composition of the EFT contribution changes with kinematic restrictions as seen in

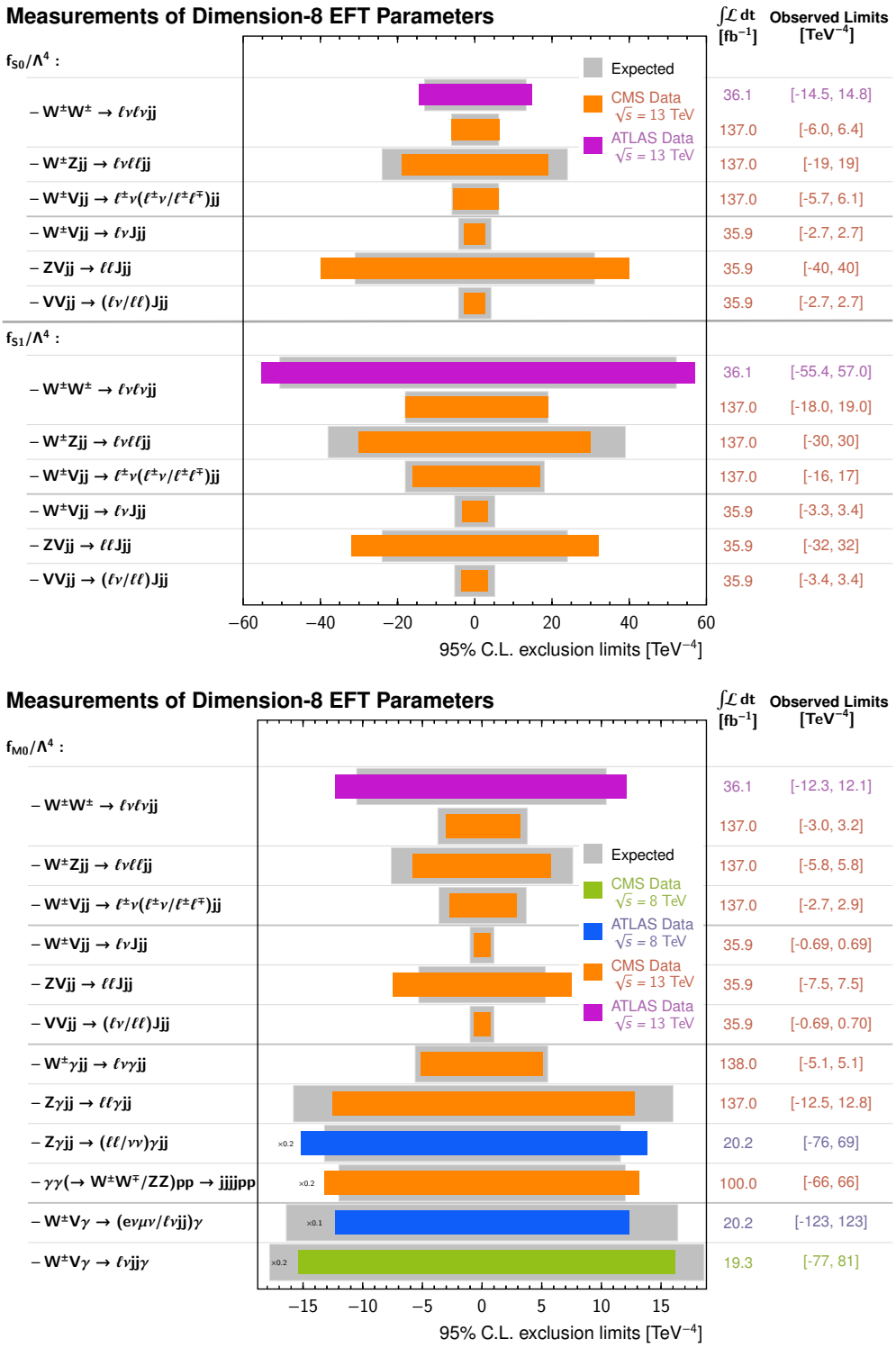


Figure 9.40: Overview of exclusion limits on dimension-eight EFT parameters f_{S0}/Λ^4 and f_{S1}/Λ^4 (top), and f_{M0}/Λ^4 (bottom) including the first result from the ATLAS experiment at centre-of-mass energies of 13 TeV. Measurement results in final states involving leptons, jets and/or photons, where $V = W^{\pm}, Z$, are shown. Solely the most recent publications per experiment for a specific channel and, for reasons of reasonable comparison, results without any unitarisation procedure applied are shown. Exclusion limits are presented in the MG5_aMC formalism [245] and converted if necessary. Electric charges of the leptons include implicitly all combinations allowed by the SM, unless explicitly stated otherwise. Figure layout modified from Ref. [263].

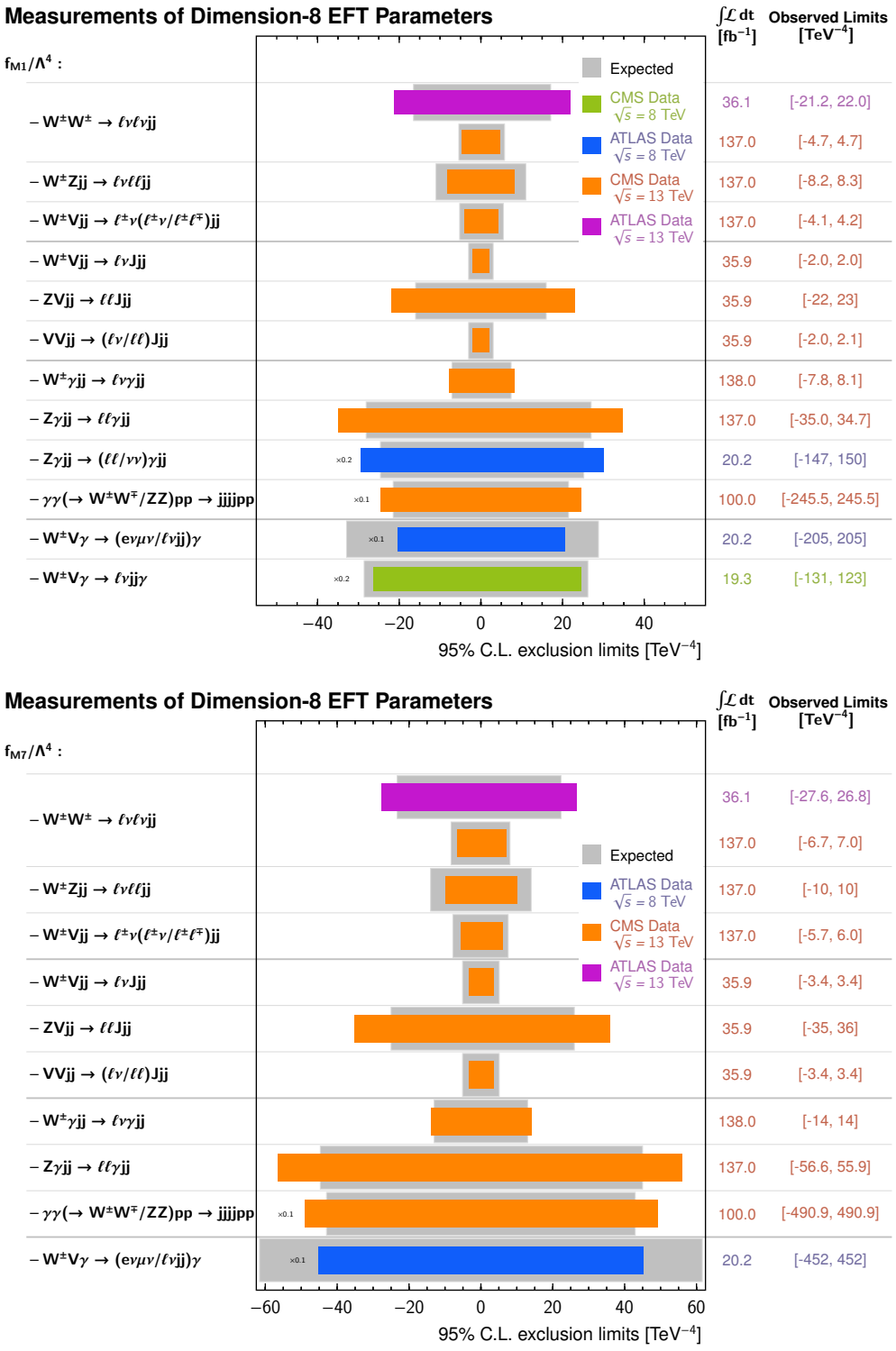


Figure 9.41: Overview of exclusion limits on dimension-eight EFT parameters f_{M1}/Λ^4 (top), and f_{M7}/Λ^4 (bottom) including the first result from the ATLAS experiment at centre-of-mass energies of 13 TeV. Measurement results in final states involving leptons, jets and/or photons, where $V = W^\pm, Z$, are shown. Solely the most recent publications per experiment for a specific channel and, for reasons of reasonable comparison, results without any unitarisation procedure applied are shown. Exclusion limits are presented in the MG5_aMC formalism [245] and converted if necessary. Electric charges of the leptons include implicitly all combinations allowed by the SM, unless explicitly stated otherwise. Figure layout modified from Ref. [263].

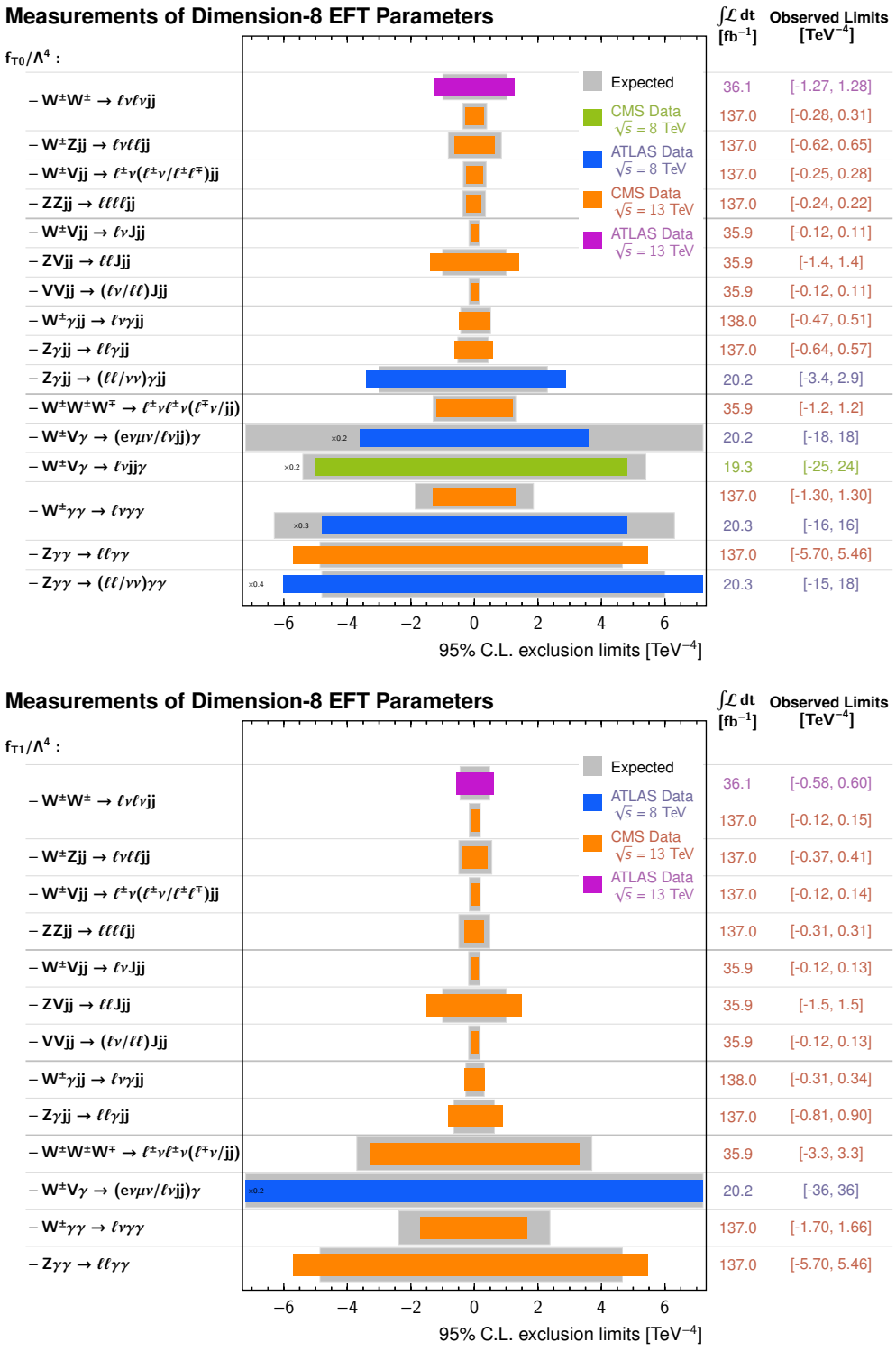


Figure 9.42: Overview of exclusion limits on dimension-eight EFT parameters f_{T0}/Λ^4 (top), and f_{T1}/Λ^4 (bottom) including the first result from the ATLAS experiment at centre-of-mass energies of 13 TeV. Measurement results in final states involving leptons, jets and/or photons, where $V = W^{\pm}, Z$, are shown. Solely the most recent publications per experiment for a specific channel and, for reasons of reasonable comparison, results without any unitarisation procedure applied are shown. Exclusion limits are presented in the MG5_aMC formalism [245] and converted if necessary. Electric charges of the leptons include implicitly all combinations allowed by the SM, unless explicitly stated otherwise. Figure layout modified from Ref. [263].

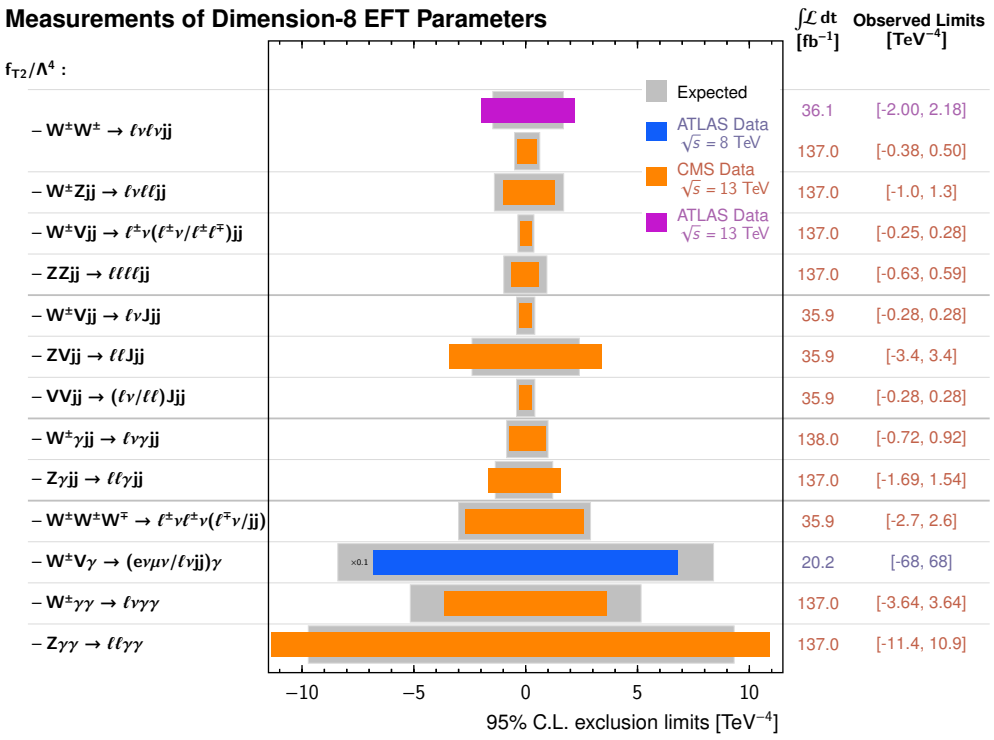


Figure 9.43: Overview of exclusion limits on dimension-eight EFT parameter f_{T2}/Λ^4 including the first result from the ATLAS experiment at centre-of-mass energies of 13 TeV. Measurement results in final states involving leptons, jets and/or photons, where $V = W^\pm, Z$, are shown. Solely the most recent publications per experiment for a specific channel and, for reasons of reasonable comparison, results without any unitarisation procedure applied are shown. Exclusion limits are presented in the MG5_aMC formalism [245] and converted if necessary. Electric charges of the leptons include implicitly all combinations allowed by the SM, unless explicitly stated otherwise. Figure layout modified from Ref. [263].

Table 9.19: Summary of parameter values for which the cross-section in the fiducial phase space (cf. Tab. 6.8) of the linear `LIN` contribution becomes equal in size to the quadratic `QUAD` contribution in the $\ell^\pm\nu_\ell\ell'^\pm\nu'_\ell jj$ final state. The resulting fiducial cross-section for the pure EFT contribution $\texttt{LIN}(x) + \texttt{QUAD}(x)$ for these parameter values are shown as well, together with the current best 95% C.L. intervals measured in the final state $W^\pm W^\pm jj \to \ell^\pm\nu_\ell\ell'^\pm\nu'_\ell jj$ [155].

Param. $\frac{f_i}{\Lambda^4}$	Value x $\texttt{LIN}(x) = \texttt{QUAD}(x)$ (TeV^{-4})	Fiducial cross-section for $\texttt{LIN}(x) + \texttt{QUAD}(x)$ (10^{-3} fb = ab)	Current best 95% C.L. interval measured in final state: $W^\pm W^\pm jj \to \ell^\pm\nu_\ell\ell'^\pm\nu'_\ell jj$
$S02$	0.94	3.54	[−6.0 , 6.4]
$S1$	3.01	2.41	[−18 , 19]
$M0$	0.57	2.48	[−3.0 , 3.2]
$M1$	1.13	4.32	[−4.7 , 4.7]
$M7$	1.57	3.62	[−6.7 , 7.0]
$T0$	0.06	3.30	[−0.28, 0.31]
$T1$	0.07	18.71	[−0.12, 0.15]
$T2$	0.32	44.03	[−0.38, 0.50]

and M families, as well as for the f_{T0}/Λ^4 parameter a factor of 4 to more than 6 separates the two values. The sensitivity to the f_{T1}/Λ^4 and even more the f_{T2}/Λ^4 parameters is superior and the region where the linear EFT term becomes dominant is only a factor of two or even less away from the current best exclusion bounds.

Yet, the sensitivity in the fully leptonic $W^\pm W^\pm jj$ final state, despite the optimisation for the EFT signal in the analysis in Ref. [155], is not sufficient with the currently available amount of data. This means that either more data or even more energetic data need to be acquired in order to populate the sensitive region, or more advanced analyses techniques are necessary. With the investigation of the fundamental ingredients of an EFT analysis, this thesis presents a major step in this direction.

From Tab. F.6, it is to be reminded that acceptances for the `LIN` and `QUAD` contributions are different and that the overall acceptance of the pure EFT contribution changes with the parameter values. In the fiducial region utilised here, the acceptance for the `LIN` terms are larger than for the `QUAD` term for all parameters, except those of the S family. Moreover, the values where $\texttt{LIN}(x) = \texttt{QUAD}(x)$, not only depend on the chosen fiducial region, but also the final state subject of the measurement. Hence, for the semi-leptonic final state $W^\pm Vjj \to (\ell^\pm\nu_\ell/\ell^\pm\ell^\mp)Jjj$, which exhibits the current global best exclusion bounds on the considered parameters (from a subset of the available data to date) [154], these values can differ substantially and need to be checked independently. Hence, no conclusions of the validity range can be drawn for the exclusion intervals obtained there. Since none of the two experiments, not ATLAS nor CMS, have published exclusion bounds in this final state with the complete Run 2 dataset, exciting times are still ahead.

Taking a step back, it is to be reminded that the linear EFT term is large only in phase space regions where the SM $W^\pm W^\pm jj$-EW6 contributes because it describes the interference of the EFT amplitude for a given operator with the SM $W^\pm W^\pm jj$-EW6 amplitude. Current analyses, however, target the energetic or massive tails of the phase space and advertise these regions to have the least SM background contributions. Per construction then, these phase space regions are dominated by the pure `QUAD` contribution of the EFT model. Hence, the current analysis strategies need to be reconsidered towards favouring regions which are dominated by the linear EFT contribution. This could either prove to be other regions of other observables than generally employed. Another possible strategy could be to report exclusion limits by solely utilising the `LIN` contribution, together with bounds from the full EFT prescription. This is a scenario which only becomes available with the amplitude decomposition technique of generating predictions. Still, per construction, the separation in phase space of the linear EFT contribution from the background of the underlying SM process is not feasible.

All previous consideration do not take into account the unitarisation of the EFT amplitudes. Of course, clipping away the massive or energetic parts of the EFT contributions, does reduce mostly the pure `QUAD` contribution, because, as seen in Fig. 9.30 and others, it reaches out to much larger energies. Hence, the discussion is to be repeated for each considered clipping energy in order to verify the validity of the obtained exclusion bounds. In a sense, clipping the EFT contribution is a first step towards solely utilising the `LIN` contribution, though, realised differently.

For the exclusion bounds using the full $\texttt{LIN} + \texttt{QUAD}$ contribution it might be worth testing the sensitivity for other, more sophisticated mass variables, as studied in Ref. [274]. Furthermore it has been shown to be beneficial to utilise a combination of bins in the m_{jj} and m_{ll} (or another mass) observable for the fitting [155]. The first allows to constrain different background processes in the low and high mass regions, as seen in the SM analysis, and the latter gives the sensitivity to the EFT signal.

Sec. 9.2.6. The signal regions only differ slightly by their lepton and jet p_T requirements and in the value of the minimum required ΔY_{jj}. Solely a requirement on the maximum of both leptons' Zeppenfeld variables is added in Ref. [155] which is not present in the signal region of this thesis. From the mild change in relative contribution of the `LIN` and `QUAD` contribution when going from the generator phase to the fiducial phase space, and the study of many kinematic distributions in Ref. [268], it is naively assumed that the differences of both signal regions have minor impact on the conclusion of this comparison. In this spirit, it does not make sense to compare to global best limits as these are obtained in a different final state (mostly $W^\pm Vjj \to \ell^\pm\nu_\ell Jjj$ [154]) and the cross-sections and signal regions do not compare.

From the findings in Sec. 9.2.5 when searching for a sensitive observable, different behaviour of the S compared to the other parameters in the jet kinematics is observed. It might hence be further necessary to optimise the phase space for the measurement separately for the parameters of this family and all others.

From the exclusion bounds as a function of the clipping energy $E_{\text{clip}} = m_{WW}$, it can be seen that the measurements in this final state only begin to touch reasonable regions. For the family of S parameters, none of the obtained exclusion contours are allowed from the unitarisation point of view. For the remaining parameters, the allowed regions are reached when clipping at 1.5 TeV or further below.

With the work in this thesis, a first step towards including the effects of EFT operators of lower mass dimension is made. The studies presented here, solely include the effects of few dimension-six operators on the prediction of the $W^{\pm}Z$-EW4 process. In order to give a consistent picture, more operators must be included and effects on more processes, most importantly on the $W^{\pm}W^{\pm}jj$ process, need to be studied.

Another important aspect to be mentioned is that NLO EW corrections to the electroweak $W^{\pm}W^{\pm}jj$-EW6 process are not included in the measurements in this thesis, nor in any other published result. These correction are sizable with more than -13% in the fiducial region. Due to them being negative, the background expectations reduce and exclusion bounds on the EFT parameters become weaker when these are considered. This circumstance presents another motivation to thoroughly study and employ precise predictions in future measurements.

In conclusion, the fundamental ground work commenced in this thesis is by no means completed. By gaining further knowledge about the EFT model under study, also in directions not thought of today, the collaborations have the possibility to adjust their analysis in order to render the results reasonable in a mathematical and physical interpretation. This is solely achievable by staying in close discussion with experts from both, the experimental and theoretical sides.

Findings from this work and all following discussions shall in the long term be incorporated to move towards more sophisticated analyses. One apparent direction is the consideration of not only one EFT operator at a time but rather many, beginning with two-dimensional exclusion contours utilising parameters of the same family and further extending to multi-dimensional exclusion limits as computing resources and theoretical model implementation in the simulation programmes allow. From studying the `CROSS` contributions in Sec. 9.2.6, it is seen that the inference between EFT operators can be quite sizable which can lead to regions with increased sensitivity.

The ultimate goal in the study of EFT models in the electroweak sector should be a global fit including many more final states beyond VBS and triboson process, such as processes including top quarks or direct Higgs boson detection. A first step in this direction is taken in Ref. [264] combining the measurements of the $W^{\pm}W^{\pm}jj$ and $ZZjj$ final states from the CMS collaboration by utilising information from HEPData [265]. Moreover, the theoretical description of the EFT model should then not only include dimension-eight but also dimension-six operators. To date no model implementation exists, which includes operators of both classes.

To begin with, a combination of various VBS and triboson final states and measurements from both, the ATLAS and CMS experiments, should be envisaged in order to gain more sensitivity on dimension-eight EFT operators and reach the physically allowed regions in terms of the EFT expansion as well as unitarity. For this, a common ground on the theoretical prescription of the signal model is required. Moreover, the availability of transparent and complete results is crucial, including detailed and separate information on uncertainty sources and their correlations, preferably utilising standardised platforms. The study of fundamental elements of dimension-eight EFT analyses in this work, such as the signal modelling and the clipping unitarisation, help shaping the way toward defining common strategies for a combination in different final states and experiments.

Chapter 10

Summary & Outlook

This thesis presents comprehensive investigations of the electroweak $W^{\pm}W^{\pm}$ scattering process ($W^{\pm}W^{\pm}jj$-EW6) in the fully leptonic final state in proton-proton collisions at a centre-of-mass energy of 13 TeV. An amount of 36.1 fb^{-1} of data taken in the years 2015 and 2016 of the LHC Run 2 data-taking period with the ATLAS detector is utilised. Containing Vector Boson Scattering Feynman diagrams, the $W^{\pm}W^{\pm}jj$-EW6 process can be employed to probe the gauge structure of the SM and the mechanism of Electroweak Symmetry Breaking, and furthermore simultaneously, the delicate interplay of these two fundamental ingredients of the SM. The research of this work comprises three central aspects.

First, the theoretical predictions of the $W^{\pm}W^{\pm}jj$ and, in particular, the fully leptonic $W^{\pm}W^{\pm}jj$-EW6 process are studied as an example for processes involving VBS. For this purpose, three different MC event generation programmes with a variety of settings are employed in this work. These are the PowhegBox programme at NLO QCD accuracy with the VBS approximation, the Sherpa programme in a LO multi-jet merged setup with up to three jets in the matrix element, as well as at LO, and the MG5_aMC programme at LO accuracy. The predictions of the three nominal setups PB+Py8, Sherpa23jLO, and MG5+Py8drec, in the fiducial region disagree and the discrepancies are not covered by the total uncertainties of the predictions. Distinct settings of each setup are investigated to find the origin of the disagreement. These include the nominal renormalisation and factorisation scales in the matrix-element calculations of each setup, as well as the parton shower configurations. A uniform hierarchy in the predictions with different scale settings is found for all three setups. Together with the non-optimal implementation of the colour-flow configurations in the parton shower of the Sherpa programme for the $W^{\pm}W^{\pm}jj$-EW6 process, which results in a significant reduction of the predicted cross-section, it could be one of the sources of the disagreement.

Second, the first observation of the $W^{\pm}W^{\pm}jj$-EW6 process with data from the ATLAS experiment taken at $\sqrt{s} = 13\,\text{TeV}$ is established by rejecting the background-only hypothesis in the SM analysis with an observed significance of 6.5σ. The expected significance, employing the Sherpa23jLO prediction for the $W^{\pm}W^{\pm}jj$-EW6 process, is 4.4σ.

The fiducial cross-section of the $W^{\pm}W^{\pm}jj$-EW6 as predicted by the SM is measured as:

$$\sigma^{\text{fid}}_{\text{meas}} = 2.89\ ^{+0.51}_{-0.48}\ (\text{stat})\ ^{+0.14}_{-0.16}\ (\text{mod})\ ^{+0.24}_{-0.22}\ (\text{sys})^{+0.08}_{-0.06}\ (\text{lumi})\,\text{fb}.$$

Per construction of the analysis, this result includes the contribution of the interference between the $W^{\pm}W^{\pm}jj$-EW6 and $W^{\pm}W^{\pm}jj$-EW4 process. This measurement is dominated by the statistical uncertainty of the data sample. All three nominal theoretical predictions agree with the measured fiducial cross-section within the total uncertainty envelopes. The predictions from PB+Py8 and MG5+Py8drec agree better with the measurement than the Sherpa23jLO prediction.

Furthermore, in this work, the components of the analysis of the SM $W^{\pm}W^{\pm}jj$-EW6 process are reutilised for a reinterpretation of the experimental data at $\sqrt{s} = 13\,\text{TeV}$ in terms of an EFT model describing BSM extensions with operators of mass dimension eight [2, 3]. For the first time, one-dimensional exclusion bounds on the coefficients of these operators are

determined in the fully leptonic final state of the $W^{\pm}W^{\pm}$ scattering process with data from the ATLAS experiment. Moreover, these bounds are the first overall dimension-eight EFT parameter exclusion bounds derived at $\sqrt{s} = 13\,\text{TeV}$ with data from the ATLAS experiment.

For these results, the novel technique of amplitude decomposition is employed for the event generation of the EFT signal contributions. It considerably improves the signal predictions and accuracy, as well as the simulation efficiency in the sensitive regions of the EFT contribution at high energies and invariant masses, which are investigated in the current analyses. Moreover, along the profound validation of this new approach in this thesis, it is found that the conventional simulation technique (with the `FULL` approach) is insufficient in terms of phase space integration accuracy in the MC event generation in the high energetic tails of the distributions. Hence, it is strongly recommended to not further utilise the `FULL` prediction but instead the amplitude decomposition method. If the latter is not yet available, an alternative strategy could be to slice the `FULL` predictions into multiple samples, depending on some energy or mass variable.

Ununitarised exclusion bounds on dimension-eight EFT coefficients are presented and compared with existing results of all final states. The results of this work cannot compete with the current best limits in this final state presented in Ref. [155] or other final states. For the latter measurement, as well as many more previous results of dimension-eight EFT parameters in various final states [18, 154, 243, 247, 249–251, 253] the conventional `FULL` prediction has been employed. Hence, the insufficiencies found in this approach can in principle affect these results. No conclusions can, however, be drawn on the size of the impact in these previous analyses, since it depends on the parameter and final state.

In this thesis, global first exclusion bounds with the improved signal modelling are presented. As such, the thesis' focus lies in the investigation of the fundamental ingredients for the analysis of dimension-eight EFT models, such as the novel signal modelling technique, the clipping unitarisation approach, and the inclusion of effects of dimension-six EFT operators.

The application of the clipping unitarisation on the EFT signal contributions is thoroughly investigated in this work, and exclusion limits obtained with this approach are presented. For the first time in the $W^{\pm}W^{\pm}jj$ final state, exclusion bounds scanning multiple values of the clipping energy are shown in this thesis.

Moreover, exclusion bounds are studied, including the impact of EFT operators with mass dimension six on the $W^{\pm}Z$-EW4 background process. The results of this study constitute the first of their kind across final states and experiments. The inclusion of dimension-six EFT operators with coefficients at their current best limit values yields no sizable effect on the exclusion bounds of the dimension-eight coefficients in the tested, still limited, configuration.

For all three major elements of this work, potential directions for both, short and long-term future studies are presented. With additional data being collected in Run 3 and further in the high luminosity (HL) phase of the LHC, the statistical accuracy of the measurements increases. This opens the path for precision measurements in the electroweak VBS sector. More sophisticated analysis objectives, such as the publication of unfolded distributions or the investigation of polarised $W^{\pm}W^{\pm}$ scattering, become experimentally achievable. Moreover, analysis techniques can advance in other directions, e. g. towards the statistical evaluation of multiple observables, the simultaneous measurement of the $W^{\pm}W^{\pm}jj$ and $W^{\pm}Zjj$ processes, or the use of multivariate techniques.

For the SM process, this enables us to re-evaluate the consistency between the measured cross-section and newer versions of the theoretical predictions, which are expected to be updated for an appropriate handling of the inconsistencies found. Moreover, effects of the partially large higher order corrections become important. Due to its comparably simple structure, the $W^{\pm}W^{\pm}$ scattering process pioneers the field of VBS predictions. Hence, it is most desirable to pursue efforts in the implementation and investigation of fully NLO accurate predictions in the available MC generation tools and the experimental analyses in close exchange of both communities. Then, the theoretical structure of the NLO accurate predictions force to examine the full $W^{\pm}W^{\pm}jj$ process, together with a dedicated analysis of the $W^{\pm}W^{\pm}jj$-EW6 process. The publication of unfolded distributions, which becomes feasible with more data available, will further acquire insight not only in this direction.

The results of the EFT reinterpretation analysis show, that experimental analyses of the $W^{\pm}W^{\pm}jj$-EW6 final state, utilising the currently available amount of data, are not yet

sensitive enough to enter physically reasonable regions of the EFT coefficients phase space. This concerns both, the limitations due to violation of unitarity of the scattering amplitudes and the mathematical implementation of the expansion series of the EFT formulation.

Nevertheless, the work of this thesis adds valuable information to the understanding of the studied EFT model. Yet, the fundamental groundwork of the thesis is by no means completed. Being aware of the shortcomings and their implications for experimental analyses will help to guide the community towards more reasonable analysis strategies. This is solely achievable by staying in close discussion with experts from the theoretical side.

In addition, measurements should aim for multidimensional exclusion bounds. By considering multiple EFT operators simultaneously, the underlying model becomes more realistic in terms of the EFT motivation. Eventually, the EFT model should describe both, dimension-six and -eight operators, a technical implementation of which is not available to date.

One evident path towards improving the sensitivity for the EFT coefficients is the combination of information. This is possible in multiple directions. Results can be combined to explore the benefits of multiple final states, which can be sensitive to different phase space regions of the coefficients. Beginning with the combination of various VBS and triboson final states, results can further be complemented with measurements of processes involving top quarks or the Higgs boson. Furthermore, the analysed dataset can be augmented by combining results of the ATLAS and CMS experiments. This not only requires a common ground on the theoretical prescription of the signal modelling in these analyses, but also the availability of transparent and complete results therefrom. The study of the fundamental elements of dimension-eight EFT analyses in this work, helps shape the way toward defining common strategies for a combination in different final states and experiments. This combined effort perhaps brings us one step closer towards unravelling the hidden mysteries of the necessary extensions of the SM.

Appendix A

Details on the MC Event Generation

A.1 Input Parameters and Generator Specifications

Tab. A.1 summarises all input parameters of the SM specified in the event generation of the samples with the PowhegBox, Sherpa, and MG5_aMC programmes.

Table A.1: Values of the SM input parameters for the MC generation of the $W^{\pm}W^{\pm}jj$ processes. Values indicated with "–" are irrelevant for the processes at hand. Further explanations, see text.

Generator	PowhegBox		Sherpa	MG5_aMC
Sample	$W^{\pm}W^{\pm}jj$-EW4	$W^{\pm}W^{\pm}jj$-EW6	all $W^{\pm}W^{\pm}jj$	all $W^{\pm}W^{\pm}jj$
EW parameters:				
G_F [10^{-5}GeV^{-2}]	1.166397	1.16639	1.166397	1.16639
α_S	0.118	0.118	0.118	0.118
EW boson masses and decay widths in units of GeV:				
m_H	–	120	126	125
Γ_H	–	0.00441	0.00418	0.00638
m_W	80.419	80.419	80.399	80.419
Γ_W	2.141	2.099	2.085	2.0476
m_Z	91.1876	91.188	91.1876	91.188
Γ_Z	2.4952	2.51	2.4952	2.4414
Fermion masses and decay widths in units of GeV:				
m_τ	1.777	1.777	1.777	1.777
Γ_τ	–	–	2.27×10^{-12}	2.27×10^{-12}
m_μ	0.1057	0.1057	0.105	massless
m_e	0.511×10^{-3}	0.511×10^{-3}	0.511×10^{-3}	massless
$m_{t/b}$	–	–	–	–
$m_{c/s/u/d}$	massless	massless	massless	massless

The matrix elements of the PowhegBox implementation do not include top quarks, which is the reason for not specifying values for its mass or decay width. τ leptons are not decayed via PowhegBox itself but subsequently with Pythia 8 [137] and Herwig 7 [138, 139] which is the reason for not specifying the τ lepton decay width in PowhegBox.

A.2 Steering Cards and Job Options

For further analysis, all showered event files are transformed into the `TRUTH1` derivation format within the ATLAS MC production framework with setting up release `20.7.8.25` of the `AtlasDerivation` project. This gives the derivation tag `p3317`.

A.2.1 PowhegBox

The integration grid an LHE event files for the PowhegBox samples have been generated privately [216]. For this the PowhegBox base `POWHEG-BOX-V2` revision `3208` has been used[1]. The process specific toolboxes `POWHEG-BOX-V2/vbf_wp_wp` and `POWHEG-BOX-V2/Wp_Wp_J_J`, for the electroweak and strong $W^{\pm}W^{\pm}jj$ processes respectively, have been used at revision `3178`[2]. The configuration file for the generation of the electroweak process is shown below.

```
1  bornktmin -1                ! [ATLAS default: -1] (-1:use Powheg default) generation cut:
2                              ! minimum kt in underlying Born
3  bornonly 0                  ! [ATLAS default: 0] (0:disabled; 1:enabled) calculate only
4                              ! Born-level process
5  bornsuppfact -1             ! [ATLAS default: -1] (-1:use Powheg default) mass parameter
6                              ! for Born suppression factor. If > 0 suppfact = 1
7  bornzerodamp 1              ! [ATLAS default: 1] (0:disabled; 1:enabled) use damping
8                              ! where the Born is strongly suppressed (or 0).
9  bottomthr -1                ! [ATLAS default: -1] (-1:use Powheg default) minimum pT in
10                             ! GeV for generating emission off b-quarks
11 bottomthrpdf -1             ! [ATLAS default: -1] (-1:use Powheg default) threshold in GeV
12                             ! at which b-quark PDF becomes non-zero
13 btildeborn -1               ! [ATLAS default: -1] (-1:use Powheg default)
14 btildecoll -1               ! [ATLAS default: -1] (-1:use Powheg default)
15 btildereal -1               ! [ATLAS default: -1] (-1:use Powheg default) for fixed order:
16                             ! distinguish real terms from Born/virtual/subtraction
17 btildevirt -1               ! [ATLAS default: -1] (-1:use Powheg default)
18 btlscalect -1               ! [ATLAS default: -1] (-1:Powheg default; 0:disabled; 1:enabled)
19                             ! use the scales of the underlying-Born configuration for the
20                             ! subtraction terms
21 btlscalereal -1             ! [ATLAS default: -1] (-1:Powheg default; 0:disabled; 1:enabled)
22                             ! compute scales that depend on the real kinematics
23 charmthr -1                 ! [ATLAS default: -1] (-1:use Powheg default) minimum pT in
24                             ! GeV for generating emission off c-quarks
25 charmthrpdf -1              ! [ATLAS default: -1] (-1:use Powheg default) threshold in GeV
26                             ! at which c-quark PDF becomes non-zero
27 check_bad_st2 1             ! [ATLAS default: -1] (-1:Powheg default)
28 colltest 1                  ! [ATLAS default: 1] (0:disabled; 1:enabled) check collinear
29                             ! limits
30 compute_rwgt 0              ! [ATLAS default: 0] (0:nominal; 1:compute reweighting factor)
31 doublefsr 0                 ! [ATLAS default: 0] (0:disabled; 1:enabled) reduce observable
32                             ! spikes by suppressing FSR emissions harder than the emitter.
33 ebeam1 6500.0               ! [ATLAS default: 6500.0] energy of beam 1 in GeV
34 ebeam2 6500.0               ! [ATLAS default: 6500.0] energy of beam 2 in GeV
35 evenmaxrat 1                ! [ATLAS default: 1] (0:disabled; 1:enabled) speed up upper-bound
36                             ! calculation by taking maximum of identical processes.
37 facscfact 1.0               ! [ATLAS default: 1.0] factorization scale factor:
38                             ! mu_fact = mu_ref * facscfact
39 fastbtlbound 1               ! [ATLAS default: 1] (0:disabled; 1:enabled) use fast btilde
40                             ! bound.
41 fixedgrid -1                 ! [ATLAS default: -1] (-1:use Powheg default)
42 flg_debug 0                  ! [ATLAS default: 0] (0:disabled; 1:enabled) write extra
43                             ! information to LHEF. Breaks PYTHIA showering.
44 foldcsi 2                    ! [ATLAS default: 2] number of folds on x (csi) integration
45 foldphi 2                    ! [ATLAS default: 2] number of folds on phi integration
46 foldy 2                      ! [ATLAS default: 2] number of folds on y integration
47 fullrwgt -1                 ! [ATLAS default: -1] (-1:use Powheg default) experimental! Must
48                             ! ONLY be used for processes with no Born-level parton radiation.
49 fullrwgtmode -1              ! [ATLAS default: -1] (-1:use Powheg default)
50 hdamp -1                    ! [ATLAS default: -1] (-1:use Powheg default) DEPRECATED, apply
```

[1] This can be downloaded from svn://powhegbox.mib.infn.it/trunk/POWHEG-BOX-V2.

[2] They can be downloaded from svn://powhegbox.mib.infn.it/trunk/User-Processes-V2/vbf_wp_wp and svn://powhegbox.mib.infn.it/trunk/User-Processes-V2/Wp_Wp_J_J, respectively.

```
                              ! damping factor for high-pt radiation: h**2/(pt2+h**2)
hfact -1                      ! [ATLAS default: -1] (-1:use Powheg default) apply dumping factor
                              ! for high-pt radiation: h**2/(pt2+h**2)
icsimax 1                     ! [ATLAS default: 1] number of intervals (<= 10) in x (csi) grid
                              ! to compute upper bounds
ih1 1                         ! [ATLAS default: 1] ([-]1:[anti]proton; [-2]2:[anti]neutron;
                              ! [-3]3:[-]pi) hadron content of beam 1
ih2 1                         ! [ATLAS default: 1] ([-]1:[anti]proton; [-2]2:[anti]neutron;
                              ! [-3]3:[-]pi) hadron content of beam 2
itmx1 3                       ! [ATLAS default: 3] number of iterations for initializing the
                              ! integration grid
itmx1rm -1                    ! [ATLAS default: -1] (-1:use Powheg default) number of iterations
                              ! for initializing the integration grid for the remnant.
itmx2 6                       ! [ATLAS default: 6] number of iterations for computing the
                              ! integral and finding upper bound
itmx2rm -1                    ! [ATLAS default: -1] (-1:use Powheg default) number of iterations
                              ! for computing the integral and finding upper bound for the
                              ! remnant.
iupperfsr 2                   ! [ATLAS default: 2] choice of FSR upper bounding functional form
iupperisr 1                   ! [ATLAS default: 1] choice of ISR upper bounding functional form
iymax 1                       ! [ATLAS default: 1] number of intervals (<= 10) in y grid to
                              ! compute upper bounds
lhans1 260000                 ! [ATLAS default: 10800] PDF set for hadron 1 (LHAGLUE numbering)
lhans2 260000                 ! [ATLAS default: 10800] PDF set for hadron 2 (LHAGLUE numbering)
lhrwgt_descr 'nominal'        ! [ATLAS default: nominal] weight description.
lhrwgt_group_combine 'none'   ! [ATLAS default: none] reweighting combination method.
lhrwgt_group_name 'nominal'   ! [ATLAS default: nominal] group description.
lhrwgt_id '0'                 ! [ATLAS default: 0] weight ID.
LOevents 0                    ! [ATLAS default: 0] (0:disabled; 1:enabled) produce LOPS events
                              ! (scalup=ptj); in this case bornonly should also be enabled.
minlo -1                      ! [ATLAS default: -1] (0:disabled; 1:enabled) use MiNLO.
ncall1 19500                  ! [ATLAS default: 800000] number of calls for initializing the
                              ! integration grid
ncall1rm -1                   ! [ATLAS default: -1] (-1:use Powheg default) number of calls for
                              ! initializing the integration grid for the remant.
ncall2 15000                  ! [ATLAS default: 800000] number of calls for computing the
                              ! integral and finding upper bound
ncall2rm -1                   ! [ATLAS default: -1] (-1:use Powheg default) number of calls for
                              ! computing the integral and finding upper bound for the remnant.
ncallfrominput -1             ! [ATLAS default: -1] (-1:disabled) read ncall parameters from
                              ! input.
noevents -1                   ! [ATLAS default: -1] (-1:use Powheg default)
novirtual -1                  ! [ATLAS default: -1] (-1:use Powheg default)
nubound 10000                 ! [ATLAS default: 500000] number of calls to setup upper bounds
                              ! for radiation
numevts 2500                  ! [ATLAS default: 110] number of events to be generated
olddij -1                     ! [ATLAS default: -1] (-1:use Powheg default)
par_2gsupp -1                 ! [ATLAS default: -1] (-1:use Powheg default)
par_diexp -1                  ! [ATLAS default: -1] (-1:use Powheg default) ISR singularity
                              ! exponent (p1)
par_dijexp -1                 ! [ATLAS default: -1] (-1:use Powheg default) FSR singularity
                              ! exponent (p2)
ptsqmin -1                    ! [ATLAS default: -1] (-1:use Powheg default) minimum pT in GeV
                              ! for generating emission off light quarks
ptsupp -1                     ! [ATLAS default: -1] (-1:use Powheg default) DEPRECATED, but some
                              ! processes complain if it is missing
radregion -1                  ! [ATLAS default: -1] (-1:all regions) only generate radiation in
                              ! the selected singular region
rand1 0                       ! [ATLAS default: 0] (0:disabled; 1:enabled) user-initiated random
                              ! seed (disabled for reproducibility)
rand2 0                       ! [ATLAS default: 0] (0:disabled; 1:enabled) user-initiated random
                              ! seed (disabled for reproducibility)
renscfact 1.0                 ! [ATLAS default: 1.0] renormalization scale factor:
                              ! mu_ren = mu_ref * renscfact
runningscales 0               ! [ATLAS default: 0] (0:use fixed factorisation/renormalisation
                              ! scale; 1:use running scale)
smartsig 1                    ! [ATLAS default: 1] (0:disabled; 1:enabled) remember equal
                              ! amplitudes
softtest 1                    ! [ATLAS default: 1] (0:disabled; 1:enabled) check soft limits
stage2init -1                 ! [ATLAS default: -1] (-1:use Powheg default)
storeinfo_rwgt 0              ! [ATLAS default: 0] (0:disabled; 1:enabled) enable new-style PDF
```

```
                              ! information
storemintupb 1                ! [ATLAS default: 1] (0:disabled; 1:enabled) cache cross sections
                              ! to speed up construction of upper bounding envelope.
testplots 0                   ! [ATLAS default: 0] (0:disabled; 1:enabled) do NLO and PWHG
                              ! distributions
testsuda 0                    ! [ATLAS default: 0] (0:disabled; 1:enabled) test Sudakov form
                              ! factor
ubsigmadetails 1              ! [ATLAS default: 1] (0:disabled; 1:enabled) output calculated
                              ! cross-sections
use-old-grid 1                ! [ATLAS default: 1] (0:disabled; 1:enabled) use old integration
                              ! grid if available
use-old-ubound 1              ! [ATLAS default: 1] (0:disabled; 1:enabled) read norm of upper
                              ! bounding function from pwgubound.dat, if present
vdecaymodew1 135              ! [ATLAS default: -] (default process-dependent) First W decay
                              ! mode
vdecaymodew2 135              ! [ATLAS default: -] (default process-dependent) Second W decay
                              ! mode
withdamp 1                    ! [ATLAS default: 1] (-1:use Powheg default) use Born-zero damping
                              ! factor.
withnegweights 1              ! [ATLAS default: 1] (0:disabled; 1:enabled) allow negative
                              ! weights
withsubtr 1                   ! [ATLAS default: 1] (0:disabled; 1:enabled) subtract real
                              ! counterterms
xupbound 2                    ! [ATLAS default: 2] increase upper bound for radiation generation
                              ! by this factor
zerowidth 0                   ! [ATLAS default: 0] (0:disabled; 1:enabled) use on-shell
                              ! quarks/bosons only
ubexcess_correct 1
```

The configuration file for the generation of strong process is shown below.

```
!Single vector boson production parameters
vdecaymodeW1 135  ! PDG code for charged decay product of the vector bosons:
                  ! 11:e-; 13 mu-; 15 tau-; -11:e+; -13 mu+ ; -15 tau+;
                  ! 113 ew- mu-; 135 e- mu- tau-;  -113 ew+ mu+; -135 e+ mu+ tau+
vdecaymodeW2 135  ! as above; must have the same sign!
numevts 100    ! number of events to be generated
ih1   1           ! hadron 1 (1 for protons, -1 for antiprotons)
ih2   1           ! hadron 2 (1 for protons, -1 for antiprotons)
ndns1 131         ! pdf set for hadron 1 (mlm numbering)
ndns2 131         ! pdf set for hadron 2 (mlm numbering)
ebeam1 6500d0     ! energy of beam 1
ebeam2 6500d0     ! energy of beam 2
! To be set only if using LHA pdfs
lhans1  260000     ! pdf set for hadron 1 (LHA numbering)
lhans2  260000     ! pdf set for hadron 2 (LHA numbering)
! To be set only if using different pdf sets for the two incoming hadrons
! QCDLambda5  0.25 ! for not equal pdf sets

! Parameters to allow or not the use of stored data
use-old-grid    1 ! if 1 use old grid if file pwggrids.dat is present (<> 1 regenerate)
use-old-ubound  1 ! if 1 use norm of upper bounding function stored in pwgubound.dat,
                  ! if present; <> 1 regenerate

ncall1   30000   ! number of calls for initializing the integration grid
itmx1    5       ! number of iterations for initializing the integration grid
ncall2   100     ! number of calls for computing the integral and finding upper bound
itmx2    45  ! number of iterations for computing the integral and finding upper bound
foldcsi   5    ! number of folds on csi integration
foldy     5     ! number of folds on  y  integration
foldphi   10     ! number of folds on phi integration
nubound  5000    ! number of bbarra calls to setup norm of upper bounding function
icsimax  1     ! <= 100, number of csi subdivision when computing the upper bounds
iymax    1     ! <= 100, number of y subdivision when computing the upper bounds
xupbound 2d0   ! increase upper bound for radiation generation

! OPTIONAL PARAMETERS

#renscfact  1d0   ! (default 1d0) ren scale factor: muren  = muref * renscfact
#facscfact  1d0   ! (default 1d0) fac scale factor: mufact = muref * facscfact
```

```
#ptsupp     0d0   ! (default 0d0)  mass param for Born suppression factor
                  ! (generation cut) If < 0 suppfact = 1
#bornonly   1      ! (default 0) if 1 do Born only
#smartsig   0      ! (default 1) remember equal amplitudes (0 do not remember)
#withsubtr  0      ! (default 1) subtract real counterterms (0 do not subtract)
withdamp    0      ! (default 0, do not use) use Born-zero damping factor
#ptsqmin    0.8    ! (default 0.8 GeV) minimum pt for generation of radiation
#charmthr   1.5    ! (default 1.5 GeV) charm treshold for gluon splitting
#bottomthr  5.0    ! (default 5.0 GeV) bottom treshold for gluon splitting
testplots  0      ! (default 0, do not) do NLO and PWHG distributions
#hfact    100d0    ! (default no dumping factor) dump factor for high-pt radiation:
                   ! > 0 dumpfac=h**2/(pt2+h**2)
#testsuda  1       ! (default 0, do not test) test Sudakov form factor
#radregion 1       ! (default all regions) only generate radiation in the selected
                   ! singular region
#charmthrpdf  1.5  ! (default 1.5 GeV) pdf charm treshold
#bottomthrpdf 5.0  ! (default 5.0 GeV) pdf bottom treshold


storemintupb 1

#iseed    12345    ! initialize random number sequence
#rand1     -1      ! initialize random number sequence
#rand2     -1      ! initialize random number sequence

#iupperisr 1 ! (default 1) choice of ISR upper bounding functional form
#iupperfsr 2 ! (default 2) choice of FSR upper bounding functional form

! Z+jet production
#bornktmin  20d0    ! (default 0d0) kt min at Born level for jet in Z+jet

#manyseeds  1       ! Used to perform multiple runs with different random
                    ! seeds in the same directory.
                    ! If set to 1, the program asks for an integer j;
                    ! The file pwgseeds.dat at line j is read, and the
                    ! integer at line j is used to initialize the random
                    ! sequence for the generation of the event.
                    ! The event file is called pwgevents-'j'.lhe



#xgriditeration 1
#parallelstage 3

storeinfo_rwgt 1
#compute_rwgt 1
#pdfreweight 1
#fullrwgt 1
#fullrwgtmode 4

check_bad_st2 0
ubexcess_correct 0

lhrwgt_descr 'nominal'        ! [ATLAS default: nominal] weight description.
lhrwgt_group_combine 'none'   ! [ATLAS default: none] reweighting combination method.
lhrwgt_group_name 'nominal'   ! [ATLAS default: nominal] group description.
lhrwgt_id '0'                 ! [ATLAS default: 0] weight ID.
```

The LHE event files are generated split by the charge of the final state W^-W^- (called `WmWm`) and W^+W^+ (called `WpWp`) and further interfaced with either Pythia 8 [137] or Herwig 7 [138, 139] for parton showering. The ATLAS MC production framework is used with setting up release `19.2.5.19.4` of the `MCProd` project. An example for a Pythia 8 steering file with default tune `AZNLO` is shown below.

```
#--------------------------------------------------------------
# Pythia8 showering with Photos
#--------------------------------------------------------------
include('MC15JobOptions/Pythia8_AZNLO_CTEQ6L1_EvtGen_Common.py')
include('MC15JobOptions/nonStandard/Pythia8_Photospp.py')
```

```
6
7  #--------------------------------------------------------------
8  # Pythia8 main31 update
9  #--------------------------------------------------------------
10 genSeq.Pythia8.UserModes += [ 'Main31:NFinal = 4' ]
11
12 #--------------------------------------------------------------
13 # EVGEN configuration
14 #--------------------------------------------------------------
15 evgenConfig.description = "POWHEG+PYTHIA8+EVTGEN, VBS WmWm + 2 jets"
16 evgenConfig.keywords    = [ "SM", "VBS", "electroweak", "WW", "2jet", "NLO" ]
17 evgenConfig.process     = "VBS ssWW"
18 evgenConfig.inputfilecheck = 'EWK_WmWm'
19 evgenConfig.minevents   = 5000
```

When using the alternate dipole recoil option, the line:

```
genSeq.Pythia8.Commands += ["SpaceShower:dipoleRecoil=on"]
```

is added to the default steering file.

An example Herwig 7 configuration file is shown below.

```
1  include("MC15JobOptions/Herwig7_701_H7UE_MMHT2014lo68cl_NNPDF3ME_LHEF_EvtGen_Common.py")
2  include("MC15JobOptions/Herwig7_701_StripWeights.py")
3
4  from Herwig7_i import config as hw
5  genSeq.Herwig7.Commands += hw.powhegbox_cmds().splitlines()
6
7  #--------------------------------------------------------------
8  # EVGEN configuration
9  #--------------------------------------------------------------
10 evgenConfig.description = "POWHEG+HERWIG7+EVTGEN, VBS WmWm + 2 jets"
11 evgenConfig.generators += ["Powheg", "Herwig7"]
12 evgenConfig.keywords = [ "SM", "VBS", "electroweak", "WW", "2jet", "NLO" ]
13 evgenConfig.process = "VBS ssWW"
14 evgenConfig.inputfilecheck = 'EWK_WmWm'
15 evgenConfig.minevents = 5000
```

The `description`, `keywords`, and `process` configurations need to be changed according to the generated process at hand, $W^{\pm}W^{\pm}jj$-EW6 or $W^{\pm}W^{\pm}jj$-EW4 (at NLO QCD) with either positively or negatively charged final state .

A.2.2 Sherpa

For the event generation and simulation of the nominal Sherpa samples the ATLAS MC production framework is used with setting up release `19.2.5.17.1` of the `MCProd` project. The steering card for the LO multi-jet merged setup for the $W^{\pm}W^{\pm}jj$-EW6 process with default core scale m_{WW} at parton level is shown below. Details and explanations to the steering scripts can be found in Ref. [133].

```
1  include("MC15JobOptions/Sherpa_2.2.2_NNPDF30NNLO_Common.py")
2
3  evgenConfig.description = "Electroweak same-sign llvvjj + 0,1j@LO"
4  evgenConfig.keywords = ["SM", "diboson", "2lepton", "jets", "VBS"]
5  evgenConfig.minevents = 100
6  evgenConfig.inputconfcheck = "222_NNPDF30NNLO_llvvjj_ss_EW6"
7
8  evgenConfig.process="""
9  (run){
10   ACTIVE[25]=1;
11   MASS[25]=126.0;
12   WIDTH[25]=0.00418;
13   MASSIVE[11]=1;
14   MASSIVE[13]=1;
15   MASSIVE[15]=1;
16   PARTICLE_CONTAINER 991[m:-1] leptons 11 -11 13 -13 15 -15;
```

```
17
18   %scales, tags for scale variations
19   FSF:=1.; RSF:=1.; QSF:=1.;
20   SCALES STRICT_METS{FSF*MU_F2}{RSF*MU_R2}{QSF*MU_Q2};
21   CORE_SCALE=VAR{Abs2(p[2]+p[3]+p[4]+p[5])};
22
23   %tags for process setup
24   NJET:=1; QCUT:=20.;
25
26   EXCLUSIVE_CLUSTER_MODE=1
27   SOFT_SPIN_CORRELATIONS=1
28
29   %solves problem with dipole QED modeling
30   ME_QED_CLUSTERING_THRESHOLD=5;
31
32   % improve integration performance
33   PSI_ITMIN=25000;
34   CDXS_VSOPT=5;
35   INTEGRATION_ERROR 0.05;
36 }(run)
37
38
39 (processes){
40   Process 93 93 -> 11 11 -12 -12 93 93 93{NJET};
41   Order (*,6); CKKW sqr(QCUT/E_CMS);
42   End process;
43
44   Process 93 93 -> 13 13 -14 -14 93 93 93{NJET};
45   Order (*,6); CKKW sqr(QCUT/E_CMS);
46   End process;
47
48   Process 93 93 -> 15 15 -16 -16 93 93 93{NJET};
49   Order (*,6); CKKW sqr(QCUT/E_CMS);
50   End process;
51
52   Process 93 93 -> 11 13 -12 -14 93 93 93{NJET};
53   Order (*,6); CKKW sqr(QCUT/E_CMS);
54   End process;
55
56   Process 93 93 -> 11 15 -12 -16 93 93 93{NJET};
57   Order (*,6); CKKW sqr(QCUT/E_CMS);
58   End process;
59
60   Process 93 93 -> 13 15 -14 -16 93 93 93{NJET};
61   Order (*,6); CKKW sqr(QCUT/E_CMS);
62   End process;
63
64   Process 93 93 -> -11 -11 12 12 93 93 93{NJET};
65   Order (*,6); CKKW sqr(QCUT/E_CMS);
66   End process;
67
68   Process 93 93 -> -13 -13 14 14 93 93 93{NJET};
69   Order (*,6); CKKW sqr(QCUT/E_CMS);
70   End process;
71
72   Process 93 93 -> -15 -15 16 16 93 93 93{NJET};
73   Order (*,6); CKKW sqr(QCUT/E_CMS);
74   End process;
75
76   Process 93 93 -> -11 -13 12 14 93 93 93{NJET};
77   Order (*,6); CKKW sqr(QCUT/E_CMS);
78   End process;
79
80   Process 93 93 -> -11 -15 12 16 93 93 93{NJET};
81   Order (*,6); CKKW sqr(QCUT/E_CMS);
82   End process;
83
84   Process 93 93 -> -13 -15 14 16 93 93 93{NJET};
85   Order (*,6); CKKW sqr(QCUT/E_CMS);
86   End process;
87 }(processes)
```

```
88
89 (selector){
90   Mass 11 -11 0.1 E_CMS;
91   PT 991 5.0 E_CMS;
92   NJetFinder 2 15. 0. 0.4 -1;
93 }(selector)
94 """
95
96 genSeq.Sherpa_i.Parameters += [ "EW_SCHEME=3", "GF=1.166397e-5" ]
```

For the $W^{\pm}W^{\pm}jj$-EW4 process the order in electroweak couplings of the processes must be changed from 6 to 4:

```
Order (*,4);
```

for each of the processes, together with the `description`, `keywords`, and `inputconfcheck` configurations to represent the strong process.

For the LO setup without multi-jet merging the additional radiation must be turned off in the process definition at matrix element level:

```
NJET:=0;
```

For the study on the impact of the renormalisation and factorisation scale the following scales are set in the steering files, where the squared scales have to be specified:

```
CORE_SCALE=VAR{sqr(80.3)};
```

for the fixed scale m_W;

```
CORE_SCALE=VAR{H_T2};
```

for the sum of all transverse masses in the event;

```
CORE_SCALE=VAR{0.25*H_T2};
```

for the sum of all transverse masses in the event divided by 2;

```
CORE_SCALE=VAR{PPerp(p[6])*PPerp(p[7])};
```

for the scale $\sqrt{p_{\mathrm{T}}(j1)p_{\mathrm{T}}(j2)}$;

```
CORE_SCALE=VAR{Abs2(p[0]+p[1])};
```

for the scale $\sqrt{s}$.

A.2.3 MG5_aMC

All MG5_aMC samples are generated privately via the setup developed at the TU Dresden [217]. This includes a local MG5_aMC version 2.6.5 with minor modifications which is run within the structures of the ATLAS MC production framework setting up release `19.2.5.37` of the `AtlasProduction` project. An example configurations file including the setup for showering with Pythia 8 [137] is printed below.

```
1 from MadGraphControl.MadGraphUtils import *
2
3 evgenConfig.generators = ["MadGraph", "Pythia8", "EvtGen"]
4
5 evgenConfig.description = 'MadGraph_lvlvjj_ss_EW6_SM_sm_sm'
6 evgenConfig.keywords = ['SM', 'diboson', 'VBS', 'WW', 'sameSign', 'electroweak',
7                          '2lepton', '2jet']
8
9 runName='run_01'
10 process_total=None
11
12 evgenConfig.inputfilecheck = runName
13
```

```
#GridPack
do_gridpack_only = "inputGenConfFile" not in dir(runArgs)

gridpack_mode=True
gridpack_dir='madevent/'
gridpack_compile=False
nevents = 1 if do_gridpack_only else 5050

if not do_gridpack_only:
    Mode=0
    nJobs=1
    Cluster_Type=None
    Cluster_Queue=None
else:
    Mode=1
    nJobs=24
    Cluster_Type='slurm'
    Cluster_Queue='haswell64'
    Cluster_Size=24


beamEnergy=-999
if hasattr(runArgs,'ecmEnergy'):
    beamEnergy = runArgs.ecmEnergy / 2.
else:
    raise RuntimeError("No center of mass energy found.")

#Fetch default LO run_card.dat and set parameters
extras = {
    'pdlabel': "'lhapdf'",
    'lhaid': 260000,
    'dynamical_scale_choice': 2,
    'auto_ptj_mjj': False,
    'cut_decays': True,
    'maxjetflavor': 5,
    'asrwgtflavor': 5,
    'ptj': 15.0,
    'ptb': 15.0,
    'ptl': 4.0,
    'drjj': 0.2,
    'drbj': 0.2,
    'drbb': 0.2,
    'drbl': 0.2,
    'drll': 0.2,
    'drjl': 0.2,
    'dral': 0.1,
    'etaj': 5.5,
    'etab': 5.5,
    'etal': 3.0,
    'mmll': 0.0,
    'use_syst': True,
    'systematics_program': 'systematics',
    'systematics_arguments': "['--mur=0.5,1,2', '--muf=0.5,1,2', '--dyn=-1,1,2,3,4'," +
      "'--pdf=errorset,NNPDF30_nlo_as_0119@0,NNPDF30_nlo_as_0117@0,CT14nlo@0,'" +
      "'MMHT2014nlo68clas118@0']"
}

extras["gridpack"] = '.true.' if do_gridpack_only else ".false."

process_dir = new_process(grid_pack=gridpack_dir)

build_run_card(run_card_old=get_default_runcard(proc_dir=process_dir),
               run_card_new='run_card.dat',
               xqcut=0,
               nevts=nevents,
               rand_seed=runArgs.randomSeed,
               beamEnergy=beamEnergy)
print_cards()
modify_run_card(run_card='run_card.dat',
                    run_card_backup='run_card_backup.dat',
                    settings=extras)
```

```
85
86 print_cards()
87
88 generate(required_accuracy=0.001,
89          run_card_loc='run_card.dat',
90          param_card_loc='param_card_pre.dat',
91          mode=Mode,
92          njobs=nJobs,
93          cluster_type=Cluster_Type,
94          cluster_queue=Cluster_Queue,
95          proc_dir=process_dir,
96          run_name=runName,
97          grid_pack=gridpack_mode,
98          gridpack_compile=gridpack_compile,
99          gridpack_dir=gridpack_dir,
100         nevents=nevents,
101         random_seed=runArgs.randomSeed)
102
103 output_suffix = gridpack_dir if do_gridpack_only else runName
104 arrange_output(run_name=runName,
105                proc_dir=process_dir,
106                outputDS=output_suffix+'._00001.events.tar.gz',
107                lhe_version=3,
108                saveProcDir=True)
109
110 if not do_gridpack_only:
111     runArgs.inputGeneratorFile=output_suffix+'._00001.events.tar.gz'
112     do_merging = False
113
114     include("MC15JobOptions/Pythia8_A14_NNPDF23LO_EvtGen_Common.py")
115     # fix for VBS processes (requires version>=8.230)
116     genSeq.Pythia8.Commands += ["SpaceShower:dipoleRecoil=on"]
117
118     include("MC15JobOptions/Pythia8_MadGraph.py")
119     include("MC15JobOptions/Pythia8_ShowerWeights.py")
```

It takes as inputs a process and a parameter card, `proc_card.dat` and `param_card.dat`, exemplarily respectively shown below.

```
1  import model sm
2  define l+ = e+ mu+ ta+
3  define vl = ve vm vt
4  define l- = e- mu- ta-
5  define vl~ = ve~ vm~ vt~
6  define p = g u c d s u~ c~ d~ s~ b b~
7  define j = g u c d s u~ c~ d~ s~ b b~
8  generate p p > l+ vl l+ vl j j QCD=0
9  add process p p > l- vl~ l- vl~ j j QCD=0
10 output -f
```

```
1  ###################################################################
2  ## PARAM_CARD AUTOMATICALY GENERATED BY THE UFO  ####################
3  ###################################################################
4
5  ####################################
6  ## INFORMATION FOR SMINPUTS
7  ####################################
8  Block SMINPUTS
9      1 1.325070e+02 # aEWM1
10     2 1.166390e-05 # Gf
11     3 1.180000e-01 # aS
12
13 ####################################
14 ## INFORMATION FOR MASS
15 ####################################
16 Block MASS
17     4 0.000000e+00 # MC
18     5 0.000000e+00 # MB
19     6 1.720000e+02 # MT
```

```
20    11 0.000000e-04 # Me
21    13 0.000000e-01 # MM
22    15 1.777000e+00 # MTA
23    23 9.118800e+01 # MZ
24    25 1.250000e+02 # MH
25 ## Not dependent paramater.
26 ## Those values should be edited following analytical the
27 ## analytical expression. Some generator could simply ignore
28 ## those values and use the analytical expression
29   22 0.000000 # a : 0.0
30   24 80.419000 # W+
31   21 0.000000 # g : 0.0
32   9000001 0.000000 # ghA : 0.0
33   9000003 80.419000 # ghWp
34   9000004 80.419000 # ghWm
35   9000005 0.000000 # ghG : 0.0
36   12 0.000000 # ve : 0.0
37   14 0.000000 # vm : 0.0
38   16 0.000000 # vt : 0.0
39   2 0.000000 # u : 0.0
40   1 0.000000 # d : 0.0
41   3 0.000000 # s : 0.0
42   251 80.419000 # G+
43
44 ####################################
45 ## INFORMATION FOR DECAY
46 ####################################
47 DECAY   6 1.508336e+00
48 DECAY  15 0.000000
49 DECAY  23 2.441404e+00
50 DECAY  24 2.047600e+00
51 DECAY  25 6.382339e-03
52 ## Not dependent paramater.
53 ## Those values should be edited following analytical the
54 ## analytical expression. Some generator could simply ignore
55 ## those values and use the analytical expression
56 DECAY  22 0.000000 # a : 0.0
57 DECAY  21 0.000000 # g : 0.0
58 DECAY  9000001 0.000000 # ghA : 0.0
59 DECAY  9000005 0.000000 # ghG : 0.0
60 DECAY  12 0.000000 # ve : 0.0
61 DECAY  14 0.000000 # vm : 0.0
62 DECAY  16 0.000000 # vt : 0.0
63 DECAY  2 0.000000 # u : 0.0
64 DECAY  4 0.000000 # c : 0.0
65 DECAY  1 0.000000 # d : 0.0
66 DECAY  3 0.000000 # s : 0.0
67 DECAY  5 0.000000 # b : 0.0
68 DECAY  11 0.000000 # e- : 0.0
69 DECAY  13 0.000000 # mu- : 0.0
70
71 ####################################
72 ## INFORMATION FOR CKMBLOCK
73 ####################################
74 Block CKMBLOCK
75     1 2.277360e-01 # cabi
76
77 ####################################
78 ## INFORMATION FOR YUKAWA
79 ####################################
80 Block YUKAWA
81    # 4 1.270000e+00 # ymc
82    # 5 4.200000e+00 # ymb
83     6 1.645000e+02 # ymt
84    # 11 5.110000e-04 # yme
85    # 13 1.056600e-01 # ymm
86    # 15 1.777000e+00 # ymtau
87 #===========================================================
88 # QUANTUM NUMBERS OF NEW STATE(S) (NON SM PDG CODE)
89 #===========================================================
90
```

```
Block QNUMBERS 9000001  # ghA
        1 0  # 3 times electric charge
        2 -1  # number of spin states (2S+1)
        3 1  # colour rep (1: singlet, 3: triplet, 8: octet)
        4 1  # Particle/Antiparticle distinction (0=own anti)
Block QNUMBERS 9000002  # ghZ
        1 0  # 3 times electric charge
        2 -1  # number of spin states (2S+1)
        3 1  # colour rep (1: singlet, 3: triplet, 8: octet)
        4 1  # Particle/Antiparticle distinction (0=own anti)
Block QNUMBERS 9000003  # ghWp
        1 3  # 3 times electric charge
        2 -1  # number of spin states (2S+1)
        3 1  # colour rep (1: singlet, 3: triplet, 8: octet)
        4 1  # Particle/Antiparticle distinction (0=own anti)
Block QNUMBERS 9000004  # ghWm
        1 -3  # 3 times electric charge
        2 -1  # number of spin states (2S+1)
        3 1  # colour rep (1: singlet, 3: triplet, 8: octet)
        4 1  # Particle/Antiparticle distinction (0=own anti)
Block QNUMBERS 9000005  # ghG
        1 0  # 3 times electric charge
        2 -1  # number of spin states (2S+1)
        3 8  # colour rep (1: singlet, 3: triplet, 8: octet)
        4 1  # Particle/Antiparticle distinction (0=own anti)
Block QNUMBERS 250  # G0
        1 0  # 3 times electric charge
        2 1  # number of spin states (2S+1)
        3 1  # colour rep (1: singlet, 3: triplet, 8: octet)
        4 0  # Particle/Antiparticle distinction (0=own anti)
Block QNUMBERS 251  # G+
        1 3  # 3 times electric charge
        2 1  # number of spin states (2S+1)
        3 1  # colour rep (1: singlet, 3: triplet, 8: octet)
        4 1  # Particle/Antiparticle distinction (0=own anti)
```

Although the Cabibbo angle for the CKM matrix is specified in the parameter card, the loaded model `sm` specifies a unitary quark mixing matrix.

Some of the dynamical scale choices used in the comparison studies are builtin in the MG5_aMC programme. They can be used by changing the `dynamical_scale_choice` switch in the `extras` dictionary of the steering script. Allowed values are:

- `-1`: MG5_aMC default, cluster scale;
- `0`: User defined (need to be added in `setscales.f`);
- `1`: Total transverse energy of the event (HT in this work);
- `2`: Sum of the transverse masses $\sum \sqrt{m^2 + p_{\mathrm{T}}^2}$ (HT in this work);
- `3`: Sum of the transverse masses divided by 2 (HT/2 in this work);
- `4`: Partonic energy $\sqrt{s}$ (SqrtS in this work).

For setting a fixed scale in MG5_aMC, the following lines:

```
'fixed_ren_scale': '.true.',
'fixed_fac_scale': '.true.',
'scale': '80.3',
'dsqrt_q2fact1': '80.3',
'dsqrt_q2fact2': '80.3',
```

have to be added to the `extras` dictionary of the steering script.

In order to use custom scales in MG5_aMC, the definition of the respective scales has to be added to the `setscales.f` file in the Fortran base code. The patch for the implementation of the m_{WW} scale is printed below.

```
31c31,37
< c
---
> c     for mVV scale
>       integer j
>       double precision pTot(0:3)
>       integer idupmww(nexternal,maxproc)
>       common /c_leshouche_inc/idupmww
>
77a84
>          rscale=0d0
84,86c91,106
<          write(*,*) "User-defined scale not set"
<          stop 21
<          rscale = 0
---
> c        --- for mVV scale
>          do i=0,3
>             pTot(i)=0d0
>          enddo
>          do j=3,nexternal
>             if( abs(idupmww(j,1)).gt.10 .and. abs(idupmww(j,1)).lt.17 ) then
>                do i=0,3
>                   pTot(i)= pTot(i) + P(i,j)
>                enddo
>             endif
>          enddo
>          rscale = dsqrt(dot(pTot,pTot))
> c        --- end mVV scale ---
```

The patch for the scale $\sqrt{p_{\mathrm{T}}(j1)p_{\mathrm{T}}(j2)}$ computation is shown below.

```
40a41,43
>       real*8 pt1pt2
>       integer njets
>
84,86c87,98
<          write(*,*) "User-defined scale not set"
<          stop 21
<          rscale = 0
---
>           pt1pt2 = 1.0
>           njets = 0
>
>           do i=nexternal-1,nexternal
>               pt1pt2 = pt1pt2*pt(P(0,i))
>               njets = njets+1
>           enddo
>
>           if(njets.ne.2) write(*,*) 'WARNING:  njets= ',njets
>           rscale=dsqrt(pt1pt2)
```

For the showering with Herwig 7 [138, 139] the ATLAS MC production framework is used setting up release `20.7.9.9.23` of the `MCProd` project. An example steering file is shown below.

```
from MadGraphControl.MadGraphUtils import *

evgenConfig.generators = ["MadGraph", "Herwig7", "EvtGen"]

evgenConfig.description = 'MadGraph_lvlvjj_ss_EW6_LSMT_sm_sm'
    evgenConfig.keywords = ['SM', 'diboson', 'VBS', 'WW', 'sameSign', 'electroweak', '2lepton',
→   '2jet']

runName='run_01'
process_total=None

evgenConfig.inputfilecheck = runName
```

```
output_suffix = runName
runArgs.inputGeneratorFile='tmp_'+output_suffix+'._00001.events.tar.gz'

#--------------------------------------------------------------
# Herwig7 (H7UE) showering
#--------------------------------------------------------------
# initialize Herwig7 generator configuration for showering of LHE files

from Herwig7_i.Herwig7_iConf import Herwig7
from Herwig7_i.Herwig7ConfigLHEF import Hw7ConfigLHEF

genSeq += Herwig7()
Herwig7Config = Hw7ConfigLHEF(genSeq, runArgs)

# configure Herwig7
Herwig7Config.me_pdf_commands(order="NLO", name="NNPDF30_nlo_as_0118")
Herwig7Config.tune_commands()
→   Herwig7Config.lhef_mg5amc_commands(lhe_filename=runArgs.inputGeneratorFile, me_pdf_order="NLO")

# add EvtGen
include("MC15JobOptions/Herwig71_EvtGen.py")

# run Herwig7
Herwig7Config.run()
```

A.3 Inconsistencies in the Event Generation

A.3.1 Lepton Flavour Universality in PowhegBox $W^{\pm}W^{\pm}jj$-EW4 Process

In the course of the studies presented in Chapter 6, an inconsistency regarding the lepton flavour universality in the implementation of the $W^{\pm}W^{\pm}jj$-EW4 process of the PowhegBox programme is found.

Considering the object selection requirements for leptons in the fiducial region being identical for electrons and muons, the predicted fiducial cross-section is expected to be equivalent for all dilepton final states, i.e. the channels $e^{\pm}e^{\pm}$, $e^{\pm}\mu^{\pm}$, $\mu^{\pm}e^{\pm}$, $\mu^{\pm}\mu^{\pm}$, within the statistical accuracy of the MC sample. Fig. A.1 (a) shows the channel distribution for the prediction of the $W^{\pm}W^{\pm}jj$-EW4 with the nominal PowhegBox implementation, PB+Py8. For reference the predictions of the nominal Sherpa setup, Sherpa23jLO and the PowhegBox setup interfaced to Herwig 7 [138, 139], PB+H7, are likewise shown in the plot. The prediction of Sherpa23jLO looks as expected while the PB+H7 prediction shows the similar inconsistencies. The first observation excludes inconsistencies in the technical implementation of the selection requirements in the fiducial region. The latter suggests the inconsistency to arise from the PowhegBox implementation and not the interface to the parton shower programme. As shown in Fig. A.1 (b), the lepton flavour distribution is found to be as expected for the implementation of the $W^{\pm}W^{\pm}jj$-EW6.

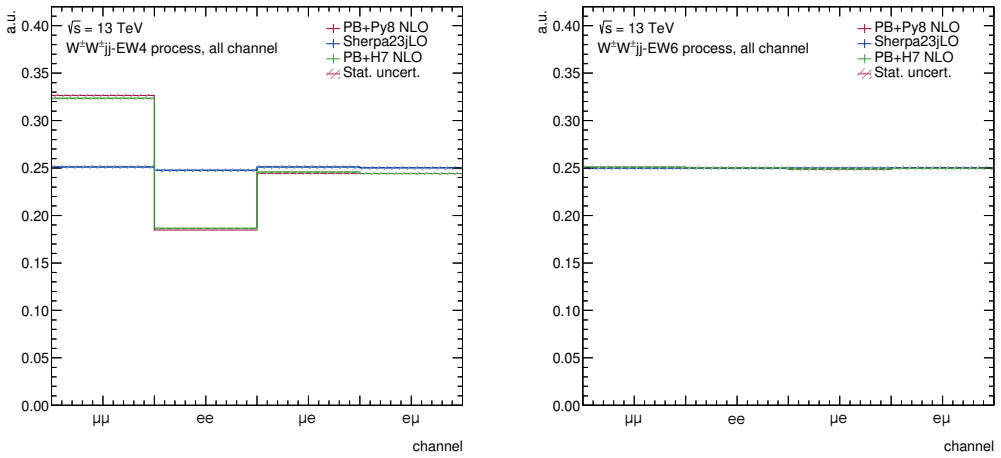
A.4 Technical Information for the Evaluation of Modelling Uncertainties

A.4.1 PowhegBox + Pythia 8

The names of the generator level weights used for the evaluation of the modelling uncertainties for the PowhegBox setups are listed exemplarily below.

```
// Mapping of Weights for sample
// mc15_13TeV.363995.PhPy8EG_NNPDF30NLO_AZNLOC6L1_EWK_WmWm.merge.DAOD_TRUTH1.e5678_p3135

// nominal scale variations
"muR = 0.5, muF = 0.5"
"muR = 0.5, muF = 1.0"
```



(a) $W^{\pm}W^{\pm}jj$-EW4 process **(b)** $W^{\pm}W^{\pm}jj$-EW6 process

Figure A.1: Prediction of the lepton flavour channel distribution in the fully leptonic final state of the $W^{\pm}W^{\pm}jj$-EW4 (left) and $W^{\pm}W^{\pm}jj$-EW6 (right) process for the POWHEGBOX + PYTHIA 8 nominal setup PB+Py8, the nominal SHERPA setup Sherpa23jLO, and the POWHEGBOX setup interfaced to HERWIG 7 PB+H7. Distributions are normalised to unit area and shown in the region after object selection (left), as defined in Tab. 6.8. Uncertainties are statistical accuracy of the MC samples only.

```
"muR = 0.5, muF = 2.0"
"muR = 1.0, muF = 0.5"
"muR = 1.0, muF = 2.0"
"muR = 2.0, muF = 0.5"
"muR = 2.0, muF = 1.0"
"muR = 2.0, muF = 2.0"
// alpha_s variations
"PDF set = 265000"
"PDF set = 266000"
// variations of nominal PDF set
"PDF set = 13100"
"PDF set = 25100"
// NNPDF30_nlo_as_0118 set variations (N=100)
"PDF set = 260001"
"PDF set = 260002"
"PDF set = 260003"
"PDF set = 260004"
"PDF set = 260005"
"PDF set = 260006"
"PDF set = 260007"
"PDF set = 260008"
"PDF set = 260009"
"PDF set = 260010"
"PDF set = 260011"
"PDF set = 260012"
"PDF set = 260013"
"PDF set = 260014"
"PDF set = 260015"
"PDF set = 260016"
"PDF set = 260017"
"PDF set = 260018"
"PDF set = 260019"
"PDF set = 260020"
"PDF set = 260021"
"PDF set = 260022"
"PDF set = 260023"
"PDF set = 260024"
"PDF set = 260025"
"PDF set = 260026"
"PDF set = 260027"
```

```
"PDF set = 260028"
"PDF set = 260029"
"PDF set = 260030"
"PDF set = 260031"
"PDF set = 260032"
"PDF set = 260033"
"PDF set = 260034"
"PDF set = 260035"
"PDF set = 260036"
"PDF set = 260037"
"PDF set = 260038"
"PDF set = 260039"
"PDF set = 260040"
"PDF set = 260041"
"PDF set = 260042"
"PDF set = 260043"
"PDF set = 260044"
"PDF set = 260045"
"PDF set = 260046"
"PDF set = 260047"
"PDF set = 260048"
"PDF set = 260049"
"PDF set = 260050"
"PDF set = 260051"
"PDF set = 260052"
"PDF set = 260053"
"PDF set = 260054"
"PDF set = 260055"
"PDF set = 260056"
"PDF set = 260057"
"PDF set = 260058"
"PDF set = 260059"
"PDF set = 260060"
"PDF set = 260061"
"PDF set = 260062"
"PDF set = 260063"
"PDF set = 260064"
"PDF set = 260065"
"PDF set = 260066"
"PDF set = 260067"
"PDF set = 260068"
"PDF set = 260069"
"PDF set = 260070"
"PDF set = 260071"
"PDF set = 260072"
"PDF set = 260073"
"PDF set = 260074"
"PDF set = 260075"
"PDF set = 260076"
"PDF set = 260077"
"PDF set = 260078"
"PDF set = 260079"
"PDF set = 260080"
"PDF set = 260081"
"PDF set = 260082"
"PDF set = 260083"
"PDF set = 260084"
"PDF set = 260085"
"PDF set = 260086"
"PDF set = 260087"
"PDF set = 260088"
"PDF set = 260089"
"PDF set = 260090"
"PDF set = 260091"
"PDF set = 260092"
"PDF set = 260093"
"PDF set = 260094"
"PDF set = 260095"
"PDF set = 260096"
"PDF set = 260097"
"PDF set = 260098"
```

```
"PDF set = 260099"
"PDF set = 260100"

// Mapping of Weights for sample
// mc15_13TeV.363997.PhPy8EG_NNPDF30NLO_AZNLOC6L1_QCD_WmWm.merge.DAOD_TRUTH1.e5678_p3135

// nominal scale variations
"muR = 0.5, muF = 0.5"
"muR = 0.5, muF = 1.0"
"muR = 0.5, muF = 2.0"
"muR = 1.0, muF = 0.5"
"muR = 1.0, muF = 2.0"
"muR = 2.0, muF = 0.5"
"muR = 2.0, muF = 1.0"
"muR = 2.0, muF = 2.0"
// alpha_s variations
"PDF set = 265000"
"PDF set = 266000"
// variations of nominal PDF set
"PDF set = 13100"
"PDF set = 25100"
```

For the estimate of the modelling uncertainties from the parton shower in Pythia 8 [137], several internal parameter are varied up- and downwards. In the PowhegBox + Pythia 8 the AZNLO tune is used. For the variations for this tune the prescriptions in Ref. [212, 224] are followed. The parameters which are varied are summarised in Tab. A.2.

Table A.2: Internal shower variation parameters for the PowhegBox + Pythia 8 setup using the AZNLO tune.

Variation name	Explanation
AZNLO EV1	Variation of AZNLO eigenvector 1 (ISR uncertainties only)
AZNLO EV2	Variation of AZNLO eigenvector 2 (ISR uncertainties only)
μ_R^{FSR}	Variation of the renormalisation scale for QCD emission in the FSR shower (factor 2 up/down)
MPI	Variation of the MPI cut-off scale

The variations are not included as internal "on-the-fly" weights but rather separate MC samples are generated. The variations are technically implemented by varying one or more Pythia 8 parameters by adding one of the following commands to the default configuration script shown in App. A.2.1:

```
genSeq.Pythia8.Commands += [ 'BeamRemnants:primordialKThard = 1.719',
                             'SpaceShower:pT0Ref = 1.919' ]
```

for the upward variation and

```
genSeq.Pythia8.Commands += [ 'BeamRemnants:primordialKThard = 1.780',
                             'SpaceShower:pT0Ref = 1.928' ]
```

for the downward variation of `AZNLO EV1`;

```
genSeq.Pythia8.Commands += [ 'BeamRemnants:primordialKThard = 1.762',
                             'SpaceShower:pT0Ref = 1.844' ]
```

for the upward variation and

```
genSeq.Pythia8.Commands += [ 'BeamRemnants:primordialKThard = 1.737',
                             'SpaceShower:pT0Ref = 2.004' ]
```

for the downward variatio of `AZNLO EV2`;

```
genSeq.Pythia8.Commands += [ 'TimeShower:renormMultFac = 2' ]
```

for the upward variation and;

```
genSeq.Pythia8.Commands += [ 'TimeShower:renormMultFac = 0.5' ]
```

for the downward variation of μ_R^{FSR};

```
genSeq.Pythia8.Commands += [
        'MultipartonInteractions:pT0Ref = 2.00289 + 0.200289' ]
```

for the upward variation and

```
genSeq.Pythia8.Commands += [
        'MultipartonInteractions:pT0Ref = 2.00289 - 0.200289' ]
```

for the downward variation of the MPI configuration.

A.4.2 Sherpa

The names of the generator level weights used for the evaluation of the modelling uncertainties for the Sherpa setups are listed exemplarily below.

```
// Mapping of Weights for sample
// mc15_13TeV.364286.Sherpa_222_NNPDF30NNLO_llvvjj_ss_EW4.merge.DAOD_TRUTH1.e6055_p3135

// nominal scale variations
"MUR0.5_MUF0.5_PDF261000"
"MUR0.5_MUF1_PDF261000"
"MUR1_MUF0.5_PDF261000"
"MUR1_MUF1_PDF261000"
"MUR1_MUF2_PDF261000"
"MUR2_MUF1_PDF261000"
"MUR2_MUF2_PDF261000"
// NNPDF30_nnlo_as_0118 set variations (N=100)
"MUR1_MUF1_PDF261001"
"MUR1_MUF1_PDF261002"
"MUR1_MUF1_PDF261003"
"MUR1_MUF1_PDF261004"
"MUR1_MUF1_PDF261005"
"MUR1_MUF1_PDF261006"
"MUR1_MUF1_PDF261007"
"MUR1_MUF1_PDF261008"
"MUR1_MUF1_PDF261009"
"MUR1_MUF1_PDF261010"
"MUR1_MUF1_PDF261011"
"MUR1_MUF1_PDF261012"
"MUR1_MUF1_PDF261013"
"MUR1_MUF1_PDF261014"
"MUR1_MUF1_PDF261015"
"MUR1_MUF1_PDF261016"
"MUR1_MUF1_PDF261017"
"MUR1_MUF1_PDF261018"
"MUR1_MUF1_PDF261019"
"MUR1_MUF1_PDF261020"
"MUR1_MUF1_PDF261021"
"MUR1_MUF1_PDF261022"
"MUR1_MUF1_PDF261023"
"MUR1_MUF1_PDF261024"
"MUR1_MUF1_PDF261025"
"MUR1_MUF1_PDF261026"
"MUR1_MUF1_PDF261027"
"MUR1_MUF1_PDF261028"
"MUR1_MUF1_PDF261029"
"MUR1_MUF1_PDF261030"
"MUR1_MUF1_PDF261031"
"MUR1_MUF1_PDF261032"
"MUR1_MUF1_PDF261033"
"MUR1_MUF1_PDF261034"
"MUR1_MUF1_PDF261035"
"MUR1_MUF1_PDF261036"
```

```
"MUR1_MUF1_PDF261037"
"MUR1_MUF1_PDF261038"
"MUR1_MUF1_PDF261039"
"MUR1_MUF1_PDF261040"
"MUR1_MUF1_PDF261041"
"MUR1_MUF1_PDF261042"
"MUR1_MUF1_PDF261043"
"MUR1_MUF1_PDF261044"
"MUR1_MUF1_PDF261045"
"MUR1_MUF1_PDF261046"
"MUR1_MUF1_PDF261047"
"MUR1_MUF1_PDF261048"
"MUR1_MUF1_PDF261049"
"MUR1_MUF1_PDF261050"
"MUR1_MUF1_PDF261051"
"MUR1_MUF1_PDF261052"
"MUR1_MUF1_PDF261053"
"MUR1_MUF1_PDF261054"
"MUR1_MUF1_PDF261055"
"MUR1_MUF1_PDF261056"
"MUR1_MUF1_PDF261057"
"MUR1_MUF1_PDF261058"
"MUR1_MUF1_PDF261059"
"MUR1_MUF1_PDF261060"
"MUR1_MUF1_PDF261061"
"MUR1_MUF1_PDF261062"
"MUR1_MUF1_PDF261063"
"MUR1_MUF1_PDF261064"
"MUR1_MUF1_PDF261065"
"MUR1_MUF1_PDF261066"
"MUR1_MUF1_PDF261067"
"MUR1_MUF1_PDF261068"
"MUR1_MUF1_PDF261069"
"MUR1_MUF1_PDF261070"
"MUR1_MUF1_PDF261071"
"MUR1_MUF1_PDF261072"
"MUR1_MUF1_PDF261073"
"MUR1_MUF1_PDF261074"
"MUR1_MUF1_PDF261075"
"MUR1_MUF1_PDF261076"
"MUR1_MUF1_PDF261077"
"MUR1_MUF1_PDF261078"
"MUR1_MUF1_PDF261079"
"MUR1_MUF1_PDF261080"
"MUR1_MUF1_PDF261081"
"MUR1_MUF1_PDF261082"
"MUR1_MUF1_PDF261083"
"MUR1_MUF1_PDF261084"
"MUR1_MUF1_PDF261085"
"MUR1_MUF1_PDF261086"
"MUR1_MUF1_PDF261087"
"MUR1_MUF1_PDF261088"
"MUR1_MUF1_PDF261089"
"MUR1_MUF1_PDF261090"
"MUR1_MUF1_PDF261091"
"MUR1_MUF1_PDF261092"
"MUR1_MUF1_PDF261093"
"MUR1_MUF1_PDF261094"
"MUR1_MUF1_PDF261095"
"MUR1_MUF1_PDF261096"
"MUR1_MUF1_PDF261097"
"MUR1_MUF1_PDF261098"
"MUR1_MUF1_PDF261099"
"MUR1_MUF1_PDF261100"
// alpha_s variations
"MUR1_MUF1_PDF269000"
"MUR1_MUF1_PDF270000"
// variation of nominal PDF set
"MUR1_MUF1_PDF25300"
"MUR1_MUF1_PDF13000"
```

For the estimate of the modelling uncertainties from the LO multi-jet merging via the CKKW-L method and the CSSHOWER parton shower from SHERPA, several internal parameter are varied up- and downwards. The parameters which are varied are summarised in Tab. A.3.

Table A.3: Internal LO multi-jet merging and shower variation parameters for the SHERPA setup.

Variation name	Explanation	Technical name	Variation value
μ_{CKKW}	Variation of the jet resolution scale in the ME+PS merging	`QCUT`	20^{+10}_{-5} GeV
ϵ_{QRES}	Variation of resummation scale `MU_Q2` (i.e. shower starting scale)	`QSF`	$1^{\times 2}_{\times 0.5}$
CSSKIN	Variation of kinematic recoil scheme	`CSS_KIN_SCHEME`	–

For this version of the SHERPA event generator, the variations are not included as internal "on-the-fly" weights but rather separate MC samples are generated. These have been officially produced in the ATLAS event generation machinery. Tab. A.4 specifies the MC sample information for the shower variation samples.

Table A.4: Summary of MC sample dataset ID (DSID) and derivations used for the modelling of the LO multi-jet merging and shower variation samples of the $W^{\pm}W^{\pm}jj$-EW6 and $W^{\pm}W^{\pm}jj$-EW4 processes in the SHERPA setup.

Process	DSID	Derivation
$W^{\pm}W^{\pm}jj$-EW6	364370 - 364374	TRUTH1
$W^{\pm}W^{\pm}jj$-EW4	364365 - 364369	TRUTH1

A.4.3 MG5_aMC + Pythia 8

The names of the generator level weights used for the evaluation of the modelling uncertainties for the MG5_aMC + PYTHIA 8 [137] setups are listed exemplarily below.

```
// Mapping of Weights for
// sample mc15_13TeV.367491.MGPy8EG_lvlvjj_ss_EW6_LSMT_sm_sm.DAOD_TRUTH1.e20190928_p3317

// dynamical scale choices
"dyn_scale_choice=sum pt"
"dyn_scale_choice=HT"
"dyn_scale_choice=HT/2"
"dyn_scale_choice=sqrts"
// nominal scale variations
"MUR=0.5 MUF=0.5 dyn_scale_choice=HT"
"MUR=0.5 dyn_scale_choice=HT"
"MUF=0.5 dyn_scale_choice=HT"
"MUR=0.5 MUF=2.0 dyn_scale_choice=HT"
"MUR=2.0 MUF=0.5 dyn_scale_choice=HT"
"MUF=2.0 dyn_scale_choice=HT"
"MUR=2.0 dyn_scale_choice=HT"
"MUR=2.0 MUF=2.0 dyn_scale_choice=HT"
// nominal scale variations
"MUR=0.5 MUF=0.5"
"MUR=0.5"
"MUF=0.5"
"MUR=0.5 MUF=2.0"
"MUR=2.0 MUF=0.5"
"MUR=2.0"
```

```
"MUF=2.0"
"MUR=2.0 MUF=2.0"
// NNPDF30_nlo_as_0118 set variations (N=100)
"PDF=260000 MemberID=1"
"PDF=260000 MemberID=2"
"PDF=260000 MemberID=3"
"PDF=260000 MemberID=4"
"PDF=260000 MemberID=5"
"PDF=260000 MemberID=6"
"PDF=260000 MemberID=7"
"PDF=260000 MemberID=8"
"PDF=260000 MemberID=9"
"PDF=260000 MemberID=10"
"PDF=260000 MemberID=11"
"PDF=260000 MemberID=12"
"PDF=260000 MemberID=13"
"PDF=260000 MemberID=14"
"PDF=260000 MemberID=15"
"PDF=260000 MemberID=16"
"PDF=260000 MemberID=17"
"PDF=260000 MemberID=18"
"PDF=260000 MemberID=19"
"PDF=260000 MemberID=20"
"PDF=260000 MemberID=21"
"PDF=260000 MemberID=22"
"PDF=260000 MemberID=23"
"PDF=260000 MemberID=24"
"PDF=260000 MemberID=25"
"PDF=260000 MemberID=26"
"PDF=260000 MemberID=27"
"PDF=260000 MemberID=28"
"PDF=260000 MemberID=29"
"PDF=260000 MemberID=30"
"PDF=260000 MemberID=31"
"PDF=260000 MemberID=32"
"PDF=260000 MemberID=33"
"PDF=260000 MemberID=34"
"PDF=260000 MemberID=35"
"PDF=260000 MemberID=36"
"PDF=260000 MemberID=37"
"PDF=260000 MemberID=38"
"PDF=260000 MemberID=39"
"PDF=260000 MemberID=40"
"PDF=260000 MemberID=41"
"PDF=260000 MemberID=42"
"PDF=260000 MemberID=43"
"PDF=260000 MemberID=44"
"PDF=260000 MemberID=45"
"PDF=260000 MemberID=46"
"PDF=260000 MemberID=47"
"PDF=260000 MemberID=48"
"PDF=260000 MemberID=49"
"PDF=260000 MemberID=50"
"PDF=260000 MemberID=51"
"PDF=260000 MemberID=52"
"PDF=260000 MemberID=53"
"PDF=260000 MemberID=54"
"PDF=260000 MemberID=55"
"PDF=260000 MemberID=56"
"PDF=260000 MemberID=57"
"PDF=260000 MemberID=58"
"PDF=260000 MemberID=59"
"PDF=260000 MemberID=60"
"PDF=260000 MemberID=61"
"PDF=260000 MemberID=62"
"PDF=260000 MemberID=63"
"PDF=260000 MemberID=64"
"PDF=260000 MemberID=65"
"PDF=260000 MemberID=66"
"PDF=260000 MemberID=67"
"PDF=260000 MemberID=68"
```

```
"PDF=260000 MemberID=69"
"PDF=260000 MemberID=70"
"PDF=260000 MemberID=71"
"PDF=260000 MemberID=72"
"PDF=260000 MemberID=73"
"PDF=260000 MemberID=74"
"PDF=260000 MemberID=75"
"PDF=260000 MemberID=76"
"PDF=260000 MemberID=77"
"PDF=260000 MemberID=78"
"PDF=260000 MemberID=79"
"PDF=260000 MemberID=80"
"PDF=260000 MemberID=81"
"PDF=260000 MemberID=82"
"PDF=260000 MemberID=83"
"PDF=260000 MemberID=84"
"PDF=260000 MemberID=85"
"PDF=260000 MemberID=86"
"PDF=260000 MemberID=87"
"PDF=260000 MemberID=88"
"PDF=260000 MemberID=89"
"PDF=260000 MemberID=90"
"PDF=260000 MemberID=91"
"PDF=260000 MemberID=92"
"PDF=260000 MemberID=93"
"PDF=260000 MemberID=94"
"PDF=260000 MemberID=95"
"PDF=260000 MemberID=96"
"PDF=260000 MemberID=97"
"PDF=260000 MemberID=98"
"PDF=260000 MemberID=99"
"PDF=260000 MemberID=100"
// alpha_s variations
"146"
"PDF=265000 MemberID=0"
// variation of nominal PDF set
"PDF=13100 MemberID=0"
"PDF=25200 MemberID=0"
// Pythia shower internal variations
"Var3cUp"
"Var3cDown"
"isr:muRfac=2.0_fsr:muRfac=2.0"
"isr:muRfac=2.0_fsr:muRfac=1.0"
"isr:muRfac=2.0_fsr:muRfac=0.5"
"isr:muRfac=1.0_fsr:muRfac=2.0"
"isr:muRfac=1.0_fsr:muRfac=0.5"
"isr:muRfac=0.5_fsr:muRfac=2.0"
"isr:muRfac=0.5_fsr:muRfac=1.0"
"isr:muRfac=0.5_fsr:muRfac=0.5"
"isr:muRfac=1.75_fsr:muRfac=1.0"
"isr:muRfac=1.5_fsr:muRfac=1.0"
"isr:muRfac=1.25_fsr:muRfac=1.0"
"isr:muRfac=0.625_fsr:muRfac=1.0"
"isr:muRfac=0.75_fsr:muRfac=1.0"
"isr:muRfac=0.875_fsr:muRfac=1.0"
"isr:muRfac=1.0_fsr:muRfac=1.75"
"isr:muRfac=1.0_fsr:muRfac=1.5"
"isr:muRfac=1.0_fsr:muRfac=1.25"
"isr:muRfac=1.0_fsr:muRfac=0.625"
"isr:muRfac=1.0_fsr:muRfac=0.75"
"isr:muRfac=1.0_fsr:muRfac=0.875"
"hardHi"
"hardLo"
"isr:PDF:plus"
"isr:PDF:minus"
```

For the estimate of the modelling uncertainties from the parton shower from Pythia 8, several internal parameter are varied up- and downwards. In the MG5_aMC + Pythia 8 the A14 tune [218] is used. For the variations for this tune the prescriptions in Ref. [284, 285] are followed. The parameters which are varied are summarised in Tab. A.5. They are

implemented as internal "on-the-fly" weights in the nominal MC samples.

Table A.5: Internal shower variation parameters for the MG5_aMC + Pythia 8 setup.

Variation name	Explanation	Technical name	Variation values
μ_R^{ISR}	Variation of the renormalisation scale for QCD emission in the ISR shower	`isr:muRfac`	$1^{\times 2}_{\times 0.5}$
μ_R^{FSR}	Variation of the renormalisation scale for QCD emission in the FSR shower	`fsr:muRfac`	$1^{\times 2}_{\times 0.5}$
c_{NS}^{ISR}	Variation of the inclusion of non-singular terms in QCD emissions in ISR	`hardHi/Lo`	± 2
ISR PDF	ISR internal PDF set variation via LHAPDF6 [286]	`isr:PDF:plus/minus`	

Appendix B

Additional Information on the Theoretical Studies

B.1 Sample Statistics, Generator Cross-sections, Acceptances, and Fiducial Cross-sections for All Setups

Tab. B.1 shows the statistics of all MC samples generated for the all processes and setups used in the studies of the $W^{\pm}W^{\pm}jj$ process in the SM in Chapter 6. The setup for these samples is explained in Sec. 6.3. Tab. B.2 shows the cross-section predictions of the $W^{\pm}W^{\pm}jj$-EW6 process in the respective generator phase space of each setup (summarised in Tables 6.6 and 6.7 for the Sherpa and MG5_aMC setups, respectively.) together with the acceptance and cross-section in the nominal fiducial region defined in Tab. 6.8 for all setups used in the studies of the SM $W^{\pm}W^{\pm}jj$ process in Chapter 6.

Tab. B.3 shows the cross-section predictions of the $W^{\pm}W^{\pm}jj$-EW4 process in the respective generator phase space of each setup (summarised in Tables 6.6 and 6.7 for the Sherpa and MG5_aMC setups, respectively.) together with the acceptance and cross-section in the nominal fiducial region defined in Tab. 6.8 for all setups used in this work.

Tab. B.4 shows the cross-section predictions of the $W^{\pm}W^{\pm}jj$-INT processes at LO $\mathcal{O}(\alpha_{EW}^5\alpha_S)$ and the inclusive $W^{\pm}W^{\pm}jj$ process at all leading orders in α_{EW} and α_S generated with the MG5_aMC nominal setup. The table summarises the cross-section in the generator phase space, defined in Tab. 6.7, and the acceptance and the cross-section in the fiducial region, defined in Tab. 6.8.

Tab. B.5 shows the acceptances and cross-sections in the fiducial regions defined in the CMS publication [14] with the first discovery of the $W^{\pm}W^{\pm}jj$-EW6 process and the studies in Ref. [141] for all setups used in the studies of the SM $W^{\pm}W^{\pm}jj$ process. Both phase space selection requirements are summarised in Tab. 6.9 with respect to the nominal phase space.

Table B.1: MC samples statistics for all processes and setups used in the studies of the $W^{\pm}W^{\pm}jj$ process in the SM in Chapter 6. For the PowhegBox configurations, the generation is split by charge into separate samples for the W^+W^+ and W^-W^- final states.

Sample label	Scale choice	N_{evnt}
$W^{\pm}W^{\pm}jj$-EW6 process:		
PB+Py8	fixed: m_W	365000 + 365000
PB+Py8drec		15000 + 25000
PB+H7		356400 + 361350
PB+H7DS		5000 + 10000
Sherpa23jLO	mWW	500000
	HT	10000
	SqrtPtJets	100000
	SqrtS	100000
	HT/2	100000
	fixed: m_W	100000
MG5+Py8drec	HT	150000
	mWW	50000
	SqrtPtJets	50000
	SqrtS	150000
	HT/2	150000
	fixed: m_W	50000
MG5+Py8	HT	50000
	SqrtPtJets	20000
	Cluster	5000
MG5+H7	HT	50000
SherpaLO	mWW	7590000
	HT	6050000
	SqrtPtJets	6300000
	SqrtS	5880000
	HT/2	5400000
	fixed: m_W	5660000
$W^{\pm}W^{\pm}jj$-EW4 process:		
PB+Py8 QCD	fixed: m_W	340000 + 340000
PB+H7 QCD		316250 + 331650
Sherpa23jLO QCD	fixed: m_W	7330000
	mWW	500000
MG5+Py8drec QCD	HT/2	50000
	HT	50000
	SqrtS	50000
Other process definitions:		
MG5+Py8drec INT	HT	50000
MG5+Py8drec INCL	HT	50000

Table B.2: Cross-section predictions of the $W^{\pm}W^{\pm}jj$-EW6 process in the respective generator phase space of each setup (summarised in Tables 6.6 and 6.7 for the Sherpa and MG5_aMC setups, respectively) together with the acceptance and cross-section in the nominal fiducial region defined in Tab. 6.8 for all setups used in the studies of the SM $W^{\pm}W^{\pm}jj$ process. Uncertainties are the statistical errors of the MC generation only.

Sample label	Scale choice	Generator cross-section [fb]	Acceptance fid. phase space	Fiducial cross-section [fb]
PB+Py8			0.107 ± 0.001	3.08 ± 0.02
PB+Py8drec	fixed: m_W	28.70 ± 0.05	0.104 ± 0.002	2.98 ± 0.07
PB+H7			0.106 ± 0.001	3.05 ± 0.02
Sherpa23jLO	mWW	40.80 ± 0.07	0.049 ± 0.001	2.01 ± 0.01
	HT	39.08 ± 0.41	0.050 ± 0.002	1.95 ± 0.09
	SqrtPtJets	48.08 ± 0.18	0.049 ± 0.001	2.34 ± 0.03
	SqrtS	37.93 ± 0.13	0.043 ± 0.001	1.65 ± 0.03
	HT/2	41.97 ± 0.36	0.048 ± 0.001	2.02 ± 0.03
	fixed: m_W	50.82 ± 0.21	0.059 ± 0.001	3.00 ± 0.04
MG5+Py8drec	HT	34.05 ± 0.09	0.076 ± 0.001	2.59 ± 0.02
	mWW	37.38 ± 0.17	0.083 ± 0.001	3.08 ± 0.05
	SqrtPtJets	36.41 ± 0.16	0.080 ± 0.001	2.93 ± 0.05
	SqrtS	32.29 ± 0.09	0.072 ± 0.001	2.33 ± 0.02
	HT/2	35.06 ± 0.09	0.079 ± 0.001	2.78 ± 0.03
	fixed: m_W	38.30 ± 0.17	0.086 ± 0.001	3.31 ± 0.05
MG5+Py8	HT	34.05 ± 0.15	0.071 ± 0.001	2.40 ± 0.04
	SqrtPtJets	36.39 ± 0.16	0.085 ± 0.001	3.07 ± 0.05
	Cluster	37.40 ± 0.17	0.083 ± 0.001	3.11 ± 0.05
MG5+H7	HT	34.05 ± 0.09	0.075 ± 0.001	2.56 ± 0.04
MG5+H7DS	SqrtPtJets	36.41 ± 0.16	0.088 ± 0.001	3.01 ± 0.07
SherpaLO	mWW	42.97 ± 0.02	0.061 ± 0.000	2.60 ± 0.00
	HT	42.56 ± 0.21	0.055 ± 0.000	2.34 ± 0.03
	SqrtPtJets	44.78 ± 0.21	0.067 ± 0.000	2.98 ± 0.07
	SqrtS	40.46 ± 0.20	0.052 ± 0.000	2.10 ± 0.04
	HT/2	43.69 ± 0.23	0.060 ± 0.000	2.63 ± 0.07
	fixed: m_W	47.01 ± 0.30	0.071 ± 0.000	3.32 ± 0.13

Table B.3: Cross-section predictions of the $W^{\pm}W^{\pm}jj$-EW4 process in the respective generator phase space of each setup (summarised in Tables 6.6 and 6.7 for the SHERPA and MG5_aMC setups, respectively) together with the acceptance and cross-section in the nominal fiducial region defined in Tab. 6.8 for all setups used in the studies of the SM $W^{\pm}W^{\pm}jj$ process. Uncertainties are the statistical errors of the MC generation only.

Sample label	Scale choice	Generator cross-section [fb]	Acceptance fid. phase space	Fiducial cross-section [fb]
PB+Py8 QCD	fixed: m_W	49.77 ± 0.09	0.013 ± 0.000	0.64 ± 0.01
PB+H7 QCD			0.015 ± 0.000	0.74 ± 0.01
Sherpa23jLO QCD	fixed: m_W	55.92 ± 0.23	0.021 ± 0.000	1.18 ± 0.03
	mWW	25.21 ± 0.04	0.017 ± 0.000	0.44 ± 0.00
MG5+Py8drec QCD	HT/2	21.97 ± 0.10	0.013 ± 0.001	0.29 ± 0.01
	HT	18.01 ± 0.08	0.013 ± 0.001	0.23 ± 0.01
	SqrtS	15.16 ± 0.07	0.012 ± 0.001	0.18 ± 0.01

Table B.4: Cross-section predictions of the interference between the $W^{\pm}W^{\pm}jj$-EW6 and $W^{\pm}W^{\pm}jj$-EW4 processes at LO $\mathcal{O}(\alpha_{EW}^5\alpha_S)$ and the inclusive $W^{\pm}W^{\pm}jj$ process at all leading orders in α_{EW} and α_S in the generator phase space of the MG5_aMC setup (cf. Tab. 6.7) together with the acceptance and cross-section in the nominal fiducial region defined in Tab. 6.8. Uncertainties are the statistical errors of the MC generation only.

Sample label	Scale choice	Generator cross-section [fb]	Acceptance fid. phase space	Fiducial cross-section [fb]
MG5+Py8drec INT	HT	2.52 ± 0.03	0.030 ± 0.001	0.08 ± 0.01
MG5+Py8drec INCL	HT	54.56 ± 0.24	0.044 ± 0.001	2.38 ± 0.05

Table B.5: Acceptance and cross-section predictions of the $W^{\pm}W^{\pm}jj$-EW6 process in the fiducial regions defined in the CMS publication [14] and in Ref. [141] (cf. Tab. 6.9) for all setups used in the studies of the SM $W^{\pm}W^{\pm}jj$ process. Uncertainties are the statistical errors of the MC generation only.

		Fid. PS from Ref. [14]		Fid. PS from Ref. [141]	
Sample label	Scale choice	Acceptance	Fid. cross-section [fb]	Acceptance	Fid. cross-section [fb]
PB+Py8	fixed: m_W	0.155 ± 0.001	4.44 ± 0.02	0.046 ± 0.001	1.31 ± 0.01
PB+Py8drec		0.155 ± 0.003	4.44 ± 0.09	0.044 ± 0.002	1.26 ± 0.04
PB+H7		0.175 ± 0.001	5.03 ± 0.02	0.046 ± 0.001	1.32 ± 0.01
PB+H7DS		0.149 ± 0.005	4.26 ± 0.15	0.044 ± 0.003	1.25 ± 0.07
Sherpa23jLO	mWW	0.068 ± 0.000	2.78 ± 0.02	0.020 ± 0.000	0.83 ± 0.01
	HT	0.069 ± 0.003	2.70 ± 0.10	0.021 ± 0.001	0.81 ± 0.06
	SqrtPtJets	0.069 ± 0.001	3.32 ± 0.04	0.021 ± 0.000	0.99 ± 0.02
	SqrtS	0.060 ± 0.001	2.26 ± 0.03	0.018 ± 0.000	0.66 ± 0.02
	HT/2	0.068 ± 0.001	2.83 ± 0.03	0.020 ± 0.000	0.83 ± 0.02
	fixed: m_W	0.081 ± 0.001	4.09 ± 0.05	0.024 ± 0.001	1.23 ± 0.03
MG5+Py8drec	HT	0.111 ± 0.001	3.78 ± 0.03	0.033 ± 0.001	1.12 ± 0.02
	mWW	0.119 ± 0.001	4.44 ± 0.06	0.036 ± 0.001	1.33 ± 0.03
	SqrtPtJets	0.118 ± 0.001	4.30 ± 0.06	0.034 ± 0.001	1.24 ± 0.03
	fixed: m_W	0.123 ± 0.002	4.70 ± 0.06	0.035 ± 0.001	1.35 ± 0.03
MG5+Py8	HT	0.096 ± 0.001	3.28 ± 0.05	0.030 ± 0.001	1.01 ± 0.03
	SqrtPtJets	0.120 ± 0.002	4.37 ± 0.06	0.033 ± 0.001	1.19 ± 0.05
	Cluster	0.116 ± 0.001	4.35 ± 0.06	0.035 ± 0.001	1.30 ± 0.03
MG5+H7	HT	0.108 ± 0.001	3.69 ± 0.05	0.032 ± 0.001	1.09 ± 0.03
MG5+H7DS	SqrtPtJets	0.113 ± 0.002	4.13 ± 0.08	0.034 ± 0.001	1.23 ± 0.05
SherpaLO	mWW	0.082 ± 0.000	3.53 ± 0.01	0.025 ± 0.000	1.07 ± 0.00
	HT	0.076 ± 0.000	3.23 ± 0.05	0.023 ± 0.000	0.97 ± 0.03
	SqrtPtJets	0.094 ± 0.000	4.20 ± 0.09	0.030 ± 0.000	1.36 ± 0.08
	SqrtS	0.070 ± 0.000	2.85 ± 0.06	0.023 ± 0.000	0.91 ± 0.05
	HT/2	0.085 ± 0.000	3.69 ± 0.11	0.028 ± 0.000	1.21 ± 0.09
	fixed: m_W	0.098 ± 0.000	4.60 ± 0.14	0.033 ± 0.000	1.56 ± 0.13

B.2 Comparison of Scale Settings for $W^{\pm}W^{\pm}jj$-EW4

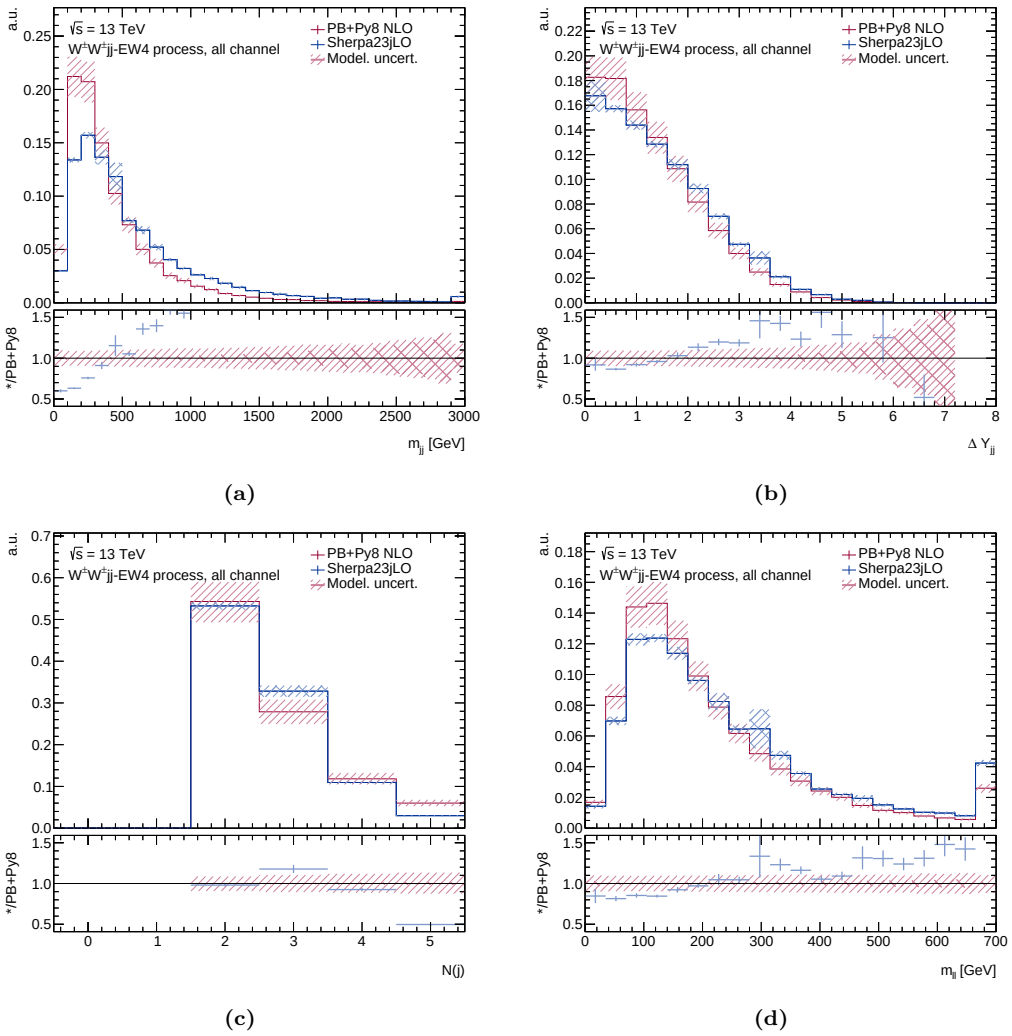


Figure B.1: Kinematic distributions comparing the different modelling setups for the $W^{\pm}W^{\pm}jj$-EW4 process, PB+Py8 (red), and Sherpa23jLO (blue), for the same scale choice m_W. Distributions are shown in the inclusive region (cf. Tab. 6.8). The invariant mass m_{jj} (a) and rapidity separation ΔY_{jj} (b) of the tagging jet system, the exclusive jet multiplicity $N(j)$ (c), and the invariant mass m_{ll} of the leading charged lepton pair (d) are shown. Distributions are normalised to unit area. The lower panel shows the relative difference with respect to the PB+Py8 prediction. The uncertainties bands are the total modelling uncertainties for the PB+Py8 prediction, while they are MC statistics only for Sherpa23jLO.

B.3 Comparison of Contributions to the $W^{\pm}W^{\pm}jj$ process

Table B.6: Summary of cross-sections for the three explicit orders at LO of the $W^{\pm}W^{\pm}jj$ process, $\mathcal{O}(\alpha_{EW}^{6}\alpha_{S}^{0})$, $\mathcal{O}(\alpha_{EW}^{4}\alpha_{S}^{2})$, and $\mathcal{O}(\alpha_{EW}^{5}\alpha_{S})$, labelled EW6, EW4 and INT, respectively, as well as their sum, labelled SUM, and the cross-section for an inclusive production of the full $W^{\pm}W^{\pm}jj$ process, labelled INCL. Relative contributions are given with respect to the sum of the three explicit contributions. Numbers are quoted for the phase space after the lepton event selection and before any jet event selection (cf. Tab. 6.8). The MG5+Py8drec setup is employed. Uncertainties are statistical uncertainties from the MC generation only.

Contribution	EW-6	EW-4	INT	SUM	INCL
Phase space after lepton event selection:					
cross-section [fb]	5.82 ± 0.06	2.74 ± 0.03	0.41 ± 0.01	8.97 ± 0.07	8.91 ± 0.10
rel. contribution to SUM	65%	30.5%	4.5%	rel. difference to SUM:	−0.67%

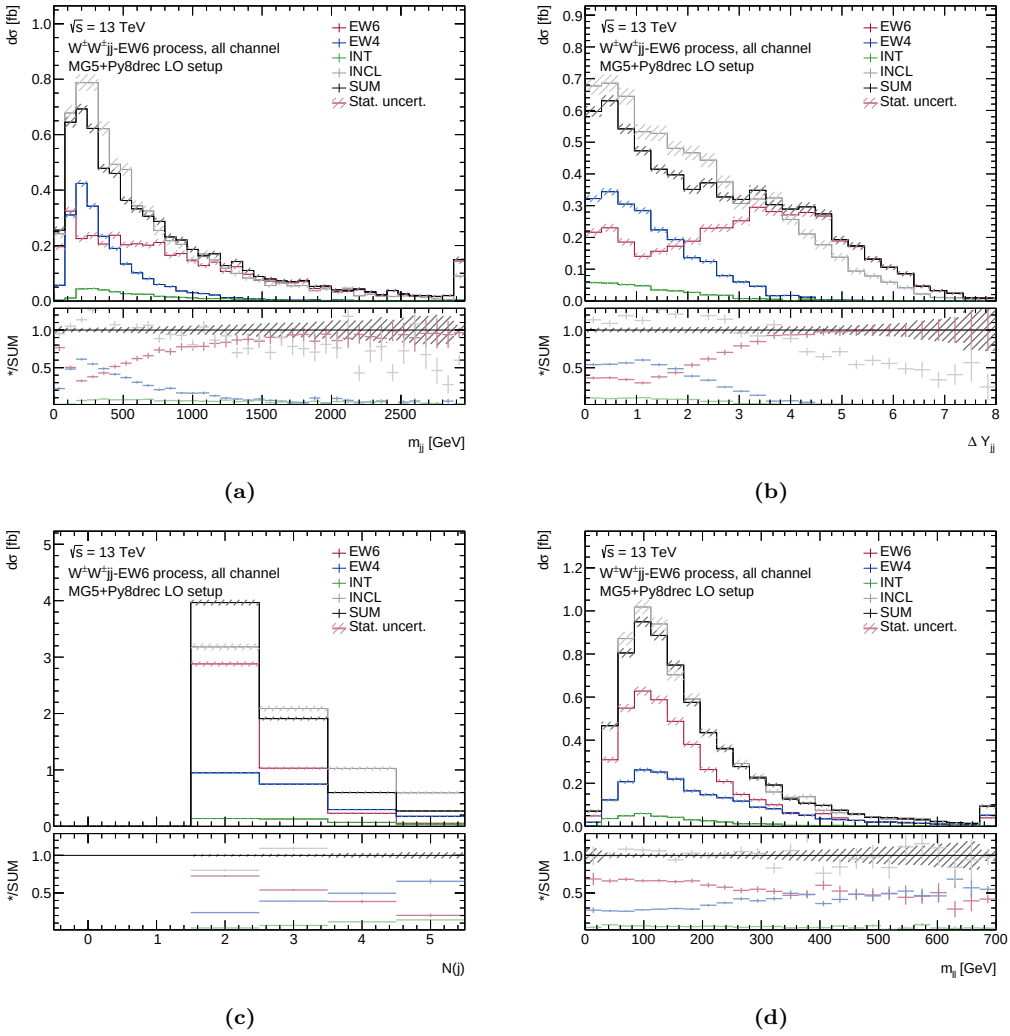


Figure B.2: Kinematic distributions comparing the LO contributions of the $W^{\pm}W^{\pm}jj$ process, the electroweak and the strong production, and its interference, labelled EW6, EW4, and INT, respectively. The sum of all contributions is also shown, labelled as SUM and compared to the inclusive prediction of the full $W^{\pm}W^{\pm}jj$ process, labelled INCL. The invariant mass m_{jj} (a) and rapidity separation ΔY_{jj} (b) of the tagging jet system, the exclusive jet multiplicity $N(j)$ (c), and the invariant mass m_{ll} of the charged lepton pair (d) are shown. Distributions are shown in the inclusive phase space (cf. Tab. 6.8). The MC samples are produced in the MG5+Py8drec setup.. The lower panel shows the relative contribution with respect to the sum. Uncertainties are statistical uncertainties from the MC generation only.

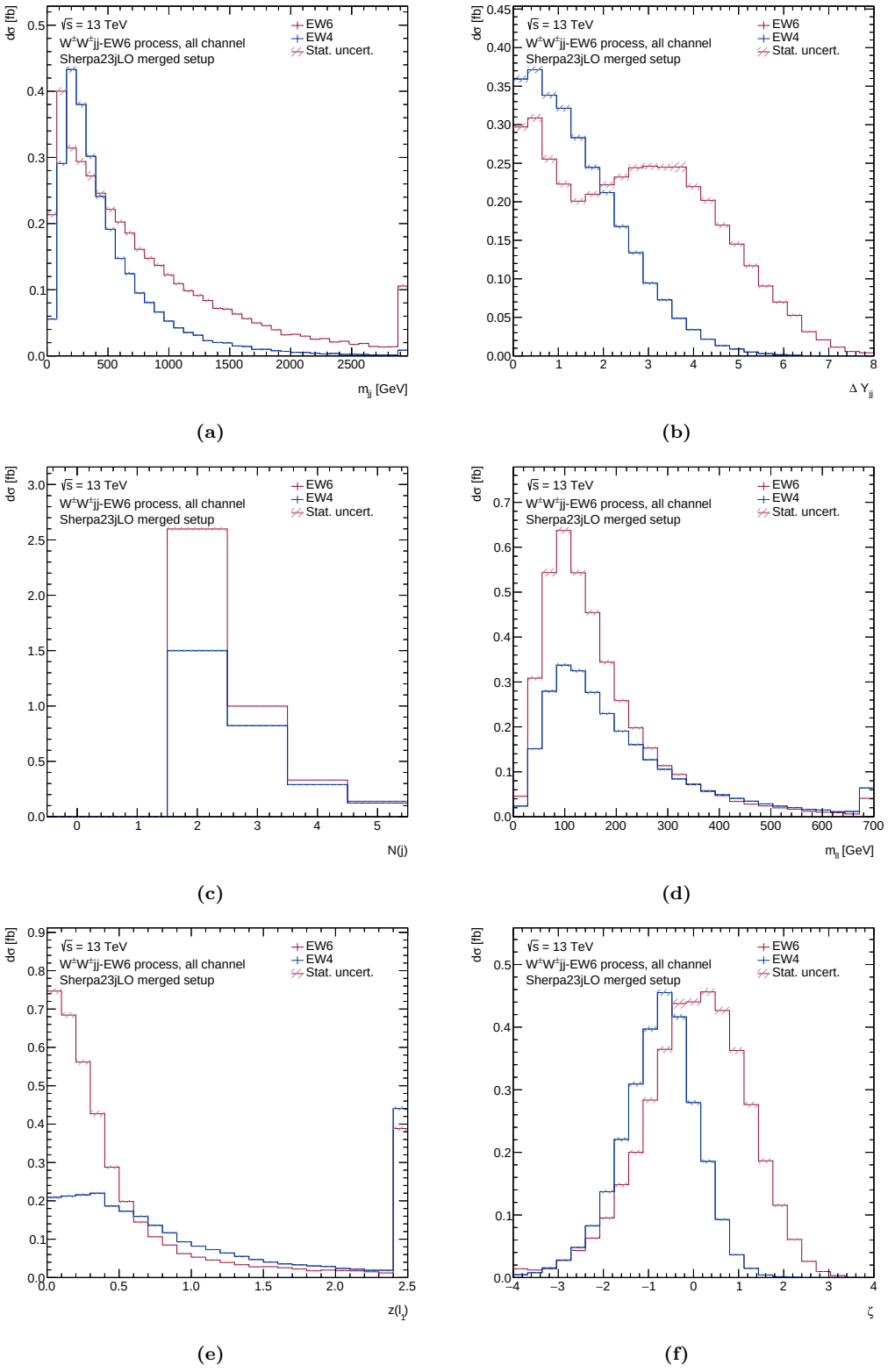


Figure B.3: Kinematic distributions comparing the $W^{\pm}W^{\pm}jj$-EW6 and $W^{\pm}W^{\pm}jj$-EW4 contributions in the Sherpa23jLO setup with the scale choice m_{WW}. The invariant mass m_{jj} (a) and rapidity separation ΔY_{jj} (b) of the tagging jet system, the exclusive jet multiplicity $N(j)$ (c), the invariant mass m_{ll} of the charged lepton pair (d), the Zeppenfeld variable of the leading charged lepton $z((l(1)))$ (e), and the lepton centrality ζ (f) are shown. Distributions are shown in the inclusive phase space (cf. Tab. 6.8). Uncertainties are statistical uncertainties from the MC generation only.

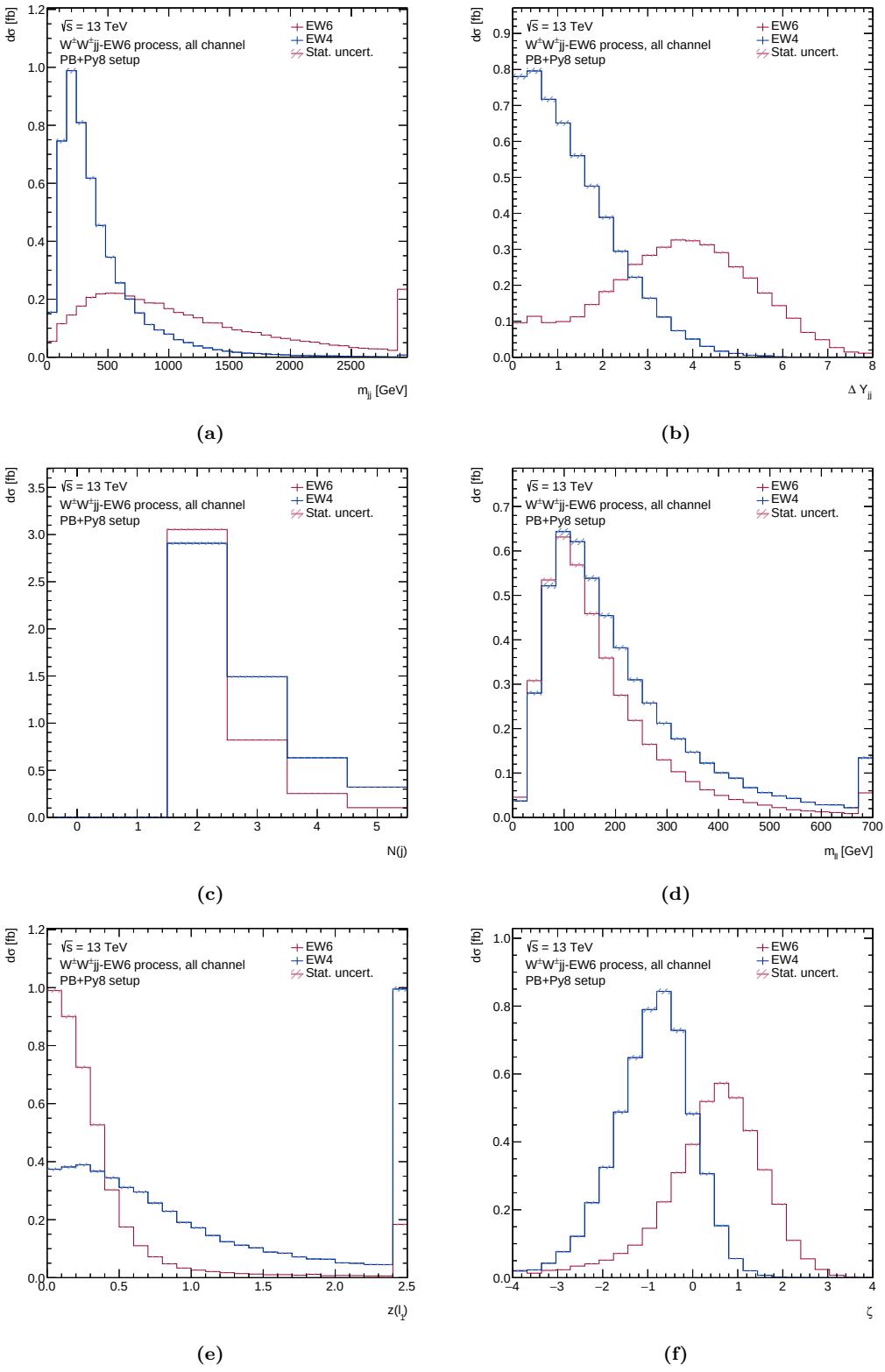


Figure B.4: Kinematic distributions comparing the LO $W^{\pm}W^{\pm}jj$-EW6 and $W^{\pm}W^{\pm}jj$-EW4 contributions in the PB+Py8 setup with the scale choice m_W. The invariant mass m_{jj} (a) and rapidity separation ΔY_{jj} (b) of the tagging jet system, the exclusive jet multiplicity $N(j)$ (c), the invariant mass m_{ll} of the charged lepton pair (d), the Zeppenfeld variable of the leading charged lepton $z((l(1)))$ (e), and the lepton centrality ζ (f) are shown. Distributions are shown in the inclusive phase space (cf. Tab. 6.8). Uncertainties are statistical uncertainties from the MC generation only.

B.4 Detailed Information on the Modelling Uncertainties

B.4.1 Detailed Perturbative QCD Matrix-element Uncertainties in the Fiducial Region

Renormalisation and Factorisation Scale Uncertainties

Tables B.7 and B.8 summarise the effects of the variation of the renormalisation and factorisation scale according to the 7-point envelope approach, detailed in Sec. 6.5.1, in the fiducial region, defined in Tab. 6.8, for the $W^{\pm}W^{\pm}jj$-EW6 and $W^{\pm}W^{\pm}jj$-EW4 processes, respectively.

Table B.7: Relative renormalisation and factorisation scale variations in the matrix element calculation with the 7-point envelope approach for the $W^{\pm}W^{\pm}jj$-EW6 process in the nominal setups with PowhegBox + Pythia 8, Sherpa, and MG5_aMC + Pythia 8 in the fiducial region, defined in Tab. 6.8 for the combined lepton flavour channel $\ell^{\pm}\ell^{\pm}$.

		Relative variations [%]		
ε_F	ε_R	PB+Py8	Sherpa23jLO	MG5+Py8drec
1.0	0.5	−0.94	+6.79	–
1.0	2.0	+0.75	−5.13	–
0.5	1.0	+0.39	+7.76	+7.35
2.0	1.0	+0.18	−6.77	−6.47
0.5	0.5	−1.75	+15.07	+7.35
2.0	2.0	+0.07	−11.56	−6.47

Table B.8: Relative renormalisation and factorisation scale variations in the matrix element calculation with the 7-point envelope approach for the $W^{\pm}W^{\pm}jj$-EW4 process in the nominal setups with PowhegBox + Pythia 8, Sherpa, and MG5_aMC + Pythia 8 in the fiducial region, defined in Tab. 6.8 for the combined lepton flavour channel $\ell^{\pm}\ell^{\pm}$.

		Relative variations [%]		
ε_F	ε_R	PB+Py8	Sherpa23jLO	MG5+Py8drec
1.0	0.5	+9.85	+29.67	+18.17
1.0	2.0	−9.27	−20.02	−14.23
0.5	1.0	+2.77	+6.71	+5.93
2.0	1.0	−2.24	−5.97	−5.35
0.5	0.5	+12.04	+38.36	+25.15
2.0	2.0	−11.79	−24.80	−18.83

PDF and α_S Uncertainties

Tables B.9 and B.10 summarise the effects of the variation of the internal eigenvectors of the nominal PDF set, its nominal value for the evolution of the strong coupling constant α_S, and the variation due to alternating the nominal PDF set from the NNPDF3.0 to the CT14 or MMHT2014 set in the fiducial region, defined in Tab. 6.8, for the $W^{\pm}W^{\pm}jj$-EW6 and $W^{\pm}W^{\pm}jj$-EW4 processes, respectively. The variation procedures are detailed in Sec. 6.5.1.

Table B.9: Relative PDF set variations including α_S variations in the matrix element calculation for the $W^{\pm}W^{\pm}jj$-EW6 process in the nominal setups with PowhegBox + Pythia 8, Sherpa, and MG5_aMC + Pythia 8 in the fiducial region, defined in Tab. 6.8 for the combined lepton flavour channel $\ell^{\pm}\ell^{\pm}$.

Sample label	PB+Py8	Sherpa23jLO	MG5+Py8drec
Nominal PDF set	NNPDF3.0nlo	NNPDF3.0nnlo	NNPDF3.0nlo
PDF error type		Relative variations [%]	
Internal variations	±1.65	±1.54	±1.59
Difference w.r.t. nominal:			
CT14	+0.48	+1.24	+0.46
MMHT2014	+0.88	+2.29	+0.48
α_S variations	±0.06	+0.34 −0.27	+0.03 −0.29

Table B.10: Relative PDF set variations including α_S variations in the matrix element calculation for the $W^{\pm}W^{\pm}jj$-EW4 process in the nominal setups with PowhegBox + Pythia 8, Sherpa, and MG5_aMC + Pythia 8 in the fiducial region, defined in Tab. 6.8 for the combined lepton flavour channel $\ell^{\pm}\ell^{\pm}$.

Sample label	PB+Py8	Sherpa23jLO	MG5+Py8drec
Nominal PDF set	NNPDF3.0nlo	NNPDF3.0nnlo	NNPDF3.0nlo
PDF error type		Relative variations [%]	
Internal variations	–	±1.54	±1.61
Difference w.r.t. nominal:			
CT14	+0.36	+0.73	+0.57
MMHT2014	+4.02	+2.07	+0.87
α_S variations	+1.49 −1.67	+2.00 −1.86	+1.03 −1.45

B.4.2 Impact of Internal Shower Parameter Variations

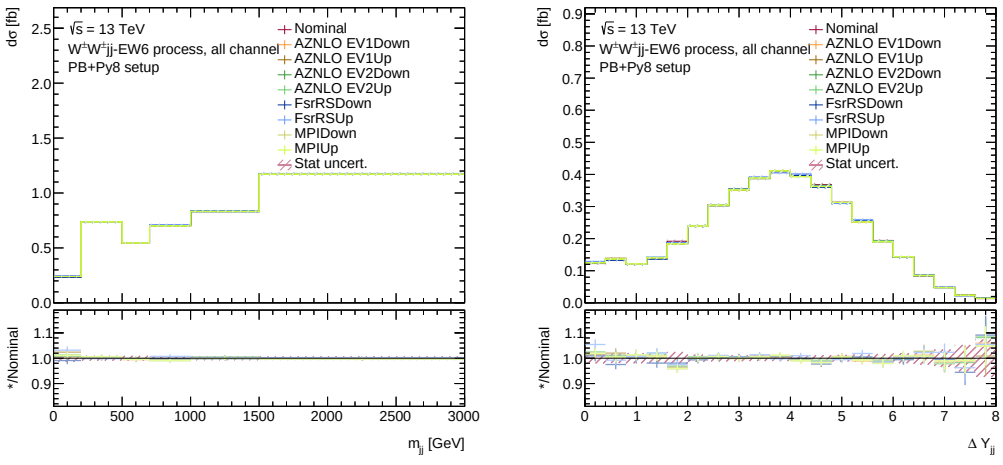
PowhegBox + Pythia 8

Tab. B.11 summarises the effects of the variation of the internal parameters of the nominal Pythia 8 tune AZNLO in the PB+Py8 setup in the fiducial region, defined in Tab. 6.8, for the $W^{\pm}W^{\pm}jj$-EW6 and $W^{\pm}W^{\pm}jj$-EW4 processes, respectively. The variations are defined in Sec. A.4.1 and the procedures are detailed in Sec. 6.5.2.

Table B.11: Relative internal shower variation as explained in Tab A.2 for the $W^{\pm}W^{\pm}jj$-EW6 and $W^{\pm}W^{\pm}jj$-EW4 processes for the PB+Py8 setup in the fiducial region for the combined lepton flavour channel $\ell^{\pm}\ell^{\pm}$.

Variation name	Relative variations [%]	
	$W^{\pm}W^{\pm}jj$-EW6	$W^{\pm}W^{\pm}jj$-EW4
AZNLO EV1 down	−0.34	−0.39
AZNLO EV1 up	−0.29	−0.13
AZNLO EV2 down	−0.29	−0.21
AZNLO EV2 up	−0.22	+0.15
$\mu_R^{\mathrm{FSR}} \times 0.5$	−0.33	−2.00
$\mu_R^{\mathrm{FSR}} \times 2$	+0.18	+0.20
MPI down	−0.41	+0.06
MPI up	−0.41	+0.06

Figures B.5 and B.6 show the impact of the variations of the shower modelling parameters of the PB+Py8 setup in the fiducial region before applying selections on the invariant mass m_{jj} and the rapidity separation ΔY_{jj} of the tagging jet system, defined in Tab. 6.8, for the $W^{\pm}W^{\pm}jj$-EW6 and $W^{\pm}W^{\pm}jj$-EW4 processes, respectively.

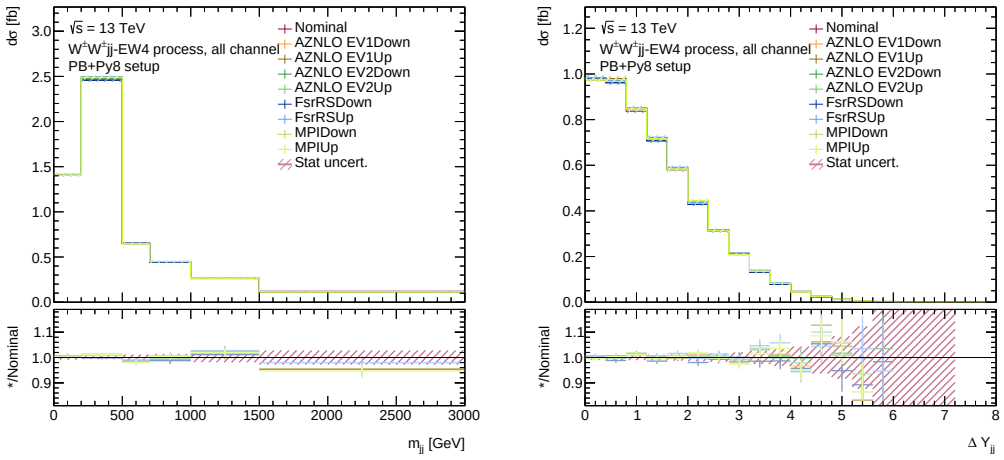


(a) **(b)**

Figure B.5: Distributions of the invariant mass m_{jj} and rapidity separation ΔY_{jj} of the tagging jet system for the nominal PB+Py8 setup and its variation of the Pythia 8 internal parameters, as explained in Sec. A.4.1 in the fiducial region before applying selections on m_{jj} and ΔY_{jj} (cf. Tab. 6.8), for the $W^{\pm}W^{\pm}jj$-EW6 process. Uncertainties are statistical uncertainties from the MC generation only.

Sherpa

Tab. B.12 summarises the effects of the variation of the internal parameters of the nominal Sherpa parton shower model in the Sherpa23jLO setup in the fiducial region, defined in



(a) **(b)**

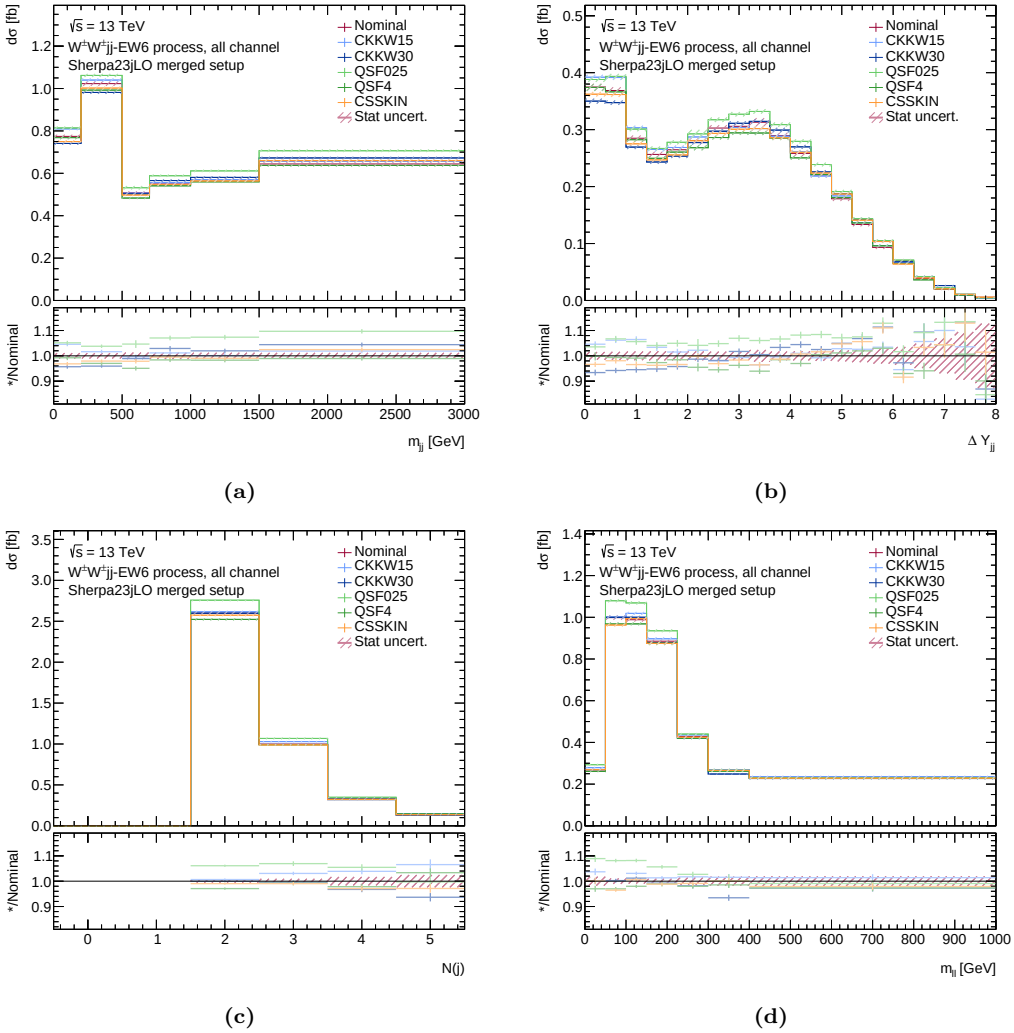
Figure B.6: Distributions of the invariant mass m_{jj} and rapidity separation ΔY_{jj} of the tagging jet system for the nominal PB+Py8 setup and its variation of the PYTHIA 8 internal parameters, as explained in Sec. A.4.1 in the fiducial region before applying selections on m_{jj} and ΔY_{jj} (cf. Tab. 6.8), for the $W^{\pm}W^{\pm}jj$-EW4 process. Uncertainties are statistical uncertainties from the MC generation only.

Tab. 6.8, for the $W^{\pm}W^{\pm}jj$-EW6 and $W^{\pm}W^{\pm}jj$-EW4 processes, respectively. The variations are defined in Sec. A.4.2 and the procedures are detailed in Sec. 6.5.2.

Table B.12: Relative internal LO CKKW-L multi-jet merging and shower variations as explained in Tab A.3 for the $W^{\pm}W^{\pm}jj$-EW6 and $W^{\pm}W^{\pm}jj$-EW4 processes in the fiducial region for the Sherpa23jLO setup for teh combined lepton flavour channel $\ell^{\pm}\ell^{\pm}$.

Variation name	Relative variations [%]	
	$W^{\pm}W^{\pm}jj$-EW6	$W^{\pm}W^{\pm}jj$-EW4
$\mu_{\text{CKKW}} - 5\,\text{GeV}$	+0.65	+4.16
$\mu_{\text{CKKW}} + 10\,\text{GeV}$	+3, 46	−5.53
$\varepsilon_{\text{QRES}} = 0.5$	+7.80	+3.88
$\varepsilon_{\text{QRES}} = 2$	−1.86	−1.53
CSSKIN scheme	+0.49	+1.67

Figures B.7 and B.8 show the impact of the variations of the merging scale and parton shower modelling parameters of the Sherpa23jLO setup in the fiducial region before applying selections on the invariant mass m_{jj} and the rapidity separation ΔY_{jj} of the tagging jet system, defined in Tab. 6.8, for the $W^{\pm}W^{\pm}jj$-EW6 and $W^{\pm}W^{\pm}jj$-EW4 processes, respectively.



(a) **(b)**

(c) **(d)**

Figure B.7: Kinematic distributions for the nominal Sherpa23jLO setup and its variation of the merging scale and internal parton shower parameters, as explained in Sec. A.4.2 in the fiducial region before applying selections on m_{jj} and ΔY_{jj} (cf. Tab. 6.8), for the $W^{\pm}W^{\pm}jj$-EW6 process. Shown are the m_{jj} (a) and ΔY_{jj} (b), the exclusive jet multiplicity $N(j)$ (c), and the invariant mass of the two leading charged leptons m_{ll} (d) in the event. Uncertainties are statistical uncertainties from the MC generation only.

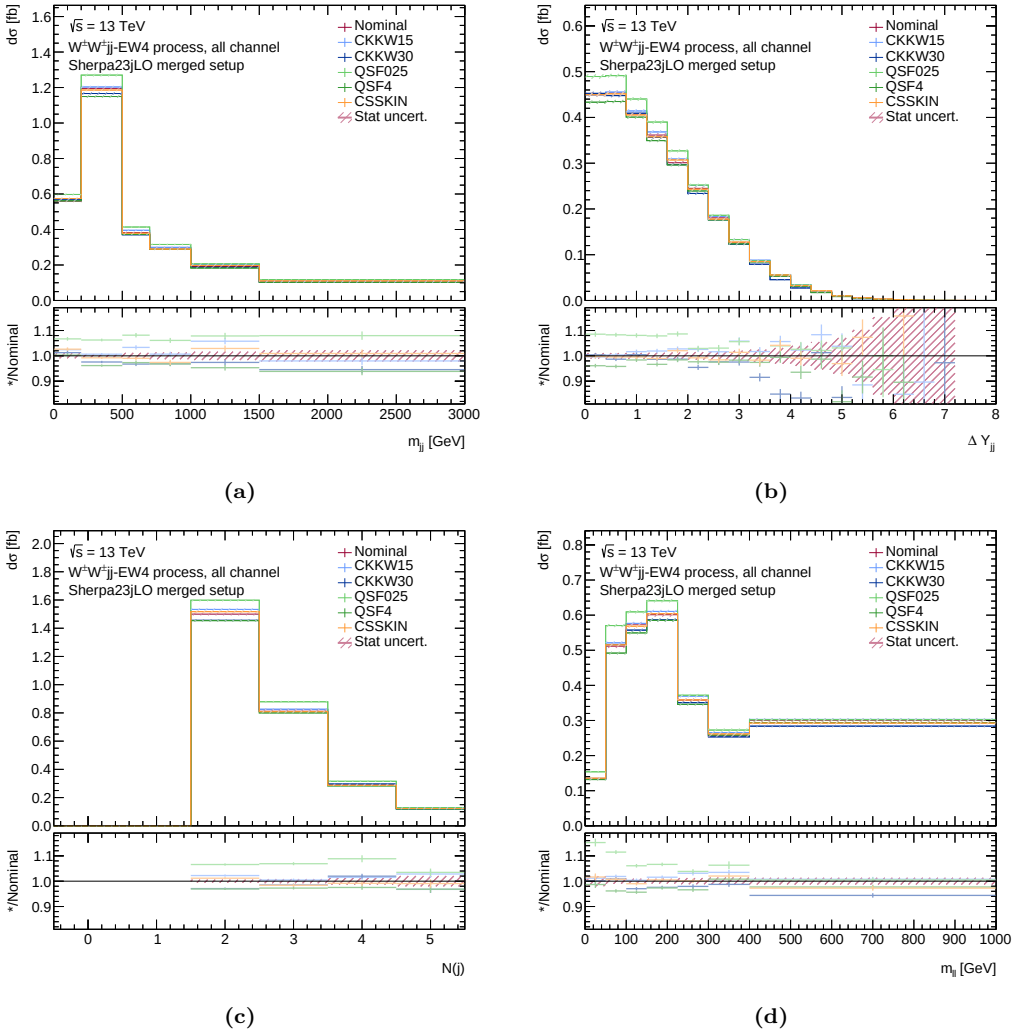


Figure B.8: Kinematic distributions for the nominal Sherpa23jLO setup and its variation of the merging scale and internal parton shower parameters, as explained in Sec. A.4.2 in the fiducial region before applying selections on m_{jj} and ΔY_{jj} (cf. Tab. 6.8), for the $W^{\pm}W^{\pm}jj$-EW4 process. Shown are the m_{jj} (a) and ΔY_{jj} (b), the exclusive jet multiplicity $N(j)$ (c), and the invariant mass of the two leading charged leptons m_{ll} (d) in the event. Uncertainties are statistical uncertainties from the MC generation only.

MG5_aMC + Pythia 8

Tab. B.13 summarises the effects of the variation of the internal parameters of the nominal Pythia 8 parton shower tun A14 in the MG5+Py8drec setup in the fiducial region, defined in Tab. 6.8, for the $W^{\pm}W^{\pm}jj$-EW6 and $W^{\pm}W^{\pm}jj$-EW4 processes, respectively. The variations are defined in Sec. A.4.3 and the procedures are detailed in Sec. 6.5.2. The input to the renormalisation scale variation envelope in the parton shower evolution is detailed in Tab. B.14 for this setup.

Table B.13: Relative internal shower variation as explained in Tab A.5 for the $W^{\pm}W^{\pm}jj$-EW6 and $W^{\pm}W^{\pm}jj$-EW4 processes in the fiducial region for the combined lepton flavour channel $\ell^{\pm}\ell^{\pm}$.

Variation name	Relative variations [%]	
	$W^{\pm}W^{\pm}jj$-EW6	$W^{\pm}W^{\pm}jj$-EW4
$\mu_R^{\mathrm{ISR+FSR}}$ envelope down	−0.16	+1.82
$\mu_R^{\mathrm{ISR+FSR}}$ envelope up	+3.78	−13.73
c_{NS}^{ISR} down	+0.02	−1.55
c_{NS}^{ISR} up	+0.84	+2.22
ISR PDF down	+0.27	−0.96
ISR PDF up	+0.33	+1.50

Table B.14: Relative shower ISR/FSR renormalisation scale variations as explained in Tab A.5 for the $W^{\pm}W^{\pm}jj$-EW6 and $W^{\pm}W^{\pm}jj$-EW4 processes in the fiducial region for the combined lepton flavour channel $\ell^{\pm}\ell^{\pm}$.

Variation		Relative variations [%]	
$\varepsilon_R^{\mathrm{ISR}}$	$\varepsilon_R^{\mathrm{FSR}}$	$W^{\pm}W^{\pm}jj$-EW6	$W^{\pm}W^{\pm}jj$-EW4
1.0	0.5	+2.00	−7.89
1.0	2.0	+0.02	+1.50
0.5	1.0	+0.57	−1.03
2.0	1.0	−0.16	+1.82
0.5	0.5	+0.36	−2.07
2.0	2.0	+3.78	−13.73

Figures B.9 and B.10 show the impact of the variations of the parton shower modelling parameters of the MG5+Py8drec setup in the fiducial region before applying selections on the invariant mass m_{jj} and the rapidity separation ΔY_{jj} of the tagging jet system, defined in Tab. 6.8, for the $W^{\pm}W^{\pm}jj$-EW6 and $W^{\pm}W^{\pm}jj$-EW4 processes, respectively.

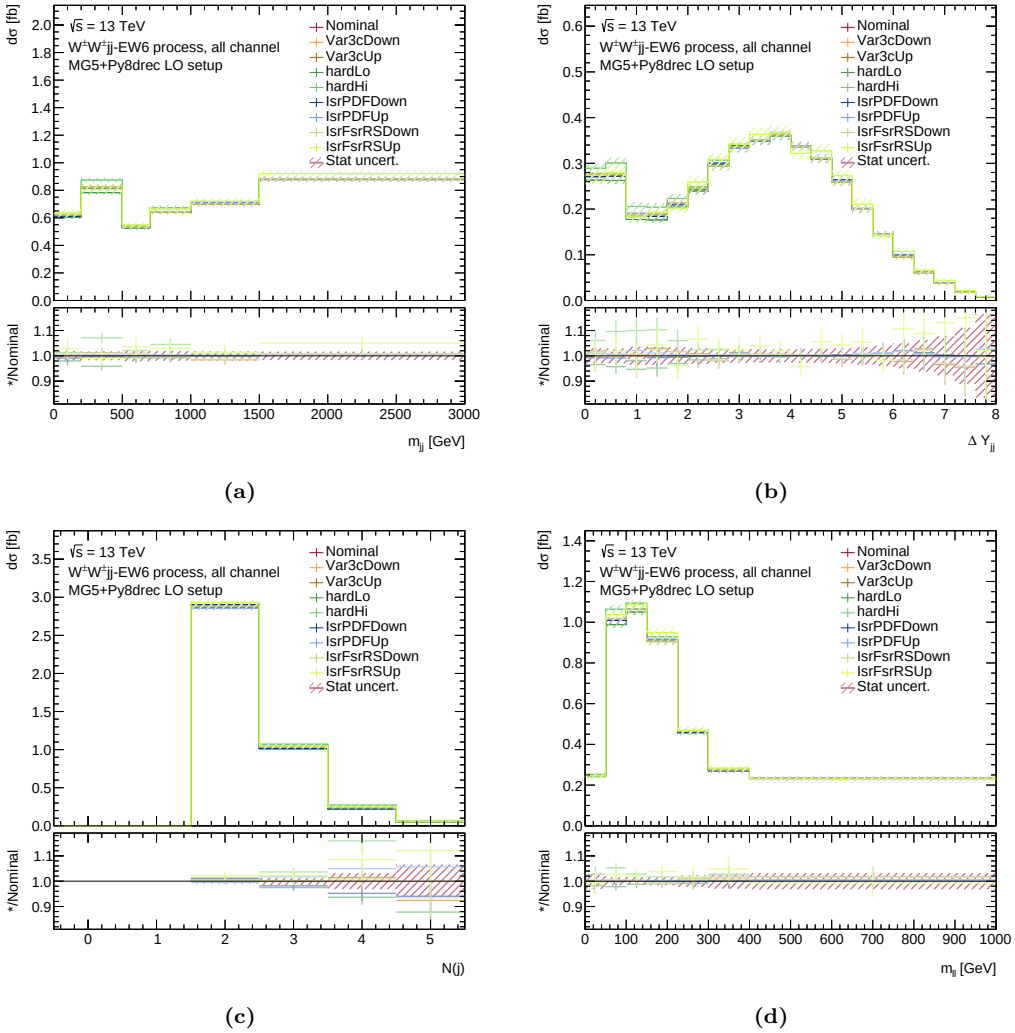


Figure B.9: Kinematic distributions for the nominal MG5+Py8drec setup and its variation of the internal parton shower parameters, as explained in Sec. A.4.3 in the fiducial region before applying selections on m_{jj} and ΔY_{jj} (cf. Tab. 6.8), for the $W^{\pm}W^{\pm}jj$-EW6 process. Shown are the m_{jj} (a) and ΔY_{jj} (b), the exclusive jet multiplicity $N(j)$ (c), and the invariant mass of the two leading charged leptons m_{ll} (d) in the event. Uncertainties are statistical uncertainties from the MC generation only.

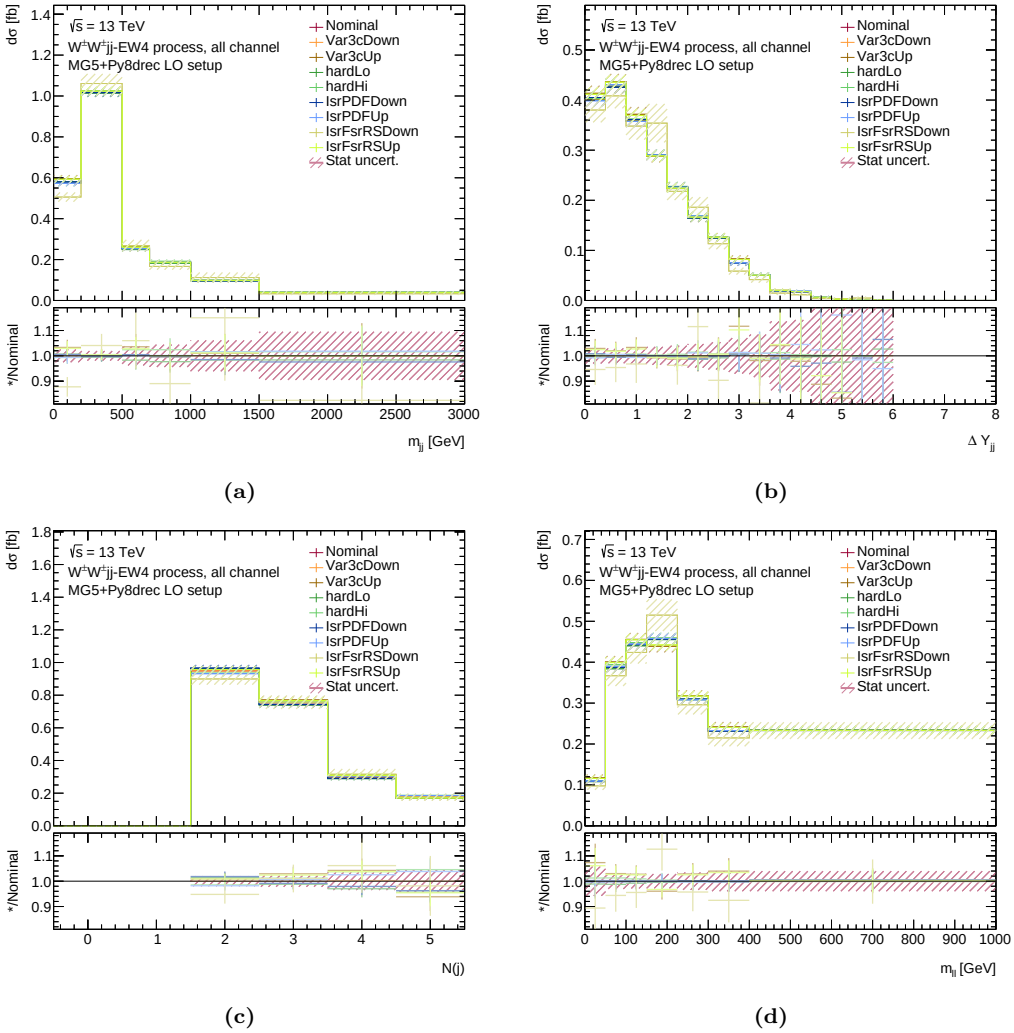


Figure B.10: Kinematic distributions for the nominal MG5+Py8drec setup and its variation of the internal parton shower parameters, as explained in Sec. A.4.3 in the fiducial region before applying selections on m_{jj} and ΔY_{jj} (cf. Tab. 6.8), for the $W^{\pm}W^{\pm}jj$-EW4 process. Shown are the m_{jj} (a) and ΔY_{jj} (b), the exclusive jet multiplicity $N(j)$ (c), and the invariant mass of the two leading charged leptons m_{ll} (d) in the event. Uncertainties are statistical uncertainties from the MC generation only.

B.5 Comparison of Scale Settings

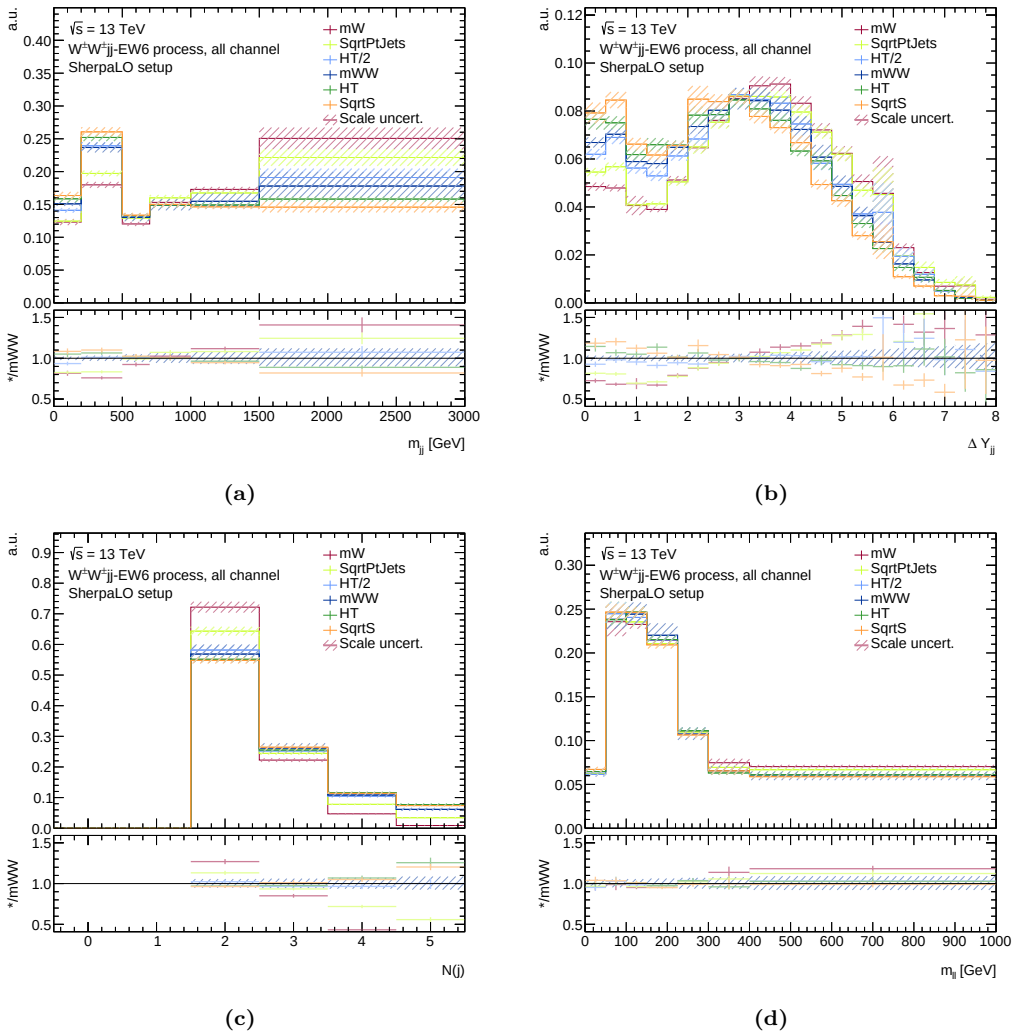


Figure B.11: Kinematic distributions comparing the predictions of the SherpaLO setup for the $W^{\pm}W^{\pm}jj$-EW6 process, for six different scale choices as defined in Sec. 6.7.1. The invariant mass m_{jj} (a) and rapidity separation ΔY_{jj} (b) of the tagging jet system, the exclusive jet multiplicity $N(j)$ (c), and the invariant mass m_{ll} of the leading charged lepton pair (d) are shown. Distributions are shown in the inclusive region (cf. Tab. 6.8) and are normalised to unit area. The lower panel shows the relative difference with respect to the predictions employing the nominal scale m_{WW}. The uncertainties bands are from the MC statistics only, except for the default setup which includes scale uncertainties from the envelope approach.

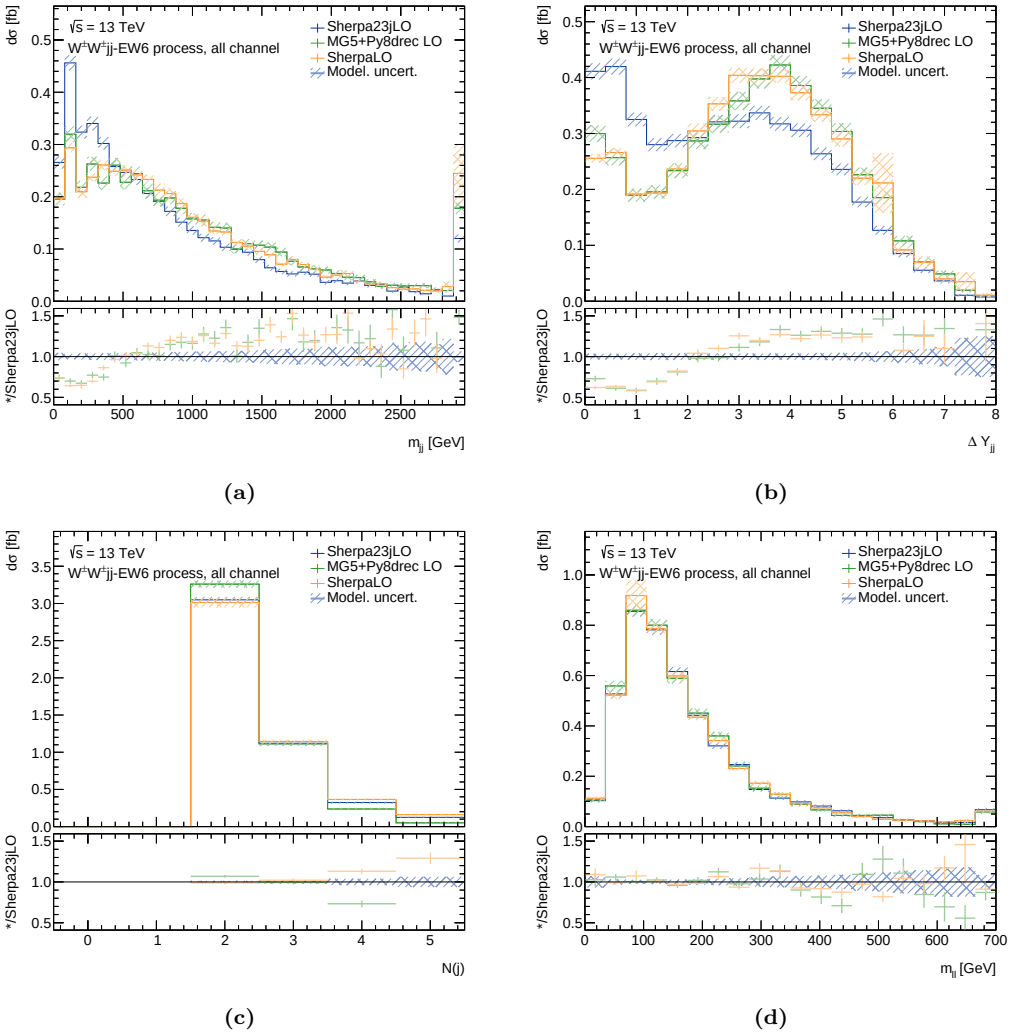


Figure B.12: Kinematic distributions comparing the different modelling setups for the $W^{\pm}W^{\pm}jj$-EW6 process, Sherpa23jLO (blue), MG5+Py8drec (green), and SherpaLO (orange), for the same dynamical scale choice SqrtPtJets, defined in Eq. (6.9). The invariant mass m_{jj} (a) and rapidity separation ΔY_{jj} (b) of the tagging jet system, the exclusive jet multiplicity $N(j)$ (c), and the invariant mass m_{ll} of the leading charged lepton pair (d) are shown. Distributions are shown in the inclusive region (cf. Tab. 6.8). The lower panel shows the relative difference with respect to the Sherpa23jLO prediction. The uncertainties bands are from the MC statistics only.

B.6 Comparison of Shower Configurations

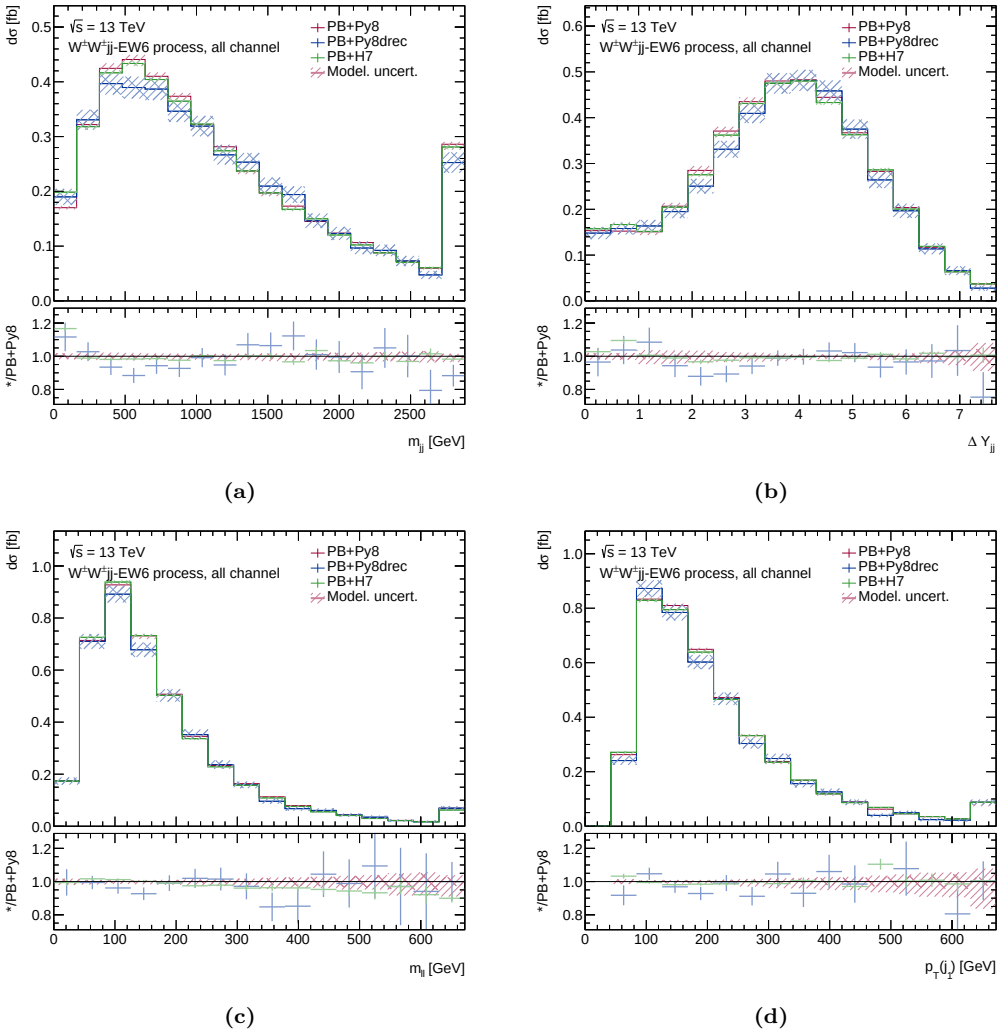


Figure B.13: Kinematic distributions comparing the predictions of different parton shower setups at NLO QCD accuracy of the $W^{\pm}W^{\pm}jj$-EW6 process with the POWHEG-BOX MC event generator. The nominal setup PB+Py8, using PYTHIA 8 with the default global recoil option, is compared against the a PYTHIA 8 setup with the dipole recoil scheme (PB+Py8drec) and the default HERWIG 7 setup (PB+H7). The invariant mass m_{jj} (a) and rapidity separation ΔY_{jj} (b) of the tagging jet system, the invariant mass of the two leading charged leptons, m_{ll} (c), and the leading jet transverse momentum (d) are shown. Distributions are shown in the inclusive region (cf. Tab. 6.8). The lower panel shows the relative difference with respect to the nominal setup PB+Py8. The uncertainties bands are from the MC statistics only, except for the default setup which includes uncertainties from the internal parton shower variations.

B.7 Effect of the QED FSR Radiation in the Parton Shower

The MC sample for the studies in Sec. 6.7.5 is generated with the SHERPA event generation programme. The nominal setup of the Sherpa23jLO sample is altered with adding the command to the default job options (cf. Sec. A.2.2):

```
ME_QED=Off;
```

which turns off the resummed higher order QED corrections to the matrix element in final state particles that do not interact via the strong force (i.e. all particles except quarks and gluons, which means QED corrections to Hadron decays are not affected) [133]. Tab. B.15 displays the sample statistics and Tab. B.16 summarises the generator cross-section, as well as the acceptance into and the cross-section in the fiducial region.

Table B.15: MC samples statistics for the generation of the $W^{\pm}W^{\pm}jj$-EW6 process with the Sherpa23jLO setup with QED FSR radiation switched off used in the studies in Sec. 6.7.5.

Sample label	Scale choice	N_{evnt}
Sherpa23jLO w/o QED FSR	mWW	10000000

Table B.16: Cross-section predictions of the $W^{\pm}W^{\pm}jj$-EW6 process in the respective generator phase space (summarised in Tab. 6.6) together with the acceptance and cross-section in the nominal fiducial region defined in Tab. 6.8 for the Sherpa23jLO setup with QED FSR radiation switched off. Uncertainties are the statistical errors of the MC generation only.

Sample label	Scale choice	Generator cross-section [fb]	Acceptance fid. phase space	Fiducial cross-section [fb]
Sherpa23jLO w/o QED FSR	mWW	39.66 ± 0.38	0.049 ± 0.001	1.93 ± 0.05

Fig. B.14 shows the selection sequence and differential distributions comparing the predictions of the $W^{\pm}W^{\pm}jj$-EW6 process with the nominal SHERPA setup with and without the QED FSR in the parton shower prescription.

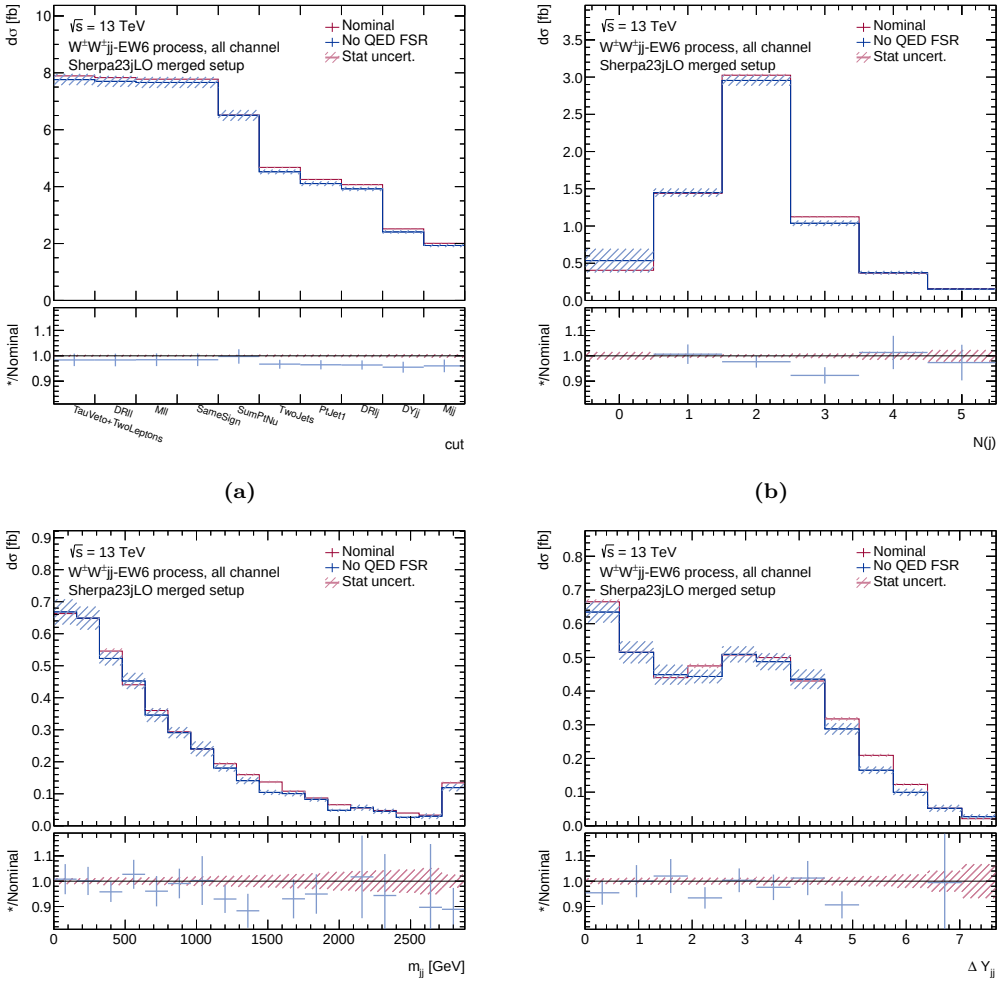


Figure B.14: Selection sequence (a) and differential distributions (b)-(d) comparing the predictions of the $W^{\pm}W^{\pm}jj$-EW6 process with and without QED FSR in the parton shower with the nominal Sherpa setup Sherpa23jLO. The inclusive jet multiplicity $N(j)$ (b) is shown in the region after the lepton event selection (cf. Tab. 6.8). The invariant mass m_{jj} (c) and ΔY_{jj} (d) distributions of the tagging jet pair is shown in the inclusive region. Uncertainties on the distributions include the MC statistical error only.

Appendix C

Details of MC Simulated Event Samples at Reconstruction Level

Unless stated otherwise, all MC simulated samples used in this thesis use the following configurations:

- MC Production campaign `MC15c` of the `mc15_13TeV` scope with pile-up profile guess for combined average 2015+2016 data-taking,
- Detector simulation tag `s2726`,
- Reconstruction tags `r7772_r7676`,
- `STDM3` derivation with tags `p3314` and `p3317` for skimmed and unskimmed production, respectively.

This appendix summarises the details for the reconstruction level MC simulated samples for all SM processes, i.e. all signal and background processes relevant in this thesis, as well as for the EFT predictions.

C.1 Reconstruction Level SM Samples

Extensive details on the event generation of the signal process $W^{\pm}W^{\pm}jj$-EW6, as well as the QCD-induced background process $W^{\pm}W^{\pm}jj$-EW4 are given in Chapter 6 and the corresponding Appendix A. Nevertheless, a list of the details of those samples which have been generated within the official ATLAS MC production framework is included in this appendix for completeness and serves as an example for describing the information shown. It is shown in Tab. C.1.

The sample description includes information such as the name (and sometimes the version) of the generator (Sherpa v.2.2.2 and PowhegBox +Pythia 8), the PDF set used

Table C.1: Event simulation details for the signal process $W^{\pm}W^{\pm}jj$-EW6 and the QCD-induced background process $W^{\pm}W^{\pm}jj$-EW4, including the dataset ID (DSID), sample description (see text for details), ATLAS MC production tag, generator cross-section times branching ratio $\sigma \equiv \sigma^{\text{gen}} \cdot \text{BR}$, higher order correction factor k, and filter efficiency ε.

DSID	Sample description	Tags	σ [fb]	k	ε
364286	Sherpa_222_NNPDF30NNLO_llvvjj_ss_EW4	e6055	25.211	1.0	1.0
364287	Sherpa_222_NNPDF30NNLO_llvvjj_ss_EW6	e6055	40.804	1.0	1.0
363995	PhPy8EG_NNPDF30NLO_AZNLOC6L1_EWK_WmWm	e5678	7.805	1.0	1.0
363996	PhPy8EG_NNPDF30NLO_AZNLOC6L1_EWK_WpWp	e5678	20.891	1.0	1.0
363997	PhPy8EG_NNPDF30NLO_AZNLOC6L1_QCD_WmWm	e5678	15.692	1.0	1.0
363998	PhPy8EG_NNPDF30NLO_AZNLOC6L1_QCD_WpWp	e5678	34.080	1.0	1.0

Table C.2: Event simulation details for the diboson processes used in the analysis, including the dataset ID (DSID), sample description (see text for details), ATLAS MC production tag, generator cross-section times branching ratio $\sigma \equiv \sigma^{\text{gen}} \cdot \text{BR}$, higher order correction factor k, and filter efficiency ε.

DSID	Sample Description	Tags	σ [fb]	k	ε
363356	Sherpa_221_NNPDF30NNLO_ZqqZll	e5525	15561	1.0	0.14024
363358	Sherpa_221_NNPDF30NNLO_WqqZll	e5525	3433.0	1.0	1.0
364250	Sherpa_222_NNPDF30NNLO_llll	e5894	1252.3	1.0	1.0
364253	Sherpa_222_NNPDF30NNLO_lllv	e5916	4581.6	1.0	1.0
364254	Sherpa_222_NNPDF30NNLO_llvv	e5916	12500	1.0	1.0
361073	Sherpa_CT10_gglllll	e3836	20.743	1.5470	1.0
361077	Sherpa_CT10_ggllvv	e4641	854.22	0.91	1.0
364283	Sherpa_222_NNPDF30NNLO_llllljj_EW6	e6055	10.523	1.0	1.0
364284	Sherpa_222_NNPDF30NNLO_lllvjj_EW6	e6055	46.691	1.0	1.0
364285	Sherpa_222_NNPDF30NNLO_llvvjj_EW6	e6055	116.21	1.0	1.0

Table C.3: Event simulation details for the evaluation of the parton shower modelling uncertainties of the $W^{\pm}Z$ process, including the dataset ID (DSID), sample description (see text for details), ATLAS MC production tag, and generator cross-section times branching ratio $\sigma \equiv \sigma^{\text{gen}} \cdot \text{BR}$. Higher order correction factor k and filter efficiency ε are equal to 1.

DSID	Sample Description	Tags	σ [fb]
361601	PowhegPy8EG_CT10nloME_AZNLOCTEQ6L1_WZlvll_mll4	e4475	4510.3
363999	PhHppEG_CT10nloME_WZlvll_mll20	e5528	2000

for the matrix element calculation (NNPDF3.0(N)NLO), if relevant the Pythia tune (AZNLOC6L1), and the process description (llvvjj_ss_EW4 or _EW6), i.e. for the fully leptonic $W^{\pm}W^{\pm}$ production and decay in association with two jets at tree-level. The sample description tag in most cases does not include information on the perturbative order, the factorisation and renormalisation scales, and more details.

Tab. C.1 and all following tables, also include the dataset ID (DSID) and event generation tags used within the official ATLAS MC production framework, and the generator level cross-sections times branching ratios $\sigma \equiv \sigma^{\text{gen}} \cdot \text{BR}$, higher order QCD correction factors k (i.e. those which are not included in the event generation of these samples), and filter selection efficiencies ε for each independent sample.

Details on the simulations of diboson processes with other massive boson combinations VV ($V \in \{W^{\pm}, Z\}$) with electroweak order $\mathcal{O}(\alpha_{EW}^4)$ (not indicated in the sample description), as well as order $\mathcal{O}(\alpha_{EW}^6)$ (indicated with "EW6" in the sample description) are listed in Tab. C.2. For these samples, the Sherpa event generator [132, 133] in different versions is employed. For semileptonic(fully leptonic) final states, version 2.2.1(2.2.2) is used. Gluon induced diboson processes are generated with version 2.1.1. While the latter employ the CT10 PDF set [129] at NLO in QCD, all other diboson samples use the NNPDF3.0 PDF set at NNLO in QCD and with $\alpha_S(m_Z) = 0.118$ [128] for matrix element level calculations. Matrix elements of samples at order $\mathcal{O}(\alpha_{EW}^4)$ are calculated and multi-jet merged (rf to Sec. 4.2.3) with up to one additional parton at NLO and up to three additional partons at LO employing OpenLoops [287] and the MEPS@NLO prescription [288]. Samples at order $\mathcal{O}(\alpha_{EW}^6)$ are generated at tree-level using Sherpa's internal matrix element generator Comix [132]. The default Sherpa Csshower [140] models the parton shower and additional phenomena (cf. Sec. 4.2) in all samples.

For the evaluation of the uncertainties associated to the parton shower and further phenomena of the modelling of the $W^{\pm}Z$ process, two additional samples are employed, as detailed in Tab. C.3. Both samples use the same configuration for the matrix element calculations at NLO QCD accuracy: the Powheg event generator and the CT10 PDF set at NLO in QCD. These calculations are interfaced to either Pythia 8 (with tune AZNLO) or Herwig ++ [138] (default tune). k-factors and filter efficiencies are equal to 1.

Details on the simulations of processes with three massive bosons VVV ($V \in \{W^{\pm}, Z\}$)

Table C.4: Event simulation details for the triboson processes used in the analysis, including the dataset ID (DSID), sample description (see text for details), ATLAS MC production tag, generator cross-section times branching ratio $\sigma \equiv \sigma^{\text{gen}} \cdot \text{BR}$, higher order correction factor k, and filter efficiency ε.

DSID	Sample Description	Tags	σ [fb]	k	ε
361620	Sherpa_CT10_WWW_3l3v	e4093	8.3430	1.0	1.0
361621	Sherpa_CT10_WWZ_4l2v	e4053	1.7340	1.0	1.0
361622	Sherpa_CT10_WWZ_2l4v	e4053	3.4299	1.0	1.0
361623	Sherpa_CT10_WZZ_5l1v	e4093	0.21783	1.0	1.0
361624	Sherpa_CT10_WZZ_3l3v	e4093	1.9248	1.0	0.44444
361625	Sherpa_CT10_ZZZ_6l0v	e4093	0.017059	1.0	1.0
361626	Sherpa_CT10_ZZZ_4l2v	e4093	0.44125	1.0	0.22542
361627	Sherpa_CT10_ZZZ_2l4v	e4093	0.44530	1.0	0.44815

and fully leptonic decay are listed in Tab. C.4. For these samples, the Sherpa event generator version 2.1.1 is employed. The CT10 PDF set [129] at NLO in QCD is employed for matrix element level calculations. Except the samples for the WWZ process, all samples are calculated with OpenLoops at NLO accuracy in QCD. The WWZ processes are generated at LO with up to two additional partons in the matrix element calculations.

Details on the simulations of the $V\gamma$ ($V \in \{W^{\pm}, Z\}$) processes with fully leptonic decay of the V boson, with electroweak order $\mathcal{O}(\alpha_{EW}^3)$ (not indicated in the sample description), as well as order $\mathcal{O}(\alpha_{EW}^5)$ (indicated with "EW5" in the sample description), are listed in Tab. C.5. All samples are generated with the Sherpa event generator including all off-shell contributions. Samples with electroweak order $\mathcal{O}(\alpha_{EW}^3)$ are generated with version 2.1.1 and PDF set CT10 at NLO QCD. Matrix elements of the QCD-induced processes are multi-jet merged (rf to Sec. 4.2.3) with up to one additional parton at NLO and up to three additional partons at LO. Samples with electroweak order $\mathcal{O}(\alpha_{EW}^5)$ use version 2.2.4 and PDF set NNPDF3.0 at NNLO in QCD and with $\alpha_S(m_Z) = 0.118$. They are LO accurate.

Details on the simulations of processes containing top quarks are listed in Tab. C.6. The production of a $t\bar{t}$ pair in association with a massive boson V ($V \in \{W^{\pm}, Z\}$) is generated at NLO QCD accuracy with the MadGraph5_aMC@NLO event generator [134]. Parton shower and further phenomena are modelled with the A14 tune [218] of Pythia 8.210 [137]. Matrix elements are calculated with the NNPDF3.0 PDF set at NLO QCD and a dynamic factorisation and renormalisation scale of $H_T/2$ as defined in Eq. (6.3).

Events with single top production in association with a massive boson V ($V \in \{W^{\pm}, Z\}$) are generated at NLO QCD accuracy with the PowhegBox v1 ($W^{\pm}t$ processes) and MadGraph5_aMC@NLO (Zt processes) event generators. PowhegBox employs the 4-flavour scheme and the corresponding CT10f4 PDF set in the matrix element calculation. The mass of the top quark and the `hdamp` configuration parameter in PowhegBox are set to 172.5 GeV likewise. Top quark spin correlations are preserved throughout the generation. In the t-channel production, they are decayed via MadSpin [168]. For both processes parton shower and further phenomena are modelled with the Perugia tune [289] of Pythia 6.428 [208].

The process of top quark pair production is generated with the PowhegBox v2 event generator calculating the matrix element at NLO QCD accuracy and with the NNPDF3.0 PDF set. The mass of the top quark and the `hdamp` configuration parameter in PowhegBox are set to $m_t = 172.5\,\text{GeV}$ and $1.5 \cdot m_t$, respectively. A filter selects events with fully leptonic decay of the $t\bar{t}$pair. Parton shower and further phenomena are modelled with the A14 tune of Pythia 8.210. Filter efficiencies for all samples involving top quark production are equal to 1.

Details on the simulations of Z boson production in association with jets are listed in Tables C.7 and C.8, for the e^+e^-, $\mu^+\mu^-$, and $\tau^+\tau^-$ decay final states. Samples are generated using the MadGraph5_aMC@NLO event generator employing LO multi-jet merging of up to four additional partons in the matrix element and the NNPDF3.0 PDF set. Parton shower and further phenomena are modelled with the A14 tune of Pythia 8.186. All samples are normalised to NNLO accurate cross-sections, i.e. exhibiting non-zero k-factors.

Details on the simulations of $W^{\pm}$ boson production in association with jets are listed in

Table C.5: Event simulation details for the $V\gamma$ ($V \in \left\{W^{\pm}, Z\right\}$) processes used in the analysis, including the dataset ID (DSID), sample description (see text for details), ATLAS MC production tag, generator cross-section times branching ratio $\sigma \equiv \sigma^{\text{gen}} \cdot \text{BR}$, higher order correction factor k, and filter efficiency ε.

DSID	Sample Description	Tags	σ [fb]	k	ε
301887	Sherpa_CT10_enugammaPt10_35	e4452	200750	1.0	1.0
301890	Sherpa_CT10_enugammaPt35_70	e3952	15329	1.0	1.0
301891	Sherpa_CT10_enugammaPt70_140	e3952	1528.2	1.0	1.0
301892	Sherpa_CT10_enugammaPt140	e3952	241.55	1.0	1.0
301888	Sherpa_CT10_munugammaPt10_35	e4452	200910	1.0	1.0
301893	Sherpa_CT10_munugammaPt35_70	e3952	15272	1.0	1.0
301894	Sherpa_CT10_munugammaPt70_140	e3952	1523.5	1.0	1.0
301895	Sherpa_CT10_munugammaPt140	e3952	241.83	1.0	1.0
301889	Sherpa_CT10_taunugammaPt10_35	e4452	200780	1.0	1.0
301896	Sherpa_CT10_taunugammaPt35_70	e3952	15297	1.0	1.0
301897	Sherpa_CT10_taunugammaPt70_140	e3952	1529.0	1.0	1.0
301898	Sherpa_CT10_taunugammaPt140	e3952	242.60	1.0	1.0
363514	Sherpa_224_NNPDF30NNLO_emnugjj_EW5	e6398	294.19	1.0	1.0
363515	Sherpa_224_NNPDF30NNLO_epnugjj_EW5	e6398	363.37	1.0	1.0
363516	Sherpa_224_NNPDF30NNLO_mumnugjj_EW5	e6398	232.45	1.0	1.0
363517	Sherpa_224_NNPDF30NNLO_mupnugjj_EW5	e6398	290.14	1.0	1.0
363518	Sherpa_224_NNPDF30NNLO_taumnugjj_EW5	e6398	172.24	1.0	1.0
363519	Sherpa_224_NNPDF30NNLO_taupnugjj_EW5	e6398	219.34	1.0	1.0
301535	Sherpa_CT10_eegammaPt10_35	e3952	52723	1.0	1.0
301899	Sherpa_CT10_eegammaPt35_70	e3952	5235.7	1.0	1.0
301900	Sherpa_CT10_eegammaPt70_140	e3952	384.73	1.0	1.0
301901	Sherpa_CT10_eegammaPt140	e3952	47.126	1.0	1.0
301536	Sherpa_CT10_mumugammaPt10_35	e3952	52724	1.0	1.0
301902	Sherpa_CT10_mumugammaPt35_70	e3952	5241.9	1.0	1.0
301903	Sherpa_CT10_mumugammaPt70_140	e3952	385.67	1.0	1.0
301904	Sherpa_CT10_mumugammaPt140	e3952	47.195	1.0	1.0
304776	Sherpa_CT10_tautaugammaPt10_35	e4687	52708	1.0	1.0
301905	Sherpa_CT10_tautaugammaPt35_70	e3952	5249.0	1.0	1.0
301906	Sherpa_CT10_tautaugammaPt70_140	e3952	384.82	1.0	1.0
301907	Sherpa_CT10_tautaugammaPt140	e3952	47.025	1.0	1.0
363510	Sherpa_224_NNPDF30NNLO_eegjj_EW5	e6398	141.37	1.0	1.0
363511	Sherpa_224_NNPDF30NNLO_mumugjj_EW5	e6398	106.54	1.0	1.0
363512	Sherpa_224_NNPDF30NNLO_tautaugjj_EW5	e6398	89.578	1.0	1.0

Table C.6: Event simulation details for processes involving top quark production used in the analysis, including the dataset ID (DSID), sample description (see text for details), ATLAS MC production tag, generator cross-section times branching ratio $\sigma \equiv \sigma^{\text{gen}} \cdot \text{BR}$, and higher order correction factor k. Filter efficiency ε are equal to 1 for all samples.

DSID	Sample Description	Tags	σ [fb]	k
410155	aMcAtNloPythia8EvtGen_MEN30NLO_A14N23LO_ttW	e5070	548.38	1.096
410218	aMcAtNloPythia8EvtGen_MEN30NLO_A14N23LO_ttee	e5070	36.865	1.120
410219	aMcAtNloPythia8EvtGen_MEN30NLO_A14N23LO_ttmumu	e5070	36.868	1.120
410220	aMcAtNloPythia8EvtGen_MEN30NLO_A14N23LO_tttautau	e5070	36.515	1.120
410050	MadGraphPythiaEvtGen_P2012_tZ_4fl_tchan_noAllHad	e4279	240.13	1.0
410015	PowhegPythiaEvtGen_P2012_Wt_dilepton_top	e3753	3583.5	1.054
410016	PowhegPythiaEvtGen_P2012_Wt_dilepton_antitop	e3753	3581.4	1.054
410503	PowhegPythia8EvtGen_A14_ttbar_hdamp258p75_dil	e5475	76932	1.139

Table C.7: Event simulation details for Z boson production in association with jets in the e^+e^- decay channel used in the analysis, including the dataset ID (DSID), sample description (see text for details), ATLAS MC production tag, generator cross-section times branching ratio $\sigma \equiv \sigma^{\text{gen}} \cdot \text{BR}$, higher order correction factor k, and filter efficiency ε.

DSID	Sample Description	Tags	σ [fb]	k	ε
	MadGraphPythia8EvtGen_A14NNPDF23LO_ …				
361628	…Zee_lowMll_Np0	e4442	2677100	1.2320	1.0
361629	…Zee_lowMll_Np1	e4442	44988	1.2320	1.0
361630	…Zee_lowMll_Np2	e4442	29292	1.2320	1.0
361631	…Zee_lowMll_Np3	e4442	6117.0	1.2320	1.0
361632	…Zee_lowMll_Np4	e4442	2209.1	1.2320	1.0
	MGPy8EG_N30NLO_ …				
363147	…Zee_Ht0_70_CVetoBVeto	e4866	1719800	1.1410	0.83272
363148	…Zee_Ht0_70_CFilterBVeto	e4866	1719300	1.1410	0.10771
363149	…Zee_Ht0_70_BFilter	e4866	1719500	1.1410	0.059158
363150	…Zee_Ht70_140_CVetoBVeto	e4866	85067	1.1410	0.71768
363151	…Zee_Ht70_140_CFilterBVeto	e4866	85049	1.1410	0.17369
363152	…Zee_Ht70_140_BFilter	e4866	85193	1.1410	0.10765
363153	…Zee_Ht140_280_CVetoBVeto	e4866	36010	1.1410	0.67282
363154	…Zee_Ht140_280_CFilterBVeto	e4866	36023	1.1410	0.19991
363155	…Zee_Ht140_280_BFilter	e4866	36060	1.1410	0.12505
363156	…Zee_Ht280_500_CVetoBVeto	e4866	8206.3	1.1410	0.62814
363157	…Zee_Ht280_500_CFilterBVeto	e4866	8217.4	1.1410	0.22730
363158	…Zee_Ht280_500_BFilter	e4866	8244.1	1.1410	0.14208
363159	…Zee_Ht500_700_CVetoBVeto	e4866	1274.6	1.1410	0.59628
363160	…Zee_Ht500_700_CFilterBVeto	e4866	1274.4	1.1410	0.24852
363161	…Zee_Ht500_700_BFilter	e4866	1274.5	1.1410	0.15262
363162	…Zee_Ht700_1000_CVetoBVeto	e4866	444.22	1.1410	0.57522
363163	…Zee_Ht700_1000_CFilterBVeto	e4866	446.15	1.1410	0.26181
363164	…Zee_Ht700_1000_BFilter	e4866	446.15	1.1410	0.16125
363165	…Zee_Ht1000_2000_CVetoBVeto	e4866	152.29	1.1410	0.55501
363166	…Zee_Ht1000_2000_CFilterBVeto	e4866	152.69	1.1410	0.27452
363167	…Zee_Ht1000_2000_BFilter	e4866	153.75	1.1410	0.16578
363168	…Zee_Ht2000_E_CMS_CVetoBVeto	e4866	5.6666	1.1410	0.53072
363169	…Zee_Ht2000_E_CMS_CFilterBVeto	e4866	5.7339	1.1410	0.29182
363170	…Zee_Ht2000_E_CMS_BFilter	e4866	5.7621	1.1410	0.17528

Table C.8: Event simulation details for Z boson production in association with jets in the $\mu^+\mu^-$, and $\tau^+\tau^-$ decay channels used in the analysis, including the dataset ID (DSID), sample description (see text for details), ATLAS MC production tag, generator cross-section times branching ratio $\sigma \equiv \sigma^{\text{gen}} \cdot \text{BR}$, higher order correction factor k, and filter efficiency ε.

DSID	Sample Description	Tags	σ [fb]	k	ε
	MGPy8EG_N30NLO_ …				
363123	…Zmumu_Ht0_70_CVetoBVeto	e4649	1714900	1.1410	0.83153
363124	…Zmumu_Ht0_70_CFilterBVeto	e4649	1715300	1.1410	0.10844
363125	…Zmumu_Ht0_70_BFilter	e4649	1715700	1.1410	0.059188
363126	…Zmumu_Ht70_140_CVetoBVeto	e4649	84555	1.1410	0.71837
363127	…Zmumu_Ht70_140_CFilterBVeto	e4649	84571	1.1410	0.17383
363128	…Zmumu_Ht70_140_BFilter	e4649	84753	1.1410	0.10797
363129	…Zmumu_Ht140_280_CVetoBVeto	e4649	35890	1.1410	0.67402
363130	…Zmumu_Ht140_280_CFilterBVeto	e4649	35891	1.1410	0.19969
363131	…Zmumu_Ht140_280_BFilter	e4649	35891	1.1410	0.12601
363132	…Zmumu_Ht280_500_CVetoBVeto	e4649	8193.6	1.1410	0.62789
363133	…Zmumu_Ht280_500_CFilterBVeto	e4649	8180.5	1.1410	0.22805
363134	…Zmumu_Ht280_500_BFilter	e4649	8170.8	1.1410	0.14285
363135	…Zmumu_Ht500_700_CVetoBVeto	e4649	1270.7	1.1410	0.59645
363136	…Zmumu_Ht500_700_CFilterBVeto	e4649	1267.4	1.1410	0.24948
363137	…Zmumu_Ht500_700_BFilter	e4649	1266.2	1.1410	0.15279
363138	…Zmumu_Ht700_1000_CVetoBVeto	e4649	442.24	1.1410	0.57064
363139	…Zmumu_Ht700_1000_CFilterBVeto	e4649	445.17	1.1410	0.26337
363140	…Zmumu_Ht700_1000_BFilter	e4649	443.56	1.1410	0.16025
363141	…Zmumu_Ht1000_2000_CVetoBVeto	e4649	148.24	1.1410	0.55454
363142	…Zmumu_Ht1000_2000_CFilterBVeto	e4649	144.80	1.1410	0.26892
363143	…Zmumu_Ht1000_2000_BFilter	e4649	147.28	1.1410	0.17087
363144	…Zmumu_Ht2000_E_CMS_CVetoBVeto	e4649	5.5138	1.1410	0.55534
363145	…Zmumu_Ht2000_E_CMS_CFilterBVeto	e4649	5.5277	1.1410	0.28747
363146	…Zmumu_Ht2000_E_CMS_BFilter	e4649	5.6967	1.1410	0.17008
363725	…Zmumu_lowMll_Ht0_70_CVetoBVeto	e4863	2813300	1.1410	0.88800
363726	…Zmumu_lowMll_Ht0_70_CFilterBVeto	e4863	2816300	1.1410	0.084627
363727	…Zmumu_lowMll_Ht0_70_BFilter	e4887	2816000	1.1410	0.027286
363728	…Zmumu_lowMll_Ht70_140_CVetoBVeto	e4863	25846	1.1410	0.66714
363729	…Zmumu_lowMll_Ht70_140_CFilterBVeto	e4887	25921	1.1410	0.25195
363730	…Zmumu_lowMll_Ht70_140_BFilter	e4887	25930	1.1410	0.080668
363731	…Zmumu_lowMll_Ht140_280_CVetoBVeto	e4863	9257.6	1.1410	0.63482
363732	…Zmumu_lowMll_Ht140_280_CFilterBVeto	e4863	9274.9	1.1410	0.26724
363733	…Zmumu_lowMll_Ht140_280_BFilter	e4887	9317.6	1.1410	0.10002
363734	…Zmumu_lowMll_Ht280_500_CVetoBVeto	e4863	1834.2	1.1410	0.59635
363735	…Zmumu_lowMll_Ht280_500_CFilterBVeto	e4887	1842.0	1.1410	0.27848
363736	…Zmumu_lowMll_Ht280_500_BFilter	e4887	1840.6	1.1410	0.12280
363737	…Zmumu_lowMll_Ht500_700_CVetoBVeto	e4863	243.36	1.1410	0.57440
363738	…Zmumu_lowMll_Ht500_700_CFilterBVeto	e4863	243.64	1.1410	0.29329
363739	…Zmumu_lowMll_Ht500_700_BFilter	e4863	243.69	1.1410	0.13905
363740	…Zmumu_lowMll_Ht700_1000_CVetoBVeto	e4863	75.079	1.1410	0.55119
363741	…Zmumu_lowMll_Ht700_1000_CFilterBVeto	e4863	74.080	1.1410	0.29501
363742	…Zmumu_lowMll_Ht700_1000_BFilter	e4863	74.099	1.1410	0.14924
363743	…Zmumu_lowMll_Ht1000_2000_CVetoBVeto	e4863	20.213	1.1410	0.54262
363744	…Zmumu_lowMll_Ht1000_2000_CFilterBVeto	e4863	19.991	1.1410	0.29845
363745	…Zmumu_lowMll_Ht1000_2000_BFilter	e4863	20.136	1.1410	0.15648
363746	…Zmumu_lowMll_Ht2000_E_CMS_CVetoBVeto	e4863	0.35612	1.1410	0.50990
363747	…Zmumu_lowMll_Ht2000_E_CMS_CFilterBVeto	e4863	0.36063	1.1410	0.30357
363748	…Zmumu_lowMll_Ht2000_E_CMS_BFilter	e4863	0.38109	1.1410	0.17245
	MadGraphPythia8EvtGen_A14NNPDF23LO_ …				
361510	…Ztautau_Np0	e3898	1398700	1.2320	1.0
361511	…Ztautau_Np1	e3898	211410	1.2320	1.0
361512	…Ztautau_Np2	e3898	67183	1.2320	1.0
361513	…Ztautau_Np3	e3898	18614	1.2320	1.0
361514	…Ztautau_Np4	e3898	7266.3	1.2320	1.0
361638	…Ztautau_lowMll_Np0	e4442	2412400	1.2320	1.0
361639	…Ztautau_lowMll_Np1	e4442	46019	1.2320	1.0
361640	…Ztautau_lowMll_Np2	e4442	28852	1.2320	1.0
361641	…Ztautau_lowMll_Np3	e4442	6051.3	1.2320	1.0
361642	…Ztautau_lowMll_Np4	e4442	2211.1	1.2320	1.0

Tab. C.9 for all leptonic decay final states. Samples are generated using the SHERPA event generator with version 2.2.1. The samples are multi-jet merged with up to two additional partons at NLO and up to four additional partons at LO in the matrix element employing the ME+PS@NLO method [288]. The NNPDF3.0 PDF set is used at NNLO in the matrix element as well as the SHERPA internal parton shower algorithm. All samples are normalised to NNLO accurate cross-sections, i.e. exhibiting non-zero k-factors.

C.2 Reconstruction Level EFT Samples

Samples including EFT effects using the nominal MG5_aMC + PYTHIA 8 setup, described in Sec. 6.3.3, have been privately simulated at reconstruction level within the ATLAS MC production framework structures. They do not have an official DSID or `e`-tag. The detector simulation is run setting up release `19.2.4.9` of the `AtlasProduction` project which reproduces conditions as in tag `s2726`. The reconstruction is run setting up release `20.7.5.1.1` of the `AtlasProd1` project which reproduces conditions as in tag `r7772_r7676`. The `STDM3` is run setting up release `20.7.8.25` of the `AtlasDerivation` project which reproduces conditions as in tag `p3317`.

The samples are generated at LO accuracy. No k-factors are available for these BSM samples. No filters have been used in their generation. The generator cross-section for all samples is summarised with information on the particle level studies in App. F.6.

C.3 Reconstruction Level aTGC Samples

Details on the simulations of $W^{\pm}Z$ boson production using a dimension-six aTGC model are listed in Tab. C.10 for all leptonic decay final states. Samples are generated using the MC@NLO event generator and interfaced to HERWIG. The samples are NLO QCD accurate. All samples are normalised to NNLO accurate cross-sections with a k-factor amounting to 1.11.

These samples incorporate additional weights generated with a matrix element reweighting method in order to transfer the nominal generated point to any point in the three dimensional space of the aTGC parameters Δg_1^Z, $\Delta\kappa_Z$, and λ_Z. The MC weight prescription reads:

$$\begin{aligned} w(\Delta g_1^Z, \Delta\kappa_Z, \lambda_Z) = w_0 \times (w_1 &+ (\Delta g_1^Z)^2 w_2 + \Delta\kappa_Z^2 w_3 + \lambda_Z^2 w_4 \\ &+ 2\Delta g_1^Z w_5 + 2\Delta\kappa_Z w_6 + 2\lambda_Z w_7 \\ &+ 2\Delta g_1^Z \Delta\kappa_Z w_8 + 2\Delta g_1^Z \lambda_Z w_9 + 2\Delta\kappa_Z \lambda_Z w_{10}). \end{aligned} \tag{C.1}$$

Table C.9: Event simulation details for $W^{\pm}$ boson production in association with jets in all decay channels used in the analysis, including the dataset ID (DSID), sample description (see text for details), ATLAS MC production tag, generator cross-section times branching ratio $\sigma \equiv \sigma^{\text{gen}} \cdot \text{BR}$, higher order correction factor k, and filter efficiency ε. Note the unit of the cross-section given in the table.

DSID	Sample Description	Tags	σ [10^3 fb]	k	ε
	Sherpa_221_NNPDF30NNLO_ …				
364156	…Wmunu_MAXHTPTV0_70_CVetoBVeto	e5340	19151.0	0.9702	0.82465
364157	…Wmunu_MAXHTPTV0_70_CFilterBVeto	e5340	19145.0	0.9702	0.13031
364158	…Wmunu_MAXHTPTV0_70_BFilter	e5340	19143.0	0.9702	0.044209
364159	…Wmunu_MAXHTPTV70_140_CVetoBVeto	e5340	945.89	0.9702	0.6743
364160	…Wmunu_MAXHTPTV70_140_CFilterBVeto	e5340	946.12	0.9702	0.24357
364161	…Wmunu_MAXHTPTV70_140_BFilter	e5340	944.8	0.9702	0.084525
364162	…Wmunu_MAXHTPTV140_280_CVetoBVeto	e5340	339.73	0.9702	0.60009
364163	…Wmunu_MAXHTPTV140_280_CFilterBVeto	e5340	339.8	0.9702	0.29256
364164	…Wmunu_MAXHTPTV140_280_BFilter	e5340	339.68	0.9702	0.10844
364165	…Wmunu_MAXHTPTV280_500_CVetoBVeto	e5340	72.084	0.9702	0.54766
364166	…Wmunu_MAXHTPTV280_500_CFilterBVeto	e5340	72.103	0.9702	0.32016
364167	…Wmunu_MAXHTPTV280_500_BFilter	e5340	72.063	0.9702	0.13137
364168	…Wmunu_MAXHTPTV500_1000	e5340	15.008	0.9702	1.0
364169	…Wmunu_MAXHTPTV1000_E_CMS	e5340	1.2349	0.9702	1.0
364170	…Wenu_MAXHTPTV0_70_CVetoBVeto	e5340	19153.0	0.9702	0.82467
364171	…Wenu_MAXHTPTV0_70_CFilterBVeto	e5340	19145.0	0.9702	0.13038
364172	…Wenu_MAXHTPTV0_70_BFilter	e5340	19143.0	0.9702	0.044154
364173	…Wenu_MAXHTPTV70_140_CVetoBVeto	e5340	944.98	0.9702	0.67483
364174	…Wenu_MAXHTPTV70_140_CFilterBVeto	e5340	946.37	0.9702	0.24414
364175	…Wenu_MAXHTPTV70_140_BFilter	e5340	945.63	0.9702	0.083353
364176	…Wenu_MAXHTPTV140_280_CVetoBVeto	e5340	339.75	0.9702	0.59858
364177	…Wenu_MAXHTPTV140_280_CFilterBVeto	e5340	339.8	0.9702	0.28805
364178	…Wenu_MAXHTPTV140_280_BFilter	e5340	339.7	0.9702	0.11088
364179	…Wenu_MAXHTPTV280_500_CVetoBVeto	e5340	72.077	0.9702	0.54829
364180	…Wenu_MAXHTPTV280_500_CFilterBVeto	e5340	72.105	0.9702	0.31969
364181	…Wenu_MAXHTPTV280_500_BFilter	e5340	72.077	0.9702	0.13865
364182	…Wenu_MAXHTPTV500_1000	e5340	15.05	0.9702	1.0
364183	…Wenu_MAXHTPTV1000_E_CMS	e5340	1.2344	0.9702	1.0
364184	…Wtaunu_MAXHTPTV0_70_CVetoBVeto	e5340	19155.0	0.9702	0.82462
364185	…Wtaunu_MAXHTPTV0_70_CFilterBVeto	e5340	19154.0	0.9702	0.12951
364186	…Wtaunu_MAXHTPTV0_70_BFilter	e5340	19152.0	0.9702	0.045128
364187	…Wtaunu_MAXHTPTV70_140_CVetoBVeto	e5340	945.58	0.9702	0.6756
364188	…Wtaunu_MAXHTPTV70_140_CFilterBVeto	e5340	946.49	0.9702	0.24245
364189	…Wtaunu_MAXHTPTV70_140_BFilter	e5340	945.87	0.9702	0.083903
364190	…Wtaunu_MAXHTPTV140_280_CVetoBVeto	e5340	339.69	0.9702	0.59884
364191	…Wtaunu_MAXHTPTV140_280_CFilterBVeto	e5340	339.84	0.9702	0.29032
364192	…Wtaunu_MAXHTPTV140_280_BFilter	e5340	339.68	0.9702	0.10575
364193	…Wtaunu_MAXHTPTV280_500_CVetoBVeto	e5340	72.078	0.9702	0.56172
364194	…Wtaunu_MAXHTPTV280_500_CFilterBVeto	e5340	71.99	0.9702	0.31863
364195	…Wtaunu_MAXHTPTV280_500_BFilter	e5340	71.944	0.9702	0.13597
364196	…Wtaunu_MAXHTPTV500_1000	e5340	15.052	0.9702	1.0
364197	…Wtaunu_MAXHTPTV1000_E_CMS	e5340	1.2342	0.9702	1.0

Table C.10: Event simulation details for $W^{\pm}Z$ boson production using an dimension-six aTGC model in all decay channels used in the EFT analysis, including the dataset ID (DSID), sample description (see text for details), ATLAS MC production tag, and generator cross-section times branching ratio $\sigma \equiv \sigma^{\text{gen}} \cdot \text{BR}$.

DSID	Sample Description	Tags	σ [fb]
361553	McAtNloHerwigEvtGen_AUET2CT10_WpZ_e_e_0_0_0	e4439	99.781
361554	McAtNloHerwigEvtGen_AUET2CT10_WmZ_e_e_0_0_0	e4439	61.584
361555	McAtNloHerwigEvtGen_AUET2CT10_WpZ_e_mu_0_0_0	e4439	99.782
361556	McAtNloHerwigEvtGen_AUET2CT10_WmZ_e_mu_0_0_0	e4439	61.579
361557	McAtNloHerwigEvtGen_AUET2CT10_WpZ_e_tau_0_0_0	e4439	99.777
361558	McAtNloHerwigEvtGen_AUET2CT10_WmZ_e_tau_0_0_0	e4439	61.585
361559	McAtNloHerwigEvtGen_AUET2CT10_WpZ_mu_e_0_0_0	e4439	99.774
361560	McAtNloHerwigEvtGen_AUET2CT10_WmZ_mu_e_0_0_0	e4439	61.578
361561	McAtNloHerwigEvtGen_AUET2CT10_WpZ_mu_mu_0_0_0	e4439	99.785
361562	McAtNloHerwigEvtGen_AUET2CT10_WmZ_mu_mu_0_0_0	e4439	61.58
361563	McAtNloHerwigEvtGen_AUET2CT10_WpZ_mu_tau_0_0_0	e4439	99.782
361564	McAtNloHerwigEvtGen_AUET2CT10_WmZ_mu_tau_0_0_0	e4439	61.581
361565	McAtNloHerwigEvtGen_AUET2CT10_WpZ_tau_e_0_0_0	e4439	99.785
361566	McAtNloHerwigEvtGen_AUET2CT10_WmZ_tau_e_0_0_0	e4439	61.571
361567	McAtNloHerwigEvtGen_AUET2CT10_WpZ_tau_mu_0_0_0	e4439	99.762
361568	McAtNloHerwigEvtGen_AUET2CT10_WmZ_tau_mu_0_0_0	e4439	61.574
361569	McAtNloHerwigEvtGen_AUET2CT10_WpZ_tau_tau_0_0_0	e4439	99.78
361570	McAtNloHerwigEvtGen_AUET2CT10_WmZ_tau_tau_0_0_0	e4439	61.556

Appendix D

Additional Analysis Details

D.1 Object and Event Selection

D.1.1 Event Preselection

Error Flags

Error flags used in the reconstruction level analysis for event cleaning as explained in Sec. 3.3.2:

```
→     if (eventInfo->errorState(xAOD::EventInfo::Tile)==xAOD::EventInfo::Error)
        return 0;
    if (eventInfo->errorState(xAOD::EventInfo::LAr)==xAOD::EventInfo::Error)
        return 0;
    if (eventInfo->errorState(xAOD::EventInfo::SCT)==xAOD::EventInfo::Error)
        return 0;
    if (eventInfo->isEventFlagBitSet(xAOD::EventInfo::Core, 18))
        return 0;
```

Nominal Analysis Trigger

Unprescaled single lepton trigger strings used in the reconstruction level analysis for experimental and simulated data are summarised in Tables D.1. Selection thresholds for several triggers have tightened throughout the data taking period used in the analysis due to the increase in instantaneous luminosity from 2015 until the end of 2016.

Trigger for Non-prompt Lepton Background Estimate

The events in data in the dijet region, defined to measure the fake factors for electrons and muons, are preselected with the following prescaled single lepton trigger chains:

- `HLT_e12_lhvloose_nod0_L1EM10VH`,
- `HLT_e40_lhvloose_nod0`, and
- `HLT_mu14`,

and the unprescaled trigger chain `HLT_mu50`.

Table D.1: Details on the unprescaled single lepton trigger strings for experimental and MC simulated data used in the analysis given by the year of data taking and precisely the run number.

Year	Run number range	Electrons	Muons
		Single-lepton trigger string for exp. data:	
2015	276261 − 284485	HLT_e24_lhmedium_L1EM20VH, HLT_e60_lhmedium, HLT_e120_lhloose	HLT_mu20_iloose_L1MU15, HLT_mu50
2016	297729 − 302919	HLT_e24_lhtight_nod0_ivarloose, HLT_e60_lhmedium_nod0, HLT_e140_lhloose_nod0	HLT_mu24_ivarmedium, HLT_mu50
2016	302918 − end	HLT_e26_lhtight_nod0_ivarloose, HLT_e60_lhmedium_nod0, HLT_e140_lhloose_nod0	HLT_mu26_ivarmedium, HLT_mu50
Year	Run number range	Electrons	Muons
		Single-lepton trigger string for MC simulated data:	
2015	276261 − 284485	HLT_e24_lhmedium_L1EM18VH, HLT_e60_lhmedium, HLT_e120_lhloose	HLT_mu20_iloose_L1MU15, HLT_mu50
2016	297729 − 302919	HLT_e24_lhtight_nod0_ivarloose, HLT_e60_lhmedium_nod0, HLT_e140_lhloose_nod0	HLT_mu24_ivarmedium, HLT_mu50
2016	302918 − end	HLT_e26_lhtight_nod0_ivarloose, HLT_e60_lhmedium_nod0, HLT_e140_lhloose_nod0	HLT_mu26_ivarmedium, HLT_mu50

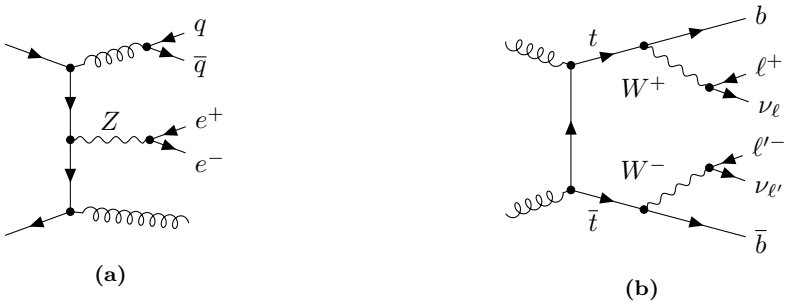


Figure D.1: Examples of Feynman diagrams of leptonic Z+jets (a) and fully-leptonic $t\bar{t}$ (b) production, both of which are processes representing the major contributions to the background due to electron charge misidentification in the $e^{\pm}e^{\pm}$ and $e^{\pm}\mu^{\pm} + \mu^{\pm}e^{\pm}$ channels, respectively, in the signal region.

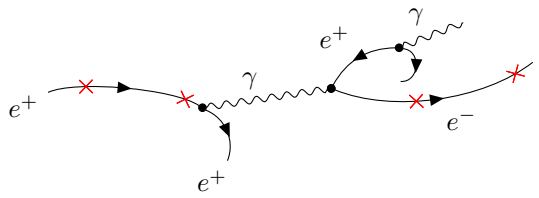


Figure D.2: Schematic illustration (not true to scale, for illustration purpose only) of the process of photon conversion and subsequent pair production of a positron. The red crosses shall schematically indicate the hits in the inner silicon detectors. The reconstructed track of the initial positron (coming from the left) is partially reconstructed with the hits of the electron from the pair production resulting in the wrong curvature and hence wrong charge measurement of the initial positron. Figure adapted from Ref. [219].

D.2 Background Estimates

D.2.1 Electron Charge Misidentification

The requirement on the two analysis leptons having the same electrical charge in the signal region helps increasing the signal fraction over backgrounds with opposite-charge leptons, such as Drell-Yan, $t\bar{t}$ and single top, and W^+W^- production. However, events from these background processes can enter the signal selection if the charge of one of the leptons is wrongly reconstructed. Although the probability for this to happen is small, it can cause a sizable background contribution in the signal region due to the comparably large cross-section of the processes exhibiting two opposite charge leptons compared to the $W^{\pm}W^{\pm}jj$-EW6 signal process. Fig. D.1 shows some example Feynman diagrams for the dominant processes contributing to the background due to lepton charge misidentification in the signal region.

A lepton's electric charge is obtained from the direction of the curvature of its associated track in the magentic field of the tracking devices of the ATLAS detector. Its mismeasurement hence either results from a mismeasurement of the track's curvature or from an incorrect track-object pairing.

Especially electrons with large transverse momentum suffer from the first effect as the track straightens with the object's p_{T}. The second effect is predominantly caused by electrons or positrons emitting a hard bremsstrahlung photon which subsequently converts into an electron-positron pair. The track of one of the secondary electrons/positrons is then identified as the primary electron's/positron's track matched to the initial electromagnetic cluster, hence obtaining in only roughly one half of the cases the correct charge. A schematic view can be seen in Fig. D.2. Both the probability of bremsstrahlung and the mismeasurement of the curvature increase with the amount of passive material traversed. This leads to the charge misidentification being large at high absolute pseudorapidities. In addition, the occupancy of the inner detector increases with $|\eta|$ which further complicates the track reconstruction.

For muons, both effects are negligible. One reason is the higher mass compared to elec-

trons which reduces the bremsstrahlung probability by four orders of magnitude due to its indirect proportionality to the squared lepton mass. In addition, muon tracks are measured not only in the inner detector but also in the muon spectrometer. The hence longer trajectory allows for a more precise measurement of the muon track. Studies with simulated data at 13 TeV shown in Fig. 8.4 of Ref. [219] support these statements. The estimation of this background is therefore only relevant for channels which exhibit electrons, i.e. the $e^{\pm}e^{\pm}$, $e^{\pm}\mu^{\pm}$, and $\mu^{\pm}e^{\pm}$ channel.

The background estimate due to the misidentification of the electron charge in the signal and control regions is evaluated in three steps, which are briefly summarised in the following based on the detailed studies performed in Ref. [219]. It is estimated with a specially selected experimental data sample employing the charge misidentification probabilities which are derived from simulation and corrected for differences seen between simulation and data. The final estimate is obtained after an energy correction of the electrons subject to charge misidentification. Sources of systematic uncertainties for this background contribution are summarised at the end of this section.

Measurement of Electron Charge Misidentification Probability and Scale Factors

The charge misidentification probability is measured in experimental and simulated data and corresponding data-to-simulation scale factors (cf Sec. 4.3.4) are computed. The need for simulation-correcting scale factors lies in the origin of the charge misreconstruction which, as stated above, primarily happens when particles traverse the detector. These detector effects are not modelled precisely enough in the GEANT4 simulation and hence need to be corrected to match what is observed in experimental data.

The scale factors are calculated in events exhibiting two electrons with identical object selection requirements as used in the analysis (summarised in Tab. 7.1). In order to ensure high statistical accuracy, the well-modelled Z boson resonance is exploited, requiring the selected events to lie within a window of $75\,\text{GeV} < m_{ll} < 105\,\text{GeV}$ around the mass of the Z boson. The procedure closely follows the recommendations outlined in Ref. [102] and [290].

The probability of finding a certain number of same-charge (sc) events n_{SC} in a total number of events with two electrons $N_{\text{OC+SC}}$ (same-charge and opposite-charge (oc)) is binomially distributed exhibiting an expectation value of same-charge events:

$$\nu_{\text{SC}\,ij} = N_{(\text{SC+OC})\,ij} \cdot p = N_{(\text{SC+OC})\,ij}\left[(1-\varepsilon_i)\varepsilon_j + (1-\varepsilon_j)\varepsilon_i\right], \tag{D.1}$$

where $\varepsilon_{i,j}$ are the independent probabilities for either of the two electrons' charge to be misidentified depending on their transverse momentum and absolute pseudorapidity binned in i, j, i.e. $\varepsilon_{i,j} \equiv \varepsilon_{i,j}(p_{\text{T}}, |\eta|)$.

The overall probability of obtaining same-charge events from charge misidentification of one electron in dielectron events can be approximated by a Poisson distribution in the limit of large $N_{(\text{SC+OC})\,ij}$ and finite expectation value:

$$P_{ij}(N_{\text{SC}}|\nu_{\text{SC}}) = P_{ij}(N_{\text{SC}\,ij}|\varepsilon_i, \varepsilon_j) = \frac{(\nu_{\text{SC}\,ij})^{N_{\text{SC}\,ij}}\, e^{-\nu_{\text{SC}\,ij}}}{N_{\text{SC}\,ij}!}, \tag{D.2}$$

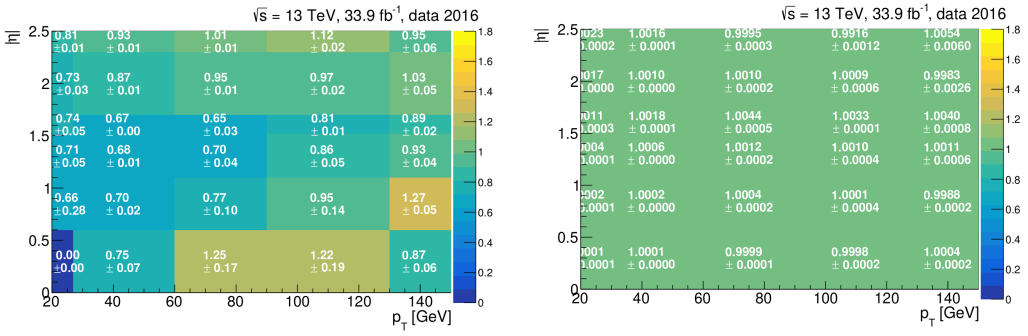
which is employed in a maximum likelihood fit to extract the $\varepsilon_{i,j}$, i.e. minimising the expression:

$$-\ln L = -\sum_{i,j} \ln L(\varepsilon_i, \varepsilon_j) = -\sum_{i,j} P_{ij}(N_{\text{SC}\,ij}|\varepsilon_i, \varepsilon_j). \tag{D.3}$$

From the measured charge misidentification rates $\varepsilon_{i,j}^{\text{data/MC}}$ in experimental data and simulations, per object scale factors (SF) for wrong and correct charge identification, respectively, can be extracted:

$$SF_{\text{wrong}} = \frac{\varepsilon^{\text{data}}}{\varepsilon^{\text{MC}}}, \text{and} \quad SF_{\text{correct}} = \frac{(1-\varepsilon^{\text{data}})}{(1-\varepsilon^{\text{MC}})}. \tag{D.4}$$

Both are shown in 2-dimensional maps in Fig. D.3 with five bins in electron transverse momentum p_{T} (measured up to 1000 GeV), and six bins in absolute pseudorapidity $|\eta|$ (excluding



(a) (b)

Figure D.3: Electron charge identification scale factors as a function of the electron's transverse momentum p_{T} and absolute pseudorapidity $|\eta|$ for wrong (a) and correct (b) charge identification. Electrons are required to pass the analysis selection of Tab. 7.1. Uncertainties are the total uncertainties of the scale factor extraction method. Figure taken from Ref. [219].

the barrel-endcap calorimeter transition region $1.37 < |\eta| < 1.52$). The p_{T} threshold in this measurement is lowered such that the effects of energy loss due to charge misidentification are captured. In addition, optimisation studies and other background estimates in this analysis involve looser p_{T} thresholds.

The data-to-simulation corrections are as large as 30% in several bins for wrong charge identification and well below 1% for the correct charge assignment.

Evaluation of Electron Charge Misidentification with Truth Information

The charge misidentification rate for the background estimate in this analysis is not taken from the likelihood estimate but rather retrieved employing the available truth information in the simulation of $Z \to e^+e^-$ events:

$$\varepsilon_i = \frac{\text{wrong charge electrons}_i}{\text{all prompt electrons}_i}, \tag{D.5}$$

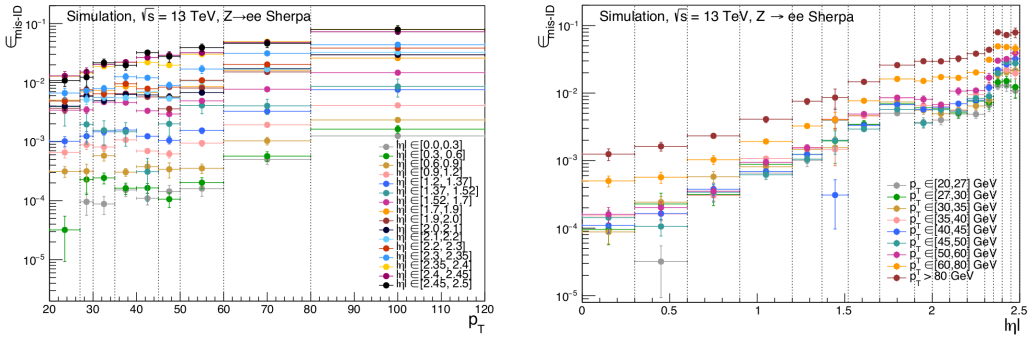
where "prompt" electrons refers to all isolated electrons from $Z \to e^+e^-$ simulated data, which are directly stemming from the Z boson decay, including those electrons subject to successive hard bremsstrahlung and conversion. In this way, background electrons from hadron decays are not entering the calculation.

This rate is again evaluated in 2-dimensional bins i of the transverse momentum p_{T} and absolute pseudorapidity of the electron after correcting with the scale factor obtained in the previous step. The results are shown in Fig. D.4.

As expected from the consideration above, the charge misidentification probability increases with transverse momentum and absolute pseudorapidity, exhibiting a range of almost two orders of magnitude between the barrel and end-cap regions. Hence, in order to suppress large contributions of the electron charge misidentification background, the pseudorapidity of electrons is restricted to the barrel region in the $e^{\pm}e^{\pm}$ channels in the signal region (cf Tab. 7.4). Hard bremsstrahlung plus subsequent conversion of the photon contribute the largest fraction to the overall electron charge misidentification probability [219].

Reweighting of Data with Opposite Charge Electrons

Eventually, real data events of opposite charge leptons are reweighted to obtain an estimate on the number of same-charge events in the signal region. Utilising opposite charge events has the advantage of high statistical accuracy of the background estimate. Experimental data is employed to avoid mismodelling in simulation, as well as detector uncertainties (besides from the charge misidentification probability measurement). In addition, real data includes contributions from processes with prompt as well as non-prompt electrons. In order to avoid



(a) **(b)**

Figure D.4: Electron charge misidentification probabilities ε_i as a function of the electron's transverse momentum p_{T} (a) and absolute pseudorapidity $|\eta|$ (b) extracted from simulation after correcting with charge identification scale factors. The measurement is divided in bins of $|\eta|$ and p_{T}, respectively. Uncertainties are statistical uncertainties of the electron sample only. Figure taken from Ref. [219].

double counting of events with non-prompt electrons in the signal region, contributions from electron charge misidentification are subtracted when estimating the background due to non-prompt leptons.

The probe events have to pass signal selection requirements as detailed in Tab. 7.4, except the same-charge requirement which is inverted. The reweighting factor is assembled from the per-event probabilities of charge misidentification $\varepsilon_i(p_{\mathrm{T}}, |\eta|) \equiv \varepsilon$ of the leading (l_1) or subleading lepton (l_2):

- $(1-\varepsilon(l_1))(1-\varepsilon(l_2))$ if the charges of both leptons are correctly identified, i.e. having an opposite charge pair;
- $\varepsilon(l_1)\varepsilon(l_2)$ if the charges of both leptons are wrongly identified, which again gives an opposite charge pair;
- $\varepsilon(l_1)\cdot(1-\varepsilon(l_2))+\varepsilon(l_2)\cdot(1-\varepsilon(l_1))$, if either one of the leptons' charge is misidentified, i.e. obtaining a same-charge event.

The overall event weight to scale the opposite charge events is then:

$$w_{ee} = \frac{\varepsilon(e_1)(1-\varepsilon(e_2)) + \varepsilon(e_2)(1-\varepsilon(e_1))}{1-(\varepsilon(e_1)+\varepsilon(e_2)) + 2\varepsilon(e_1)\varepsilon(e_2)}, \tag{D.6}$$

for events with two electrons, or:

$$w_{e\mu+\mu e} = \frac{\varepsilon(e)}{1-\varepsilon(e)}, \tag{D.7}$$

for event with one electron and one muon, where $\varepsilon(\mu) = 0$ is adopted. The final yield of background events due to electron charge misidentification can then be extracted as:

$$N^{\mathrm{bkg}}_{\text{charge misID}} = N_{\mathrm{OC}} \cdot w_{\ell\ell}, \tag{D.8}$$

where N_{OC} is the number of real data events with opposite charge leptons selected in the region stated above.

Electron Energy and Resolution Correction

Electrons subject to hard bremsstrahlung carry over some of their energy to the emitted photon whose energy may be deposited outside the fixed-size cluster in the electromagnetic calorimeter identified with the original electron. This leakage leads to a reduced reconstructed energy and resolution for these electrons compared to electrons not undergoing

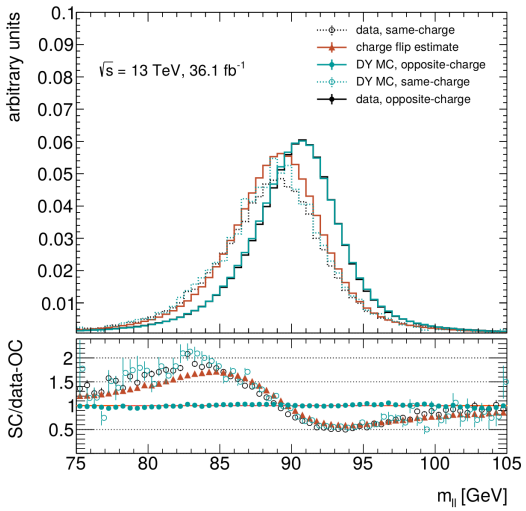


Figure D.5: Distribution of the invariant mass of two opposite (solid, black and green) and same-charge (dashed) electrons in simulation (green) and experimental data (black). The background estimate of same-charge events due to electron charge misidentification is shown in red. The distributions are obtained after the event preselection and lepton event selection (cf. Tab. 7.4), without a requirement on m_{ll}, and the additional restriction on barrel electrons in the $e^{\pm}e^{\pm}$ channel. No jet selection requirements are imposed. Distributions are normalised to unit area. The lower pad shows the ratio with respect to opposite charge events in experimental data. Uncertainties are statistical only. Figure taken from Ref. [219].

hard bremsstrahlung. As described above, this process is the leading source for electron charge misidentification. Hence, both phenomena are highly correlated. Fig. D.5 shows the distribution of the invariant mass of the two leading leptons m_{ll} around the mass of the Z boson for same-charge and opposite charge events in experimental data and simulation. A shift towards lower values of m_{ll} of the Z boson resonance is clearly visible for same-charge events. In addition, the width of the distribution is increased for this type of events.

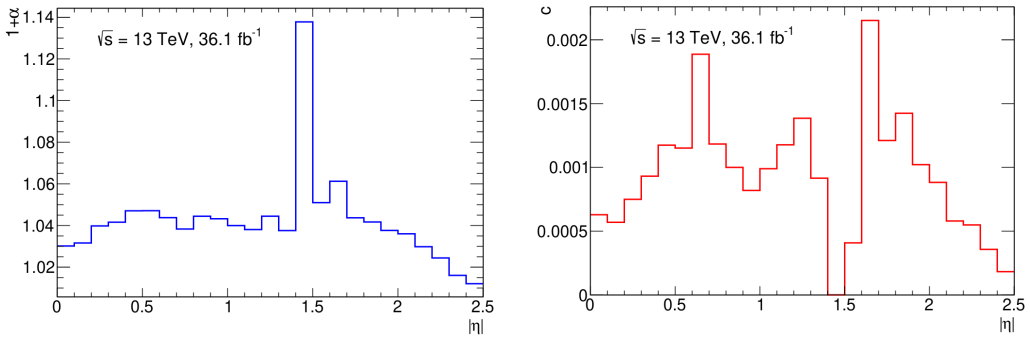
These observations make the reweighting procedure described above insufficient to correctly estimate the kinematics of the background contribution due to electron charge misidentification as this procedure solely alters the event count in a respective p_{T} and $|\eta|$ bin and not the kinematics of the misidentified electron. Hence, a correction to the transverse momentum of the original electron p_T^{orig} in the opposite charge lepton event in experimental data is applied to obtain:

$$p_T^{\mathrm{corr}} = \frac{p_T^{\mathrm{orig}}}{1+\alpha} + \Delta E. \tag{D.9}$$

The first term adds a residual energy scale correction via the factor $1/(1+\alpha)$. The second, constant term is used to smear the transverse momentum with the gaussian distributed smearing factor ΔE, in order to reflect the worsened resolution of the electrons with misidentified charge due to bremsstrahlung. Both of these corrections are obtained utilising the energy response $p_T^{\mathrm{reco}}/p_T^{\mathrm{truth}} - 1$, a measure for the difference of the transverse momenta derived at particle (truth) and reconstruction level. They are determined from simulation and in bins of absolute transverse momentum $|\eta|$. The energy scale correction is defined as:

$$\alpha = \frac{\left(\frac{p_T^{\mathrm{reco}}}{p_T^{\mathrm{truth}}} - 1\right)^{\mathrm{correct}}}{\left(\frac{p_T^{\mathrm{reco}}}{p_T^{\mathrm{truth}}} - 1\right)^{\mathrm{wrong}}}, \tag{D.10}$$

a measure of the energy response difference for electrons with correctly and wrongly identified charges. As before, the correct charge is determined from truth information in simulation. The constant term correction follows from pseudo-experiments of the Gaussian distributed



(a) **(b)**

Figure D.6: Residual energy scale correction factor $1 + \alpha$ (a) and constant term c (in GeV) (b) as a function of the reconstructed electron's absolute pseudorapidity $|\eta|$. Figure taken from Ref. [219].

quantity ΔE, with mean value 0 and width:

$$c = \left\langle \frac{p_T^{\text{reco}}}{p_T^{\text{truth}}} \right\rangle^{\text{wrong}} - \left\langle \frac{p_T^{\text{reco}}}{p_T^{\text{truth}}} \right\rangle^{\text{correct}} . \tag{D.11}$$

Fig. D.6 shows the values for the correction factors $1 + \alpha$ and c as a function of absolute pseudorapidity $|\eta|$ of the reconstructed electron. As expected, the correction of the first term is above 1 reflecting the energy response shift towards lower values. The resolution correction is mild with approx. $(1 - 2)$ MeV.

The resulting distribution in m_{ll} of the corrected estimate of same-charge lepton events derived from opposite charged events in real data is shown in red in Fig. D.5. It describes the same-charge event distribution obtained from simulated and real data well and has the advantage of increased statistical accuracy.

In the case of an $e^{\pm}e^{\pm}$ channel event, it is impossible to infer which of the electron's charge is misidentified in same-charge experimental data. Hence, in real opposite charge data. the electron on which to apply the transverse momentum correction of Eq. (D.9) is chosen randomly. This choice defines the charge of the resulting same-charge electron pair event.

The background estimate due to electron charge misreconstruction is eventually validated in an inclusive same-charge region, based on the selection requirements in the signal region, with inverted Z boson mass window selection, and omitting the missing transverse momentum and the VBS selection requirements (cf Tab. 7.4). Fig. D.7 shows the m_{ll} distribution. More kinematic distributions for validation can be found in Ref. [219]. The background estimate agrees reasonably well with a slight misalignment of the Z boson peak resulting from the overestimation of the energy correction. Systematic uncertainties are chosen such that this effect is covered.

D.2.2 Non-prompt Leptons from Hadron Decays or Misidentified Jets

The object selection criteria for analysis leptons are designed to balance the requirements of a pure and yet highly efficient signal process selection. They are based on the fact that the signal exhibits two prompt leptons. However, processes with non-prompt leptons can enter the signal region when the non-prompt lepton is identified as an analysis object. The measurement of the probability for this to occur is subject of the non-prompt background estimation.

Non-prompt leptons, as they will be called in brief throughout the thesis, include two categories of charged lepton objects: Jets that are wrongly identified as charged leptons[1];

[1]These leptons are usually called "fake" leptons. For simplicity both categories are summarised in the term "non-prompt" leptons in this thesis.

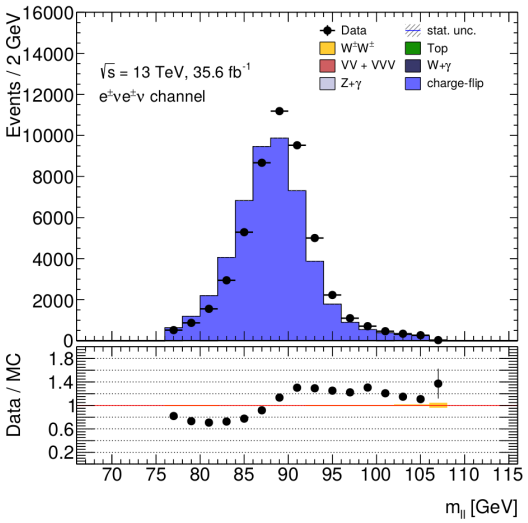
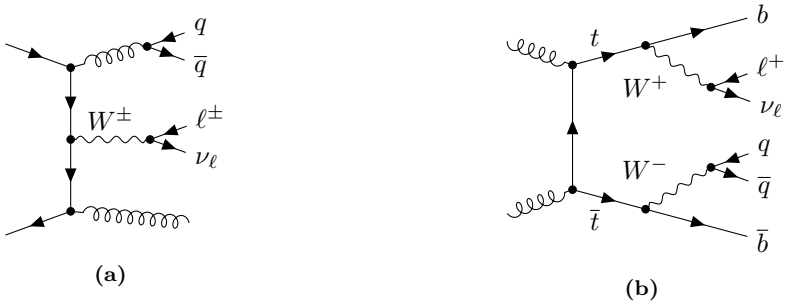


Figure D.7: Distribution of the invariant mass of the two leading leptons in the $e^{\pm}e^{\pm}$ channel in the inclusive same-charge region based on the selection requirements in the signal region, inverting the Z boson mass window selection, and omitting the missing transverse momentum and the VBS selection requirements (cf Tab. 7.4). Experimental data is compared to the background estimates, most dominantly in this region is the background contribution from events due to electron charge misidentification. The background contribution from events with non-prompt leptons is not estimated in this region. The lower pad shows the ratio of the experimental data to the full background estimate. Uncertainties are statistical only. Figure taken from Ref. [219].

and leptons from secondary decays of mostly unstable hadrons that are wrongly associated to the primary vertex. Jets and electrons share some similarities in their detector signatures, which makes it more likely for electrons to be misidendified as a jet, while non-prompt muons are more probable to be produced in hadron decays, due to their decay branching fractions [41].

Background processes with non-prompt leptons are hence SM processes producing a charged lepton together with multiple hadronic jets, one of which is reconstructed as an `analysis` lepton. Dominant processes entering the signal region with non-prompt leptons are $W^{\pm}$+jets and $t\bar{t}$ production, both of which contain a leptonic $W^{\pm}$ decay and multiple jets, as depicted in Fig. D.8. Other processes, such as semi-leptonic diboson production (W^+W^-, $W^{\pm}Z$, or ZZ), contribute to this source of background. However, their overall event count in the signal region is minor due to the comparably small diboson production cross-section. This is confirmed with MC simulation studies, as shown in Fig. D.9. Processes



(a) **(b)**

Figure D.8: Examples of Feynman diagrams of leptonic $W^{\pm}$+jets (a) and semi-leptonic $t\bar{t}$(b) production, both of which are processes representing the major contributions to the background due to non-prompt leptons in the signal region. $\ell^{\pm}$ can be an electron or muon.

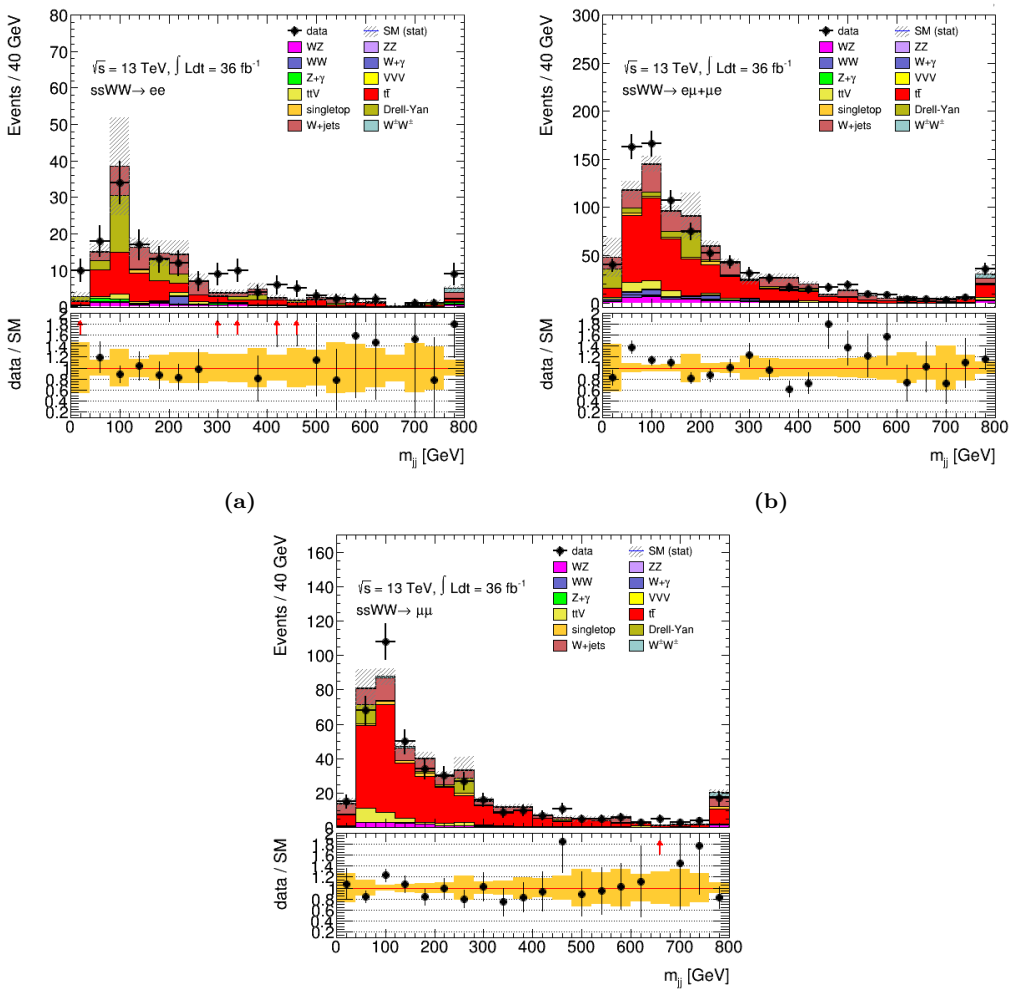


Figure D.9: Distribution of the tagging jet invariant mass m_{jj} in three channels, $e^{\pm}e^{\pm}$ (a), $e^{\pm}\mu^{\pm} + \mu^{\pm}e^{\pm}$ (b), and $\mu^{\pm}\mu^{\pm}$ (c), in the signal region without VBS selection requirements (cf Tab. 7.4) and requiring two leptons one of which selected as `analysis` and `anti-analysis` (i.e. the non-prompt candidate) object (cf Sec. D.2.2) respectively. Shown is data (black) compared to the overall (stacked colour) prediction taken from MC simulation. Uncertainties are statistical only. Figure taken from Ref. [232].

Table D.2: Summary of `anti-analysis` electron selection criteria used for the non-prompt background estimate with respect to the `analysis` selection (cf Tab. 7.1). Non-prompt electron candidates are selected with the `electron` analysis selection except the requirement of either failing the `Gradient` isolation or the `Tight` identification WP selections.

Observable	Cut value `anti-analysis` selection (w.r.t. to `analysis` selection)
p_{T}	✓
$\lvert\eta\rvert$	✓
Identification WP	`Medium`
$\lvert z_0 \times \sin\theta\rvert$	✓
d_0/σ_{d_0}	✓
Isolation WP	–
Author	✓
Non-prompt candidate	(! `Gradient` iso.) || (! `Tight` ID)

where both analysis leptons are misreconstructed from jets are neglegted as their contribution is considered to be very small in the signal region with the requirement of two well isolated leptons when compared to the accuracy of the background estimate.

The contribution of the non-prompt background in the analysis relevant regions is estimated in a similar manner as the electron charge misidentification background. First, the number of a non-prompt lepton passing the `analysis` and a modified (`anti-analysis`) selection is measured in data. Their ratio is defined as the "fake factor". It is calculated independently for electrons and muons due to the rather different non-prompt origins. Then, this fake factor is used to weight events from a specially selected data sample in order to estimate the background contribution in the respective region. This is called the "fake factor method". Both quantities, the fake factor and the final background contribution are retrieved from experimental data as MC simulation is not considered to reliably model the effects that cause non-prompt leptons, such as hadronisation and jet fragmentation.

This section briefly outlines the two steps and its challenges to obtain the non-prompt background estimate together with its uncertainties based on the calculations in Ref. [232] and [233], which rely on a method conceptualised in the Run 1 analysis of this process [291].

Lepton Fake Factor Measurement and Systematic Uncertainties

The measurement of the fake factor relies on the assumption that prompt leptons are mostly leptons which are reconstructed with high quality and isolated from other detector activity, i.e. leptons that fulfill the `analysis` (short `ana`) object selections, while non-prompt leptons are considered to fail some of the requirements for `analysis` leptons. Hence, a set of selection criteria is to be defined that is predominantly fulfilled by non-prompt leptons. This set is called `anti-analysis` (short `anti-ana`) selection[2] in the following and is listed in Tables D.2 and D.3 for electrons and muons, respectively. Its definition is a compromise between providing a data sample which is as pure as possible in non-prompt leptons while at the same time having enough statistics for the fake factor calculation in different kinematical regions categorised in transverse momentum and pseudorapidity of the lepton. Eventually, these two goals must be balanced against each other with regard to minimising the uncertainty of the final background estimate.

The fake factor, hence the fraction for non-prompt leptons, assumed to populate the

[2]It is to be made clear here that the attribute (non-)prompt is based on the true (parton level) origin of a lepton, while `analysis` or `anti-analysis` are referring to the selection criteria that these leptons fulfill. Hence, `analysis` as well as `anti-analysis` leptons can in principle be prompt or non-prompt.

Table D.3: Summary of `anti-analysis` muon selection criteria used for the non-prompt background estimate with respect to the `analysis` selection (cf Tab. 7.2). Non-prompt muon candidates are selected with the muon `analysis` selection except the requirement of either failing the `Gradient` isolation WP selection or the longitudinal impact parameter requirement.

Observable	Cut value `anti-analysis` selection (w.r.t. to `analysis` selection)
p_{T}	✓
$\lvert\eta\rvert$	✓
Identification WP	✓
$\lvert z_0 \times \sin\theta\rvert$	✓
d_0/σ_{d_0}	< 10
Isolation WP	–
Non-prompt candidate	(! `Gradient` iso.) $\lvert\rvert$ $(d_0/\sigma_{d_0} > 3)$

`anti-analysis` sample, to enter the `analysis` selection, is then defined as:

$$f_\ell(p_{\mathrm{T}}) = \frac{N^{\mathrm{data}}_{\text{ana }\ell}(p_{\mathrm{T}}) - N^{\text{MC prompt}}_{\text{ana }\ell}(p_{\mathrm{T}})}{N^{\mathrm{data}}_{\text{anti-ana }\ell}(p_{\mathrm{T}}) - N^{\text{MC prompt}}_{\text{anti-ana }\ell}(p_{\mathrm{T}})}, \tag{D.12}$$

which is the ratio of the number of events with leptons selected as `analysis` over `anti-analysis` objects in a specially selected data sample $N^{\mathrm{data}}_{\text{ana/anti-ana }\ell}(p_{\mathrm{T}})$ subtracted by the prompt lepton contamination, which is estimated from MC simulated events based on the `MCTruthClassifier` tool as described in Sec. 4.3.3, $N^{\text{MC prompt}}_{\text{ana/anti-ana }\ell}(p_{\mathrm{T}})$. It is calculated in bins of transverse momentum of both lepton candidates in order to account for kinematical dependencies in the faking object.

The fake factor is measured in a so-called "dijet" region that is unlikely to be populated with any prompt leptons and by employing the jet balance method. This selection allows to count the events where a jet is reconstructed as an `analysis` lepton compared to where it is reconstructed as an `anti-analysis` lepton. It is detailed in Tab. D.4.

The events are preselected as in the signal region (cf Tab. 7.4), except for adapting the single lepton trigger chains to the use of `anti-analysis` leptons. Due to the looser selection requirements for `anti-analysis` leptons, trigger chains with looser requirements on the lepton isolation, identification, and transverse momentum have to be employed. These are mostly prescaled and detailed in App. D.1.1. Events are further required to have at least one `analysis` selected jet (central or forward[3]) and exactly one lepton which either satisfies the `analysis` or `anti-analysis` selection depending on whether to be considered for the numerator or denominator of Eq. (D.12), respectively. The selected lepton and the tag jet, defined to be the leading transverse momentum jet in the event, shall be balanced against each other in the transverse plane, i.e. requiring their azimuthal angle separation to be greater than 2.8. According to the MC studies shown in Fig. D.9, $t\bar{t}$ production, featuring heavy flavour jets as a possible source for non-prompt leptons, was found to be the dominant contribution of processes exhibiting an `anti-analysis` leptons, i.e a non-prompt candidate, in the signal region. Therefore events with heavy flavour jets are selected for the fake factor measurement by demanding the tag jet to be a b-tagged jet. The contribution from prompt leptons stemming from leptonic $W^{\pm}$ boson decays is dominant in this region [233]. It is reduced by employing its Jacobian peak feature, rejecting events with the sum of the transverse mass[4] of the charged lepton and missing transverse momentum system, m_T, and the track-based missing transverse momentum $E^{\mathrm{miss}}_{T,\text{ track}}$ exceeding 50 GeV.

[3]The separation into central and forward jets is however made at $|\eta| = 2.5$ in the dijet region compared to $|\eta| = 2.4$ in the signal region.

[4]This transverse mass is defined as $m_T = \sqrt{2p_{\mathrm{T}}E^{\mathrm{miss}}_T(1-\cos\Delta\Phi)}$.

Table D.4: Selection requirements for events to enter the dijet region used for the measurement of the lepton fake factors.

Requirement	Cut value	Explanation
Event preselection:		
As in signal region (cf Tab. 7.4), except adapted trigger chains (see text)		
$N(j)$	≥ 1	Minimum number of jets
j_1	b-tagged	Tag jet ($\equiv$ leading p_{T} jet) is b-tagged
$N(\ell_{\text{ana/anti-ana}})$	$== 1$	Number of charged leptons (e or μ) with `analysis`/`anti-analysis` selection (cf Tables 7.1, 7.2, D.2 and D.3)
Trigger match	$\ell_{\text{ana/anti-ana}}$	Selected lepton must have fired one of the event triggers
$\left\lvert\Delta\Phi(\ell_{\text{ana/anti-ana}}, j_1)\right\rvert$	> 2.8	Candidate lepton and tagging jet are back-to-back in transverse plane
$(m_T + E^{\text{miss}}_{T,\text{ track}})$	$< 50\,\text{GeV}$	Maximum sum of transverse mass and track-based missing transverse energy

It is to be noted that the procedure of overlap removals between leptons and jets in this region is different from the signal region (cf Sec. 3.4.5). The `heavy flavour` WP as used in the signal region, would remove a large fraction of the non-prompt lepton candidates from heavy flavour decays, which are the objects of study here. Hence overlaps are removed with the `lepton favoured` WP, which always keeps the lepton while rejecting the overlapping jet[5].

The `anti-analysis` lepton as selected in this region has substantially different isolation characteristics compared to the `analysis` lepton. The reason for this is instrinsic in the definition of the `anti-analysis` lepton to be required to fail the isolation criteria of the `analysis` lepton. In order to mitigate this effect, the transverse momentum of the `anti-analysis` lepton is redefined as: $p_T^{\text{anti-ana}} = p_{\mathrm{T}} + p_T^{\text{cone30}}$, in order to capture the residual transverse momentum of the underlying jet via adding the sum of its tracks' transverse momenta (from the primary vertex with $p_{\mathrm{T}} > 1.0\,\text{GeV}$) within a cone of $R = 0.3$ around the lepton's track. Detailed studies on this can be found in Ref. [232, 233]. The fake factor of Eq. (D.12) is hence derived in bins of p_{T} of the `analysis` leptons and in bin of the corrected $p_T^{\text{anti-ana}}$ of the lepton selected as `anti-ana`. Likewise all following quantities on the way to estimate this background contribution are calculated with the corrected transverse momentum of the `anti-ana` lepton.

Fig. D.10 shows the (corrected) transverse momentum distribution in experimental data and MC simulation for prompt leptons for the `analysis` and `anti-analysis` selected electrons and muons in the dijet region used to calculated the fake factors. The MC simulated data shows the prompt contamination in this region which is relevant only for the `analysis` selected lepton samples with large transverse momentum. Major contributions come from $W^{\pm}/Z$+jets and $t\bar{t}$ production.

The final fake factor measurement as a function of the lepton transverse momentum together with the statistical and full systematic uncertainties is shown in Fig. D.11 for electrons and muons. The electron fake factor is calculated separately for central barrel ($|\eta| < 1.37$) and end-cap ($1.52 < |\eta| < 2.47$) electrons. The transverse momentum of the electrons(muons) is lowered to 15(20) GeV in the fake factor measurement in order to capture migration effects due to isolation characteristics of the `anti-analysis` selected lepton[6] and to allow for

[5] This difference between the signal and dijet region selection alters the isolation characteristics of the lepton object between the two regions. This is an effect that needs to be studied and accounted for in future analyses in order to improve the background estimate.

[6] This can be seen from the increase in the fake factor for the lowest bin of the p_{T} of the lepton.

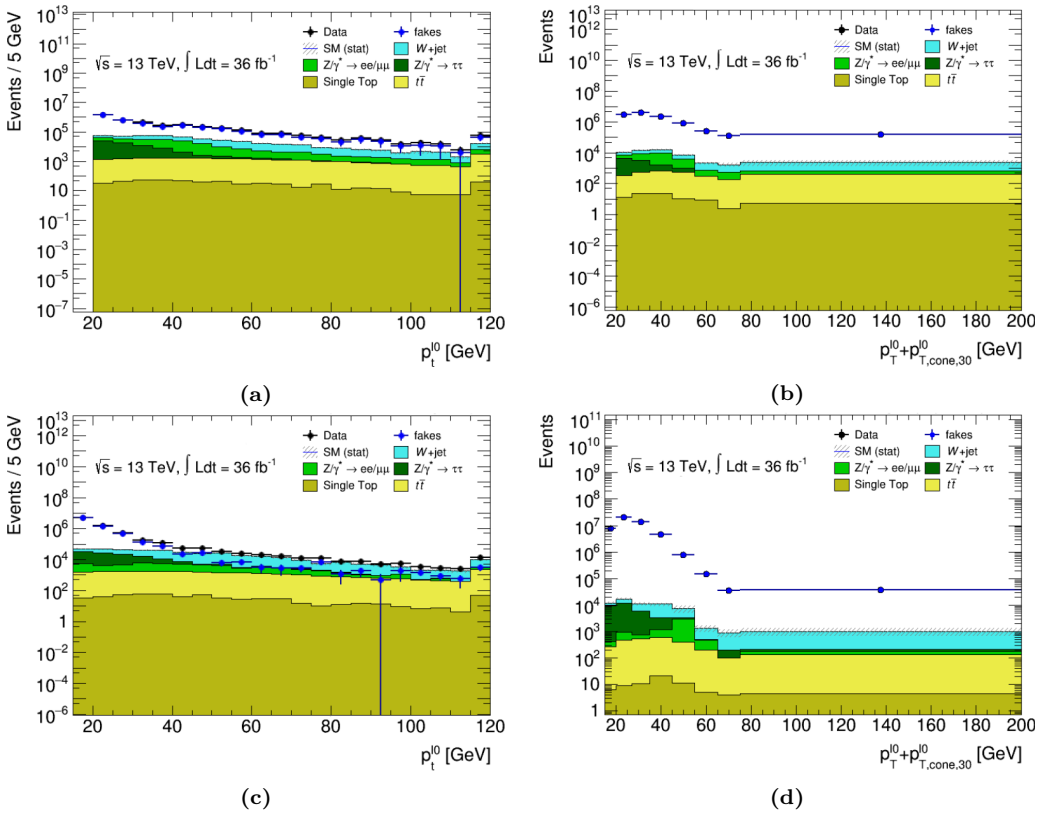


Figure D.10: Distribution of the (corrected) transverse momentum of `analysis` (left) and `anti-analysis` (right) electrons (top) and muons (bottom) in experimental data (black) and from MC simulation considering only prompt leptons in the final state (stacked colour) in the dijet region. The "fakes" contribution (blue) shows the MC subtracted data which is the input for the numerator (left) and denominator (right) for the fake factor measurement in Eq. (D.12). Only statistical uncertainties are shown. Figure taken from Ref. [232].

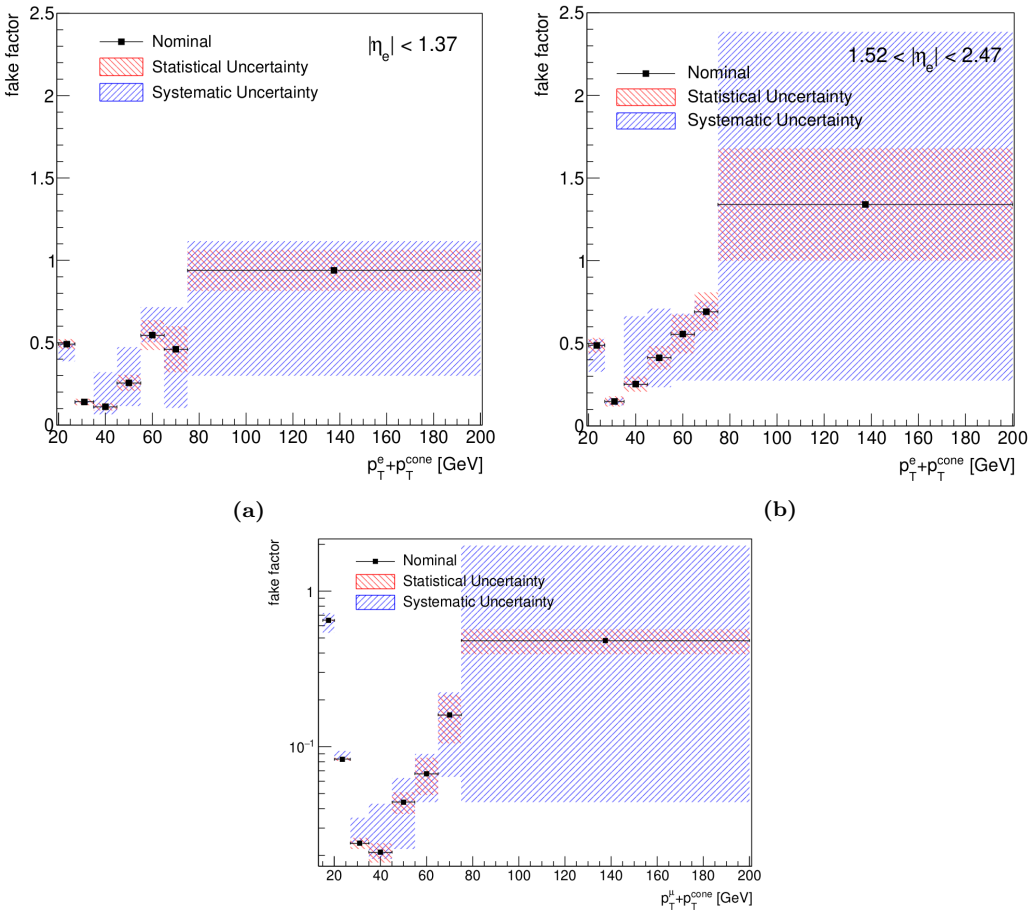


Figure D.11: Fake factor as a function of lepton transverse momentum for central barrel ($|\eta| < 1.37$) (a) and end-cap ($1.52 < |\eta| < 2.47$) (b) electrons, and muons (c). Total uncertainties are shown, divided into statistical and full systematic sources. The systematic uncertainties are calculated as the envelope of all fake factor variations. Note the logarithmic scale for muon fake factor distribution. Figure taken from Ref. [233].

Table D.5: Numerical values and statistical uncertainties of the fake factor for central barrel electrons ($|\eta| < 1.37$) in bins of electron p_{T} for the nominal method and each individual systematic variation. Numbers taken from Ref. [232].

fake factor	pT[20, 27]	pT[27, 35]	pT[35, 45]	pT[45, 55]	pT[55, 65]	pT[65, 75]	pT[75, 200]
nominal	0.491 ± 0.031	0.140 ± 0.020	0.111 ± 0.023	0.256 ± 0.049	0.546 ± 0.091	0.460 ± 0.140	0.939 ± 0.125
MT+MET-up	0.493 ± 0.030	0.138 ± 0.019	0.115 ± 0.022	0.261 ± 0.045	0.559 ± 0.084	0.656 ± 0.091	0.802 ± 0.016
MT+MET-down	0.488 ± 0.032	0.137 ± 0.020	0.110 ± 0.025	0.283 ± 0.053	0.503 ± 0.097	0.351 ± 0.149	1.117 ± 0.255
$\Delta\phi(\ell, j)$-up	0.489 ± 0.035	0.134 ± 0.021	0.105 ± 0.025	0.224 ± 0.048	0.593 ± 0.093	0.356 ± 0.144	0.928 ± 0.177
$\Delta\phi(\ell, j)$-down	0.506 ± 0.029	0.140 ± 0.018	0.111 ± 0.022	0.260 ± 0.046	0.545 ± 0.084	0.546 ± 0.120	0.882 ± 0.103
jetPt	0.493 ± 0.032	0.146 ± 0.021	0.115 ± 0.024	0.259 ± 0.049	0.550 ± 0.091	0.460 ± 0.140	0.939 ± 0.125
nbJet=0	0.387 ± 0.009	0.130 ± 0.008	0.321 ± 0.012	0.473 ± 0.015	0.716 ± 0.180	0.716 ± 0.180	0.716 ± 0.180
Subtract-up	0.488 ± 0.031	0.138 ± 0.020	0.106 ± 0.023	0.248 ± 0.049	0.529 ± 0.092	0.434 ± 0.143	0.888 ± 0.115
Subtract-down	0.493 ± 0.031	0.142 ± 0.020	0.115 ± 0.023	0.264 ± 0.049	0.563 ± 0.090	0.485 ± 0.136	0.989 ± 0.132
Jet pT Reweight	0.445 ± 0.055	0.137 ± 0.037	0.065 ± 0.023	0.115 ± 0.033	0.603 ± 0.047	0.104 ± 0.105	0.299 ± 0.260

Table D.6: Numerical values and statistical uncertainties of the fake factor for central end-cap electrons ($1.37 < |\eta| < 2.5$) in bins of electron p_{T} for the nominal method and each individual systematic variation. Numbers taken from Ref. [232].

fake factor	pT[20, 27]	pT[27, 35]	pT[35, 45]	pT[45, 55]	pT[55, 65]	pT[65, 75]	pT[75, 200]
nominal	0.487 ± 0.046	0.148 ± 0.031	0.253 ± 0.046	0.412 ± 0.071	0.556 ± 0.117	0.691 ± 0.117	1.340 ± 0.340
MT+MET-up	0.483 ± 0.045	0.152 ± 0.031	0.241 ± 0.043	0.443 ± 0.070	0.565 ± 0.106	0.668 ± 0.117	1.075 ± 0.189
MT+MET-down	0.495 ± 0.047	0.156 ± 0.033	0.271 ± 0.052	0.364 ± 0.074	0.664 ± 0.107	0.749 ± 0.056	0.885 ± 0.084
$\Delta\phi(\ell, j)$-up	0.471 ± 0.051	0.158 ± 0.035	0.247 ± 0.051	0.474 ± 0.085	0.283 ± 0.107	0.546 ± 0.149	1.189 ± 0.266
$\Delta\phi(\ell, j)$-down	0.478 ± 0.042	0.170 ± 0.031	0.274 ± 0.046	0.389 ± 0.066	0.645 ± 0.104	0.757 ± 0.102	1.319 ± 0.326
jetPt	0.523 ± 0.048	0.149 ± 0.033	0.235 ± 0.045	0.429 ± 0.073	0.555 ± 0.117	0.691 ± 0.117	1.340 ± 0.340
nbJet=0	0.525 ± 0.011	0.234 ± 0.013	0.644 ± 0.016	0.710 ± 0.014	0.274 ± 0.316	0.274 ± 0.316	0.274 ± 0.316
Subtract-up	0.484 ± 0.046	0.146 ± 0.031	0.248 ± 0.046	0.406 ± 0.071	0.545 ± 0.118	0.676 ± 0.118	1.317 ± 0.337
Subtract-down	0.489 ± 0.046	0.151 ± 0.031	0.257 ± 0.046	0.419 ± 0.071	0.568 ± 0.117	0.705 ± 0.115	1.363 ± 0.342
Jet pT Reweight	0.328 ± 0.068	0.124 ± 0.048	0.297 ± 0.100	0.234 ± 0.061	0.680 ± 0.092	0.452 ± 0.138	2.385 ± 1.729

further studies and adjustments during the analysis preparation.

The sources of systematic uncertainties considered for the fake factor measurement are detailed in Ref. [233] and shall only briefly be reviewed here. They include:

- Individual variations of the selection requirements of the dijet region:
  $\Delta^{+}(p_T(j)) = +5\,\mathrm{GeV}$,
  $\Delta^{\pm}((m_T + E^{\mathrm{miss}}_{T,\,\mathrm{track}})) = \pm 5\,\mathrm{GeV}$, and
  $\Delta^{\pm}(\left|\Delta\Phi(\ell_{\mathrm{ana/anti\text{-}ana}}, j_1)\right|) = \pm 0.1$;

- Variation of the prompt lepton contamination subtraction from MC simulation by $\Delta^{\pm}(\text{MC subtr.}) = \pm 10\%$ derived from the discrepancy between experimental and MC simulated data in a dedicated control region (cf. Ref. [233]);

- Variation due to the removal of the b-tag requirement on the tag jet accounts for the uncertainty due to different jet flavour composition in the dijet and the signal region;

- Variation due to application of the reweighting of the tag jet transverse momentum to account for the difference between the tag jet and underlying jet (i.e. the non-prompt lepton candidate) p_{T} spectrum (cf. Ref. [233]).

The impact of the individual variations on the fake factor measurement in all bins of the lepton p_{T} can be retrieved from Tab. D.5, D.6, and D.7. As the explanations of this background estimate, these are taken from Ref. [232].

Background Estimate in All Regions

The final background contribution is estimated in experimental data which is selected with the selection requirements of the region of interest (e.g. cf. Tab. 7.4 for the signal region selection), except that only one of the leptons is asked to pass the `analysis` selection while

Table D.7: Numerical values and statistical uncertainties of the fake factor for muons in bins of muon p_{T} for the nominal method and each individual systematic variation. Numbers taken from Ref. [232].

fake factor	pT [15, 20]	pT[20, 27]	pT[27, 35]	pT[35, 45]	pT[45, 55]	pT[55, 65]	pT[65, 75]	pT[75, 200]
nominal	0.649 ± 0.007	0.083 ± 0.002	0.024 ± 0.002	0.021 ± 0.003	0.044 ± 0.007	0.067 ± 0.018	0.160 ± 0.055	0.481 ± 0.088
MT+MET-up	0.649 ± 0.007	0.082 ± 0.002	0.082 ± 0.002	0.020 ± 0.003	0.045 ± 0.007	0.068 ± 0.018	0.207 ± 0.062	0.523 ± 0.086
MT+MET-down	0.648 ± 0.007	0.083 ± 0.003	0.024 ± 0.002	0.022 ± 0.004	0.044 ± 0.007	0.054 ± 0.020	0.207 ± 0.060	0.389 ± 0.081
$\Delta\phi(\ell, j)$-up	0.645 ± 0.008	0.083 ± 0.003	0.024 ± 0.002	0.021 ± 0.004	0.045 ± 0.008	0.064 ± 0.021	0.064 ± 0.058	0.438 ± 0.092
$\Delta\phi(\ell, j)$-down	0.646 ± 0.006	0.083 ± 0.002	0.024 ± 0.002	0.020 ± 0.003	0.043 ± 0.006	0.076 ± 0.017	0.174 ± 0.050	0.448 ± 0.078
jetPt-up	0.650 ± 0.007	0.083 ± 0.002	0.024 ± 0.002	0.021 ± 0.003	0.045 ± 0.007	0.069 ± 0.018	0.159 ± 0.018	0.481 ± 0.088
nbJet=0	0.724 ± 0.003	0.094 ± 0.001	0.035 ± 0.001	0.025 ± 0.002	0.022 ± 0.004	0.060 ± 0.015	0.026 ± 0.053	0.044 ± 0.134
Subtract-up	0.648 ± 0.007	0.083 ± 0.002	0.024 ± 0.002	0.019 ± 0.003	0.037 ± 0.007	0.044 ± 0.019	0.096 ± 0.062	0.370 ± 0.082
Subtract-down	0.649 ± 0.007	0.083 ± 0.002	0.025 ± 0.002	0.022 ± 0.003	0.050 ± 0.007	0.090 ± 0.017	0.224 ± 0.052	0.591 ± 0.099
Jet pT Reweight	0.539 ± 0.077	0.093 ± 0.007	0.025 ± 0.004	0.043 ± 0.019	0.063 ± 0.014	0.085 ± 0.025	0.141 ± 0.110	1.962 ± 0.492

another one must pass the `anti-analysis` selection[7]. This region is commonly referred to as the `ana+anti-ana` region. Based on the kinematics of the `anti-analysis` lepton, which is considered to be the non-prompt lepton candidate, the fake factor is applied as an event weight to these events after subtracting contributions from events with prompt leptons and electrons which are subject to charge misidentification.

In the $e^{\pm}e^{\pm}$ and $\mu^{\pm}\mu^{\pm}$ channels, this results in a background event estimate as follows:

$$N^{\mathrm{bkg}}_{\text{non-prompt}} = \sum_i f_\ell(i) \cdot \left(N^{\mathrm{data}}_{\text{ana } \ell\text{+anti-ana } \ell}(i) - N^{\text{MC prompt}}_{\text{ana } \ell\text{+anti-ana } \ell}(i) - N^{\text{data charge misID}}_{\text{ana } \ell\text{+anti-ana } \ell}(i) \right), \tag{D.13}$$

where $N^{\mathrm{data}}_{\text{ana+anti-ana}}$ is the event yield in the region selecting one `analysis` and one `anti-analysis` lepton, $N^{\text{MC prompt}}_{\text{ana+anti-ana}}$ is the number of events in this region which exhibit two prompt leptons based on MC simulation information, and $N^{\text{data charge misID}}_{\text{ana+anti-ana}}$ is the number of events in the $e^{\pm}e^{\pm}$ channel in which one of the electrons undergoes charge misidentification[8]. The latter also contains events where the electron which is selected as an `anti-analysis` object is subject to charge misidentification. Hence, charge misidentification probabilities for these objects have to be derived in addition to the ones for `analysis` electrons summarised in Sec. D.2.1. These are obtained in a slightly modified manner whose exact methodology and numbers shall not be content of this thesis. They can be obtained from Ref. [219, 232]. The fake factor is applied in bins of the corrected transverse momentum (and pseudorapidity) of the `anti-analysis` muon(electron), denoted as i.

In the $e^{\pm}\mu^{\pm} + \mu^{\pm}e^{\pm}$ channels both, the electron and the muon fake factor need to be applied to a separate set of events where either the electron or the muon is selected as the `anti-analysis` lepton, i.e. the non-prompt candidate from a misidendified jet:

$$\begin{aligned} N^{\mathrm{bkg}}_{\text{non-prompt}} = &\sum_i f_e(i) \cdot \left(N^{\mathrm{data}}_{\text{ana } \mu\text{+anti-ana } e}(i) - N^{\text{MC prompt}}_{\text{ana } \mu\text{+anti-ana } e}(i) - N^{\text{data charge misID}}_{\text{ana } \mu\text{+anti-ana } e}(i) \right) \\ &+ \sum_i f_\mu(i) \cdot \left(N^{\mathrm{data}}_{\text{ana } e\text{+anti-ana } \mu}(i) - N^{\text{MC prompt}}_{\text{ana } e\text{+anti-ana } \mu}(i) - N^{\text{data charge misID}}_{\text{ana } e\text{+anti-ana } \mu}(i) \right). \end{aligned} \tag{D.14}$$

D.2.3 Non-prompt Electrons from Photon Conversions

Massive boson production with leptonic decay in association with I/FSR photons can contribute to the signal region event yield if:

[7] This especially means that the trigger chains used for this background estimate stay unchanged in these regions which implies that events exist where the `anti-analysis` lepton cannot fire the event trigger. The event selection inefficiencies caused by this are studied and found to be approx. 10(20)% for electrons(muons). These corrections are not applied to the nominal background estimate, as they have not been ready in time. It is argued that these are well within the systematic uncertainties of the method [232].

[8] These are mainly processes such as Z+jets, $t\bar{t}$ and single top production.

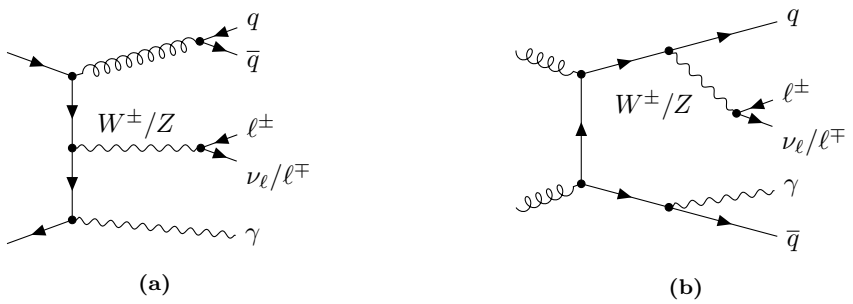


Figure D.12: Examples of Feynman diagrams of the leptonic $V\gamma$+jets process, where a massive boson $V \in \left\{W^{\pm}, Z\right\}$ is produced in association with an ISR (a) ot FSR (b) photon and jets. This class of processes can enter the signal region if the photon converts into an electron-positron pair, one of which forms a same-charge pair with an additional lepton from the massive boson decay.

- The photon converts into an electron/positron pair[9], and
- One of the leptons from the $W^{\pm}$ or Z decay forms a pair of same electrical charge leptons with one of the conversion objects, and
- at least two high energetic jets are present.

Processes of such kind consequently comprise genuine $W^{\pm}$ or Z boson production in association with a photon (which subsequently converts) and jets, as depicted in Fig. D.12, where all final state physics objects need to be energetic enough to be selected into the signal region. The origin of the photon can, however, be manifold. Events with photons produced in hadron decays or jet fragmentation and quark bremsstrahlung are accounted for in the estimate of the non-prompt background, addressed in the previous section. Events with photons with moderate energy from lepton bremsstrahlung in events with Z bosons are accounted for in the estimate of the background due to electron charge misidentification as this is estimated from experimental data involving opposite charge leptons from the Z boson resonance. Hence, the only missing contribution is of events with $W^{\pm}$ or Z boson production together with jets and prompt energetic photons, denoted as $W^{\pm}\gamma$ and $Z\gamma$ in the following.

In order to estimate this background contribution, a dedicated region is designed in which experimental data is compared to MC simulated events. From this, a scale factor is extracted which is used to adjust the event yields obtained from MC simulation of the $W^{\pm}\gamma$ and $Z\gamma$ processes in all regions utilised in the analysis. In this way, inefficiencies in the modelling of these processes in simulations are corrected. In fact, the event yield of the $Z\gamma$ process in the signal region is zero, only leaving $W^{\pm}\gamma$ events to be corrected. This, however, does not change the procedure to estimate this background. It is detailed in Ref. [220] and briefly summarised in the following.

The method again exploits Z boson production and its well reconstructable mass peak. The idea is to use events with photon FSR, and subsequent conversion, from one of the muons of the Z boson decay: $Z \to \mu^+\mu^-\gamma^* \to \mu^+\mu^- e^+ e^-$. Hence, after the event preselection, which is identical to the signal region selection (cf Tab. 7.4), two opposite charge muons and one electron, all of which passing the `analysis` selection requirements (cf Tables 7.2 and 7.1), are required which together form a system with invariant mass within $75\,\text{GeV} < |m_{\mu\mu e} - m_Z| < 100\,\text{GeV}$ around the Z boson mass. The electron is assumed to originate from the photon conversion. In order to suppress contributions from processes involving a leptonically decaying $W^{\pm}$ boson, such as $W^{\pm}Z$, $W^{\pm}\gamma$, and $W^{\pm}$+jets, the missing transverse momentum is required to not exceed 30 GeV. By construction, this region is orthogonal to the signal region. The total event yields from MC simulation and experimental data in this region, summarised in Tab. D.8, show reasonable purity in the $Z\gamma$ contribution. In the MC simulation of the $Z\gamma$ and Z+jets processes events with photons with overlapping

[9] As explained when estimating the background due to lepton charge misidentification, the cross-section for photon conversion into muons is suppressed by more than four orders of magnitude compared to electrons.

Table D.8: Event yields of experimental data, all relevant processes estimated from MC simulation in the $Z\gamma$ region, where $V \in \{W^{\pm}, Z, \gamma\}$ (excluding the $Z\gamma$ process), and their sum (denoted "total simulation"). Event yields for the $Z\gamma$ and Z+jets processes are quoted after removing overlaps between the two simulated samples. Uncertainties are statistical only. Numbers taken from Ref. [232].

Process	Event yield
$Z\gamma$	24.60 ± 3.32
Z+jets	3.02 ± 1.54
Other $VV + VVV$	6.66 ± 0.32
Top	1.49 ± 0.51
Total simulation	35.76 ± 3.71
Data	57.00 ± 7.55

kinematic properties can occur[10]. This overlap is removed by rejecting Z+jets simulated events if they contain a photon[11] satisfying the generator level cuts of the $Z\gamma$ MC sample ($p_{\mathrm{T}}(\gamma) > 10\,\mathrm{GeV}$ and $\Delta R(\ell, \gamma) < 0.1$). The modelling of the invariant masses in this region is shown in Fig. D.13.

From the event yields in this region a normalisation factor is obtained:

$$\mathrm{SF}_{W^{\pm}\gamma} = \frac{N^{\mathrm{data}} - N^{\mathrm{MC}}_{\text{other } VV+VVV} - N^{\mathrm{MC}}_{\mathrm{top}}}{N^{\mathrm{MC}}_{Z\gamma} + N^{\mathrm{MC}}_{Z+\mathrm{jets}}}, \tag{D.15}$$

$$= 1.77 \pm 0.36, \tag{D.16}$$

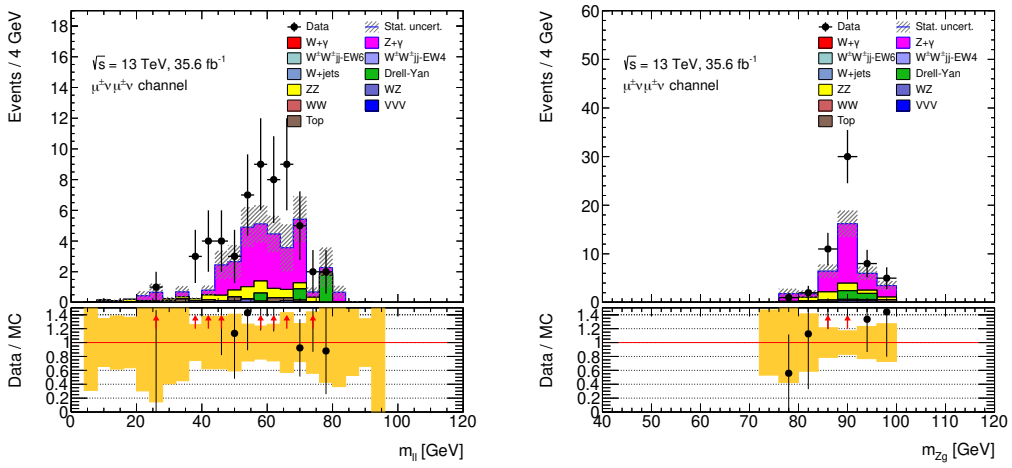
which is used to correct the $W^{\pm}\gamma$ contribution in all relevant regions of the statistical analyses.

D.3 Validation of the Background Modelling

Seven validation regions are defined, six of which select two same-charge leptons and one triboson VR. Their selection requirements with respect to the signal region (cf Tab. 7.4) are summarised in Tab. D.9 and D.10, respectively. They are briefly explained in the following. Only the most relevant example distributions in each VR are shown. The reader is referred to Ref. [232] for more insights, where the kinematic distributions are taken from. All distributions are shown with statistical uncertainties from data and MC simulation only. Event yields in experimental data and estimated background contributions for all processes are shown in Tab. D.11.

The "same-charge inclusive" VR is the most inclusive region looked at. The requirement on the missing transverse momentum E_T^{miss} is omitted as well as any jet selection requirements in the event, except the b-jet veto. With these requirements, the signal region is part of this validation region. However, the fraction of events passing the signal region selection is small compared to the overall event content of this VR. With this VR, the lepton kinematics can be inspected in a region where the background contributions due to electron charge misidentification and non-prompt leptons are sizable if not dominant. The subleading lepton transverse momentum in the $e^{\pm}e^{\pm}$ channel, the dilepton invariant mass m_{ll} in the $e^{\pm}\mu^{\pm} + \mu^{\pm}e^{\pm}$ channel, and both the distribution of E_T^{miss} and the number of jets $N(j)$ in the combined channel in this region are exemplary shown in Fig. D.14. While an overall good agreement with experimental data is obtained, a missmodelling in m_{ll} around the Z boson resonance is seen in the $e^{\pm}\mu^{\pm} + \mu^{\pm}e^{\pm}$ channel, which is further occurring at low E_T^{miss} and $N(j)$. This

[10] This is due to the parton shower algorithms including FSR photon radiation.
[11] This is done excluding photons from hadron decays via truth information.



(a) **(b)**

Figure D.13: Distribution of the invariant mass of the dilepton and dilepton+photon system, m_{ll} (a) and $m_{Z\gamma}$ (b), respectively, in the $Z\gamma$ region. Shown is data (black) compared to the overall prediction taken from MC simulation (stacked colour). Uncertainties are statistical only. The lower pad shows the experimental data relative to the sum of all SM predictions. The residual disagreement is considered to be due to mismodelling of the $Z\gamma$ process in simulation and corrected for with the derived scale factor $\mathrm{SF}_{Z\gamma}$. Figure taken from Ref. [220].

Table D.9: Definition with respect to the signal region (cf Tab. 7.4) of all validation regions selecting two same-charge leptons. Selection requirements are tightening from left to right. The event preselection in all validation regions follows the signal region, as well as most lepton event selection requirements. Exceptions are the inverted invariant mass selection around the Z boson mass in the $e^{\pm}e^{\pm}$ channels and the missing transverse momentum requirement which is omitted for some of the regions. Jet event selection requirements are as stated for each region. The requirements on the VBS observables are mostly inverted if not omitted entirely.

Observable	Cut value w.r.t. signal region in all same-charge channels ($e^{\pm}e^{\pm}$, $\mu^{\pm}\mu^{\pm}$, $e^{\pm}\mu^{\pm}$, $\mu^{\pm}e^{\pm}$)					
	Inclusive	Low-$N(j)$	Top non-prompt	Top EW	Low-m_{jj}	Low-ΔY_{jj}
	Event preselection as in signal region					
	Lepton event selection as in signal region, except: Inverted Z boson veto, i.e. $\lvert m_{ee} - m_Z \rvert < 15\,\mathrm{GeV}$ ($e^{\pm}e^{\pm}$ channel only)					
E_T^{miss}	–	✓	–	–	✓	✓
	Jet event selection:					
$N(j)$	–	< 2	✓	✓	✓	✓
$p_{\mathrm{T}}(j_1)$	–	–	✓	✓	✓	✓
$p_{\mathrm{T}}(j_2)$	–	–	✓	✓	✓	✓
N(b-jet)	✓	✓	$= 1$	≥ 2	✓	✓
	VBS selection:					
m_{jj} [GeV]	–	–	–	–	< 500	> 200
$\Delta Y(jj)$	–	–	–	–	–	< 2.0

Table D.10: Definition with respect to the signal region (cf. Tab. 7.4) of the "trilepton" validation region. The event preselection follows the signal region. The lepton event selection requirements are altered such that exactly one `veto` lepton with transverse momentum larger than 15 GeV needs to be present in the event. The special requirements in the $e^{\pm}e^{\pm}$ channels are omitted, as well as the E_T^{miss} selection. No jet event selection requirements are imposed except for the veto on b-tagged jets in the event.

Observable	Cut value w.r.t. signal region in trilepton validation region $\ell\ell'\ell''$, $\ell^{(\prime\prime)} = e^{\pm}$ or $\mu^{\pm}$
Event preselection as in signal region	
Lepton event selection as in signal region, except:	
$N(\ell_{\text{veto}})$	$== 1$
$p_{\text{T}}(\ell_{\text{veto}})$	$> 15\,\text{GeV}$
$\lvert m_{ee} - m_Z \rvert$	–
$\lvert \eta_e \rvert$	–
E_T^{miss}	–
No jet event selection, except:	
N(b-jet)	✓

could indicate a mismodelling of the $Z\gamma$ contribution. The mismodelled kinematical regions are not selected into the signal region and hence, do not play a major role in the analysis.

The "same-charge low-$N(j)$" VR is designed to test the largest background sources, i.e. the backgrounds due to $W^{\pm}Z$ processes, the non-prompt leptons and electron charge misidentification. The lepton selection requirements are unchanged w.r.t. the signal region, except the inversion of the Z boson mass window in the $e^{\pm}e^{\pm}$ channels. Events are required to have at most one selected jet, inverting the selection requirements on the number of jets of the signal region. Fig. D.15 shows the subleading lepton transverse momentum for events where the subleading lepton is either an electron or a muon.

The "same-charge top non-prompt" VR is used to test the modelling of the background due to non-prompt leptons. With the requirement of exactly one b-jet in the event, this region is populated with events in which a b-jet is identified as an isolated lepton. Fig. D.16 shows the subleading lepton p_{T} for events where the subleading lepton is either an electron or a muon. Fig. D.17 shows the $N(j)$ and m_{jj} distributions in the combined channels.

The "same-charge top EW" VR select only events with at least two b-tagged jets, hence further tightening the requirements of the "same-charge top non-prompt" VR. The region is enriched in events from $t\bar{t}V$ production as well as electron charge misidentification, where one of the leptons is either reconstructed from a jet or with a wrong charge. The upper panels in Fig. D.18 show the E_T^{miss} and $N(j)$ distributions in the combined channels.

The "same-charge low-m_{jj}" and "same-charge low-ΔY_{jj} " VRs have similar requirements as the signal region. These allow to test the background modelling in regions with similar background composition as the signal region. For the first, the selection on the tagging jet invariant mass is inverted and the ΔY_{jj} requirement omitted. The focus here is laid on testing the modelling of the non-prompt background where statistics are larger compared to the signal region. The distribution of subleading lepton p_{T} in the $e^{\pm}\mu^{\pm} + \mu^{\pm}e^{\pm}$ channels, and the m_{jj} in the combined channels in this region are shown in the lower panels of Fig. D.18. In the "same-charge low-ΔY_{jj}" VRs events with $m_{jj} > 200\,\text{GeV}$ and $\Delta Y_{jj} < 2.0$ are selected. By inverting the requirement on the pseudorapidity separation of the tagging jets, the modelling of QCD-induced processes can be studied, such as $W^{\pm}Z$ and ZZ production, as well as backgrounds from non-prompt leptons. The upper panels of Fig. D.19 show the $N(j)$ and m_{jj} distributions in the combined channels for this region. The agreement between data and background estimate is good in both regions.

A "trilepton" VR is built from two `analysis` selected leptons and one `veto` selected lepton

Table D.11: Event yields and their statistical uncertainties split in $e^{\pm}e^{\pm}$, $\mu^{\pm}\mu^{\pm}$, $e^{\pm}\mu^{\pm}$, and $\mu^{\pm}e^{\pm}$ channels in all same-charge validation regions and the trilepton validation region. The term "charge-flip" refers to background contributions due to electron charge misidentification. The term "fakes" refers to background contributions due to non-prompt leptons. The last column shows the ratio between experimental data and the combined background estimations (from MC simulation and data-driven methods).

ee channel	Data	$W^{\pm}W^{\pm}$ EWK	$W^{\pm}W^{\pm}$ QCD	WZ	ZZ	$W+\gamma$	$Z+\gamma$	VVV	Top	Charge-flip	Fakes	Data/MC
SS inclusive VR	998.00 ± 31.59	15.60 ± 0.17	6.26 ± 0.08	115.80 ± 2.41	8.37 ± 0.29	21.01 ± 7.46	3.84 ± 1.15	0.95 ± 0.07	3.19 ± 0.38	603.53 ± 1.44	201.56 ± 26.90	1.02 ± 0.04
SS Low M_{jj} VR	67.00 ± 8.19	3.61 ± 0.08	2.76 ± 0.05	19.16 ± 0.60	0.80 ± 0.07	0.75 ± 0.28	0.07 ± 0.04	0.23 ± 0.03	1.71 ± 0.29	15.13 ± 0.26	28.65 ± 4.93	0.92 ± 0.13
SS Low ΔY_{jj} VR	27.00 ± 5.20	1.65 ± 0.05	2.55 ± 0.05	7.03 ± 0.24	0.17 ± 0.02	0.08 ± 0.04	0.02 ± 0.02	0.10 ± 0.02	0.36 ± 0.06	4.76 ± 0.15	11.29 ± 3.31	0.96 ± 0.22
SS Low n_{jet} VR	239.00 ± 15.46	3.99 ± 0.08	1.10 ± 0.03	59.98 ± 1.91	2.08 ± 0.16	9.85 ± 6.14	0.48 ± 0.29	0.54 ± 0.06	0.94 ± 0.24	80.63 ± 0.55	91.08 ± 8.27	0.95 ± 0.07
SS top-fakes VR	116.00 ± 10.77	2.52 ± 0.09	1.43 ± 0.05	10.02 ± 0.50	0.73 ± 0.07	0.09 ± 0.07	0.08 ± 0.05	0.13 ± 0.03	12.72 ± 0.75	34.62 ± 0.40	70.87 ± 6.85	0.87 ± 0.09
SS top-EW VR	91.00 ± 9.54	0.26 ± 0.03	0.15 ± 0.02	1.37 ± 0.13	0.14 ± 0.02	0.03 ± 0.03	0	0.01 ± 0.01	20.11 ± 0.78	41.80 ± 0.43	31.32 ± 5.92	0.96 ± 0.12
$\mu\mu$ channel	Data	$W^{\pm}W^{\pm}$ EWK	$W^{\pm}W^{\pm}$ QCD	WZ	ZZ	$W+\gamma$	$Z+\gamma$	VVV	Top	Charge-flip	Fakes	Data/MC
SS inclusive VR	726.00 ± 26.94	42.49 ± 0.28	23.26 ± 0.16	408.45 ± 6.63	29.10 ± 0.60	0	0.32 ± 0.32	3.64 ± 0.14	7.39 ± 0.24	0	105.51 ± 3.62	1.17 ± 0.05
SS Low M_{jj} VR	96.00 ± 9.80	10.02 ± 0.15	10.05 ± 0.10	47.48 ± 0.81	1.38 ± 0.07	0	0	0.71 ± 0.06	4.01 ± 0.18	0	14.70 ± 1.40	1.09 ± 0.11
SS Low ΔY_{jj} VR	31.00 ± 5.57	3.97 ± 0.08	7.66 ± 0.09	16.20 ± 0.42	0.38 ± 0.03	0	0	0.24 ± 0.03	1.09 ± 0.10	0	4.03 ± 0.92	0.92 ± 0.17
SS Low n_{jet} VR	387.00 ± 19.67	12.38 ± 0.15	4.53 ± 0.07	244.58 ± 6.12	13.08 ± 0.45	0	0	2.35 ± 0.11	2.25 ± 0.13	0	50.14 ± 2.71	1.18 ± 0.06
SS top-fakes VR	118.00 ± 10.86	6.13 ± 0.13	4.63 ± 0.09	18.13 ± 0.48	0.70 ± 0.05	0	0.01 ± 0.01	0.34 ± 0.04	25.04 ± 0.48	0	53.03 ± 2.56	1.09 ± 0.10
SS top-EW VR	96.00 ± 9.80	0.56 ± 0.04	0.57 ± 0.04	2.61 ± 0.19	0.11 ± 0.02	0	0	0.11 ± 0.03	40.33 ± 0.61	0	21.16 ± 1.85	1.47 ± 0.16
$e\mu$ channel	Data	$W^{\pm}W^{\pm}$ EWK	$W^{\pm}W^{\pm}$ QCD	WZ	ZZ	$W+\gamma$	$Z+\gamma$	VVV	Top	Charge-flip	Fakes	Data/MC
SS inclusive VR	1318.00 ± 36.30	39.39 ± 0.27	20.72 ± 0.15	432.25 ± 5.46	32.77 ± 0.58	77.55 ± 11.00	31.72 ± 5.45	3.36 ± 0.13	10.24 ± 0.65	151.97 ± 1.91	388.09 ± 17.59	1.11 ± 0.04
SS Low M_{jj} VR	171.00 ± 13.08	9.24 ± 0.13	9.01 ± 0.10	59.42 ± 1.11	2.09 ± 0.13	6.59 ± 1.84	1.28 ± 0.51	0.74 ± 0.06	4.42 ± 0.29	21.88 ± 0.75	45.65 ± 6.36	1.07 ± 0.09
SS Low ΔY_{jj} VR	67.00 ± 8.19	4.00 ± 0.08	7.06 ± 0.09	19.00 ± 0.54	0.57 ± 0.04	2.40 ± 1.04	0.10 ± 0.04	0.36 ± 0.04	1.26 ± 0.10	5.73 ± 0.39	13.82 ± 3.93	1.23 ± 0.18
SS Low n_{jet} VR	642.00 ± 25.34	11.25 ± 0.15	4.06 ± 0.07	250.54 ± 4.70	12.70 ± 0.38	46.54 ± 9.01	6.95 ± 1.59	2.08 ± 0.10	4.00 ± 0.54	84.05 ± 1.45	184.84 ± 13.04	1.06 ± 0.05
SS top-fakes VR	252.00 ± 15.87	5.77 ± 0.13	4.14 ± 0.08	23.72 ± 0.66	1.10 ± 0.07	4.30 ± 1.38	0.40 ± 0.32	0.35 ± 0.04	35.02 ± 1.70	109.02 ± 1.61	93.05 ± 8.98	0.91 ± 0.07
SS top-EW VR	279.00 ± 16.70	0.54 ± 0.04	0.53 ± 0.04	3.48 ± 0.25	0.17 ± 0.03	0.38 ± 0.31	0.06 ± 0.04	0.05 ± 0.02	48.78 ± 1.37	142.07 ± 1.71	35.77 ± 8.38	1.20 ± 0.08
μe channel	Data	$W^{\pm}W^{\pm}$ EWK	$W^{\pm}W^{\pm}$ QCD	WZ	ZZ	$W+\gamma$	$Z+\gamma$	VVV	Top	Charge-flip	Fakes	Data/MC
SS inclusive VR	1285.00 ± 35.85	36.54 ± 0.25	19.17 ± 0.14	382.08 ± 4.80	28.21 ± 0.53	91.02 ± 13.14	39.59 ± 3.96	2.70 ± 0.12	8.63 ± 0.55	98.80 ± 1.28	504.79 ± 14.86	1.06 ± 0.03
SS Low M_{jj} VR	125.00 ± 11.18	8.66 ± 0.12	8.29 ± 0.09	52.25 ± 1.01	1.96 ± 0.11	2.85 ± 1.24	0.85 ± 0.47	0.55 ± 0.05	4.10 ± 0.28	11.74 ± 0.42	50.37 ± 4.93	0.88 ± 0.09
SS Low ΔY_{jj} VR	43.00 ± 6.56	3.64 ± 0.08	6.42 ± 0.08	17.00 ± 0.43	0.50 ± 0.04	1.67 ± 1.08	0.01 ± 0.01	0.24 ± 0.03	1.24 ± 0.10	3.04 ± 0.22	13.00 ± 2.84	0.92 ± 0.15
SS Low n_{jet} VR	603.00 ± 24.56	10.55 ± 0.13	3.76 ± 0.06	204.33 ± 4.05	9.53 ± 0.32	45.44 ± 8.59	5.84 ± 1.48	1.69 ± 0.10	2.85 ± 0.42	50.82 ± 0.96	247.96 ± 10.63	1.03 ± 0.05
SS top-fakes VR	182.00 ± 13.49	5.29 ± 0.12	3.94 ± 0.08	19.82 ± 0.68	1.01 ± 0.08	4.70 ± 3.11	0.00 ± 0.00	0.28 ± 0.04	25.99 ± 0.83	57.01 ± 0.94	105.11 ± 7.09	0.82 ± 0.07
SS top-EW VR	194.00 ± 13.93	0.58 ± 0.05	0.41 ± 0.03	3.10 ± 0.47	0.27 ± 0.06	0.95 ± 0.86	0.04 ± 0.04	0.07 ± 0.02	43.05 ± 1.35	78.88 ± 1.03	49.56 ± 6.74	1.10 ± 0.09
$\ell\ell\ell$ channel	Data	$W^{\pm}W^{\pm}$ EWK	$W^{\pm}W^{\pm}$ QCD	WZ	ZZ	$W+\gamma$	Z+jets	VVV	Top	—	—	Data/MC
TriLepton Inclusive CR	7840.00 ± 88.54	0.02 ± 0.01	0.01 ± 0.00	5274.70 ± 17.84	1032.11 ± 7.22	0.04 ± 0.04	2310.01 ± 216.44	32.40 ± 0.35	157.55 ± 4.47	—	—	0.89 ± 0.02

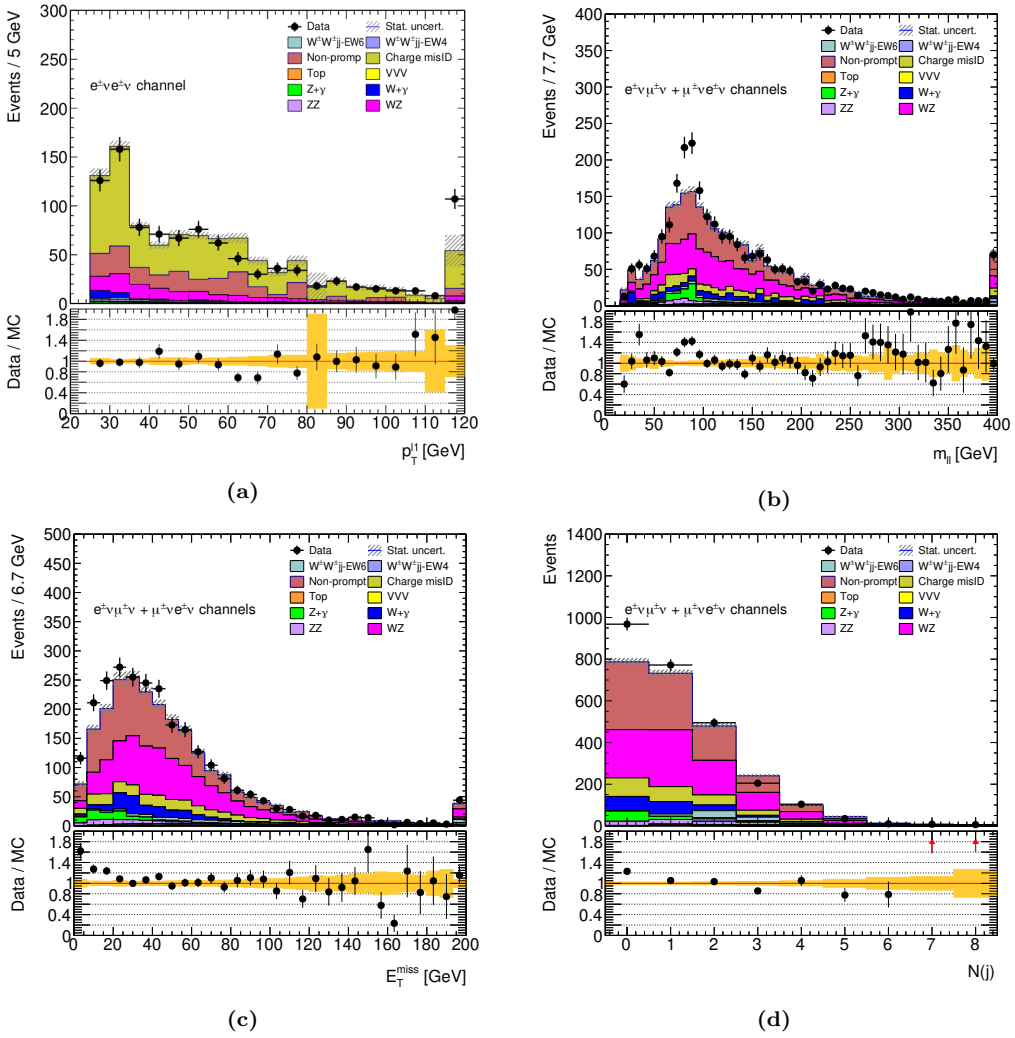
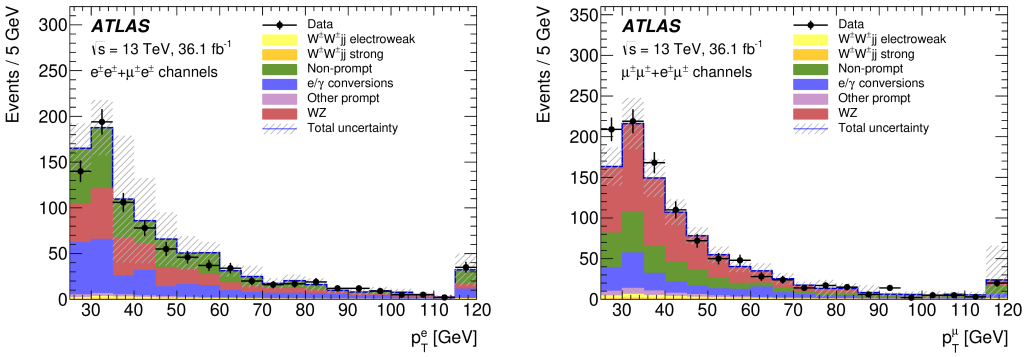
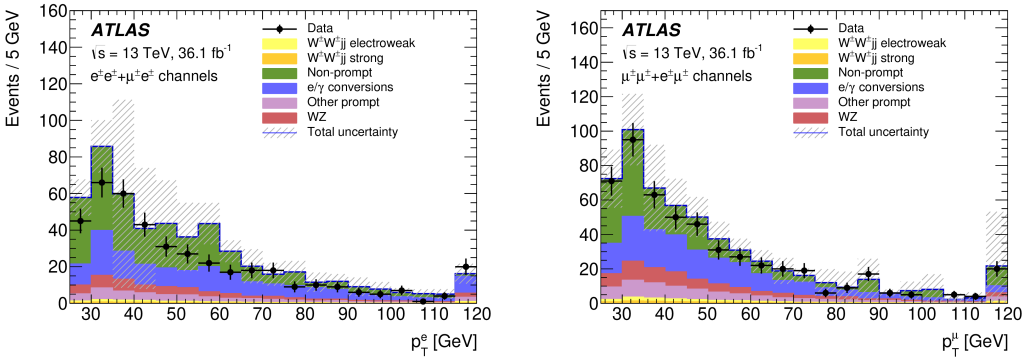


Figure D.14: Distributions in the "same-charge inclusive" validation region of the subleading lepton transverse momentum in the $e^{\pm}e^{\pm}$ channels (a), the invariant mass of the dilepton system m_{ll} (b), the missing transverse momentum E_T^{miss} (c), and the number of jets in the event $N(j)$ (d) in the $e^{\pm}\mu^{\pm} + \mu^{\pm}e^{\pm}$ channels. Uncertainties are statistical only for both the distribution of the experimental data, as well as MC simulated events. The lower pad shows the experimental data relative to the sum of all SM predictions. Figures taken from Ref. [232].



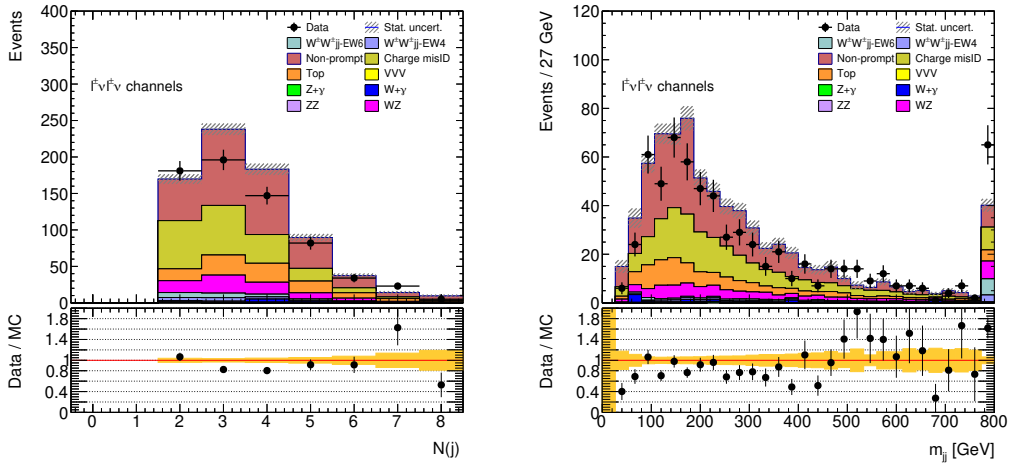
(a) **(b)**

Figure D.15: Distributions in the "same-charge low-$N(j)$ " validation region of the subleading lepton transverse momentum for events where the subleading lepton is an electron (a) and a muon (b). The hatched band represents the statistical and systematic uncertainties of the background prediction added in quadrature. "Other prompt" comprises MC-based predictions of the processes of $t\bar{t}V$, ZZ, and triboson production. The last bin of each distribution includes the overflow. Figures taken from Ref. [1].



(a) **(b)**

Figure D.16: Distributions in the "same-charge top non-prompt" validation region. Shown are the subleading lepton transverse momentum for events where the subleading lepton is an electron (a) and a muon (b). The hatched band represents the statistical and systematic uncertainties of the background prediction added in quadrature. "Other prompt" comprises MC-based predictions of the processes of $t\bar{t}V$, ZZ, and triboson production. The last bin of each distribution includes the overflow. Figures taken from Ref. [1].



(a) **(b)**

Figure D.17: Distributions in the "same-charge top non-prompt" validation region of the number of jets in the event $N(j)$ (a), and the invariant mass of the tagging jet system m_{jj} (b) in the combined channels. Uncertainties are statistical only for both the distribution of the experimental data, as well as MC simulated events. The lower pad shows the experimental data relative to the sum of all SM predictions. Figures taken from Ref. [232].

in order to test the modelling of the $W^{\pm}Z$ process in a region with no jet requirements except vetoing events containing b-tagged jets. By omitting a large set of selection requirements compared to the $W^{\pm}Z$ control region, discussed in Sec. 8.4.1, this background contribution can be studied with larger statistics. The lower panels of Fig. D.19 show the invariant mass of the dilepton system with m_{ll} closest to the Z boson mass, and the trilepton system m_{lll} in the combined channels.

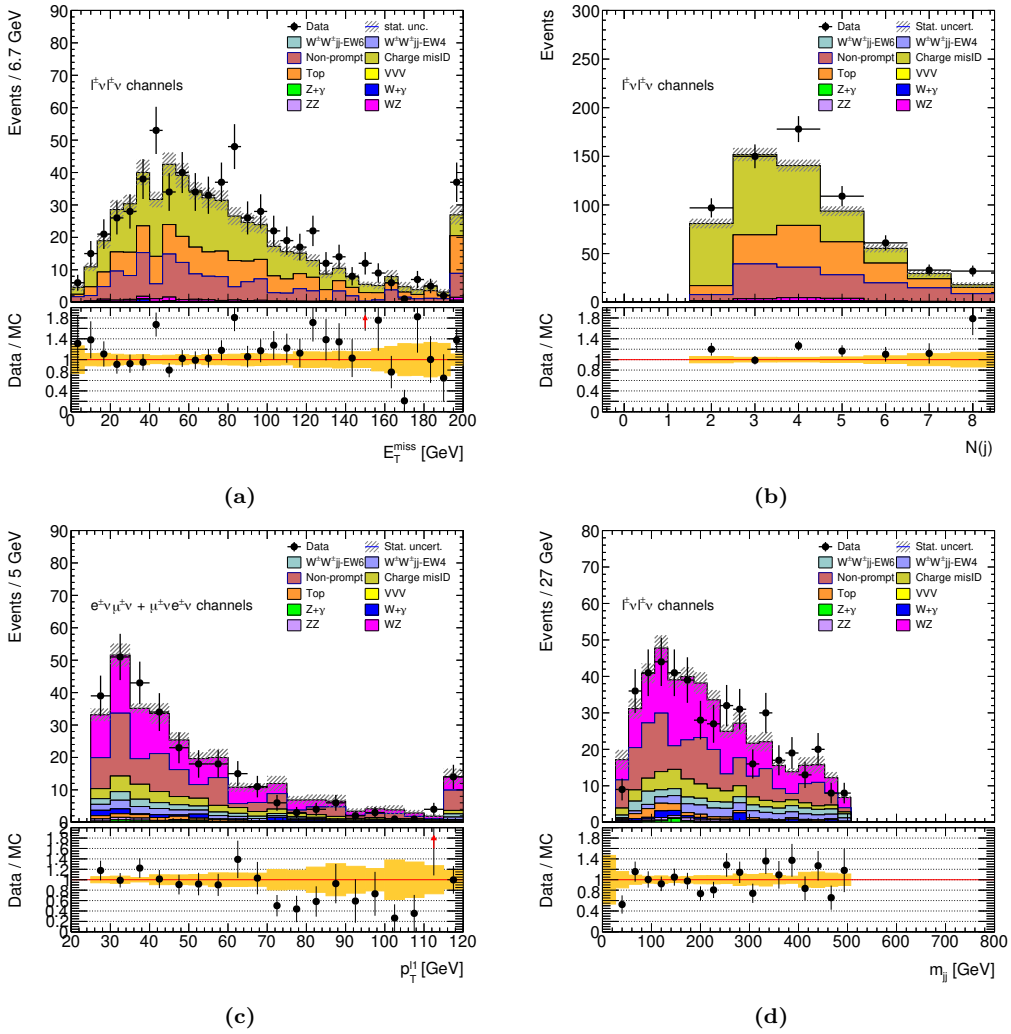


Figure D.18: Distributions in the "same-charge top EW" validation region of the missing transverse momentum E_T^{miss} (a), and the number of jets in the event $N(j)$ (b) in the combined channels, and distributions in the "same-charge low-m_{jj} " validation region of the subleading lepton transverse momentum in the $e^{\pm}\mu^{\pm} + \mu^{\pm}e^{\pm}$ channels (c) and the invariant mass of the tagging jet system m_{jj} (d) in the combined channels. Uncertainties are statistical only for both the distribution of the experimental data, as well as MC simulated events. The lower pad shows the experimental data relative to the sum of all SM predictions. Figures taken from Ref. [232].

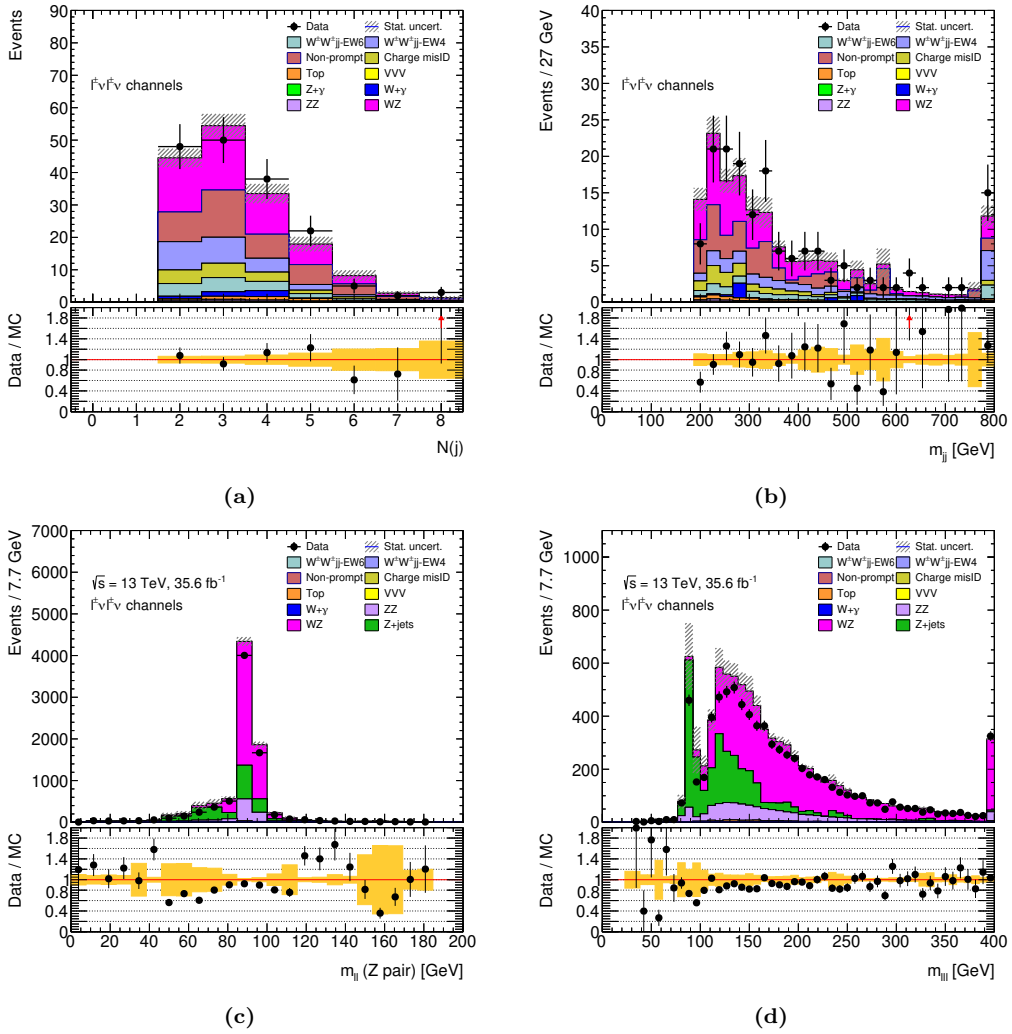


Figure D.19: Distributions in the "same-charge low-ΔY_{jj} " validation region of the number of jets in the event $N(j)$ (a) and the invariant mass of the tagging jet system m_{jj} (b), and distributions in the "trilepton" validation region of the invariant mass of the dilepton system with invariant mass closest to the Z boson mass m_{ll} (c) and of the trilepton system m_{lll} (d) in the combined channels. Uncertainties are statistical only for both the distribution of the experimental data, as well as MC simulated events. The lower pad shows the experimental data relative to the sum of all SM predictions. Figures taken from Ref. [232].

D.4 Systematic Uncertainties

D.4.1 Experimental Uncertainties

D.4.2 Modelling Uncertainties

Derivation of the Folding Prescription

The probability of finding $N(R_j)^{\text{test}}$ events in bin j at reconstruction level:

$$P(R_j)^{\text{test}} = \frac{\sum_i \left(P(R_j|T_i)^{\text{in}} \cdot P(T_i)^{\text{test}}\right)}{\sum_i P(T_i|R_j)^{\text{in}}}, \tag{D.17}$$

shall be expressed with quantities accessible from the information of the input and the test datasets. The experimental probability (empirical probability) is used to express the relative frequency of an event to occur in bin k of region A:

$$P(A_k) = \frac{N(A_k)}{N(A)}, \tag{D.18}$$

where $N(A_k)$ is the event count in bin k of region A and $N(A) = \sum_k N(A_k)$ is the total event population of A. Then the denominator of Eq. (D.17) becomes:

$$\sum_i P(T_i|R_j)^{\text{in}} = \frac{\sum_i P(T_i \cap R_j)^{\text{in}}}{P(R_j)^{\text{in}}}, \tag{D.19}$$

$$= \frac{\sum_i N(T_i \cap R_j)^{\text{in}}}{N(T \cap R)^{\text{in}}} \cdot \frac{N(R)^{\text{in}}}{N(R_j)^{\text{in}}}, \tag{D.20}$$

$$= \frac{\sum_i N(T_i \cap R_j)^{\text{in}}}{N(R_j)^{\text{in}}} \cdot \frac{N(R)^{\text{in}}}{N(T \cap R)^{\text{in}}}, \tag{D.21}$$

$$= C_j^{\text{fid}} \cdot \frac{N(R)^{\text{in}}}{N(T \cap R)^{\text{in}}}, \tag{D.22}$$

which eventually is expressed with the fiducial correction C_j^{fid}, i.e. the fraction of events passing the reconstruction level selection criteria that also pass the selection criteria at particle level.

The numerator of Eq. (D.17) becomes:

$$\sum_i \left(P(R_j|T_i)^{\text{in}} \cdot P(T_i)^{\text{test}}\right) = \sum_i \left(\frac{P(T_i \cap R_j)^{\text{in}}}{P(T_i)^{\text{in}}} \cdot P(T_i)^{\text{test}}\right), \tag{D.23}$$

$$= \sum_i \left(\frac{N(T_i \cap R_j)^{\text{in}}}{N(T \cap R)^{\text{in}}} \cdot \frac{N(T)^{\text{in}}}{N(T_i)^{\text{in}}} \cdot \frac{N(T_i)^{\text{test}}}{N(T)^{\text{test}}}\right), \tag{D.24}$$

$$= \sum_i \left(\frac{N(T_i \cap R_j)^{\text{in}}}{N(T_i)^{\text{in}}} N(T_i)^{\text{test}}\right) \cdot \frac{N(T)^{\text{in}}}{N(T \cap R)^{\text{in}} N(T)^{\text{test}}}, \tag{D.25}$$

$$= \sum_i \left(\mathcal{M}_{ji}^{\text{res}} \cdot N(T_i)^{\text{test}}\right) \cdot \frac{N(T)^{\text{in}}}{N(T \cap R)^{\text{in}} N(T)^{\text{test}}}, \tag{D.26}$$

which is expressed with the response matrix $\mathcal{M}_{ji}^{\text{res}}$, i.e. a 2-dimensional matrix in the $R \cap T$ space where all rows i are normalised with the event count $N(T_i)$ in the respective particle level bin i.

The event count of the test dataset per bin j at reconstruction level can then be assembled from Equations (D.22) and (D.26):

$$N(R_j)^{\text{test}} = P(R_j)^{\text{test}} \cdot N(R)^{\text{test}}, \tag{D.27}$$

$$= \frac{1}{C_j^{\text{fid}}} \sum_i \left(\mathcal{M}_{ji}^{\text{res}} \cdot N(T_i)^{\text{test}}\right) \frac{N(T)^{\text{in}} N(R)^{\text{test}}}{N(T)^{\text{test}} N(R)^{\text{in}}}, \tag{D.28}$$

Table D.12: Details on the experimental uncertainties for all objects relevant to the analysis, as well as for the entire event prescription. For each object type and category, the full label used in the statistical analysis (as occurring in figures and result tables), and a short description are listed.

Category	Full label	Comment
Electrons:		
Trigger eff.	EL_EFF_Trigger_Total_1NPCOR_PLUS_UNCOR	
Energy scale	EG_SCALE_ALLCORR	Nominal energy scale uncertainty (methodology as in Run 1)
	EG_SCALE_E4SCINTILLATOR	Additional systematic uncertainties due to changes between Run 1 and Run 2 conditions
	EG_SCALE_LARCALIB_EXTRA2015PRE	
	EG_SCALE_LARTEMPERATURE_EXTRA2015PRE	
	EG_SCALE_LARTEMPERATURE_EXTRA2016PRE	
Energy resol.	EG_RESOLUTION_ALL	
Reconstruction eff.	EL_EFF_Reco_Total_1NPCOR_PLUS_UNCOR	
Identification eff.	EL_EFF_ID_CorrUncertaintyNP	15 correlated components
	EL_EFF_ID_SIMPLIFIED_UncorrUncertaintyNP	16 uncorrelated components
Isolation eff.	EL_EFF_Iso_Total_1NPCOR_PLUS_UNCOR	
Muons:		
Trigger eff.	MUON_EFF_TrigStatUncertainty	Statistical component
	MUON_EFF_TrigSystUncertainty	Systematic component
Momentum scale	MUON_SCALE	
Momentum resol.	MUON_ID	From inner detector
	MUON_MS	From muon spectrometer
Reconstruction	MUON_EFF_STAT	Statistical component for muons with $p_{\mathrm{T}} > 15\,\mathrm{GeV}$
& identification	MUON_EFF_SYS	Systematic component for muons with $p_{\mathrm{T}} > 15\,\mathrm{GeV}$
efficiency	MUON_EFF_STAT_LOWPT	Statistical component for muons with $p_{\mathrm{T}} < 15\,\mathrm{GeV}$
	MUON_EFF_SYST_LOWPT	Systematic component for muons with $p_{\mathrm{T}} < 15\,\mathrm{GeV}$
Track-to-vertex association eff.	MUON_TTVA_STAT	Statistical component
	MUON_TTVA_SYS	Systematic component
Isolation eff.	MUON_ISO_STAT	Statistical component
	MUON_ISO_SYS	Systematic component
Jets:		
Energy scale	JET_EffectiveNP	8 components from in-situ calibration
	JET_EtaIntercalibration_Modeling	Uncert. on η-intercalibrations (modelling, statistics/ method, non-closure)
	JET_EtaIntercalibration_TotalStat	
	JET_EtaIntercalibration_NonClosure	
	JET_Pileup_PtTerm	Uncert. on individual terms in the pile-up subtraction (Eq. (3.7))
	JET_Pileup_RhoTopology	
	JET_Pileup_OffsetNPV	
	JET_Pileup_OffsetMu	
	JET_Flavor_Composition	Uncert. on flavour composition
	JET_Flavor_Response	Uncert. on samples' flavour response
	JET_BJES_Response	Uncert. on b-jets
	JET_PunchThrough_MC15	Uncert. for punch-through jets
	JET_RelativeNonClosure_MC15	MC simulation non-closure
	JET_SingleParticle_HighPt	High-p_{T} jet behaviour
Energy resol.	JET_JER_SINGLE_NP	
JVT eff.	JET_JvtEfficiency	
b-tag ineff.	FT_EFF_Eigen_B	
	FT_EFF_Eigen_C	
	FT_EFF_Eigen_L	
	FT_EFF_extrapolation	Extrapolation to high-p_{T} jets
	FT_EFF_extrapolation_from_charm	Uncertainty on tau jets
E_T^{miss}:		
Soft tracks energy scale	MET_SoftTrk_Scale	Longitudinal scale uncert.
Soft tracks energy resol.	MET_SoftTrk_ResoPara	Longitudinal and
	MET_SoftTrk_ResoPerp	Transverse resol. uncertainty

Table D.13: Relative impact of experimental systematic uncertainties on the event yields of all predictions based on MC simulation in all flavour-split and the combined channel in the signal region condensed in six categories. Lepton uncertainties comprise all variations in the measurement of electrons and muons, except the trigger efficiency which is quoted as separate value. Jet uncertainties comprise all variations in the measurement of jets, except the variations of the flavour tagging which are quoted as b-tag inefficiency uncertainties.

Process	Systematic Uncertainty [%]					
Channel	Leptons	Trigger eff.	Jet	b-tag ineff.	Pile-up rwt.	E_T^{miss}
$W^\pm Z$						
$e^\pm e^\pm$	1.52	0.03	9.58	2.49	2.99	0.93
$e^\pm \mu^\pm + \mu^\pm e^\pm$	1.24	0.09	5.03	2.23	3.49	0.79
$\mu^\pm \mu^\pm$	3.07	0.43	8.45	2.40	3.33	1.63
$W^\pm W^\pm jj$-EW4						
$e^\pm e^\pm$	1.62	0.02	3.41	2.56	4.99	0.41
$e^\pm \mu^\pm + \mu^\pm e^\pm$	1.19	0.08	3.04	2.48	0.45	0.22
$\mu^\pm \mu^\pm$	0.34	0.41	2.85	2.48	0.33	1.89
Other prompt						
$e^\pm e^\pm$	2.90	0.03	16.50	8.98	6.67	2.82
$e^\pm \mu^\pm + \mu^\pm e^\pm$	2.90	0.09	13.85	5.31	9.45	3.21
$\mu^\pm \mu^\pm$	3.73	0.39	22.17	8.57	4.73	1.96
Top						
$e^\pm e^\pm$	2.57	0.03	17.65	15.02	8.73	1.75
$e^\pm \mu^\pm + \mu^\pm e^\pm$	3.27	0.08	11.97	9.04	10.69	4.16
$\mu^\pm \mu^\pm$	2.66	0.39	14.27	13.83	4.18	1.62
ZZ						
$e^\pm e^\pm$	3.59	0.03	15.71	2.23	1.22	4.84
$e^\pm \mu^\pm + \mu^\pm e^\pm$	3.10	0.10	15.76	2.35	3.20	3.26
$\mu^\pm \mu^\pm$	5.70	0.36	35.18	2.89	4.58	3.24
VVV						
$e^\pm e^\pm$	1.66	0.02	13.09	2.96	19.37	< 0.01
$e^\pm \mu^\pm + \mu^\pm e^\pm$	1.27	0.07	13.39	3.77	24.66	0.46
$\mu^\pm \mu^\pm$	2.48	0.47	16.85	4.95	6.87	< 0.01
$V\gamma$						
$e^\pm e^\pm$	1.39	0.01	7.75	1.90	4.75	< 0.01
$e^\pm \mu^\pm + \mu^\pm e^\pm$	1.40	0.13	37.74	2.94	14.14	< 0.01
$W^\pm \gamma$						
$e^\pm e^\pm$	1.40	0.01	7.05	1.97	4.11	< 0.01
$e^\pm \mu^\pm + \mu^\pm e^\pm$	1.13	0.14	33.36	2.94	14.17	< 0.01
$Z\gamma$						
$e^\pm e^\pm$	1.26	0.02	16.22	1.08	12.57	< 0.01
$e^\pm \mu^\pm + \mu^\pm e^\pm$	22.01	0.07	370.44	3.10	11.51	< 0.01
$W^\pm W^\pm jj$-EW6 (Sherpa23jLO)						
$e^\pm e^\pm$	1.45	0.02	2.28	1.81	0.48	0.26
$e^\pm \mu^\pm + \mu^\pm e^\pm$	1.14	0.08	2.22	1.76	0.97	0.17
$\mu^\pm \mu^\pm$	1.83	0.47	2.28	1.74	2.42	0.21

Detailed Information on PDF, α_S, and Scale Uncertainties

Table D.14: Relative renormalisation and factorisation scale variations in the matrix element calculation with the 7-point envelope approach for the $WZjj$-EW4, $WZjj$-EW6, for their sum labelled $W^{\pm}Z$, the $W^{\pm}W^{\pm}jj$-EW4, and $W^{\pm}W^{\pm}jj$-EW6 processes in the combined $\ell^{\pm}\ell^{\pm}$ channel in the signal region (cf. Tab. 7.4).

ε_F	ε_R	Relative variations [%]					
		$W^{\pm}Z$			$W^{\pm}W^{\pm}jj$		
		EW4	EW6	EW4+EW6	EW4	EW6	
						Sherpa23jLO	MG5+Py8drec
1.0	0.5	+29.92	–	+25.57	+29.72	+6.62	–
1.0	2.0	−20.55	–	−17.56	−20.00	−5.00	–
0.5	1.0	+0.63	+8.14	+1.72	+6.35	+7.85	+7.58
2.0	1.0	−0.04	−7.06	−1.06	−5.68	−6.83	−6.64
0.5	0.5	+30.92	+8.14	+27.61	+37.94	+14.97	+7.58
2.0	2.0	−20.42	−7.06	−18.47	−24.55	−11.49	−6.64

Table D.15: Relative PDF set variations including α_S variations in the matrix element calculation for the $WZjj$-EW4, $WZjj$-EW6, for their sum labelled $W^{\pm}Z$, the $W^{\pm}W^{\pm}jj$-EW4, and $W^{\pm}W^{\pm}jj$-EW6 processes in the combined $\ell^{\pm}\ell^{\pm}$ channel in the signal region (cf. Tab. 7.4). Nominal PDF set: NNPDF3.0nnlo for all samples.

PDF error type	Relative variations [%]					
	$W^{\pm}Z$			$W^{\pm}W^{\pm}jj$		
	EW4	EW6	EW4+EW6	EW4	EW6	
					Sherpa23jLO	MG5+Py8drec
Intern. vars.	±1.09	±1.64	±1.19	±1.94	±1.69	±1.65
Difference w.r.t. nominal: NNPDF3.0nnlo						
CT14	+1.01	+0.12	+0.85	+0.78	+0.94	+0.84
MMHT2014	+2.21	+1.90	+2.16	+2.34	+2.25	+0.56
α_S vars.	+2.72 −2.18	−0.02 −0.07	+2.24 −1.81	+2.02 −2.07	±0.36	+0.05 −0.31

Appendix E

Additional Details on the Cross-section Measurement

E.1 Control Regions

E.1.1 $W^{\pm}Z$ Control Region

Table E.1: Estimated event yields and total uncertainties of the processes of the other prompt background category in the $W^{\pm}Z$ control region before the statistical analysis. "Other prompt" comprises MC-based predictions of the processes of $t\bar{t}V$, ZZ, and triboson production. Numbers are given in the combined $\ell\ell'\ell''$ channel, with $\ell^{(\prime\prime)} = e^{\pm}$ or $\mu^{\pm}$.

Process	$\ell\ell'\ell''$ channel
Other prompt:	
- $t\bar{t}V$	6.17 ± 2.06
- ZZ	14.12 ± 3.21
- VVV	1.26 ± 0.40

Table E.2: Relative impact of experimental systematic uncertainties on the event yields of all predictions based on MC simulation in the $W^{\pm}Z$ control region condensed in six categories. Lepton uncertainties comprise all variations in the measurement of electrons and muons, except the trigger efficiency which is quoted as separate value. Jet uncertainties comprise all variations in the measurement of jets, except the variations of the flavour tagging which are quoted as b-tag inefficiency uncertainties.

Process	Systematic Uncertainty [%]					
	Leptons	Trig. eff.	Jet	b-tag ineff.	Pile-up rwt.	E_T^{miss}
$W^{\pm}Z$	1.60	0.23	6.29	1.98	1.46	0.83
Other prompt	1.50	0.24	9.69	5.23	2.89	2.85
- $t\bar{t}V$	1.65	0.26	7.31	13.41	1.61	0.46
- ZZ	1.40	0.23	10.67	1.92	3.67	4.13
- VVV	1.78	0.21	10.44	2.21	0.46	0.25
$Z\gamma$	1.23	0.23	61.25	1.99	7.01	23.15
$W^{\pm}W^{\pm}jj$-EW6	1.19	0.01	0.13	1.11	42.73	< 0.01

Table E.3: Relative renormalisation and factorisation scale variations in the matrix element calculation with the 7-point envelope approach for the $W^{\pm}Z$-EW4, $W^{\pm}Z$-EW6, the combined $W^{\pm}Z$ and $W^{\pm}W^{\pm}jj$-EW6 processes in the $W^{\pm}Z$ control region.

ε_F	ε_R	Relative variations [%]			
		$W^{\pm}Z$-EW4	$W^{\pm}Z$-EW6	$W^{\pm}Z$	$W^{\pm}W^{\pm}jj$-EW6
1.0	0.5	+28.74	–	+34.94	–
1.0	2.0	−20.23	–	−22.12	–
0.5	1.0	−0.04	+6.72	+0.47	+5.48
2.0	1.0	−0.31	−5.93	−0.74	−5.21
0.5	0.5	+29.51	+6.72	+27.75	+5.48
2.0	2.0	−20.08	−5.93	−18.99	−5.21

Table E.4: Relative PDF set variations including α_S variations in the matrix element calculation for the $W^{\pm}Z$-EW4, $W^{\pm}Z$-EW6, the combined $W^{\pm}Z$, and $W^{\pm}W^{\pm}jj$-EW6 processes in the $W^{\pm}Z$ control region. Nominal PDF set: NNPDF3.0nnlo

PDF error type	Relative variations [%]			
	$W^{\pm}Z$-EW4	$W^{\pm}Z$-EW6	$W^{\pm}Z$	$W^{\pm}W^{\pm}jj$-EW6
Internal variations	±1.30	±1.59	±1.32	±3.52
Difference w.r.t. nominal: NNPDF3.0nnlo				
CT14	+0.73	+0.62	+0.72	−1.42
MMHT2014	+1.58	+2.13	+1.62	+1.98
α_S variations	+2.33 −2.32	+0.03 −0.11	±2.15	+0.76 −1.26

E.1.2 Low-m_{jj} Control Region

Table E.5: Estimated event yields and total uncertainties of the processes of the other prompt background category in the low-m_{jj} control region before the statistical analysis. "Other prompt" comprises MC-based predictions of the processes of $t\bar{t}V$, ZZ, and triboson production. Numbers are given in all lepton charge and flavour split channels, as well as the combined $\ell^{\pm}\ell^{\pm}$ channel.

Process	Channel			
	e^+e^+	e^-e^-	$e^+\mu^+ + \mu^+e^+$	$e^-\mu^- + \mu^-e^-$
Other prompt				
- $t\bar{t}V$	0.12 ± 0.06	0.04 ± 0.03	0.59 ± 0.22	0.18 ± 0.08
- ZZ	0.12 ± 0.07	0.10 ± 0.06	0.46 ± 0.13	0.48 ± 0.17
- VVV	0.03 ± 0.02	0.02 ± 0.01	0.15 ± 0.06	0.11 ± 0.04

Process	Channel		
	$\mu^+\mu^+$	$\mu^-\mu^-$	$\ell^{\pm}\ell^{\pm}$
Other prompt			
- $t\bar{t}V$	0.31 ± 0.12	0.18 ± 0.08	1.43 ± 0.49
- ZZ	0.19 ± 0.05	0.14 ± 0.05	1.48 ± 0.37
- VVV	0.13 ± 0.05	0.05 ± 0.02	0.48 ± 0.16

E.2 Modelling Uncertainties in the Signal and Low-m_{jj} Control Region

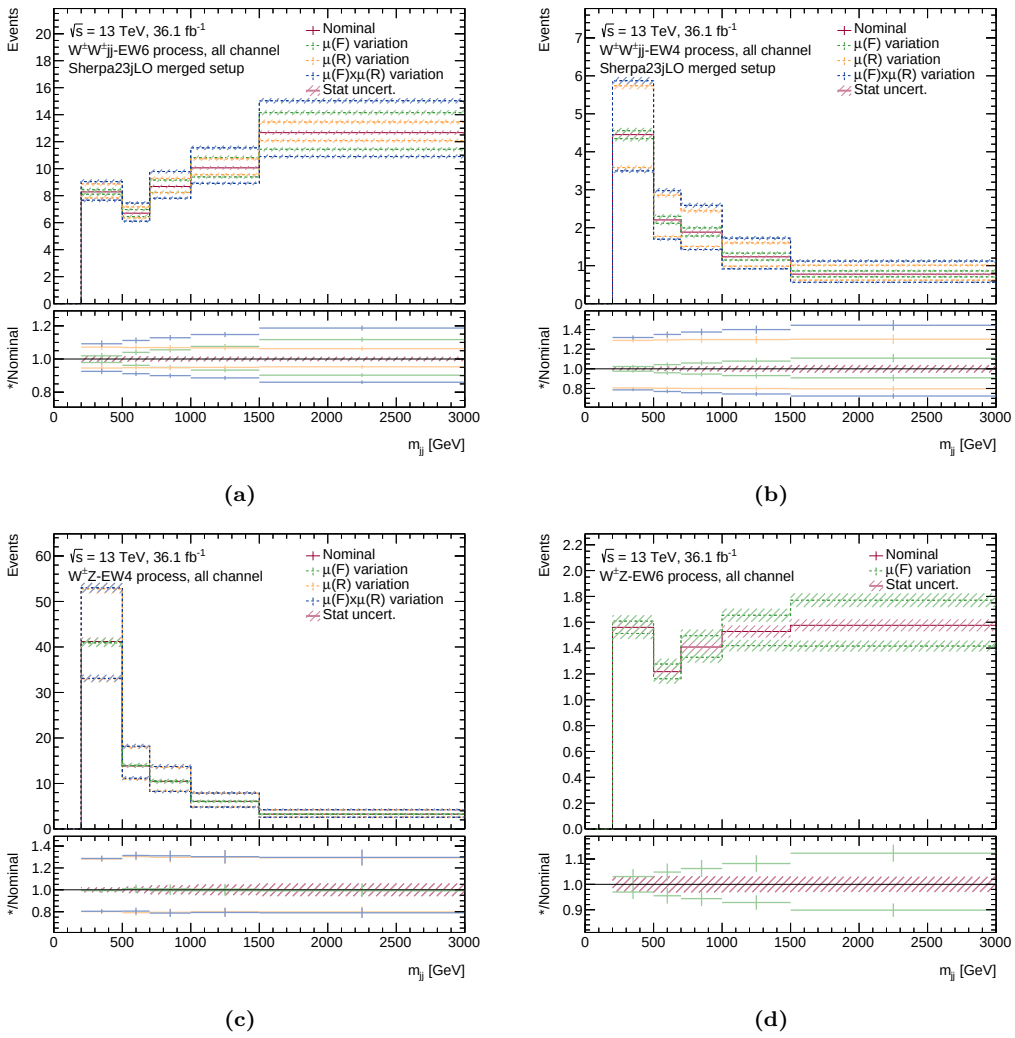


Figure E.1: Distribution of the invariant mass of the tagging jet system m_{jj} in the signal region and low-m_{jj} control region for the nominal estimates and the 7-point variations of the renormalisation and factorisation scales. Shown are the distributions for the $W^{\pm}W^{\pm}jj$-EW6 (a), $W^{\pm}W^{\pm}jj$-EW4 (b), $W^{\pm}Z$-EW4 (c), and $W^{\pm}Z$-EW6 (d) processes in the combined $\ell^{\pm}\ell^{\pm}$ channel. The lower panel shows the relative difference of the variations with respect to the nominal estimate. Uncertainties are statistical only.

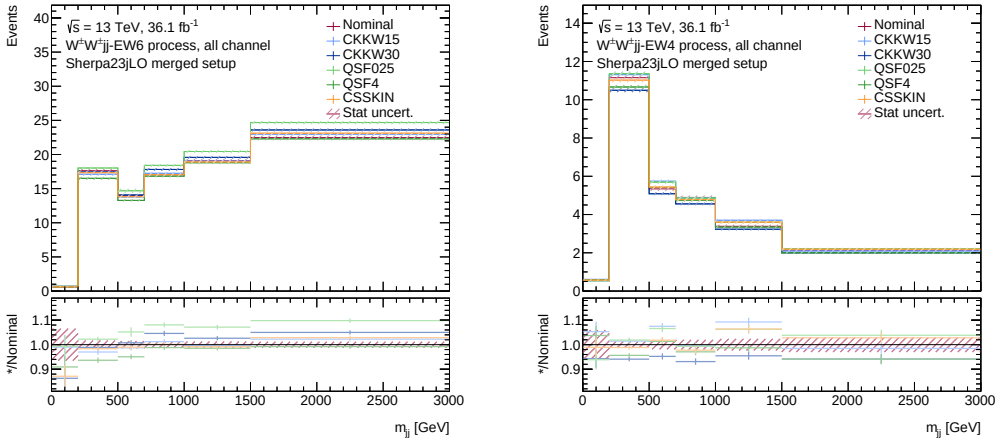


Figure E.2: Kinematic distributions for the nominal Sherpa23jLO setup and its variation of the merging scale and internal parton shower parameters, as explained in Sec. A.4.2 in the fiducial region without m_{jj} requirement (cf. Tab. 6.8), for the $W^{\pm}W^{\pm}jj$-EW6 (a) and $W^{\pm}W^{\pm}jj$-EW4 (b) processes, as input to the folding procedure (cf. Sec. 7.6.2). Uncertainties are statistical uncertainties from the MC generation only.

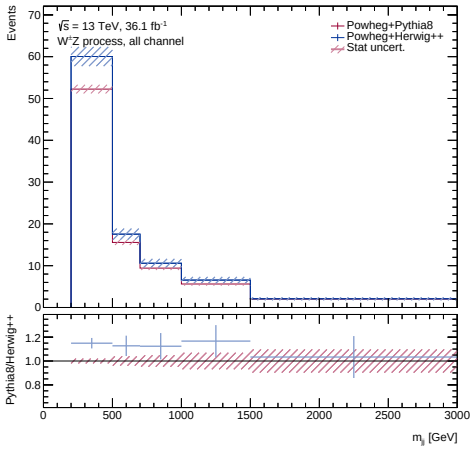


Figure E.3: Distribution of the invariant mass of the tagging jet system m_{jj} in the signal region and low-m_{jj} control region for the $W^{\pm}Z$-EW4 process estimated from POWHEG interfaced to PYTHIA 8 (red) and `HERWIG++` (blue) in the combined $\ell^{\pm}\ell^{\pm}$ channel. The lower panel shows the relative difference which is utilised to estimate the relative uncertainty from parton shower modelling on the nominal SHERPA prediction. Uncertainties are statistical only.

E.3 Results

E.3.1 Results of Fit to Asimov Data

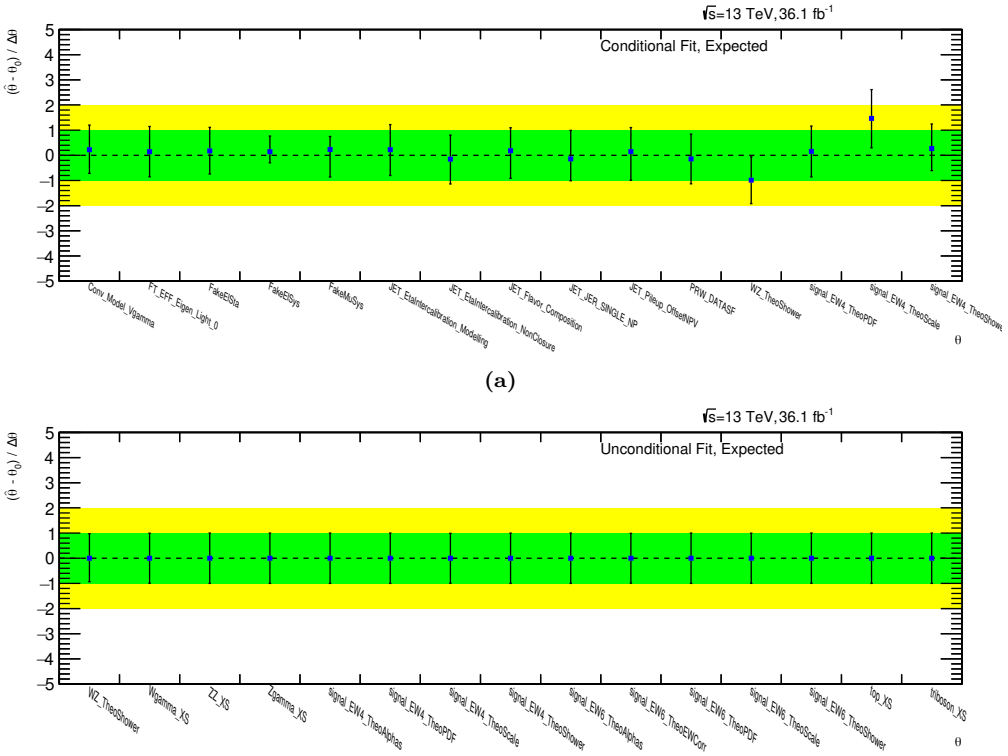


Figure E.4: Pulls of the nuisance parameters for the full unconditional, i.e. including μ as a free parameter, (a) and the background-only fit, i.e. with $\mu = 0$, (b) to Asimov data. Only a subset of the 15 NPs with largest pulls are shown. Prediction of the 1 and 2 standard deviations before the fit are indicated with the green and yellow bands, respectively.

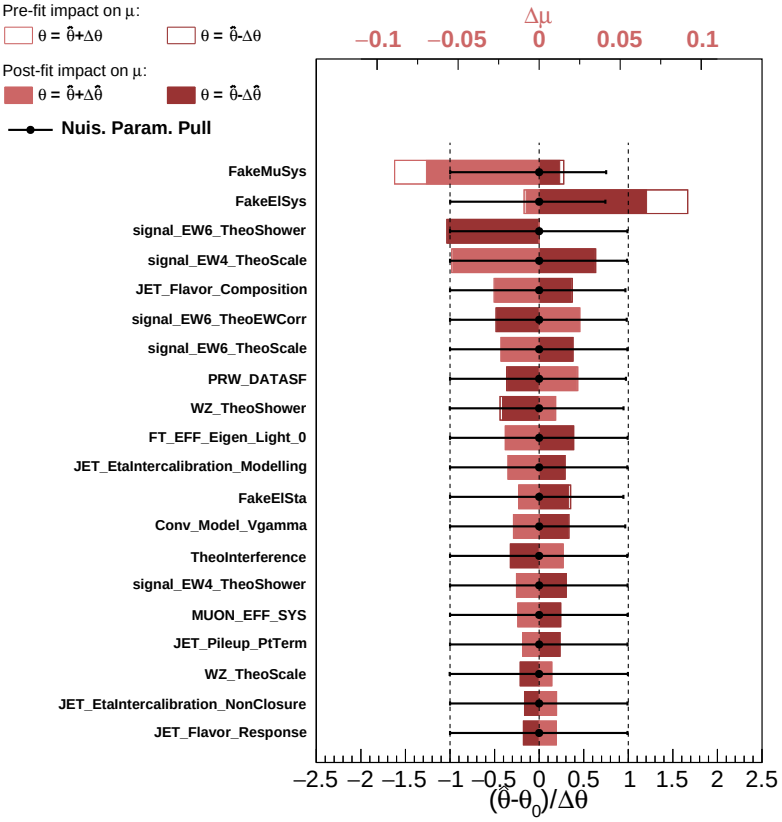


Figure E.5: Impact of the nuisance parameters on the measured, i.e. best fit signal strength $\hat{\mu}$ before (empty brown rectangles) and after (filled brown rectangles) the fit to Asimov data. The impact is quantified with the upper scale. NPs are ranked by their impact after the fit including only the 20 NPs with highest impact. The black points show the pull and the relative uncertainties after the fit $\Delta\hat{\theta}$ of each NP, quantified on the lower scale. NPs associated to the statistical uncertainties of the background estimates are not considered for the impact. NPs associated with experimental uncertainties with several independent components are indicated by their index in the set. Figure taken from Ref. [232].

Table E.6: Estimated event yields and their total uncertainties of all SM processes in the $W^{\pm}Z$ control region after the statistical analysis of the Asimov dataset. "Other prompt" comprises MC-based predictions of the processes of $t\bar{t}V$, ZZ, and triboson production. The "non-prompt" and "charge misID" background estimates are not taken into account in this region. The Asimov dataset in this region is generated from an upstream and independent fit to the $W^{\pm}Z$ control region to observed experimental data. Numbers are given in the combined $\ell\ell'\ell''$ channel, with $\ell^{(\prime\prime)} = e^{\pm}$ or $\mu^{\pm}$.

Process	$\ell\ell'\ell''$ channel
$W^{\pm}Z$	178.78 ± 14.90
$W^{\pm}W^{\pm}jj$-EW4	–
Other prompt	21.55 ± 3.80
Non-prompt	–
Charge misID	–
$V\gamma$	2.68 ± 1.63
$W^{\pm}W^{\pm}jj$-EW6	< 0.01
Total expected	203.01 ± 14.33
Asimov data*	203.99

Table E.7: Estimated event yields and their total uncertainties of all SM processes in all channels, including the combined $\ell^\pm\ell^\pm$ channel, in the signal region after the statistical analysis of the Asimov dataset. "Other prompt" comprises MC-based predictions of the processes of $t\bar{t}V$, ZZ, and triboson production. Uncertainties on the $W^\pm W^\pm jj$-EW6 signal process include absolute normalisation uncertainties (cf. Tab. 7.12), which are not considered in the statistical analysis (cf. Sec. 8.3).

Process	Channel						
	e^+e^+	e^-e^-	$e^+\mu^+ + \mu^+e^+$	$e^-\mu^- + \mu^-e^-$	$\mu^+\mu^+$	$\mu^-\mu^-$	$\ell^\pm\ell^\pm$
$W^\pm Z$	1.70 ± 0.40	1.18 ± 0.35	12.53 ± 2.02	8.10 ± 1.58	4.99 ± 0.79	3.31 ± 0.67	31.80 ± 4.36
$W^\pm W^\pm jj$-EW4	0.38 ± 0.14	0.16 ± 0.06	3.02 ± 1.05	1.21 ± 0.43	1.80 ± 0.62	0.76 ± 0.26	7.34 ± 2.49
Other prompt	0.17 ± 0.05	0.14 ± 0.04	0.90 ± 0.23	0.60 ± 0.24	0.36 ± 0.11	0.19 ± 0.06	2.36 ± 0.53
Non-prompt	4.08 ± 1.43	2.31 ± 1.00	9.35 ± 3.19	6.34 ± 2.51	0.57 ± 0.07	0.67 ± 0.16	23.32 ± 6.81
Charge misID	1.33 ± 0.23	1.17 ± 0.23	3.48 ± 0.36	2.95 ± 0.38	–	–	8.93 ± 0.79
$V\gamma$	0.41 ± 0.21	0.62 ± 0.34	2.65 ± 1.36	0.80 ± 0.64	–	–	4.47 ± 2.21
$W^\pm W^\pm jj$-EW6	3.80 ± 0.94	1.49 ± 0.37	16.49 ± 4.05	6.45 ± 1.59	9.14 ± 2.26	3.50 ± 0.87	40.88 ± 10.03
Total expected	11.87 ± 2.21	7.07 ± 1.65	48.41 ± 6.42	26.45 ± 4.14	16.86 ± 2.54	8.42 ± 1.17	119.09 ± 13.78
Asimov data	11.87	7.07	48.41	26.45	16.86	8.42	119.09

Table E.8: Estimated event yields and their total uncertainties of all SM processes in all channels, including the combined $\ell^\pm\ell^\pm$ channel, in the low-m_{jj} control region after the statistical analysis of the Asimov dataset. "Other prompt" comprises MC-based predictions of the processes of $t\bar{t}V$, ZZ, and triboson production. Uncertainties on the $W^\pm W^\pm jj$-EW6 signal process include absolute normalisation uncertainties (cf. Tab. 7.12), which are not considered in the statistical analysis (cf. Sec. 8.3).

Process	Channel						
	e^+e^+	e^-e^-	$e^+\mu^+ + \mu^+e^+$	$e^-\mu^- + \mu^-e^-$	$\mu^+\mu^+$	$\mu^-\mu^-$	$\ell^\pm\ell^\pm$
$W^\pm Z$	1.83 ± 0.38	1.42 ± 0.39	12.51 ± 1.91	9.35 ± 1.54	5.22 ± 0.80	3.59 ± 0.53	33.93 ± 4.67
$W^\pm W^\pm jj$-EW4	0.24 ± 0.07	0.15 ± 0.05	1.99 ± 0.58	1.15 ± 0.34	1.16 ± 0.34	0.64 ± 0.18	5.32 ± 1.50
Other prompt	0.28 ± 0.08	0.16 ± 0.06	1.20 ± 0.25	0.77 ± 0.17	0.63 ± 0.13	0.37 ± 0.09	3.40 ± 0.63
Non-prompt	0.71 ± 0.21	4.37 ± 1.53	12.77 ± 3.74	8.62 ± 2.67	2.43 ± 1.21	1.18 ± 0.18	30.08 ± 7.78
Charge misID	1.70 ± 0.29	1.77 ± 0.40	4.01 ± 0.46	3.56 ± 0.51	–	–	11.03 ± 1.15
$V\gamma$	0.18 ± 0.09	0.26 ± 0.13	0.28 ± 0.97	2.20 ± 1.07	–	–	2.93 ± 1.76
$W^\pm W^\pm jj$-EW6	0.64 ± 0.11	0.47 ± 0.08	2.97 ± 0.48	1.99 ± 0.33	1.83 ± 0.30	1.11 ± 0.18	9.01 ± 1.46
Total expected	5.57 ± 0.78	8.61 ± 2.10	35.73 ± 4.38	27.63 ± 3.56	11.26 ± 1.44	6.89 ± 0.58	95.69 ± 8.61
Asimov data	5.57	8.61	35.73	27.63	11.26	6.77	95.68

E.3.2 Distributions in All Lepton Charge and Flavour Channels

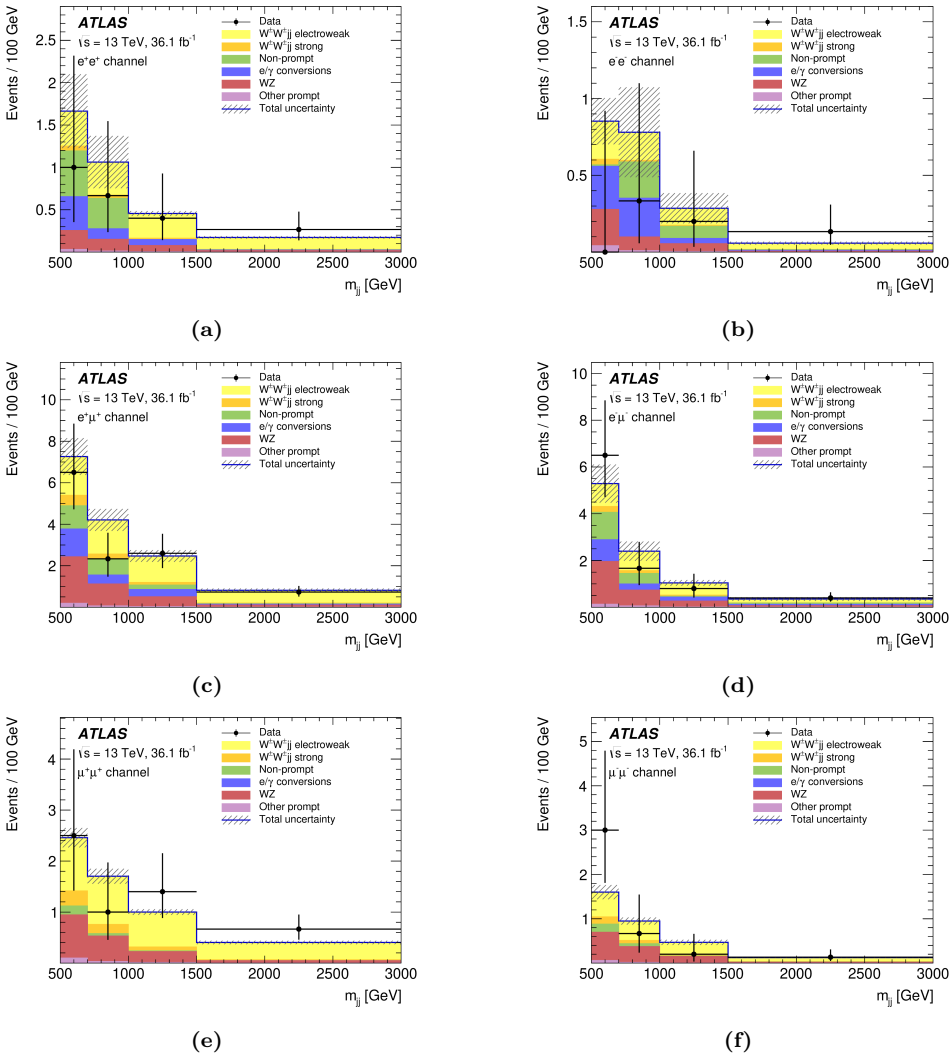


Figure E.6: Distribution of the invariant mass of the tagging jets, m_{jj}, in the e^+e^+ (a), e^-e^- (b), $e^+\mu^+$ (c), $e^-\mu^-$ (d), $\mu^+\mu^+$ (e), and $\mu^-\mu^-$ (f) channel in the signal region after the fit to observed data. Expected signal and background yields are coloured and stacked with the hatched band representing the statistical and systematic uncertainties of the background prediction. The background predictions from electron charge misidentification and $V\gamma$ processes are combined into the e/γ conversion category. The other prompt category comprises predictions of the processes of $t\bar{t}V$, ZZ, and triboson production. The last bin of the distribution includes all events with $m_{jj} > 3000\,\text{GeV}$. The lower panel shows the experimental data with respect to the total expected estimate. Figures taken from Ref. [1].

Appendix F

Simulation of EFT Signal Samples

F.1 Sample Generation using Madgraph

For the generation of the samples including EFT effects the MG5_aMC programme interfaced to Pythia 8 is used. The framework, setup and main configuration files are identical to the SM sample generation, described in App. A.2.3. Solely the inputs, precisely the process and parameter cards, are adjusted to serve the case of the alternative EFT model and extended parameter set including the EFT coefficients.

In order to generate events with decomposed EFT effects (cf. Eq. (9.3)), the `model` name and the `generate` command have to be adapted in the `process_card.dat`. An example process card for the generation of a sample with linear EFT effects of the f_{S1} parameter is shown below.

```
import model SM_LSMT_Ind5_UFO
define l+ = e+ mu+ ta+
define  vl = ve vm vt
define l- = e- mu- ta-
define vl~ = ve~ vm~ vt~
define p = g u c d s u~ c~ d~ s~ b b~
define j = g u c d s u~ c~ d~ s~ b b~
generate p p > l+ vl l+ vl j j QCD=0 S1^2==1 S0=0 S2=0 M0=0 M1=0 M2=0 M3=0 M4=0 M5=0 M6=0 M7=0
 T0=0 T1=0 T2=0 T3=0 T4=0 T5=0 T6=0 T7=0 T8=0 T9=0 @1
add process p p > l- vl~ l- vl~ j j QCD=0 S1^2==1 S0=0 S2=0 M0=0 M1=0 M2=0 M3=0 M4=0 M5=0
 M6=0 M7=0 T0=0 T1=0 T2=0 T3=0 T4=0 T5=0 T6=0 T7=0 T8=0 T9=0 @1
```

The `generate` command is build from the individual parts as:

```
generate [process] [SM couplings] [EFT couplings] [EFT couplings = 0]
```

where the second to last part (`EFT couplings`) has to be adapted to create all individual term of Eq. (9.3) or a `FULL` sample. The configuration is as follows, exemplarily for the f_{M0} and f_{M1} parameters:

```
LIN(SM,M0)      -->  M0^2==1 ...          (all other couplings set to zero)
QUAD(M0)        -->  M0^2==2 ...          (all other couplings set to zero)
CROSS(M0,M1)    -->  M0^2==1 M1^2==1 ...  (all other couplings set to zero)
FULL(SM,M0)     -->  M0=1 ...             (all other couplings set to zero)
FULL(SM,M0,M1)  -->  M0=1 M1=1 ...        (all other couplings set to zero)
```

The individual samples can then be combined to a full sample as described in Sec. 9.2.1. This prescription can be used for all M, and T parameters, as well as the f_{S1}/Λ^4. As explained in Sec. 2.3.3, the coefficients of the parameters f_{S0}/Λ^4 and f_{S2}/Λ^4 have to be set

simultaneously and to the same value. Hence, the recipe for generating samples including these two parameters extends because one needs to specify two or even three parameters in one process definition. In addition, it is technically not possible to set two parameters for the `QUAD` notation, i.e.

```
S0^2==2 S2^2==2
```

in one line, which further lengthens the commands. The `generate` command for the samples of the linear term with the f_{S0} and f_{S2} parameters, `LIN` ($S0$,$S2$), reads:

```
generate p p > l+ vl l+ vl j j QCD=0 S0^2==1 S2=0 @1
add process p p > l- vl~ l- vl~ j j QCD=0 S0^2==1 S2=0 @1
add process p p > l+ vl l+ vl j j QCD=0 S2^2==1 S0=0 @1
add process p p > l- vl~ l- vl~ j j QCD=0 S2^2==1 S0=0 @1
```

The `QUAD` ($S0$,$S2$) sample generation command includes the `CROSS` term of the f_{S0} and f_{S2} parameters and reads:

```
generate p p > l+ vl l+ vl j j QCD=0 S0^2==2 S2=0 @1
add process p p > l- vl~ l- vl~ j j QCD=0 S0^2==2 S2=0 @1
add process p p > l+ vl l+ vl j j QCD=0 S2^2==2 S0=0 @1
add process p p > l- vl~ l- vl~ j j QCD=0 S2^2==2 S0=0 @1
add process p p > l+ vl l+ vl j j QCD=0 S0^2==1 S2^2==1 @1
add process p p > l- vl~ l- vl~ j j QCD=0 S0^2==1 S2^2==1 @1
```

The `CROSS` ($S0$,$S2$,$S1$) term between all three S parameters is generated with the command:

```
generate p p > l+ vl l+ vl j j QCD=0 S0^2==1 S1^2==1  @1
add process p p > l- vl~ l- vl~ j j QCD=0 S0^2==1 S1^2==1  @1
add process p p > l+ vl l+ vl j j QCD=0 S2^2==1 S1^2==1  @1
add process p p > l- vl~ l- vl~ j j QCD=0 S2^2==1 S1^2==1  @1
```

Here again, all other parameters have to be set to zero in each process `generate` and `add process` line. This has been omitted with focus on the important parts of the command. The `FULL` sample with the f_{S0} and f_{S2} parameters can be generated simply with the general command listed above.

An example `param_card.dat` is printed below for the case of the interference sample of the three S parameters. The values for the parameters have to be given in units of GeV, just as all other input parameters as well.

```
1  ###################################################################
2  ## PARAM_CARD AUTOMATICALY GENERATED BY THE UFO  ####################
3  ###################################################################
4
5  ####################################
6  ## INFORMATION FOR SMINPUTS
7  ####################################
8  Block SMINPUTS
9      1 1.325070e+02 # aEWM1
10     2 1.166390e-05 # Gf
11     3 1.180000e-01 # aS
12
13 ####################################
14 ## INFORMATION FOR MASS
15 ####################################
16 Block MASS
17     4 0.000000e+00 # MC
18     5 0.000000e+00 # MB
19     6 1.720000e+02 # MT
20    11 0.000000e-04 # Me
21    13 0.000000e-01 # MM
22    15 1.777000e+00 # MTA
23    23 9.118800e+01 # MZ
24    25 1.250000e+02 # MH
25 ##  Not dependent paramater.
```

```
## Those values should be edited following analytical the
## analytical expression. Some generator could simply ignore
## those values and use the analytical expression
  22 0.000000 # a : 0.0
  24 80.419000 # W+
  21 0.000000 # g : 0.0
  9000001 0.000000 # ghA : 0.0
  9000003 80.419000 # ghWp
  9000004 80.419000 # ghWm
  9000005 0.000000 # ghG : 0.0
  12 0.000000 # ve : 0.0
  14 0.000000 # vm : 0.0
  16 0.000000 # vt : 0.0
  2 0.000000 # u : 0.0
  1 0.000000 # d : 0.0
  3 0.000000 # s : 0.0
  251 80.419000 # G+

#####################################
## INFORMATION FOR DECAY
#####################################
DECAY   6 1.508336e+00
DECAY  15 2.270000e-12
DECAY  23 2.441404e+00
DECAY  24 2.047600e+00
DECAY  25 6.382339e-03
##  Not dependent paramater.
## Those values should be edited following analytical the
## analytical expression. Some generator could simply ignore
## those values and use the analytical expression
DECAY  22 0.000000 # a : 0.0
DECAY  21 0.000000 # g : 0.0
DECAY  9000001 0.000000 # ghA : 0.0
DECAY  9000005 0.000000 # ghG : 0.0
DECAY  12 0.000000 # ve : 0.0
DECAY  14 0.000000 # vm : 0.0
DECAY  16 0.000000 # vt : 0.0
DECAY  2 0.000000 # u : 0.0
DECAY  4 0.000000 # c : 0.0
DECAY  1 0.000000 # d : 0.0
DECAY  3 0.000000 # s : 0.0
DECAY  5 0.000000 # b : 0.0
DECAY  11 0.000000 # e- : 0.0
DECAY  13 0.000000 # mu- : 0.0

#####################################
## INFORMATION FOR CKMBLOCK
#####################################
Block CKMBLOCK
    1 2.277360e-01 # cabi

#####################################
## INFORMATION FOR ANOINPUTS
#####################################
Block ANOINPUTS
    1 8.000000e-12 # FS0
    2 2.000000e-11 # FS1
    3 8.000000e-12 # FS2
    4 0.000000e-10 # FM0
    5 0.000000e-10 # FM1
    6 0.000000e-10 # FM2
    7 0.000000e-10 # FM3
    8 0.000000e-10 # FM4
    9 0.000000e-10 # FM5
   10 0.000000e-10 # FM6
   11 0.000000e-10 # FM7
   12 0.000000e-10 # FT0
   13 0.000000e-10 # FT1
   14 0.000000e-10 # FT2
   15 0.000000e-10 # FT3
   16 0.000000e-10 # FT4
```

```
97    17 0.000000e-10 # FT5
98    18 0.000000e-10 # FT6
99    19 0.000000e-10 # FT7
100   20 0.000000e-10 # FT8
101   21 0.000000e-10 # FT9
102
103 ###################################
104 ## INFORMATION FOR WOLFENSTEIN
105 ###################################
106 Block Wolfenstein
107     1 2.253000e-01 # lamWS
108     2 8.080000e-01 # AWS
109     3 1.320000e-01 # rhoWS
110     4 3.410000e-01 # etaWS
111
112 ###################################
113 ## INFORMATION FOR YUKAWA
114 ###################################
115 Block YUKAWA
116     4 1.270000e+00 # ymc
117     5 4.200000e+00 # ymb
118     6 1.645000e+02 # ymt
119    11 5.110000e-04 # yme
120    13 1.056600e-01 # ymm
121    15 1.777000e+00 # ymtau
122 #===========================================================
123 # QUANTUM NUMBERS OF NEW STATE(S) (NON SM PDG CODE)
124 #===========================================================
125
126 Block QNUMBERS 9000001  # ghA
127         1 0  # 3 times electric charge
128         2 -1  # number of spin states (2S+1)
129         3 1  # colour rep (1: singlet, 3: triplet, 8: octet)
130         4 1  # Particle/Antiparticle distinction (0=own anti)
131 Block QNUMBERS 9000002  # ghZ
132         1 0  # 3 times electric charge
133         2 -1  # number of spin states (2S+1)
134         3 1  # colour rep (1: singlet, 3: triplet, 8: octet)
135         4 1  # Particle/Antiparticle distinction (0=own anti)
136 Block QNUMBERS 9000003  # ghWp
137         1 3  # 3 times electric charge
138         2 -1  # number of spin states (2S+1)
139         3 1  # colour rep (1: singlet, 3: triplet, 8: octet)
140         4 1  # Particle/Antiparticle distinction (0=own anti)
141 Block QNUMBERS 9000004  # ghWm
142         1 -3  # 3 times electric charge
143         2 -1  # number of spin states (2S+1)
144         3 1  # colour rep (1: singlet, 3: triplet, 8: octet)
145         4 1  # Particle/Antiparticle distinction (0=own anti)
146 Block QNUMBERS 9000005  # ghG
147         1 0  # 3 times electric charge
148         2 -1  # number of spin states (2S+1)
149         3 8  # colour rep (1: singlet, 3: triplet, 8: octet)
150         4 1  # Particle/Antiparticle distinction (0=own anti)
151 Block QNUMBERS 250  # G0
152         1 0  # 3 times electric charge
153         2 1  # number of spin states (2S+1)
154         3 1  # colour rep (1: singlet, 3: triplet, 8: octet)
155         4 0  # Particle/Antiparticle distinction (0=own anti)
156 Block QNUMBERS 251  # G+
157         1 3  # 3 times electric charge
158         2 1  # number of spin states (2S+1)
159         3 1  # colour rep (1: singlet, 3: triplet, 8: octet)
160         4 1  # Particle/Antiparticle distinction (0=own anti)
```

Important to note is, that the `LIN`, as well as any other interference samples between two processes is not compatible with using the default dynamical scale in MG5_aMC, the cluster scale, as it is not defined for such process definitions [273]. Hence, the dynamical scale for all samples has to be adjusted to any of the other dynamical scales, as described in App. A.2.3. As for the nominal SM sample generated with this setup, the scale for the

samples including EFT effects is set to 2, which is the sum of the transverse mass [226], labelled HT in this thesis, unless explicitly stated otherwise.

F.2 Technical implementation of the Variable m_{WW} at Matrix-Element Level

The invariant mass of the $W^{\pm}W^{\pm}$ boson system is obtained from the information of the matrix element particle in the event record of the MG5_aMC output. It is stored in the final reconstructed event samples and can hence be derived after the full simulation of the events. Nothing needs to be adjusted in the event generation step.

In the MG5_aMC setup, matrix element particles are stored with `status` code 22 or 23 and barcode below 200.000. In order to select $W^{\pm}$, particles with PDG-ID 24 are selected. From the two particles found, the invariant mass is built from the sum of their energy-momentum four vectors.

F.3 The True Invariant Mass of the $W^{\pm}W^{\pm}$ System

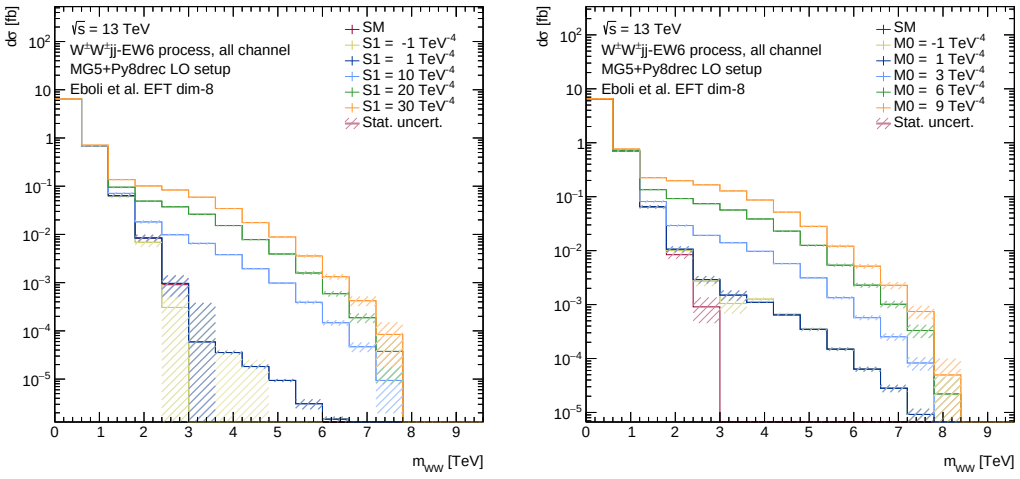


Figure F.1: Invariant mass of the $W^{\pm}W^{\pm}$ system, m_{WW}, at matrix-element level for different values of the f_{S1}/Λ^4 (a) and f_{M0}/Λ^4 (b) parameters. The nominal value (cf. Tab. 9.3) is shown in green. The distributions are shown in the loose region (cf. Tab. 6.8). The amplitude decomposition method is used for the EFT distributions. Note the large range of the x-axis covering values up to 10 TeV for m_{WW}. Uncertainties are statistical uncertainties from the MC generation only.

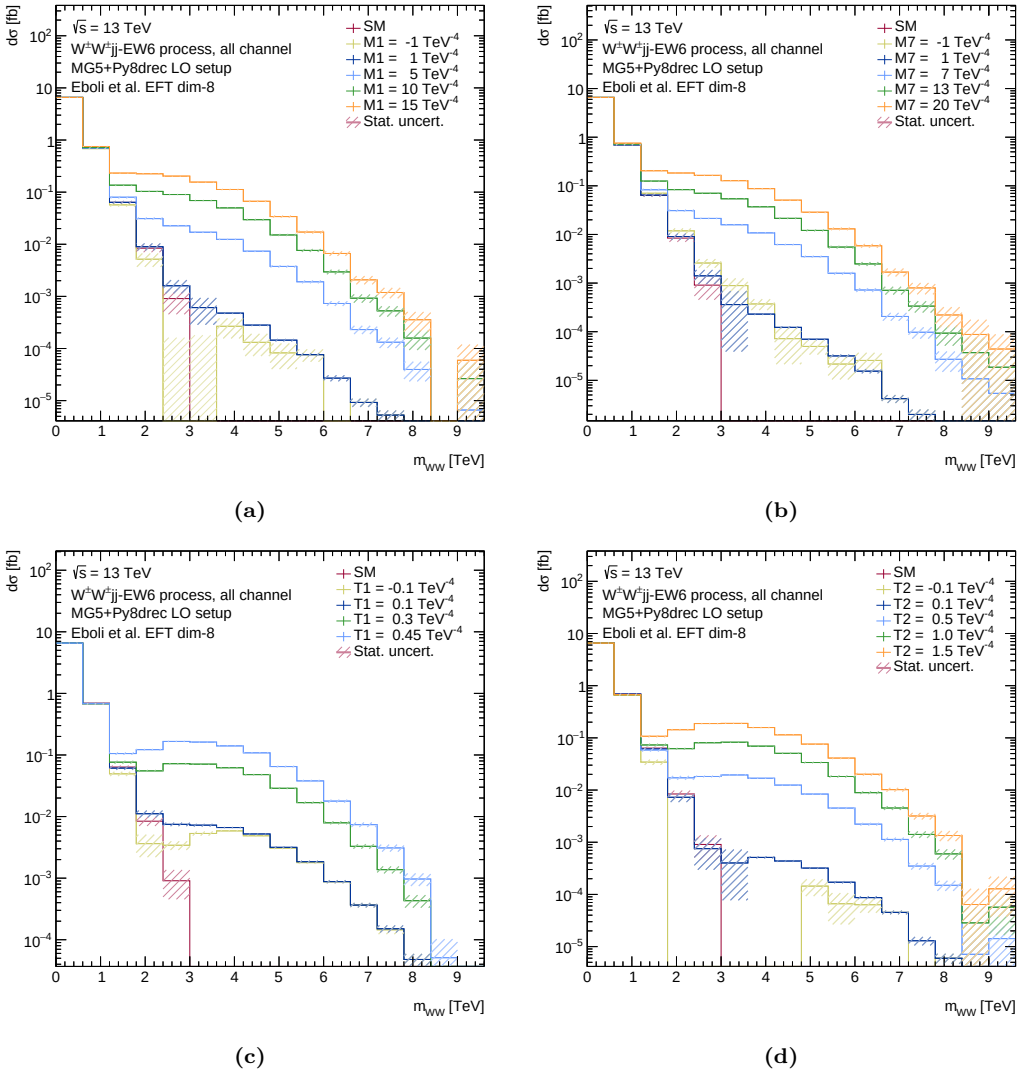


Figure F.2: Invariant mass of the $W^{\pm}W^{\pm}$ system, m_{WW}, at matrix-element level for different values of the f_{SM1}/Λ^4 (a), f_{M7}/Λ^4 (b), f_{T1}/Λ^4 (c), and f_{T2}/Λ^4 (d) parameters. The nominal value (cf. Tab. 9.3) is shown in green. The distributions are shown in a loose region including all events with exactly two leptons with the object selection requirements shown in Tab. 6.8. The amplitude decomposition method is used for the EFT distributions. Note the large range of the x-axis covering values up to 10 TeV for m_{WW}. Uncertainties are statistical uncertainties from the MC generation only.

F.4 Distributions of Two-dimensional EFT Effects

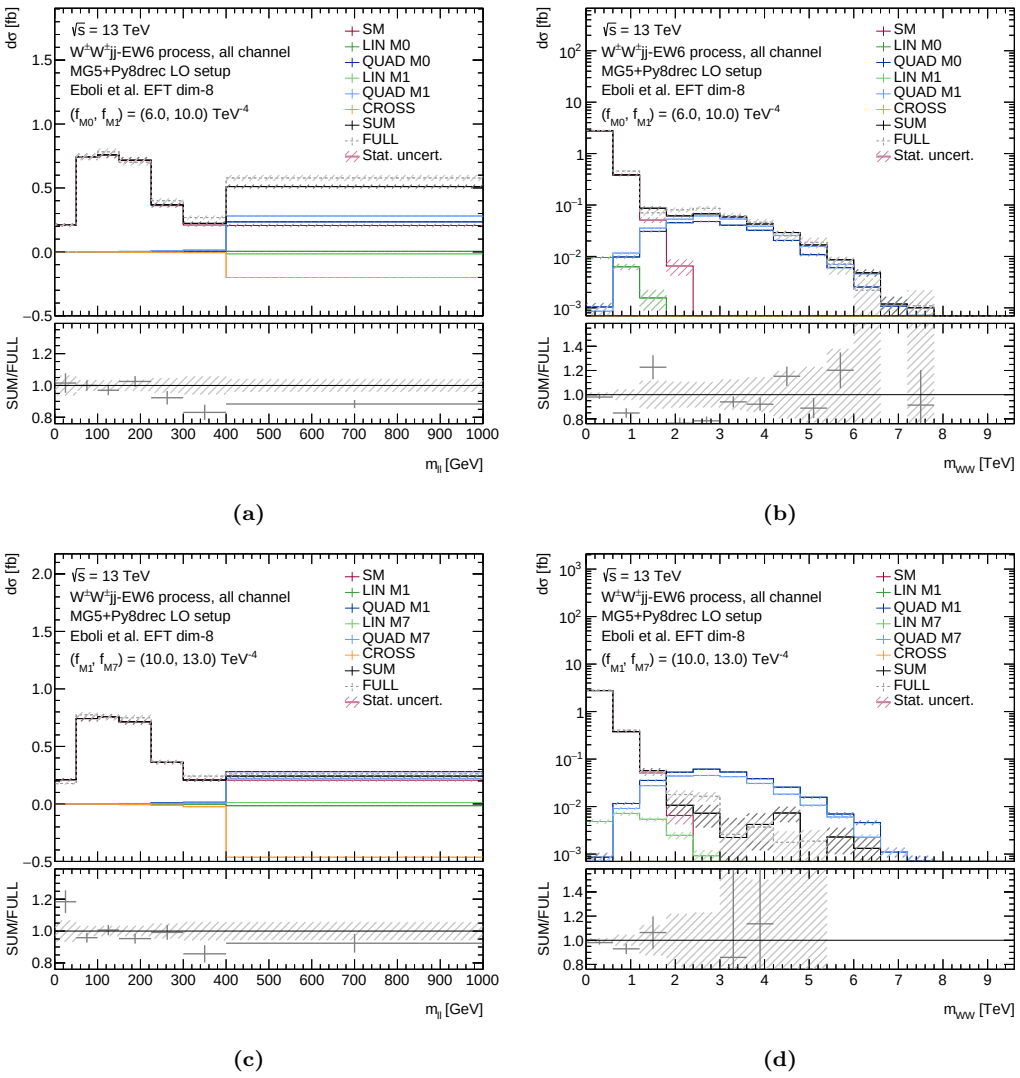


Figure F.3: Distributions of the invariant mass of the leading lepton pair, m_{ll} (a,c), and the $W^{\pm}W^{\pm}$ system, m_{WW} (b,d), for the nominal valuesof the two-dimensional inter-family parameter pairs $f_{M0}/\Lambda^4 - f_{M1}/\Lambda^4$ (a,b), and $f_{M1}/\Lambda^4 - f_{M7}/\Lambda^4$ (c,d) in the fiducial region. Shown are the SM prediction, the decomposed `LIN`, `QUAD`, and `CROSS` EFT contributions and their sum, labelled `SUM`, together with the prediction of an independently simulated sample of the full prediction of the SM with the EFT extension, labelled `FULL`. The simulation of the `CROSS` contribution between the $\mathcal{O}_{M0}$ and $\mathcal{O}_{M7}$ operators was not available in the FeynRules model version used for this validation. The lower panel shows the ratio of the `SUM` with respect to the `FULL` prediction. Uncertainties are statistical uncertainties from the MC generation only. The last bin includes the overflow.

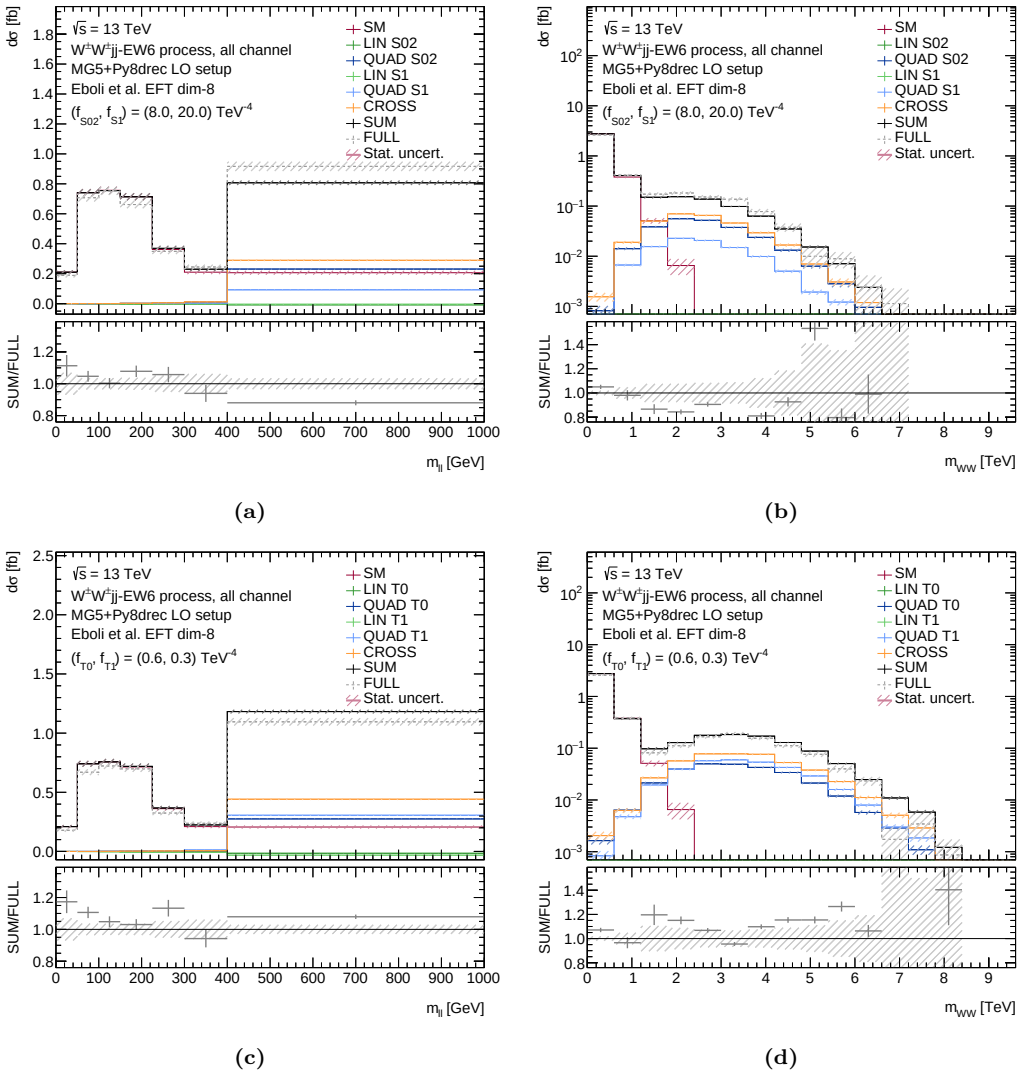


Figure F.4: Distributions of the invariant mass of the leading lepton pair, m_{ll} (a,c), and the $W^{\pm}W^{\pm}$ system, m_{WW} (b,d), for the nominal valuesof the two-dimensional inter-family parameter pairs f_{S02}/Λ^4 $-f_{S1}/\Lambda^4$ (a,b), and f_{T0}/Λ^4 $-f_{T1}/\Lambda^4$ (c,d) in the fiducial region. Shown are the SM prediction, the decomposed `LIN`, `QUAD`, and `CROSS` EFT contributions and their sum, labelled `SUM`, together with the prediction of an independently simulated sample of the full prediction of the SM with the EFT extension, labelled `FULL`. The simulation of the `CROSS` contribution between the $\mathcal{O}_{M0}$ and $\mathcal{O}_{M7}$ operators was not available in the FeynRules model version used for this validation. The lower panel shows the ratio of the `SUM` with respect to the `FULL` prediction. Uncertainties are statistical uncertainties from the MC generation only. The last bin includes the overflow.

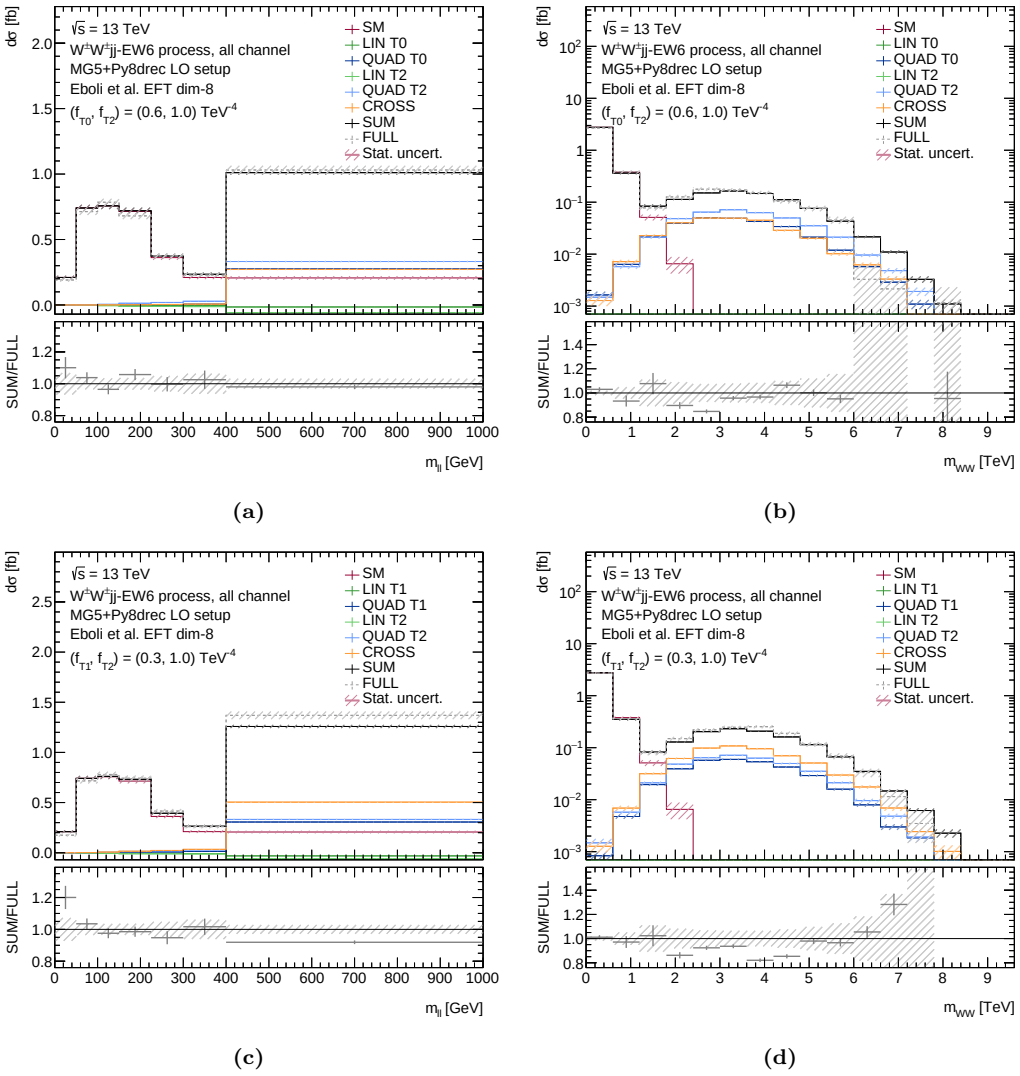


Figure F.5: Distributions of the invariant mass of the leading lepton pair, m_{ll} (a,c), and the $W^{\pm}W^{\pm}$ system, m_{WW} (b,d), for the nominal valuesof the two-dimensional inter-family parameter pairs f_{T0}/Λ^4 $-f_{T2}/\Lambda^4$ (a,b), and f_{T1}/Λ^4 $-f_{T2}/\Lambda^4$ (c,d) in the fiducial region. Shown are the SM prediction, the decomposed `LIN`, `QUAD`, and `CROSS` EFT contributions and their sum, labelled `SUM`, together with the prediction of an independently simulated sample of the full prediction of the SM with the EFT extension, labelled `FULL`. The simulation of the `CROSS` contribution between the $\mathcal{O}_{M0}$ and $\mathcal{O}_{M7}$ operators was not available in the FeynRules model version used for this validation. The lower panel shows the ratio of the `SUM` with respect to the `FULL` prediction. Uncertainties are statistical uncertainties from the MC generation only. The last bin includes the overflow.

F.5 Investigation of the Decomposition Non-closure

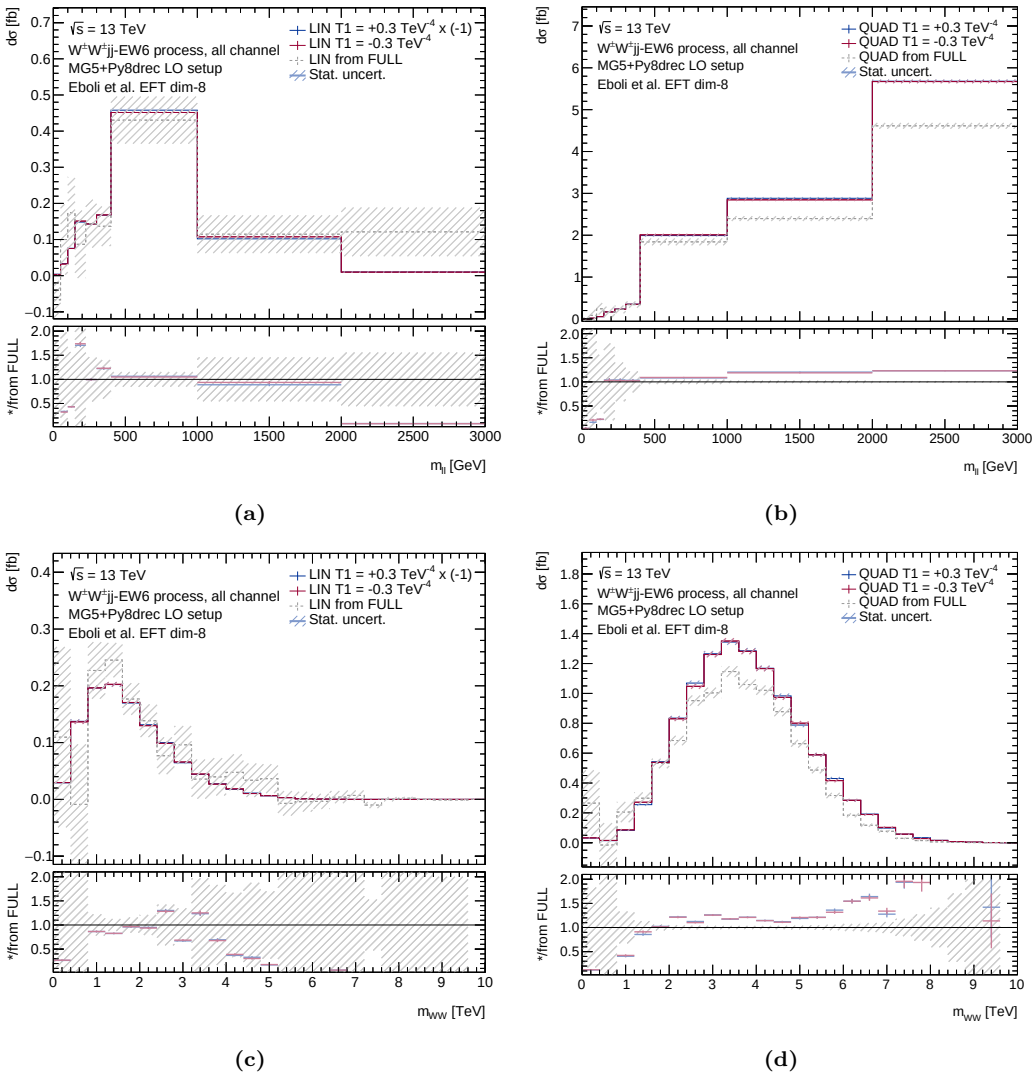


Figure F.6: Comparison of the `LIN` (a,c) and `QUAD` (b,d) contribution obtained from the amplitude decomposition method (blue and red) compared to retrieving them from independent `FULL` and SM samples employing Equations (9.11) and (9.12) (dashed grey). Shown are the invariant mass of the leading lepton pair, m_{ll} (a,b), and the $W^{\pm}W^{\pm}$ system, m_{WW} (c,d), for the f_{T1}/Λ^4 parameter in a loose region including all events with exactly two leptons with the object selection requirements shown in Tab. 6.8. The contributions from the decomposition method are illustrated for identical positive (blue) and negative (red) values of f_{T1}/Λ^4. The lower panel shows the ratio of the predictions from the amplitude decomposition method with respect to the contributions obtained from the `FULL` prediction. Uncertainties are statistical uncertainties from the MC generation only. The last bin includes the overflow.

F.6 Sample Statistics, Cross-sections, and Acceptances for the Final Setup

Table F.1: Cross-section predictions of the decomposed EFT `LIN`, `QUAD`, and `CROSS` contributions of the $W^{\pm}W^{\pm}jj$-EW6 process for all relevant parameters f_i/Λ^4 in the generator phase space of the MG5_aMC setup (cf. Tab. 6.7) together with the acceptance and cross-section in the nominal fiducial region defined in Tab. 6.8. Uncertainties are the statistical errors of the MC generation only.

Parameter(s)	Value(s)	Gen. mode	Generator cross-section [fb]	Acceptance fid. region [1]	Fiducial cross-section [fb]
$S02$	8.0	`LIN`	-0.153 ± 0.003	0.095 ± 0.001	-0.015 ± 0.001
$S02$	8.0	`QUAD`	1.097 ± 0.005	0.116 ± 0.001	0.127 ± 0.002
$S1$	20.0	`LIN`	-0.093 ± 0.002	0.081 ± 0.001	-0.008 ± 0.001
$S1$	20.0	`QUAD`	0.460 ± 0.002	0.116 ± 0.001	0.053 ± 0.001
$S02$ – $S1$	8.0 , 20.0	`CROSS`	1.398 ± 0.007	0.118 ± 0.001	0.165 ± 0.002
$M0$	6.0	`LIN`	0.071 ± 0.003	0.182 ± 0.002	0.013 ± 0.001
$M0$	6.0	`QUAD`	1.068 ± 0.006	0.127 ± 0.002	0.136 ± 0.002
$M1$	10.0	`LIN`	-0.093 ± 0.003	0.207 ± 0.002	-0.019 ± 0.001
$M1$	10.0	`QUAD`	1.282 ± 0.007	0.130 ± 0.002	0.167 ± 0.002
$M7$	13.0	`LIN`	0.073 ± 0.003	0.204 ± 0.002	0.015 ± 0.001
$M7$	13.0	`QUAD`	0.909 ± 0.005	0.137 ± 0.002	0.124 ± 0.002
$M0$ – $M1$	6.0, 10.0	`CROSS`	-1.082 ± 0.010	0.109 ± 0.001	-0.117 ± 0.002
$M0$ – $M7$	6.0, 13.0	`CROSS`	1.349 ± 0.011	0.130 ± 0.002	0.176 ± 0.002
$M1$ – $M7$	10.0, 13.0	`CROSS`	-1.959 ± 0.009	0.133 ± 0.002	-0.261 ± 0.003
$T0$	0.6	`LIN`	-0.062 ± 0.002	0.266 ± 0.002	-0.016 ± 0.001
$T0$	0.6	`QUAD`	1.058 ± 0.006	0.147 ± 0.002	0.155 ± 0.002
$T1$	0.3	`LIN`	-0.223 ± 0.002	0.180 ± 0.002	-0.040 ± 0.001
$T1$	0.3	`QUAD`	1.124 ± 0.006	0.152 ± 0.002	0.171 ± 0.002
$T2$	1.0	`LIN`	-0.375 ± 0.003	0.182 ± 0.002	-0.068 ± 0.001
$T2$	1.0	`QUAD`	1.398 ± 0.008	0.150 ± 0.002	0.210 ± 0.003
$T0$ – $T1$	0.6, 0.3	`CROSS`	1.592 ± 0.008	0.153 ± 0.002	0.244 ± 0.003
$T0$ – $T2$	0.6, 1.0	`CROSS`	1.098 ± 0.008	0.146 ± 0.002	0.161 ± 0.002
$T1$ – $T2$	0.3, 1.0	`CROSS`	2.029 ± 0.006	0.148 ± 0.002	0.300 ± 0.004

Appendix G

Additional Details on the EFT Reinterpretation

G.1 Exclusion Bounds Without Systematic Uncertainties

Parameter	95% C.L. interval [TeV^{-4}]	
$\frac{f_i}{\Lambda^4}$	Expected	Observed
$S02$	$[-12, 12]$	$[-13, 13]$
$S1$	$[-46, 47]$	$[-52, 53]$
$M0$	$[-9.1, 8.9]$	$[-10.2, 10.0]$
$M1$	$[-13, 14]$	$[-15, 15]$
$M7$	$[-20, 19]$	$[-22, 21]$
$T0$	$[-0.81, 0.85]$	$[-0.90, 0.92]$
$T1$	$[-0.37, 0.40]$	$[-0.41, 0.44]$
$T2$	$[-1.1, 1.3]$	$[-1.3, 1.5]$

Table G.1: Expected and observed one-dimensional exclusion intervals at the 95% C.L. for all EFT parameters of the considered model [2, 3] relevant in the $W^{\pm}W^{\pm}jj$-EW6 process without considering systematic uncertainties on all predictions. The expected limits are obtained with pseudo-experiments. No unitarisation procedure is applied.

G.2 Event Yields in Bins of m_{ll}

Table G.2: Estimated event yields and their statistical uncertainties of all SM processes differentially in bins of the invariant dilepton mass, m_{ll}, in the signal region as input to the EFT reinterpretation analysis. "Other prompt" comprises MC-based predictions of the processes of $t\bar{t}V$, ZZ, and triboson production. The yields of experimental data taken in the years 2015 and 2016 in Run 2 of the LHC with the ATLAS detector are given as well. Numbers are given in the combined $\ell^{\pm}\ell^{\pm}$ channel.

Process	Event yields in bins of m_{ll} (lower bin edge in GeV)						
	0	50	100	150	225	300	400
$W^{\pm}Z$	2.93 ± 0.17	8.26 ± 0.32	8.27 ± 0.39	6.55 ± 0.27	3.03 ± 0.17	1.67 ± 0.17	1.19 ± 0.12
$W^{\pm}W^{\pm}jj$-EW4	0.21 ± 0.01	0.81 ± 0.03	1.20 ± 0.04	1.56 ± 0.04	1.22 ± 0.04	0.97 ± 0.03	1.36 ± 0.04
Other prompt	0.23 ± 0.03	0.67 ± 0.08	0.50 ± 0.05	0.45 ± 0.05	0.20 ± 0.05	0.17 ± 0.03	0.14 ± 0.02
Non-prompt	5.78 ± 2.12	3.88 ± 1.33	2.95 ± 1.50	4.07 ± 1.73	1.91 ± 1.31	2.86 ± 1.59	1.78 ± 1.31
Charge misID	1.03 ± 0.10	1.67 ± 0.14	1.95 ± 0.19	1.96 ± 0.22	1.20 ± 0.17	0.52 ± 0.10	0.61 ± 0.13
$V\gamma$	0.44 ± 0.36	0.76 ± 0.41	2.29 ± 1.29	0.47 ± 0.37	0.37 ± 0.29	0.09 ± 0.06	0.05 ± 0.05
$W^{\pm}W^{\pm}jj$-EW6 (MG5+Py8drec)	3.00 ± 0.18	11.01 ± 0.36	12.57 ± 0.40	11.50 ± 0.36	5.76 ± 0.26	3.20 ± 0.17	3.03 ± 0.18
Total expected	13.62 ± 2.17	27.06 ± 2.20	29.73 ± 2.07	26.56 ± 1.84	13.69 ± 1.39	9.48 ± 1.61	8.16 ± 1.34
Data 2015/16	9	23	25	24	23	9	9

Table G.3: Estimated event yields and their statistical uncertainties of the linear and quadratic EFT signal contributions of all relevant operators at their nominal parameter values (cf. Tab. 9.3) in bins of the invariant dilepton mass, m_{ll}, in the signal region as input to the EFT reinterpretation analysis. Numbers are given in the combined $\ell^{\pm}\ell^{\pm}$ channel.

Param.	Value	Contr.	Event yields in bins of m_{ll} (lower bin edge in GeV)							
$\frac{f_i}{\Lambda^4}$	$\frac{1}{\text{TeV}^4}$		0	50	100	150	225	300	400	$\sum$
$S02$	8.0	LIN	< 0.01	-0.02 ± 0.01	-0.04 ± 0.01	-0.08 ± 0.02	-0.07 ± 0.02	-0.05 ± 0.02	-0.13 ± 0.03	-0.40 ± 0.05
		QUAD	< 0.01	< 0.01	0.01 ± 0.01	0.06 ± 0.01	0.09 ± 0.01	0.22 ± 0.02	3.06 ± 0.07	3.46 ± 0.07
$S1$	20.0	LIN	< 0.01	< 0.01	-0.02 ± 0.01	-0.04 ± 0.01	-0.01 ± 0.01	-0.02 ± 0.01	-0.09 ± 0.02	-0.19 ± 0.03
		QUAD	< 0.01	< 0.01	< 0.01	0.03 ± 0.00	0.04 ± 0.00	0.09 ± 0.01	1.22 ± 0.03	1.38 ± 0.03
$M0$	6.0	LIN	< 0.01	0.03 ± 0.01	0.03 ± 0.01	0.06 ± 0.01	0.03 ± 0.01	0.04 ± 0.02	0.09 ± 0.04	0.29 ± 0.05
		QUAD	< 0.01	< 0.01	0.01 ± 0.01	0.04 ± 0.01	0.09 ± 0.01	0.17 ± 0.03	2.99 ± 0.11	3.31 ± 0.11
$M1$	10.0	LIN	< 0.01	< 0.01	-0.02 ± 0.02	-0.08 ± 0.02	-0.07 ± 0.02	-0.09 ± 0.02	-0.23 ± 0.04	-0.49 ± 0.06
		QUAD	$-$	< 0.01	0.03 ± 0.01	0.07 ± 0.01	0.12 ± 0.02	0.35 ± 0.05	3.58 ± 0.14	4.16 ± 0.15
$M7$	13.0	LIN	< 0.01	0.02 ± 0.02	0.01 ± 0.01	0.04 ± 0.02	0.01 ± 0.03	0.12 ± 0.03	0.23 ± 0.05	0.40 ± 0.07
		QUAD	$-$	0.02 ± 0.02	0.01 ± 0.01	0.09 ± 0.02	0.06 ± 0.01	0.17 ± 0.02	3.03 ± 0.13	3.38 ± 0.13
$T0$	0.6	LIN	< 0.01	< 0.01	-0.02 ± 0.01	-0.03 ± 0.02	-0.08 ± 0.02	-0.09 ± 0.02	-0.23 ± 0.03	-0.45 ± 0.05
		QUAD	< 0.01	0.01 ± 0.00	0.01 ± 0.00	0.05 ± 0.01	0.06 ± 0.01	0.11 ± 0.01	3.54 ± 0.12	3.78 ± 0.12
$T1$	0.3	LIN	< 0.01	-0.02 ± 0.005	-0.07 ± 0.01	-0.14 ± 0.02	-0.12 ± 0.01	-0.13 ± 0.02	-0.48 ± 0.04	-0.96 ± 0.05
		QUAD	$-$	< 0.01	0.03 ± 0.01	0.13 ± 0.02	0.14 ± 0.02	0.22 ± 0.03	4.09 ± 0.13	4.63 ± 0.14
$T2$	1.0	LIN	< 0.01	-0.02 ± 0.01	-0.08 ± 0.01	-0.19 ± 0.02	-0.19 ± 0.02	-0.22 ± 0.02	-0.90 ± 0.05	-1.61 ± 0.06
		QUAD	$-$	0.02 ± 0.01	0.08 ± 0.02	0.21 ± 0.02	0.29 ± 0.03	0.40 ± 0.03	4.23 ± 0.15	5.23 ± 0.16

G.3 Systematic Uncertainties

Table G.4: Relative impact of experimental systematic uncertainties on the event yields of all background predictions based on MC simulation in bins of m_{ll} in the signal region condensed in seven categories. Lepton uncertainties comprise all variations in the measurement of electrons and muons, respectively, including the trigger efficiency. Jet uncertainties comprise all variations in the measurement of jets, except the variations of the jet energy resolution and the flavour tagging which are quoted as JER and b-tag inefficiency uncertainties, respectively.

Process	Exp. syst. uncertainties in bins of m_{ll} (lower bin edge in GeV) [%]						
Unc. source	0	50	100	150	225	300	400
$W^{\pm}Z$							
Electrons	0.30	0.38	0.27	0.83	0.80	0.89	1.81
Muons	0.92	0.99	0.96	1.12	1.27	1.41	1.83
Jets (w/o JER)	3.53	3.39	6.47	4.07	11.92	4.98	9.83
JER	−0.67	3.56	4.73	0.55	−2.81	4.86	2.19
b-tag ineff.	2.18	2.20	2.09	2.11	2.29	2.267	2.46
Pile-up rwt.	3.87	−1.80	3.91	0.47	1.71	−1.47	4.63
E_T^{miss}	1.12	0.04	0.12	0.31	0.60	0.53	0.01
$W^{\pm}W^{\pm}jj$-EW4							
Electrons	0.46	0.18	0.21	0.41	0.37	0.62	0.55
Muons	1.54	1.11	1.07	1.14	1.35	1.91	1.66
Jets (w/o JER)	2.79	5.32	2.24	3.51	1.62	3.50	2.19
JER	1.26	1.38	−0.45	0.84	−0.40	−0.18	0.47
b-tag ineff.	2.26	2.32	2.35	2.43	2.45	2.41	2.50
Pile-up rwt.	−3.33	−0.58	−0.91	−2.75	4.98	0.17	−1.48
E_T^{miss}	0.29	0.23	0.03	0.14	0.06	0.08	0.20
Other prompt							
Electrons	4.96	3.19	0.88	1.97	7.56	1.27	1.25
Muons	1.38	0.98	1.55	2.87	2.32	3.76	3.71
Jets (w/o JER)	4.05	8.42	9.49	16.09	8.42	3.05	11.72
JER	11.85	2.97	8.94	8.30	−6.51	−4.56	6.21
b-tag ineff.	2.16	1.91	2.16	2.39	1.73	1.94	2.82
Pile-up rwt.	−4.65	17.33	−13.60	2.44	21.50	13.03	−4.75
E_T^{miss}	0.85	2.82	3.89	1.57	7.20	0.85	0.58
$V\gamma$							
Electrons	0.41	0.59	0.33	0.80	1.07	2.36	2.02
Muons	0.86	1.41	0.63	0.57	1.60	0.24	1.97
Jets (w/o JER)	0.11	0.11	0.15	0.38	0.07	0.17	0.36
JER	−0.01	9.16	0.51	15.42	0.12	−45.44	0.01
b-tag ineff.	1.54	2.36	3.39	1.49	2.21	2.44	4.42
Pile-up rwt.	−33.52	−10.40	−11.75	13.11	−10.62	1.06	−11.47
E_T^{miss}	< 0.01	< 0.01	< 0.01	< 0.01	< 0.01	< 0.01	< 0.01

Table G.5: Relative impact of experimental systematic uncertainties on the event yields of the quadratic component of EFT signal predictions, which is used as uncertainty of the full EFT signal prediction, in bins of m_{ll} in the signal region condensed in seven categories. Lepton uncertainties comprise all variations in the measurement of electrons and muons, respectively, including the trigger efficiency. Jet uncertainties comprise all variations in the measurement of jets, except the variations of the jet energy resolution and the flavour tagging which are quoted as JER and b-tag inefficiency uncertainties, respectively.

Process	Exp. syst. uncertainties in bins of m_{ll} (lower bin edge in GeV) [%]						
Unc. source	0	50	100	150	225	300	400
$S02$ QUAD							
Electrons	11.69	32.66	10.39	4.25	40.32	15.32	9.84
Muons	18.69	53.50	14.10	8.49	66.05	24.07	13.82
Jets (w/o JER)	58.03	110.36	17.05	12.97	76.28	28.07	18.20
JER	3.34	−23.43	−2.91	−5.40	11.40	5.80	3.01
b-tag ineff.	23.52	13.28	8.81	19.49	17.45	14.64	13.24
Pile-up rwt.	23.20	20.25	−15.03	19.15	7.00	4.07	1.20
E_T^{miss}	6.81	19.61	5.13	2.69	23.55	8.76	4.86
$S1$ QUAD							
Electrons	28.33	26.69	47.12	6.40	13.74	2.63	10.78
Muons	45.64	42.45	80.15	11.77	22.93	5.48	15.57
Jets (w/o JER)	51.50	69.81	96.32	13.72	23.36	6.87	19.63
JER	8.30	8.23	47.01	−2.10	3.00	−0.65	3.45
b-tag ineff.	39.71	27.03	21.58	17.34	18.73	16.42	12.74
Pile-up rwt.	22.94	19.74	12.33	33.40	0.77	−4.33	−2.13
E_T^{miss}	16.66	15.50	28.24	3.88	7.52	2.05	5.44
$M0$ QUAD							
Electrons	8.62	7.68	83.97	41.48	18.01	14.57	10.35
Muons	14.53	12.78	153.97	74.64	31.58	24.20	14.80
Jets (w/o JER)	16.90	14.43	162.52	78.45	32.07	24.83	17.20
JER	−2.68	11.86	−26.23	23.12	13.53	−5.11	2.86
b-tag ineff.	28.63	61.07	31.64	25.95	34.28	26.91	23.10
Pile-up rwt.	28.20	22.55	−37.01	2.16	1.13	1.12	−0.73
E_T^{miss}	5.41	4.62	50.71	24.67	9.68	8.49	4.92
$M1$ QUAD							
Electrons	–	77.16	55.45	56.62	15.66	1.74	11.36
Muons	–	127.25	91.87	93.79	29.57	2.39	16.46
Jets (w/o JER)	–	144.81	104.83	107.27	29.98	5.37	19.82
JER	–	23.17	−42.47	17.19	5.43	1.63	2.70
b-tag ineff.	–	42.34	13.44	24.54	23.35	20.36	22.89
Pile-up rwt.	–	−32.03	−27.63	11.22	10.06	−11.40	1.19
E_T^{miss}	–	46.46	33.54	33.14	9.47	0.15	5.81

Table G.6: Relative impact of experimental systematic uncertainties on the event yields of the quadratic component of EFT signal predictions, which is used as uncertainty of the full EFT signal prediction, in bins of m_{ll} in the signal region condensed in seven categories. Lepton uncertainties comprise all variations in the measurement of electrons and muons, respectively, including the trigger efficiency. Jet uncertainties comprise all variations in the measurement of jets, except the variations of the jet energy resolution and the flavour tagging which are quoted as JER and b-tag inefficiency uncertainties, respectively.

Process	Exp. syst. uncertainties in bins of m_{ll} (lower bin edge in GeV) [%]						
Unc. source	0	50	100	150	225	300	400
$M7$ QUAD							
Electrons	–	166.33	113.09	30.11	29.94	10.85	3.92
Muons	–	260.36	177.19	46.98	46.81	22.63	3.64
Jets (w/o JER)	–	279.03	187.93	50.58	43.97	22.51	5.77
JER	–	−50.29	45.58	−10.24	−2.95	2.00	1.98
b-tag ineff.	–	68.47	22.95	17.22	27.98	24.96	23.69
Pile-up rwt.	–	−81.52	−17.51	39.35	7.38	24.74	−4.58
E_T^{miss}	–	100.24	68.00	18.17	16.42	6.34	0.74
$T0$ QUAD							
Electrons	65.52	50.43	38.86	19.05	48.17	25.76	4.60
Muons	103.67	80.31	60.69	30.57	77.11	39.28	4.96
Jets (w/o JER)	123.55	85.44	74.82	41.67	93.20	47.42	4.54
JER	19.61	0.14	25.04	6.69	19.91	4.15	1.19
b-tag ineff.	39.23	43.70	40.70	37.84	42.29	37.06	36.06
Pile-up rwt.	12.66	7.12	7.30	−2.93	2.97	16.45	0.55
E_T^{miss}	39.07	30.19	23.21	11.15	29.21	15.01	1.08
$T1$ QUAD							
Electrons	–	54.10	42.05	1.88	16.65	6.45	7.72
Muons	–	87.60	74.02	3.46	31.99	12.25	9.70
Jets (w/o JER)	–	102.79	82.13	5.88	31.22	10.45	10.39
JER	–	16.39	12.55	−4.92	5.80	0.89	1.07
b-tag ineff.	–	25.47	48.44	39.75	33.92	35.29	34.08
Pile-up rwt.	–	1.13	2.79	−3.11	0.33	−10.00	−1.12
E_T^{miss}	–	32.51	25.24	0.68	9.89	3.29	3.17
$T2$ QUAD							
Electrons	–	63.69	22.52	19.86	36.87	34.17	8.08
Muons	–	103.48	36.97	31.59	60.24	56.78	10.79
Jets (w/o JER)	–	124.60	43.32	37.09	68.14	65.25	11.84
JER	–	21.10	5.74	10.76	12.32	7.30	2.80
b-tag ineff.	–	38.05	31.58	35.14	36.47	34.79	35.75
Pile-up rwt.	–	7.80	−1.11	6.14	9.84	7.54	−3.48
E_T^{miss}	–	36.52	14.10	11.44	21.70	20.36	3.71

Table G.7: Summary of experimental uncertainties from the estimation of the backgrounds due to electron charge misidentification and non-prompt leptons in bins of m_{ll} in the signal region. These uncertainties are conceptualised and derived within the the respective estimation methods outlined in Sections D.2.1 to D.2.3.

Category	Exp. syst. uncertainties in bins of m_{ll} (lower bin edge in GeV) [%]						
Unc. source	0	50	100	150	225	300	400
Charge misID:							
Charge ID SF	$^{+5.25}_{-2.99}$	$^{+4.31}_{-2.99}$	$^{+5.30}_{-2.99}$	$^{+4.35}_{-2.99}$	$^{+4.16}_{-2.99}$	$^{+4.16}_{-2.99}$	$^{+2.84}_{-2.99}$
Energy correction	± 0.54	± 4.71	± 3.82	± 11.45	∓ 2.62	± 19.48	± 0.92
Non-prompt:							
f_e statistical	± 14.74	± 9.15	± 10.07	± 8.30	± 11.67	± 11.14	± 12.86
f_e systematic	$^{+23.04}_{-56.89}$	$^{+16.18}_{-43.69}$	$^{+7.78}_{-32.22}$	$^{-0.03}_{-31.38}$	$^{+0.26}_{-37.76}$	$^{-0.66}_{-36.36}$	$^{+0.14}_{-37.30}$
f_μ statistical	± 3.31	± 6.13	± 2.12	± 6.79	± 3.41	± 2.99	± 0.10
f_μ systematic	$^{+41.72}_{-3.79}$	$^{+49.82}_{-11.32}$	$^{+30.76}_{+6.29}$	$^{+63.33}_{-23.86}$	$^{+38.23}_{+2.22}$	$^{+41.12}_{-3.23}$	$^{+22.29}_{+14.25}$

Table G.8: Relative impact of modelling uncertainties on the event yields of the $W^\pm Z$, $W^\pm W^\pm jj$-EW4, and $W^\pm W^\pm jj$-EW6 background predictions based on MC simulation in bins of m_{ll} in the signal region. Results for the $W^\pm Z$ process are the combined impact on the $WZjj$-EW6 and $WZjj$-EW4 processes. The uncertainty sources contain the effect from the variation of the renormalisation and factorisation scales μ_R/μ_F, the nominal PDF set and its strong coupling value α_S, the parton shower and/or merging parameters/algorithms, and, for the $W^\pm W^\pm jj$-EW6 process, the interference between the $W^\pm W^\pm jj$-EW6 and $W^\pm W^\pm jj$-EW4 processes.

Process	Mod. uncertainties in bins of m_{ll} (lower bin edge in GeV) [%]						
Unc. source	0	50	100	150	225	300	400
$W^\pm Z$							
μ_R/μ_F env.	28.07	25.94	25.14	25.29	25.01	23.43	21.54
PDF set env.	2.49	2.35	2.40	2.05	2.29	2.28	3.80
α_S	1.84	1.79	2.55	2.56	2.15	2.21	−2.06
Parton shower	7.29	3.09	11.02	7.92	100.49	28.06	27.21
$W^\pm W^\pm jj$-EW4							
μ_R/μ_F env.	38.44	37.70	37.29	37.23	37.67	38.36	38.37
PDF set env.	2.86	2.94	3.01	3.19	3.35	6.79	4.36
α_S	2.21	2.28	2.01	1.94	1.85	1.84	1.87
Parton shower	−100.00	26.45	18.16	8.80	19.26	21.59	20.54
$W^\pm W^\pm jj$-EW6							
μ_R/μ_F env.	$^{6.14}_{-5.50}$	$^{7.00}_{-6.17}$	$^{6.98}_{-6.16}$	$^{7.66}_{-6.71}$	$^{8.18}_{-7.12}$	$^{8.83}_{-7.62}$	$^{10.51}_{-8.91}$
PDF set env.	1.39	1.84	2.26	1.65	1.70	1.80	2.38
α_S	−0.15	0.02	−0.04	0.17	−0.07	0.03	0.45
Parton shower	1.00	0.71	0.79	0.67	0.21	1.21	0.55
EW4-EW6 Interf.	0.98	3.26	1.47	1.98	2.77	3.76	3.14

Table G.9: Relative impact of modelling uncertainties on the event yields of the quadratic component of EFT signal predictions, which is used as uncertainty of the full EFT signal prediction, in bins of m_{ll} in the signal region. The uncertainty sources contain the effect from the variation of the renormalisation and factorisation scales μ_R/μ_F, the nominal PDF set and its strong coupling value α_S, and the parton shower parameters.

Process	Mod. uncertainties in bins of m_{ll} (lower bin edge in GeV) [%]						
Unc. source	0	50	100	150	225	300	400
$S02$ QUAD							
μ_R/μ_F env.	6.74 −5.88	8.88 −7.62	12.80 −10.59	11.36 −9.55	11.78 −9.85	12.02 −10.05	14.51 −11.86
PDF set env.	2.51	3.45	3.16	4.37	2.45	3.43	4.22
α_S	0.33	0.72	1.05	0.99	0.67	0.85	0.57
Parton shower	39.10	11.92	11.87	3.22	8.75	1.59	3.84
$S1$ QUAD							
μ_R/μ_F env.	9.23 −7.97	9.24 −8.01	11.15 −9.35	10.44 −8.83	11.79 −9.87	12.02 −10.05	14.66 −11.97
PDF set env.	2.61	2.88	6.12	2.09	6.95	2.78	4.44
α_S	0.58	−0.02	0.40	0.59	−0.30	0.74	0.82
Parton shower	34.24	22.11	5.60	4.45	6.62	9.89	3.97
$M0$ QUAD							
μ_R/μ_F env.	5.64 −5.15	9.40 −8.13	11.67 −9.82	9.91 −8.45	11.15 −9.39	12.99 −10.79	14.98 −12.21
PDF set env.	2.95	168.40	36.86	3.55	3.76	3.16	6.68
α_S	0.14	−18.98	−6.86	0.80	−0.39	0.79	0.82
Parton shower	49.33	97.88	54.69	3.90	5.92	5.42	4.80
$M1$ QUAD							
μ_R/μ_F env.	– –	10.20 −8.63	10.49 −8.84	12.24 −10.20	12.16 −10.18	12.35 −10.30	14.95 −12.19
PDF set env.	–	2.72	3.07	12.94	7.26	2.87	4.14
α_S	–	0.95	1.10	−0.76	1.69	0.46	1.04
Parton shower	–	2.80	11.02	8.65	22.84	9.92	5.71
$M7$ QUAD							
μ_R/μ_F env.	– –	5.62 −5.30	7.02 −6.17	12.29 −10.25	12.20 −10.13	12.74 −10.58	14.56 −11.91
PDF set env.	–	3.42	2.44	4.55	7.61	3.17	5.73
α_S	–	−1.14	0.36	0.59	−0.96	1.17	1.12
Parton shower	–	48.65	6.57	7.27	2.70	4.67	10.55
$T0$ QUAD							
μ_R/μ_F env.	10.36 −8.85	9.59 −8.25	11.19 −9.47	13.21 −10.97	13.88 −11.45	13.23 −10.96	15.33 −12.47
PDF set env.	7.23	3.68	5.92	4.90	4.89	10.21	5.50
α_S	1.75	0.32	1.11	1.96	< 0.01	1.31	0.81
Parton shower	107.98	7.33	13.41	26.33	7.68	5.18	5.92
$T1$ QUAD							
μ_R/μ_F env.	– –	10.48 −8.95	12.73 −10.61	13.03 −10.80	14.34 −11.78	15.31 −12.43	15.08 −12.30
PDF set env.	–	2.21	2.77	5.49	5.17	4.57	4.66
α_S	–	0.68	0.72	1.25	0.68	1.27	1.38
Parton shower	–	20.78	9.15	6.77	6.29	7.88	2.20
$T2$ QUAD							
μ_R/μ_F env.	– –	12.88 −10.71	13.04 −10.84	12.85 −10.70	13.49 −11.15	13.95 −11.49	15.39 −12.52
PDF set env.	–	4.13	3.33	4.02	4.57	13.36	4.78
α_S	–	1.34	1.38	1.73	1.18	0.05	1.12
Parton shower	–	24.24	9.03	3.55	4.20	9.02	3.37

G.4 The Clipping Unitarisation Approach

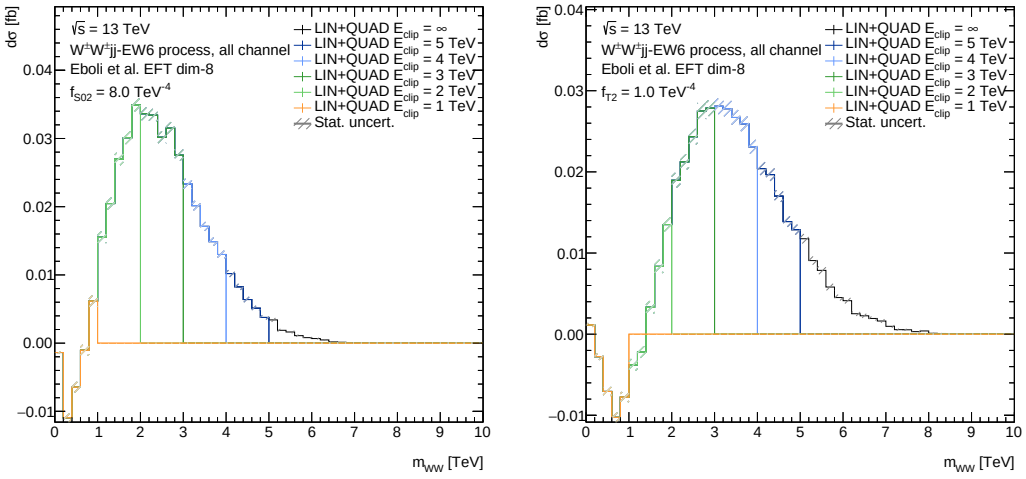


Figure G.1: Distributions of the invariant mass of the $W^{\pm}W^{\pm}$ system, m_{WW}, at matrix element level for the EFT prediction without the SM contribution at various clipping energies E_{clip}. The distributions are shown for the f_{S02}/Λ^4 (a) and f_{T2}/Λ^4 (b) parameters set to their nominal values (cf. Tab. 9.3) for events with exactly two leptons with object selection requirements shown in Tab. 6.8 at particle level. Uncertainties are statistical uncertainties from the MC generation only.

G.5 Impact of Dimension-6 EFT Effects from the $W^{\pm}Z$-EW4 Process

Table G.10: Effect of the aTGC parameters Δg_1^Z, $\Delta\kappa_Z$, and λ_Z on the MC predicted event yields of the $W^{\pm}Z$ process compared to the SM prediction in bins of the invariant dilepton mass, m_{ll} in the signal region. Shown is the impact when the three parameters are independently set to their best limits values [283].

Parameter	Effect in bins of m_{ll} (lower bin edge in GeV) [%]						
	0	50	100	150	225	300	400
Δg_1^Z	$^{+0.13}_{-0.09}$	$^{-0.19}_{+0.18}$	$^{-0.06}_{+0.09}$	$^{-0.08}_{+0.18}$	$^{-0.47}_{+0.61}$	$^{+0.03}_{+0.08}$	$^{+0.08}_{+0.16}$
$\Delta\kappa_Z$	$^{-0.05}_{+0.06}$	$^{-0.05}_{+0.05}$	$^{-0.06}_{+0.07}$	$^{-0.04}_{+0.05}$	$^{-0.05}_{+0.06}$	$^{-0.05}_{+0.07}$	$^{-0.21}_{+0.23}$
λ_Z	$^{-0.37}_{+0.39}$	$^{-0.37}_{+0.42}$	$^{-0.64}_{+0.71}$	$^{-0.78}_{+1.04}$	$^{-1.10}_{+1.62}$	$^{-1.09}_{+1.32}$	$^{-4.71}_{+5.32}$

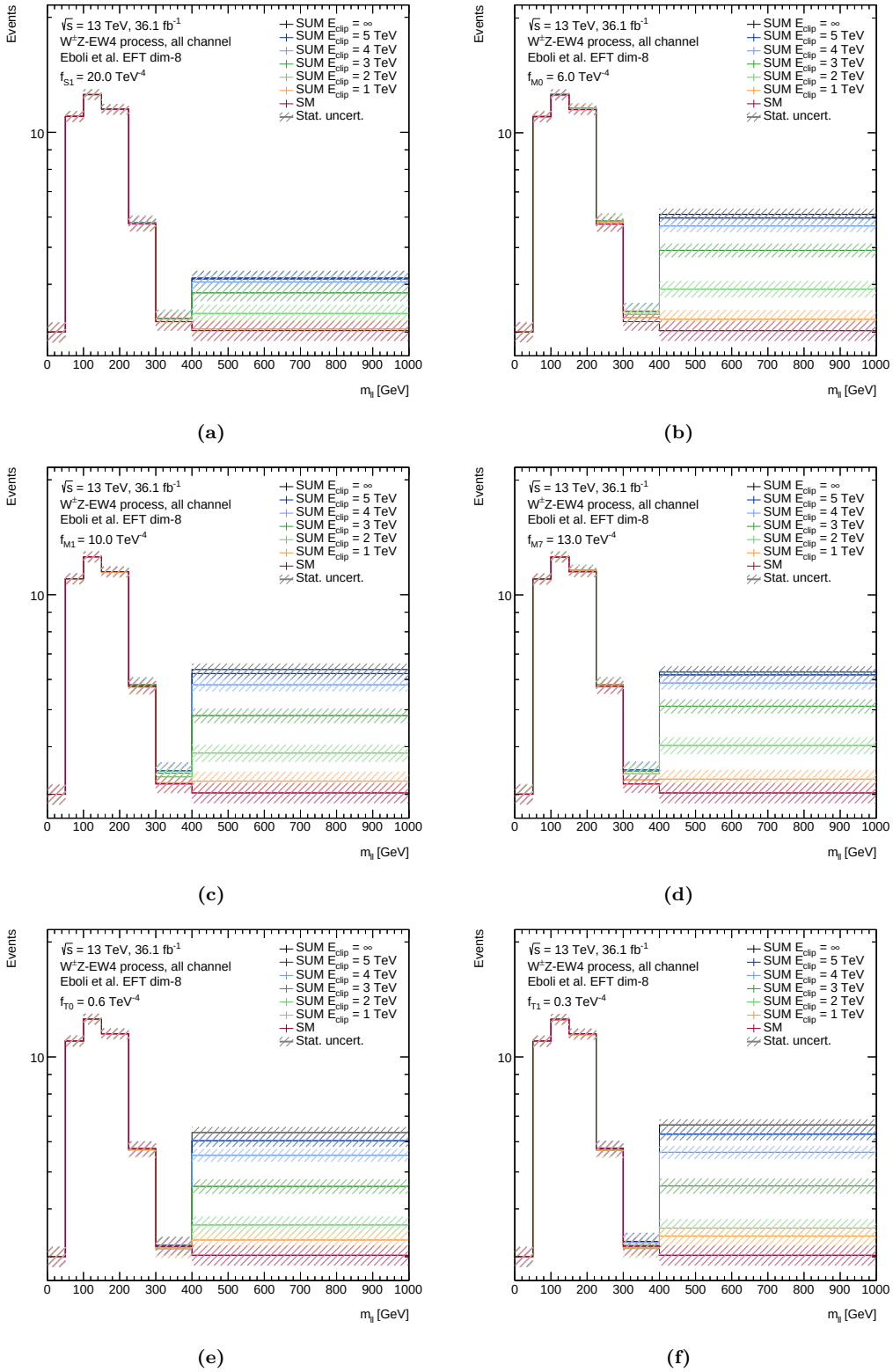


Figure G.2: Distributions of the invariant mass of the leading lepton pair, m_{ll}, for the SUM prediction at various clipping energies E_{clip}. The distributions are shown for the parameters f_{S1}/Λ^4 (a), f_{M0}/Λ^4 (b), f_{M1}/Λ^4 (c), f_{M7}/Λ^4 (d), f_{T0}/Λ^4 (e) and f_{T1}/Λ^4 (f) set to their nominal values (cf. Tab. 9.3) in the combined $\ell^{\pm}\ell^{\pm}$ channel in the signal region at reconstruction level. The SM prediction is shown as well (red). Uncertainties are statistical uncertainties from the MC generation only. The last bin includes the overflow.

List of Figures

2.1 Summary of several Standard Model total and fiducial production cross section measurements with the ATLAS experiment. 12
2.2 Triple self-interaction vertices of the electroweak gauge bosons at LO. 13
2.3 Quartic self-interaction vertices of the electroweak gauge bosons at LO. . . . 13
2.4 Interaction vertices for the Higgs boson with the electroweak gauge bosons. . 14
2.5 Feynman diagrams contributing to the process of vector boson scattering $VV \to VV$ at LO. 14
2.6 Feynman diagrams of the seven processes contributing to the vector boson scattering $W^+W^+ \to W^+W^+$ at LO. 15
2.7 Kinematic sketch of the W^+W^+ scattering reaction in the centre-of-mass frame of the W^+W^+ system. 15
2.8 Cross-section of longitudinally polarised gauge-boson scattering in the channel $W^+W^- \to W^+W^-$ as a function of the centre-of-mass energy. 17
2.9 Cross-section of the polarised gauge-boson scattering in all possible massive boson final states $V_LV_L \to V_LV_L$ as a function of the centre-of-mass energy with and without including the Higgs exchange contributions. 17
2.10 The four-fermion vertex in the Fermi theory translates into the exchange of a $W^\pm/Z$ boson in the full electroweak SM. 19

3.1 Scheme of the CERN accelerator complex. 26
3.2 Outline of the LHC schedule. 27
3.3 Schematic view of the ATLAS detector at the LHC. 27
3.4 Schematic view of the ATLAS inner detector. 29
3.5 Schematic view of the ATLAS pixel detector. 30
3.6 Schematic view of the ATLAS muon spectrometer. 31
3.7 Schematic view of the ATLAS calorimeter system. 32
3.8 The ATLAS TDAQ system in Run 2 35
3.9 Total integrated luminosity and data quality in 2015 and 2016. 37
3.10 Combined number of interactions per crossing in 2015 and 2016 38
3.11 Data and Monte Carlo simulated events processing chain 38

4.1 Unpolarised NNLO NNPDF3.0 parton distribution functions (PDFs) multiplied by the Bjorken variable for protons. 49
4.2 Structure of Monte Carlo event generation components for pp-collisions . . . 50

5.1 Schematic Feynman diagram of VBS processes at the LHC. 58
5.2 Representation of Feynman diagrams of the $VVjj$-EW6 process at LO in the t- and u-channels. 60
5.3 Representation of Feynman diagrams of $VVjj$-EW6 at LO in the s-channel. . 60
5.4 Representation of Feynman diagrams of the $VVjj$-EW4 process at LO 61
5.5 Contributing perturbative orders of the $VVjj$ process at LO and NLO at the LHC. 64
5.6 Representation of Feynman diagrams of the $W^\pm W^\pm jj$ process at NLO in QCD and electroweak couplings. 66

6.1 Differential distribution of the Zeppenfeld variable of the third-leading jet from predictions matched to parton showers at LO and NLO. 77
6.2 Distribution of the Zeppenfeld variable for the third-leading jet for all leading orders of the $W^{\pm}W^{\pm}jj$ process, $W^{\pm}W^{\pm}jj$-EW6, $W^{\pm}W^{\pm}jj$-EW4 and their interference, their sum and the prediction for the inclusive $W^{\pm}W^{\pm}jj$ process in the inclusive phase space. 93
6.3 Kinematic distributions comparing the LO contributions of the $W^{\pm}W^{\pm}jj$ process, the electroweak and the strong production, and its interference, and their sum. 94
6.4 Kinematic distributions comparing the LO contributions of the $W^{\pm}W^{\pm}jj$ process, the electroweak and the strong production, and its interference, and their sum generated with the MG5+Py8drec setup. 95
6.5 Two-dimensional distribution of m_{jj} and ΔY_{jj} of the tagging jet system for the LO components of the $W^{\pm}W^{\pm}jj$ process, $W^{\pm}W^{\pm}jj$-EW6, $W^{\pm}W^{\pm}jj$-EW4, and their interference. 96
6.6 Kinematic distributions comparing the different nominal modelling setups for the $W^{\pm}W^{\pm}jj$-EW6 process, PB+Py8, Sherpa23jLO, and MG5+Py8drec. . . 99
6.7 Kinematic distributions of the third-leading jet comparing the different nominal modelling setups for the $W^{\pm}W^{\pm}jj$-EW6 process, PB+Py8, Sherpa23jLO, and MG5+Py8drec. 100
6.8 Kinematic distributions comparing the different nominal modelling setups for the $W^{\pm}W^{\pm}jj$-EW4 process, PB+Py8, Sherpa23jLO, and MG5+Py8drec. . . 102
6.9 Kinematic distributions comparing the different nominal modelling setups for the $W^{\pm}W^{\pm}jj$-EW6 process, PB+Py8, Sherpa23jLO, and MG5+Py8drec, with the same nominal scale choice m_W. 106
6.10 Distribution of the invariant mass m_{jj} of the tagging jet pair for the $pp \to e^+\nu_e\mu^+\nu_\mu jj$ process at LO and NLO QCD for two different scale choices, taken from Ref. [161]. 107
6.11 Kinematic distributions comparing the predictions of the Sherpa23jLO setup for the $W^{\pm}W^{\pm}jj$-EW6 process for six different scale choices. 108
6.12 Kinematic distributions comparing the predictions of the MG5+Py8drec setup for the $W^{\pm}W^{\pm}jj$-EW6 process for six different scale choices. 109
6.13 Kinematic distributions of typical VBS observables comparing the predictions of different parton shower setups at LO of the $W^{\pm}W^{\pm}jj$-EW6 process. . . . 111
6.14 Distribution of the invariant mass of the two charged leptons comparing the predictions of different parton shower setups at LO of the $W^{\pm}W^{\pm}jj$-EW6 process. 112
6.15 Kinematic distributions of jets comparing the predictions of different parton shower setups at NLO in QCD of the $W^{\pm}W^{\pm}jj$-EW6 process. 113
6.16 Impact of the VBS approximation at NLO QCD in the 2-dimensional plane of the transverse mass and the rapidity separation of the tagging jets. 116
6.17 Distribution of the relative NLO EW correction to the LO $W^{\pm}W^{\pm}jj$-EW6 process, k(NLO EW), as a function of m_{jj}. 117

7.1 Display of a candidate experimental $pp \to W^{\pm}W^{\pm}jj \to \mu^+\mu^+jj + E_T^{\text{miss}}$ event from proton-proton collisions at a centre-of-mass energy of 13 TeV recorded with the ATLAS detector in the Run 2 data-taking period of the LHC. . . . 123
7.2 Folding information in m_{jj} and m_{ll} for the processes $W^{\pm}W^{\pm}jj$-EW6 and $W^{\pm}W^{\pm}jj$-EW4. 142

8.1 Kinematic distributions in the $W^{\pm}Z$ control region. 159
8.2 Impact of the jet energy resolution and pileup reweighting data scale factors systematic uncertainties on the nominal predictions estimated from MC simulation in the signal and low-m_{jj} control region. 164
8.3 Distribution of the invariant mass of the tagging jet system in the signal region and low-m_{jj} control region of the nominal background estimate due to electron charge misidentification and its uncertainties in all channels. 165

8.4 Distribution of the invariant mass of the tagging jet system in the signal region and low-m_{jj} control region of the nominal background estimate due to non-prompt leptons and its uncertainties in all channels. 166
8.5 Distribution of the invariant mass of the tagging jet system in the signal region and low-m_{jj} control region of the $W^{\pm}W^{\pm}jj$-EW6 signal estimate and its modelling uncertainties in the combined $\ell^{\pm}\ell^{\pm}$ channel. 167
8.6 Distribution of the invariant mass of the tagging jet system in the signal region and low-m_{jj} control region of the $W^{\pm}W^{\pm}jj$-EW4 and $W^{\pm}Z$ estimates and their modelling uncertainties in the combined $\ell^{\pm}\ell^{\pm}$ channel. 168
8.7 Scan of the likelihood function with dependence on μ or the fit to the expected and the observed experimental data. 170
8.8 Distribution of the invariant mass of the tagging jets, m_{jj}, in the combined channel $\ell^{\pm}\ell^{\pm}$ in the signal region before and after the fit to observed data. . . 173
8.9 Distribution of the invariant mass of the tagging jets, m_{jj}, in in the $W^{\pm}Z$ control region and all channels of the low-m_{jj} control regions before and after the fit to observed data. 174
8.10 Pulls of the nuisance parameters for the unconditional, and the background-only fit to observed data. 175
8.11 Impact of the nuisance parameters on the measured signal strength $\hat{\mu}$ before and after the fit to observed data. 177
8.12 Comparison of the measured fiducial cross-section and the nominal theoretical predictions of the analysis, Sherpa23jLO, PB+Py8, and MG5+Py8drec. . . . 180

9.1 Overview of exclusion limits on dimension-eight EFT parameters f_{S0}/Λ^4 and f_{S1}/Λ^4, and f_{M0}/Λ^4 with the ATLAS and CMS experiments at centre-of-mass energies of 8 and 13 TeV in final states involving leptons, jets and/or photons. 187
9.2 Overview of exclusion limits on dimension-eight EFT parameters f_{M1}/Λ^4, and f_{M7}/Λ^4 with the ATLAS and CMS experiments at centre-of-mass energies of 8 and 13 TeV in final states involving leptons, jets and/or photons. 188
9.3 Overview of exclusion limits on dimension-eight EFT parameters f_{T0}/Λ^4, and f_{T1}/Λ^4 with the ATLAS and CMS experiments at centre-of-mass energies of 8 and 13 TeV in final states involving leptons, jets and/or photons. 189
9.4 Overview of exclusion limits on dimension-eight EFT parameter f_{T2}/Λ^4 with the ATLAS and CMS experiments at centre-of-mass energies of 8 and 13 TeV in final states involving leptons, jets and/or photons. 190
9.5 Two-dimensional expected and observed 95% C.L. exclusion limits for the aQGC parameters α_4 and α_5 obtained by analyses of the $W^{\pm}Vjj$, $W^{\pm}W^{\pm}jj$, and $W^{\pm}Zjj$ VBS final states with the ATLAS experiment. 193
9.6 193
9.7 Invariant mass of the $W^{\pm}W^{\pm}$ system at matrix element level for different values of the f_{S02}/Λ^4 and f_{T0}/Λ^4 parameters compared to the SM prediction. 200
9.8 Kinematic distributions of invariant (transverse) masses of the leptonic decay products of the $W^{\pm}W^{\pm}$ system for different values of the f_{S02}/Λ^4 parameter and the SM prediction in the loose region at particle level. 201
9.9 Kinematic distributions related to the leptonic decay products of the $W^{\pm}W^{\pm}$ system for different values of the f_{S02}/Λ^4 parameter and the SM prediction in the loose region at particle level. 202
9.10 Distribution of the transverse momentum of the leading jet in the event, $p_{\mathrm{T}}(j_1)$ for different values of the f_{S02}/Λ^4, f_{M0}/Λ^4, and f_{T0}/Λ^4 parameters compared to the SM prediction. 204
9.11 Distributions of the invariant mass of the leading lepton pair for different values of the f_{M0}/Λ^4 and f_{T0}/Λ^4 parameters and the SM prediction in the loose region at particle level. 205

9.12 Distributions of the invariant mass of the leading lepton pair, m_{ll}, and the $W^{\pm}W^{\pm}$ system, m_{WW}, for the nominal values of the f_{S1}/Λ^4, and f_{M0}/Λ^4 parameters in the fiducial region showing the decomposed EFT contributions and their sum, compared to an independent full prediction of the SM with the EFT extension. 210
9.13 Distribution of the invariant mass of the leading lepton pair, m_{ll}, for the nominal values of the f_{S02}/Λ^4, f_{M1}/Λ^4, and f_{M7}/Λ^4 parameters in the fiducial region showing the decomposed EFT contributions and their sum, compared to an independent full prediction of the SM with the EFT extension. 211
9.14 Distributions of the transverse momentum of the leading jet $p_{\mathrm{T}}(j_1)$, and the invariant mass of the $W^{\pm}W^{\pm}$ system, m_{WW}, for the nominal value of the f_{T0}/Λ^4 parameter in the loose region showing the decomposed EFT contributions and their sum, compared to an independent full prediction of the SM with the EFT extension. 212
9.15 Distributions of the invariant mass of the tagging jet and the leading lepton pair for the nominal value of the f_{T0}/Λ^4 parameter in the fiducial region showing the decomposed EFT contributions and their sum, compared to an independent full prediction of the SM with the EFT extension. 212
9.16 Distribution of the invariant mass of the leading lepton pair, m_{ll}, for the nominal values of the f_{T1}/Λ^4, and f_{T2}/Λ^4 parameters in the fiducial region showing the decomposed EFT contributions and their sum, compared to an independent full prediction of the SM with the EFT extension. 213
9.17 Distributions of the invariant mass of the lepton pair and the $W^{\pm}W^{\pm}$ system for the f_{T0}/Λ^4 parameters in the loose region showing the `LIN` and `QUAD` EFT contributions from the amplitude decomposition approach compared to retrieving them from independent `FULL` samples of the SM with the EFT extension. 215
9.18 Distributions of the invariant mass of the $W^{\pm}W^{\pm}$ system and the leading lepton pair in a restricted generator phase space with a minimum requirement on m_{ll} of 500 GeVfor the f_{T0}/Λ^4 parameter showing the decomposed EFT contributions and their sum, compared to an independent full prediction of the SM with the EFT extension. 217
9.19 Normalised kinematic distributions of the transverse momentum of the leading lepton and leading jet of the `LIN` and `QUAD` contributions for different values of the f_{S1}/Λ^4 parameter in the loose region at particle level. 220
9.20 Normalised kinematic distributions of the invariant mass of the leading lepton and tagging jet pair of the `LIN` and `QUAD` contributions for different values of the f_{S1}/Λ^4 parameter in the loose region at particle level. 221
9.21 Distributions of the invariant mass of the leading lepton pair, m_{ll}, in the combined $\ell^{\pm}\ell^{\pm}$ channel in the signal region at reconstruction level for the background estimates, experimental data taken in the years 2015 and 2016 with the ATLAS detector, and different signal predictions. 224
9.22 Distribution of the invariant leading lepton mass and impact of experimental uncertainties on the $W^{\pm}W^{\pm}jj$-EW6 and $W^{\pm}Z$ process in the signal region. . 232
9.23 Distribution of the invariant leading lepton mass and impact of experimental uncertainties on the `QUAD` contribution of the EFT signal predictions for the parameters f_{S02}/Λ^4, f_{S1}/Λ^4, f_{M0}/Λ^4, and f_{M1}/Λ^4 in the signal region. . . . 233
9.24 Distribution of the invariant leading lepton mass and impact of experimental uncertainties on the `QUAD` contribution of the EFT signal predictions for the parameters f_{M7}/Λ^4, f_{T0}/Λ^4, f_{T1}/Λ^4, and f_{T2}/Λ^4 in the signal region. 234
9.25 Distribution of the invariant mass of the dilepton system in the signal region of the nominal background estimate due to electron charge misidentification and non-prompt leptons, and their uncertainties in the combined channel. . . 235
9.26 Distribution of the invariant leading lepton mass and impact of theoretical modelling uncertainties on the $W^{\pm}W^{\pm}jj$-EW6, $W^{\pm}W^{\pm}jj$-EW4, and $W^{\pm}Z$ process in the signal region. 236

9.27 Distribution of the invariant leading lepton mass and impact of modelling uncertainties on the QUAD contribution of the EFT signal predictions for the parameters f_{S02}/Λ^4, f_{S1}/Λ^4, f_{M0}/Λ^4, and f_{M1}/Λ^4 in the signal region. . . . 237
9.28 Distribution of the invariant leading lepton mass and impact of modelling uncertainties on the QUAD contribution of the EFT signal predictions for the parameters f_{M7}/Λ^4, f_{T0}/Λ^4, f_{T1}/Λ^4, and f_{T2}/Λ^4 in the signal region. 238
9.29 Schematic for the illustration of the clipping unitarisation procedure. 240
9.30 Distribution of the invariant mass of the $W^{\pm}W^{\pm}$ system separately for the LIN and QUAD EFT contributions for all relevant parameters. 241
9.31 Fiducial cross-section of the SUM contribution as a function of the clipping energy E_{clip} for all relevant parameters. 242
9.32 Distributions of the invariant mass of the leading lepton pair, m_{ll}, for the EFT prediction without the SM contribution at various clipping energies E_{clip} in the fiducial region. 243
9.33 Distributions of the invariant mass of the leading lepton pair, m_{ll}, for the SUM prediction at various clipping energies E_{clip} in the signal region at reconstruction level. 243
9.34 Distribution of the invariant mass of the two leading leptons, m_{ll}, for the SM $W^{\pm}W^{\pm}jj$-EW6 prediction and experimental data taken in the years 2015 and 2016 with the ATLAS detector in the signal region at reconstruction level; two-dimensional distribution of the invariant mass of the $W^{\pm}W^{\pm}$ system, m_{WW} at matrix-element level and m_{ll} at reconstruction level for the SM $W^{\pm}W^{\pm}jj$-EW6 process; and mean value of m_{WW} at ME level as a function of m_{ll} at reconstruction level. 245
9.35 Expected and observed upper and lower exclusion bounds at 95% C.L., and unitarity bounds on the parameters f_{S02}/Λ^4, f_{S1}/Λ^4, f_{M0}/Λ^4, f_{M1}/Λ^4 as a function of the clipping energy $E_{\text{clip}} = m_{WW}$. 246
9.36 Expected and observed upper and lower exclusion bounds at 95% C.L., and unitarity bounds on the parameters f_{M7}/Λ^4, f_{T0}/Λ^4, f_{T1}/Λ^4, f_{T2}/Λ^4 as a function of the clipping energy $E_{\text{clip}} = m_{WW}$. 247
9.37 Invariant mass of the dilepton system in the loose region showing the effects of the aTGC parameters Δg_1^Z, $\Delta\kappa_Z$, and λ_Z on the event yield of the $W^{\pm}Z$ process. 250
9.38 Invariant mass of the dilepton system in the signal region showing the effects of the aTGC parameters Δg_1^Z, $\Delta\kappa_Z$, and λ_Z on the event yield of the $W^{\pm}Z$ process. 251
9.39 Invariant mass of the dilepton system in the loose and signal regions showing the minimal/maximal effects of the aTGC parameters Δg_1^Z, $\Delta\kappa_Z$, and λ_Z on the event yield of the $W^{\pm}Z$ process. 252
9.40 Overview of exclusion limits on dimension-eight EFT parameters f_{S0}/Λ^4 and f_{S1}/Λ^4, and f_{M0}/Λ^4 including the first result from the ATLAS experiment at centre-of-mass energies of 13 TeV. 255
9.41 Overview of exclusion limits on dimension-eight EFT parameters f_{M1}/Λ^4, and f_{M7}/Λ^4 including the first result from the ATLAS experiment at centre-of-mass energies of 13 TeV. 256
9.42 Overview of exclusion limits on dimension-eight EFT parameters f_{T0}/Λ^4, and f_{T1}/Λ^4 including the first result from the ATLAS experiment at centre-of-mass energies of 13 TeV. 257
9.43 Overview of exclusion limits on dimension-eight EFT parameter f_{T2}/Λ^4 including the first result from the ATLAS experiment at centre-of-mass energies of 13 TeV. 258

A.1 Prediction of the lepton flavour channel distribution in the fully leptonic final state of the $W^{\pm}W^{\pm}jj$-EW4 and the $W^{\pm}W^{\pm}jj$-EW6 process. 279

B.1 Kinematic distributions comparing the different nominal modelling setups for the $W^{\pm}W^{\pm}jj$-EW4 process, PB+Py8, and Sherpa23jLO, with the same nominal scale choice m_W. 294
B.2 Kinematic distributions comparing the LO contributions of the $W^{\pm}W^{\pm}jj$ process, the electroweak and the strong production, and its interference, and their sum, with the inclusive prediction. 296
B.3 Kinematic distributions comparing the electroweak and the strong production of the $W^{\pm}W^{\pm}jj$ process generated with the Sherpa23jLO setup. 297
B.4 Kinematic distributions comparing the electroweak and the strong production of the $W^{\pm}W^{\pm}jj$ process generated with the PB+Py8 setup. 298
B.5 Impact of the internal parton shower variation on the PB+Py8 setup for the $W^{\pm}W^{\pm}jj$-EW6 process. 301
B.6 Impact of the internal parton shower variations on the PB+Py8 setup for the $W^{\pm}W^{\pm}jj$-EW4 process. 302
B.7 Impact of the merging scale and internal parton shower variations on the Sherpa23jLO setup for the $W^{\pm}W^{\pm}jj$-EW6 process. 303
B.8 Impact of the merging scale and internal parton shower variations on the Sherpa23jLO setup for the $W^{\pm}W^{\pm}jj$-EW4 process. 304
B.9 Impact of the internal parton shower variations on the MG5+Py8drec setup for the $W^{\pm}W^{\pm}jj$-EW6 process. 306
B.10 Impact of the internal parton shower variations on the MG5+Py8drec setup for the $W^{\pm}W^{\pm}jj$-EW4 process. 307
B.11 Kinematic distributions comparing the predictions of the SherpaLO setup for the $W^{\pm}W^{\pm}jj$-EW6 process for six different scale choices. 308
B.12 Kinematic distributions comparing the setups Sherpa23jLO, MG5+Py8drec, and SherpaLO for the $W^{\pm}W^{\pm}jj$-EW6 process with the same nominal scale choice SqrtPtJets. 309
B.13 Additional kinematic distributions comparing the predictions of different parton shower setups at NLO in QCD of the $W^{\pm}W^{\pm}jj$-EW6 process. 310
B.14 Selection sequence and differential distributions comparing the predictions of the $W^{\pm}W^{\pm}jj$-EW6 process with and without QED FSR in the parton shower with the nominal SHERPA setup Sherpa23jLO. 312

D.1 Examples of Feynman diagrams of Z+jets and $t\bar{t}$ production representing the major contributions to the background due to electron charge misidentification in the signal region. 325
D.2 Schematic illustration of the process of photon conversion and subsequent pair production. 325
D.3 Electron charge identification scale factors. 327
D.4 Electron charge misidentification probabilities. 328
D.5 Invariant electron pair mass in opposite and same-charge events. 329
D.6 Residual energy scale correction factor $1 + \alpha$ and constant term c for the electron transverse momentum correction. 330
D.7 Distribution of the invariant mass of the two leading leptons in the $e^{\pm}e^{\pm}$ channel in the inclusive same-charge region. 331
D.8 Examples of Feynman diagrams of $W^{\pm}$+jets and $t\bar{t}$ production representing the major contributions to the background due to non-prompt leptons in the signal region. 331
D.9 Distribution of the tagging jet invariant mass m_{jj} in the signal region without VBS selection requirements and requiring two leptons one of which selected as `analysis` and `anti-analysis` object. 332
D.10 Distribution of the (corrected) transverse momentum of `analysis` and `anti-analysis` electrons and muons in the dijet region. 336
D.11 Fake factor as a function of lepton transverse momentum for central barrel and end-cap electrons, and muons. 337
D.12 Examples of Feynman diagrams of $V\gamma$+jets production. 340

D.13 Distribution of the invariant mass of the dilepton and dilepton+photon system in the $Z\gamma$ region. . . . 342
D.14 Kinematic distributions in the "same-charge inclusive" validation region. . . . 345
D.15 Kinematic distributions in the "same-charge low-$N(j)$ " validation region. . . 346
D.16 Subleading lepton kinematic distributions in the "same-charge top non-prompt" validation region. . . . 346
D.17 Jet kinematic distributions in the "same-charge top non-prompt" validation region. . . . 347
D.18 Kinematic distributions in the "same-charge top EW" validation region. . . . 348
D.19 Kinematic distributions in the "same-charge low-ΔY_{jj}" validation region. . . 349

E.1 Distribution of m_{jj} in the signal region and low-m_{jj} control region for the nominal estimates and 7-point renormalisation and factorisation scale variations of the $W^{\pm}W^{\pm}jj$-EW6, $W^{\pm}W^{\pm}jj$-EW4, $W^{\pm}Z$-EW4, $W^{\pm}Z$-EW6 processes. . 358
E.2 Impact of the merging scale and internal parton shower variations on the Sherpa23jLO setup for the $W^{\pm}W^{\pm}jj$-EW6 and $W^{\pm}W^{\pm}jj$-EW4 processes in the fiducial region without m_{jj} requirement. . . . 359
E.3 Distribution of the invariant mass of the tagging jet system m_{jj} in the signal region and low-m_{jj} control region for the $W^{\pm}Z$-EW4 process estimated from POWHEG interfaced to PYTHIA 8 and HERWIG++ in the combined $\ell^{\pm}\ell^{\pm}$ channel. . . . 359
E.4 Pulls of the nuisance parameters for the unconditional, and the background-only fit to Asimov data. . . . 360
E.5 Impact of the nuisance parameters on the measured signal strength $\hat{\mu}$ before and after the fit to Asimov data. . . . 361
E.6 Distribution of the invariant mass of the tagging jets, m_{jj}, in the $e^{\pm}e^{\pm}$ channels in the signal region before and after the fit to observed data. . . . 364

F.1 Invariant mass of the $W^{\pm}W^{\pm}$ system at matrix-element level for different values of the f_{S1}/Λ^4 and f_{M0}/Λ^4 parameters compared to the SM prediction in the loose region. . . . 369
F.2 Invariant mass of the $W^{\pm}W^{\pm}$ system at matrix-element level for different values of the f_{SM1}/Λ^4, f_{M7}/Λ^4, f_{T1}/Λ^4, and f_{T2}/Λ^4 parameters compared to the SM prediction in a loose region. . . . 370
F.3 Distributions of the invariant mass of the leading lepton pair and the $W^{\pm}W^{\pm}$ system for the nominal values of the two-dimensional inter-family M parameter pairs in the fiducial region showing the decomposed EFT contributions and their sum, compared to an independent full prediction of the SM with the EFT extension. . . . 371
F.4 Distributions of the invariant mass of the leading lepton pair and the $W^{\pm}W^{\pm}$ system for the nominal values of the two-dimensional inter-family S and T parameter pairs in the fiducial region showing the decomposed EFT contributions and their sum, compared to an independent full prediction of the SM with the EFT extension. . . . 372
F.5 Distributions of the invariant mass of the leading lepton pair and the $W^{\pm}W^{\pm}$ system for the nominal values of the two-dimensional inter-family T parameter pairs in the fiducial region showing the decomposed EFT contributions and their sum, compared to an independent full prediction of the SM with the EFT extension. . . . 373
F.6 Distributions of the invariant mass of the leading lepton pair and the $W^{\pm}W^{\pm}$ system for the f_{T1}/Λ^4 parameter in the loose region showing the `LIN` and `QUAD` EFT contributions from the amplitude decomposition approach compared to retrieving them from independent `FULL` samples of the SM with the EFT extension. . . . 374

G.1 Distributions of the invariant mass of the $W^{\pm}W^{\pm}$ system at matrix element level for the EFT prediction without the SM contribution at various clipping energies E_{clip} in the fiducial region. 385
G.2 Distributions of the invariant mass of the leading lepton pair, m_{ll}, for the SUM prediction at various clipping energies E_{clip} in the signal region at reconstruction level for the parameters f_{S1}/Λ^4, f_{M0}/Λ^4, f_{M1}/Λ^4, f_{M7}/Λ^4, f_{T0}/Λ^4 and f_{T1}/Λ^4. 386

List of Tables

2.1 SM fermions and their quantum numbers. 8
2.2 SM bosons and their quantum numbers 9
2.3 Masses of the SM fermions. 9
2.4 Masses of the SM bosons. 10
2.5 Additional input parameters of the SM 11
2.6 Dimension-eight operators in the Éboli and Gonzalez–Garcia model. 21

3.1 Summary of LHC *pp*-Runs and design parameters. 26
3.2 Relative energy resolution of the ATLAS calorimeters. 33
3.3 Luminosity and pileup conditions summary of 2015 and 2016 36

5.1 Comparison of the predicted cross-section for fully leptonic final states of the $VVjj$-EW6 and the $VVjj$-EW4 processes. 63
5.2 Overview of measurements involving VBS at the LHC. 70
5.3 Overview of selection requirements in recent analyses of the $VVjj$-EW6 process at the LHC. 72

6.1 Summary of possible orders of the strong and electroweak couplings, α_S and α_{EW}, respectively, at LO and NLO, the type of the contributing corrections, the quantitative fixed-order NLO corrections, and availability of parton shower matched predictions. 75
6.2 Review of the event generation specifics of the $W^{\pm}W^{\pm}jj$ process in Run 1 and Run 2 of the LHC. 78
6.3 Summary of event generation details for the modelling of the $W^{\pm}W^{\pm}jj$-EW6 process. 80
6.4 Summary of event generation details for the modelling of the $W^{\pm}W^{\pm}jj$-EW4 process. 81
6.5 Summary of event generation details for the modelling of the $W^{\pm}W^{\pm}jj$ process. 82
6.6 Generator level phase space for the Sherpa event generation of all $W^{\pm}W^{\pm}jj$ processes 84
6.7 Generator level phase space for the MG5_aMC LO event generation of all $W^{\pm}W^{\pm}jj$ processes 84
6.8 Definition of the nominal fiducial phase space 86
6.9 Comparison of fiducial phase space definitions of Ref. [14], [141] and [1]. . . . 88
6.10 Summary of cross-sections for the three decomposed orders at LO, their sum and an inclusive production of the $W^{\pm}W^{\pm}jj$ process. 92
6.11 Predictions on the fiducial cross-section of the $W^{\pm}W^{\pm}jj$-EW6 process for the PB+Py8, Sherpa23jLO, and MG5+Py8drec MC event generation setups. . . 97
6.12 Predictions on the fiducial cross-section of the $W^{\pm}W^{\pm}jj$-EW4 process for the PB+Py8, Sherpa23jLO, and MG5+Py8drec MC event generation setups. . . 101
6.13 Predictions of the fiducial cross-section of the $W^{\pm}W^{\pm}jj$-EW6 process for different nominal settings of renormalisation and factorisation scales in the PB+Py8, Sherpa23jLO, MG5+Py8drec, and SherpaLO MC event generation setups. 104

6.14 Predictions on the fiducial cross-section of the $W^{\pm}W^{\pm}jj$-EW6 process for different parton shower setups for the PowhegBox and MG5_aMC event generators. . . . 110
6.15 Predictions of the cross-section of the $W^{\pm}W^{\pm}jj$-EW6 process in the fiducial phase space defined in Ref. [14]. . . . 114
6.16 Predictions of the cross-section of the process $pp \to \mu^{+}\nu_{\mu}e^{+}\nu_{e}jj$ in the fiducial phase space defined in Ref. [141]. . . . 115
6.17 Fiducial cross-section prediction of the $W^{\pm}W^{\pm}jj$-EW6 process for the nominal setup Sherpa23jLO and without QED FSR radiation. . . . 117
6.18 Predictions on the fiducial cross-section of the $W^{\pm}W^{\pm}jj$-EW6 process for the PB+Py8, Sherpa23jLO, and MG5+Py8drec MC event generation setups rescaled to NLO EW accuracy. . . . 118
6.19 Summary of MC event generation setups capable of the generation of the $W^{\pm}W^{\pm}jj$ process. . . . 120

7.1 Summary of electron selection criteria. . . . 126
7.2 Summary of muon selection criteria. . . . 126
7.3 Summary of jet selection criteria. . . . 126
7.4 Definition of the signal region of the analyses. . . . 129
7.5 Estimated event yields and statistical uncertainties of all relevant background processes in the combined $\ell^{\pm}\ell^{\pm}$ channel in the signal region before the statistical analyses. . . . 131
7.6 Summary of experimental object and event uncertainties used in the analyses. 133
7.7 Relative impact of experimental systematic uncertainties on the event yields of all predictions based on MC simulation in the signal region. . . . 134
7.8 Summary of experimental uncertainties from background estimation procedures used in the analyses. . . . 135
7.9 Estimated event yields and uncertainties of the background due to electron charge misidentification in all relevant channels in the signal region. . . . 136
7.10 Estimated event yields and uncertainties of the background due to non-prompt leptons in all channels in the signal region. . . . 137
7.11 Summary of modelling uncertainties used in the analyses. . . . 138
7.12 Relative impact of modelling uncertainties on the event yields of the $W^{\pm}Z$, $W^{\pm}W^{\pm}jj$-EW4, and $W^{\pm}W^{\pm}jj$-EW6 predictions based on MC simulation in the signal region. . . . 143
7.13 Normalisation uncertainties on MC estimated cross-section predictions for minor backgrounds. . . . 144
7.14 Estimated event yields and total uncertainties of the $W^{\pm}W^{\pm}jj$-EW6 signal and all background processes, as well as experimental data in all channels in the signal region before the statistical analyses. . . . 145

8.1 Summary of existing results on the cross-section measurement of the $W^{\pm}W^{\pm}jj$ process at 13 TeV at the LHC. . . . 148
8.2 Details on all regions entering the fitting procedure for the SM analysis. . . . 151
8.3 Definition of the $W^{\pm}Z$ control region. . . . 157
8.4 Estimated event yields and total uncertainties of the $W^{\pm}W^{\pm}jj$-EW6 signal and all background processes, as well as experimental data in the $W^{\pm}Z$ control region before the statistical analysis. . . . 158
8.5 Relative impact of experimental systematic uncertainties on the event yields of all predictions based on MC simulation in the $W^{\pm}Z$ control region. . . . 158
8.6 Relative impact of modelling uncertainties on the $W^{\pm}Z$ and $W^{\pm}W^{\pm}jj$-EW6 event yields in the $W^{\pm}Z$ control region. . . . 158
8.7 Estimated event yields and total uncertainties of the $W^{\pm}W^{\pm}jj$-EW6 signal and all background processes, as well as experimental data in all channels in the low-m_{jj} control region before the statistical analysis. . . . 161
8.8 List of nuisance parameters included for each process in the signal region and low-m_{jj} ($W^{\pm}Z$) control region. . . . 162

8.9 Estimated event yields and their total uncertainties of all SM processes and event yields of experimental data in all channels in the signal region after the statistical analysis. . . . 171
8.10 Estimated event yields and their total uncertainties of all SM processes and event yields of experimental data in all channels in the low-m_{jj} control region after the statistical analysis. . . . 172
8.11 Estimated event yields and total uncertainties of all SM processes and event yields of experimental data in the $W^{\pm}Z$ control region after the statistical analysis. . . . 173
8.12 Symmetrised impact of uncertainties on the measured fiducial cross-section split into categories. . . . 179

9.1 Overview of VBS and triple boson measurements that include exclusion limits on aQGC or dimension-eight EFT parameters with the ATLAS and CMS experiments at centre-of-mass energies of 8 and 13 TeV in final states involving leptons, jets and/or photons. . . . 185
9.2 One-dimensional expected and observed 95% C.L. for the aQGC parameters α_4 and α_5 with K-matrix unitarisation obtained in Ref. [86] and conversion into the dimension-eight EFT parameters of Ref. [2, 3]. . . . 194
9.3 Nominal values of all relevant parameters as used for the amplitude decomposition method and the subsequent scaling of the individual contributions. . . . 199
9.4 Generator cross-section predictions for the decomposed `LIN` and `QUAD` contributions, as well as their sum with the SM prediction and the `FULL` prediction of an individual sample for all relevant parameters at their nominal values. . . . 206
9.5 Generator cross-section predictions for the decomposed `CROSS` contributions, as well as the two-dimensional sum of all relevant contributions with the SM prediction and the `FULL` prediction of an individual sample for all relevant parameters at their nominal values. . . . 207
9.6 Fiducial cross-section predictions for the decomposed `LIN` and `QUAD` contributions, as well as their sum with the SM prediction and the `FULL` prediction of an individual sample for all relevant parameters at their nominal values. . . . 208
9.7 Fiducial cross-section predictions for the decomposed `CROSS` contributions, as well as the two-dimensional sum of all relevant contributions with the SM prediction and the `FULL` prediction of an individual sample for all relevant parameters at their nominal values. . . . 208
9.8 Generator and fiducial cross-section predictions for the SM, the decomposed `LIN` and `QUAD` contributions, as well as their sum and the `FULL` prediction of an individual sample for the f_{T0}/Λ^4 parameter in a restricted generator phase space with a minimum requirement on m_{ll} of 500 GeV. . . . 216
9.9 Generator and fiducial cross-section predictions for the decomposed `LIN` and `QUAD` contributions for the f_{S1}/Λ^4 parameter and the scaling factor between the cross-section prediction of the nominal parameter value and each tested point. . . . 218
9.10 Relative impact of experimental systematic uncertainties on the event yields of the `QUAD` contribution of all EFT signal predictions in the combined $\ell^{\pm}\ell^{\pm}$ channel in the signal region. . . . 227
9.11 Relative impact of modelling uncertainties on the event yields of the `QUAD` contribution of all EFT signal predictions in the combined $\ell^{\pm}\ell^{\pm}$ channel in the signal region. . . . 228
9.12 Definition of various sets for the study of the impact of the systematic uncertainties on the expected exclusion bounds. . . . 229
9.13 Expected and observed one-dimensional exclusion intervals at the 95% C.L. for all EFT parameters of the considered model relevant in the $W^{\pm}W^{\pm}jj$-EW6 process with the nominal set of systematic uncertainties. . . . 235

9.14 Expected and observed one-dimensional exclusion intervals at the 95% C.L. for all EFT parameters of the considered model relevant in the $W^{\pm}W^{\pm}jj$-EW6 process applying an energy cutoff of 1.5 TeV with the nominal set of systematic uncertainties. . . . 248
9.15 Best limit values of the aTGC parameters Δg_1^Z, $\Delta\kappa_Z$, and λ_Z and effect on the MC predicted event yields of the $W^{\pm}Z$ process in two regions. . . . 249
9.16 Three dimensional effect of the aTGC parameters Δg_1^Z, $\Delta\kappa_Z$, and λ_Z on the MC predicted event yields of the $W^{\pm}Z$ process in two regions. . . . 250
9.17 Combined effect of the aTGC parameters Δg_1^Z, $\Delta\kappa_Z$, and λ_Z on the MC predicted event yields of the $W^{\pm}Z$ process compared to the SM prediction in bins of the invariant dilepton mass, m_{ll} in the signal region. . . . 253
9.18 Expected and observed 95% C.L. intervals of all considered dimension-eight EFT parameters when effects of dimension-six EFT operators are included as systematic uncertainties on the event yield of the $W^{\pm}Z$ process. . . . 253
9.19 Summary of parameter values and fiducial cross-sections for which the cross-section in the fiducial phase space of the linear `LIN` contribution becomes equal in size to the quadratic `QUAD` contribution in the $\ell^{\pm}\nu_{\ell}\ell'^{\pm}\nu'_{\ell}jj$ final state. . . . 258

A.1 SM parameters as input for MC generation of the $W^{\pm}W^{\pm}jj$ processes. . . . 265
A.2 Internal shower variation parameters for the PowhegBox + Pythia 8 setup using the AZNLO tune. . . . 281
A.3 Internal LO multi-jet merging and shower variation parameters for the Sherpa setup. . . . 284
A.4 Summary of MC sample information for multi-jet merging and parton shower variations in the Sherpa setup. . . . 284
A.5 Internal shower variation parameters for the MG5_aMC + Pythia 8 setup. 287

B.1 MC samples statistics for all SM $W^{\pm}W^{\pm}jj$ processes and setups. . . . 290
B.2 Generator cross-section, acceptance and fiducial cross-section predictions of the $W^{\pm}W^{\pm}jj$-EW6 process in the nominal fiducial region. . . . 291
B.3 Generator cross-section, acceptance and fiducial cross-section predictions of the $W^{\pm}W^{\pm}jj$-EW4 process in the nominal fiducial region. . . . 292
B.4 Generator cross-section, acceptance and fiducial cross-section predictions of the interference between the $W^{\pm}W^{\pm}jj$-EW6 and $W^{\pm}W^{\pm}jj$-EW4 processes at LO $\mathcal{O}(\alpha_{EW}^5\alpha_S)$, labelled INT, and the inclusive $W^{\pm}W^{\pm}jj$ process at all leading orders in α_{EW} and α_S, labelled INCL, in the nominal fiducial region. 292
B.5 Generator cross-section, acceptance and fiducial cross-section predictions of the $W^{\pm}W^{\pm}jj$-EW6 process in the fiducial regions of Ref. [14] and [141]. . . . 293
B.6 Summary of cross-sections for the three explicit orders at LO, their sum and an inclusive production of the $W^{\pm}W^{\pm}jj$ process in the phase space after the lepton event selection. . . . 295
B.7 Relative scale variation for the $W^{\pm}W^{\pm}jj$-EW6 process in the nominal setups in the fiducial region. . . . 299
B.8 Relative scale variation for the $W^{\pm}W^{\pm}jj$-EW4 process in the nominal setups in the fiducial region. . . . 299
B.9 Relative PDF set variations including α_S variations for the $W^{\pm}W^{\pm}jj$-EW6 process in the nominal setups in the fiducial region. . . . 300
B.10 Relative PDF set variations including α_S variations for the $W^{\pm}W^{\pm}jj$-EW6 process in the nominal setups in the fiducial region. . . . 300
B.11 Relative internal parton shower variation for the processes $W^{\pm}W^{\pm}jj$-EW6 and $W^{\pm}W^{\pm}jj$-EW4 for the PB+Py8 setup in the fiducial region. . . . 301
B.12 Relative internal merging and shower variations for the $W^{\pm}W^{\pm}jj$-EW6 and $W^{\pm}W^{\pm}jj$-EW4 processes for the Sherpa23jLO setup in the fiducial region. . 302
B.13 Relative internal parton shower variations for the processes $W^{\pm}W^{\pm}jj$-EW6 and $W^{\pm}W^{\pm}jj$-EW4 for the MG5+Py8drec setup in the fiducial region. . . . 305

B.14 Relative parton shower ISR/FSR renormalisation scale variations for the processes $W^{\pm}W^{\pm}jj$-EW6 and $W^{\pm}W^{\pm}jj$-EW4 for the MG5+Py8drec setup in the fiducial region. . . . 305
B.15 MC samples statistics for the generation of the $W^{\pm}W^{\pm}jj$-EW6 process with the Sherpa23jLO setup without QED FSR radiation. . . . 311
B.16 Generator cross-section, acceptance and fiducial cross-section predictions of the $W^{\pm}W^{\pm}jj$-EW6 process in the fiducial region for the Sherpa23jLO setup without QED FSR radiation. . . . 311

C.1 Event simulation details for the signal process $W^{\pm}W^{\pm}jj$-EW6 and the QCD-induced background process $W^{\pm}W^{\pm}jj$-EW4. . . . 313
C.2 Event simulation details for the diboson processes used in the analysis. . . . 314
C.3 Event simulation details for the evaluation of the parton shower modelling uncertainties of the $W^{\pm}Z$ process. . . . 314
C.4 Event simulation details for the triboson processes used in the analysis. . . . 315
C.5 Event simulation details for the $V\gamma$ ($V \in \{W^{\pm}, Z\}$) processes used in the analysis. . . . 316
C.6 Event simulation details for processes involving top quark production used in the analysis. . . . 316
C.7 Event simulation details for Z boson production in association with jets in the e^+e^- decay channel used in the analysis. . . . 317
C.8 Event simulation details for Z boson production in association with jets in the $\mu^+\mu^-$, and $\tau^+\tau^-$ decay channels used in the analysis. . . . 318
C.9 Event simulation details for $W^{\pm}$ boson production in association with jets in all leptonic decay channels used in the analysis. . . . 320
C.10 Event simulation details for $W^{\pm}Z$ production with aTGC in all leptonic decay channels used in the EFT analysis. . . . 321

D.1 Unprescaled single-lepton trigger strings for experimental and MC simulated data used in the analysis. . . . 324
D.2 Summary of `anti-analysis` electron selection criteria for the non-prompt background estimate. . . . 333
D.3 Summary of `anti-analysis` muon selection criteria for the non-prompt background estimate. . . . 334
D.4 Definition of the dijet region used for the fake factor measurement. . . . 335
D.5 Numerical values and statistical uncertainties of the fake factor for central barrel electrons in bins of electron p_{T} for the nominal method and each individual systematic variation. . . . 338
D.6 Numerical values and statistical uncertainties of the fake factor for central end-cap electrons in bins of electron p_{T} for the nominal method and each individual systematic variation. . . . 338
D.7 Numerical values and statistical uncertainties of the fake factor for muons in bins of muon p_{T} for the nominal method and each individual systematic variation. . . . 339
D.8 Event yield in the $Z\gamma$ region. . . . 341
D.9 Definition with respect to the signal region of all validation regions selecting two same-charge leptons. . . . 342
D.10 Definition with respect to the signal region of the trilepton validation region. 343
D.11 Event yields and their statistical uncertainties in all validation regions. . . . 344
D.12 Details on the experimental object and event uncertainties employed in the analyses. . . . 351
D.13 Relative impact of experimental systematic uncertainties on the event yields of all predictions based on MC simulation in the signal region in all relevant channels. . . . 352
D.14 Relative scale variation for the $W^{\pm}Z$, $W^{\pm}W^{\pm}jj$-EW4, and $W^{\pm}W^{\pm}jj$-EW6 processes in the signal region. . . . 353

D.15 Relative variations of the PDF set and its α_S value for the processes $W^{\pm}Z$, $W^{\pm}W^{\pm}jj$-EW4, and $W^{\pm}W^{\pm}jj$-EW6 in the signal region. 353

E.1 Estimated event yields and total uncertainties of the processes of the other prompt background category in the $W^{\pm}Z$ control region before the statistical analysis. 355
E.2 Relative impact of experimental systematic uncertainties on the event yields of all predictions based on MC simulation in the $W^{\pm}Z$ control region. 355
E.3 Relative scale variation for the $W^{\pm}Z$-EW4, $W^{\pm}Z$-EW6, the combined $W^{\pm}Z$, and $W^{\pm}W^{\pm}jj$-EW6 processes in the $W^{\pm}Z$ control region. 356
E.4 Relative PDF set variations including α_S variations for the $W^{\pm}Z$-EW4, $W^{\pm}Z$-EW6, the combined $W^{\pm}Z$, and $W^{\pm}W^{\pm}jj$-EW6 processes in the $W^{\pm}Z$ control region. 356
E.5 Estimated event yields and total uncertainties of the processes of the other prompt background category in the low-m_{jj} control region before the statistical analysis. 357
E.6 Estimated event yields and their total uncertainties of all SM processes in the $W^{\pm}Z$ control region after the statistical analysis of the Asimov dataset. . . . 361
E.7 Event yields and their total uncertainties of all SM processes in all channels in the signal region after the statistical analysis of the Asimov dataset. 362
E.8 Estimated event yields and their total uncertainties of all SM processes in all channels in the low-m_{jj} control region after the statistical analysis of the Asimov dataset. 363

F.1 Generator cross-section, acceptance and fiducial cross-section predictions of the EFT contribution $W^{\pm}W^{\pm}jj$-EW6 process in the nominal fiducial region. 375

G.1 Expected and observed one-dimensional exclusion intervals at the 95% C.L. for all EFT parameters of the considered model relevant in the $W^{\pm}W^{\pm}jj$-EW6 process without considering systematic uncertainties. 377
G.2 Estimated event yields and statistical uncertainties of all background processes, as well as experimental data differentially in bins of the invariant dilepton mass, m_{ll}, in the signal region. 378
G.3 Estimated event yields and statistical uncertainties of the linear and quadratic EFT signal contributions of all relevant operators at their nominal parameter values in bins of the invariant dilepton mass, m_{ll}, in the signal region. 379
G.4 Relative impact of experimental systematic uncertainties on the event yields of all background predictions based on MC simulation in bins of m_{ll} in the signal region. 380
G.5 Relative impact of experimental systematic uncertainties on the event yields of all EFT signal predictions based on MC simulation in bins of m_{ll} in the signal region. 381
G.6 Relative impact of experimental systematic uncertainties on the event yields of all EFT signal predictions based on MC simulation in bins of m_{ll} in the signal region. 382
G.7 Summary of experimental uncertainties from the data-driven estimation of the backgrounds due to electron charge misidentification and non-prompt leptons in bins of m_{ll} in the signal region. 383
G.8 Relative impact of modelling uncertainties on the event yields of the $W^{\pm}Z$, $W^{\pm}W^{\pm}jj$-EW4, and $W^{\pm}W^{\pm}jj$-EW6 background predictions based on MC simulation in bins of m_{ll} in the signal region. 383
G.9 Relative impact of modelling uncertainties on the event yields of the EFT signal predictions in bins of m_{ll} in the signal region. 384
G.10 Effect of the aTGC parameters Δg_1^Z, $\Delta\kappa_Z$, and λ_Z on the MC predicted event yields of the $W^{\pm}Z$ process compared to the SM prediction in bins of the invariant dilepton mass, m_{ll} in the signal region. 385

Bibliography

[1] ATLAS Collaboration, *Observation of Electroweak Production of a Same-Sign W Boson Pair in Association with Two Jets in pp Collisions at $\sqrt{s} = 13$ TeV with the ATLAS Detector*, Phys. Rev. Lett. **123** (2019) 161801, arXiv: 1906.03203 [hep-ex] (cit. on pp. v, vii, 1, 70, 72–74, 76, 78–81, 85–88, 95, 118, 120, 123, 124, 129, 141, 147, 148, 157, 174, 178–180, 203, 223, 346, 364, 375).

[2] O. J. P. Eboli, M. C. Gonzalez-Garcia, and J. K. Mizukoshi, *$p\ p \to j\ j\ e^{\pm}\ mu^{\pm}\ nu\ nu$ and $j\ j\ e^{\pm}\ mu^{\mp}\ nu\ nu$ at $O(\alpha(em)^6)$ and $O(\alpha(em)^4\ \alpha(s)^2)$ for the study of the quartic electroweak gauge boson vertex at CERN LHC*, Phys. Rev. D **74** (2006) 073005, arXiv: hep-ph/0606118 (cit. on pp. v, vii, 2, 20, 21, 124, 183, 184, 186, 194, 198, 222, 232, 235, 248, 261, 377).

[3] O. J. P. Éboli and M. C. Gonzalez–Garcia, *Classifying the bosonic quartic couplings*, Phys. Rev. **D93** (2016) 093013, arXiv: 1604.03555 [hep-ph] (cit. on pp. v, vii, 2, 20–22, 124, 183, 184, 186, 194, 198, 222, 232, 235, 248, 261, 377).

[4] Eduardo da Silva Almeida, O. J. P. Éboli, and M. C. Gonzalez–Garcia, *Unitarity constraints on anomalous quartic couplings*, Phys. Rev. D **101** (11 2020) 113003, URL: https://link.aps.org/doi/10.1103/PhysRevD.101.113003 (cit. on pp. v, vii, 22, 192, 246, 247).

[5] Sheldon L. Glashow, *Partial-Symmetries of Weak Interactions*, Nuclear Physics **22** (1961) 579 (cit. on pp. 1, 4).

[6] C. N. Yang and R. L. Mills, *Conservation of Isotopic Spin and Isotopic Gauge Invariance*, Phys. Rev. **96** (1 1954) 191 (cit. on pp. 1, 4).

[7] *Precision electroweak measurements on the Z resonance*, Phys.Rept. **427** (2006) 257, arXiv: hep-ex/0509008 [hep-ex] (cit. on p. 1).

[8] Georges Aad et al., *Observation of a new particle in the search for the Standard Model Higgs boson with the ATLAS detector at the LHC*, Phys.Lett. **B716** (2012) 1, arXiv: 1207.7214 [hep-ex] (cit. on pp. 1, 10).

[9] Serguei Chatrchyan et al., *Observation of a new boson at a mass of 125 GeV with the CMS experiment at the LHC*, Phys.Lett. **B716** (2012) 30, arXiv: 1207.7235 [hep-ex] (cit. on pp. 1, 10).

[10] Utpal Sarkar, *Particle and Astroparticle Physics*, CRC Press. pp. 429, 2007 (cit. on p. 1).

[11] M. C. Brak, "The Hierarchy Problem in the Standard Model and Little Higgs Theories", MA thesis: NIKHEF, 2004 (cit. on pp. 1, 12).

[12] Gianfranco Bertone, Dan Hooper, and Joseph Silk, *Particle Dark Matter: Evidence, Candidates and Constraints*, Physics Reports **405** (2005) 279 (cit. on p. 1).

[13] ATLAS Collaboration, *Evidence for Electroweak Production of $W^{\pm}W^{\pm}jj$ in pp Collisions at $\sqrt{s} = 8$ TeV with the ATLAS Detector*, Phys. Rev. Lett. **113** (2014) 141803, arXiv: 1405.6241 [hep-ex] (cit. on pp. 1, 23, 27, 69, 73, 76, 78, 120, 144, 147, 184, 186, 196).

[14] CMS Collaboration, *Observation of Electroweak Production of Same-Sign W Boson Pairs in the Two Jet and Two Same-Sign Lepton Final State in Proton–Proton Collisions at* 13 *TeV*, Phys. Rev. Lett. **120** (2018) 081801, arXiv: 1709.05822 [hep-ex] (cit. on pp. 1, 69, 70, 72–74, 76, 78, 87, 88, 93, 95, 103, 112–114, 147–149, 178, 181, 183, 199, 239, 289, 293).

[15] ATLAS Collaboration, *Observation of electroweak $W^{\pm}Z$ boson pair production in association with two jets in pp collisions at $\sqrt{s} = 13$ TeV with the ATLAS detector*, Phys. Lett. B **793** (2019) 469, arXiv: 1812.09740 [hep-ex] (cit. on pp. 1, 69, 70, 72, 150, 154, 156, 170).

[16] ATLAS Collaboration, *Observation of electroweak production of two jets and a Z-boson pair with the ATLAS detector at the LHC*, (2020), arXiv: 2004.10612 [hep-ex] (cit. on pp. 1, 70, 72).

[17] CMS Collaboration, *Observation of electroweak production of W with two jets in proton-proton collisions at s=13 TeV*, Physics Letters B **811** (2020) 135988, ISSN: 0370-2693, URL: http://dx.doi.org/10.1016/j.physletb.2020.135988 (cit. on pp. 1, 69, 70, 72).

[18] CMS Collaboration, *Measurement of the electroweak production of $Z\gamma$ and two jets in proton-proton collisions at $\sqrt{s} = 13$ TeV and constraints on dimension 8 operators*, (2021) (cit. on pp. 1, 69, 70, 72, 185, 186, 197, 199, 222, 262).

[19] Benedikt Biedermann, Ansgar Denner, and Mathieu Pellen, *Complete NLO corrections to W^+W^+ scattering and its irreducible background at the LHC*, JHEP **10** (2017) 124, arXiv: 1708.00268 [hep-ph] (cit. on pp. 1, 62, 64–68, 74, 75, 98, 101, 114–118, 180).

[20] G. Kane, *Modern elementary particle physics: explaining and extending the standard model; 2nd ed.* Cambridge University Press, 2017, ISBN: 978-1-107-16508-3, URL: https://cds.cern.ch/record/2244793 (cit. on p. 3).

[21] Michael E. Peskin and Dan V. Schroeder, *An Introduction To Quantum Field Theory*, Westview Press, 1995 (cit. on pp. 3, 11).

[22] David Griffiths, *Introduction to elementary particles*, John Wiley & Sons, 2008 (cit. on pp. 3, 11).

[23] Francis Halzen and Martin Alan, *Quarks and Leptons: An Introductory Course in Modern Particle Physics*, John Wiley and Sons, 1984 (cit. on p. 3).

[24] Antonio Pich, "Effective field theory: Course", *Les Houches Summer School in Theoretical Physics, Session 68: Probing the Standard Model of Particle Interactions*, 1998 949, arXiv: hep-ph/9806303 (cit. on p. 3).

[25] D. B. Kaplan, *Lectures on effective field theory*, 2016, URL: https://www.ictp-saifr.org/wp-content/uploads/2015/05/Kaplan1.pdf (visited on 01/27/2021) (cit. on pp. 3, 19).

[26] Emmy Noether, *Invariant variation problems*, Transport Theory and Statistical Physics **1** (1971) 186 (cit. on p. 4).

[27] E. Fermi, *Versuch einer Theorie der β-Strahlen. I*, Zeitschrift fur Physik **88** (1934) 161 (cit. on pp. 4, 7).

[28] A. Salam, *Elementary Particle Theory*, Almqvist and Wiksell, 1968 (cit. on p. 4).

[29] Steven Weinberg, *A Model of Leptons*, Phys. Rev. Lett. **19** (1967) 1264 (cit. on p. 4).

[30] F.J. Hasert et al., *Observation of Neutrino Like Interactions Without Muon Or Electron in the Gargamelle Neutrino Experiment*, Phys.Lett. **B46** (1973) 138 (cit. on p. 5).

[31] *Experimental observation of isolated large transverse energy electrons with associated missing energy at $\sqrt{s} = 540$ GeV*, Physics Letters B **122** (1983) 103, ISSN: 0370-2693 (cit. on p. 5).

[32] *Experimental observation of lepton pairs of invariant mass around* $95\,\mathrm{Gev/c^2}$ *at the CERN SPS collider*, Physics Letters B **126** (1983) 398, ISSN: 0370-2693 (cit. on p. 5).

[33] *Observation of single isolated electrons of high transverse momentum in events with missing transverse energy at the CERN pp collider*, Physics Letters B **122** (1983) 476, ISSN: 0370-2693 (cit. on p. 5).

[34] *Evidence for* $Z^0 \to e^+e$ *at the CERN pp collider*, Physics Letters B **129** (1983) 130, ISSN: 0370-2693 (cit. on p. 5).

[35] Peter Higgs, *Broken Symmetries and the Masses of Gauge Bosons*, Phys. Rev. Lett. **13** (1964) 508 (cit. on p. 6).

[36] F. Englert and R. Brout, *Broken Symmetry and the Mass of Gauge Vector Mesons*, Phys. Rev. Lett. **13** (9 1964) 321 (cit. on p. 6).

[37] G. S. Guralnik, C. R. Hagen, and T. W. B. Kibble, *Global Conservation Laws and Massless Particles*, Phys. Rev. Lett. **13** (20 1964) 585 (cit. on p. 6).

[38] F. L. Wilson, *Fermi's Theory of Beta Decay*, American Journal of Physics **36** (1968) (cit. on p. 7).

[39] David J. Gross and Frank Wilczek, *Ultraviolet Behavior of Non-Abelian Gauge Theories*, Phys. Rev. Lett. **30** (26 1973) 1343, URL: https://link.aps.org/doi/10.1103/PhysRevLett.30.1343 (cit. on p. 7).

[40] H. David Politzer, *Reliable Perturbative Results for Strong Interactions?*, Phys. Rev. Lett. **30** (1973) 1346 (cit. on p. 7).

[41] Particle Data Group et al., *Review of Particle Physics*, Progress of Theoretical and Experimental Physics **2020** (2020), 083C01, ISSN: 2050-3911, eprint: https://academic.oup.com/ptep/article-pdf/2020/8/083C01/34673722/ptaa104.pdf, URL: https://doi.org/10.1093/ptep/ptaa104 (cit. on pp. 9–11, 44, 49, 331).

[42] F. J. Dyson, *The Radiation Theories of Tomonaga, Schwinger, and Feynman*, Phys. Rev. **75** (3 1949) 486, URL: https://link.aps.org/doi/10.1103/PhysRev.75.486 (cit. on p. 11).

[43] *Standard Model Summary Plots Summer 2019*, tech. rep., CERN, 2019, URL: https://cds.cern.ch/record/2682186 (cit. on pp. 12, 69).

[44] G Ross, *Grand Unified Theories*, Westview Press, 1984 (cit. on p. 12).

[45] K. Nakamura et al., *Grand Unified Theories*, Journal of Physics G **37** (2010) 075021 (cit. on p. 12).

[46] B. Abi et al., *Measurement of the Positive Muon Anomalous Magnetic Moment to 0.46 ppm*, Phys. Rev. Lett. **126** (14 2021) 141801, URL: https://link.aps.org/doi/10.1103/PhysRevLett.126.141801 (cit. on p. 12).

[47] Ansgar Denner and T. Hahn, *Radiative corrections to W+ W- —> W+ W- in the electroweak standard model*, Nucl. Phys. **B525** (1998) 27, arXiv: hep-ph/9711302 [hep-ph] (cit. on pp. 15–17).

[48] Vernon D. Barger, King-man Cheung, Tao Han, and R.J.N. Phillips, *Strong* W^+W^+ *scattering signals at pp supercolliders*, Phys. Rev. D **42** (1990) 3052 (cit. on pp. 15, 16).

[49] Christian Gumpert, "Measurement of Electroweak Gauge Boson Scattering in the Channel $pp \to W^\pm W^\pm jj$ with the ATLAS Detector at the Large Hadron Collider", Presented 27 Feb 2015, 2014, URL: https://cds.cern.ch/record/2003240 (cit. on pp. 15, 63, 76).

[50] C. Bittrich, "Study of Polarization Fractions in the Scattering of Massive Gauge Bosons $W^\pm Z \to W^\pm Z$ with the ATLAS Detector at the Large Hadron Collider", Presented 2015, 2015, URL: https://cds.cern.ch/record/2014124 (cit. on pp. 15, 17).

[51] Ian J.R. Aitchison, *Supersymmetry and the MSSM: An Elementary introduction*, (2005), arXiv: hep-ph/0505105 [hep-ph] (cit. on p. 18).

[52] Roberto Contino, "The Higgs as a Composite Nambu-Goldstone Boson", *Theoretical Advanced Study Institute in Elementary Particle Physics: Physics of the Large and the Small*, 2011 235, arXiv: 1005.4269 [hep-ph] (cit. on p. 18).

[53] Giuliano Panico and Andrea Wulzer, *The Composite Nambu-Goldstone Higgs*, vol. 913, Springer, 2016, arXiv: 1506.01961 [hep-ph] (cit. on p. 18).

[54] Duccio Pappadopulo, Andrea Thamm, Riccardo Torre, and Andrea Wulzer, *Heavy Vector Triplets: Bridging Theory and Data*, JHEP **09** (2014) 060, arXiv: 1402.4431 [hep-ph] (cit. on p. 18).

[55] G. F. Giudice, C. Grojean, A. Pomarol, and R. Rattazzi, *The Strongly-Interacting Light Higgs*, JHEP **06** (2007) 045, arXiv: hep-ph/0703164 (cit. on p. 18).

[56] Domenec Espriu and Federico Mescia, *Unitarity and causality constraints in composite Higgs models*, Phys. Rev. D **90** (2014) 015035, arXiv: 1403.7386 [hep-ph] (cit. on p. 18).

[57] Wolfgang Kilian, *Electroweak Symmetry Breaking: The Bottom-Up Approach*, Springer, 2003 (cit. on pp. 18, 19).

[58] Raquel Gomez-Ambrosio, "Studies of Gauge Couplings at LHC: the Effective Field Theory Approach", PhD thesis, 2017 (cit. on pp. 19, 20).

[59] Céline Degrande et al., *Effective field theory: A modern approach to anomalous couplings*, Annals of Physics **335** (2013) 21, ISSN: 0003-4916, URL: http://dx.doi.org/10.1016/j.aop.2013.04.016 (cit. on p. 20).

[60] J. Beringer et al., *Review of Particle Physics*, Phys. Rev. D **86** (1 2012) 010001, URL: https://link.aps.org/doi/10.1103/PhysRevD.86.010001 (cit. on pp. 20, 191).

[61] J. Abdallah et al., *Measurement of the e+ e- —> W+ W- gamma cross-section and limits on anomalous quartic gauge couplings with DELPHI*, Eur. Phys. J. C **31** (2003) 139, arXiv: hep-ex/0311004 (cit. on pp. 20, 191).

[62] P. Achard et al., *Study of the $W^+W^-\gamma$ process and limits on anomalous quartic gauge boson couplings at LEP*, Phys. Lett. B **527** (2002) 29, arXiv: hep-ex/0111029 (cit. on pp. 20, 191).

[63] G. Abbiendi et al., *Measurement of the $W^+W^-\gamma$ cross-section and first direct limits on anomalous electroweak quartic gauge couplings*, Phys. Lett. B **471** (1999) 293, arXiv: hep-ex/9910069 (cit. on pp. 20, 191).

[64] Victor Mukhamedovich Abazov et al., *Search for anomalous quartic $WW\gamma\gamma$ couplings in dielectron and missing energy final states in $p\bar{p}$ collisions at $\sqrt{s} = 1.96$ TeV*, Phys. Rev. D **88** (2013) 012005, arXiv: 1305.1258 [hep-ex] (cit. on pp. 20, 191).

[65] G. Abbiendi et al., *Constraints on anomalous quartic gauge boson couplings from nu anti-nu gamma gamma and q anti-q gamma gamma events at LEP-2*, Phys. Rev. D **70** (2004) 032005, arXiv: hep-ex/0402021 (cit. on pp. 20, 191).

[66] ATLAS Collaboration, *$ZZ \to \ell^+\ell^-\ell'^+\ell'^-$ cross-section measurements and search for anomalous triple gauge couplings in 13 TeV pp collisions with the ATLAS detector*, Phys. Rev. D **97** (2018) 032005, arXiv: 1709.07703 [hep-ex] (cit. on p. 20).

[67] ATLAS Collaboration, *Measurement of ZZ production in the $\ell\ell\nu\nu$ final state with the ATLAS detector in pp collisions at $\sqrt{s} = 13$ TeV*, JHEP **10** (2019) 127, arXiv: 1905.07163 [hep-ex] (cit. on p. 20).

[68] ATLAS Collaboration, *Measurement of the $Z\gamma \to \nu\bar{\nu}\gamma$ production cross section in pp collisions at $\sqrt{s} = 13$ TeV with the ATLAS detector and limits on anomalous triple gauge-boson couplings*, JHEP **12** (2018) 010, arXiv: 1810.04995 [hep-ex] (cit. on p. 20).

[69] C. Arzt, M. B. Einhorn, and J. Wudka, *Patterns of deviation from the standard model*, Nucl. Phys. B **433** (1995) 41, arXiv: hep-ph/9405214 (cit. on p. 21).

[70] M.C. Gonzalez–Garcia O.J.P. Éboli, *Anomalous quartic interaction among electroweak gauge bosons*, 2012, URL: http://feynrules.irmp.ucl.ac.be/wiki/AnomalousGaugeCoupling#no1 (visited on 01/26/2021) (cit. on pp. 21, 195, 198).

[71] Marco Sekulla, "Anomale Kopplungen, Resonanzen und Unitarität in Vektorboson-Streuung", PhD thesis: Universität Siegen, 2015, URL: https://dspace.ub.uni-siegen.de/handle/ubsi/979 (cit. on pp. 21, 22).

[72] Adam Alloul, Neil D. Christensen, Céline Degrande, Claude Duhr, and Benjamin Fuks, *FeynRules 2.0 - A complete toolbox for tree-level phenomenology*, Comput. Phys. Commun. **185** (2014) 2250, arXiv: 1310.1921 [hep-ph] (cit. on p. 22).

[73] D. Zeppenfeld and S. Willenbrock, *Probing the three-vector-boson vertex at hadron colliders*, Phys. Rev. D **37** (7 1988) 1775, URL: https://link.aps.org/doi/10.1103/PhysRevD.37.1775 (cit. on p. 22).

[74] U. Baur and D. Zeppenfeld, *Unitarity Constraints on the Electroweak Three Vector Boson Vertices*, Phys. Lett. B **201** (1988) 383 (cit. on p. 22).

[75] Ana Alboteanu, Wolfgang Kilian, and Juergen Reuter, *Resonances and Unitarity in Weak Boson Scattering at the LHC*, JHEP **11** (2008) 10, arXiv: hep-ph/0806.4145 (cit. on pp. 22, 184).

[76] Michael S. Chanowitz, *Quantum corrections from nonresonant W W scattering*, Phys. Rept. **320** (1999) 139, arXiv: hep-ph/9903522 (cit. on pp. 22, 184).

[77] S. U. Chung et al., *Partial wave analysis in K-matrix formalism*, Annalen der Physik **507** (1995) 404, eprint: https://onlinelibrary.wiley.com/doi/pdf/10.1002/andp.19955070504, URL: https://onlinelibrary.wiley.com/doi/abs/10.1002/andp.19955070504 (cit. on pp. 22, 184).

[78] B. E. Lindquist et al., *Recommendations from the Anomalous Gauge Coupling Task-force*, (2017), URL: https://cds.cern.ch/record/2261444 (cit. on pp. 23, 192, 240).

[79] L. Evans and P. Bryant, *LHC Machine*, JINST **3** (2008) S08001, URL: https://cds.cern.ch/record/1129806 (cit. on pp. 25, 26).

[80] ATLAS Collaboration, *The ATLAS Experiment at the CERN Large Hadron Collider*, JINST **3** (2008) S08003 (cit. on pp. 25–29, 31–33).

[81] Esma Mobs, *The CERN accelerator complex - 2019. Complexe des accélérateurs du CERN - 2019*, (2019), General Photo, URL: https://cds.cern.ch/record/2684277 (cit. on pp. 25, 26).

[82] K. Aamodt et al., *The ALICE Experiment at the CERN LHC*, Journal of Instrumentation **3** (2008) S08002 (cit. on p. 26).

[83] CMS Collaboration, *The CMS experiment at the CERN LHC*, JINST **3** (2008) S08004 (cit. on p. 26).

[84] A. Augusto et al., *The LHCb Detector at the LHC*, Journal of Instrumentation **3** (2008) S08005 (cit. on p. 26).

[85] CERN, *High Luminosity LHC Project Schedule*, 2020, URL: https://project-hl-lhc-industry.web.cern.ch/content/project-schedule (visited on 02/05/2021) (cit. on p. 27).

[86] ATLAS Collaboration, *Measurement of $W^{\pm}W^{\pm}$ vector-boson scattering and limits on anomalous quartic gauge couplings with the ATLAS detector*, Phys. Rev. D **96** (2017) 012007, arXiv: 1611.02428 [hep-ex] (cit. on pp. 27, 76, 184–186, 194, 196).

[87] ATLAS Collaboration, "ATLAS Collaboration Maps", General Photo, 2019, URL: https://cds.cern.ch/record/2654110 (cit. on p. 27).

[88] B. Abbott et al., *Production and integration of the ATLAS Insertable B-Layer*, JINST **13** (2018) T05008, arXiv: 1803.00844 [physics.ins-det] (cit. on p. 29).

[89] H. Pernegger, *The Pixel Detector of the ATLAS experiment for LHC Run-2*, Journal of Instrumentation **10** (2015) C06012 (cit. on p. 30).

[90] The ATLAS collaboration, *Operation of the ATLAS trigger system in Run 2*, Journal of Instrumentation **15** (2020) P10004, ISSN: 1748-0221, URL: http://dx.doi.org/10.1088/1748-0221/15/10/P10004 (cit. on p. 35).

[91] ATLAS Collaboration, *Luminosity Public Results Run2*, 2021, URL: https://twiki.cern.ch/twiki/bin/view/AtlasPublic/LuminosityPublicResultsRun2 (visited on 03/22/2021) (cit. on pp. 36–38).

[92] W. Herr and B. Muratori, *Concept of Luminosity*, CERN 2006-002 (2006) (cit. on p. 37).

[93] G. Avoni et al., *The new LUCID-2 detector for luminosity measurement and monitoring in ATLAS*, JINST **13** (2018) P07017 (cit. on p. 37).

[94] *Luminosity determination in pp collisions at $\sqrt{s} = 13$ TeV using the ATLAS detector at the LHC*, tech. rep. ATLAS-CONF-2019-021, CERN, 2019, URL: http://cds.cern.ch/record/2677054 (cit. on p. 38).

[95] James Catmore et. al, *The ATLAS data processing chain: from collisions to papers*, 2018, URL: https://indico.cern.ch/event/757797/contributions/3142011/attachments/1733780/2803340/inductionday_SWC.pdf (visited on 03/24/2021) (cit. on p. 38).

[96] The ATLAS Collaboration, *EventLoop*, 2020, URL: https://twiki.cern.ch/twiki/bin/viewauth/AtlasProtected/EventLoop (cit. on p. 39).

[97] L. Hauswald and F. Socher et al, *Repository for ELCore analysis framework*, 2015, URL: https://gitlab.cern.ch/ELCore/ELCore (visited on 10/03/2019) (cit. on p. 39).

[98] F. Socher, C. Bittrich, F. Iltzsche, T. Herrmann, and S. Todt, *Common Analysis Framework*, 2020, URL: https://gitlab.cern.ch/atlas-germany-dresden-vbs-group/CommonAnalysisFramework (cit. on p. 39).

[99] C Burgard, R Gugel, and K Lehmann et al, *ATLAS Common Analysis Framework*, 2014, URL: https://atlas-caf.web.cern.ch (cit. on p. 39).

[100] R. Brun and F. Rademakers, *ROOT — An object oriented data analysis framework*, Nucl. Instrum. Meth. A **389** (1997) 81, ISSN: 0168-9002 (cit. on p. 39).

[101] ATLAS Collaboration, *Early Inner Detector Tracking Performance in the 2015 Data at $\sqrt{s} = 13$ TeV*, ATL-PHYS-PUB-2015-051, 2015, URL: https://cds.cern.ch/record/2110140 (cit. on p. 39).

[102] ATLAS Collaboration, *Electron reconstruction and identification in the ATLAS experiment using the 2015 and 2016 LHC proton–proton collision data at $\sqrt{s} = 13$ TeV*, Eur. Phys. J. C **79** (2019) 639, arXiv: 1902.04655 [hep-ex] (cit. on pp. 40–42, 55, 130, 326).

[103] ATLAS Collaboration, *Electron and photon energy calibration with the ATLAS detector using 2015–2016 LHC proton–proton collision data*, JINST **14** (2019) P03017, arXiv: 1812.03848 [hep-ex] (cit. on p. 40).

[104] ATLAS Collaboration, *Electron and photon energy calibration with the ATLAS detector using LHC Run 1 data*, Eur. Phys. J. C **74** (2014) 3071, arXiv: 1407.5063 [hep-ex] (cit. on p. 40).

[105] Walter Lampl et al., *Calorimeter Clustering Algorithms: Description and Performance*, ATL-LARG-PUB-2008-002, 2008, URL: https://cds.cern.ch/record/1099735 (cit. on pp. 40, 43).

[106] ATLAS Collaboration, *Improved electron reconstruction in ATLAS using the Gaussian Sum Filter-based model for bremsstrahlung*, ATLAS-CONF-2012-047, 2012, URL: https://cds.cern.ch/record/1449796 (cit. on p. 40).

[107] ATLAS Collaboration, *Muon reconstruction performance of the ATLAS detector in proton–proton collision data at $\sqrt{s} = 13$ TeV*, Eur. Phys. J. C **76** (2016) 292, arXiv: 1603.05598 [hep-ex] (cit. on pp. 41, 42, 55).

[108] ATLAS Collaboration, *Documentation of IsolationSelectionTool*, 2021, URL: https://twiki.cern.ch/twiki/bin/viewauth/AtlasProtected/IsolationSelectionTool (visited on 05/08/2021) (cit. on p. 43).

[109] ATLAS Collaboration, *Jet energy scale measurements and their systematic uncertainties in proton–proton collisions at $\sqrt{s} = 13$ TeV with the ATLAS detector*, Phys. Rev. D **96** (2017) 072002, arXiv: 1703.09665 [hep-ex] (cit. on p. 43).

[110] ATLAS Collaboration, *Jet energy measurement with the ATLAS detector in proton–proton collisions at $\sqrt{s} = 7$ TeV*, Eur. Phys. J. C **73** (2013) 2304, arXiv: 1112.6426 [hep-ex] (cit. on p. 43).

[111] M. Cacciari, G. P. Salam, and G. Soyez, *The anti-k_t jet clustering algorithm*, JHEP **04** (2008) 063, arXiv: 0802.1189 [hep-ph] (cit. on pp. 43, 83, 87).

[112] Matteo Cacciari and Gavin P. Salam, *Dispelling the N^3 myth for the kt jet-finder*, Phys.Lett. **B641** (2006) 57, arXiv: hep-ph/0512210 [hep-ph] (cit. on p. 43).

[113] ATLAS Collaboration, *Performance of pile-up mitigation techniques for jets in pp collisions at $\sqrt{s} = 8$ TeV using the ATLAS detector*, Eur. Phys. J. C **76** (2016) 581, arXiv: 1510.03823 [hep-ex] (cit. on p. 43).

[114] ATLAS Collaboration, *Tagging and suppression of pileup jets with the ATLAS detector*, ATLAS-CONF-2014-018, 2014, URL: https://cds.cern.ch/record/1700870 (cit. on pp. 44, 55).

[115] ATLAS Collaboration, *Optimisation of the ATLAS b-tagging performance for the 2016 LHC Run*, ATL-PHYS-PUB-2016-012, 2016, URL: https://cds.cern.ch/record/2160731 (cit. on p. 44).

[116] ATLAS Collaboration, *Expected performance of the ATLAS b-tagging algorithms in Run-2*, ATL-PHYS-PUB-2015-022, 2015, URL: https://cds.cern.ch/record/2037697 (cit. on p. 44).

[117] ATLAS Collaboration, *E_T^{miss} performance in the ATLAS detector using 2015–2016 LHC pp collisions*, ATLAS-CONF-2018-023, 2018, URL: https://cds.cern.ch/record/2625233 (cit. on p. 45).

[118] ATLAS Collaboration, *Performance of missing transverse momentum reconstruction with the ATLAS detector using proton–proton collisions at $\sqrt{s} = 13$ TeV*, Eur. Phys. J. C **78** (2018) 903, arXiv: 1802.08168 [hep-ex] (cit. on p. 45).

[119] D Adams et al., *Recommendations of the Physics Objects and Analysis Harmonisation Study Groups 2014*, tech. rep. ATL-PHYS-INT-2014-018, CERN, 2014, URL: https://cds.cern.ch/record/1743654 (cit. on pp. 45, 46).

[120] S. Farrell, *Overlap Removal Tools*, 2017, URL: https://indico.cern.ch/event/631313/contributions/2683959/attachments/1518878/2373377/Farrell_ORTools_ftaghbb.pdf (visited on 05/31/2021) (cit. on p. 45).

[121] ATLAS Collaboration, *Overlap removal tools*, 2020, URL: https://gitlab.cern.ch/atlas/athena/blob/master/PhysicsAnalysis/AnalysisCommon/AssociationUtils/README.rst (visited on 05/31/2021) (cit. on p. 46).

[122] Matteo Cacciari, Gavin P Salam, and Gregory Soyez, *The catchment area of jets*, Journal of High Energy Physics **2008** (2008) 005, ISSN: 1029-8479, URL: http://dx.doi.org/10.1088/1126-6708/2008/04/005 (cit. on p. 46).

[123] Andy Buckley, Jonathan Butterworth, et al., *General-purpose event generators for LHC physics*, Phys.Rept. **504** (2011) 145, arXiv: 1101.2599 [hep-ph] (cit. on pp. 47–50).

[124] S. Höche, "Introduction to parton-shower event generators", *Theoretical Advanced Study Institute in Elementary Particle Physics: Journeys Through the Precision Frontier: Amplitudes for Colliders*, 2014, arXiv: 1411.4085 [hep-ph] (cit. on pp. 47, 49).

[125] DESY HERA-Proposal, *HERA 81-10*, 1981 (cit. on p. 48).

[126] None None, *Design Report Tevatron 1 Project (Second Printing November 1982)*, (1982), URL: https://www.osti.gov/biblio/1413194 (cit. on p. 48).

[127] L. A. Harland-Lang, A. D. Martin, P. Motylinski, and R. S. Thorne, *Parton distributions in the LHC era: MMHT 2014 PDFs*, Eur. Phys. J. C **75** (2015) 204, arXiv: 1412.3989 [hep-ph] (cit. on pp. 48, 89).

[128] R. D. Ball et al., *Parton distributions for the LHC Run II*, JHEP **04** (2015) 040, arXiv: 1410.8849 [hep-ph] (cit. on pp. 48, 49, 82–84, 89, 314).

[129] Sayipjamal Dulat et al., *New parton distribution functions from a global analysis of quantum chromodynamics*, Phys. Rev. D **93** (2016) 033006, arXiv: 1506.07443 [hep-ph] (cit. on pp. 48, 89, 314, 315).

[130] T. Gleisberg, Stefan Hoeche, et al., *Event generation with SHERPA 1.1*, JHEP **0902** (2009) 007, arXiv: 0811.4622 [hep-ph] (cit. on p. 50).

[131] M. Rauch, *Vector-Boson Fusion and Vector-Boson Scattering*, (2016), arXiv: 1610.08420 [hep-ph] (cit. on pp. 50, 58, 60, 62, 65–68, 95, 97, 105, 114, 150).

[132] Tanju Gleisberg and Stefan Höche, *Comix, a new matrix element generator*, JHEP **12** (2008) 039, arXiv: 0808.3674 [hep-ph] (cit. on pp. 51, 76, 83, 314).

[133] E. Bothmann et al., *Event Generation with Sherpa 2.2*, SciPost Phys. **7** (2019) 034, arXiv: 1905.09127 [hep-ph] (cit. on pp. 51, 76, 270, 311, 314).

[134] J. Alwall et al., *The automated computation of tree-level and next-to-leading order differential cross sections, and their matching to parton shower simulations*, JHEP **07** (2014) 079, arXiv: 1405.0301 [hep-ph] (cit. on pp. 51, 65, 75, 76, 78, 79, 315).

[135] B. Jäger and G. Zanderighi, *NLO corrections to electroweak and QCD production of W+W+ plus two jets in the POWHEG BOX*, Journal of High Energy Physics **2011** (2011), ISSN: 1029-8479, URL: http://dx.doi.org/10.1007/JHEP11(2011)055 (cit. on pp. 51, 65, 67, 74, 75, 82).

[136] T. Melia, P. Nason, R. Rontsch, and G. Zanderighi, W^+W^+ *plus dijet production in the POWHEGBOX*, Eur. Phys. J. C **71** (2011) 1670, arXiv: 1102.4846 [hep-ph] (cit. on pp. 51, 68, 74, 75, 82).

[137] Torbjörn Sjöstrand et al., *An Introduction to PYTHIA 8.2*, Comput. Phys. Commun. **191** (2015) 159, arXiv: 1410.3012 [hep-ph] (cit. on pp. 52, 53, 67, 75, 78, 79, 265, 269, 272, 281, 284, 315).

[138] M. Bahr et al., *Herwig++ physics and manual*, Eur. Phys. J. C **58** (2008) 639, arXiv: 0803.0883 [hep-ph] (cit. on pp. 52, 53, 67, 75, 76, 79, 265, 269, 277, 278, 314).

[139] J. Bellm et al., *Herwig 7.0/Herwig++ 3.0 release note*, Eur. Phys. J. C **76** (2016) 196, arXiv: 1512.01178 [hep-ph] (cit. on pp. 52, 53, 67, 75, 76, 79, 265, 269, 277, 278).

[140] Steffen Schumann and Frank Krauss, *A Parton shower algorithm based on Catani-Seymour dipole factorisation*, JHEP **03** (2008) 038, arXiv: 0709.1027 [hep-ph] (cit. on pp. 52, 53, 76, 83, 314).

[141] A. Ballestrero et al., *Precise predictions for same-sign W-boson scattering at the LHC*, (2018), arXiv: 1803.07943 [hep-ph] (cit. on pp. 52, 62–65, 67, 74–77, 79, 82, 87, 88, 92, 95, 97, 100, 103, 104, 107, 110, 112, 114–116, 120, 121, 289, 293).

[142] Stefan Hoeche, Frank Krauss, Steffen Schumann, and Frank Siegert, *QCD matrix elements and truncated showers*, JHEP **0905** (2009) 053, arXiv: 0903.1219 [hep-ph] (cit. on pp. 53, 76, 79, 83).

[143] Nils Lavesson and Leif Lonnblad, *Merging parton showers and matrix elements: Back to basics*, JHEP **04** (2008) 085, arXiv: 0712.2966 [hep-ph] (cit. on p. 53).

[144] S. Frixione and B. R. Webber, *Matching NLO QCD computations and parton shower simulations*, JHEP **06** (2002) 029, arXiv: hep-ph/0204244 (cit. on pp. 53, 76).

[145] P. Nason, *A new method for combining NLO QCD with shower Monte Carlo algorithms*, JHEP **11** (2004) 040, arXiv: 0409146 [hep-ph] (cit. on pp. 53, 76, 79).

[146] S. Frixione, P. Nason, and C. Oleari, *Matching NLO QCD computations with parton shower simulations: the POWHEG method*, JHEP **11** (2007) 070, arXiv: 0709.2092 [hep-ph] (cit. on pp. 53, 76, 79).

[147] Bo Andersson, Sandipan Mohanty, and Fredrik Soderberg, *The Lund fragmentation process for a multigluon string according to the area law*, Eur. Phys. J. C **21** (2001) 631, arXiv: hep-ph/0106185 (cit. on p. 54).

[148] Stefan Gieseke, Frashër Loshaj, and Patrick Kirchgaeßer, *Soft and diffractive scattering with the cluster model in Herwig*, Eur. Phys. J. C **77** (2017) 156, arXiv: 1612.04701 [hep-ph] (cit. on p. 54).

[149] S. Agostinelli et al., *GEANT4 – a simulation toolkit*, Nucl. Instrum. Meth. A **506** (2003) 250, URL: http://www.sciencedirect.com/science/article/pii/S0168900203013688 (cit. on p. 54).

[150] The ATLAS Collaboration, *MCTruthClassifier*, 2020, URL: https://gitlab.cern.ch/atlas/athena/-/tree/21.2/PhysicsAnalysis/MCTruthClassifier (cit. on p. 55).

[151] ATLAS Collaboration, *Performance of b-jet identification in the ATLAS experiment*, JINST **11** (2016) P04008, arXiv: 1512.01094 [hep-ex] (cit. on p. 55).

[152] D. L. Rainwater, R. Szalapski, and D. Zeppenfeld, *Probing color singlet exchange in Z + two jet events at the CERN LHC*, Phys. Rev. **D54** (1996) 6680, arXiv: 9605444 [hep-ph] (cit. on p. 62).

[153] ATLAS Collaboration, *Measurements of electroweak Wjj production and constraints on anomalous gauge couplings with the ATLAS detector*, Eur. Phys. J. C **77** (2017) 474, arXiv: 1703.04362 [hep-ex] (cit. on p. 62).

[154] CMS Collaboration, *Search for anomalous electroweak production of vector boson pairs in association with two jets in proton–proton collisions at 13 TeV*, Phys. Lett. B **798** (2019) 134985, arXiv: 1905.07445 [hep-ex] (cit. on pp. 62, 69, 70, 72, 185, 186, 191, 192, 197, 199, 222, 254, 259, 262).

[155] CMS Collaboration, *Measurements of production cross sections of WZ and same-sign WW boson pairs in association with two jets in proton–proton collisions at $\sqrt{s} = 13$ TeV*, Phys. Lett. B **809** (2020) 135710, arXiv: 2005.01173 [hep-ex] (cit. on pp. 63, 69, 70, 72, 73, 78, 95, 147, 148, 181, 183–186, 192, 197, 222, 224, 239, 254, 258, 259, 262).

[156] S. Todt et al., *Support note for measurement of electroweak $W^{\pm}W^{\pm}jj$ production at $\sqrt{s} = 13$ TeV*, tech. rep., CERN, 2018, URL: https://cds.cern.ch/record/2309552 (cit. on p. 63).

[157] R. Covarelli, M. Pellen, and Marco Zaro, *Vector-Boson scattering at the LHC: Unraveling the electroweak sector*, Int. J. Mod. Phys. A **36** (2021) 2130009, arXiv: 2102.10991 [hep-ph] (cit. on pp. 64, 69, 75, 89).

[158] Sally Dawson, *The effective W approximation*, Nuclear Physics B **249** (1985) 42, ISSN: 0550-3213, URL: https://www.sciencedirect.com/science/article/pii/0550321385900380 (cit. on p. 64).

[159] M.J. Duncan, G.L. Kane, and W.W. Repko, *WW physics at future colliders*, Nuclear Physics B **272** (1986) 517, ISSN: 0550-3213, URL: https://www.sciencedirect.com/science/article/pii/0550321386902348 (cit. on p. 64).

[160] R.N. Cahn and Sally Dawson, *Production of very massive Higgs bosons*, Physics Letters B **136** (1984) 196, ISSN: 0370-2693, URL: https://www.sciencedirect.com/science/article/pii/0370269384911808 (cit. on p. 64).

[161] B. Jager, C. Oleari, and D. Zeppenfeld, *Next-to-leading order QCD corrections to W+ W+ jj and W- W- jj production via weak-boson fusion*, Phys. Rev. D **80** (2009) 034022, arXiv: 0907.0580 [hep-ph] (cit. on pp. 65, 67, 74, 82, 83, 104, 105, 107).

[162] A. Denner, L. Hosekova, and S. Kallweit, *NLO QCD corrections to W+ W+ jj production in vector-boson fusion at the LHC*, Phys. Rev. D **86** (2012) 114014, arXiv: 1209.2389 [hep-ph] (cit. on pp. 65, 67, 74, 104).

[163] F. Campanario, M. Kerner, L. D. Ninh, and D. Zeppenfeld, *Next-to-leading order QCD corrections to W^+W^+ and W^-W^- production in association with two jets*, Phys. Rev. D **89** (2014) 054009, arXiv: 1311.6738 [hep-ph] (cit. on pp. 65, 68, 74, 114).

[164] J. Baglio et al., *Release Note - VBFNLO 2.7.0*, (2014), arXiv: 1404.3940 [hep-ph] (cit. on pp. 65, 68, 74).

[165] T. Figy, C. Oleari, and D. Zeppenfeld, *Next-to-leading order jet distributions for Higgs boson production via weak boson fusion*, Phys. Rev. D **68** (2003) 073005, arXiv: hep-ph/0306109 (cit. on p. 65).

[166] K. Arnold et al., *VBFNLO: A Parton level Monte Carlo for processes with electroweak bosons*, Comput. Phys. Commun. **180** (2009) 1661, arXiv: 0811.4559 [hep-ph] (cit. on pp. 65, 74).

[167] J. Baglio et al., *VBFNLO: A Parton Level Monte Carlo for Processes with Electroweak Bosons – Manual for Version 2.7.0*, (2011), arXiv: 1107.4038 [hep-ph] (cit. on pp. 65, 74, 82).

[168] Pierre Artoisenet, Rikkert Frederix, Olivier Mattelaer, and Robbert Rietkerk, *Automatic spin-entangled decays of heavy resonances in Monte Carlo simulations*, JHEP **03** (2013) 015, arXiv: 1212.3460 [hep-ph] (cit. on pp. 65, 75, 315).

[169] B. Jager, C. Oleari, and D. Zeppenfeld, *Next-to-leading order QCD corrections to W+W- production via vector-boson fusion*, JHEP **07** (2006) 015, arXiv: hep-ph/0603177 (cit. on p. 67).

[170] B. Jager, C. Oleari, and D. Zeppenfeld, *Next-to-leading order QCD corrections to Z boson pair production via vector-boson fusion*, Phys. Rev. D **73** (2006) 113006, arXiv: hep-ph/0604200 (cit. on p. 67).

[171] G. Bozzi, B. Jager, C. Oleari, and D. Zeppenfeld, *Next-to-leading order QCD corrections to W+ Z and W- Z production via vector-boson fusion*, Phys. Rev. D **75** (2007) 073004, arXiv: hep-ph/0701105 (cit. on p. 67).

[172] F. Campanario, N. Kaiser, and D. Zeppenfeld, *$W\gamma$ production in vector boson fusion at NLO in QCD*, Phys. Rev. D **89** (2014) 014009, arXiv: 1309.7259 [hep-ph] (cit. on p. 67).

[173] B. Jager and G. Zanderighi, *Electroweak W+W-jj prodution at NLO in QCD matched with parton shower in the POWHEG-BOX*, JHEP **04** (2013) 024, arXiv: 1301.1695 [hep-ph] (cit. on p. 67).

[174] B. Jäger, A. Karlberg, and G. Zanderighi, *Electroweak $ZZjj$ production in the Standard Model and beyond in the POWHEG-BOX V2*, JHEP **03** (2014) 141, arXiv: 1312.3252 [hep-ph] (cit. on p. 67).

[175] B. Jager, A. Karlberg, and J. Scheller, *Parton-shower effects in electroweak $WZjj$ production at the next-to-leading order of QCD*, Eur. Phys. J. **C79** (2019) 226, arXiv: 1812.05118 [hep-ph] (cit. on p. 67).

[176] T. Melia, K. Melnikov, R. Rontsch, and G. Zanderighi, *Next-to-leading order QCD predictions for W^+W^+jj production at the LHC*, JHEP **12** (2010) 053, arXiv: 1007.5313 [hep-ph] (cit. on pp. 68, 74, 82, 83).

[177] T. Melia, K. Melnikov, R. Rontsch, and G. Zanderighi, *NLO QCD corrections for W^+W^- pair production in association with two jets at hadron colliders*, Phys. Rev. D **83** (2011) 114043, arXiv: 1104.2327 [hep-ph] (cit. on p. 68).

[178] B. Biedermann et al., *Next-to-leading-order electroweak corrections to $pp \to W^+W^- \to$ 4 leptons at the LHC*, JHEP **06** (2016) 065, arXiv: 1605.03419 [hep-ph] (cit. on p. 68).

[179] B. Biedermann, A. Denner, and L. Hofer, *Next-to-leading-order electroweak corrections to the production of three charged leptons plus missing energy at the LHC*, JHEP **10** (2017) 043, arXiv: 1708.06938 [hep-ph] (cit. on p. 68).

[180] S. Kallweit, J. M. Lindert, S. Pozzorini, and M. Schönherr, *NLO QCD+EW predictions for $2\ell 2\nu$ diboson signatures at the LHC*, JHEP **11** (2017) 120, arXiv: 1705.00598 [hep-ph] (cit. on p. 68).

[181] B. Biedermann, A. Denner, and M. Pellen, *Large electroweak corrections to vector-boson scattering at the Large Hadron Collider*, Phys. Rev. Lett. **118** (2017) 261801, arXiv: 1611.02951 [hep-ph] (cit. on pp. 68, 74, 116).

[182] A. Denner, S. Dittmaier, P. Maierhöfer, M. Pellen, and C. Schwan, *QCD and electroweak corrections to WZ scattering at the LHC*, JHEP **06** (2019) 067, arXiv: 1904.00882 [hep-ph] (cit. on p. 68).

[183] A. Denner, R. Franken, M. Pellen, and T. Schmidt, *NLO QCD and EW corrections to vector-boson scattering into ZZ at the LHC*, JHEP **11** (2020) 110, arXiv: 2009.00411 [hep-ph] (cit. on p. 68).

[184] T. Gleisberg, Stefan. Hoeche, F. Krauss, M. Schonherr, S. Schumann, et al., *Event generation with SHERPA 1.1*, JHEP **0902** (2009) 007, arXiv: 0811.4622 [hep-ph] (cit. on pp. 68, 79).

[185] B. Biedermann et al., *Automation of NLO QCD and EW corrections with Sherpa and Recola*, Eur. Phys. J. **C77** (2017) 492, arXiv: 1704.05783 [hep-ph] (cit. on pp. 68, 76, 118, 121).

[186] M. Schönherr, *An automated subtraction of NLO EW infrared divergences*, Eur. Phys. J. C **78** (2018) 119, arXiv: 1712.07975 [hep-ph] (cit. on p. 68).

[187] CMS Collaboration, *Summaries of CMS cross section measurements*, 2021, URL: https://twiki.cern.ch/twiki/bin/view/CMSPublic/PhysicsResultsCombined (visited on 09/02/2021) (cit. on p. 69).

[188] M. Pellen, *Exploring the scattering of vector bosons at LHCb*, Phys. Rev. D **101** (2020) 013002, arXiv: 1908.06805 [hep-ph] (cit. on p. 69).

[189] CMS Collaboration, *Evidence for electroweak production of four charged leptons and two jets in proton-proton collisions at s=13TeV*, Physics Letters B **812** (2021) 135992, ISSN: 0370-2693, URL: http://dx.doi.org/10.1016/j.physletb.2020.135992 (cit. on pp. 69, 70, 72).

[190] ATLAS Collaboration, *Search for the electroweak diboson production in association with a high-mass dijet system in semileptonic final states in pp collisions at $\sqrt{s} =$ 13 TeV with the ATLAS detector*, Phys. Rev. D **100** (2019) 032007, arXiv: 1905.07714 [hep-ex] (cit. on pp. 69, 70, 72).

[191] *Search for vector boson scattering at the LHC Run 2 with CMS data in the semileptonic $l\nu qq$ final state*, tech. rep., CERN, 2021, URL: https://cds.cern.ch/record/2776799 (cit. on pp. 70, 72).

[192] ATLAS Collaboration, *Evidence for electroweak production of two jets in association with a $Z\gamma$ pair in pp collisions at $\sqrt{s} = 13$ TeV with the ATLAS detector*, Phys. Lett. B **803** (2020) 135341, arXiv: 1910.09503 [hep-ex] (cit. on pp. 70, 72).

[193] CMS Collaboration, *Measurements of production cross sections of polarized same-sign W boson pairs in association with two jets in proton–proton collisions at $\sqrt{s} = 13$ TeV*, Phys. Lett. B **812** (2021) 136018, arXiv: 2009.09429 [hep-ex] (cit. on pp. 69, 73, 147–149, 181).

[194] ATLAS Collaboration, *Measurement of the electroweak production of dijets in association with a Z-boson and distributions sensitive to vector boson fusion in proton–proton collisions at $\sqrt{s} = 8$ TeV using the ATLAS detector*, JHEP **04** (2014) 031, arXiv: 1401.7610 [hep-ex] (cit. on p. 71).

[195] ATLAS Collaboration, *Differential cross-section measurements for the electroweak production of dijets in association with a Z boson in proton–proton collisions at ATLAS*, (2020), arXiv: 2006.15458 [hep-ex] (cit. on p. 71).

[196] CMS Collaboration, *Study of vector boson scattering and search for new physics in events with two same-sign leptons and two jets*, Phys. Rev. Lett. **114** (2015) 051801, arXiv: 1410.6315 [hep-ex] (cit. on pp. 73, 76, 78, 95, 186, 206).

[197] *Prospects for the study of vector boson scattering in same sign WW and WZ interactions at the HL-LHC with the upgraded CMS detector*, (2016) (cit. on p. 73).

[198] ATLAS Collaboration, *Prospects for the measurement of the $W^{\pm}W^{\pm}$ scattering cross section and extraction of the longitudinal scattering component in pp collisions at the High-Luminosity LHC with the ATLAS Experiment*, ATL-PHYS-PUB-2018-052, 2018, URL: https://cds.cern.ch/record/2652447 (cit. on p. 73).

[199] ATLAS Collaboration, *Modelling of the vector boson scattering process $pp \to W^{\pm}W^{\pm}jj$ in Monte Carlo generators in ATLAS*, ATL-PHYS-PUB-2019-004, 2019, URL: https://cds.cern.ch/record/2655303 (cit. on pp. 74, 75, 79, 100, 103, 120, 121).

[200] ATLAS and CMS Collaborations, *Comparison of ATLAS and CMS VBS Monte Carlo simulation*, ATL-PHYS-PUB-2020-026, 2020, URL: https://cds.cern.ch/record/2737267 (cit. on pp. 74, 77, 79, 100).

[201] M. Chiesa, Ansgar Denner, Jean-Nicolas Lang, and Mathieu Pellen, *An event generator for same-sign W-boson scattering at the LHC including electroweak corrections*, Eur. Phys. J. C **79** (2019) 788, arXiv: 1906.01863 [hep-ph] (cit. on pp. 75, 118, 121).

[202] S. Actis, A. Denner, L. Hofer, A. Scharf, and S. Uccirati, *Recursive generation of one-loop amplitudes in the Standard Model*, JHEP **04** (2013) 037, arXiv: 1211.6316 [hep-ph] (cit. on p. 75).

[203] Stefano Actis et al., *RECOLA: REcursive Computation of One-Loop Amplitudes*, Comput. Phys. Commun. **214** (2017) 140, arXiv: 1605.01090 [hep-ph] (cit. on p. 75).

[204] W. Kilian, T. Ohl, and J. Reuter, *WHIZARD: Simulating Multi-Particle Processes at LHC and ILC*, Eur. Phys. J. **C71** (2011) 1742, arXiv: 0708.4233 [hep-ph] (cit. on pp. 76, 184).

[205] M. Moretti, T. Ohl, and J. Reuter, *O'Mega: An Optimizing matrix element generator*, (2001) 1981, arXiv: 0102195 [hep-ph] (cit. on pp. 76, 184).

[206] Alessandro Ballestrero, Aissa Belhouari, Giuseppe Bevilacqua, Vladimir Kashkan, and Ezio Maina, *PHANTOM: A Monte Carlo event generator for six parton final states at high energy colliders*, Comput. Phys. Commun. **180** (2009) 401, arXiv: 0801.3359 [hep-ph] (cit. on p. 76).

[207] B. Cabouat and T. Sjöstrand, *Some Dipole Shower Studies*, Eur. Phys. J. C **78** (2018) 226, arXiv: 1710.00391 [hep-ph] (cit. on pp. 76, 77).

[208] Torbjorn Sjöostrand, Stephen Mrenna, and Peter Z. Skands, *PYTHIA 6.4 Physics and Manual*, JHEP **05** (2006) 026, arXiv: hep-ph/0603175 (cit. on pp. 78, 315).

[209] Peter Skands, Stefano Carrazza, and Juan Rojo, *Tuning PYTHIA 8.1: the Monash 2013 Tune*, Eur. Phys. J. C **74** (2014) 3024, arXiv: 1404.5630 [hep-ph] (cit. on pp. 78, 114).

[210] Vardan Khachatryan et al., *Event generator tunes obtained from underlying event and multiparton scattering measurements*, Eur. Phys. J. C **76** (2016) 155, arXiv: 1512.00815 [hep-ex] (cit. on p. 78).

[211] Albert M Sirunyan et al., *Extraction and validation of a new set of CMS PYTHIA8 tunes from underlying-event measurements*, Eur. Phys. J. C **80** (2020) 4, arXiv: 1903.12179 [hep-ex] (cit. on p. 78).

[212] ATLAS Collaboration, *Measurement of the Z/γ^* boson transverse momentum distribution in pp collisions at $\sqrt{s} = 7$ TeV with the ATLAS detector*, JHEP **09** (2014) 145, arXiv: 1406.3660 [hep-ex] (cit. on pp. 79, 281).

[213] S. Höche, "Status of the Sherpa Event Generator", Multi-Boson Interactions Workshop, 2018, URL: https://indico.cern.ch/event/700961/contributions/3069895 (cit. on pp. 80, 81, 85, 118).

[214] Simone Alioli, Paolo Nason, Carlo Oleari, and Emanuele Re, *A general framework for implementing NLO calculations in shower Monte Carlo programs: the POWHEG BOX*, JHEP **06** (2010) 043, arXiv: 1002.2581 [hep-ph] (cit. on pp. 79, 82).

[215] M. Ciccolini, A. Denner, and S. Dittmaier, *Electroweak and QCD corrections to Higgs production via vector-boson fusion at the LHC*, Phys. Rev. D **77** (2008) 013002, arXiv: 0710.4749 [hep-ph] (cit. on p. 82).

[216] M.-A. Pleier A. Johnson, "PowhegBox Signal sample generation of LHE files" (cit. on pp. 82, 266).

[217] S. Todt and C. Bittrich et al, *Repository for helper tools developed by local working group*, 2020, URL: https://gitlab.cern.ch/atlas-germany-dresden-vbs-group/otherTools (visited on 03/20/2020) (cit. on pp. 84, 272).

[218] ATLAS Collaboration, *ATLAS Pythia 8 tunes to 7 TeV data*, ATL-PHYS-PUB-2014-021, 2014, URL: https://cds.cern.ch/record/1966419 (cit. on pp. 85, 91, 286, 315).

[219] Giulia Gonella, "Observation and Measurement of the Electroweak $W^{\pm}W^{\pm}jj$ Process in Proton-Proton Collisions at $\sqrt{s} = 13$ TeV with the ATLAS Detector", Presented 25 Oct 2019, 2019, URL: https://cds.cern.ch/record/2714995 (cit. on pp. 87, 124, 128, 130, 136, 163, 165, 235, 325–331, 339).

[220] Chilufya Mwewa, "Observation of the electroweak production of two same-sign W bosons in proton-proton collisions with the ATLAS detector", Presented 2020, 2019, URL: https://cds.cern.ch/record/2730081 (cit. on pp. 87, 130, 340, 342).

[221] ATLAS Collaboration, *HEPData entry of the Observation of Electroweak Production of a Same-Sign W Boson Pair in Association with Two Jets in pp Collisions at $\sqrt{s} = 13$ TeV with the ATLAS Detector*, 2021, URL: https://www.hepdata.net/record/ins1738841 (visited on 10/07/2021) (cit. on p. 87).

[222] Jon Butterworth et al., *PDF4LHC recommendations for LHC Run II*, J. Phys. G **43** (2016) 023001, arXiv: 1510.03865 [hep-ph] (cit. on p. 90).

[223] ATLAS Collaboration, *Measurement of the Z/γ^* boson transverse momentum distribution in pp collisions at $\sqrt{s} = 7$ TeV with the ATLAS detector.*, (2014), URL: https://cds.cern.ch/record/1696339 (cit. on p. 91).

[224] ATLAS Collaboration, *Recommendations for MC tunes: systematic uncertainties and non-pQCD corrections*, 2021, URL: https://twiki.cern.ch/twiki/bin/view/AtlasProtected/MCTuningRecommendations#Prescription_for_AZNLO_tune (visited on 11/23/2021) (cit. on pp. 91, 281).

[225] S. Todt, C. Bittrich, P. Kirchgaesser, A. Papaefstathiou, and S. Plätzer, *Soft QCD Effects in VBS/VBF Topologies*, (2021), arXiv: 2110.01623 [hep-ph] (cit. on p. 112).

[226] MadGraph, *What are the default dynamic factorization and renormalization scales in MadEvent?*, 2021, URL: https://cp3.irmp.ucl.ac.be/projects/madgraph/wiki/FAQ-General-13 (visited on 12/06/2021) (cit. on pp. 113, 369).

[227] MadGraph5$_a$*MC@NLOLaunchpad* and S. Todt, *Dynamical scale settings in the same-sign WW process*, 2022, URL: https://answers.launchpad.net/mg5amcnlo/+question/684056 (visited on 07/07/2022) (cit. on pp. 113, 198).

[228] M. Pellen, "Private communication", 2017 (cit. on pp. 115, 117, 163).

[229] C. Bittrich, "Evidence for Scattering of Electroweak Gauge Bosons in the $W^{\pm}Z$ Channel with the ATLAS Detector at the Large Hadron Collider", Presented 14 Jul 2020, 2020, URL: http://cds.cern.ch/record/2719126 (cit. on p. 120).

[230] C. Bittrich S. Todt, "Overview of VBF/VBS setups", Internal ATLAS Meeting, 2019, URL: https://indico.cern.ch/event/837597/contributions/3513129/attachments/1889343/3115433/2019-08-01-VBF_VBS_setups.pdf (cit. on p. 120).

[231] ATLAS Collaboration, *Jet-Based Event Cleaning*, 2022, URL: https://twiki.cern.ch/twiki/bin/view/AtlasProtected/HowToCleanJets2016#IsBadBatMan_Event_Flag_and_EMEC. (visited on 01/18/2022) (cit. on pp. 127, 128).

[232] C. Bittrich et al., *Support note for measurement of electroweak $W^{\pm}W^{\pm}jj$ production at $\sqrt{s} = 13$ TeV*, tech. rep., CERN, 2018, URL: https://cds.cern.ch/record/2309552 (cit. on pp. 130, 137, 141, 159, 163, 166, 170, 173, 175, 177, 178, 235, 332, 333, 335, 336, 338, 339, 341, 345, 347–349, 361).

[233] Emily Marie Duffield, "Observation of the electroweak production of two W bosons with the same electric charge in association with two jets in pp collisions at $\sqrt{s} = 13$ TeV with the ATLAS detector", 2019, URL: https://cds.cern.ch/record/2687964 (cit. on pp. 130, 136, 333–335, 337, 338).

[234] John Butler et al., *Search for Triboson $W\pm W$ $W\pm\rightarrow\pm$ $\pm$ Production and Anomalous Quartic Gauge Couplings in 8 TeV ATLAS Data*, tech. rep., CERN, 2015, URL: https://cds.cern.ch/record/2030159 (cit. on p. 144).

[235] F. Iltzsche, "Observation of Electroweak Same-Charge $W^{\pm}W^{\pm}jj$ Production at $\sqrt{s} =$ 13 TeV with the ATLAS Detector at the LHC", Presented 27 Sep 2019, 2019, URL: https://cds.cern.ch/record/2697175 (cit. on pp. 144, 150, 153, 157, 163, 170, 174, 176).

[236] G. D. Cowan, *Statistical data analysis*, Oxford Univ. Press, 1998, ISBN: 978-0-198-50155-8, URL: https://cds.cern.ch/record/358560 (cit. on pp. 150, 178).

[237] F. James, *Statistical Methods in Experimental Physics; 2nd ed.* World Scientific, 2006, ISBN: 978-9-812-56795-6, URL: https://cds.cern.ch/record/1019859 (cit. on pp. 150, 178).

[238] Todt S. et al Iltzsche F. Herrmann T., *Repository for statistical analysis framework*, 2022, URL: https://gitlab.cern.ch/atlas-germany-dresden-vbs-group/StatisticTool (visited on 04/21/2022) (cit. on p. 150).

[239] Kyle Cranmer, George Lewis, Lorenzo Moneta, Akira Shibata, and Wouter Verkerke, *HistFactory: A tool for creating statistical models for use with RooFit and RooStats*, tech. rep. CERN-OPEN-2012-016, New York U., 2012, URL: https://cds.cern.ch/record/1456844 (cit. on pp. 150, 162, 168).

[240] W. Verkerke and D. Kirkby, *The RooFit toolkit for data modeling*, 2003, arXiv: physics/0306116 [physics.data-an] (cit. on p. 150).

[241] P. Azzi et al., *Report from Working Group 1: Standard Model Physics at the HL-LHC and HE-LHC*, CERN Yellow Rep. Monogr. **7** (2019) 1, ed. by Andrea Dainese et al., arXiv: 1902.04070 [hep-ph] (cit. on p. 180).

[242] Max Vincent Stange, "Data-driven estimation of the non-prompt background in same charged $W^{\pm}W^{\pm}$ scattering within the ATLAS experiment", Presented 05 Nov 2020, 2020, URL: http://cds.cern.ch/record/2746597 (cit. on p. 181).

[243] CMS Collaboration, *A search for $WW\gamma$ and $WZ\gamma$ production and constraints on anomalous quartic gauge couplings in pp collisions at $\sqrt{s} = 8$ TeV*, Phys. Rev. D **90** (2014) 032008, arXiv: 1404.4619 [hep-ex] (cit. on pp. 184–186, 222, 262).

[244] *Search for exclusive $\gamma\gamma \rightarrow WW$ and $\gamma\gamma \rightarrow ZZ$ production in final states with jets and forward protons*, tech. rep., CERN, 2022, URL: https://cds.cern.ch/record/2803716 (cit. on pp. 184–186, 191).

[245] Celine Degrande et al., "Monte Carlo tools for studies of non-standard electroweak gauge boson interactions in multi-boson processes: A Snowmass White Paper", *Community Summer Study 2013: Snowmass on the Mississippi*, 2013, arXiv: 1309.7890 [hep-ph] (cit. on pp. 184, 185, 187–190, 194, 255–258).

[246] ATLAS Collaboration, *Measurements of $W^{\pm}Z$ production cross sections in pp collisions at $\sqrt{s} = 8$ TeV with the ATLAS detector and limits on anomalous gauge boson self-couplings*, Phys. Rev. D **93** (2016) 092004, arXiv: 1603.02151 [hep-ex] (cit. on pp. 184–186, 196, 199, 227).

[247] CMS Collaboration, *Evidence for electroweak production of four charged leptons and two jets in proton–proton collisions at $\sqrt{s} = 13$ TeV*, Phys. Lett. B **812** (2021) 135992, arXiv: 2008.07013 [hep-ex] (cit. on pp. 185, 186, 197, 199, 222, 262).

[248] ATLAS Collaboration, *Search for anomalous electroweak production of WW/WZ in association with a high-mass dijet system in pp collisions at $\sqrt{s} = 8$ TeV with the ATLAS detector*, Phys. Rev. D **95** (2017) 032001, arXiv: 1609.05122 [hep-ex] (cit. on pp. 184–186, 191, 193, 199).

[249] *EW Wgamma plus 2 jets at 13 TeV full run 2*, tech. rep., CERN, 2022, URL: https://cds.cern.ch/record/2809554 (cit. on pp. 185, 186, 197, 199, 222, 262).

[250] ATLAS Collaboration, *Studies of $Z\gamma$ production in association with a high-mass dijet system in pp collisions at $\sqrt{s} = 8$ TeV with the ATLAS detector*, JHEP **07** (2017) 107, arXiv: 1705.01966 [hep-ex] (cit. on pp. 184–186, 191–193, 196, 219, 222, 227, 262).

[251] CMS Collaboration, *Search for the production of $W^{\pm} W^{\pm} W^{\mp}$ events at $\sqrt{s} = 13$ TeV*, Phys. Rev. D **100** (2019) 012004, arXiv: 1905.04246 [hep-ex] (cit. on pp. 185, 186, 197, 222, 262).

[252] ATLAS Collaboration, *Study of $WW\gamma$ and $WZ\gamma$ production in pp collisions at $\sqrt{s} = 8$ TeV and search for anomalous quartic gauge couplings with the ATLAS experiment*, Eur. Phys. J. C **77** (2017) 646, arXiv: 1707.05597 [hep-ex] (cit. on pp. 184–186, 192, 196, 219, 227).

[253] CMS Collaboration, *Measurements of the $pp \to W^{\pm}\gamma\gamma$ and $pp \to Z\gamma\gamma$ cross sections at $\sqrt{s} = 13$ TeV and limits on anomalous quartic gauge couplings*, (2021), arXiv: 2105.12780 [hep-ex] (cit. on pp. 185, 186, 197, 222, 262).

[254] ATLAS Collaboration, *Evidence of $W\gamma\gamma$ Production in pp Collisions at $\sqrt{s} = 8$ TeV and Limits on Anomalous Quartic Gauge Couplings with the ATLAS Detector*, Phys. Rev. Lett. **115** (2015) 031802, arXiv: 1503.03243 [hep-ex] (cit. on pp. 184–186, 191, 192, 196, 219).

[255] ATLAS Collaboration, *Measurements of $Z\gamma$ and $Z\gamma\gamma$ production in pp collisions at $\sqrt{s} = 8$ TeV with the ATLAS detector*, Phys. Rev. D **93** (2016) 112002, arXiv: 1604.05232 [hep-ex] (cit. on pp. 184–186, 191–193, 196, 219, 227).

[256] J. Reuter, Wolfgang Kilian, and Marco Sekulla, *Simplified Models for New Physics in Vector Boson Scattering - Input for Snowmass 2013*, (2013), arXiv: 1307.8170 [hep-ph] (cit. on p. 184).

[257] A. Alboteanu, W. Kilian, and J. Reuter, *Resonances and Unitarity in Weak Boson Scattering at the LHC*, JHEP **0811** (2008) 010, arXiv: 0806.4145 [hep-ph] (cit. on p. 184).

[258] CMS Collaboration, *Evidence for exclusive $\gamma\gamma \to W^+W^-$ production and constraints on anomalous quartic gauge couplings in pp collisions at $\sqrt{s} = 7$ and 8 TeV*, JHEP **08** (2016) 119, arXiv: 1604.04464 [hep-ex] (cit. on p. 186).

[259] ATLAS Collaboration, *Measurement of exclusive $\gamma\gamma \to W^+W^-$ production and search for exclusive Higgs boson production in pp collisions at $\sqrt{s} = 8$ TeV using the ATLAS detector*, Phys. Rev. D **94** (2016) 032011, arXiv: 1607.03745 [hep-ex] (cit. on pp. 186, 196).

[260] Raquel Gomez-Ambrosio, *Studies of Dimension-Six EFT effects in Vector Boson Scattering*, Eur. Phys. J. C **79** (2019) 389, arXiv: 1809.04189 [hep-ph] (cit. on pp. 186, 248).

[261] Riccardo Bellan et al., *A sensitivity study of VBS and diboson WW to dimension-6 EFT operators at the LHC*, JHEP **05** (2022) 039, arXiv: 2108.03199 [hep-ph] (cit. on pp. 186, 248).

[262] CMS Collaboration, *Measurement of electroweak WZ boson production and search for new physics in $WZ+$ two jets events in pp collisions at $\sqrt{s} = 13$ TeV*, Phys. Lett. B **795** (2019) 281, arXiv: 1901.04060 [hep-ex] (cit. on p. 186).

[263] C. Bittrich, *Summary Plots*, 2022, URL: https://gitlab.cern.ch/atlas-physics/sm/StandardModelTools_SummaryPlots/SummaryPlots (visited on 07/07/2022) (cit. on pp. 187–190, 255–258).

[264] Max Neukum, "Combination of Limits on Anomalous Quartic Gauge Couplings in the leptonic same-sign WW and ZZ Vector Boson Scattering at 13 TeV with the CMS Experiment", MA thesis: Karlsruhe Institute of Technology (KIT), 2019 (cit. on pp. 192, 260).

[265] HEPData, *HEPData: Repository for publication-related High-Energy Physics data*, 2022, URL: https://www.hepdata.net/ (visited on 07/21/2022) (cit. on pp. 192, 260).

[266] *aTGC combination ATLAS+CMS using 7 TeV data*, (2016) (cit. on p. 192).

[267] CMS Collaboration, *Measurements of the $pp \to ZZ$ production cross section and the $Z \to 4\ell$ branching fraction, and constraints on anomalous triple gauge couplings at $\sqrt{s} = 13$ TeV*, Eur. Phys. J. C **78** (2018) 165, arXiv: 1709.08601 [hep-ex] (cit. on p. 194).

[268] Stefanie Todt, *Auxiliary Material on the Simulation of EFT Signal Samples With the Amplitude Decomposition Approach*, 2022, URL: https://doi.org/10.5281/zenodo.7098059 (cit. on pp. 194, 200, 202, 203, 209, 218, 219, 259).

[269] Olivier Mattelaer, *On the maximal use of Monte Carlo samples: re-weighting events at NLO accuracy*, Eur. Phys. J. C **76** (2016) 674, arXiv: 1607.00763 [hep-ph] (cit. on p. 197).

[270] S.Todt, *MadGraph reweighting validation with aQGCs in same-sign $W^\pm W^\pm$ VBS process*, Presented 07.02.2018 at the VBSCan mid-term meeting, 2018, URL: https://indico.cern.ch/event/689505/contributions/2888133/attachments/1596591/2529164/2018-02-07_MadGraphReweighting_CardsComparison.pdf (cit. on p. 197).

[271] Heiko Menzel, "Validierung von Umgewichtungen simulierter Verteilungen des Prozesses $W^\pm W^\pm \to W^\pm W^\pm$", Presented 2012, 2012, URL: https://cds.cern.ch/record/2815406 (cit. on p. 197).

[272] FeynRules, *AnomalousGaugeCoupling: SM-LS012-LM017-LT012-Ind5-UFO-June19*, 2022, URL: http://feynrules.irmp.ucl.ac.be/attachment/wiki/AnomalousGaugeCoupling/SM_LS012_LM017_LT012_Ind5_UFO_June19.tar.gz (visited on 06/30/2022) (cit. on p. 198).

[273] MadGraph5$_a$*MC@NLOLaunchpad* and S. Todt, *Simulation of EFT samples with amplitude decomposition*, 2022, URL: https://answers.launchpad.net/mg5amcnlo/+question/683400 (visited on 07/07/2022) (cit. on pp. 198, 214, 368).

[274] Stefanie Todt, "Investigation of mass reconstruction techniques for resonances in the scattering of $W^\pm W^\pm \to W^\pm W^\pm$ at the LHC", Presented 04 Jun 2015, 2015, URL: https://cds.cern.ch/record/2000966 (cit. on pp. 200, 201, 222, 259).

[275] Z. Yifan, *VBS ZZjj 2l2 status report*, 2022, URL: https://indico.cern.ch/event/1183197/contributions/4970996/attachments/2484251/4265341/VBSZZjj_llvv_SMEW_FINAL.pdf (cit. on pp. 214, 219).

[276] D. Sampsonidou, *WZjj: Decomposition Closure tests*, 2019, URL: https://indico.cern.ch/event/842562/contributions/3536339/attachments/1895984/3128013/aQGCs_WZjj_22_8_DSampsonidou.pdf (cit. on p. 214).

[277] E. Soldatov, *Zy→ EWK full Run 2: aQGC request*, 2019, URL: https://indico.cern.ch/event/868693/contributions/3661859/attachments/1957097/3251310/aqgc_reint_05122019.pdf (cit. on pp. 214, 216).

[278] H. Mildner, *WW+WZ EFT Combination: Towards global EFT fits of SM precision measurements*, 2019, URL: https://indico.cern.ch/event/863326/contributions/3637958/attachments/1944896/3254237/hmildner_WW_WZ_EFTcombi_update.pdf (cit. on pp. 214, 219).

[279] S. Todt, *EFT Signal Sample Modeling in $W^\pm W^\pm jj$*, 2019, URL: https://indico.cern.ch/event/822754/contributions/3558562/attachments/1907441/3150929/ssWW_Dim8MCstudies.pdf (cit. on p. 216).

[280] et. al. J.F. Laporte J. Manjarres Ramos, *FLIT*, 2013, URL: https://twiki.cern.ch/twiki/bin/view/AtlasProtected/FLIT (cit. on p. 225).

[281] G. Cowan, K. Cranmer, E. Gross, and O. Vitells, *Asymptotic formulae for likelihood-based tests of new physics*, Eur. Phys. J. C **71** (2011) 1554, arXiv: 1007.1727 [physics.data-an] (cit. on pp. 225, 229), Erratum: Eur. Phys. J. C **73** (2013) 2501.

[282] G. Gounaris et al., "Triple gauge boson couplings", *AGS / RHIC Users Annual Meeting*, 1996 525, arXiv: hep-ph/9601233 (cit. on p. 248).

[283] CMS Collaboration, *Search for anomalous triple gauge couplings in WW and WZ production in lepton + jet events in proton–proton collisions at* $\sqrt{s} = 13$ *TeV*, JHEP **12** (2019) 062, arXiv: 1907.08354 [hep-ex] (cit. on pp. 248–253, 385).

[284] ATLAS Collaboration, *Recommendations for MC tunes: systematic uncertainties and non-pQCD corrections*, 2021, URL: https://twiki.cern.ch/twiki/bin/view/AtlasProtected/MCTuningRecommendations#Recommended_setup (visited on 11/23/2021) (cit. on p. 286).

[285] PYTHIA 8, *PYTHIA 8 Manual: Automated Variations of Shower Parameters for Uncertainty Bands*, 2021, URL: https://pythia.org/manuals/pythia8235/Welcome.html (visited on 11/23/2021) (cit. on p. 286).

[286] Andy Buckley et al., *LHAPDF6: parton density access in the LHC precision era*, The European Physical Journal C **75** (2015), ISSN: 1434-6052, URL: http://dx.doi.org/10.1140/epjc/s10052-015-3318-8 (cit. on p. 287).

[287] Fabio Cascioli, Philipp Maierhofer, and Stefano Pozzorini, *Scattering Amplitudes with Open Loops*, Phys. Rev. Lett. **108** (2012) 111601, arXiv: 1111.5206 [hep-ph] (cit. on p. 314).

[288] Stefan Höche, Frank Krauss, M. Schönherr, and Frank Siegert, *QCD matrix elements + parton showers: The NLO case*, JHEP **04** (2013) 027, arXiv: 1207.5030 [hep-ph] (cit. on pp. 314, 319).

[289] Peter Zeiler Skands, *Tuning Monte Carlo Generators: The Perugia Tunes*, Phys. Rev. D **82** (2010) 074018, arXiv: 1005.3457 [hep-ph] (cit. on p. 315).

[290] Jean-Francois Arguin et al., *Support Note for Electron ID: charge mis-identification*, tech. rep. ATL-COM-PHYS-2017-1014, CERN, 2017, URL: https://cds.cern.ch/record/2273365 (cit. on p. 326).

[291] ATLAS Collaboration, *Same Sign* $W^{\pm}W^{\pm}$ *Production and Limits on Anomalous Quartic Gauge Couplings*, tech. rep. ATL-COM-PHYS-2013-990, CERN, 2013, URL: https://cds.cern.ch/record/1561731 (cit. on p. 333).